Optimization of the Influence of Longitudinal and Lateral Non-Uniformity on the Performance of an Electromagnetic Calorimeter

Dissertation zur Erlangung des Doktorgrades (Dr. rer. nat.)

im Fachgebiet Experimentalphysik
Prof. Dr. Kai-Thomas Brinkmann
II. Physikalisches Institut
Justus-Liebig-Universität Gießen

vorgelegt von

M. Sc. Stefan Diehl
aus Hungen - Inheiden

Gießen, 2015

Contents

Zusammenfassung

Elektromagnetische Kalorimeter (EMC) gehören zu den Schlüsselkomponenten aktueller und zukünftiger Experimente der Hadronen- und Teilchenphysik, da sie die einzige Möglichkeit zur präzisen Energiemessung von Photonen und anderen elektromagnetischen Proben darstellen. Der PANDA Detektor, welcher zur Untersuchung der Wechselwirkung eines gekühlten Anti-Protonenstrahls mit einem ruhenden Target am Hochenergie-Speicherring (HESR) der geplanten Einrichtung für Anti-Protonen- und Ionen-Forschung (FAIR) in Darmstadt eingesetzt werden soll, wird zwei verschiedenen Kalorimeter enthalten. Im Target-Spektrometer, welches die Region um den Interaktionspunkt abdeckt, kommt ein auf anorganischen Szintillationskristallen aus Bleiwolframat basierendes Kalorimeter zum Einsatz. Die Kristalle werden hierbei in Form eines Fasses mit Endkappen auf beiden Seiten um den Interaktionspunkt angeordnet. Dieser Kalorimetertyp ermöglicht ein kompaktes Design in Kombination mit einer exzellenten Energieauflösung. Der Bereich der kleinsten Vorwärtswinkel des Aufbaus wird durch ein separates Vorwärts-Spektrometer abgedeckt. In diesem Teil des Detektors wird ein Sampling - Kalorimeter mit sogenannten Shashlyk - Modulen zum Einsatz kommen. Eine besondere Herausforderung für beide Kalorimetertypen ergibt sich durch die benötigte Abdeckung des dynamischen Energiebereichs von 10 MeV bis zu 15 GeV. Neben der Art des Kalorimeters wird die Performance der beiden Detektoren auch durch die laterale und longitudinale Homogenität des Energieansprechverhaltens maßgeblich bestimmt. In dieser Arbeit soll daher der Einfluss von Inhomogenitätseffekten auf die Energieauflösung der Kalorimeter diskutiert werden. Weiterhin werden Ansätze zur Minimierung der Nicht-Linearität und zur Verbesserung der Performance beider Kalorimeter vorgestellt. Im Fall des Shashlyk - Kalorimeters konnte eine Verbesserung der lateralen Inhomogenität sowie eine Verringerung der Lichtabschwächung in den Modulen durch ein neues, verbessertes Design der Shashlyk - Module erreicht werden. Durch diese Optimierungen konnte die laterale Inhomogenität von mehr als $\pm$ 17 % auf weniger als $\pm$ 2 % reduziert werden. Zur weiteren Optimierung der Energieauflösung wurden verschiedene Algorithmen zur Extraktion der Energieinformation aus der Signalform verglichen. Zusammengenommen konnte durch alle Optimierungen eine signifikante Verbesserung der Energie- und Ortsauflösung im Energiebereich unterhalb von 1 GeV erreicht werden. Die Energieauflöung für den kompletten untersuchten Energiebereich von 50 MeV bis 12 GeV kann durch die Parametrisierung $\sigma/E = 3.54\ \%/\sqrt{E/\mathrm{GeV}} \oplus 1.34\ \%$ beschrieben werden. Für die Zeitauflösung wurden Werte im Bereich von $100\ \mathrm{ps}/\sqrt{E/\mathrm{GeV}}$ erzielt. Mit diesen Ergebnissen konnte erstmals gezeigt werden, dass das Shashlyk - Kalorimeter des PANDA Detektors in der Lage ist, Photonen im Energiebereich unterhalb von 1 GeV, zumindest bis zu Minimalenergien von 50 MeV, mit einer ausreichenden Energieauflösung nachzuweisen. Um die experimentellen Resultate zu reproduzieren und den Einfluss verschiedener Aspekte auf die Energieauflösung zu untersuchen, wurde der Prototyp des

Shashlyk - Kalorimeters in GEANT4 implementiert. Basierend auf der durch GEANT4 simulierten Energiedeposition wurden schließlich verschiedene Modelle zur Reproduktion der experimentellen Energieauflösung verglichen. Bei der Optimierung des Ansprechverhaltens der Fasskomponente des elektromagnetischen Kalorimeters des Target-Spektrometers muss ein besonderes Augenmerk auf den Energiebereich unterhalb von 1 GeV gelegt werden, da ein Großteil der nachzuweisenden Photonen in diesem Bereich erwartet wird. Einer der kritischen Parameter bei niedrigen Photonenenergien ist das Untergrundrauschen der Elektronik. Für die aktuelle Version des ASIC, welcher für die Auslese der beiden auf die Rückseite der Bleiwolframat-Kristalle geklebten Lawinen-Photo-Dioden (APD) gedacht ist, konnte erstmals gezeigt werden, dass eine Standardabweichung des elektronischen Rauschen von unter 1 MeV erreicht werden kann. Der Vergleich verschiedener Methoden zur Extraktion der Energieinformation aus der Signalform hat gezeigt, dass ein Fit der Signalform im Vergleich zu einer einfachen Suche des Maximums eine Verbesserung der Energieauflösung im Energiebereich unterhalb von 100 MeV bewirkt. Ein ähnlicher Effekt kann auch durch eine Integration der Signalform über einen beschränkten Bereich um das Extremum des Pulses erreicht werden. Ein weiterer Schwerpunkt dieser Arbeit liegt auf der Untersuchung des Einflusses der Nichtlinearität der Lichtsammlung auf die Energieauflösung. Diese Nicht-Linearität wird durch die Fokussierung des Szintillationslichtes an der abgeschrägten Seitenfläche des Kristalls ausgelöst und bewirkt eine Positionsabhängigkeit des Energie-Ansprechverhaltens, welches letztendlich zu einer nicht-linearen Energierekonstruktion und zu einer Verschlechterung der Energieauflösung führt. Es konnte gezeigt werden, dass ein Aufrauen der am stärksten abgeschrägten Seite des Kristalls mit einer mittleren Rauigkeit von 0.3 μm zu eine Reduktion der Nicht-Linearität der Lichtsammlung von Typ 2 Kristallen von ursprünglich etwa 30 % bis auf unter 5 % bewirkt. Basierend auf den aufgerauten Kristallen, welche als eine 3 $\times$ 3 Untereinheit in den aktuellen Prototypen des Fassteils des EMC eingebaut wurden, konnte der Einfluss der Uniformität der Lichtsammlung auf die Energieauflösung erstmals im Energiebereich unterhalb von 1 GeV untersucht werden. Es konnte experimentell gezeigt werden, dass die Reduktion der Nicht-Linearität durch das Aufrauen der Seitenfläche die relative Energieauflösung im Energiebereich oberhalb von 200 MeV verbessert, während die Energieauflösung für Energien zwischen 50 MeV und 200 MeV in etwa gleich bleibt und im Energiebereich unterhalb von 50 MeV nur eine geringe Verschlechterung beobachtet werden kann. Insbesondere der konstante Term der Parametrisierung der Energieauflösung konnte von mehr als 2 % für komplett polierte Kristalle auf 0.5 % für Kristalle mit einer aufgerauten Seitenfläche reduziert werden. Um ein besseres Verständnis des Einflusses der Nicht-Linearität der Lichtsammlung auf die Energieauflösung zu erhalten und um eine Eichung des Prototypen mit kosmischen Myonen zu ermöglichen, wurde ein detailliertes Modell des aktuellen Prototypen inklusive des Szintillationsprozesses und der Lichtsammlung in GEANT4 implementiert. Mit einem speziell entwickelten Modell zur Berechnung der Ansprechverhaltens der Kristalle basierend auf der Energiedeposition, der Nichtlinearität der Lichtsammlung und weiteren empirischen Größen konnte eine gute Übereinstimmung der simulierten Werte mit den experimentellen Resultaten erzielt werden.

Abstract

Electromagnetic calorimeters (EMCs) are one of the key components of present and future hadron and particle physics experiments, since they provide the only possibility for an accurate and efficient energy measurement of electromagnetic probes. The PANDA detector which is planned to be operated at the High Energy Storage Ring (HESR) of the future Facility for Anti-Proton and Ion Research (FAIR) at Darmstadt to study the interaction of cooled anti-protons with a fixed target will apply two different calorimeter concepts. In the target spectrometer, covering the region around the interaction point, a calorimeter based on inorganic scintillation crystals made of lead-tungstate ($PbWO_4$), arranged as a barrel with caps on both sides will be installed to achieve a compact design and an excellent energy resolution. The most forward angles of the setup will be covered by a separate forward spectrometer. In this part, a shashlyk type sampling calorimeter will be implemented. A special advantage for both calorimeters is the coverage of the large dynamic range from 10 MeV up to 15 GeV. Despite the different concepts, the performance of both detectors can be limited by a lateral and longitudinal inhomogeneity of the energy response. This work will discuss the influence of such inhomogeneities on the resolutions of the calorimeters and present concepts to minimize their impact and to improve the performance. For the shashlyk EMC a significant improvement of the lateral homogeneity and a reduction of the light attenuation variation in the modules has been achieved by a new, improved design of the shashlyk modules. With these improvements the lateral inhomogeneity could be reduced from up to $\pm$ 17 % to less than $\pm$ 2 %. To further optimize the energy resolution, different feature extraction and calibration methods are compared. As a result of all optimizations, a significant improvement of the energy and position resolution has been achieved in the energy range below 1 GeV. The energy resolution for the complete energy range from 50 MeV to 12 GeV can be parametrized by $\sigma/E = 3.54\ \%/\sqrt{E/\mathrm{GeV}} \oplus 1.34\ \%$ and a time resolution close to 100 ps$/\sqrt{E/\mathrm{GeV}}$ has been achieved. Altogether it has been proven for the first time that the shashlyk calorimeter of the PANDA detector provides a sufficient performance for the detection of low energetic photons at least down to an energy of 50 MeV. To reproduce the experimental results and to study the impact of different aspects on the energy resolution, the shashlyk EMC prototype has been implemented in GEANT4 and different models for the reproduction of the experimental energy resolution have been compared. For the performance of the barrel part of the target EMC, a special focus has to be set to the energy region below 1 GeV, since most of the detected photons will be in this range. A first crucial parameter for this energy region is the electronic noise. For the current version of the front-end electronics ASIC (APFEL), which is foreseen for the readout of the Avalanche Photo Diodes (APDs) glued to the rear face of the lead tungstate crystals, it has been shown for the first time that a standard deviation of the electronic noise of less than 1 MeV can be achieved. The comparison of different feature

extraction methods showed that a fit of the pulse-shape can improve the energy resolution at energies below 100 MeV compared to a simple peak sensing feature extraction. A similar behavior can be observed for an integration of a limited region of the pulse. The main focus of this work is set on the investigation of the influence of the non-uniformity in light collection on the energy resolution. This non-uniformity is introduced by a focusing of the scintillation light due to the tapered side faces of the crystals and causes a position dependence of the energy response, which finally leads to a non-linear response and a deterioration of the energy resolution. It has been shown that a de-polishing of the most tapered lateral side face to an average roughness of 0.3 μm reduces the non-uniformity in light collection of type 2 crystals from originally around 30 % down to a level of less than 5 %. Based on these de-polished crystals, implemented as a 3 $\times$ 3 sub-array in the current barrel EMC prototype, the influence of the light collection uniformity on the energy resolution for energies below 1 GeV has been investigated for the first time. It has been proven experimentally that a reduction of the non-uniformity by the de-polishing procedure improves the relative energy resolution for energies above 200 MeV, while the energy resolution between 50 MeV and 200 MeV stays approximately at the same level and only a slight deterioration is expected for energies below 50 MeV. Especially the constant term of the parametrization of the energy resolution has been reduced from more than 2 % to 0.5 % in case of de-polished crystals. To provide a more detailed study of the influence of the non-uniformity on the energy resolution and to obtain a calibration of the prototype with cosmic muons, a detailed model of the current barrel EMC prototype, including the scintillation process and the light collection has been implemented in GEANT4. With a special model, calculating the response of the crystals based on the energy deposition distribution, including the non-uniformity and other empirical values, a good agreement with the experimental results has been achieved.

Preface

Electromagnetic calorimeters are essential components of most of the currently existing high energy physics detectors, since they provide the only possibility for an effective detection of photons and an accurate energy measurement for electromagnetic probes in general. Therefore, the information obtained by electromagnetic calorimeters gives a significant contribution to the reconstruction of the invariant mass of particles and excited states produced by collisions in high energy physics detectors. The requirements introduced by the envisaged physics goals make it necessary to design the calorimeter in a way that its energy, position and time resolution are below a certain limit, determined by the simulation of the envisaged physics channels. To reach this objective on the one side a proper selection of the calorimeter type and its components is mandatory, but on the other side also the longitudinal and lateral uniformity of the energy response are some of the most critical parameters which have to be optimized to gain an optimal performance of the electromagnetic calorimeter for all incident angles and over the complete energy range. This work will present the results, obtained with two close to final prototypes of the barrel part of the target electromagnetic calorimeter and of the forward shashlyk calorimeter of the PANDA detector which will be built at the future Facility for Antiproton and Ion Research (FAIR) in Darmstadt, Germany, to show the influence of different kinds of non-uniformity on the performance of the prototypes in comparison to GEANT4 simulations. To optimize the performance of the prototypes different feature extraction and calibration methods will be compared. In addition, different concepts for the optimization of the uniformity will be presented and discussed on the basis of test beam results and simulations.

The first chapter of this work starts with a short motivation of hadron and particle physics research in general and an overview over the planed FAIR facility and the PANDA detector. In the second part of the chapter, an introduction to the physics and to different concepts of electromagnetic calorimeters is given. Finally the PANDA electromagnetic calorimeters, which are the basis of this work, are described in detail. The second chapter gives an overview over the MAMI accelerator facility in Mainz, which has been used for the tests of different prototypes of the PANDA electromagnetic calorimeters in the energy range below 1 GeV. In addition, the design of the different prototypes will be presented. The third and fourth chapter show the performance of the prototypes and compare different feature extraction and calibration methods. Furthermore, concepts for the reduction of the lateral and longitudinal non-uniformity of the prototypes will be presented and their influence on the energy response will be shown based on experimental results and GEANT4 simulations. The fifth chapter will give a detailed discussion of the different factors influencing the performance of the prototypes, with a special focus on the deterioration of the energy response by longitudinal and lateral non-uniformity effects. Finally, an outlook on future concepts of calorimetry will be given.

Chapter 1

Motivation and introduction

Since the time of the old Greeks, mankind is thinking about the smallest constituents of matter and their interactions. In the last century a significant progress has been made in this field. Starting with the discovery of the electron and the postulation of a first atomic model with negatively charged electrons homogeneously distributed in the positively charged atom by J.J. Thomson in 1897. Continuing with the famous scattering experiment of α particles on a thin gold foil by Ernest Rutherford in 1911, leading to the theory of a small positively charged nucleus, surrounded by a significantly larger cloud of negative electrons [ER11]. While the shells of the atoms could be soon better understood by the theories of Niels Bohr in 1912, it took until 1932, when James Chadwick discovered the neutron [JC32] to get a closer understanding of the nucleus as a combination of positive protons and neutrally charged neutrons. A few years later in 1935 H. Yukawa developed the model of exchange forces, explaining the stability of the positively charged nucleus by a strong force between the nucleons [LB86]. As an exchange particle of this force, the pion was proposed and finally discovered in the cosmic radiation by Cecil Powell in 1947 [OP47]. Based on these discoveries the Quantum Electrodynamics (QED) was developed in the 1940s and 1950s as a relativistic quantum theory for charged particles by J. Schwinger, R. Feynman and S. Tomonaga. In the following years new particle accelerator were built, enabling the study of interaction effects between the particles with higher and higher energies, resulting in the discovery of more and more new particles. Based on all these discoveries the quark model was proposed by M. Gell-Mann in 1964 [GM64]. With this model, particles like protons, neutrons and mesons were no longer elementary particles, they could now be described as a composition of quarks. Particles with this property were from there on called hadrons. Depending on the composition of the hadron they are divided into mesons, representing a quark-antiquark pair ($q\bar{q}$), and baryons, which are composed of three quarks (qqq). To describe the interaction of quarks the Quantum Chromodynamics (QCD) was developed. All investigations made up to now are combined in the Standard Model (SM) of particle physics, which was already developed in the early 1970s and describes the elementary particles and their interactions. The Standard Model divides the elementary particles in two types, quarks and leptons and groups them in three generations according to their mass and stability. The first generation includes the lightest and most stable quarks while the particles of the following generations are heavier and less stable. Each of the quarks has a corresponding antiparticle with an inverted charge and parity. In a similar way, the leptons are grouped in three generations. Fig. 1.1 shows

the arrangement of the different quarks and leptons in the three generations as well as their mass and electrical charge. All particles shown are Fermions and have a spin of 1/2.

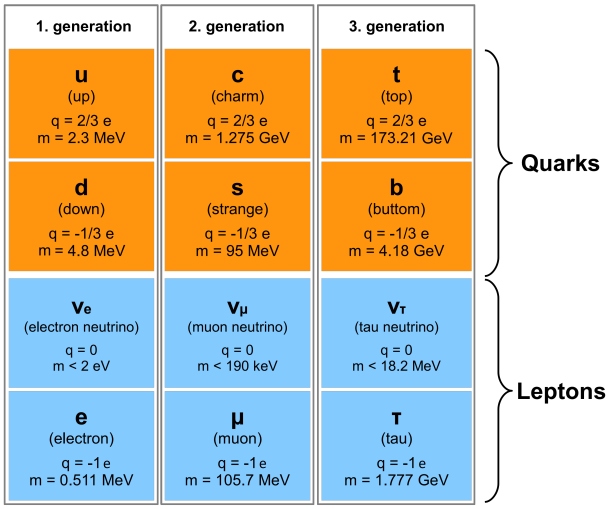

Figure 1.1: Arrangement of the different quarks and leptons in the three generations of the Standard Model. For each particle the rest mass and the electrical charge are given according to [PDG14].

The particles of the Standard Model interact via four fundamental forces, the electromagnetic force, the strong and weak nuclear force and the gravitational force, which is not part of the Standard Model. Electromagnetic and gravitational forces are well known from the daily life, they couple to the electrical charge and the mass of particles and have in principle an infinite range, with a strength behaving like $1/r^2$ with the distance r. In contrast to this, the strong and weak nuclear forces can act only over very short ranges, which makes them only important for the description of nuclear and sub-nuclear processes. The fundamental forces interact between the particles by exchanging bosons. Table 1.1 shows an overview over the fundamental forces, their strength and range and the corresponding exchange bosons.

force	exchange boson	rel. strength	range
electromagnetic	photon	1/137	∞
strong	gluon (8 $\times$)	1	10^{-15} m
weak	vector bosons (W^+, W^-, Z^0)	10^{-6}	10^{-18} m
gravitation	not part of SM	$6 \cdot 10^{-39}$	∞

Table 1.1: Fundamental forces and their exchange bosons. [CRN14]

The weak nuclear force is responsible for the transformation of particles into other particles, for example in a radioactive decay, while the interaction between quarks is initiated by the strong force which couples to the color charge of the quarks. Each quark has one of the three possible color charges (red, blue, green), while anti quarks have a corresponding anti-color. The gluons as the exchange bosons of the strong force carry a combination of a color and an anti-color. For bound objects like hadrons, the color of the constituents has to be distributed in a way that the mixture of the colors is white. The exact interaction of the quarks within a hadronic system can be described by QCD calculations, which are predicting a wide range

of possible excitations and configurations of quarks and gluons. In the past, a lot of these excitations have been found with different detector setups and accelerators in accordance to theoretical calculations based on Standard Model QCD. Nevertheless, there are still a lot of open questions, like the existence of more rare excitations and special configurations like glueballs (systems of bound gluons), hybrids (mesons with an excited gluon) and multiquark states (systems consisting of more than three valence quarks), which are predicted by QCD but mostly not observed yet. To study such complex hadronic systems and excitations, in a first step accelerators with a high luminosity and an excellent beam quality are needed to get a sufficient production yield for the predicted states. After producing these states and systems they will decay after a very short lifetime. Due to this, the only way to proof their existence is to detect the decay products and to reconstruct mass, momentum and quantum numbers of the initial excitation or compound system based on the theoretical predictions. For this purpose a fast, efficient and precise detector system, consisting of several sub-detectors is needed to detect all decay products. In particular for the reconstruction of mass and momentum the most critical parameter is given by the energy measurement. For electromagnetically interacting particles, an Electromagnetic Calorimeter (EMC) is the only way to measure the energy with a high precision. In addition to this, the position reconstruction of the EMC is the only way to determine the emission angle of photons with a high efficiency. Since most of the decay chains contain one or more electromagnetic interacting particles, the EMC is crucial for the performance of the complete detector system, which makes it necessary to develop individually optimized systems for each high energy physics detector setup.

1.1 The FAIR facility

The future international Facility for Antiproton and Ion Research (FAIR) which is presently under construction at the site of the already existing GSI, Helmholtzzentrum für Schwerionenforschung Darmstadt (GSI) will provide an accelerator with a high luminosity and an excellent beam quality. With these key features it will enable new experiments in the fields of hadron and nuclear physics as well as atomic and plasma physics. Fig. 1.2 shows a schematic view of the new FAIR accelerators (red) and the existing GSI accelerators and buildings (blue). The new facility will use the existing accelerators of GSI like the linear accelerator UNILAC and the SIS-18 synchrotron as pre-accelerators to fill the new main synchrotron SIS-100/300 with protons or heavy ions. In addition a new linear proton accelerator (p-LINAC) will be constructed to optimize the filling of SIS 18 with protons. The main accelerator SIS 100/300 will consist of two independent synchrotrons with a circumference of 1100 m each. According to their names the two synchrotrons will have a magnetic rigidity of 100 Tm and 300 Tm [BKS05]. The repetition rate of 1 Hz and the ramp speed of the magnets of 4 Tesla per second for the SIS 100 will result in extremely high beam intensities of pulsed uranium ion (q=28+) beams with energies of 1 GeV/u and proton beams with energies up to 29 GeV [BKS05]. The SIS 300 synchrotron will be used to produce ion beams with energies up to 35-45 GeV/u. As a special feature, the combination of both rings can be used to provide a proton or ion beam for up to four experiments in parallel [BKS05]. The beams from the new synchrotrons will be used for several experiments spread over the four main research directions of FAIR: APPA (Atomic, Plasma Physics and Applications), CBM (Compressed Baryonic Matter), NUSTAR (Nuclear Structure, Astrophysics and Reactions) and PANDA (Antiproton Annihilation at Darmstadt) [HHG06, FAIRexp].

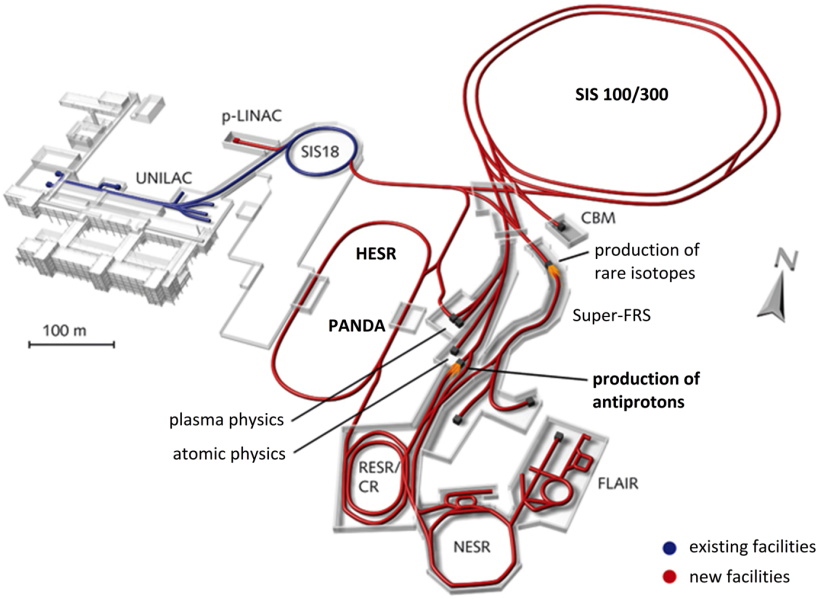

Figure 1.2: Schematic view of the new FAIR accelerators (red) and the existing GSI facility (blue) [GSI14]. The PANDA detector will be placed at the High Energy Storage Ring (HESR).

The focus of the following part will be on the accelerators needed to supply the PANDA experiment with a cooled anti-proton beam. For this purpose the high energetic protons from SIS 100 are guided onto an anti-proton production target. The produced anti-protons are collected in the collector ring, in which they are focused and cooled by a stochastic cooling. After this, they are finally injected into the High Energy Storage Ring (HESR), which is shown in figure 1.3.

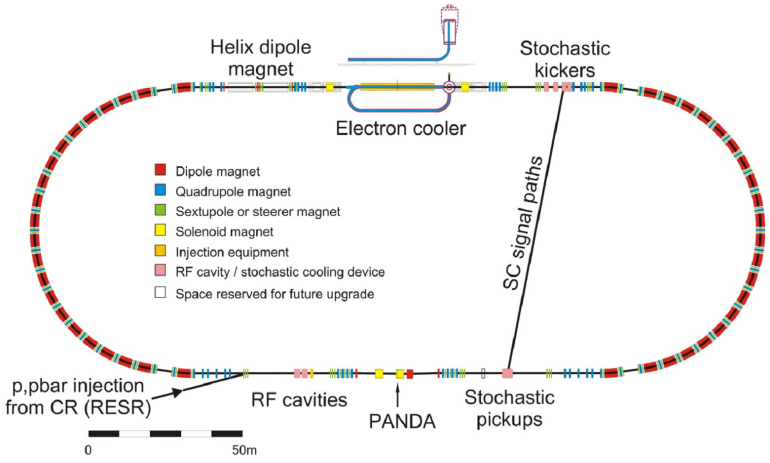

Figure 1.3: Schematic view of the HESR with the magnets and the setups for anti proton cooling [RM11]. With the dipole magnets a beam rigidity of up to 50 Tm can be achieved. The PANDA detector will be positioned in the center of one straight section of the ring, while the electron cooler and the stochastic kickers will be positioned on the opposite side of the ring.

The anti-protons stored in this ring will have momenta between 1.55 GeV/c and 15 GeV/c [RM11]. To guarantee a constant beam quality and to compensate the interaction of the anti-protons with each other and with the target in the detector, an active beam cooling is required. This will be achieved by a combination of a high energy electron cooling and a stochastic cooling of the anti-protons in the ring [RM11]. The HESR can be operated in two configurations. In a high resolution mode, a momentum resolution of $\sigma_p/p < 2 \cdot 10^{-5}$ can be achieved for anti proton momenta between 1.5 GeV/c and 9 GeV/c at a Luminosity of $2 \cdot 10^{31}$ cm^{-2}s^{-1}. In contrast to this the luminosity can be increased up to $2 \cdot 10^{32}$ cm^{-2}s^{-1} in the high luminosity mode deteriorating the momentum resolution to $\sigma_p/p \approx 10^{-4}$ at the same time [RM11]. In this mode, the complete momentum range up to 15 GeV/c will be accessible.

1.2 The PANDA experiment

The PANDA detector will use the cooled anti-proton beam of the HESR, which will collide with a fixed target of liquid hydrogen or a solid target of heavy nuclei inside the detector. In these interactions a large variety of excited states and exotic hadronic systems can be produced. To study these systems the detector has to fulfill a series of requirements to get the optimal resolution for the invariant mass, momentum and vertex reconstruction. The first part of this section will focus on a selection of physics topics, which are envisaged to be studied with the PANDA detector. Based on the requirements from this part, the second part of the section will show the setup of the envisaged PANDA detector.

1.2.1 The physics program of the PANDA detector

The physics program of the PANDA detector focuses on the investigation of the hadron structure and the properties of the strong interaction. The first main pillar of the physics program is the hadron spectroscopy. In this field especially the charmonium, D meson and baryon spectroscopy will be of interest. In addition, the PANDA detector will be used to search for gluonic excitations and to study further QDC dynamics [EP14]. The second pillar of research will be the investigation of the nuclear structure. In this field especially time-like form factors of the proton, transition distribution amplitudes and parton distributions will be investigated [EP14]. In addition to this PANDA will investigate the properties of hadrons in matter and search for hypernuclei [EP14]. The following part will give an overview over some selected physics topics. A more detailed description of all physics cases can be found in the "Physics Performance Report for: PANDA" [PPR09].

Hadron Spectroscopy

The PANDA detector in combination with the cooled anti-proton beam from the HESR opens up new perspectives for hadron spectroscopy. While in e^+e^- colliders only states with $J^{PC} = 1^{--}$ can be directly produced due to the quantum number conservation for the virtual photon, $p\bar{p}$ collisions can form states with all quantum numbers directly. In addition, resonance scans can be performed with the HESR, during which the production yield is scanned with a well defined anti-proton energy. In these scans, the resolution is only

limited by the momentum spread of the cooled anti-proton beam, which can be as low as $\sigma_p/p < 2 \cdot 10^{-5}$ in the high resolution mode. Due to this advantage a large variety of hadronic states shown in fig. 1.4 can be accessed with the PANDA detector.

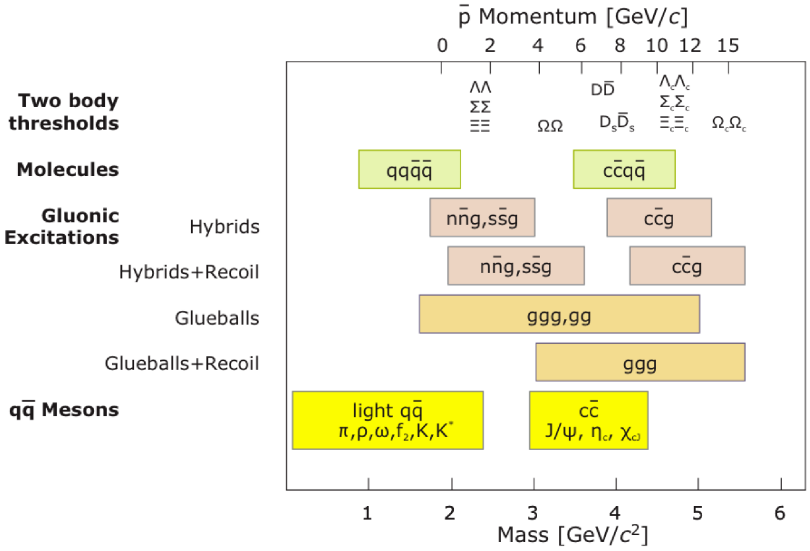

Figure 1.4: Overview over already discovered and predicted hadronic objects in the mass and momentum range which will be accessible with PANDA [VM13].

While the momentum range below 2 GeV/c was already investigated with $p\bar{p}$ collisions at the Low Energy Antiproton Ring (LEAR) at CERN in the past, PANDA will enable the study of the energy range between 1.5 GeV/c and 15 GeV/c with $p\bar{p}$ annihilation for the first time. The investigation of the predicted QCD bound states like charmonium-, D-meson- and baryon-states will contribute significantly to the understanding of QCD [PPR09].

Especially in the field of **D meson spectroscopy** there are still a lot of open questions. Since the discovery of new open charm mesons at BELLE, CLEO and BaBar there is a growing interest in the characterization of these charmed mesons of which some do not even fit into the quark model predictions for heavy-light systems [PPR09]. For the D and D_s mesons, LHCb has recently published new results [LHCb14-1, LHCb14-2], but the width of the D_s meson has still a large uncertainty, which can only be improved with a high precision experiment like PANDA, which will show a mass resolution down to around 100 keV for a resonance mass scan [EP14].

In addition the **charmonium spectrum** shown in figure 1.5 offers a large variety of research topics. In the last decade more charmonium states than expected have been discovered with experiments like BES III and BELLE II, including also states which can not be described by the present theories and models, like the X(3872) which is very narrow and shows an isospin violating decay [EP14]. Although its quantum numbers are known from LHCb, an exact measurement of the width is needed to really understand its origin. Simulations show that the mass resolution of PANDA for this state will be twenty times better than at the present B factories [LGR13]. Besides these precision measurements of already discovered states, there are also a few states which have been predicted but not yet discovered. One of these is the h'_c ($n = 2, {}^1P_1$) state which is a candidate for a test of the flavor independence of the

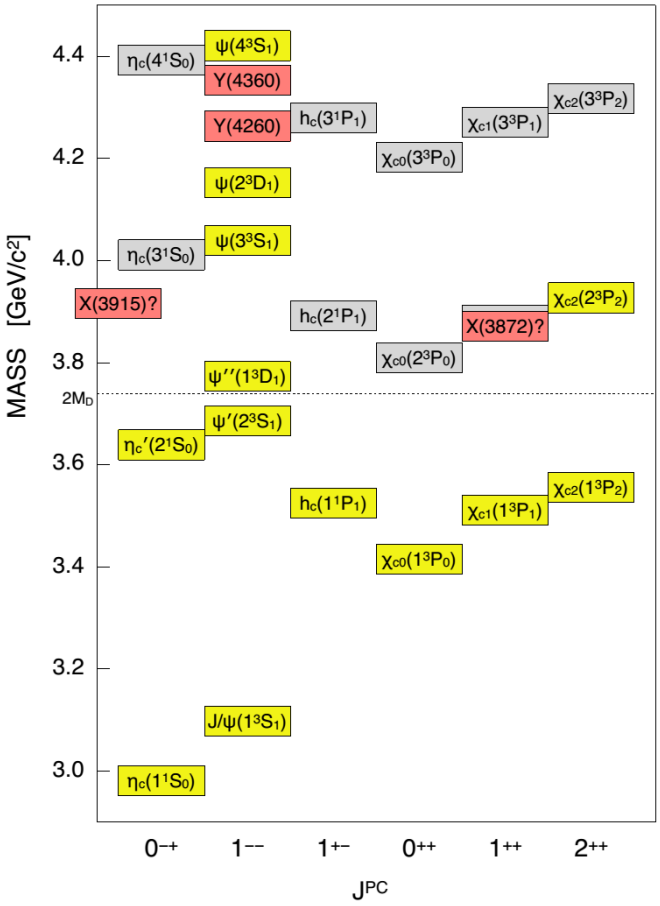

Figure 1.5: The charmonium mass spectrum with all discovered and predicted states up to 2012 as a function of the spin parity J^{PC} [RM12]. The yellow states are predicted and already discovered. The gray states are predicted but not yet discovered and the red states are discovered but have not been predicted. The dashed line represents the mass limit of the open charm ($D\bar{D}$) threshold.

quark-antiquark potential [LGR13]. Due to its quantum numbers ($J^{PC} = 0^{-+}$) it can not be observed in B decays, because the factorization limit forbids a decay like $0^{-+} \rightarrow 0^{-+}1^{+-}$ [LGR13]. However, its ground state $h_c(n = 1)$ has already been observed in the decay $\psi' \rightarrow h_c\ \pi^0$ [LGR13]. Since the isospin violating nature of this decay is also true for the decay of the resonances $\psi(4040)$ or $\psi(4160)$ in which the h'_c could be produced, a small branching fraction has to be expected [LGR13]. Therefore, PANDA with its high luminosities is an excellent opportunity to discover this state. Another state which is due to its small width of 8.3 MeV [BGS05] much more promising for the study of the flavor independence of the quark-antiquark potential is the ${}_3F^4$ charmonium state. This state has not yet been observed, because it is suppressed in radiative decays at BES III and in B meson decays at BELLE II, due to the blocking of the angular barrier, which suppresses the transition from L=3 to the L=0 ground state by a factor 2L+1=7 [LGR13]. In contrast to this, the production of high-L-states is not suppressed in proton anti-proton collision, which makes PANDA to an excellent candidate for the search of this state. In addition to these examples, there are a

lot more states in the charmonium spectrum which can be discovered or better characterized with PANDA.

Another focus of PANDA will be the search for **exotic states**. Since gluons are the exchange particles of the strong interaction, they carry color charge in form of a color and an anti-color. Due to this property, they are able to couple on particles which also carry color charge. In the normal case, if gluons are only seen as exchange bosons of the strong force, the coupling partners would be three quarks or a quark and an anti-quark, resulting in normal baryons and mesons. In addition to this, the theory of the strong interaction allows the gluons to behave like principal components of particles, which leads to hybrids consisting of a quark, an anti-quark and an excited gluon but also to pure "glueballs" consisting of two or more excited gluons. An easy way to identify such exotic states are their quantum numbers. Due to the additional degrees of freedom carried by the gluons, states containing gluons as principle components can have spin-exotic quantum numbers like $J^{PC} = 0^{--}, 0^{+-}, 1^{-+}, 2^{+-}$, which are not allowed for normal mesonic states consisting of a quark and an anti-quark [DB05]. For gluonic states with non exotic quantum numbers it is possible to compare their properties with model predictions or lattice QDC calculations and to search for an overpopulation of the meson spectrum [DB05]. Figure 1.6 gives an overview over the predicted glueball and hybrid states in comparison to the experimental charmonium spectrum.

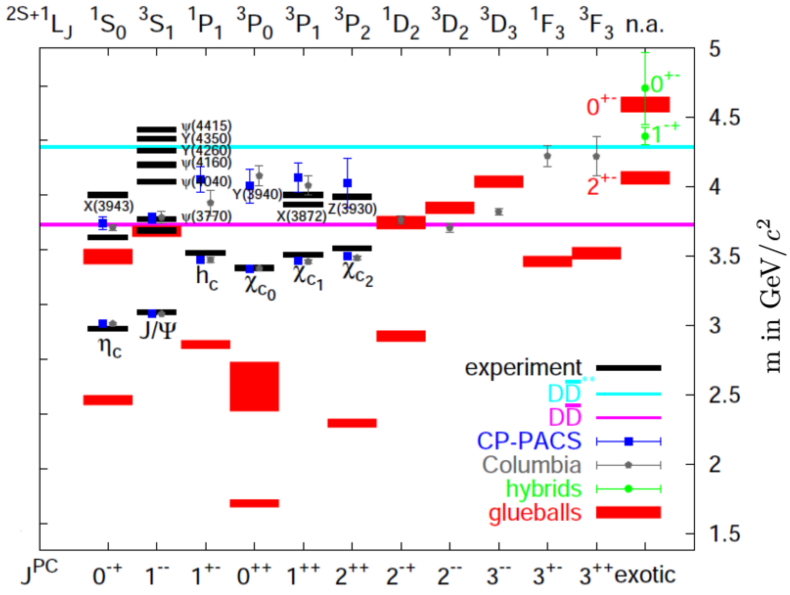

Figure 1.6: Charmonium mass spectrum with the predicted glueballs (red) and hybrids (green) as a function of the spin quantum numbers for a mass range from 1.5 GeV/c^2 up to 5 GeV/c^2. The solid lines indicate the $D\bar{D}$ and $D\bar{D}^{**}$ thresholds. For comparison the experimentally discovered charmonium states and states predicted by lattice QDC (CP-PACS and Columbia) are shown [BKM05].

The lattice QCD predicts a large variety of around 15 **glueballs** with different quantum numbers and masses in the energy range accessible with PANDA. Especially the mass of these objects is of great interest for the understanding of the mass generation of strongly interacting particles, because gluons themselves are massless and the mass of the glueballs is therefore only generated by the strong interaction [VM13]. Calculations with pure SU(3)

gauge theory predict the mass range of the glueballs between 1.7 GeV/c^2 and 5 GeV/c^2 [CAD05]. However, a significant amount of glueballs is predicted to have masses between 3 GeV/c^2 and 5 GeV/c^2 [CAD05], a mass region which makes the identification much easier, because there are much less meson states which in addition are predicted to be significantly narrower than the ones in the light-quark sector [VM13]. With the PANDA detector it will be possible for the first time to do a systematic search of the predicted glueball states.

First results, indicating the existence of **hybrids** have been obtained with anti-proton annihilation experiments. The $\pi_1(1400)$ and the $\pi_1(1600)$ with the exotic quantum numbers $J^{PC} = 1^{-+}$ have been identified with the crystal barrel experiment at the Low Energy Antiproton Ring (LEAR) in a $p\bar{p}$-annihilation at rest with significant statistics [AAA98, JR01]. For PANDA especially charmonium hybrids are of interest, because they are predicted for the same mass region like the glueballs between 3 and 5 GeV/c^2, where an identification should be easily possible. A promising candidate for a $[c\bar{c}g]$ hybrid state is the Y(4260). The production cross section of this state can be estimated to be $\sigma(\bar{p}p \rightarrow y(4260)) = 1.9 \pm 0.2nb$ [LGR13]. In the high resolution mode of the HESR this corresponds to 16400 events which will be seen with PANDA per day [LGR13]. However, this state with the quantum numbers of $J^{PC} = 1^{--}$ has not been observed yet at other experiments. One reason could be the significantly reduced cross sections for the $e^+e^- \rightarrow Y(4260)$ production at BES III and for the production from initial state radiation at BELLE II [LGR13]. According to [LGR13] it would take for example more than 8 years of data taking to see only 30000 events with a Y(4260) at BELLE II.

In addition to the investigation of the mesonic and exotic states described in the last sections, also a deeper understanding of the **baryon spectrum** is a primary goal of the PANDA experiment. The investigation of the missing elements of the baryon spectrum is a key element for the understanding of the non-perturbative QCD and for the verification of quark model predictions. For this reason several studies have been performed in the past at already existing electron accelerators, focusing on baryons consisting of light quarks. In contrast to this the region of heavier baryons, containing strange and charm quarks is rarely investigated, which opens up a large discovery potential for PANDA [UW11]. Especially exited S=-2 and S=-3 baryons in the strange baryon sector and the pair production of charmed baryons are topics of interest for PANDA [UW11].

Nuclear structure investigations

In addition to the hadron spectroscopy, PANDA is also well suited for nuclear structure investigations. An important method to obtain structural information of the nucleon is given by the real and virtual Compton-scattering of photons on the nucleus. Especially the **inclusive deep-inelastic scattering** can be used to study quark and anti quark distributions in the nucleon via a measurement of the forward virtual Compton amplitude [FRS03]. With the anti-protons from the HESR it will be possible to study the crossed-channel Compton scattering of the exclusive $\bar{p}$p annihilation into two photons [FRS03]. With the planed luminosity of $2 \cdot 10^{32}\text{cm}^{-2}\text{s}^{-1}$ for the HESR, a few thousand of this events can be expected in PANDA per month for $\sqrt{s}$=3.2 GeV [FRS03]. It has been shown that this process can be well described with the model of Generalized Parton Distributions (GPDs) for large s, $|t|$ and $|u| \sim s$ values [FRS03]. Due to this a measurement of the differential cross sections of the Compton scattering in the crossed-channel and in the related exclusive annihilation channels with different

particles, like a vector or a scalar meson or a lepton pair in the final state can be compared with theoretical calculations based on GPDs, which will provide a deeper understanding of the annihilation process and its description with Quantum Chromodynamics (QCD) and quark models [PANp14, PPR09].

Another property of interest for the investigation of the nuclear structure is the **time-like form factor of the proton**. The electromagnetic form factors of hadrons are used to describe their internal structure. The form factors can be expressed as a function of the four momentum transfer[1] $q^2 = \omega^2 - \vec{q}^2$ and are differentiated based on this variable into two regions, the space like ($q^2 < 0$) and the time like ($q^2 > 0$) region. The space like form factor can be accessed via electron scattering and has been extensively studies in theory and various experiments especially at Jefferson Laboratory (USA) during the last decades [MKJ00, AP10, CFP07]. In contrast to this, the time like form factor of the proton, which can be accessed by measuring the cross section of the proton anti-proton annihilation into an electron positron pair $\bar{p} + p \rightarrow e^+ + e^-$ has only been accurately studied in the low Q^2 region down to the threshold [SMB10, PANp14]. For higher values of Q^2 up to 15 GeV^2 the only existing data has been obtained by the E760 and the E835 experiment at Fermilab showing a limited statistics, due to which a separate measurement of the electric $|G_E|$ and magnetic $|G_M|$ form factor was not possible [PANp14, TAA93, MA99]. The PANDA experiment will enable the study of the time like proton form factor in the complete momentum range from the kinematic threshold of $q^2 = 4m_p^2c^2$ up to 22 GeV$^2/c^2$ [PPR09]. Compared to E760 and E835 PANDA will provide an significantly improved statistics and angular coverage which will enable the separate measurement of $|G_E|$ and $|G_M|$ for the first time [PPR09, SMB10]. Exploiting the process $\bar{p}p \rightarrow e^+e^-\pi^0$ will also enable the investigation of the pion cloud in the nucleus [PPR09].

Modifications of hadrons in nuclear matter

Besides the study of anti-proton proton collisions PANDA can also be used for the study of anti-proton nucleus collisions by replacing the frozen hydrogen cluster jet target by a solid atomic wire or fiber target made of carbon (^{12}C) or other materials. A special focus of these investigations is the modification of the rest mass and lifetime of hadrons in nuclear matter, due to the partial restoration of chiral symmetry in a nuclear medium [PPR09, STT07]. For mesons containing light quarks (i.e. π, ω, K) already a lot of intensive studies have been performed at experiments like Crystal Barrel/TAPS at ELSA, Crystal Ball at MAMI and Hades at GSI [VM10]. With PANDA it will be possible to extend these investigations up to hadrons containing charm quarks for the first time [PB12]. Figure 1.7 shows the measured mass splitting for π and K mesons and the theoretically predicted mass split for the heavier D meson. In addition to the investigation of the D meson mass splitting especially the measurement of the J/ψ nucleon dissociation cross section as well as the study of the behavior of anti-baryons, hyperons and anti-hyperons in nuclei are topics of great interest [PB12, PBS11]. A special requirement of these measurements in addition to a good resolution of the electromagnetic calorimeter is a high radiation resistance of the electromagnetic calorimeter and the inner tracking detectors due to the high proton and neutron background caused by the nuclear targets [PPR09].

[1] With the energy transfer ω and the three momentum transfer $\vec{q}$.

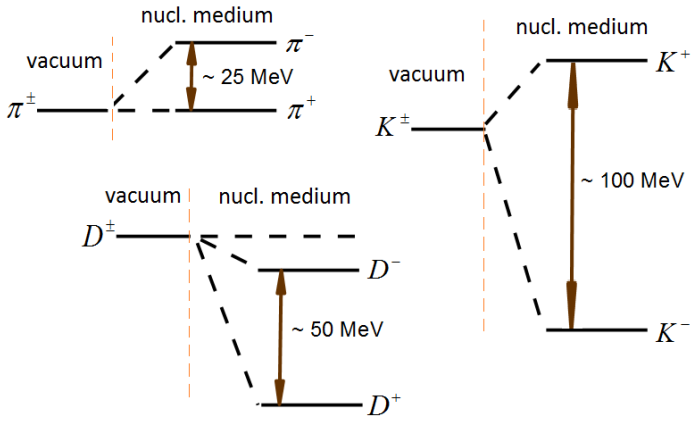

Figure 1.7: Modification of the invariant mass of mesons in a nuclear medium due to the partial restoration of chiral symmetry. While the splitting of the π and K mass have been already measured, the value for the D meson is based on theoretical calculations and varies between around 50 MeV and 100 MeV depending on the theoretical model. Data taken from [PB12, PANp14].

Hypernuclar Physics

Conventional atomic nuclei consist of protons and neutrons, which themselves consist of up- and down- quarks. If one or more of these light quarks of a nucleon are replaced by a strange quark, a new degree of freedom called strangeness is introduced and the baryon is called hyperon. Examples for light hyperons are the Lambda hyperon ($\Lambda = \text{uds}$), the Sigma hyperons (i.e. $\Sigma^+ = \text{uus}$), the Xi hyperons (i.e. $\Xi^0 = \text{uss}$) and the Omega hyperon (i.e. $\Omega^- = \text{sss}$) with masses between 1.1 and 1.7 GeV/c^2 [PDG14]. The lifetime of these systems is typically in the order of 10^{-10}s which is long enough to become bound in the nucleus [PDG14, ABP12]. If one or more nuclei of a nucleus are replaced by a hyperon, the resulting system consisting of the core of the remaining nucleus and the hyperon(s) is called hypernucleus. The investigation of such systems can provide a deeper understanding of the nucleus as many body system and of the forces acting in it [ABP12]. In addition to this it will enable the investigation of the behavior of strange baryons in nuclear matter [ASL14, ABP12].

The existence of the lightest hypernuclei has already been discovered between 1947 and 1965 in experiments investigating the interactions of cosmic rays [ABP12]. Nevertheless, there are only a few double Λ-hyperons like the ${}^{6}_{\Lambda\Lambda}He$ known up to today [JKA13]. The PANDA detector in combination with the high quality and high intensity anti-proton beam of the HESR can be used to study those systems with high statistics. The production has to be performed in two steps (see figure 1.8). In a first step, the anti-proton beam from the HESR will be used to produce low momentum Ξ hyperons within an internal target (i.e. ^{12}C) at threshold in the reactions $\bar{p} + p \rightarrow \Xi^- + \bar{\Xi}^+$ or $\bar{p} + n \rightarrow \Xi^- + \bar{\Xi}^0$ followed by a re-scattering of the Ξ^- within the target. The anti-hyperons produced in this reaction can be used as a trigger for the reaction. If the Ξ hyperons, which have left the first target, are then stopped in a special external absorber target made of ${}^{9}Be$, ${}^{10,11}B$ or ${}^{12,13}C$, they will undergo an atomic transition and finally convert in two Λ hyperons in the reaction $\Xi^- p \rightarrow \Lambda\Lambda$ with a proton from the secondary target [ABP12, PPR09, ASL13].

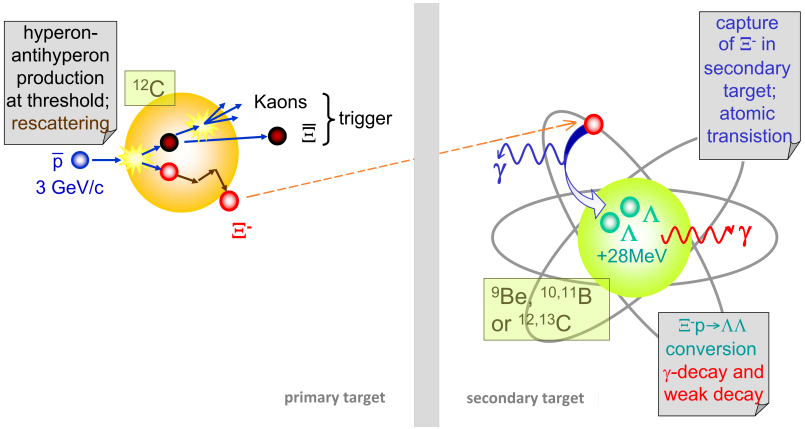

Figure 1.8: Production of double Λ hypernuclei in two steps. In a first step, the anti-proton beam from the HESR will be used to produce Ξ hyperons within an internal target followed by a re-scattering of the Ξ^- within the target. In a second step, the Ξ hyperons are stopped in a special external absorber target, where they undergo an atomic transition and finally convert in two Λ hyperons. Picture modified from [PPR09].

Performing high-precision gamma-ray spectroscopy allows to gain information about these double Λ hypernuclei. For this purpose the backward end cap of the electromagnetic calorimeter and the micro-vertex detector will be replaced by a high-purity germanium detector array [ASL13].

1.2.2 The setup of the PANDA detector

The physics program described in the last section can only be realized with a specially optimized detector setup. A common requirement of most of the physics topics is in addition to the high energy- and spatial- resolution a nearly 4π coverage of the solid angle. In addition a high radiation resistance against photons, but also against protons and slow neutrons produced in spallation processes during experiments with nuclear targets is required for all detector components [TPR05]. Another very important requirement for nearly all physics topics is an excellent and highly efficient detection of photons and lepton pairs, since most of the decay channels contain one or more photons or leptons in the final state [TPR05]. For this purpose the implementation of a highly-segmented electromagnetic calorimeter with a low energy threshold for detection and energy measurement of photons, electrons and positrons over the complete dynamic range from a few MeV up to a few GeV is mandatory not only for event reconstruction but also for background reduction [TPR05]. For the energy measurement of muons also an outer muon detector with a high stopping power is required. For hadron spectroscopy, especially for charmonium physics and the search for exotics, in addition to the already announced requirements a good Kaon identification and a good vertex reconstruction for charged Kaons and other charged particles are needed over the complete dynamic range [TPR05]. The particle identification can be realized with Cherenkov detectors, while for the tracking and vertex reconstruction inner tracking detectors and a micro vertex detector have to be implemented. For the momentum reconstruction of charged particles also a magnetic field in the region of the inner tracking detectors is required.

Since PANDA will be a fixed target experiment with a large boost of the produced particles in forward direction, an asymmetric detector setup with a target spectrometer and an extended forward spectrometer is needed. Figure 1.9 shows a schematic view of the planed PANDA detector with the two spectrometer parts.

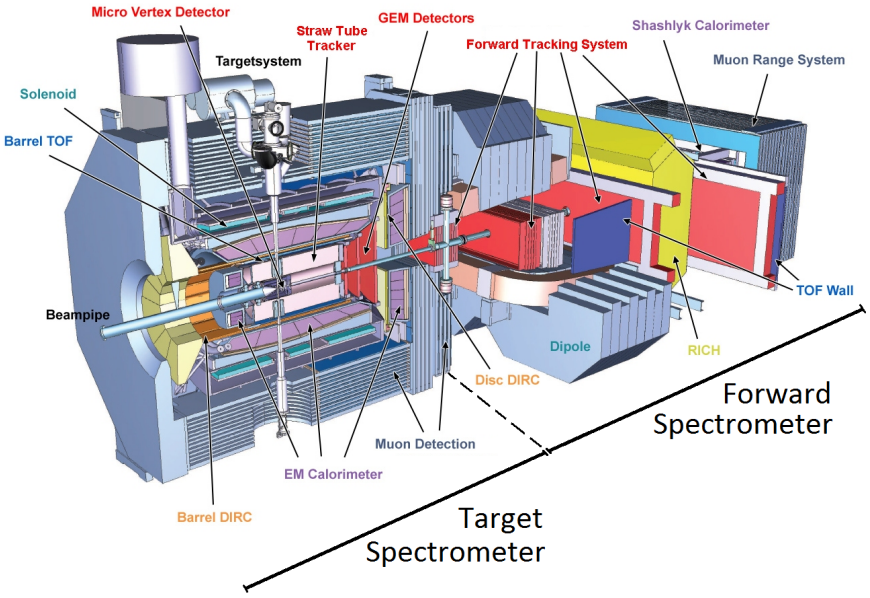

Figure 1.9: Schematic view of the PANDA experiment, consisting of the target spectrometer (left) and the forward spectrometer (right) [PAN14].

The target spectrometer is positioned around the interaction point between the anti-proton beam and the target, covering the solid angle above 5° in vertical and 10° in horizontal direction. The area directly surrounding the interaction point is covered by the micro-vertex detector, which is surrounded by the Straw Tube Tracker on the side face and by GEM detectors in the forward region of the target spectrometer. This tracking detectors are surrounded by the particle identification in the Detection of Internally Reflected Cherenkov Light (DIRC) and Time Of Flight (TOF) detectors in transverse direction and by the Disc DIRC detector in the forward part. Further outward these detectors are followed by the electromagnetic calorimeter barrel with its forward and backward end caps. All these inner detectors are surrounded by the solenoid magnet which creates a maximal magnetic field of 2 T in the inner region. The complete inner target spectrometer is covered by the muon detector in transverse and forward directions. In the region below 5° in vertical and 10° in horizontal direction a hole is left in the target spectrometer which is covered by the separated forward spectrometer. This spectrometer begins with a 2 Tm dipole magnet to bend the trajectories of charged particles. The tracking detectors of the forward spectrometer are positioned in front and behind the dipole magnet and behind the Ring Imaging Cherenkov Counter (RICH) detector. Behind the magnet and behind the last racking detector, TOF walls are inserted for time of flight measurements. The end part of the forward spectrometer is occupied by the forward shashlyk electromagnetic calorimeter followed by the muon range system. In the following sections a more detailed description of the single detector components will be given for the target and the forward spectrometer.

The Target Spectrometer

Figure 1.10 provides a detailed view of the target spectrometer with the single sub detectors described in the following section.

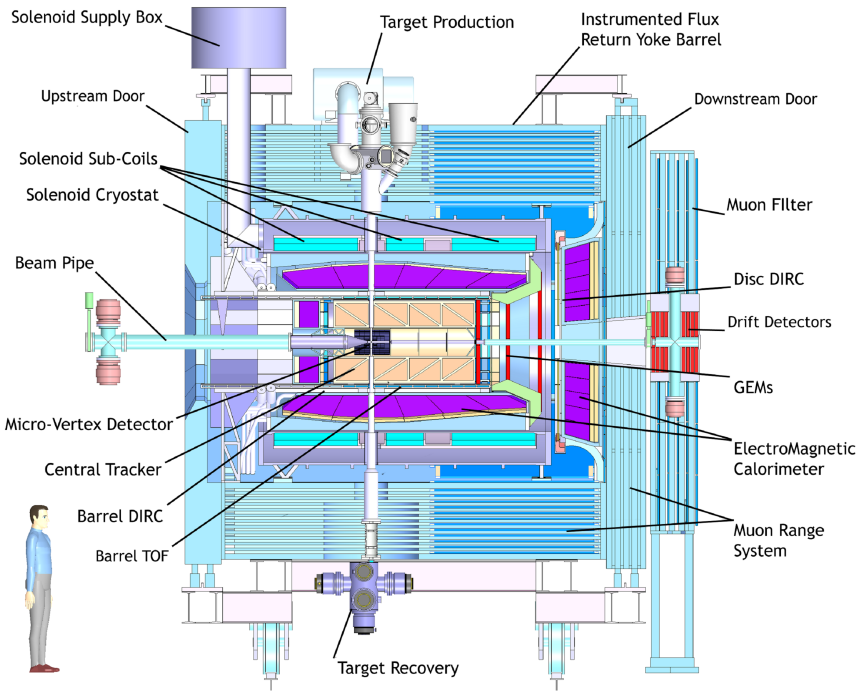

Figure 1.10: Side view of the target spectrometer of the PANDA detector with the single sub detector systems, the beam pipe and the target system. [TDma09]

The target system: For most of the envisaged physics cases a pure proton target is required for the anti-proton proton collisions. For this reason hydrogen has been chosen as the primary target material. Nevertheless, the target system should also be able to handle deuterium as an efficient neutron target and heavier gases like N_2 and noble gases from He up to Kr, which can be used to study in medium modifications [TDta12]. The main challenge of the target system is to introduce a very small solid cluster of matter into the center of the storage ring beam pipe without deteriorating the ultra high vacuum of this region or influencing the beam quality [TDta12]. To fulfill this requirement, a cluster jet or pellet target system will be used. In this system a jet of small clusters or pellets of particles with sizes in the micro- or nanometer region is crossing the anti-proton beam in transverse direction.

To realize a **cluster target**, atomic clusters have to be produced in a first step. For this purpose a pre-cooled gas is expanded into a vacuum through a convergent-divergent Laval-type nozzle with an opening of typically $10 - 100\mu m$ [TDta12]. In this process, the gas adiabatically cools down and forms a supersonic beam in which the particles can condensate to nano-structures [TDta12]. Such a gas jet is able to pass several meters in vacuum with nearly no divergence. The size of the clusters and the intensity of the beam strongly depend on the design of the nozzle and the size of the opening and can be adapted to the individual

needs by optimizing these components [TDta12]. Typical cluster sizes are in the order of 10^3 - 10^5 atoms per cluster which allows the approximation of a homogeneous volume density for the cluster beam [TDta12]. The final volume density of the beam strongly depends on the pressure of the gas which is inserted into the nozzle. To achieve a high cluster jet density which is desired for PANDA the hydrogen has to be in liquid phase with insertion pressures of $p_0 \leq 25bar$ [TDta12]. Figure 1.11 shows a schematic sketch of the cluster-jet source developed for PANDA. After leaving the nozzle, the cluster-jet beam is shaped by a conical skimmer stage and by a collimator before it finally enters the vacuum pipe leading to the interaction point inside the detector which is separated from the target system by two vacuum valves and two additional vacuum stages.

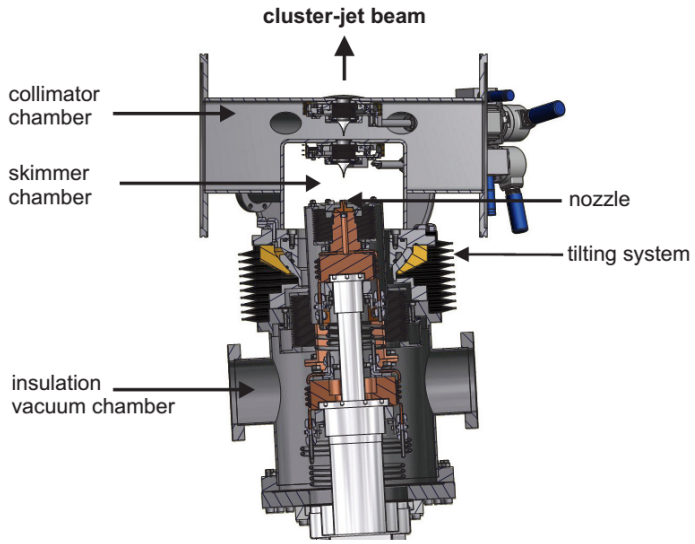

Figure 1.11: Schematic sketch of the front part of the cluster-jet source [TDta12]. The collimated cluster-jet beam is leaving the source into a vacuum pipe leading to the interaction point.

On the other side of the interaction point a beam dump for the cluster-jet beam is installed in form of an off-axis turbo molecular pump separated from the interaction point by three differentially pumped vacuum stages which are also evacuated with turbo molecular pumps [TDta12]. The off-axis turbo molecular pump can be replaced with a pellet catcher pot, if a pellet target is used.

The second option, which can be used for the target system of the PANDA detector is a **pellet target**. The main advantages of such a system are the high effective target thickness and the possibility of an exact target tracking within the beam pipe. On the other side strong thickness variations may be a problem [TDta12]. The pellets can be produced in a triple point chamber. In such a chamber a liquid at cryogenic temperatures is injected in a chamber with the same element in gaseous form or helium gas through a small nozzle. If this nozzle is periodically excited by a piezoelectric transducer, the jet starts oscillating along the surface of the nozzle and if the amplitude of the oscillation equals the jet radius, drops are formed in the jet [TDta12]. With this method a continuous and homogenous flow of drops can be produced which is injected through a thin injection capillary into the vacuum pipe, where it can be tracked with optical detectors [TDta12]. An already existing pellet target

developed at Uppsala and successfully operated at the former CELSIUS accelerator and at COSY in Jülich provides $25 - 30\mu m$ thick pellets with around 10^{15} atoms per pellet and an intensity of 5000 - 20000 pellets per second in a beam with a diameter of 3 mm [TDta12]. The PANDA pellet target will be based on this design with several improvements for the use in an anti-proton beam.

The micro vertex detector (MVD): The MVD is the innermost detector of the PANDA setup, directly surrounding the interaction point with a maximal radius of 15 cm and a length of 46 cm. A high resolution MVD is required in PANDA to measure the primary interaction vertex and the secondary decay vertices especially for charmed and strange hadrons [TDm11]. Like all other detectors the MVD has to cover nearly the complete polar angle (3° - 150°). Another main requirement is a high spatial resolution of less than 100 μm in z direction and only a few tens of μm in xy-direction, which is needed to resolve the decay vertices of D-mesons with an average decay length of only 123 μm for a D^0 [TDm11]. A third main requirement on the MVD setup is a low material budget to avoid an impact on the performance of the outer detectors. Especially for the EMC it is very important to minimize photon conversions in active or passive parts of the MVD. In addition to this, multiple scattering of particles in the MVD will degrade the tracking performance of the complete detector. Due to these restrictions, the MVD has to consist of light and low Z materials and the maximal thickness is limited to less than 10 % of one radiation length [TDm11]. Since the MVD is the innermost detector, all components have to be highly radiation hard to ensure a long term operation. Figure 1.12 shows a schematic picture of the planed MVD design.

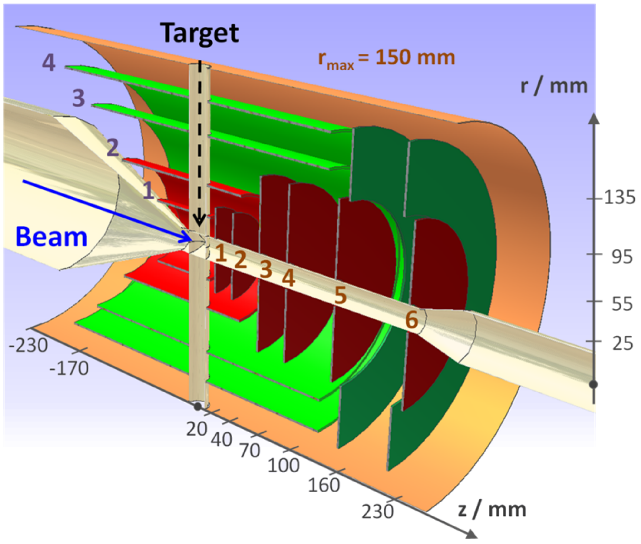

Figure 1.12: Schematic view of the Micro Vertex Detector. The detector consist of a barrel part which is surrounding the beam pipe in longitudinal direction and a forward disc part with 6 discs oriented transverse to the beam pipe. The hole intersecting the detector in transverse direction represents the target pipe. [TDm11]

To fulfill the needs of a fixed target experiment, the MVD is spitted into a barrel and a forward region. The barrel part consists out of four layers with a radius between 2.5 cm and 13.5 cm which are required to reach a minimum of four MVD hit points per track [TDm11].

The length of the barrel layers is varying. While the outer two layers have the full length, the length is decreasing gradually for the inner layers. The forward region consists of four discs to improve the resolution for low polar angles. The first two small discs are inserted in the second barrel layer, while the following two larger discs are inserted in the third barrel layer. The last two discs with the same size like disc 3 and 4 are positioned after the barrel part and surrounded by larger rings to cover the full barrel size.

The two inner barrel layers and all forward discs will consist of silicon hybrid pixel detectors (red components in fig. 1.12), while the two outer barrel layers and the outer parts of the last two forward discs will be equipped with double-sided silicon micro-strip detectors (green part in fig. 1.12) [TDm11]. For the pixel detectors quadratic pixels with a pixel size of 100 μm will be used grouped in readout units of 116 x 110 cells, corresponding to an area of $1.3 cm^2$ [TDm11]. All four different sensor geometries have to consist of multiples of this readout units and only differ in their length. The micro-strip detectors will consist of three differently shaped sensor types. In the barrel part sensors with a squared or rectangular shape and a strip pitch size of 130 μm will be arranged in a paddle-wheel design, while in the outer region of the forward discs, sensors with a trapezoidal design and a strip pitch size of 67.5 μm will be used to achieve a better resolution [TDm11]. The complete MVD will consist of approximately 10.3 million pixels and 200.000 strip sensors [TDm11].

Both silicon detector types work basically after the same principle. If a charged particle crosses the detector, electron-hole pairs are created in the silicon by ionization. The energy loss of charged particles in silicon strongly depends on their velocity and can be calculated with the Bethe-Bloch equation. From literature we know that per 3.6 eV of deposited energy on average 1 electron-hole (e-h) pair is generated in silicon [RFR06]. If an electric flied is applied to the silicon pixel and the energy deposition happens in the depletion zone, electrons and holes drift in opposite directions. On this way a current is generated on the electrodes of the pixels or on the anode/cathode strips of the strip detectors, which is significantly higher than the dark current and can be detected by the readout electronics [RFR06].

The straw tube and the gaseous micro pattern tracker: The tracking detectors represent the second detection layer of the PANDA experiment, directly surrounding the MVD. Also for this detector the physics program of PANDA provides a series of requirements which have to be fulfilled. Especially for the hadron spectroscopy program a full coverage of the azimuthal angle is mandatory. Considering the large Lorentz-boost of a fixed target experiment, especially the forward directions are important for an efficient operation. Nevertheless, even for the highest anti-proton momenta light particles like electrons, muons and pions will be emitted into the backward region of the detector [TDtr12]. For this reason, like for the MVD also a nearly full coverage of the polar angle (0° - 150°) is required. While the reconstruction of the decay vertex of short lived particles like D^0 can be excellently realized with the MVD, Hyperons and K_S mesons have much longer decay lengths (i.e. 8 cm for the Λ hyperon), which are additionally increased by the Lorentz-boost to several tens of centimeters, especially in forward direction [TDtr12]. For this reason, the straw tube tracker of the barrel region has to be extended in forward direction to ensure an efficient tracking and vertex reconstruction for this particles. To ensure the envisaged momentum resolution of $\sigma_p/p = 1\%$ and a good vertex reconstruction, the tracking detectors need a high spatial resolution and a high acceptance over the complete momentum range from about 100 MeV/c up to 8 GeV/c [TDtr12]. The count rate capability has to be in the region of $2 \cdot 10^8$ particles per second for the complete

tracking system and like for the MVD, the material budget has to be as low as possible to avoid an influence on the EMC performance by multiple scattering [TDtr12].

Like the MVD, the tracking detectors of the target spectrometer will consist of two parts. The barrel region will be covered by a Straw Tube Tracker (STT) consisting of aluminized Mylar tubes, while the forward region will be covered by gaseous micro-pattern detectors with amplification stages made of Gas Electron Multiplier (GEM) foils, arranged in three planes [TDtr12]. Figure 1.13 (left) shows the arrangement of the tracking detectors in the PANDA detector. The STT will directly surround the MVD with an asymmetric expansion in forward directions. The GEM detectors in form of three discs with increasing diameter will be positioned after the STT. The right part of figure 1.13 shows a detailed schematic sketch of the STT.

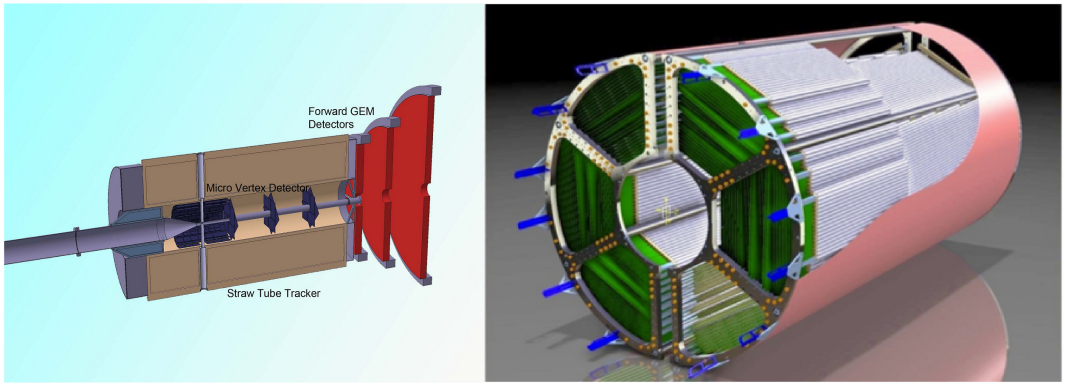

Figure 1.13: Overview of the tracking detectors of the target spectrometer with the straw tube tracker and the forward GEM detectors (left) and schematic drawing of the straw tube tracker barrel (right). [TDtr12]

The tracking detectors are an important component of the PANDA detector. They are used to measure the momentum of charged particles with a transverse momentum component, which are bend on a circular transverse trajectory by the magnetic field of the solenoid magnet. By measuring the trajectory of the particles as a combination of the hit points in the MVD and in the STT, the radius r of the circular motion can be calculated, which is directly proportional to the particles momentum $p = q \cdot B \cdot r$ with the charge of the particle q and the magnetic field B. Another application field of the central STT will be the particle identification of Kaons with energies below the DIRC threshold by energy loss measurements.

The **central STT**, covering the polar angle from 10° to 140°, will consist of 4636 1.5 m long single straw tubes with a diameter of 10 mm and a wall thickness of only 27 μm arranged as a cylindrical volume around the interaction point [TDtr12]. A single straw tube is a cylindrical tube made of Mylar with a conductive inner layer made of aluminum, which acts as a cathode. The tube is filled with gas (i.e. Ar + 10 % CO_2) at a pressure of 2 bar and a thin (20 μm) anode wire is strained in its center [TDtr12]. For the operation a positive voltage of a few keV is applied between the wire and the surrounding tube. If a charged particle passes such a tube, it ionizes the gas and the electrons drift to the anode wire while the ions are collected by the cathode wall. Since the field strange becomes stronger close to the thin wire, the accelerated electrons cause secondary gas ionization during collisions with the gas molecules in this region. With this amplification of a factor $10^4 - 10^5$, a measurable signal can be obtained for the

readout [TDtr12]. With an additional measurement of the drift time of the electron reaching the inner wire first, an additional information for the minimal distance between track and wire can be extracted. From the number of ionization electrons per track length also the specific energy loss of a charged particle dE/dx can be extracted for particle identification purposes. However, due to the low amount of produced ionization electrons and due to their large fluctuations this quantity shows a relatively large error, limiting the energy resolution to around 8 % in prototype tests [TDtr12]. In the final detector arrangement the straw tubes will be closely packed in several layers and glued together to achieve up to 27 hits in radial direction, which ensures a good spatial resolution and a good energy loss measurement capability with an material budget of only 1.23 % of one radiation length [TDtr12].

In the forward region, for angles between 5° and 22°, particles do not cross the STT or hit only a part of it. For this reason the tracking is done by three **GEM detector** plates which are placed in forward direction 1.1 m, 1.4 m and 1.9 m away from the target with an increasing outer diameter between 45 cm and 74 cm [TDg12]. The GEM detectors represent a special form of a time projection chamber (TPC). Each of the three GEM discs consists of a thin cylindrical shaped disc volume which is filled with gas. Like in the straw tubes, a crossing charged particle ionizes the gas along its track and produces a certain amount of electrons and ions. For the readout, each of the GEM discs has a double-sided read-out pad plane in its center, which allows a position sensitive charge collection. For the amplification of the charge created by the crossing particle, the read-out pad is surrounded on both sides by three layers of Gas Electron Multiplier (GEM) foils [TDg12]. After a small gas volume a cathode-plane and a window foil are added on each side of the detector [TDg12]. The key component of this structure are the GEM foils, which consist of insulating polyamide foils with a thickness of only 50 μm. The surface of the foils is coated with a 2 - 5 μm thick layer of copper. Finally photo-lithographic methods are used to perforate the foils with a pattern of double conical holes with a diameter of around 50 μm [TDg12]. If in this configuration only a moderate voltage of 300-400 V is applied between the central pad and the two cathode pads, the small diameter of the holes will lead to electric fields in the order of 50 kV/cm inside the passage, which is enough to let a primary electron create an avalanche during its passage [TDg12]. With a combination of three GEM foils gains of approximately 10^4 can be achieved under stable conditions [TDg12]. Due to the high amount of holes in the GEM plates, position resolution of less than 100 μm and high count rate capabilities can be achieved with this concept [TDg12].

Particle Identification (PID): The identification of charged particles is a mandatory requirement for many of the physics topics which will be studied with PANDA. For this purpose a special particle identification concept is needed in addition to the energy loss (dE/dx) measurements of the tracking and the information obtained from the muon detector system and from the electromagnetic calorimeter [CS14]. The central components for particle identification in the target spectrometer will be provided by Cherenkov detectors based on the DIRC concept, split off in a barrel DIRC which covers the angles between 22° and 140° and a Disc DIRC for the forward direction of the target spectrometer [CS14].

The **barrel DIRC** will consist of 80 rectangular radiator bars made of synthetic fused silica (quartz) with a high quality polished surface [HDG14]. The use of quartz as a radiator material provides the advantages of a higher light yield, a lower detection threshold and larger emission angles due to the high refraction index of n=1.47, compared to classical gas filled

Cherenkov detectors. Each bar has a dimension of 17 mm × 32 mm × 2400 mm and the total barrel will have a length of 2.4 m and a radius of 0.48 m [HDG14]. For the readout, focusing optics are attached to the end face of the bars, which will be read out by approximately 15000 channels of multi-channel plate (MCP) photo multipliers [HDG14]. Figure 1.14 shows a schematic picture of the arrangement of the radiator bars, the focusing optics and the photo sensors of the barrel DIRC.

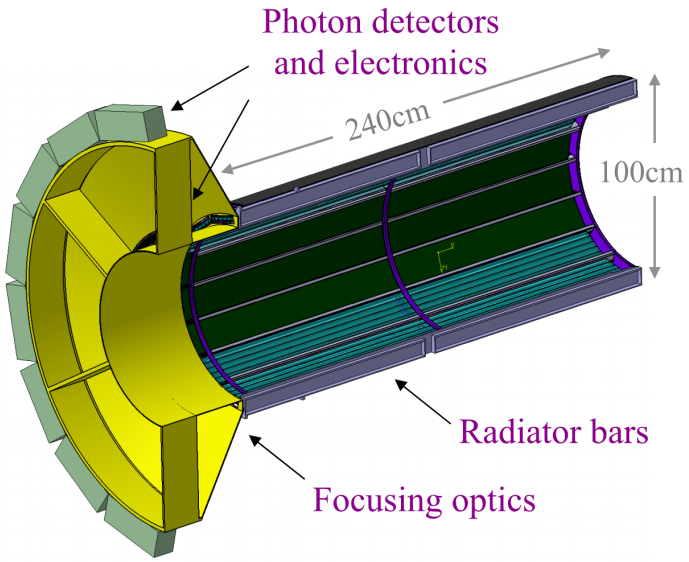

Figure 1.14: Schematic drawing of the PANDA barrel DIRC showing the radiator bars, the focusing optics and the position of the photo sensors [HDG14].

If a charged particle crosses the radiator bars with a velocity larger than the speed of light in the quartz bars ($c_{quartz} = c_0/n = c_0/1.47$), it emits Cherenkov radiation under a well defined forward angle, given by the formula

$$\vartheta_{Ch} = arccos\left(\frac{1}{n\beta}\right) \tag{1.1}$$

with the refraction index n for quartz and $\beta = v/c$. The light produced along the track propagates via internal reflection inside the radiator bars to the end of the bars where it enters the expansion volume of the focusing optics, which has an reduced index of refraction to increase initially small angular differences [HDG14]. Another purpose of the focusing units is the projection of the light on the MCPs [HDG14]. From a combination of the position ($RMS_p \approx 150\ \mu m$) and time ($\sigma_t < 50$ ps) information of the photons arriving at the position sensitive MCPs with the trajectory of the charged particle which is known from the inner tracking detectors, the Cherenkov angle can be reconstructed [HDG14]. From this value the velocity of the particle can be calculated with equation 1.1 and with the particles momentum also known from the inner tracking detectors, the particles mass can be reconstructed and the charged particle can be clearly identified.

In the forward direction of the target spectrometer a **disc DIRC** design will be used in a distance of 2 m from the interaction point, covering the region between 5° and 22° [MDG14]. This detector will consist of four 2 cm thick fused silica plates with the shape of a regular

dodecagon and a cut out for the beam pipe, representing the four independent quadrants of the disc [MDG14]. The surface has to be polished to reach a high optical quality, guaranteeing a high degree of internally reflected light. The working principle of this detector is basically the same like for the barrel part only the focusing optics which are attached on the outer side face of the disc to guide the light to the MCPs are designed in a different way to fit in the detector arrangement.

The barrel time of flight detector: To detect conversions of photons in the inner tracking detectors and especially in the barrel DIRC and to improve the relative timing between the barrel and the forward spectrometer, it is planed to add a **scintillating tile (SciTil) detector** between the DIRC and the EMC [GOS11]. The aim for such a detector is to achieve an excellent timing performance of $\sigma_t < 100\ ps$ with a minimal material budget to avoid photon conversions. In classical timing devices consisting of long scintillator bars a thick active volume is needed to reduce the light attenuation and to detect a sufficient amount of light with the Photomultiplier Tube (PMT) mounted at the end of the bars. The development and further improvement of SiPMs in the last years enabled the new concept of a segmented barrel time of flight detector with an individual Silicon Photomultiplier (SiPM) readout of each segment which combines an excellent timing performance with a minimal thickness. Figure 1.15 shows the design concept for such a detector consisting of 5760 single 2.85×2.85 cm large and 0.5 cm thick scintillator tiles made of an inorganic scintillator material (i.e. EJ228 or EJ232) and read out with two $3 \times 3mm^2$ SiPMs per module [GOS11].

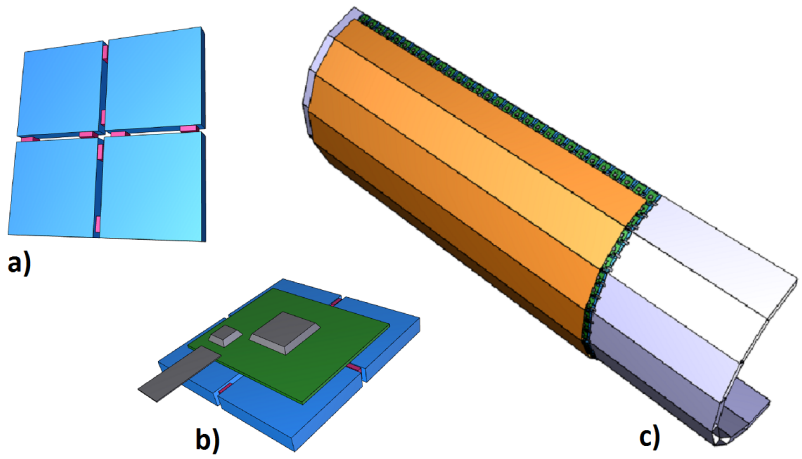

Figure 1.15: Design of the barrel SciTil time of flight detector. a) Arrangement of four inorganic scintillating tiles with a readout of two SiPMs per tile. b) Quad-module with readout electronics on the back side. c) Half barrel of the SciTil detector with eight super modules containing 360 scintillator tiles with an individual readout of each tile. [GOS11]

The tiles will be grouped in quad modules with the individual front end electronics on each module. This quad modules will be arranged in 16 super modules with 90 quad modules each, which form the barrel [GOS11]. In recent prototype studies time resolution of less than 100 ps have been achieved [BGM14].

The electromagnetic calorimeter (EMC): The EMC is one of the central components of the PANDA detector because it is the only device for a precise energy measurement of high energetic photons and other electromagnetically interacting particles like electrons. In addition, it provides the possibility to gain an efficient position information for photons. The calorimeter will directly surround the DIRC detectors. It will be made of 15552 lead tungstate ($PbWO_4$) (PWO) crystals, split of in a barrel component and a forward and backward end cap to cover the full solid angle. The EMC will be described in more detail in section 1.3.

The magnet: For the reconstruction of particle tracks in the inner tracking detectors, a magnetic field is required. For an optimal tracking a homogenous longitudinal magnetic field of 2 T is desirable. In addition, the magnet has to provide enough free space in the inner region to mount all inner detectors up to the EMC. To fulfill this requirements a superconducting solenoid magnet with an external iron return yoke has been selected for the PANDA detector [TDma09]. The external return yoke will be combined with the muon detector which will be described in the next paragraph. Figure 1.16 shows a design view of the barrel magnet yoke (left) and an schematic view of the magnet coils cross section with the three sub coils, the cryostat and the coil former.

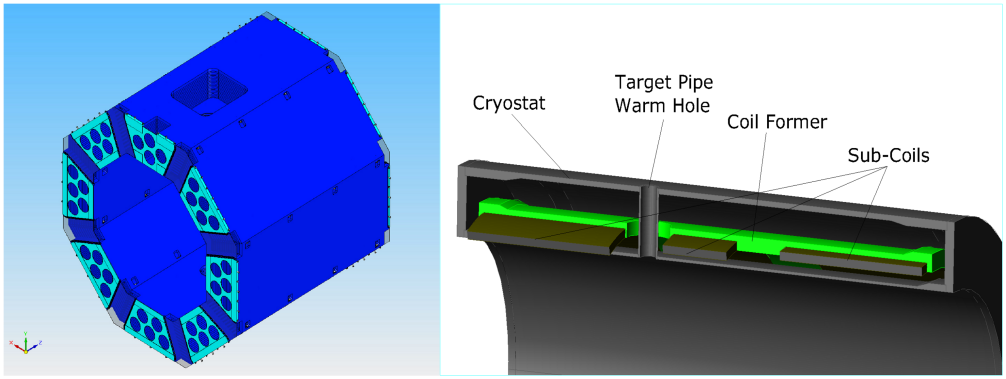

Figure 1.16: Schematic drawing of the barrel part of the magnet yoke with the insertion for the target system on top (left) and detailed drawing of a part of the magnet coil with the coil former, the three sub coils and the cryostat (right). The thermal screens and the cooling pipes are not shown in the picture. The total weight of the solenoid magnet will be around 300 t [TDma09].

The complete magnet is surrounded by a cryostat, insulating the cooling of the semiconductor wires. As a semiconductor, NbTi is used in a Rutherford-type cable[2] configuration which is twisted inside the coil former made of an aluminum alloy [TDma09]. The cooling is realized by liquid helium flowing in pipes on the outer side of the coil former. To obtain a good homogeneity in spite of the need for a hole to insert the target pipe, the magnet consists of three sub coils connected in series [TDma09]. The central coil will have 104 turns and the two outer coils 232 turns. The operating current will be 5 kA. With this configuration an uniformity of the 2 T magnetic field of 1.6 % can be achieved in the region of the tracking detectors [TDma09]. The complete solenoidal magnet of the target spectrometer will be covered by a flux-return yoke made of iron. This yoke is on the one side needed to increase

[2]Several cables are put together and compacted to achieve a rectangular shape, which is important for the radial alignment.

the strength of the magnetic field in the tracking region without building a stronger solenoid and on the other side it improves the orientation of the field flux lines and reduces radial components [TDma09].

The muon detectors: While the electromagnetically interacting particles like photons, electrons and positrons are absorbed by the EMC, most of the particles which pass the EMC and even the solenoid magnet of the target spectrometer are high energetic muons and pions. The detection and identification of these muons and especially their separation from the pions plays an important role for several physics topics, for example for Drell-Yan processes, semi-leptonic D-meson decays and J/Ψ decays [AB14].

For the detection of the muons and pions a range system will be used, which is included in the barrel part and in the forward section of the solenoid magnets iron yoke. For this purpose these two components of the yoke consist of laminated iron layers. While the 3 cm thick (6 cm for the first and last layer) iron layers of the yoke act as an absorber material for the muons in which the minimal ionizing particles deposit around 1.5 GeV per meter, every second layer consists of 3 cm thick mini-drift-tubes (MTD) as an active detector component [TDm11]. The complete system of the barrel region will consist of 13 layers with an active double layer mounted in front of the first iron plate [TDm11]. In the forward region, energies and momenta of the particles are increased due to the Lorentz boost, which makes an increase of the absorber thickness necessary. For this reason the forward door of the return yoke consists of five layers of 6 cm thick iron absorbers intersected with six active MTD layers [TDm11]. In addition, a muon filter with five additional 6 cm thick layers will be added behind the yoke [TDm11]. The MTD detectors work with the same principles like normal drift tubes. To obtain a longitudinal position information with an accuracy of around 1 cm only additional capacitively coupled strips are added to the rectangular aluminum tubes which enable a double sided read out of the tubes [TDm11].

For low energies ($E \ll 1$ GeV) which are common for the barrel region of the target spectrometer muons as well as pions can be stopped in the detector system, which enables a determination of their energy with a certain error [VR09]. For the separation of muons and pions in addition to the deposited energy also the distance traveled in the sampling structure is an important parameter. While low energetic charged pions deposit most of their energy in the first layers of the detector with a falling tail to further layers, low energetic muons deposit most of their energy at the point where they are absorbed in the detector, which strongly depends on their initial energy. Thus, a separation of the two particle types is easily possible by their energy deposition profile. At higher energies in the forward part of the target spectrometer and especially in the forward spectrometer, muons pass the system without being absorbed leaving a straight ionization trace with only slight direction changes by multiple scattering. In contrast, hadrons like pions and protons produce a hadronic shower which deposits a major part of its energy in the detector system contained in a larger volume of the detector compared to high energetic muons [VR09].

The Forward Spectrometer

Figure 1.17 provides a detailed view of the forward spectrometer which covers the region below 5° in vertical and 10° in horizontal direction.

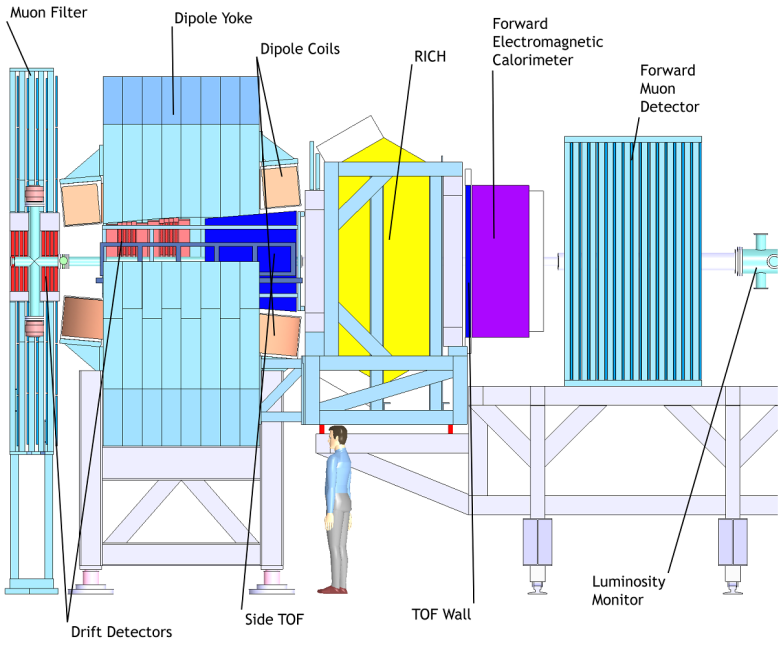

Figure 1.17: Side view of the forward spectrometer of the PANDA detector with the single sub detector systems. The muon filters on the left side containing the first drift detectors are part of the target spectrometer. [TDma09]

The forward dipole magnet: The main requirement on the forward dipole magnet is the production of a 2 Tm magnetic field with a minimized extension of the magnet in beam direction. However, the magnet size is determined by a trade-off between the field quality and the costs for the forward spectrometer which will grow quadratically in terms of the area which has to be covered with increasing distance to the interaction point. Considering this trade-off a 2.5 m long magnet with a height of 3.9 m and a width of 5.3 m has been chosen [TDma09]. Figure 1.18 shows a design drawing of the dipole magnet with the coils and the

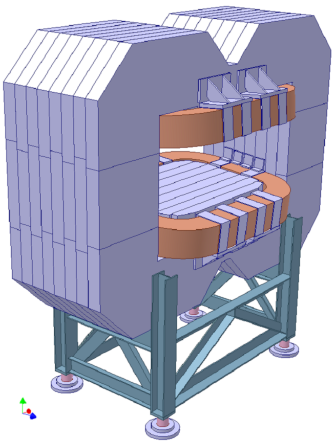

Figure 1.18: Schematic drawing of the dipole magnet of the forward spectrometer. The coils (brown) and the flux return yoke (gray) can be nicely identified. [TDma09]

flux return yoke. The segmented return yoke surrounding the coils will be made of low carbon steel. It is designed in a way that particles passing the forward hole in the target spectrometer can cross the hole inside the magnet without hitting the yoke. The conductor coils will be made of copper to provide a lower resistance for the conductor current of 2.16 kA and have a diameter of 3.0 $\times$ 2.4 cm^2 [TDma09]. The total weight of the dipole will be 220 t [TDma09].

The forward tracking detectors: The tracking system in forward direction will be used to measure the trajectories of charged particles bend by the field of the dipole magnet in the complete angular range of the forward spectrometer. For this purpose one pair of independent tracking drift detectors will be placed in front of the magnet, one inside the magnet to track particles with low momenta and one behind the dipole magnet, in front and behind the RICH detector [TDtr12]. Each of the six detectors will be made of four double layers of straw tubes in the same design like for the STT of the target spectrometer. The number of straw tubes per tracking unit will increase gradually with growing distance from the target spectrometer, from 32 straws and an area of 0.83 m^2 for the first unit up to 148 straws and an area of 8.86 m^2 for the sixth unit [JS14]. The straw tubes of the first and the fourth double layers will be mounted on a support frame in vertical direction and the two intermediate layers under a small angle of +5° and -5°, respectively, relative to the other two layers [TDtr12, JS14]. Figure 1.19 shows a schematic drawing of one of the double layers of straw tubes with the readout on the top side of the straws.

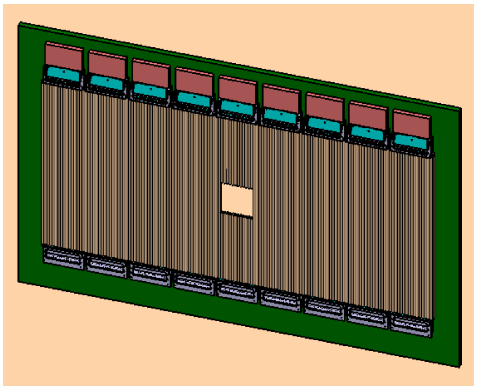

Figure 1.19: Schematic picture of the double layer straw tubes, which are mounted on a rectangular support frame around the beam pipe in the forward spectrometer. The readout will be performed with preamplifier cards, which are shown in red. [TDtr12]

Each of the tracking stations will have an material budget of only 0.3 % of one radiation length and provide a position resolution of $\sigma_p = 0.1mm$ [JS14]. Due to the modular design it will be possible to reconstruct the tracks in each layer separately.

The forward particle identification (PID and TOF): For the PID in forward directions higher particle energies have to be handled compared to the target spectrometer region due to the Lorentz boost of the particles. To guarantee an efficient π/K and K/p separation under these conditions a dual radiator RICH made of a silica aerogel and a C_4F_{10} gas radiator similar to the RICH used in the HERMES experiment [TAS14] are planed to be used for particle identification in the forward spectrometer [TDtr12]. With refraction indices of 1.0304

and 1.00137 respectively, these radiators will provide an efficient particle identification in the momentum range between 2 and 15 GeV/c with a total material budget of approximately 10.8 % of a radiation length [TDtr12]. For the collection of the light, mirrors will be used which focus the Cherenkov light produced by charged particles on an arrangement of photo sensors (i.e. PMT or hybrid photo detectors) placed on the side face of the active volume [TDtr12]. The identification of particles with momenta below 2 GeV/c will be realized in the forward spectrometer with time of flight stop detectors. The forward TOF wall will be placed between the Cherenkov detector and the shashlyk calorimeter around 7.5 m away from the interaction point. It will consist of 140 cm long and 2.5 cm thick organic scintillator bars made of Bicron 408 positioned vertically and read out on the top and bottom end with a light guide and a photomultiplier tube [SB14]. In the central region 20 5 cm wide bars will be used to achieve a better spatial resolution and rate capability, while further outside on each side 23 10 cm wide bars will be added to cover the complete area of the forward spectrometer [SB14]. With this setup it will be possible to reach a time resolution of $\sigma_t \approx 50$ ps [SB14]. For very slow particles which are not able to pass the dipole magnet, additional time of flight detectors have to be added inside the magnet. For this purpose, on each side of the magnet ten scintillator plates with a width of 10 cm and a thickness of 2.5 cm but a length of only 80-100 cm will be mounted [SB14]. Due to the high magnetic field the readout has to be performed with small field resistant PMTs or SiPMs [SB14].

The forward shashlyk calorimeter (FSC) : Like in the target spectrometer the Cerenkov detector is followed by an electromagnetic calorimeter in the forward spectrometer. In this case a shashlyk type sampling calorimeter, consisting of lead and scintillator plates read out by wavelength shifting fibers will be used. The FSC will be described in more detail in section 1.3.

The forward muon detector: The forward muon system is the last detector of the forward spectrometer, positioned around 9 m away from the interaction point. It will be built with the same principle like the system of the target spectrometer, only optimized for higher particle energies up to 10 GeV by using sixteen 6 cm thick iron layers intersected by layers of rectangular aluminum MTDs [TDm11]. Like already described for the forward region of the target spectrometer, at higher energies in the GeV region which are common in the forward spectrometer muons normally pass the system without being absorbed leaving a straight ionization trace with only slight direction changes by multiple scattering. In contrast to this, hadrons like pions and protons produce an hadronic shower which deposits a major part of its energy in the detector system and covers a larger volume of the detector than high energetic muons [VR09]. Because of this it is possible to use the forward muon system with its large absorber volume also as a hadronic calorimeter with an acceptable energy resolution [VR09].

The luminosity detector: The exact measurement of the time integrated luminosity L for a time interval dt is an important parameter for the determination of the cross section σ of a decay channel. According to $N = L \cdot \sigma$ it provides a direct correlation between the number of events N measured in an time interval dt and the cross section [TDl15]. For the determination of the luminosity a special luminosity detector will be used in PANDA. This detector will be placed behind the forward muon system, approximately 11 m away from the interaction point.

It will be positioned directly around the beam pipe, covering the full azimuthal angle. The detector will have an radius of 15 cm and consist of four planes with 400 cooled high voltage monolithic active pixel sensors (HV-MAPS) which enable the reconstruction of the tracks of particles scattered during an interaction to very small polar angles θ between 3 mrad and 8 mrad [TDl15]. Based on the reconstructed particle tracks, the shape of the cross section of this particles can be reconstructed and a fit to simulations of the angular particle distribution finally provides the time integrated luminosity [TDl15]. With this detector it is envisaged to achieve an accuracy in the luminosity measurement better than 5 % [TDl15].

1.3 The PANDA electromagnetic calorimeters

The electromagnetic calorimeters of the target and the forward spectrometer of PANDA are essential components of the detector. They provide the only possibility to measure the energy of photons directly with an error of only a few percent and an efficiency of more than 99% [TDe09]. For hadronic interactions of anti-protons with protons, the detection of secondary photons and other electromagnetically interacting particles plays an important role to reconstruct many of the envisaged physics channels and to reduce the background produced by other reactions. Especially in the field of charmonium spectroscopy there are a lot of channels with one or even more photons and other electromagnetic interacting particles in the final state, like the following charmonium decays, which belong to the benchmark channels of PANDA, illustrate [PPR09].

$$\overline{p}\,p \;\rightarrow\; J/\Psi\;\pi^0\;\pi^0 \;\rightarrow\; e^+\;e^-\;\gamma\;\gamma\;\gamma\;\gamma \tag{1.2}$$

$$\overline{p}\,p \;\rightarrow\; J/\Psi\;\gamma \;\rightarrow\; e^+\;e^-\;\;\gamma \tag{1.3}$$

$$\overline{p}\,p \;\rightarrow\; \chi_{c1,c2}\;\gamma \;\rightarrow\; J/\Psi\;\gamma\;\gamma \;\rightarrow\; e^+\;e^-\;\gamma\;\gamma \tag{1.4}$$

$$\overline{p}\,p \;\rightarrow\; h_c \;\rightarrow\; \eta_c\;+\;\gamma \;\rightarrow\; \gamma\;\gamma\;\gamma \tag{1.5}$$

In parallel to decay channels which are of interest for the physics analysis, a significant amount of background reactions, also including several photons in the final state take place. For reaction 1.2 important background contributions are given for example by [PPR09]:

$$\overline{p}\,p \;\rightarrow\; \pi^+\;\pi^-\;\pi^0\;\pi^0 \;\rightarrow\; \pi^+\;\pi^-\;4\gamma \tag{1.6}$$

$$\overline{p}\,p \;\rightarrow\; J/\Psi\;\omega\;\pi^0 \;\rightarrow\; e^+\;e^-\;\;5\gamma \tag{1.7}$$

To clearly separate the channel of interest from the background, a high efficiency for photon detection is needed, which can only be provided by an electromagnetic calorimeter. Finally, for the reconstruction of the invariant mass of the announced and many other states which are of interest for PANDA, a high precision in terms of an excellent energy and position resolution is required over the complete energy range from some MeV up to around 15 GeV which can also only be realized with an electromagnetic calorimeter.

The following subsection will provide an overview over the physics processes which are taking place in an electromagnetic calorimeter and will discuss the factors which influence the energy, position and time resolution of electromagnetic calorimeters. Based on this fundamental principles different concepts for electromagnetic calorimeters will be presented and compared.

Finally the decision for the EMC concepts which will be used in the PANDA detector will be presented and motivated on the basis of the requirements given by the physics channels to be studied and by the overall detector setup.

1.3.1 The physics of electromagnetic calorimeters

The processes taking place in an electromagnetic calorimeter can be described in three steps. In a first step the incoming radiation or charged particle has to interact with the active and passive materials of the calorimeter. During this process the complete energy of the electromagnetic probe or only a part of it will be deposited in the active material of the calorimeter. In the second step, this deposited energy will produce secondary low energetic scintillation photons or electron - ion pairs, depending on the type of calorimeter. The amount of this secondary photons or electrons is proportional to the energy of the primary high energetic electromagnetic probe and has to be measured in a third step. For this purpose in case of photons as secondary objects, a photo-sensor is used to measure their quantity. In case of gaseous calorimeters, where electron-ion pairs are produced, the charge is collected and its distribution is measured over time. Since for PANDA only calorimeters based on scintillators will be used, only this type will be described in more detail in the following section.

Interaction of high energetic photons and charged particles with matter

The electromagnetic interaction of radiation with matter can be split up in two types of interactions. On the one side, the interaction of charged particles and on the other side the interaction of high energetic photons with matter. Since both types are important for the understanding of an electromagnetic calorimeter, they will be discussed in the following section.

Charged particles

For charged particles several effects are contributing to the energy loss during the passage of matter. The most important effects are the **inelastic scattering on atomic electrons** and the **elastic scattering off nuclei**. In addition to this the **emission of Bremsstrahlung**, the emission of **Cherenkov radiation** and **nuclear reactions** also contribute to the total energy loss of charged particles [WRL94].

For heavy charged particles like muons and pions the last three effects can be neglected and only the scattering effects have to be considered. However, for heavy particles the energy loss is dominated by the inelastic scattering on atomic electrons. A formula for this energy loss by ionization and excitation of the electrons has been derived by Bethe and Bloch in the years 1930-1933 [GB12]:

$$-\left(\frac{dE}{dx}\right)_{ion} = K \cdot z^2 \cdot \rho \cdot \frac{Z}{A} \cdot \frac{1}{\beta^2} \cdot \left(\frac{1}{2} \cdot ln\left(\frac{2m_e c^2 \beta^2 \gamma^2 \epsilon_{max}}{I^2}\right) - \beta^2 - \frac{\delta}{2}\right) \tag{1.8}$$

With the constant $K = 4\pi N_A r_e^2 m_e c^2 \approx 0.3071 MeV/(g/cm^2)$. The other parameter and variables used in this formula are defined in the following way:

- N_A: Avogadro Constant ($6.022 \cdot 10^{23} mol^{-1}$)
- $z = Q/e$: Charge of the primary particle in units of the elementary charge.
- Z: Nuclear charge (atomic number) of the absorber material.
- A: Atomic weight of the absorber medium in g/mol
- ρ: Density of the absorber medium in g/cm^3
- m_e: Rest mass of an electron (0.511 MeV/c^2)
- $\delta = \delta(\beta\gamma)$: Density-effect correction
- $\beta = v/c$: Particle speed in units of c for the primary particle $\rightarrow \gamma = 1/\sqrt{1-\beta^2}$
- $\epsilon_{max} \approx 2(\gamma - 1)$: Maximum energy transfer in a single collision in MeV.
- $I \approx 16\ eV \cdot Z^{0.9}$: Mean excitation potential of the absorber medium.

Figure 1.20 illustrates the mean energy loss of charged heavy particles in different materials calculated with the Bethe-Bloch formula. For energies between $\beta\gamma \approx 0.1$ and $\beta\gamma \approx 1000$ the accuracy is in the order of a few % [PDGbb14]. For higher energies radiative effects have to be taken into account especially for lighter particles like muons and pions [PDGbb14].

The typical behavior of the energy loss is similar for all absorber materials. Starting at low energies, it decreases with $1/\beta^2$ until it reaches its minimum for a $\beta\gamma$ between 3 and 4. Particles with an energy in this range like for example cosmic muons are called minimum ionizing particles (MIP) and show an energy loss due to ionization between 1 and 2 MeV/(g/cm^2) for absorber materials with $Z > 1$ [GB12]. After this minimum the energy loss starts to increase again with a logarithmic behavior due to relativistic effects until it reaches a constant level called the Fermi-plateau caused by a saturation of the large energy transfer to δ-electrons[3].

While the Bethe-Bloch formula (1.8) describes the statistical mean energy loss of a charged particle, the real energy loss of a single charged particle shows large fluctuations. This fact plays a role especially for thin detectors in which the particles only deposit a small fraction of their energy. For the case of cosmic muons with a mean energy of 4 GeV [PDG14] and a minimum ionizing energy loss of 1-2 MeV/(g/cm^2) even a scintillation crystal with a length of several tens of centimeters has to be treated like a "thin" detector. In this case the energy loss has to be described by a highly-skewed Landau distribution [PDG14].

$$f(\Delta E) = \frac{A}{\sqrt{2\pi}} \cdot e^{-\frac{1}{2}\cdot\left(C\cdot(\Delta E - \Delta_p) + e^{-C\cdot(\Delta E - \Delta_p)}\right)} \tag{1.9}$$

with the amplitude of the distribution A, the most probable momentum loss Δ_p and a parameter C containing the thickness of the layer and the mean excitation potential I. The most probable energy loss in this case is given by [PDG14]:

$$\Delta_p = \xi \cdot \left[ln\left(\frac{2mc^2\beta^2\gamma^2}{I}\right) + ln\left(\frac{\xi}{I}\right) + 0.200 - \beta^2 - \delta \right] \tag{1.10}$$

with $\xi = (K/2)(Z/A)(x/\beta^2)$ MeV for a detector thickness of x in g/cm^2. The other parameters are defined in the same way like for equation 1.8. In contrast to the mean energy loss per

[3]Electrons ionized from the atomic shell with an energy large enough to cause secondary ionization.

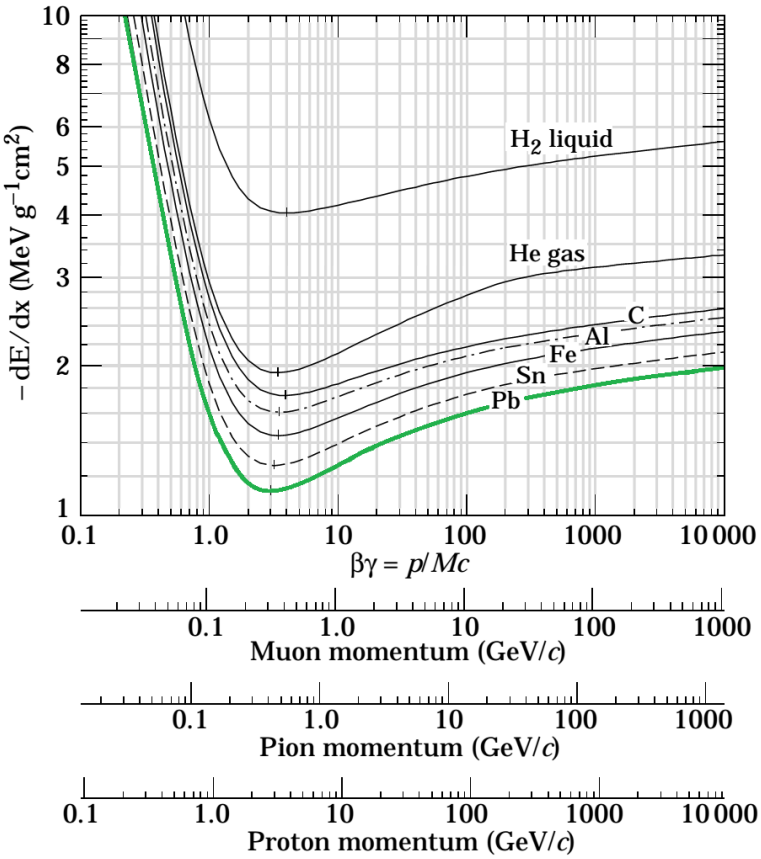

Figure 1.20: Mean energy loss of charged heavy particles in materials with increasing nuclear charge from H_2 (Z=1) up to Pb (Z=82) calculated with the Bethe-Bloch formula as a function of $\beta\gamma$ and the corresponding momenta for muons, pions and protons [PDGbb12]. Especially lead (green line) with its high nuclear charge shows a high stopping power which makes it an excellent candidate for sampling calorimeters.

path length described by the Bethe-Bloch equation, which is independent of the absorber thickness, the most probable energy loss in a "thin" absorber layer scales with the absorber thickness x according to $x \cdot (a \cdot ln(x) + b)$ with constants a and b [PDG14].

In contrast to heavy charged particles, electrons and positrons have to be treated differently due to their low mass and due to the fact that the electrons are identical with the electrons they ionize. Figure 1.21 shows the contributions to the energy loss fraction per radiation length (left axis) and the mass attenuation coefficient in g/cm^2 (right axis) of this particles in a lead absorber [PDG14]. The figure illustrates that for electrons and positrons ionization only plays a role for low energies of less than a few hundred MeV with a strong $1/\beta^2$ increase down to lower energies. In parallel to this the electrons and positrons lose a significant amount of their energy by emitting Bremsstrahlung, which increases nearly linearly for higher energies and becomes the dominating effect after a critical, material dependent energy point (see eqn. 1.34). For low energies of less than a few tens of MeV also the M∅ller scattering for electrons and the Bhabha scattering for positrons add a contribution which disappears again in the very low energy regime. Up to energies of a few tens of MeV also the annihilation of positrons

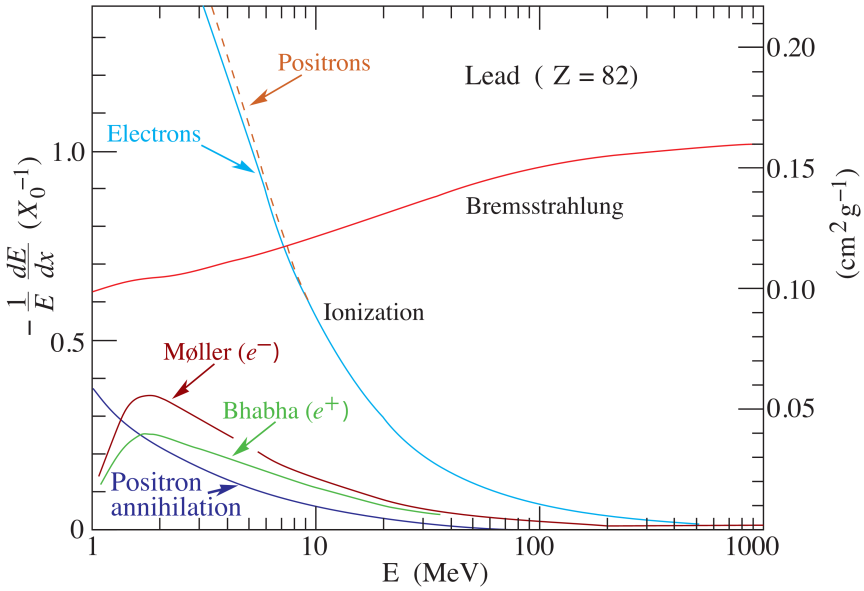

Figure 1.21: Energy loss fraction per radiation length (rigth axis) and mass attenuation coefficient (left axis) of electrons and positrons in a lead absorber (Z=82, $X_0 = 5.82 g/cm^2$, $\rho = 11.342 g/cm^3$) [PDG14].

becomes relevant with an increasing energy loss for lower energies. Nevertheless, compared to the ionization and down to less than 1 MeV even compared to the emission of Bremsstrahlung, the energy loss of positrons by annihilation is significantly lower.

The energy loss of electrons due to ionization can be derived from the first momentum of the MØller cross section [PDG14]:

$$-\frac{dE}{dx} = \frac{1}{2} \cdot K \cdot \frac{Z}{A} \cdot \frac{1}{\beta^2} \left[ln\left(\frac{m_e c^2 \beta^2 \gamma^2 (m_e c^2 (\gamma - 1)/2)}{I^2} \right) + (1 - \beta^2) - \frac{2\gamma - 1}{\gamma^2} ln(2) + \frac{1}{8} \left(\frac{\gamma - 1}{\gamma} \right)^2 - \delta \right] \tag{1.11}$$

With the parameters already described for equation 1.8. This formula is quite similar to the Bethe-Bloch equation for heavy charged particles. Considering that the maximal energy transfer ϵ_{max} in an electron-electron collision is due to the identity of the particles given by half of the kinetic energy of the primary electron, which is at relativistic energies given by $\epsilon_{max} = m_e c^2 (\gamma - 1)/2$, they only differ by $ln(2)$ [PDG14]. For positrons the complete kinetic energy can be transferred. The energy loss for these particles is described by a more complicated expression but finally shows a similar behavior (see fig. 1.21). In general the energy loss of electrons and positrons by ionization can be approximated by $-dE/dx \propto Z \cdot ln(E)$ [PDG14].

Independent of the energy loss due to ionization, an energy loss by the **emission of Bremsstrahlung** occurs when a charged particle is decelerated in the coulomb field of an atomic nucleus. The relative cross section of this process can be approximated as a function of the frequency by [PDG14]

$$\frac{d\sigma}{d\nu} \propto Z^2 \cdot \frac{e^4}{m^2 c^4} \cdot \frac{1}{\nu} \frac{1}{E} \tag{1.12}$$

and the energy loss per length is given for high energies by [CG93]

$$-\frac{dE}{dx} = 4\alpha N_A \frac{Z^2}{A} z^2 \left(\frac{1}{4\pi\epsilon_0} \cdot \frac{e^2}{mc^2}\right)^2 \cdot E \cdot ln\left(\frac{183}{Z^{1/3}}\right) \tag{1.13}$$

with the mass of the particle m and the fine structure constant $\alpha = 1/137$. Due to the $1/m^2$ behavior, the process can be neglected for heavy charged particles, but plays an important role for electrons and positrons. For high energetic electrons this formula can be simplified by introducing the classical electron radius $r_e = e^2/4\pi\epsilon_0 m_e c^2$ to [CG93]

$$-\frac{dE}{dx} = 4\alpha \cdot N_A \cdot \frac{Z^2}{A} \cdot r_e \cdot E \cdot ln\left(\frac{183}{Z^{1/3}}\right) \tag{1.14}$$

With the definition of the radiation length X_0 the energy loss can be described by [CG93]

$$-\frac{dE}{dx} = \frac{E}{X_0} \tag{1.15}$$

The radiation length is a constant, only depending on the atomic number and the nuclear charge of the absorber material. It describes the length after which the energy of an initial electron or positron with energy E_0 is reduced down to E_0/e with Euler´s number e. For Bremsstrahlung emitted only due to interactions with the nucleus it can be directly derived from equation 1.14 to be [CG93]:

$$X_0 = \frac{A}{4\alpha \cdot N_A \cdot Z^2 \cdot r_e^2 \cdot ln(183/Z^{1/3})} \propto \frac{1}{Z^2} \tag{1.16}$$

If the emission of Bremsstrahlung emitted in interactions with the atomic shell is taken into account as well, an additional contribution with an Z proportionality resulting in a replacement of Z^2 by $Z \cdot (Z+1)$ will finally lead to the following formula [CG93]:

$$X_0 = \frac{716,4 \cdot A}{Z \cdot (Z+1) \cdot ln\left(\frac{287}{\sqrt{Z}}\right)} \left[\frac{g}{cm^2}\right] \tag{1.17}$$

For a mixture of elements the inverse radiation length $1/X_0$ can be approximately described by summation of the inverse radiation lengths of the compounds, weighted with the density ρ_i of the single compounds, leading to the expression [CG93]:

$$X_0 = \frac{1}{\sum \frac{\rho_i}{X_0^i}} \tag{1.18}$$

Finally, by solving equation 1.15 the electron energy as a function of the interaction depth can be obtained, only depending on the radiation length X_0 [CG93]:

$$E(x) = E_0 \cdot e^{-\frac{x}{X_0}} \tag{1.19}$$

In addition to the already described effects, fast charged particles also lose energy by emitting **Cherenkov radiation**. If the speed of a particle crossing a medium is larger than the speed

of light in this medium ($v_p > c_n = c_0/n$) it will emit Cherenkov radiation in a forward cone with an opening angle of [JVJ55]:

$$\vartheta = arcos\left(\frac{1}{\beta \cdot n}\right) \tag{1.20}$$

The number of Cherenkov photons with a wavelength λ emitted per traveling distance of a particle with charge z/e in the medium is given by [JVJ55]:

$$\frac{d^2N}{dxd\lambda} = 2\pi \cdot \alpha \cdot z^2 \cdot \left(1 - \frac{1}{\beta^2 \cdot n^2}\right) \cdot \frac{1}{\lambda^2} \tag{1.21}$$

The last equation nicely shows the $\frac{1}{\lambda^2}$ behavior of the emission intensity resulting in a large increase of the amount of Cherenkov radiation emitted in the UV wavelength region. The same behavior is also responsible for the blue glowing of the water in nuclear reactors. The effect of the Cherenkov radiation on the total energy loss is relatively small, but of great interest for detector applications. In addition to the use for particle identification detectors based on Cherenkov radiation, it also adds a small fraction of light to the total light output of inorganic scintillators due to the fast electrons and positrons of the electromagnetic shower. Especially for heavy scintillators with a low light yield, like $PbWO_4$, this has to be considered.

High energetic photons

The interaction of high energetic photons strongly depends on their energies. In principle there are four different effects contributing to the interaction of photons with matter.

The simplest effect is a **coherent scattering** of the photons also known as Raleigh scattering. It can be described as an elastic scattering of photons on individual atoms or molecules with a change of the direction of the light, but without an energy transfer. It is based on the electric polarization of particles. If an electromagnetic light wave is crossing matter, the oscillation of the electric field component initiates an oscillation of the electrons of atoms or molecules with the same frequency, which therefore act as dipoles emitting light of the same frequency in all directions. The cross section σ_R of this process is proportional to $1/\lambda^4$ because the atoms or molecules have to be much smaller than the wavelength of the photons interacting with them. Therefore, Raleigh scattering only occurs at low energies and is relevant for scintillation photons but can be neglected for photons in the MeV range and above.

The dominating effect for low energies is given by the **photo effect**. During a photo effect a primary photon is absorbed by an electron of the atomic shell and transfers its complete energy to this electron which afterwards leaves the atom with a kinetic energy equal to the energy of the primary photon reduced by the binding energy E_B^n of the electron on shell number n [MRR95].

$$E_{kin}^{e^-} = E_\gamma - E_B^n \tag{1.22}$$

After the shell electron has left the atom, the hole is filled by electrons from higher shells under the emission of characteristic x-rays. The cross section of the photo effect shows the largest values for electrons from the inner atomic shells, especially for K-shell electrons, due to the absorption of the recoil momentum by the nucleus. Thus, the effect is also called inner

photo effect. Due to this momentum transfer, the cross section also shows several edges which occur when the photon energy equals the electron energy on a certain shell. Considering this edges the cross section of the Photo effect is given by [MRR95]:

$$\sigma_P = \begin{cases} 4\sqrt{2} \cdot \alpha^4 \cdot \sigma_0 \cdot \frac{Z^5}{\left(\frac{E_\gamma}{m_e \cdot c^2}\right)^{\frac{7}{2}}} \sim \frac{Z^5}{E^{\frac{7}{2}}} & E_\gamma > E_B^{(1)} \\ 1.5 \cdot \alpha^4 \cdot \sigma_0 \cdot \frac{Z^5}{\frac{E_\gamma}{m_e \cdot c^2}} \sim \frac{Z^5}{E_\gamma} & E_\gamma \gg E_B^{(1)} \end{cases} \tag{1.23}$$

with the cross section of the Thomson scattering $\sigma_0 = \frac{8}{3} \cdot \pi \cdot \frac{e^2}{m_e \cdot c^2}$, the electron rest mass m_e, the fine structure constant $\alpha = 1/137$ and the binding energy o the innermost shell $E_B^{(1)}$. The high Z dependence of this cross section can be explained by the self interaction of shell electrons with each other and causes a dominance of the effect especially for high Z elements.

For energies in the order of a few hundred keV up to a few MeV the **Compton effect** becomes dominant. While the photo-effect shows the highest cross sections for inner shells, the Compton effect occurs on the quasi-free electrons of the outer atomic shells. The incoming photon with an energy E_γ undergoes an elastic scattering with the outer shell electron during which a part of the photon energy is transferred to the electron, which afterwards leaves the atom with this energy. The photon with an reduced energy E_γ^* is scattered under an angle ϕ_γ relative to its initial direction. Due to the energy and momentum conservation, the energy of the scattered photon can be calculated by the formula [MRR95]:

$$\frac{E_\gamma^*}{E_\gamma} = \frac{1}{1 + \frac{E_\gamma}{m_e c^2}(1 - cos(\phi_\gamma)} \tag{1.24}$$

The maximal energy transfer will take place if the photon is scattered in backward direction. In this case the energy of the electron is given by [MRR95]:

$$E_e^{max} = \frac{E_\gamma}{1 + \frac{2E_\gamma}{m_e \cdot c^2}} \tag{1.25}$$

The cross section for a single electron can be derived from the Klein-Nishina formula. For complete atoms it is proportional to the number of electrons Z contained in the atom and can be described by [MRR95]:

$$\sigma_C = \begin{cases} \sigma_0 \cdot Z \cdot \left(1 - 2\left(\frac{E_\gamma}{m_e c^2}\right) + \frac{26}{5} \cdot \left(\frac{E_\gamma}{m_e c^2}\right)^2 + ...\right) & E_\gamma < m_e c^2 \\ \frac{\pi \cdot r_e^2 m_e c^2 Z}{E_\gamma}\left(\frac{1}{2} + ln\left(\frac{2E_\gamma}{m_e c^2}\right)\right) \sim \frac{Z}{E_\gamma} & E_\gamma \gg m_e c^2 \end{cases} \tag{1.26}$$

with the cross section of the Thomson scattering $\sigma_0 = \frac{8}{3} \cdot \pi \cdot \frac{e^2}{m_e \cdot c^2}$ and the classical electron radius $r_e \approx 2.818 \cdot 10^{-15} m$.

If the energy of the incoming photon exceeds a certain threshold energy, the **production of an electron positron pair** becomes possible in the Coulomb field of a nucleus. The threshold for this process is given by the rest-mass of an electron and a positron and the energy transferred to the recoil nucleus [MRR95]:

$$E_{thr} = 2m_e \cdot c^2 \cdot \left(1 + \frac{m_e}{m_{nucl}}\right) \tag{1.27}$$

Considering that the mass of the nucleus is much larger than the electron mass ($m_{nucl} \gg m_e$) it reduces to $E_{thr} = 2m_e \cdot c^2 \approx 1.022\ MeV$. The photon energy exceeding this threshold is transferred to the electron positron pair as kinetic energy. Due to the recoil momentum which has to be transferred in this reaction, a recoil object is mandatory. With its high mass, the nucleus is the preferred recoil partner. Nevertheless, the effect is also possible in the field of a shell electron but with a significantly reduced cross-section. The cross section of the pair-production in the field of a nucleus can be given by [MRR95]:

$$\sigma_{pp} = \begin{cases} \sim & Z^2 \cdot ln(E_\gamma) \qquad 5m_e c^2 \leq E_\gamma \leq 50 m_e c^2 \\ & 12\alpha Z^2 r_e^2 \qquad\quad E_\gamma > 10^3 m_e c^2 \end{cases} \tag{1.28}$$

It increases logarithmically after the threshold until it reaches a constant level for high energies. In analogy to the radiation length for the emission of Bremsstrahlung, a similar quantity can by defined for the conversion of photons by pair production. For this purpose one defines the mean free path Λ_p, which is directly connected to the radiation length X_0 by [WRL94]:

$$\Lambda_p = \frac{9}{7} \cdot X_0 \tag{1.29}$$

It describes the length of the material after which the number of primary photons is reduced by a factor $1/e$.

The **total cross** section for high energetic photons is given by the sum of the cross sections of the single processes [MRR95].

$$\sigma_{all} = \sigma_P + \sigma_C + \sigma_{pp} \tag{1.30}$$

A **comparison of the cross sections** of the effects shows that the photo-effect will dominate for high Z materials ($\sigma_P \propto Z^5$) and at low energies. In the medium energy regime around a few MeV and especially for low Z materials ($\sigma_P \propto Z$) the Compton effect will be the dominant process. At higher energies the pair production will dominate all other effects since it is the only effect with a cross section increasing with higher energies and reaching a constant level for very high energies, while all other cross sections are decreasing for an increase in energy. While this behavior is the same for most materials, the exact energies for which an effect becomes dominant strongly depends on the nuclear charge Z of the absorber material. Figure 1.22 shows the attenuation coefficient for high energetic photons and the contributions of the single effects described in the last paragraph for a $PbWO_4$ crystal as absorber material [BHS14]. The attenuation coefficient μ describes the inverse of the length after which the number of photons is reduced by a factor $1/e$ due to interactions with the absorber material. It is directly proportional to the cross section σ_{all} with the atomic density n_{at} as a proportionality factor, which can be expressed with the density ρ, the relative atomic mass A_r and the atomic mass unit u [MRR95]:

$$\mu = n_{at} \cdot \sigma_{all} = \frac{\rho}{A \cdot u} \cdot \sigma_{all} \tag{1.31}$$

Due to this proportionality, the attenuation coefficients shown in figure 1.22 nicely represent the behavior which has been expected for the cross sections of the single effects for a high Z material. Also the edges of the photo effect due to the shell effects are nicely visible.

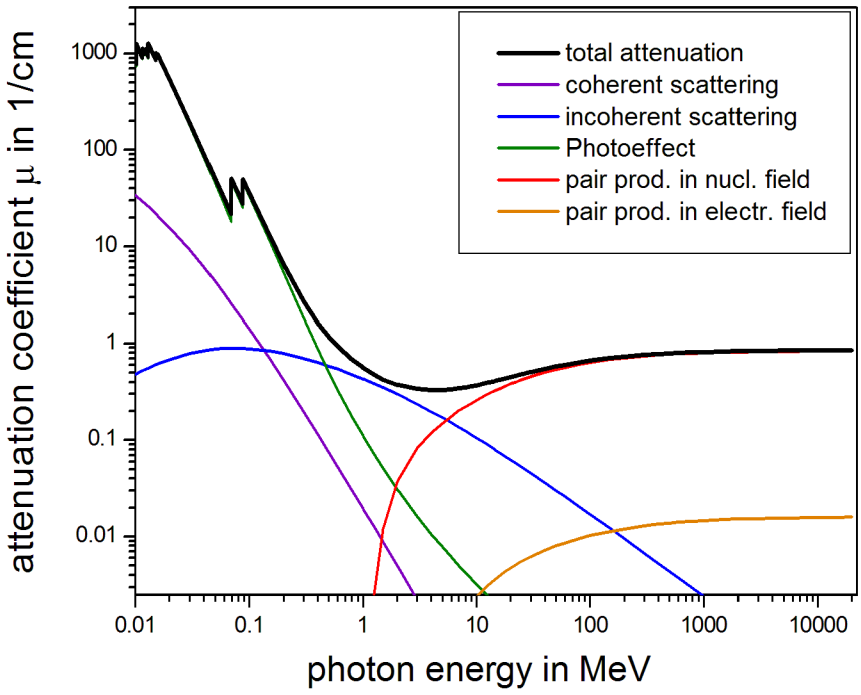

Figure 1.22: Attenuation coefficient of high energetic photons in a lead tungsten crystal ($PbWO_4$). The total cross section is shown by the black line. The cross section of the single contributing effects are represented by the colored lines: photo effect (green), Compton effect (blue), pair production in the Coulomb field of a nucleus and an electron (red and orange) and Raleigh scattering (purple). The data is taken from [BHS14].

The total cross section is first decreasing with increasing energies due to the reduction of the cross sections of the photo- and the Compton- effect and after its minimum at a few MeV increasing again due to the pair production until it reaches the constant level of the pair production cross section at energies of a few hundred MeV.

The attenuation coefficient μ can also be used to describe the exponential reduction of the intensity I_0 of primary photons by interaction processes as a function of the absorber thickness x [CG93]:

$$I(x) = I_0 \cdot e^{-\mu \cdot x} \tag{1.32}$$

Electromagnetic shower development

For energies larger than 10 MeV pair production becomes the dominating interaction process of photons and for even higher energies above 100 MeV it is almost the only process contributing to the total cross section. If such a high energetic photon hits an absorber it will travel a certain distance corresponding on average to the mean free path (see eqn. 1.29) before it undergoes a pair production. The high energetic electron and positron produced on this way continue crossing the material and lose energy by the emission of Bremsstrahlung. If the energy of the emitted photons is high enough, another pair production will take place. This way a cascade with an increasing number of particles will be produced. Figure 1.23 shows a schematic picture of the development of such an electromagnetic shower.

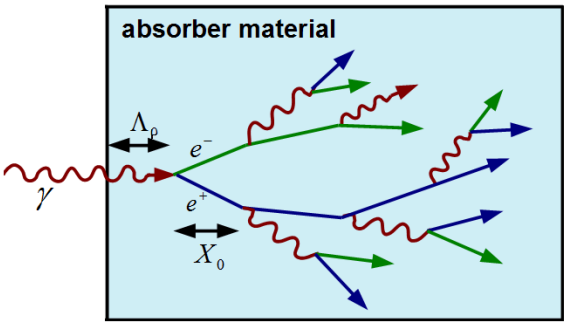

Figure 1.23: Development of an electromagnetic shower. The primary high energetic photon (red) undergoes an pair production after an average distance given by the mean free path (Λ_P). The energy loss of the resulting electron (green) and positron (blue) by the emission of Bremsstrahlung scales with the radiation length X_0.

The development of such a shower continues until the energy of the Bremsstrahlungs photons is below the threshold level for pair production and they are absorbed by a photo effect or until the energy of the electrons and positrons reaches a level at which the energy loss per path length by ionization is more probable than the energy loss by the emission of Bremsstrahlung (see figure 1.21). Since the latter case occurs at higher energies, it defines the formal stopping point of the shower development by the following condition:

$$\left(\frac{dE}{dx}\right)_{brems} \leq \left(\frac{dE}{dx}\right)_{ionization} \tag{1.33}$$

Based on a fit of empirical values a parametrization of this critical energy point can be given for solid and liquid materials by [GB12]:

$$E_C = \frac{610\ MeV}{Z + 1.24} \tag{1.34}$$

and for gases by [GB12]:

$$E_C = \frac{710\ MeV}{Z + 0.92} \tag{1.35}$$

For energies significantly larger than the critical energy, the energy loss by the emission of Bremsstrahlung is dominating the energy loss by ionization, thus the energy loss of the electrons and positrons can be described by equation 1.15 and the radiation length X_0 (see equation 1.17) can be taken as a scaling parameter for this process. Since the mean free path of the pair production can also be expressed in terms of the radiation length ($\Lambda_p = 9/7 \cdot X_0$), this parameter can be used as a basic unit for the shower scaling in longitudinal direction. The position of the shower maximum x_{max} for an initial energy E_0 in longitudinal direction is given approximately by the following expressions for photons and electrons as a function of the critical energy E_C and the radiation length X_0 [LR09]:

$$x^{\gamma}_{max} = \left[1.01 \cdot ln\left(\frac{E_0}{E_C}\right) - 0.505\right] \cdot X_0 \qquad x^{e}_{max} = \left[1.01 \cdot ln\left(\frac{E_0}{E_C}\right) - 1.01\right] \cdot X_0 \tag{1.36}$$

The two equations nicely show the logarithmic behavior of the shower scaling as a function of the initial energy. The difference between photons and electrons can be explained by the circumstance that an initial photon first travels a distance according to its mean free path length until it undergoes the first pair production, while an initial electron directly starts with the emission of Bremsstrahlung, which leads to a shift of the shower. The center of gravity on the longitudinal shower axis is directly correlated with the shower maximum and given by [LR09]:

$$x_{cg}^{\gamma} = x_{max}^{\gamma} + 1.7 \cdot X_0 \qquad x_{cg}^{e} = x_{max}^{e} + 1.4 \cdot X_0 \tag{1.37}$$

Like for the shower maximum also the center of gravity is reached earlier if the shower is initiated by electrons. The main application of the formula for the shower maximum is the approximation of the shower length, exploiting that 98 % of the shower energy are deposited within $2.5 \cdot x_{max}$ [CG93]. The longitudinal shower profile can be described with $t = x/X_0$ as [LS75, LL85]:

$$\frac{dE}{dt} = E_0 \cdot \frac{(\beta \cdot t)^{\alpha-1} \cdot \beta}{\Gamma(\alpha)} \cdot e^{-\beta \cdot t} \tag{1.38}$$

with the constants $\beta \approx 0.5$ and $\alpha \approx= \beta \cdot x_{max}/X_0$ which show a logarithmic energy dependance and have to be determined individually for each detector material.

In transverse direction the spread of the shower at high energies ($E \gg E_C$) is mainly influenced by the angular distribution of the emitted Bremsstrahlungs photons and by multiple scattering of the electrons and positrons [CG93]. For low energies the angular distributions of the photo effect and of the Compton effect also have to be considered, which can be neglected for $E \gg E_C$ [CG93]. The scaling of the transverse spread of the shower can be described by the Molière-Radius R_M, which describes the transverse spread of the shower during a distance of one radiation length X_0 in longitudinal direction. It is directly correlated to the radiation length and the critical energy and can be calculated by [CG93]:

$$R_M = \frac{21.2\ MeV}{E_C} X_0 \approx \frac{7 \cdot A}{Z \cdot \rho} \tag{1.39}$$

with the nuclear charge Z, the mass number A and the density ρ. The Molière-Radius can be used as a material independent unit for the description of the shower spread. Within a cylinder of radius $r = R_M$ on average 90 % of the total shower energy is contained, while a cylinder with a radius of $2 \cdot R_M$ already contains 95 % of the shower energy and within a radius of $3.5 \cdot R_M$ almost 99 % of the shower is covered [PDG14]. The shower profile in transverse direction can be parametrized as a function of the distance r to the shower axis by [ACH05]:

$$\frac{dE}{dr} = A_1 \cdot e^{-\frac{r}{\lambda_1}} + A_2 \cdot e^{-\frac{r}{\lambda_2}} \tag{1.40}$$

with constants A_1, λ_1 and A_2, λ_2 which have to be determined for each calorimeter individually. The two addends of this formula reflect the different behavior of the high energetic center of the shower and the low energetic reactions in the outer shower regions which lead to a tail of the transverse shower profile.

Figure 1.24 illustrates a typical longitudinal and transverse shower profile in a cesium iodide crystal for different energies between 100 MeV and 2 GeV [HK85].

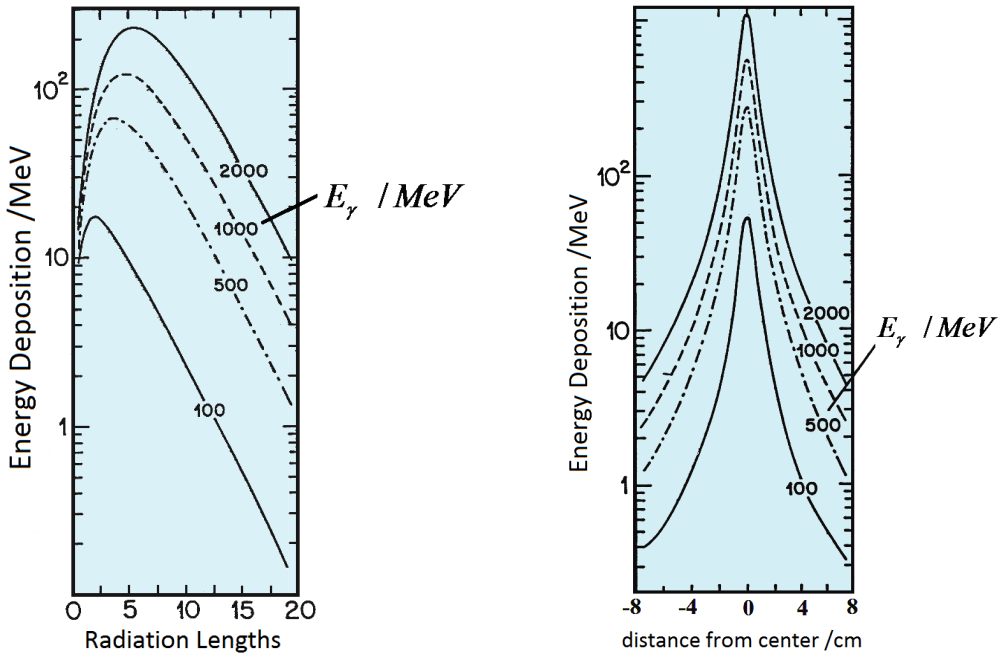

Figure 1.24: Longitudinal (left) and transverse (right) shower profile in a cesium iodide crystal for different energies between 100 MeV and 2 GeV. The picture is modified from [HK85].

The figure shows that most of the shower energy is deposited in the first part of the shower in longitudinal direction and in the center of the shower for transverse directions. Nevertheless, it is important to detect the complete shower if possible, because the shower shape shows large fluctuations for single events, especially at low energies, which finally lead to a significant smearing of the detected energy if only a part of the shower is detected in longitudinal or transverse direction.

1.3.2 Comparison of different calorimeter concepts

In the last section it has been shown how the energy of primary high energetic particles, especially photons and electrons, is absorbed in matter. To measure this energy an active medium is needed in which the complete or at least a part of the energy is deposited and converted into a measurable signal. Based on this one separates two types of calorimeters. On the one hand homogenous calorimeters in which the complete energy is deposited in the active medium and on the other hand sampling calorimeters in which heavy materials are used as converters for primary particles and the energy is only measured partially in active sampling parts. The following section will discuss the basic concept of the different electromagnetic calorimeter types, compare their advantages and disadvantages and show examples how they can be realized.

Homogeneous calorimeters

In the case of homogeneous calorimeters the complete detector consists of a high Z active material which at the same time acts as absorber medium for the incoming radiation. The active material which produces the measurable signal out of the deposited energy can be based in general on three effects, the emission of Cherenkov light, the emission of scintillation light and the production of free electrons by ionization.

Active absorbers based on the **Cherenkov effect** use the fact that charged particles emit light when they pass a medium with a velocity larger than the speed of light in the medium (see also section 1.3.1). Since an electromagnetic shower contains a lot of relativistic electrons, Cherenkov light is emitted when they travel inside the medium in addition to the emission of Bremsstrahlung. The Cherenkov light which is in the visible and UV range can be detected with photo-sensors attached to the active medium. The amount of emitted Cherenkov light is proportional to the total distance all electrons and positrons travel inside the medium and therefore proportional to the energy of the incoming photon or electron. The advantage of such calorimeters is the nearly instantaneous emission of the Cherenkov light which provides a fast response. In the past such a calorimeter has been realized with modules made of lead glass (55 % PbO, 45 % SiO_2) in the OPAL experiment, which showed resolutions of around $5\,\%/\sqrt{E/GeV}$ [PDGdet14]. In addition to this worse resolution, caused by the low intensity of the Cherenkov light per deposited energy unit, also linearity problems of the energy response have been observed [ST99].

The second option are active absorbers based on the **scintillation effect**. Such calorimeters normally consist of units made of inorganic scintillation crystals like thallium doped cesium iodide (CsI:Tl), lead tungstate ($PbWO_4$) or bismuth germanate (BGO). If radiation hits such crystals, the electrons of the band structure are excited and fall back to the ground state in several steps under the emission of scintillation light. The amount of emitted scintillation photons is proportional to the incoming energy with a good linearity of the energy response. The scintillation light which is commonly in the visible range can be detected with commercial photo-sensors. Due to the high intensity of this light compared to the Cherenkov light, such calorimeters show an excellent energy resolution of typically $(2-3)\%/\sqrt{E/GeV} \oplus (0.5-1.4)\%$ [PDGdet14]. In addition to this, the high Z elements contained in the inorganic crystals provide a high stopping power for electromagnetic probes with short radiation lengths, enabling a compact design of the calorimeter. The main disadvantage of such calorimeter is given by the high costs for the production of the large volume crystals.

The third option are calorimeters based on **ionization** which consist of an active volume filled with liquid noble gases (i.e. Ar, Kr, Xe). The radiation which passes this volume ionizes the gas and the produced electrons can be collected on electrodes by an electric field. The number of electrons and therefore the charge collected on the electrodes is proportional to the energy of the incoming radiation, if it is completely absorbed in the active volume. Due to the low density and low Z of the gases, such calorimeters show a quite high radiation length which makes them inefficient for the detection of high energetic photons or electrons and causes the need for large detector volumes. The liquid krypton calorimeter of the NA48 experiment for example has a length of $27X_0$, resulting in an acceptable energy resolution of $3.2\%/\sqrt{E/GeV} \oplus 0.42\% \oplus 0.09\%/(E/GeV)$ [PDGdet14]. Another disadvantage of this calorimeter type is the high operational costs for the gases and their cooling.

Sampling calorimeters

For sampling calorimeters the absorber medium and the active medium are split up into two components. For the absorber medium cheap high Z elements like lead, iron or tungsten can be taken, while the active component can use the same materials and principles like homogeneous calorimeters.

While calorimeters based on the ionization of noble gases have the disadvantage of a low stopping power if they are used as homogenous calorimeters, this disadvantage can be neutralized by intersecting the gas volume with a passive high Z absorber material. A possible realization of such a principle would be the use of alternating lead layers and flat ionization chambers or the integration of the absorber layers for example as electrodes in one large ionization chamber. A setup based on ionization has been used for example in the liquid Argon calorimeter of the ATLAS experiment with an "accordion" structure of lead layers and ionization chambers, providing an energy resolution of $10\%/\sqrt{E/GeV} \oplus 0.4\% \oplus 0.3\%/(E/GeV)$ [PDGdet14].

For sampling calorimeters based on scintillation detectors, in principle two concepts exist. The first is like for the ionization chambers given by alternating layers of a high Z absorber material and active scintillator layers. Since the stopping of the incoming radiation is provided by the absorber material, there is no need for expensive high Z scintillation crystals. Cheaper low Z organic plastic-scintillators can be used as an active material. However, due to a better radiation resistance and a higher light yield also concepts using inorganic scintillators are currently under investigation [BDG14]. For the readout of such a scintillating tile calorimeter and especially for the light transportation to the photo-sensor also different concepts exist. In a first concept the light is transported to the photo-sensor on the side or in the corners of the modules with wavelength shifting light guides or fibers coupled to the scintillating tiles (see figure 1.25 (left)). The disadvantage of this method is the existence of a region with a low Z material in between the modules which causes inhomogeneities in the energy response. This problem can be solved or at least reduced by using single wavelength shifting (WLS) fibers inserted through holes drilled through the module in longitudinal direction, which are read out by a photo sensor at the end of the module. This concept is known as a shashlyk-calorimeter. A schematic drawing of such a calorimeter is shown in figure 1.25 (right).

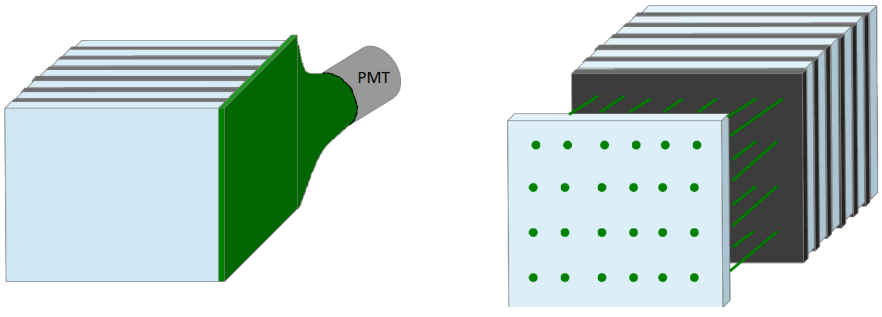

Figure 1.25: Left picture: Schematic drawing of a scintillating tile calorimeter with the scintillator tiles (blue), the absorber plates (gray) and the wavelength shifting light guide on the side of the module (green). Right picture: Schematic drawing of a shashlyk calorimeter with the absorber plates (gray), the scintillator tiles (blue) and the WLS fibers (green). The photo sensor is placed on the rear side of the module.

Due to the typically low light yield per MeV most of the calorimeters exploiting this concept are optimized for high energy physics experiments. One of the state of the art shashlyk calorimeter has been developed for the COMPASS experiment at CERN showing typical energy resolutions of $4.8\%/\sqrt{E/GeV} \oplus 0.1\%$ for energies larger than 1 GeV [VP06]. The only existing shashlyk calorimeter optimized for energies in the MeV range, starting with a threshold of 50 MeV, was developed for the KOPIO experiment, with typical energy resolutions of $2.7\%/\sqrt{E/GeV} \oplus 2\%$ for the latest prototypes [GSA08].

Another concept differing from the principle of scintillating tiles is given by a spaghetti-calorimeter. In this concept the absorber material consists of a massive block of a high Z material in which inorganic scintillating fibers are inserted through homogeneously distributed longitudinal holes (see figure 1.26).

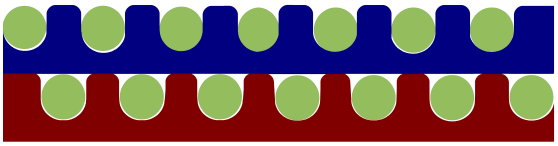

Figure 1.26: Schematic cross section of a Spaghetti calorimeter module of the H1 SpaCal. The green circles represent the fibers which are inserted in the holes of the surrounding absorber material (blue and red). The layers are shifted against each other to achieve a better homogeneity. Picture modified from [H197].

The fibers which are read out by a photo-senor at the rear side of the module act as an active medium and provide the light transportation at the same time. While such a calorimeter shows a quite fast response it has the great disadvantage of a strong inhomogeneity of the energy response if a particle hits the fibers directly. The concept has been applied in the past for the H1 SpaCal at DESY providing an energy resolution of $7.1\%/\sqrt{E/GeV} \oplus 0.6\%$ [H197]

Energy-, position-, and time resolution of electromagnetic calorimeters

After different concepts of electromagnetic calorimeters and their typical energy resolution have been presented in the last section, this section will focus on the factors which influence the energy-, position-, and time resolution of homogeneous and sampling electromagnetic calorimeters. The descriptions will focus on calorimeters based on scintillators, but can be made in an analogue way for calorimeters based on ionization.

Energy Resolution

The basis for an energy measurement with an electromagnetic calorimeter is the amount of energy deposited by the electromagnetic shower inside the active medium. This energy is directly proportional to the trace length $L \propto E_0/E_C$ of all charged shower particles within the active medium [CG93]. Under real conditions, shower particles can only be detected up to a certain minimal energy $\epsilon_{min} \ll E_0$ leading to a reduction of the measurable trace length of the shower particles L_{mess} which can be expressed by [CG93]:

$$L_{mess} = K(\epsilon_{min}) \cdot \frac{E_0}{E_C} \cdot X_0 \quad \propto \quad E_0 \tag{1.41}$$

with

$$K(\epsilon_{min}) = \left[1 + \frac{2.29 \cdot \epsilon_{min}}{E_C} \cdot ln\left(1.50 \cdot \frac{\epsilon_{min}}{E_C}\right)\right] \cdot e^{2.29 \cdot \frac{\epsilon_{min}}{E_C}} \tag{1.42}$$

The equation shows that also for this case the proportionality to the initial energy is conserved. Even if only a part of the shower is detected, for example in a sampling calorimeter, this assumption is still true which is an important condition for the linearity of the energy response. Since the number of photons produced by the scintillation process and the signal created by commonly used photo-sensors also show a linear proportionality, this assumption can be still made for the finally detected signal.

In the ideal case of a **homogeneous electromagnetic calorimeter** almost the complete energy is deposited in the active calorimeter medium. Therefore, in this case only the fluctuations of the energy deposition in the shower itself give a contribution to the intrinsic energy resolution $\sigma(E)_{intr.}$ of the shower. This fluctuations are a direct result of the variation of the net track length of the charged shower particles which can be described with Poisson statistics. They typically give a contribution of [RKB98]:

$$\left(\frac{\sigma(E)}{E}\right)_{intr.} \approx \frac{0.5\%}{\sqrt{E/GeV}} \tag{1.43}$$

In addition to this shower fluctuations there are different other statistical processes like the statistics of the scintillation process, the light absorption in the crystal and the detection of the light in the photo-sensor which contribute to the energy resolution of the calorimeter. Since all of this processes are of statistical nature, they can be summarized in the statistical term of the energy resolution

$$\left(\frac{\sigma(E)}{E}\right)_{stat.} = \frac{a}{\sqrt{E}} \tag{1.44}$$

with a constant a including all the contributing effects. The contribution of the photon statistics strongly depends on the light yield of the used scintillator and internal quenching effects during the scintillation process. Together with the other processes the typical contribution of these effects to the statistical term of the energy resolution of a homogenous electromagnetic calorimeter is in the order of $(2-3)\%/\sqrt{E}$ and therefore dominates the contribution of the intrinsic shower fluctuations.

For a **sampling calorimeter** in principle the same considerations can be made, but it has to be considered that only a part of the primary energy is deposited in the active medium, while the other part is lost in the absorber material, causing a reduced statistics of the scintillation photons which directly leads to a worsening of the energy resolution compared to homogenous calorimeters. Since the fraction of the energy deposited in the active medium also fluctuates from event to event, this statistical "sampling fluctuations" provide an additional factor which deteriorates the energy resolution of such a calorimeter.

For a calorimeter consisting of alternating active and passive layers (see figure 1.27), the number of crossing points N between shower particles and active layers can be expressed as a function of the trace length of the shower particles and the effective distance d_{eff} between two absorber layers [CG93].

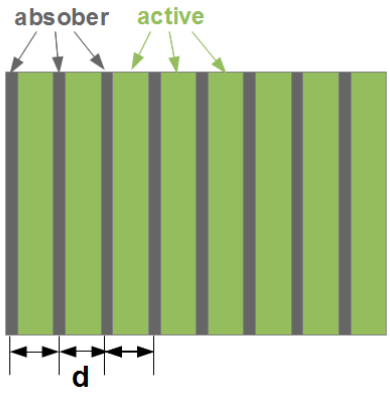

Figure 1.27: Schematic view of a sampling calorimeter consisting of alternating active (green) and passive (gray) layers. The distance d is shown for the first 3 layers.

$$N = \frac{L_m}{d_{eff}} \tag{1.45}$$

with $d_{eff} = d/cos(\vartheta)$ averaged over all angles ϑ between shower particles and shower axis.

Based on this formula and Poisson statistics the contribution of the intrinsic shower fluctuations to the relative energy resolution can be expressed as [CG93]

$$\frac{\sigma(E)}{E} = \frac{\sqrt{N}}{N} = \sqrt{\frac{E_C \cdot d_{eff}}{K(\epsilon_{min}) \cdot X_0 \cdot E_0}} \propto \sqrt{\frac{d}{\langle cos(\vartheta) \rangle}} \cdot \frac{1}{\sqrt{E}} \tag{1.46}$$

This expression shows that it is advantageous for the energy resolution to reduce the distance d between the absorber layers by using thin layers. On the other side thin active and passive layers can cause additional Landau-fluctuations due to a strong variation of the energy loss of the minimum ionizing shower electrons in ionization processes (see equation 1.9) and of the ionizing collisions itself. The contribution of this effect to the relative energy resolution can be expressed with the average energy loss per detector layer ΔE and a constant k by [CG93]:

$$\left(\frac{\sigma(E)}{E}\right)_{Landau} \propto \frac{1}{\sqrt{N} \cdot ln(k \cdot \Delta E)} \propto \frac{1}{\sqrt{E_0}} \tag{1.47}$$

Due to their statistical nature the Landau-fluctuations also give a contribution to the $1/\sqrt{E}$ term of the energy resolution, which can be reduced by increasing the average energy loss ΔE in the single layers. Therefore, a trade-off between sampling fluctuations and Landau-fluctuations has to be found for the optimization of the layer thickness. Together with the statistical contribution described for homogenous calorimeters this contributions cause a typical statistical term for sampling calorimeters of $\geq (3-4)\%/\sqrt{E}$ up to around $\geq 20\%/\sqrt{E}$ for calorimeters with thick absorber layers, optimized for a high stopping power.

The second contribution to the energy resolution of homogeneous and sampling electromagnetic calorimeters is given by instrumental effects of the photo-sensor and the readout electronics. This can be for example statistical noise contributions or fluctuations of the baseline.

In general, such contributions depend for example on the signal to noise ratio and are therefore energy dependent. They normally show the following proportionality:

$$\left(\frac{\sigma(E)}{E}\right)_{instr.} \propto \frac{1}{E} \tag{1.48}$$

This contribution especially plays a role for low gain photo-sensors with a bad signal to noise ratio. While it gives an important contribution for example for an Avalanche Photo Diode (APD) based readout, it can normally be neglected for a PMT readout due to the high gain and low intrinsic noise of this devices.

The last important contribution to the energy resolution is caused by a non-uniformity in light collection or production, non linearity effects of the photo-sensor, the electronics or the Analogue to Digital Converter (ADC) and calibration errors. The contribution of this effects to the relative energy resolution is energy independent and can be expressed as

$$\left(\frac{\sigma(E)}{E}\right)_{sys.} = const. \tag{1.49}$$

The different terms contributing to the total energy resolution have to be added quadratically ($\oplus$). Therefore, the total energy resolution of both electromagnetic calorimeter types can be expressed by:

$$\frac{\sigma(E)}{E} = \frac{a}{E} \oplus \frac{b}{\sqrt{E}} \oplus c = \sqrt{\frac{a^2}{E^2} + \frac{b^2}{E} + c^2} \tag{1.50}$$

with constants a, b, c depending on the factors described in this paragraph. In addition to the described contributions, longitudinal and lateral leakage of the electromagnetic shower and losses due to a non hermetic coverage can also influence the energy resolution. Such effects mainly occur at high energies but can become dominant in this region due to the small impact of the statistical term.

Position resolution

The reconstruction of the interaction point of photons in the electromagnetic calorimeter is the only possibility for an effective determination of the azimuthal and polar angle of their path, which are mandatory for the calculation of invariant masses. Therefore, the position resolution of the electromagnetic calorimeter gives an important contribution to the reconstruction of decay channels which contain photons in the final state. The basis for a position reconstruction in an electromagnetic calorimeter is its spatial segmentation in single units with an individual readout. In this case, the upper limit of the position resolution is determined by the size of one unit. This upper limit is especially important for very low energies at which no or only a very artificial shower development can be observed. At higher energies ($E \gg E_C$) with a proper shower development, the position resolution can be further improved by calculating the center of gravity of the shower. For this purpose the size of a single calorimeter unit should be not significantly larger than one Molière-Radius to ensure a shower spread over several detector units and to guarantee a separate detection

of different photons or particles hitting the calorimeter close to each other. Of course, for smaller detection units the position resolution will improve, but at the same time the energy depositions and therefore the scintillation light output of each unit will decrease and the costs for the individual readout of each unit will increase. As a trade-off one Molière-Radius is used as a good compromise for most calorimeters.

The most simple method to extract the position information is given by the center of gravity with a linear weighting

$$x_{lin} = \frac{\sum_i E_i \cdot x_i}{\sum_i E_i} \tag{1.51}$$

with the energy E_i and the center x_i of the individual detection units. The disadvantage of this method is given by the fact that most of the energy is deposited in the central module which therefore dominates the surrounding module in which a significantly smaller part of the energy is deposited. This leads to a discrepancy between the reconstructed and the real interaction position, which has to be corrected by an empirical correction function [GAA77].

A better method can be obtained if the transverse shower profile (see equation 1.40) is taken into account. The exponential decrease of the shower in transverse direction can be considered by using a logarithmic weighting of the relative energy fraction in the single modules. With this modification the center of gravity algorithm can be expressed as [TCA92]

$$x_{ln} = \frac{\sum_i \omega_i \cdot x_i}{\sum_i \omega_i} \tag{1.52}$$

with

$$\omega_i = \left\{ \begin{array}{ll} 0 & \text{if } W_0 + ln\left(\frac{E_i}{E_{sum}}\right) \leq 0 \\ W_0 + ln\left(\frac{E_i}{E_{sum}}\right) & \text{else} \end{array} \right\} \tag{1.53}$$

and the cluster energy $E_{sum} = \sum E_i$. The threshold parameter $W_0 = ln(E_{thr}/E_{sum})$ represents the logarithm of the energy fraction of the single crystal threshold.

The resolution of the reconstructed position is proportional to the fluctuation of the energy deposited in the single units. Since this energy becomes higher for larger initial photon/ electron energies the statistical fluctuations in the single units are reduced for higher energies. In addition for higher energies, more modules are above the threshold and therefore contribute to the center of gravity algorithm. Besides these statistical effects, the position resolution is also influenced by energy independent contributions like calibration errors and a lateral non-uniformity of the energy response. Altogether the following parametrization can be made for the position resolution:

$$\sigma_x = \frac{a_x}{\sqrt{E}} \oplus b_x = \sqrt{\frac{a_x^2}{E} + b_x^2} \tag{1.54}$$

with constants a_x and b_x. With the described position reconstruction methods position resolutions which are significantly better than the size of one single unit can be obtained, especially for high energies.

Time resolution

In general the time resolution of the calorimeter is especially important for time of flight measurements of e^+/e^-, relative to a start detector. In the case of PANDA it is also important for a relative timing of the single detectors since no trigger detector will be used. The main factors which influence the time resolution are the type of the active medium and in case of scintillators also the photo sensor. In addition to this the signal processing and treatment make an important contribution. For scintillators as active medium the time resolution can be defined as the spread of the arrival time of the first photon or for practical application as the spread of the arrival time of a certain number of photons causing the signal to exceed a certain threshold level. Therefore, especially the rise time of the scintillation signal, the light yield of the scintillator, the size/ shape of the scintillator and the timing characteristics of the photo sensor play an important role since these parameters directly influence the spread in the timing of the rising edge of the signal. The increase of the number of scintillation photons for higher energies cause an improvement of the timing statistics and therefore also an improvement of the statistical term of the time resolution. In addition to these statistical terms, contributions like the spread of the travel time of the photons in the scintillator or of the electrons in the photomultiplier tube, but also the time spread caused by the readout electronics are energy independent and therefore have to be expressed in form of a constant term. The two contributions lead to the following parametrization of the time resolution with constants a_t and b_t, showing a similar shape like the position resolution.

$$\sigma_t = \frac{a_t}{\sqrt{E}} \oplus b_t = \sqrt{\frac{a_t^2}{E} + b_t^2} \tag{1.55}$$

1.3.3 Requirements for the PANDA electromagnetic calorimeters

The decision which calorimeter concept provides the best performance for an individual detector setup and its physics goals is a project specific decision under consideration of the individual requirements and the budget and time lines of the detector project. The following section will present the requirements which have been taken into account for the PANDA electromagnetic calorimeters.

property	target EMC	forward spectrometer EMC
energy resolution σ_E/E	$\leq 1\% \oplus \frac{\leq 2\%}{\sqrt{E/GeV}}$	$1\% \oplus \frac{2-3\%}{\sqrt{E/GeV}}$
energy threshold (for incoming photon)	10 MeV (20 MeV)	10 MeV (20 MeV)
single crystal / module threshold	3 MeV	3 MeV
single crystal / module noise $\sigma_{Noise}{}^*$	1 MeV	1 MeV
horizontal angular coverage	$>10°$	0° - 10°
vertical angular coverage	$>5°$	0° - 5°

Table 1.2: Overview over the basic requirements of the PANDA target and forward electromagnetic calorimeters [TDe09, TDf15]. (*energy equivalent)

To achieve the physics goals, the requirements listed in table 1.2 have been fixed in the PANDA Technical Design Reports (TDR) for the electromagnetic calorimeter of the target spectrometer [TDe09] and for the forward shashlyk calorimeter [TDf15].

Energy resolution

The energy resolution is a crucial parameter for the PANDA EMC since it directly influences the error of the invariant mass determination, for example for J/Ψ states. In addition, a good energy resolution is needed for the determination of the E/p ratio of electrons and positrons and for the identification of light mesons like π^0 and η which contribute significantly to the background events [TDe09]. For the target as well as for the forward spectrometer the resolution limit at high energies and therefore the constant term is directly determined by the aim to distinguish electrons and positrons from pions over their E/p ratio. Since the tracking detectors provide a momentum resolution of approximately 1% also the constant term of the EMC should be at least in this region to avoid a deterioration of the E/p ratio by the energy measurement [TDe09]. At low energies previous experiments showed that a width of a reconstructed π^0-meson of less than 8 MeV/c^2 and a η width of less than 30 MeV/c^2 are desirable for their identification. [TDe09]. To achieve this requirement a statistical term of 2 % is needed in the target spectrometer [TDe09]. In the forward spectrometer this value can be increased up to 2-3 % due to the higher energies provided by the Lorentz boost of the collision products [TDf15].

Energy threshold

The energy threshold of the calorimeter is especially important for the reconstruction of low energetic photons. Since many of the background channels contain such low energetic photons a proper reconstruction and rejection of this background events is only possible if all of the photons are detected. Considering the physics program of PANDA many interesting channels especially in the field of charmonium physics have a production ratio which is significantly lower than the expected background contribution. Therefore, a study of those channels is only possible with an efficient background rejection. However, the low energetic threshold is limited by different factors like the electronic noise of the single channels and the distribution of the deposited energy at very low energies. Therefore, a threshold of 10 MeV or in the worst case 20 MeV is a reasonable goal for the target as well as for the forward shashlyk EMC [TDe09, TDf15]. Simulations showed that for a threshold of 10 MeV only 1 % of the π^0-mesons cannot be reconstructed, while for a 30 MeV threshold this number increases to 10 % [TDf15]. The requirement of a detection threshold of 10 MeV for the calorimeter directly leads to a single crystal threshold of 3 MeV since in the worst case the incoming photon or electron deposits its energy in between 4 modules, which leads to a single module energy deposition of 2.5 MeV. Since this case is very unlikely, a single crystal threshold of 3 MeV is sufficient to realize a total threshold of 10 MeV in most of the cases.

Angular coverage

A full coverage of the complete solid angle is required especially for the background rejection, since background particles like neutral pions can only be reconstructed and rejected if both

decay photons are detected by the EMC. This becomes especially crucial for background channels with several photons in the final state. However, a full 4π coverage is not possible due to the beam pipe and due to other mechanical reasons. Therefore, at least a 99 % 4π coverage in the center of mass frame is envisaged [TDe09].

Special requirements for the sub parts of the EMC

In addition to this general requirements, the sub parts of the calorimeter have to fulfill specific requirements, which are listed in table 1.3.

specific property	backward part $\geq 140°$	barrel part $22° \leq \theta < 140°$	forward part $5° \leq \theta < 22°$	shashlyk EMC $0° \leq \theta < 5°$
energy range from E_{thr} to	0.7 GeV	7.3 GeV	14.6 GeV	15 GeV
spatial resolution σ_θ	0.5° (4.8 mm)	0.3° (3.0mm)	0.1° (3.5mm)	0.025° (3.5mm)
max. hit rate per detector	100 kHz	100 kHz	500 kHz	≈1 MHz
shaping time	400 ns	400 ns	100 ns	-
rad. hardness (dose per year)	10 Gy	10 Gy	125 Gy	1000 Gy

Table 1.3: Specific requirements for the sub parts of the PANDA target and forward electromagnetic calorimeters [TDe09, TDf15]. For the forward shashlyk EMC the PMT signal will be used directly without shaping and the annual dose is given for the region close to the beam pipe.

Dynamic energy range

To determine the energy range which has to be covered by the single parts of the calorimeter, a simulation of the photon energy distribution has been performed with a DPM[4] based event generator [TDe09, TDf15]. The results for the maximal antiproton energy of 15 GeV are shown in figure 1.28. The figure shows that the highest photon energies up to 15 GeV have to be handled in the forward spectrometer while the maximum photon energy decreases for larger angles like it can be expected for a fixed target experiment. Especially for the forward end cap of the target spectrometer a large variation of the maximal photon energy occurs between the inner and the outer regions. A similar case can be observed between the forward and the backward regions of the barrel part, while the backward end cap only has to detect photons up to a few hundred MeV. The right part of figure 1.28 also illustrates that even in the forward region the detection of low energetic photons down to the threshold level plays an important role.

Spatial resolution

The required spatial resolution can be approximated by looking at the requirement of a neutral pion signal width of less than 8 MeV/c^2. Simulations showed that a resolution of $\leq 0.1°$ for the forward end cap, $\leq 0.3°$ for the barrel part and $\leq 0.5°$ for the backward end cap are needed to fulfill this requirement [TDe09]. In the forward spectrometer the minimal opening angle of the two photons from a π^0-decay is only around 1°. Simulations showed that due

[4]Dual Parton Model: Theoretical model for the simulation of antiproton - proton collisions.

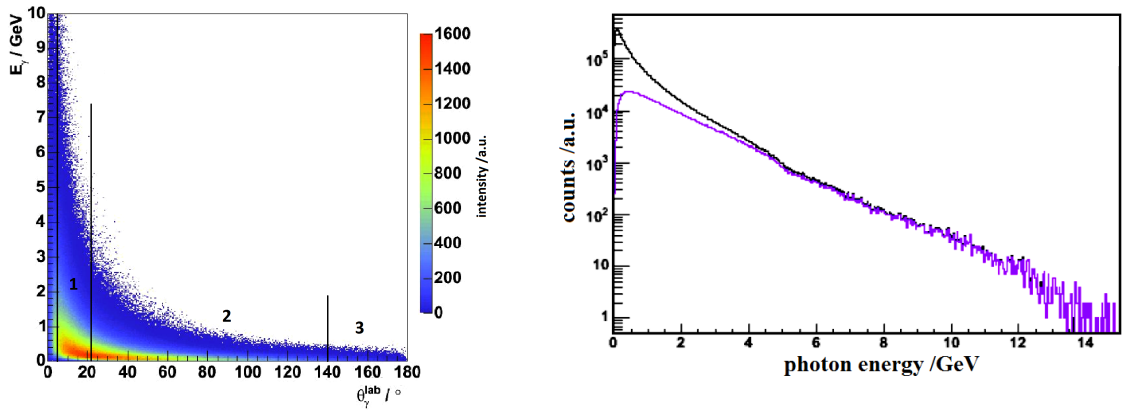

Figure 1.28: Photon energy distribution of the PANDA electromagnetic calorimeters for an anti-proton energy of 15 GeV simulated with a DPM generator. Left: Photon energy vs. laboratory angle for the complete PANDA detector with the Forward spectrometer below 5°, the forward end cap of the target spectrometer (1), the barrel part of the target spectrometer (2) and the backward end cap (3) (fig. modified from [TDe09]). Right: Intensity vs. photon energy for an anti-proton energy of 15 GeV for the forward spectrometer (purple) and for the complete detector (black) (fig. modified from [TDf15]).

to the large distance between the calorimeter of the forward spectrometer and the collision point of 8 m, a position resolution of 3.5 mm (0.25°) at 15 GeV is sufficient [TDf15]. Since the opening angles of the photons from the π^0 become larger for lower energies, an increase of this values with $1/\sqrt{E}$ is acceptable.

Rate capability and shaping time

To determine the hit rate of the calorimeter another simulation has been made with the DPM generator [TDe09, TDf15]. These simulations showed for the barrel and backward part hit rates of 60 kHz with proton targets and up to 100 kHz for heavier targets [TDe09]. For the forward end cap rates up to 500 kHz have been observed for the inner regions, decreasing with the distance to the beam pipe [TDe09]. In the forward spectrometer rates up to 1 MHz can be reached for the modules close to the beam pipe while in the outer regions the hit rate decreases down to around 300 kHz [TDf15]. To handle these rates, a fast scintillator material and a fast readout are needed, especially in the forward spectrometer. In addition, the shaping time has to be as low as possible to avoid pile-up. Nevertheless, a longer shaping time improves the noise level. Therefore, a compromise between the acceptable pile-up and the noise level is needed. If a sampling ADC is used for the readout, many of the pile-up events can be recovered, which makes a pile up rate of 10 % acceptable [TDe09]. Under these conditions a shaping time of 100 ns for the forward end cap and even 400 ns in the barrel and backward part of the EMC can be applied [TDe09].

Radiation hardness

Since PANDA is a fixed target experiment most of the scattering fragments will be boosted in forward directions. Therefore, the radiation doses will also reach significantly increased

values in this region. In the case of heavier targets a high rate of hadrons and especially neutrons has to be considered as well. Simulations showed that for the forward spectrometer a dose of 25 rad/h, corresponding to approximately 1 kGy per year has to be expected for the modules close to the beam axis [TDf15]. In the forward end cap of the target spectrometer a dose of 125 Gy/a can be expected wile the barrel and the backward part will only be exposed to an annual dose of less than 10 Gy [TDe09]. For proton targets the dose of the backward end cap is even significantly lower (0.15 Gy/a) [TDe09].

Additional requirements

In addition to the performance requirements described in the last section, the calorimeter of the target spectrometer also has to be as compact as possible to reduce the costs for the solenoidal magnet which has to cover the complete calorimeter. For the forward spectrometer this is not necessary, since a dipole magnet at the beginning of the spectrometer will be used.

Based on these requirements a decision about the type of the PANDA electromagnetic calorimeters has been made which will be explained in detail in the following sections.

1.3.4 The EMC of the target spectrometer

The only calorimeter concept which can fulfill the resolution requirements for the target spectrometer described in the last section in combination with a high compactness is a homogeneous calorimeter made of inorganic scintillation crystals.

Scintillator material

Since the costs for the solenoid magnet increase with the third to fourth power of the radius [GL94], a high Z scintillation material has to be chosen to limit the overall costs of the PANDA detector. In addition, to reach the envisaged rate capability, a fast decay time of the scintillation process is mandatory. Considering this requirements only a few inorganic scintillator materials can be considered. A comparison of these materials is given in table 1.4.

	$PbWO_4$	BGO	CeF_3	LYSO:Ce
ρ $[g/cm^3]$	8.28	7.13	6.16	7.40
X_0 $[cm]$	0.89	1.12	1.77	1.14
R_M $[cm]$	2.00	2.30	2.60	2.30
decay time τ_{decay} $[ns]$	6.5	300	30	40
maximal emission λ_{max} $[nm]$	420	480	330	420
index of refraction n @ λ_{max}	2.24 / 2.17	2.15	1.63	1.82
relative light yield [% of NaI]	0.6 at +20°C, 2.5 at -25°C	9	5	75
dE/dx (MIP) [MeV/cm]	10.2	9.0	6.2	9.6

Table 1.4: Main properties of selected scintillator materials [TDe09, PDG14]. All materials are non hygroscopic. The light yield of $PbWO_4$ is given for its improved high purity version which is also referred to as PWO-II. The relative energy loss is given for minimal ionizing particles (MIP).

The comparison of the different materials shows that $PbWO_4$ is the most compact and also the fastest scintillation material. On the other hand it shows a quite low light yield of only 0.6 % of NaI at room temperature and 2.5 % at -25°C. BGO also has a very short radiation length and shows a higher light yield than PWO but with a significantly longer decay constant that would lead to serious limitations of the count rate capability especially in the forward end cap [TDe09]. CeF_3 has an acceptable light yield and decay time, but a significantly longer radiation length. The last material, LYSO:Ce, combines a short radiation length with an excellent light yield and a short decay time. Considering these materials, LYSO:Ce would be an ideal candidate for the target EMC also due to its excellent radiation hardness [RYZ13]. However, LYSO:Ce is a relatively new material and has never been used for a high energy physics calorimeter setup so far. As a result of this, there is no experience available for the achievable homogeneity of a mass production. In addition to this, the production is quite expensive due to the high melting point and the costs of the raw material [RYZ13]. CeF_3 has up to now neither been used for a large scale high energy physics calorimeter and up to now it is not possible to produce high quality crystals with up to 20 X_0 in length [TDe09]. BGO has been successfully used in several calorimeters like L3 at CERN, but in addition to the long decay time, there are no mass production capacities available today. At the start time of the crystal production for PANDA PWO was a relatively cheap alternative with a lot of production capacities at BTCP in Russia where most of the CMS crystals, also made of PWO, were produced. Due to these advantages and due to the short decay time and the high compactness provided by this material it was chosen for the EMC of the target spectrometer [TDe09].

Crystal growth: Large PWO crystals can either be grown by the Czochralski method like it is performed at the Bogoroditsk Techno-Chemical plant (BTCP) or by a modified Bridgman method which is applied for example at the Shanghai Institute of Ceramics (SICCAS) [TDe09].

For the **Czochralski method** which is shown in figure 1.29 the crystal melt is heated up in an open crucible made of platinum to avoid impurities.

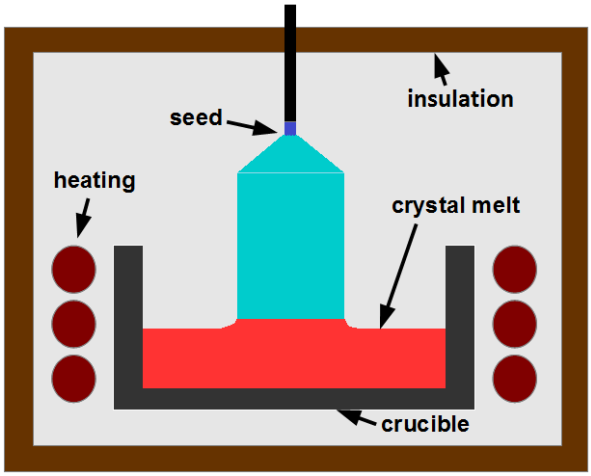

Figure 1.29: Setup for crystal growth with the Czochralski method.

A crystal seed with the right orientation is then dipped from the upper side into the melt. After the surface of the seed is molten and a homogenous boundary layer has formed it is slowly pulled upwards. The diameter of the pulled crystal can be controlled by the pulling speed and the temperature gradient and can reach values of up to several centimeters per hour [DBP10]. To avoid defects in the crystal structure a slow pulling speed in the order of tenth of a millimeter per minute is mandatory [DBP10]. Therefore, the growth of large crystal ingots with a length of up to 25 cm is very time consuming and requires a large effort in stabilizing the growing conditions over a longer time interval.

For the **Bridgman method** an oven with two temperature zones is used. While the temperature in the upper part is above the melting point of the crystal, it is reduced below the melting point in the lower part. The crystal melt is placed in a closed cylindrical crucible with a conical shape at the bottom [DBP10]. During the insertion of this crucible into the oven from the top, the raw material is molten. If the bottom of the crucible reaches the region of the oven with the lower temperature, the crystallization starts in the narrow tip of the crucible. From this initial crystallization region a single crystal starts growing into the melt, which acts as a seed [DBP10]. If the crucible is then lowered further down under rotation, the melt crystallizes in the junction of the temperature zones. For this process, a low speed is needed as well to avoid the formation of defects during the crystallization [DBP10].

All final version PANDA crystals which exist up to now have been produced by the Czochralski method at BTCP. Nevertheless, since BTCP does no longer exist, there are actually R&D programs in progress to continue with the mass production at SICCAS (Shanghai, China) and CRYTUR (Prague, Czech Republic).

Scintillation mechanism: $PbWO_4$ is an intrinsic scintillator. The tungsten ions are configured in two types of oxygen tetrahedrons while each lead ion is surrounded by eight oxygen ions from this tetrahedrons [FKM96]. The luminescence centers which emit the scintillation light are given by regular WO_4^{2-} centers and structure point defect centers of the host matrix [FKM96]. In high quality crystals the emission of light due to charge transfer transitions in the WO_4^{2-} centers gives the dominant effect with a 40 nm width (FWHM) blue luminescence peak at 420 nm [FKM96, TDe09]. Such crystals are transparent in the complete visible energy range and therefore show a clear color. Figure 1.30 shows the luminescence spectrum of the scintillation light in comparison to the transmission spectrum of the crystal.

Since this luminescence effect has a large Stokes shift, there is a strong temperature dependence of the light yield with a nearly linear gradient between -25°C and 20°C of around $-3\ \%/K$ [TDe09]. Due to this temperature quenching, the luminescence mechanism shows a fast decay time of only 6.5 ns [TDe09]. To avoid additional slow components it is extremely important to keep the amount of point defects and impurities in the crystal as low as possible.

Quality improvement: Since large quantities of PWO were already produced for the CMS electromagnetic calorimeter [CMS97] and the photon spectrometer of ALICE (PHOS) [DCZ07] at CERN as well as for the hybrid calorimeter (HYCAL) at JLAB [GL02], there were a lot of experiences available on this material. However, the average light yield of PWO at room temperature measured with a PMT with bi-alkali photocathode for CMS crystals is only in the order of 8-11 photo electrons per MeV [AKL02] which is sufficient for the announced experiments since only high energetic electromagnetic probes have to be detected.

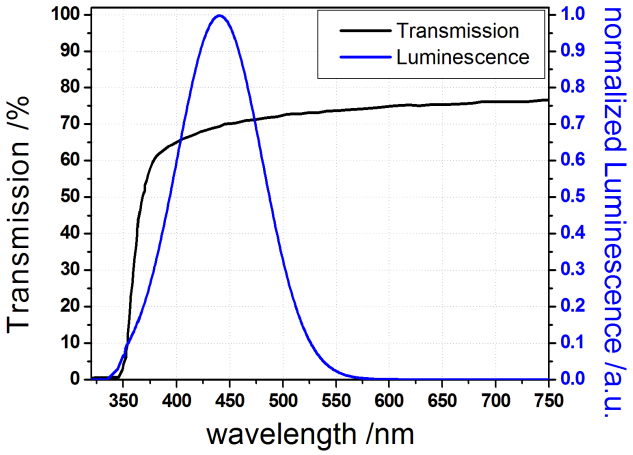

Figure 1.30: Luminescence and transmission spectra of high quality $PbWO_4$. Data taken from [TDe09].

Since PANDA requires a measurement of energies down to 10 MeV such a low light yield would lead to strong limitations of the energy resolution at low energies and to an increase of the low energetic threshold. Therefore, a R&D program was initiated to improve the light yield. By a better control of the raw material, the melt composition and by an improvement of the growing and doping procedure, a significant improvement of the crystal structure and a reduction of defects could be achieved [TDe09]. Therefore, less doping with lanthanum and yttrium was needed to guarantee the radiation hardness of the crystals. These improvements finally lead to a light yield of 17 - 22 photo electrons per MeV at room temperature, measured with a bi-alkali photocathode, which is around 80 % higher than for the average CMS crystals [TDe09]. This second generation PWO is also referred to as PWO-II.

In addition to this improvements of the crystal quality, the PANDA EMC will be operated at -25 °C which additionally increases the light yield by a factor of ≈ 3.5 compared to operation at room temperature.

Calorimeter design

To cover the complete solid angle of the target spectrometer a design made of a barrel with a forward and a backward end cap has been chosen. Figure 1.31 shows a schematic drawing of the barrel part and the forward end cap with their mechanical support structures.

The barrel part with an axial depth of 2.5 m will consist of 11360 crystals and the forward end cap which will be placed 2.05 m away from the interaction point will contain additional 3600 crystals. Another 592 crystals will be placed in the backward end cap which is placed 0.55 m away from the target in backward direction. The barrel covering a solid angle of 84.7 % of 4π will have an inner radius of 0.57 m and an outer radius of 0.95 m. The forward and backward end caps will reach from the beam pipe up to an outer radius of 0.92 m and 0.3 m, respectively, and cover a solid angle of 3.2 % and 5.5 % of 4π. [TDe09]

To achieve a so called “flat-pack” barrel design in which all crystal front faces are oriented to one point, the single crystals have to be shaped in the form of a tapered parallelepiped

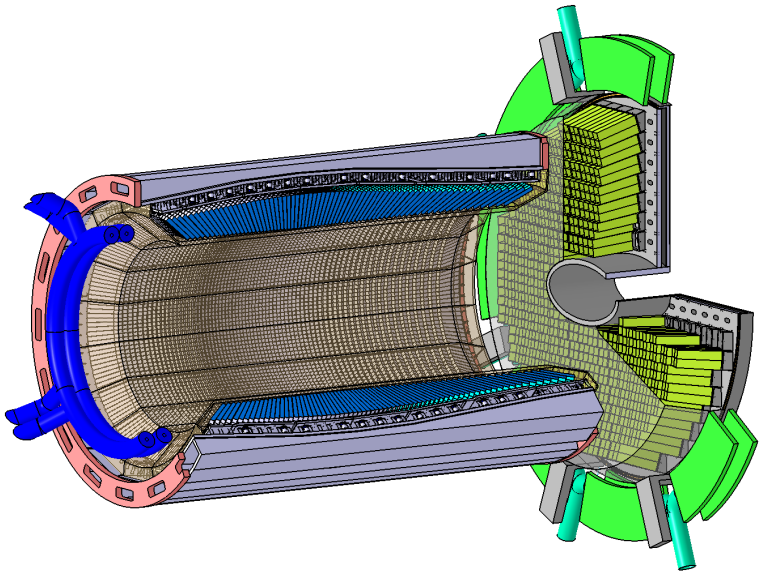

Figure 1.31: Schematic view of the PANDA target EMC with the barrel part and the forward end cap [PAN14]. The backward end cap is not shown in the picture.

[TDe09]. For the realization of the envisaged position resolution, the crystal front face should be in the order of one Molière-Radius which corresponds to 2.0 cm for PWO. With this condition 160 crystals are needed to cover one ring of the barrel with its inner radius of 0.57 m. In longitudinal direction 18 crystal geometries with a different degree of tapering are needed to cover the barrel. Due to the symmetry of the barrel around the central point, this number can be reduced to 11. The arrangement of these 11 crystal types within a longitudinal cross section of the barrel and a radial cross section of the barrel center are shown in figure 1.32.

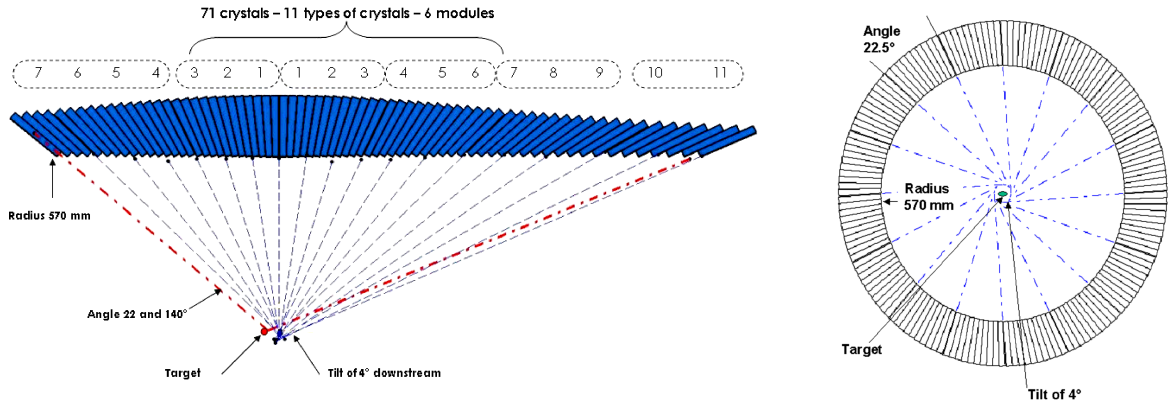

Figure 1.32: Left: Cross section of a barrel slice consisting of 11 crystal geometries. Each geometry number in the upper row corresponds to 4 crystals of this type. The lines around the crystal types indicate the six packages of one slice. The dashed red line indicates the maximal angle, starting from the target, under which electromagnetic probes can be detected. The center of the barrel is tilted by 4° in beam direction relative to the target point [TDe09]. Right: Cross section of a radial barrel ring with its 160 crystals [TDe09].

The figure also shows that the central point, to which all crystal front faces are aligned is not identical with the target. It is tilted by 4° in beam direction to avoid the passage of electromagnetic probes through the dead material in between two crystals. [TDe09]

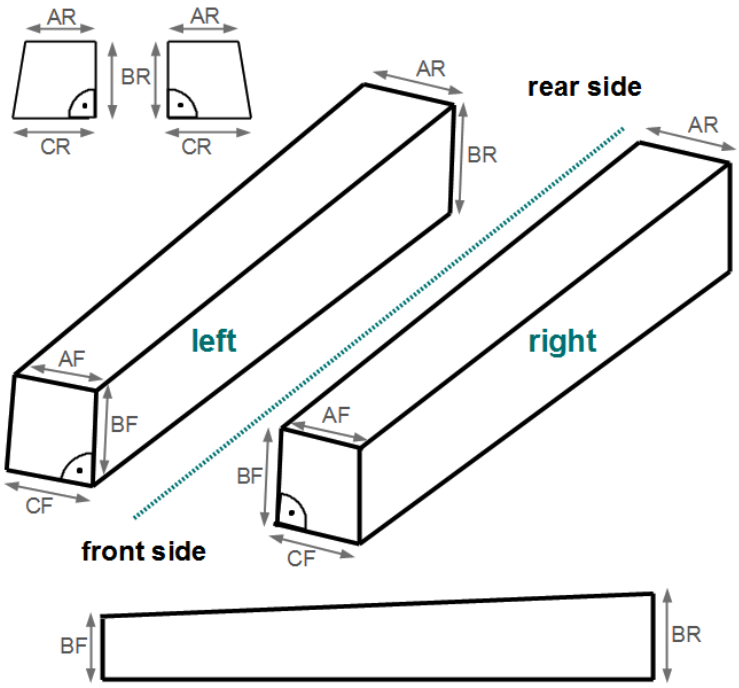

Figure 1.33: Geometry of the PANDA PWO crystals. The dimensions of the side faces AF, BF, CF and AR, BR and CR are defined by the 11 crystal geometries listed in table 1.5. The dashed green line shows the symmetry axis between the mirror symmetric versions (left and right) of each crystal type. All crystals have a length of 20 cm. [TDe09]

Type	AF /mm	BF /mm	CF /mm	AR /mm	BR /mm	CR /mm	Volume /cm^3
1	21.21	21.28	21.27	29.04	28.75	29.12	126.68
2	21.18	21.28	21.39	28.78	28.75	29.07	126.56
3	21.17	21.28	21.51	28.63	28.75	28.81	125.79
4	21.17	21.28	21.60	27.90	27.22	28.45	120.85
5	21.17	21.28	21.69	27.35	27.22	28.01	119.69
6	21.19	21.28	21.78	26.72	27.22	27.47	118.35
7	21.22	21.28	21.86	26.23	25.47	26.99	112.9
8	21.23	21.28	21.91	25.70	25.47	26.51	111.75
9	21.23	21.28	21.95	25.14	25.47	26.00	110.52
10	21.25	21.28	22.00	24.70	24.42	25.56	107.01
11	21.25	21.28	22.02	24.35	24.42	25.23	106.25

Table 1.5: Dimensions of the 11 barrel geometries of the PANDA PWO crystals. The arrangement of the six listed sides is indicated in figure 1.33. The end cap crystals have quadratic front and rear faces with a dimension in the forward end cap of AF = BF = CF = 24.38 mm and AR = BR = CR = 26.00 mm and in the backward end cap AF = BF = CF = AR = BR = CR = 24.35 mm. [TDe09]

Figure 1.33 shows a schematic picture of the crystal geometry. The tapered parallelepiped is defined by the three front sides AF, BF and CF and the three rear sides AR, BR and CR. Each crystal geometry exists in two mirror symmetric versions (left and right). The length of the crystal between the parallel front and rear faces is 20 cm for all crystal geometries corresponding to 22.5 X_0. The average weight of one crystal is 0.98 kg. Table 1.5 lists the dimensions of the different types of PANDA PWO crystals.

Figure 1.34 shows a picture of two crystals of the most tapered geometry (type 1).

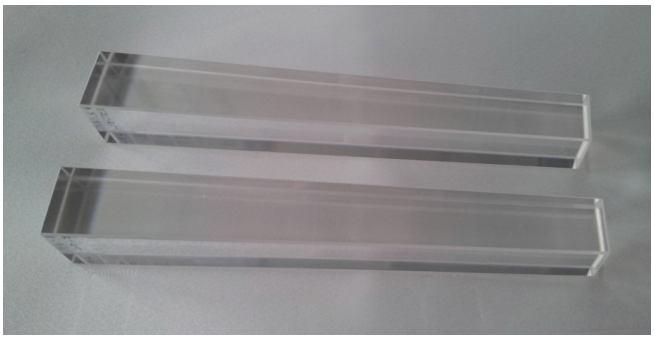

Figure 1.34: Picture of two type 1 crystals, which represent the most tapered geometry.

To improve the light yield all crystals are wrapped on the side faces as well as on the front face with mirror reflective VM2000 foil, a 63.5 μm thick multilayer polymer. The wrapped crystals are grouped in units of 4×10 crystals in carbon fiber alveoles. The total thickness of the carbon layer in between two crystals is 400 μm. Including the VM2000 foil and the gap for mechanical tolerance, the average distance between two crystals can be approximated to be 680 μm. The carbon alveole units are arranged in larger packs and finally assembled to one slice with $71 \times 10 = 710$ crystals. In radial direction 16 of this slices form the complete barrel. In the forward and backward end cap also carbon alveoles are used to arrange the crystals, but with smaller sub units of only 16 crystals to realize the circular geometry of the end caps. [TDe09]

Photo sensors

Like the crystals the photo sensors for the readout of the target EMC crystals also have to fulfill several requirements. Especially in the barrel region of the target spectrometer high transverse magnetic fields of up to 2 T have to be handled. Therefore, and due to the requirement of a compact design, classical PMTs are not an option. Since a relatively high gain is required due to the low light yield of the PWO crystals as well, the only alternative at the time when the design was fixed in 2009 was given by an Avalanche Photo Diode (APD) based readout. With significant progress in the field of silicon photomultiplier over the last years, these devices may be an option for future calorimeters based on PWO. To detect a higher amount of light, to reduce the noise and fake event level and to gain a redundancy it was decided to equip each crystal of the barrel, the backward end cap and the outer region of the forward end cap with two rectangular Large Area Avalanche Photo-diodes (LAAPDs). Only in the inner part of the forward end cap it was decided to use Vacuum Photo Tetrodes (VPTTs) due to their higher count rate capability. In addition to this, the component of the

magnetic field transverse to the axis of the photo tube is significantly reduced in this region. [TDe09]

Large Area Avalanche Photo diodes (LAAPDs): An APD is a semiconductor based photon detector with an internal gain. Figure 1.35 shows a schematic drawing of the different semiconductor layers inside an APD.

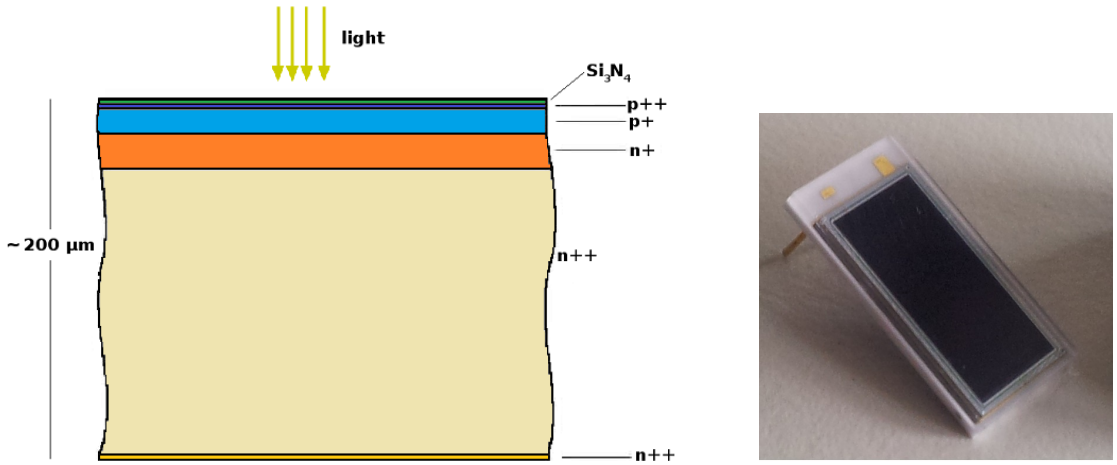

Figure 1.35: Schematic picture of an APD, modified from [CMS97] (left) and picture of an PANDA LAAPD (right).

The light enters the APD through the silicon nitride [Si_3N_4] top layer (green) which acts as an entrance window to reduce the light losses by reflections on the silicon surface [TDe09]. After the light has passed this layer and the thin p^{++} layer (dark blue) it is absorbed in the p^{+} layer (light blue) by creation of electron-hole pairs. Due to a voltage of approximately 400 V which is applied between the highly doped p^{++} and n^{++} electrode layers at the beginning and end of the APD, an electric field inside the APD forces the electrons to drift in the direction of the p-n junction. In this region the electric field reaches a value of up to 10^7 V/m and accelerates the electrons to create further electron hole pairs [TDe09]. The electrons freed in these processes are also accelerated and can produce additional electron hole pairs. Depending on the applied voltage and on the layer thickness a gain of more than 3000 can be reached in such an avalanche before the APD reaches its breakdown voltage. In the case of PANDA, the gain is chosen between 50 and 200 to achieve a stable long term operation. After the avalanche formation the electrons drift through an additional layer of n doped material before the charge is collected in the lower n^{++} doped electrode [TDe09].

The typical quantum efficiency of a PANDA LAAPDs is shown in figure 1.36 (left) in comparison with the luminescence spectrum of PWO. The average weighted quantum efficiency in the luminescence region of PWO is approximately 76 %, which is roughly three times higher than for a PMT with a classical bi-alkali photocathode.

The electric field inside the APD is directly proportional to the applied reverse voltage U_R. Therefore, the **gain** M of the APD strongly depends on this parameter. It is defined as the ratio between the amplification at a given voltage and the amplification for gain 1, which is typically measured at low voltages (i.e. 50 V). Figure 1.36 (right) shows typical gain voltage

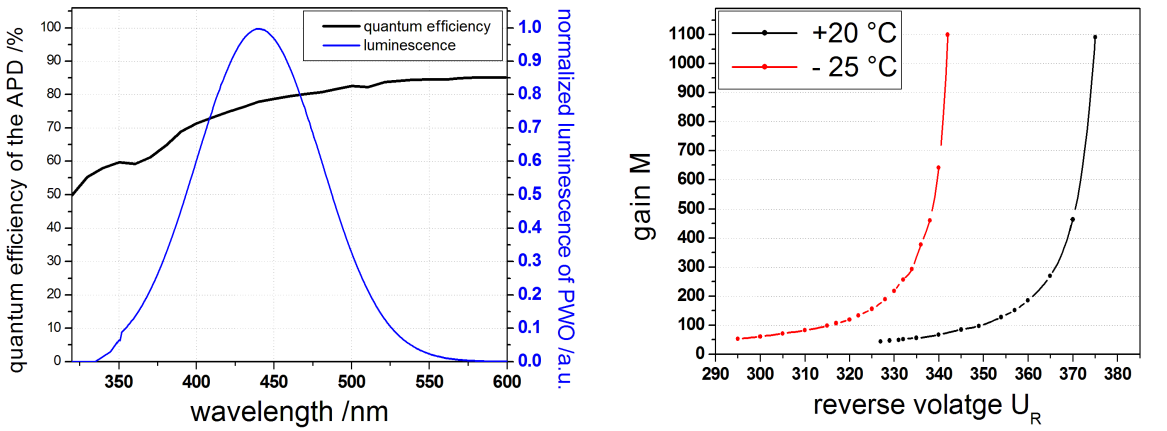

Figure 1.36: Quantum Efficiency of a typical PANDA LAAPD in comparison to the luminescence spectrum of PWO (left) and gain voltage correlation for a typical PANDA LAAPD at room temperature (black) and at -25 °C (red) (right).

curves for a PANDA LAAPD at room temperature and at the operation temperature of -25 °C. The figure illustrates that the gradient of the gain function is increasing with increasing voltage/ gain. Especially above a gain of 200-300 the gain rises rapidly, making a stable long term operation very difficult for this region. Therefore, a gain of up to 200 should be used for a stable operation. Nevertheless, in this region the voltage also has to be stabilized to $\pm 0.1\ V$ for a proper gain determination [TDe09]. Figure 1.36 (right) also shows a strong impact of the temperature on the gain of the APD. This decrease of the gain with increasing temperature can be explained with an increasing amount of interactions of the avalanche electrons with phonons, resulting in an reduction of the avalanche amplification. At a gain of 50 this effect is in the order of 2% per °C. Therefore, the temperature has to be stabilized to a level of $\pm 0.1\ °C$ as well. [TDe09]

Another important parameter of an APD is the **dark current** I_d which is composed of the surface current I_s and the bulk current I_b. While the surface current is gain independent, the bulk current increases with the gain. Therefore, the total dark current can be expressed for a fixed temperature as a linear function of the gain [TDe09]:

$$I_d = I_b \cdot M + I_s \tag{1.56}$$

The dark current can be decreased by a decrease of the temperature but increases for example with the radiation damage of the silicon material [TDe09].

Another important parameter of an APD is the **excess noise factor** F which parametrizes the statistical fluctuations of the APD gain σ_M. Those fluctuations are introduced on the one side by the statistical fluctuations of the amplification process, but also by inhomogeneities of the amplification region [TDe09]. Its gain dependence can be expressed with the ratio between the ionization coefficients for electrons and holes k by [TDe09]

$$F \approx k \cdot M + \left(2 - \frac{1}{M}\right) \cdot (1 - k) \tag{1.57}$$

The excess noise factor is quite important since it gives a significant contribution to the statistical term of the energy resolution σ_E measured with an APD, especially at low energies [TDe09]:

$$\frac{\sigma_E}{E} = \frac{1}{\sqrt{E}} \cdot \sqrt{\frac{F}{N_{eh}}} \tag{1.58}$$

with the number of produced electron hole pairs N_{eh}. For PANDA LAAPDs it is in the order of F = 2.2 at gain 50 and F = 2.7 at gain 150 (see eqn. 4.41).

Another effect which can influence the energy measurement with an APD is the **nuclear counter effect**. It occurs when minimum ionizing charged particles like leakage electrons from the shower or muons pass the APD. In this process typically 100 electron hole pairs per micrometer are produced. For a PANDA LAAPD this can result in a signal corresponding to several MeV of photon energy since the light output of PWO is very low. To reduce this effect the conversion layer was minimized for the PANDA APDs, similar to the design for CMS. [TDe09]

The main advantages of an APD are in addition to the insensitivity to magnetic fields and the small thickness of only 200 μm also the high quantum efficiency of around 70-80 % at 420 nm and the moderate costs [TDe09]. Disadvantages are given by the low gain and by the limitation of the count rate due to the shaping time. The described APD design was optimized for the readout of PWO crystals by the CMS collaboration [CMS97]. However, the APDs used for CMS have an area of only $5 \times 5\ mm^2$. Therefore, a R&D program was carried out by the PANDA collaboration in cooperation with Hamamatsu to increase the size of the APDs. In the final design a size of $7 \times 14\ mm^2$ is considered. These APDs are therefore referred to as Large Area Avalanche Photo Diodes (LAAPDs). [TDe09]

Vacuum photo triodes and tetrodes (VPTs/ VPTTs): Vacuum photo triodes or tetrodes are functioning according to the basic principle of electron amplification in a dynode system like in a conventional photomultiplier tube. The main differences are the use of planar dynodes and the use of only a few amplification stages. Both differences provide a significantly increased magnetic field resistance compared to classical PMTs. In addition, a compact design, a high rate capability (> 500 kHz) and a high radiation hardness can be achieved [TDe09]. Figure 1.37 shows a schematic drawing of a VPTT.

Typically the photocathode is at ground level, while the first and the second dynode have potentials of 0.5 kV and 1 kV, respectively. The anode which is positioned in between the two dynodes has the highest potential of 1.2 kV. The anode and the first dynode are carried out as fine metal meshes to enable the passage of the electrons [TDe09]. The photons which reach the photocathode interact in a photo-effect and cause the emission of electrons. These photo electrons are accelerated in the electric field and produce secondary electrons on the first dynode, which are further accelerated to the anode. The electrons which pass the anode mesh hit the second dynode, which consists of a solid metal plate. During this process secondary electrons are emitted which are accelerated back to the anode, where they are collected [TDe09]. Typical gain values are in the order of 50 or higher and the quantum efficiency is in the order of > 20% at 430 nm [KRS14, TDe09].

For VPTTS a typical gain drop down to 50 % at the relevant field strength of 0.88-0.97 T in the inner part of the forward end cap can be observed [KRS14]. Therefore, a gain of at least

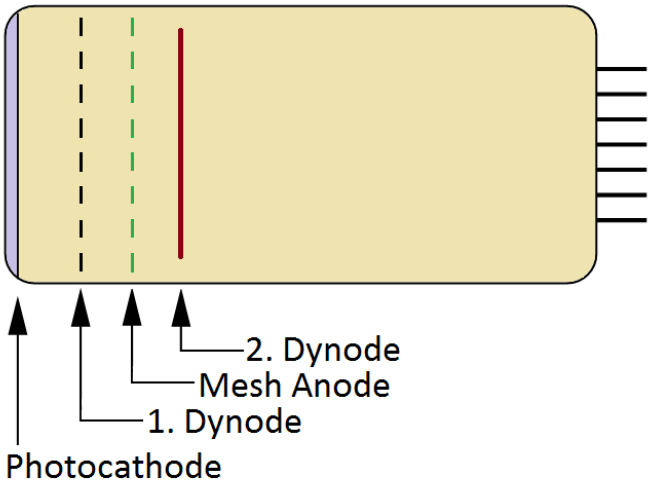

Figure 1.37: Schematic picture of a VPTT with the first dynode and the anode carried out as fine planar metal meshes to enable the passage of the electrons [TDe09]. For the case of a VPT, the first dynode is removed.

45-50 is needed to compensate this effect. The current VPTT generation from Hamamatsu meets this requirements [KRS14].

Readout chain

The amplification and shaping of the APD/ VPTT signals will be performed with two different concepts. Both readout concepts have to provide a large dynamic range to cover the complete energy range from 1 MeV up to 7.3 GeV in the barrel and up to 14.6 GeV in the forward end cap with sufficient accuracy. For the barrel part and the backward end cap a special low-noise and low-power charge preamplifier and shaper ASIC (**APFEL**) was developed at GSI [PW12] to fulfill the main requirement of

- a compact design
- a low noise level
- and a low power consumption of less than 100 mW per detector

for the operation within the cooled volume of the EMC [TDe09]. In the forward end cap more space is available inside the cooled volume. Therefore, the readout will be performed with a low-noise discrete component pre-amplifier (**LNP**) developed at Basel University (Basel pre-amp) with a separate four-stage shaper. This units will also be operated within the cooled volume of the EMC and are in addition to the low noise level and the low power consumption specially optimized for

- a high count rate capability of up to 500 kHz
- and a short pulse width to reduce pile-up

which are very important characteristics in forward directions [TDe09].

APFEL ASIC: Each crystal will be equipped with two APDs which will be read out by a common ASIC with two independent channels. The ASIC board which is shown in figure 1.38 (left) will be directly plugged to the pins of the APDs and operated within the cooled volume.

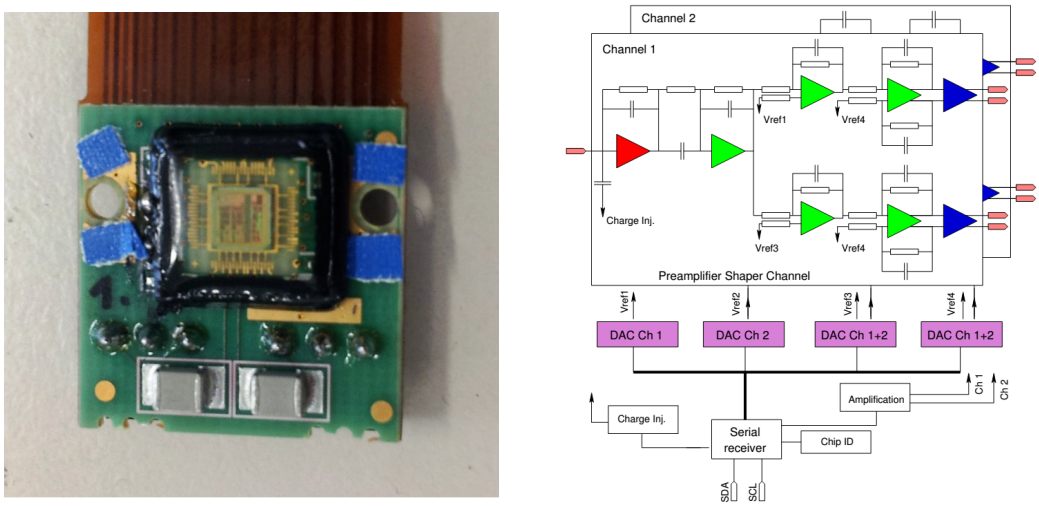

Figure 1.38: Picture (left) and wiring diagram [PW12] (right) of the current version (1.4) of the APFEL ASIC developed for PANDA. Each ASIC board will be used for the readout of both APDs of one crystal (channel 1 and 2) and produce a high and a low gain output for each APD.

The right part of figure 1.38 shows how the APD signals are treated within one of the ASIC channels. Each signal is split in a high gain and a low gain branch with a programmable amplification ratio of 16 or 32 between the two branches to achieve a sufficient digitization accuracy in the Analogue to Digital Converter over the entire energy range [PW12]. This ratio has to be optimized in a way that the dominant energy range of the barrel of up to a few hundred MeV can be treated by the high gain to provide a better signal to noise ratio for an optimal energy resolution at low energies. The maximal input charge of 8 pC provides with the given amplification a dynamic range of more than 10.000. The noise level is expected to be in the order of 0.74 fC. Each of the channels contains a shaper with an integration time of (251 ± 2) ns. The baseline of each branch is independently programmable via reference voltages. The count rate capability of the ASIC is 500 kHz which is sufficient for the barrel and backward end cap with an expected maximal count rate of 100 kHz. The power consumption is in the order of 55 mW per APD. [PW12]

LNP preamplifier: The 2×4 cm^2 large low noise low power (LNP) preamplifier is based on discrete components with a fast, integrated operational amplifier. It performs a linear conversion of the input charge into a positive output signal of up to 2 V. Since this output signal has a long decay time of 25 μs an additional analog shaper is needed. This shaper reduces the pulse width to approximately 280 ns and provides a single-ended dual-gain output. It is specially optimized to handle count rates of up to 500 kHz that are expected in the forward end cap. The power consumption is varying between 45 mW and 90 mW depending on rate and input charge for both APDs. [GT13]

Digitization and data treatment: Up to now, only a concept for the readout scheme of the forward end-cap of the barrel EMC exists. Therefore, this scheme, shown in figure 1.39, will be presented as an example for the readout of the electromagnetic calorimeter of the target spectrometer.

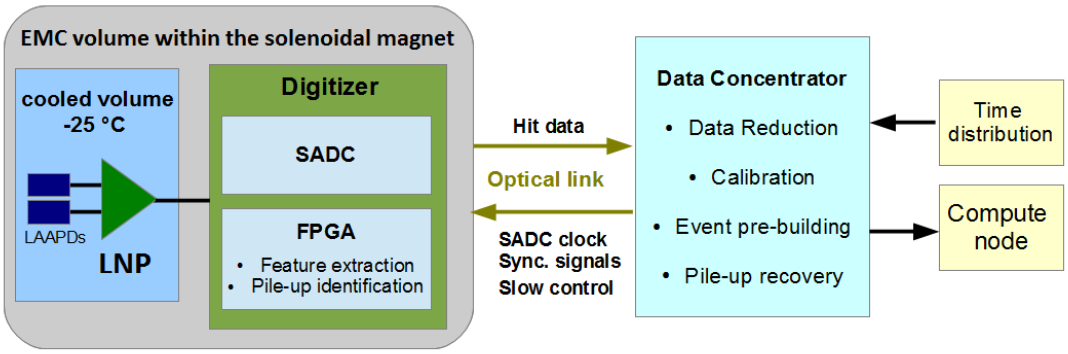

Figure 1.39: Current status of the readout chain of the forward end cap of the PANDA EMC. Principle taken from [KHK11]. The ASIC and the digitizer will be placed in the EMC volume inside the solenoid magnet while the data concentrator and the compute node will be placed outside of the detector and connected to the inner parts via an optical link.

The ASIC in the barrel and backward end cap and the LNP in the forward end cap will be placed inside the cold volume of the EMC directly behind the APDs. The signals will be lead out of the cold volume with flex-cables. In the forward end cap, this cables from the LNP pre-amplifiers are connected to a shaper board and finally to a digitizer board in the warm part of the EMC volume. On this digitizer board the signals are recorded with a sampling ADC (SADC) at a sampling rate of 50 MHz [TDe09]. After digitization, the signal height, the integral over a threshold and the event time are extracted in an FPGA[5] [KHK11]. Based on the integral over amplitude ratio pile up events are identified [GT13]. If an event has no pile-up, only the feature extracted data will be forwarded. If a pile-up event is detected, the complete pulse shape will be further processed. The digitizer sends the hit data via an optical link to the data concentrator which will be positioned outside the calorimeter volume. In the other direction it receives the SADC clock, synchronization signals and the slow control information from this link. The data concentrator is responsible for the communication protocols, the time ordering of the data, the data reduction and event pre-building, the calibration and the pile-up recovery [KHK11]. It finally sends the processed data to the compute node. As an input it receives the time distribution data from the complete PANDA data acquisition system.

For the barrel part, a similar concept with a few changes of the arrangement of the components will be used. For example, due to space reasons, the digitization of the signals can not be performed within the solenoid magnet. A preliminary readout scheme is presented for the current barrel EMC prototype in section 2.3.2.

[5]Field Programmable Gate Array

1.3.5 The EMC of the forward spectrometer

The design of the electromagnetic calorimeter of the forward spectrometer has a lot more flexibility than the one of the target spectrometer. On the one hand the length / thickness of the calorimeter can be larger than for the target spectrometer, since the forward spectrometer has only a dipole magnet at the beginning and is not covered by a solenoid. Nevertheless, the thickness of the electromagnetic calorimeter in forward direction is limited by the envisaged size of the muon detector and by the overall size of the forward spectrometer, which has been adapted to the dimensions of the experimental hall. On the other hand, a relatively large area of 1.54×2.97 m^2 has to be covered due to the large distance of 7.8 m to the interaction point [TDf15]. To cover this area with a homogenous crystal calorimeter made of PWO, nearly 10.000 crystals would be needed. Therefore, this option would introduce additional costs which reach nearly the level of the complete barrel part of the target calorimeter. Due to the larger space, a sampling calorimeter can be taken as an alternative. Section 1.3.2 shows that from the presented sampling calorimeter concepts, only a specially optimized shashlyk calorimeter can fulfill the resolution requirements at low energies. Shashlyk calorimeters have been successfully used over the last decades at several experiments like for the E865 [AGG92] and the PHENIX [GD96] experiment at Brookhaven National Laboratory (BNL) and for the HERA-B detector at DESY [AG94]. Also more recent high energy physics detectors like LHCb [IM09] at CERN´s Large Hadron Collider (LHC) and the COMPASS experiment [VP06] at CERN apply calorimeters of this type. Most of the calorimeters announced up to now are optimized for high energies typically above several hundreds of MeV. The only shashlyk calorimeter which was optimized for energies in the sub-GeV range with a threshold of several tens of MeV is the electromagnetic calorimeter intended for the KOPIO experiment at BNL [AIK04, GSA08]. It uses $(11 \times 11 \times 61)$ cm^3 large modules consisting of 300 alternating layers of 0.275 mm thick lead and 1.5 mm thick plastic scintillator tiles which are read out by 72 bend wavelength shifting (WLS) fibers, crossing the module in a 12×12 matrix in longitudinal direction and are coupled to the photo sensors at the rear end of the module [GSA08]. While calorimeters optimized for the detection of high energies typically consist of relatively thick lead plates to gain a high absorption power, the KOPIO design nicely shows that for a good energy resolution at low energies a high active sampling fraction is needed to reduce sampling fluctuations and to get a large amount of energy deposition in the active medium. In the case of the KOPIO modules this is realized with relatively thin lead plates and significantly thicker scintillator tiles. A further improvement of the energy resolution would be possible by using even thinner lead plates which on the other hand would cause a significant increase of the module length to provide a sufficient absorption volume [ADI04]. Therefore, the given dimensions have been taken as a trade off. With the last prototype of this calorimeter an energy resolution of

$$\frac{\sigma}{E} \approx 2\% \oplus \frac{2.7\%}{\sqrt{E/GeV}} \tag{1.59}$$

could be achieved with an APD based readout [GSA08]. The time resolution for an APD readout is in the order of 90 $ps/\sqrt{E/GeV}$, while with a PMT based readout a time resolution of 100 $ps/\sqrt{E/GeV}$ has been achieved [GSA08]. Unfortunately no long term experiences under real experimental conditions exist, since the KOPIO experiment was canceled due to funding issues after the R&D phase [KOP15]. Nevertheless, based on the very promising

performance of the prototypes it was decided to use a shashlyk calorimeter for the forward spectrometer of the PANDA detector of a similar layout.

Design of the individual modules

The design of the PANDA modules is based on the described KOPIO modules and has been optimized in several steps to fulfill the special requirements of the PANDA forward spectrometer. During this optimization process different versions of the modules have been produced by the Institute for High Energy Physics (IHEP) in Protvino (Russia) and tested in different energy ranges [KSM09, SD12]. This work will compare the improvements made between the version tested in 2011/2012 (version A) and the current version tested in 2013 (version B). Therefore, only the design of these versions will be described in this section. More details on earlier versions can be found in [TDf15]. Figure 1.40 shows a schematic drawing of a longitudinal cross section of one module (left) and the layout of the four scintillator tiles of the module with the holes for the WLS fibers (right).

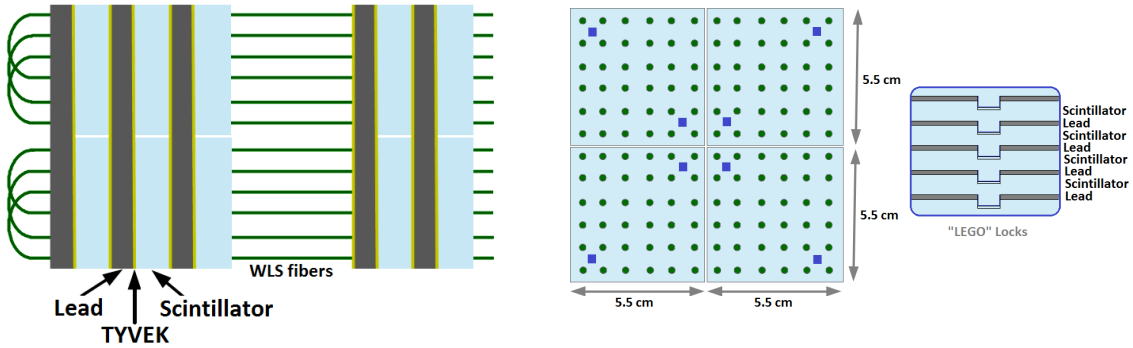

Figure 1.40: Design of a shashlyk module, consisting of four cells. Left: Longitudinal cross section with alternating layers of 0.275 mm thick lead sheets and 1.5 mm thick scintillator tiles. Only the first three and last two of the 380 layers are shown. In the current version (B) a $100\mu m$ thick sheet of reflective paper (TYVEK) is added on both sides of each scintillator tile [TDf15]. Right: Layout of the four scintillator tiles in each layer of the module. Each cell has a 6×6 matrix of holes for the insertion of the WLS fibers (green) and in the current version (B) two pin-holes (dark blue squares) to fix the position of the tile relative to the next layer. The principle of this so called "LEGO" locks is shown in the small insert of the figure.

One module consists of 380 layers of 0.275 mm thick lead sheets and 1.5 mm thick scintillator tiles [TDf15]. In comparison to the KOPIO modules, the number of layers has been increased by 26.6 % from 300 to 380 which was necessary to provide a sufficient energy resolution for high energies up to 15 GeV. Since the results obtained with the KOPIO modules concerning the energy resolution at low energies were already sufficient and since a further decrease of the lead sheet size would increase the module length even more, it was decided to adapt the concept. To reach the envisaged position resolution and to increase the count rate capability each (11×11) cm^2 large module is divided into four cells with a front face of (5.5×5.5) cm^2 each which is a little bit smaller than the effective Molière-Radius of 5.98 cm [TDf15]. While the lead sheets are common for all four cells, the scintillator tiles are separated for the four cells and optically isolated with white paint. For the scintillator tiles, an organic plastic scintillator material is used. Based on earlier experiences with the KOPIO modules concerning the

radiation hardness and the light output it was decided to use polystyrene doped with 1.5 % paraterphenile and 0.04 % 1,4-Bis-(5-phenyloxazol-2-yl)-benzol (POPOP) [TDf15]. The tiles are produced by injecting the melted raw material into a specially manufactured mould. To fix the position of the layers relative to each other, pin-holes, also called "LEGO" locks, are added to the scintillator tiles which are shown in the right part of figure 1.40. Each cell is intersected by 36 holes with a diameter if 1.3 mm, which are arranged as a 6 $\times$ 6 matrix with a distance between two holes of 9.3 mm [TDf15]. Through this holes 18 1.0 mm thick wavelength shifting (WLS) fibers are inserted, bend at the front of the module and reinserted in another hole. The 36 ends of these fibers, which collect the light from the scintillator tiles are bundled at the rear side of the module and read out with a PMT. To stabilize the module mechanically four thin metal bars (one per cell) are inserted through longitudinal holes in the module. Figure 1.41 shows a 3D drawing of the shashlyk module with its four cells and a detailed view of its front and rear part with open covers.

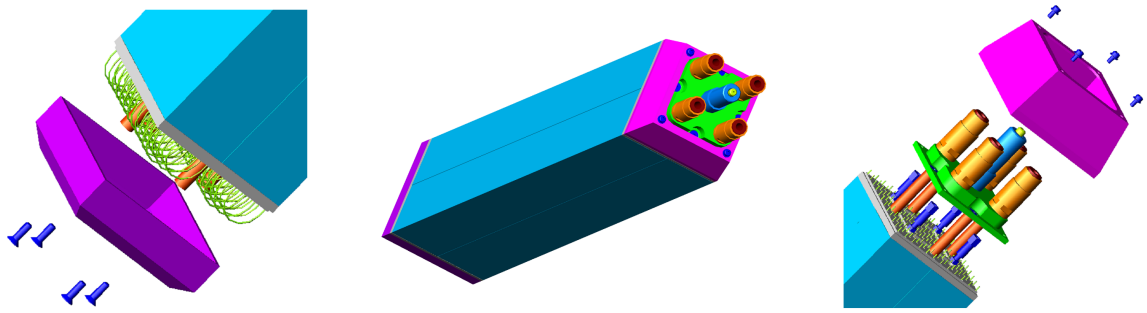

Figure 1.41: 3D drawings of a shashlyk module (center) and its front and rear part (left and right) [TDf15].

In **version A** the division of the scintillator tiles was performed by cutting the originally (11×11) cm^2 large scintillator tile into four parts. Since the large tiles had only one pin-hole in each corner of the tile, the result was only one pin-hole in each cell. To insulate the single cells optically, the cut inner side faces were painted with white color. In contrast to this, the outer side faces were left open and the complete active part of the module was covered with white reflective paper (TYVEK) to improve the light collection. In addition to this, a layer of black paper was added to the outer surface to avoid optical crosstalk between the modules. On the surface between the scintillator tiles and the lead sheets only an air gap of 37.5 μm and no reflector was added. Therefore, only totally reflected light was collected. In this configuration the module had a total length of 69.8 cm (19.6 X_0). [TDf15]

Since this version of the modules caused several problems, especially with the homogeneity of the light output for different interaction positions [SD12], a new version was produced at IHEP Protvino (**version B**). For this version a new mould was used to produce the scintillator tiles of the individual cells separately [TDf15]. For a better alignment a second pin-hole was added to the inner corner of each cell. In addition all four side faces of the scintillator tiles are now painted with white color to avoid cross talk and to improve the light collection homogeneity [TDf15]. The outer side faces of the module are covered with black paper to improve the light tightness of the module. To increase the light yield and to guarantee the long term stability of the light collection homogeneity, (0.175 ± 0.025) mm thick sheets of white reflective paper (TYVEK) were added in between the scintillator tiles and the

lead sheets [TDf15]. This modification increased the active module length to approximately 81 cm. For a final version the total module length has to be decreased again, for example by using thinner TYVEK sheets and by a redesign of the voltage supply for the PMT. Another improvement was achieved by the replacement of the WLS fibers from BICRON (BCF-91A) by new ones from KURARAY (Y-11(200)) with a higher light output and by an improvement of the bending procedure of the fibers to avoid cracks in the bending region which would increase the longitudinal inhomogeneity and decrease the light output. In addition to the announced changes, several mechanical improvements were performed for the current version.

Table 1.6 gives an overview over the most important design parameters of the shashlyk modules for version A and B.

property	version A	version B
lateral dimension of a module	$(11 \times 11)\ cm^2$ ($\approx 0.8°$)	$(11 \times 11)\ cm^2$ ($\approx 0.8°$)
lateral dimension of a single cell	$(5.5 \times 5.5)\ cm^2$ ($\approx 0.4°$)	$(5.5 \times 5.5)\ cm^2$ ($\approx 0.4°$)
length of the active part	19.6 X_0 (69.8 cm)	19.6 X_0 ($\approx$ 81 cm)
total module length (without PMT)	79.3 cm	90.5 cm
thickness of the lead plates	0.275 mm	0.275 mm
thickness of the scintillator tile	1.5 mm	1.5 mm
thickness of the TYVEK (760 pc.)	-	$(0.175 \pm 0.025)\ mm$
air gap scintillator-lead/TYVEK	37.5 μm	12.5 μm
number of WLS fibers per cell	18 (bent at the front)	18 (bent at the front)
length of one bent WLS fiber	$\approx$ 1.9 m	$\approx$ 2.1 m
type and diameter of a WLS fiber	Bycron (BCF-91A), 1.0 mm	Kuraray (Y-11(200)), 1.0 mm
mass of one module	$\approx$ 22.5 kg	$\approx$ 22.9 kg

Table 1.6: Design values of the shashlyk EMC modules. The values are taken from [TDf15, KSM09].

Properties of the scintillator material and the WLS fibers

The organic scintillator material (polystyrene doped with 1.5 % paraterphenile and 0.04 % POPOP) has been developed at IHEP Protvino and intensively tested for the KOPIO experiment [ADI04]. Like other organic scintillator materials, which are typically aromatic compounds, it is a mixture of a primary fluorescent material (paraterphenile) and a wavelength shifter material (POPOP) which are mixed with a polymerizing material (polystyrene) to form a transparent solid material. The scintillation process in such materials is based on the excitation of molecules of the primary scintillator material by the incoming radiation, followed by a de-excitation back to the ground state under the emission of light, which is typically in the UV region. Since UV photons are absorbed very fast in a plastic material like polystyrene, a wavelength shifter has to be added to shift the wavelength of the scintillation photons to the visible energy range, where they can pass the scintillator and fit to the sensitivity range of the photo-sensor. The luminescence spectrum of a pure paraterphenile single crystal with an emission maximum at around 380 nm and the luminescence spectrum of a POPOP ($C_{24}H_{16}N_2O_2$) doped plastic scintillator based on polystyrene with paraterphenile as fluorescent material are shown in figure 1.42. The figure shows that the wavelength shifter POPOP decreases the energy of the photons and therefore shifts the maximum of the

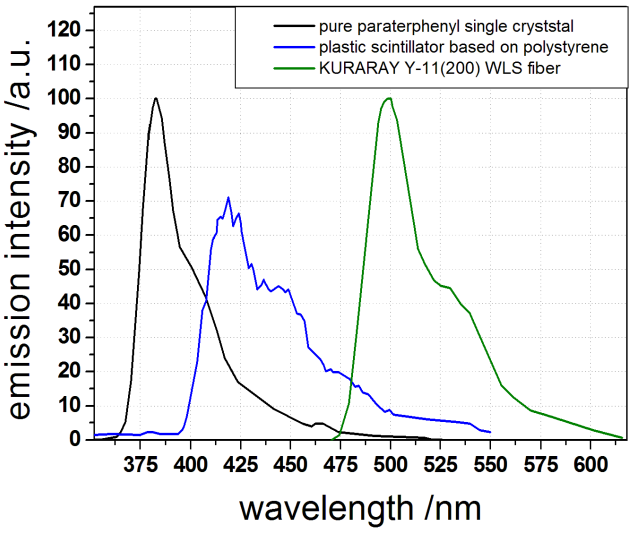

Figure 1.42: Luminescence spectra of pure paraterphenile (black) and of a POPOP doped plastic scintillator based on polystyrene with parateroehnile as flurescent material (blue) [TGP12]. In addition the emission spectrum of the Kuraray Y-11(200) WLS fibers is shown [KUR15].

emission spectrum to around 420 nm. The KOPIO collaboration has measured a light yield of the plastic scintillator material of (54 ± 6) % of anthracene which corresponds to around (9400 ± 1000) photons per MeV [ADI04]. The decay time of the emission of the primary UV photons by the paraterphenile is in the order of only 5 ns [CG93]. Considering the decay time of the wavelength shifter of only 1.6 ns [CG93], the total decay time of the scintillator material is in the region of a few nanoseconds which is typical for organic scintillators.

The wavelength shifting fibers used for the light transportation to the PMT (Kuraray Y-11(200)) have their maximal excitation wavelength at 430 nm which nicely fits to the emission of POPOP at 420 nm. The re-emission spectrum of the light is shown in figure 1.42. It shows a maximal emission wavelength of around 500 nm and tails up to 600 nm [KUR15]. The WLS fibers are specially optimized for a high light yield and an attenuation length of more than 3.5 m [KUR15].

Readout concept

The WLS fibers which are bundled at the rear side of each cell are read out with conventional PMTs. For the forward spectrometer, PMTs with a high rate capability and a high peak current stability are an essential requirement. In addition a fast response and signal rise time, which are needed to keep the fast output signal of the plastic scintillators short to reduce the pile up at high rates, can be reached with PMTs. An alternative for the readout with PMTs could be the use of silicon photomultipliers, which can also provide the announced advantages of PMTs in combination with a much more compact design. This option is currently under investigation for different other sampling calorimeter projects (i.e. [AK14]), but not considered for PANDA. Table 1.7 gives an overview over the basic properties of the currently favored Hamamatsu R7899 PMTs. The main feature of this PMT type is the high pulse height linearity up to an output current of 100 mA which is needed since the fast scintilla-

parameter	value
diameter of the entrance window	25 mm
number of dynodes	10
cathode material	bi-alkali
spectral response	300 nm - 650 nm
wavelength of max. quantum efficiency λ_{max}	420 nm
quantum efficiency at λ_{max}	27 %
quantum efficiency at 500 nm	14 %
gain at 1500 V	$2 \cdot 10^6$
output signal rise time	1.6 ns
electron transit time	16 ns
variation of transit time	0.7 ns
pulse height linearity @ 1500 V (± 2%)	100 mA

Table 1.7: Properties of the Hamamatsu R7899 PMTs, which are currently favored for the readout of the shashlyk modules [Ham00].

tion characteristics of the organic scintillator material produces a high amount of light on short time scales and therefore a large peak current of the PMT for high initial energies. In addition, a short output signal rise time and a small variation of the transit time are provided. The quantum efficiency of the standard blue sensitive bi-alkali (KCsSb) photocathode in comparison to the emission spectrum of the WLS fibers is shown in figure 1.43.

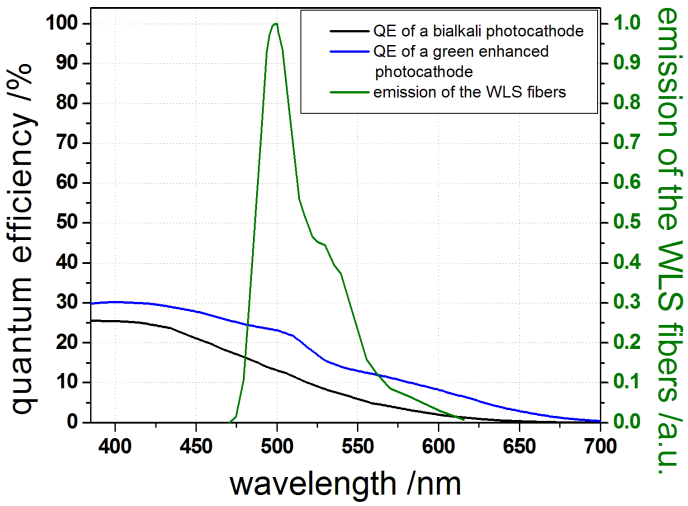

Figure 1.43: Quantum efficiency (QE) of a standard blue sensitive (black) and a green enhanced prismatic (blue) bi-alkali photocathode [Ham15] in comparison to the emission spectrum of the WLS fibers (green) [KUR15].

A disadvantage of this PMT is the relatively low quantum efficiency for the green emission light of the WLS fibers, with a weighted average of the quantum efficiency over the complete emission region of the WLS fibers of only 10.8 %. By changing the standard bi-alkali (KCsSb) photocathode to a green-enhanced bi-alkali (RbCsSb) photocathode this value could be increased up to 19.6 % [MS05]. The quantum efficiency of a R329-EGP PMT with a special

green-enhanced prismatic photocathode is shown in figure 1.43 in comparison to a standard bi-alkali photocathode. It especially introduces a large increase of the sensitivity in the relevant region around 500 nm. However, a final decision including the cost aspect has not been made up to now.

The high voltage supply of the PMTs is provided by a Cockcroft-Walton cascade generator, which is directly integrated into the base and supplied by a low voltage source [TDf15]. Figure 1.44 shows a picture of a Cockcroft-Walton unit attached to a PMT.

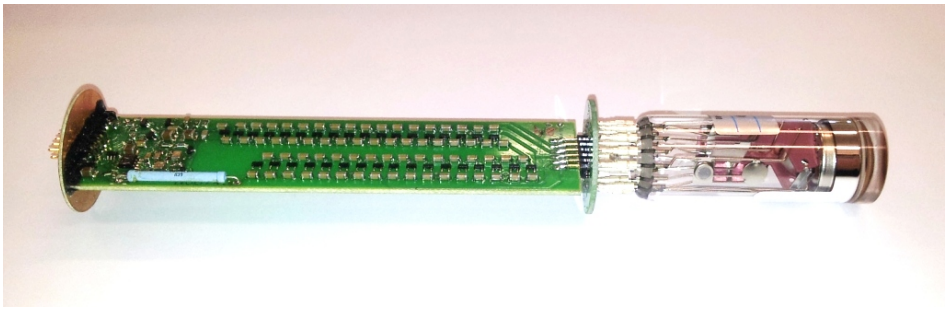

Figure 1.44: Picture of a Cockcroft Walton unit attached to a Hamamatsu R7899 PMT.

The main requirement for this device is to provide a sufficient voltage and current stability for the PMT even at rates up to 1-2 MHz. The current length of this modules of 15 cm has to be decreased in the final version to fit into the overall design length of the shashlyk EMC. This is possible since for the shashlyk calorimeter of the LHCb detector a Cockcroft-Walton unit for the high voltage supply of the same PMT model has been designed with half of the length [GGK07].

For the digitization of the signals currently two concepts are under discussion. The first concept foresees a digitization of the signals with a 14-15 bit sampling ADC with a sampling rate of at least 120 MHz [TDf15]. As a second concept a split of the signal into two branches with different gain/ attenuation like for the target EMC is possible to cover the complete dynamic range with two 12-13 bit sampling ADC channels with a sufficient accuracy. However, the first concept is currently favored [TDf15]. The signal processing will be handled similar to the target EMC, but is not yet fixed up to now. The main requirements are a fast signal treatment to handle the fast output signals and high rates and the implementation of a pile-up recovery, since even with a decay time of a few nanoseconds, a significant amount of pileup can be expected at the highest rates under the most forward angles [TDf15].

Calorimeter layout and characteristics

The shashlyk EMC is covering the innermost 5° in vertical and 10° in horizontal direction. Therefore, an area of (1.54 × 2.97) m^2 has to be covered at a distance of 7.8 m from the interaction point, which corresponds to $28 \times 54 = 1512$ cells [TDf15]. Figure 1.45 shows a drawing of the shashlyk wall with the support frame surrounding the modules. The frame can be split in two parts which can be assembled on the left and right side of the beam pipe and afterwards moved together. Due to the influence of the magnetic dipole field on charged particles and especially electrons, the arrangement of the modules is a bit asymmetric (12

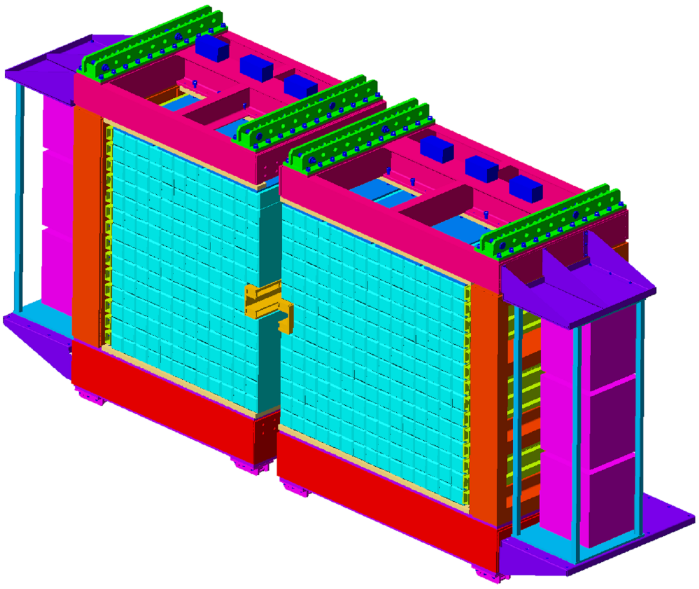

Figure 1.45: Front view of the shashlyk EMC with the beam pipe in the center [TDf15].

modules on the left and 15 modules on the right) to ensure the detection of electrons with an angle close to 10° [TDf15].

Table 1.8 gives an overview over the main physics properties of the shashlyk EMC in comparison to the target EMC.

property	shashlyk EMC	target EMC
number of individual units	$378 \times 4 = 1512$	15552
number of readout channels	1512	< 31104
effective density $[g/cm^3]$	2.7^A / 2.62^B	8.28
effective radiation length X_0 [cm]	3.49^A / 4.05^B	0.89
effective Molière-Radius R_M [cm]	5.98	2.0
active calorimeter depth	19.6 X_0	22.5 X_0
relative unit size	0.92 R_M	≈ 1.07 R_M

Table 1.8: Parameters of the shashlyk EMC for calorimeter physics in comparison to the target EMC made of PWO crystals [TDf15, KSM09, TDe09]. The super-scripts ^{A} and ^{B} indicate the version of the modules. The number of readout channels of the target EMC is smaller than the given value, since crystals of the forward end cap which are read out by a VPTT have only one channel per unit.

The comparison shows that, due to the use of a low Z organic scintillator material, the effective radiation length and the Molière-Radius are significantly larger for the shashlyk EMC. Therefore, the individual detector units have to be larger in all dimensions.

Chapter 2

The MAMI facility for detector tests and the current PANDA EMC prototypes

To test and to improve the energy-, position-, and time- resolution and to optimize the readout concept, several prototypes have been constructed for the target and the forward shashlyk EMC of PANDA. This work will show the influence of longitudinal and lateral non-uniformity on the performance of an electromagnetic calorimeter and present concepts to improve this non-uniformity on the basis of the current PANDA EMC prototype for the barrel part of the target spectrometer (PROTO120) and with the last two prototypes of the forward shashlyk EMC. All announced prototypes have been tested with a tagged photon beam in the energy range below 1 GeV in the A2 hall of the Mainz Microtron (MAMI) in Mainz (Germany). This chapter will describe the setup of the current prototypes as well as the MAMI accelerator and the Bremsstrahlungstagger of the A2 hall which is needed to provide a tagged photon beam for the detector tests. In addition, the first large scale barrel EMC prototype (PROTO60) will be described shortly, since it consists of less tapered crystals than PROTO120 and will therefore be used to compare the influence of the crystal geometry on the light collection and the energy resolution.

2.1 The Mainz Microtron MAMI

All detector tests have been performed with a tagged photon beam in the A2 hall of the Mainz Microtron (MAMI). The tagged photon beam has been produced from the incoming electron beam by the Mainz-Glasgow Bremsstrahlungstagger. This section will describe the functional principles of the electron accelerator MAMI and the Bremsstrahlungstagger.

2.1.1 The electron accelerator

The electron accelerator MAMI consists of an electron source with a linear pre-accelerator (LINAC), a cascade of three racetrack-microtrons (RTM1 - RTM3) and a harmonic double sided microtron (HDSM). With the combination of all microtrons it is possible to produce a

continuous electron beam with a current of up to 100 μA and a maximal energy of 1.5 GeV [IKP15]. Figure 2.1 shows an overview over the layout of the accelerator complex with the single microtrons and the experimental halls.

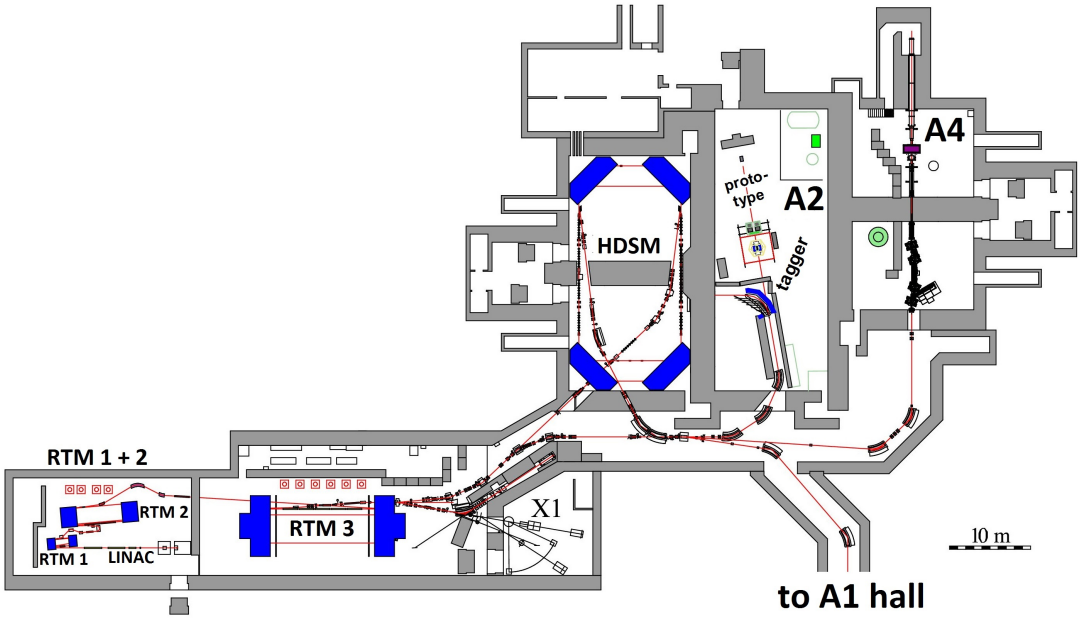

Figure 2.1: Layout of the MAMI accelerator complex with the racetrack mictrotrons and the experimental halls. Picture modified from [IKP15].

Electron source and injector LINAC

The un-polarized electron beam which is used to produce the photons for the detector tests is generated with a thermic electron gun, which accelerates the electrons emitted from an heated cathode to an energy of around 100 keV with a current of up to 100 μA [SGK08]. For experiments with polarized electrons an alternative electron source is available, which induces the emission of polarized photo-electrons ($\sim$ 75 % polarization) from an semiconductor crystal (i.e. GaAs) by a laser [ANA97]. With this source a beam current of up to 30 μA [SGK08] can be achieved. The electrons which are leaving the electron source are accelerated by a linear injector accelerator with three accelerating sections to an energy of 3.97 MeV. This pre-accelerator is also adjusting the injection phase of the electrons to the acceleration phase of the first microtron.

Racetrack microtrons

The pre-accelerated electrons are injected in the first microtron. Each of the racetrack microtrons consist of a linear acceleration section operating in a continuous wave mode at a frequency of 2.45 GHz and two dipole magnets which use a homogenous magnetic field to bend the electrons to a circular trace until their direction is turned by 180°. Since the electrons are accelerated only in one linear section, their energy remains constant in the second

linear section and the second dipole magnet leads the trace exactly to the beginning of the acceleration section. With a constant energy gain in the acceleration section in each turn, the electron trace can be exactly calculated. For a constant magnetic dipole field, the radius of the circular trace in the magnets increases in each turn with increasing electron energy. Therefore, the maximal number of turns is limited by the size of the dipole magnets. With the first racetrack-microtron (RTM 1) a maximal energy of 14.9 MeV can be reached in 18 turns [B115]. The electrons ejected from this microtron are injected in a second, larger racetrack microtron (RTM 2) with a higher magnetic field, which increases the energy in 51 turns up to 180 MeV [B115]. The electrons ejected from this microtron can be used directly for the experiments or they can be injected in the third microtron, which can increase the energy in maximal 90 turns up to 855 MeV [B115]. During this process beams with intermediate energies of 180 - 855 MeV can be extracted in energy steps of 15 MeV [B115]. Figure 2.2 shows a schematic drawing of the path of the electron beam from the source through the three racetrack microtrons.

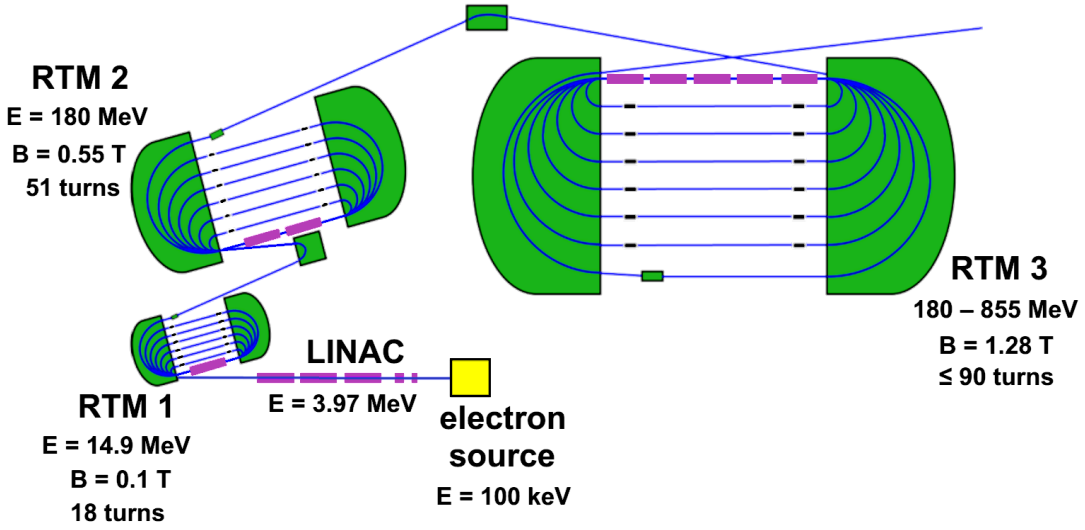

Figure 2.2: Schematic drawing of the electron source with the linear pre-accelerator (LINAC) and the three racetrack mictrotrons (RTM1 - RTM3). Concept taken from [ADe12].

Table 2.1 summarizes the most important parameters of the three racetrack-microtrons.

	RTM 1	RTM 2	RTM 3
input energy	3.97 MeV	14.86 MeV	180 MeV
output energy	14.86 MeV	180 MeV	855.1 MeV
turns	18	51	≤ 90
magnetic field	0.103 T	0.555 T	1.284 T
acceleration length	0.8 m	3.55 m	8.87 m
number of klystrons	1	2	5
energy gain per turn	0.599 MeV	3.24 MeV	7.5 MeV

Table 2.1: Parameters of the racetrack microtrons of the MAMI accelerator [B115].

For the described detector tests the 855 MeV electrons from RTM 3 were guided directly onto the radiator of the Bremsstrahlungstagger. To gain even higher energies of up to 1.5 GeV, the electrons can be injected in the harmonic double sided microtron HDSM which works after the same principle like the racetrack microtrons, but with an acceleration in both linear sections and a varying magnetic field, which is compensating the variation of the energy in the two dipole magnets. More details on the HDSM can be found in [B115].

2.1.2 The Mainz-Glasgow Tagger

The Mainz-Glasgow Tagger is used to produce a beam of energy marked photons from the primary electron beam of MAMI. Figure 2.3 shows a schematic drawing of the tagger with the electron traces in the magnetic field.

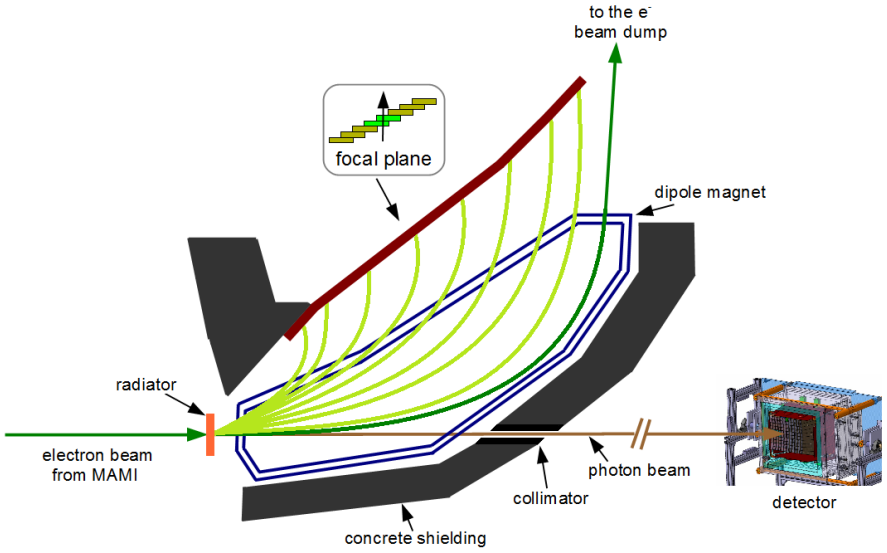

Figure 2.3: Top view of the Mainz-Glasgow Bremsstrahlungstagger. Concept taken from [MU09].

The primary electron beam is hitting a thin[1] radiator foil made of nickel or copper at the beginning of the setup. During this process some of the electrons are decelerated by the atomic nuclei of the radiator foil and lose energy by the emission of Bremsstrahlung. Due to the high primary electron energy, the emitted photons show a large Lorentz-boost in forward directions which leads to a quite narrow emission angle of the photons ($\theta \propto m_e/p_{beam}$). The produced continuous photon beam is collimated by a lead collimator and can interact with the prototypes after a distance of 10.5 - 14.5 m. To minimize the beam divergence at this distance a collimator of 1 mm and 1.5 mm diameter has been used. Since the distance between the radiator and the collimator in the tagger is around 2.5 m, the diameter of the Gaussian shaped beam spot at the detector position, 14.5 m away from the collimator can be calculated with geometrical considerations to 11.6 mm and 17.5 mm, respectively, for the two selected collimator diameters. By energy conservation the energy of the emitted photons E_γ and the energy of the decelerated electrons E_{e^-} are directly connected to the beam energy E_{beam}:

$$E_{beam} = E_\gamma + E_{e^-} \tag{2.1}$$

[1]For the test measurements 5 and 10 μm thick foils have been used

With this connection, the energy of the emitted photons can be determined by an energy measurement of the decelerated electrons. For this purpose a magnetic field[2] of $B = 1.02 - 1.83\ T$ [JA08], generated by a dipole magnet is used to bend the electrons on circular traces with an energy dependent radius:

$$r_e = \frac{p_e}{e \cdot B} = \frac{\sqrt{\frac{E_{e^-}^2}{c^2} - m_0^2 \cdot c^2}}{e \cdot B} \propto E_{e^-} \tag{2.2}$$

with the electron momentum p_e, the electron rest mass m_0 and the speed of light c. For the measurement of the radius, the electrons are detected by a ladder of 353 overlapping plastic scintillator bars (see fig. 2.3) located in the focal plane of the dipole magnet. The 80 mm long, 2 mm thick and 9-32 mm wide scintillator bars are read out individually with a PMT [MKA08]. The width of the modules varies along the ladder to keep the energy steps constant over the entire energy range [MKA08]. By requiring a coincidence between two neighboring overlapping modules, the PMT noise can be suppressed and the position resolution can be improved. The geometrically determined detection range of the ladder reaches from 5% up to 93 % of the primary electron energy [MKA08]. For an electron energy of 855 MeV, which has been used for the prototype tests, a range from 43 MeV up to 795 MeV can be covered with an accuracy of the photon energy of ±0.54 MeV for the highest energies and ±1.34 MeV for the lowest energies [AN13]. The time resolution of one tagger channel is in the order of 170 ps [MKA08], which enables a very good timing in coincidence measurements with the prototypes.

Figure 2.4 (left) shows the correlation of selected tagger channels with the photon energy for a primary electron beam of 855 MeV, while the right part of this figure shows the normalized tagger rate as a function of the photon energy for selected channels. It represents the $1/E_\gamma$ dependence of the differential cross section for the emission of Bremsstrahlung (see equation 1.12). More details about the tagger can be found in [MKA08] and [JA08].

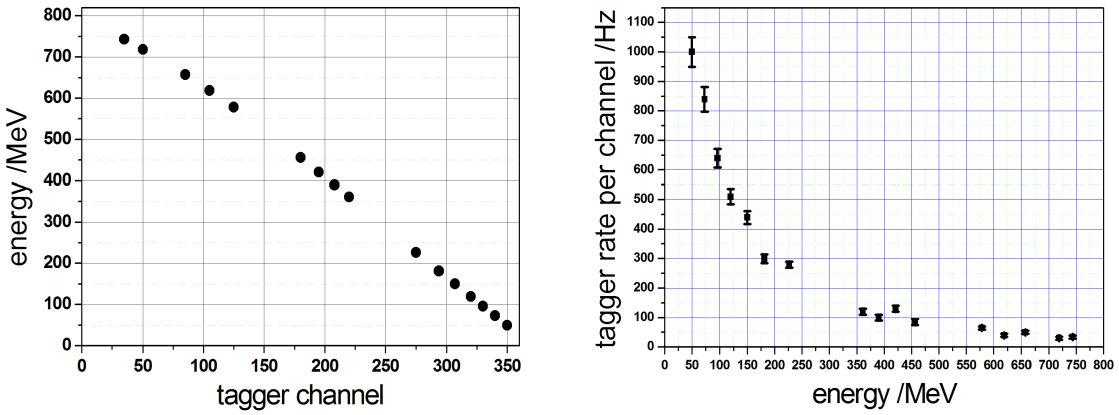

Figure 2.4: Correlation between the tagger channels and the photon energy for an electron beam energy of 855 MeV (left) and relative rate distribution for the single photon energies (right).

[2]Depending on the primary photon energy.

2.2 The first large scale barrel EMC prototype: PROTO60

The first large scale prototype of the barrel EMC was used to test the performance of cooled PWO-II crystals in the final geometry with an APD readout under real conditions. It consists of 60 type 6 PWO-II crystals which are arranged relative to the beam in a way like at their position within a barrel slice shown in figure 2.5.

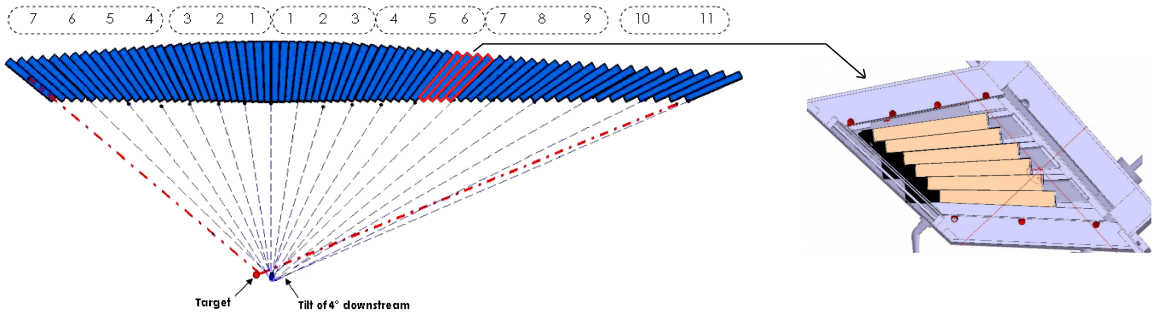

Figure 2.5: Position of the PROTO60 crystals within a barrel slice. The type 6 crystals are reaching in the barrel slice from crystal 21 to crystal 24, relative to the symmetry center [TDe09].

While the marked part of the barrel slice will consist of one alveole with 4×10 type 6 crystals, PROTO 60 is enlarged by two crystal rows of type 6 crystals to a 6×10 matrix to enable test measurements with larger crystal clusters. The right part of figure 2.5 shows the staggering of the crystals relative to each other within the cross section of the slice which results from the barrel arrangement. Like in the final configuration the crystals are wrapped with reflective VM2000 foil and placed in carbon fiber alveoles for mechanical stability. For this prototype several small alveoles for 2 × 2 crystals each were used and later on packed together.

The readout of this prototype is performed by a single 10 × 10 mm^2 LAAPD (Hamamatsu S8664-1010SPL) per crystal. The coupling of the LAAPD to the crystals is done by optical grease. The signals from the LAAPDs are amplified with a 4 fold pulse amplifier, which is a previous version of the low noise low power (LNP) preamplifiers described in section 1.3.4. The complete prototype including the preamplifiers is placed in an insulating housing and cooled down to -25°C. The signals which are lead out of the cooled volume by special backplanes are digitized by 50 MHz commercial sampling ADCs. More details on this prototype can be found in [KBD11] and [MM13].

2.3 The current barrel EMC prototype: PROTO120

The current barrel EMC prototype is build in a close to final design. It will be used to finalize the barrel mechanics and the readout, monitoring and cooling concept. PROTO 120 consists of a matrix of 12×10 PWO-II crystals, subdivided into three parts of 4×10 crystals, representing the first three geometries of the barrel slice. The crystals of type 1, 2 and 3 will be arranged exactly like in the final slice. Figure 2.6 shows the position of the slice section, represented by PROTO120.

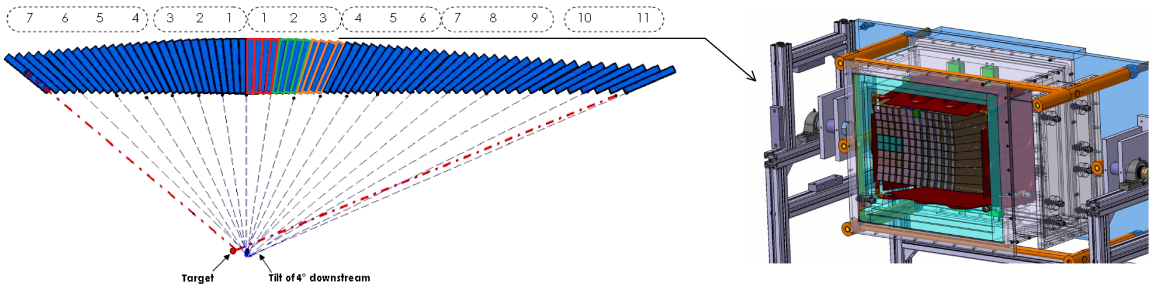

Figure 2.6: Position of the PROTO120 crystals within a barrel slice. The 4×10 matrix of type 1 crystals (red) is starting directly at the symmetry axis of the slice, followed by a 4×10 matrix of type 2 crystals (green) and a 4×10 matrix of type 3 crystals (orange) [TDe09].

2.3.1 The layout of the prototype

Each crystal is equipped with two $7 \times 14\ mm^2$ large LAAPDs of the final version (see section 1.3.4), which are glued to the rear side of the crystal with silicon glue (Dow Corning 3145 RTV MIL-A-46146). The complete rear side including the LAAPDs is covered by a capsule with reflective foil on the remaining crystal parts. The front face of the crystal is also covered with a reflective capsule, which will be used for the insertion of the light monitoring fibers. The lateral side faces are wrapped with the 63.5 μm thick [TDe09] mirror reflective polymer foil VM2000. Figure 2.7 (left) shows a picture of the crystals equipped with the LAAPDs and wrapped in VM2000.

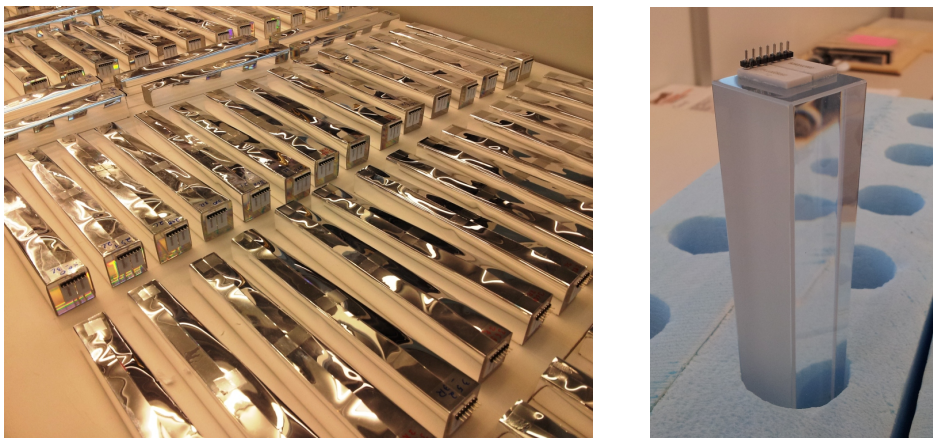

Figure 2.7: Picture of crystals wrapped with VM2000 and equipped with two LAAPDs (left) and picture of a crystal with one de-polished side face (right).

Each set of 40 crystals of the three types is placed in a carbon fiber alveole. Several flat temperature sensors [JS09] are integrated between the VM2000 and the carbon layer to control the temperature distribution in the prototype. The thickness of the carbon walls inside the alveole pack is $2 \times 200\mu m = 400\mu m$ [TDe09]. Together with the thickness of the VM2000 and an additional gap for mechanical tolerances, an average distance between the crystals of approximately 680 μm can be achieved [TDe09]. Between two alveole packs an additional gap for the thermal expansion and the mechanical assembly has to be introduced, which increases

the distance between two crystals in this region to around 900 μm [TDe09]. For type 2 a 3×3 matrix in one corner of the alveole has been equipped with crystals with the most tapered lateral side face roughed up to $R_a = 0.3\ \mu m$ to reduce the non-uniformity in light collection. A picture of such a crystal already equipped with the two LAAPDs is shown in figure 2.7 (right). More details about the crystal and APD configuration of the prototype can be found in appendix A.

For the mounting of the units, aluminum inserts are glued in the alveole on the rear side of the crystals with epoxy glue. After inserting and fixing the ASIC boards, additional back-plates with a varying geometry are screwed onto the inserts to create a planar end-face. With this preparation it becomes possible to mount the complete alveole onto the cooled back plane with openings for the cables. The complete crystal matrix is surrounded by cooled copper walls and a cooled front cover made of plastic material and a thin aluminum front plate. The cooling of the prototype to -25°C is provided by a cooling circuit filled with a mixture of 60 % methanol and 40 % water as cooling liquid. The side walls are made of thick insulating material and a plastic case. The complete structure is screwed to a massive central aluminum plate, which is separating the cold and the warm part of the detector. Between the cooled crystal back-plate and the aluminum plate a gap of a few centimeters is left for the connection of the ASICS to the distributor boards. Figure 2.8 (left) shows a picture of the type 2 alveole mounted on the back plane and surrounded by the side cooling and housing structures. The right part of figure 2.8 shows a schematic CAD drawing of the complete prototype with the cooling and housing structures, but without the front cover.

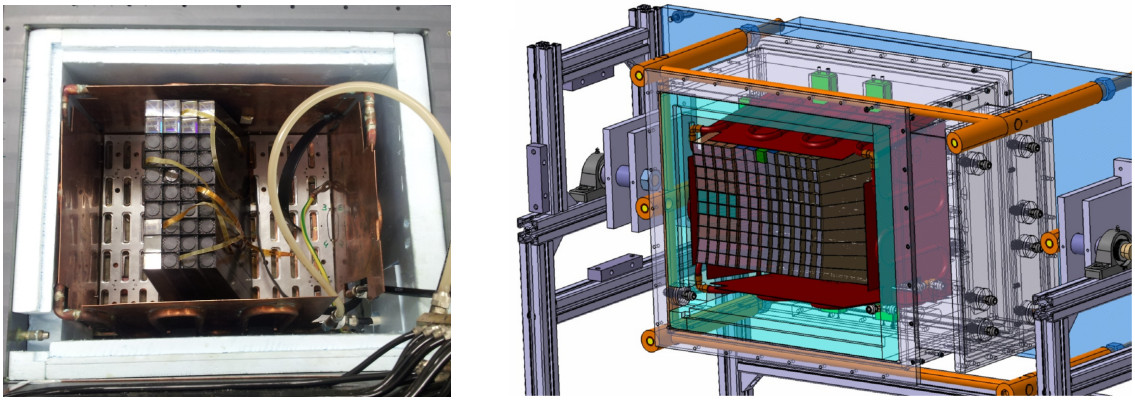

Figure 2.8: Picture of the open prototype with the type 2 section mounted (left) and CAD drawing of PROTO120 seen from the front side with removed front cover (right). The crystals are surrounded by the cooling plates and the isolating housing.

Due to the barrel geometry, only the central crystal of the first column of the type 1 alveole is aligned approximately to a line perpendicular to the front cover, leading to the central point of the barrel, which is tilted 4° downstream compared to the target. All other crystals are also facing to this central point of the barrel and therefore show an angle relative to the flat front cover of the prototype, which has to be taken into account for test measurements with straight beams. Figure 2.9 shows a vertical cross-section through the center of the sixth crystal column of PROTO120 (left) and a horizontal cross-section through the center of the fifth crystal row (right). All positions are given relative to the left upper corner of the prototypes front face (see fig. 2.8 (right)).

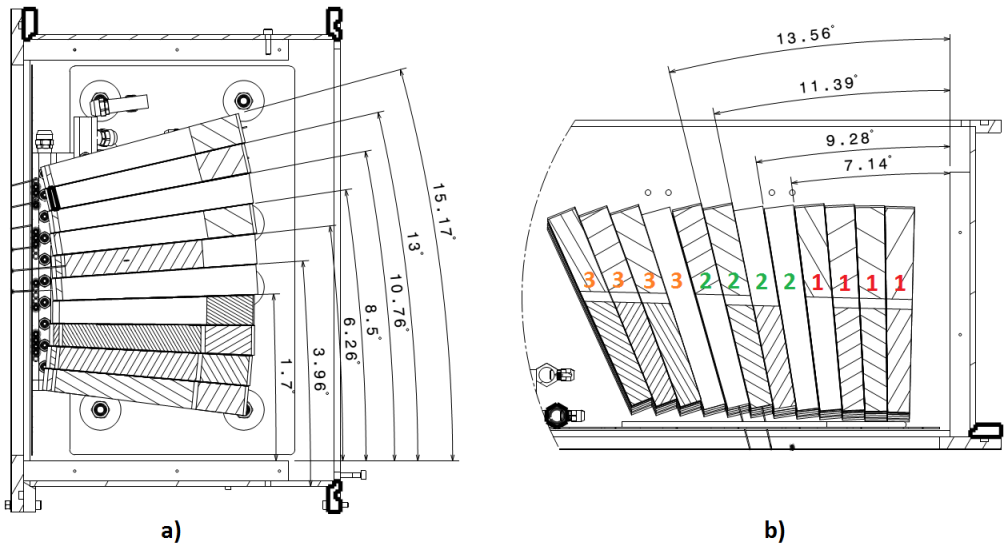

Figure 2.9: Cross section through the crystal arrangement of PROTO 120 in vertical direction (a) at the position of the sixth crystal column and in horizontal direction (b) at the position of the fifth crystal row relative to the left upper corner of the front of the detector housing in figure 2.8. The angles are measured relative to a line perpendicular to the front cover which represents the central symmetry axis of the barrel in longitudinal direction.

For the alignment of the interaction position and the relative angle of the photon beam, an xy$\vartheta\varphi$-table has been constructed. Figure 2.10 shows a picture of the prototype mounted on the xy$\vartheta\varphi$-table and aligned to the crystal axis of a crystal in the center of the type 2 alveole. In the A2 Hall of MAMI, the prototype is placed approximately 14.5 m away from the tagger. Therefore, the photons have to traverse a quite long distance through the ambient air. To reject electrons and positrons which have been produced due to conversions of the photon beam in air, a thin plastic paddle is mounted directly in front of the prototype, which identifies passing electrons.

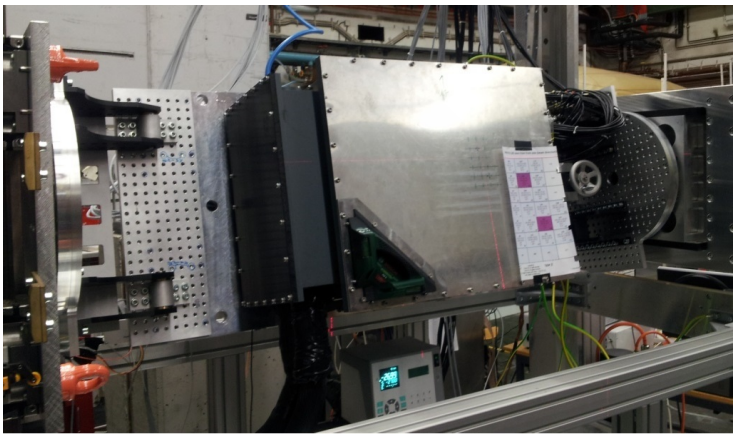

Figure 2.10: Picture of the prototype mounted on the xy$\vartheta\varphi$-table and aligned to the crystal axis for the center of the type 2 alveole.

2.3.2 Readout and data acquisition concept

The amplification and the shaping of the LAAPD signals is performed by the current version 1.5 of the APFEL ASIC (see section 1.3.4). The output signal of the ASIC is transported to the connector boards via double layer flex-cables which are optimized for a minimal noise pick-up. This flex cables are also used for the high voltage supply of the LAAPDs, the low voltage supply of the ASIC and for the slow control information of the ASICs. While the high and low voltage cables are directly connected to the connector boards, the signal and slow control information is lead out of the cooled volume via flat cables to a buffer board, placed in the warm volume behind the central aluminum plate of the prototype. Also the slow control of the ASICS, which is connected to the buffer boards via an additional board in the warm volume, is connected to the ASICS via these flat cables. The connection to the sampling ADCs is realized with specially shielded cables, which are transporting the differential signals with the information of the high and low gain of the two APDs. Figure 2.11 shows the cabled front-end-electronics connected to selected crystals of an alveole which is still in the mounting frame, placed in a climate chamber. In addition to the signal and high voltage cables, also the shielded low voltage cable and a flat cable for the slow control have to be guided out of the detector volume.

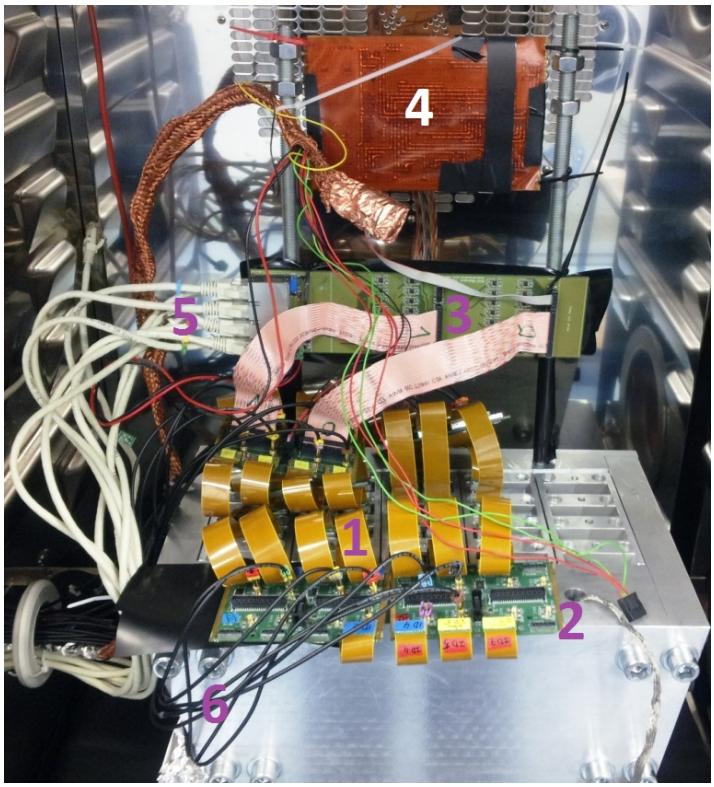

Figure 2.11: Picture of the front end electronics of PROTO120 connected for testing purposes to selected crystals of an alveole equipped with 10×4 crystals, which is still in the massive mounting frame. The flex cables of the ASICS (1), the connector boards (2), the concentrator boards (3) and the board for the connection of the slow control can be seen. The signal cables (5) and the high voltage cables (6) are connected with the sampling ADC and the high voltage units which are placed outside the climate chamber.

Figure 2.12 shows a scheme of the **data acquisition electronics**.

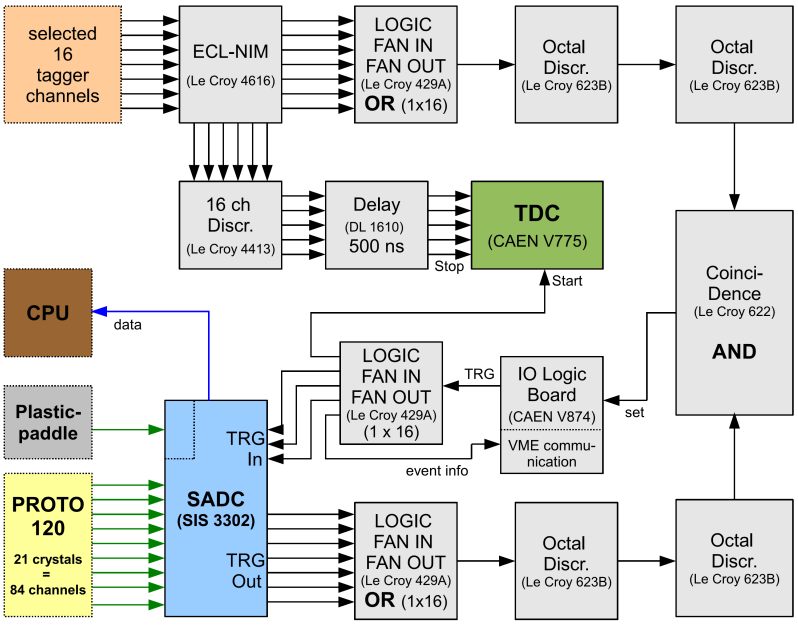

Figure 2.12: Data acquisition scheme for the PROTO120 beam-times. The green arrows show the connection of the raw signals between the detector modules and the sampling ADCs, while the blue arrow shows the internal data submission form the SADCs to the CPU via the VME bus. The black arrows show connections with standard logic ECL or NIM signals.

For the coincidence with the tagger and the trigger generation standard NIM[3] and CAMAC[4] modules have been used. The signals from the prototype and the plastic paddle are directly connected to the 50 MHz, 16 bit sampling ADC (SIS 3302). For this sampling ADC an internal leading edge trigger threshold can be set in the software for each channel. If one of the PROTO120 signals connected to the ADC is above this threshold, a trigger output signal is generated. The "OR" of this trigger output of all connected PROTO120 channels is connected to the coincidence module. To gain a well defined signal, two octal discriminators are intersected. In between these discriminators a variable delay can be placed to adjust the timing of the signal. On the other side of the scheme the information of the 16 tagger channels is converted into the NIM standard and split in two parts. The first part of the 16 signals is delayed and used as "stop" signal for a Time to Digital Converter (TDC). This TDC is set to a range of 140 ns and a resolution of 8 bit. With this configuration the time information of the tagger can be recorded with a resolution of around 550 ps. On the other side the "OR" of the 16 tagger channels is connected to the coincidence module via two discriminators, like the OR of the SADC trigger output. If a coincidence between one of the tagger channels and one of the detector channels exists, a Flip-Flop is set in the I/O logic board and a trigger signal for the readout is generated. This signal is split into several output channels. On the one side it is triggering the data acquisition of all ADC boards in a common readout mode and on the other side is used as a start signal for the TDC which records the relative time information of the tagger. In addition it gives the event information to the VME bus via the I/O logic

[3]Nuclear Instrumentation Modul-Standard
[4]Computer Aided Measurement And Control

board. This step is necessary because the readout is blocked until the acquisition of the event is finished. After the readout is ready again, the I/O logic board gets this information from the VME bus and resets the Flip-Flop, which enables the recoding of the next event.

2.4 The forward shashlyk EMC prototypes

For the forward shashlyk EMC two prototypes have been tested with energies below 1 GeV at MAMI in 2011/2012 and 2014. All prototypes consist of an array of modules with 2×2 cells each, with the designs described in section 1.3.5.

2.4.1 The prototype tested in 2011/2012

The first prototype consisted of a 3×3 array of **version A modules** (see section 1.3.5) with $6 \times 6 = 36$ cells. The readout was performed with Philips XP1911/1912 photo-multiplier tubes with passive voltage dividers and a 3×3 matrix in one corner equipped with eight Hamamatsu R7899 photo-multiplier tubes with an active Cockcroft-Walton high voltage cascade generator. Picture 2.13 shows the arrangement of the module array during the two beam-times in December 2011 and April 2012.

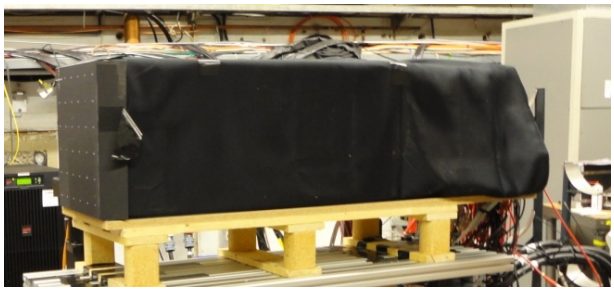

Figure 2.13: Pictures of the shashlyk EMC prototype tested in 2011/2012 with 3×3 modules (6×6 cells) of type A.

To fix the modules together and to avoid gaps in between the modules, the complete matrix was fixed with tension belts. Since the version A modules of this prototype were not light tight, they were covered with an additional layer of black paper and the complete outer surface of the prototype was covered with two layers of a black toweling. A plastic scintillator paddle is placed in front of the prototype to reject electrons and positrons produced due to photon conversion in air. More details about this prototype which is further on referred to as **"version A prototype"** can be found in [SD12].

2.4.2 The prototype tested in 2014

The current prototype consists of a 2×2 array of the improved **version B modules** (see section 1.3.5) with $4 \times 4 = 16$ cells. It will be referred to as **"version B prototype"**. The readout of all cells is performed with Hamamatsu R7899 photo multiplier tubes with active Cockcroft-Walton high voltage cascade generators. The arrangement of the modules during the beam-time is shown in figure 2.14.

Figure 2.14: Picture of the new shashlyk EMC prototype tested in 2014 with 2 × 2 modules (4 × 4 cells) of type B.

The four modules are fixed together on the front and rear side with tape to avoid gaps in between the modules. Although the version B modules are more light tight than the previous version, the outer surface of the prototype has been covered with black toweling to avoid any effects of the ambient light. The prototype is placed on a xy-table to scan different interaction positions of the photon beam.

2.4.3 Data acquisition of the shashlyk prototypes

Figure 2.15 shows a scheme of the data acquisition electronics used for the readout of the shashlyk cells during the 2014 beam-time. Since the internal trigger of the used ADC did not work properly, each signal of the 16 shashlyk cells was actively split to generate a timing and trigger signal. While one part of the signal goes directly into the 160 MHz, 12 bit sampling ADC (WIENER AVM 16), the other part is lead to a constant fraction discriminator with a threshold set just above the noise-level of the PMTs. The 16 logic output channels are converted to the NIM standard and the "OR" of the 16 channels is used for the coincidence with the tagger. For the tagger 15 channels have been selected. The sixteenth channel provides an internal "OR" of the other 15 channels. All channels are converted to the NIM standard and refreshed by a discriminator. While the 15 channels with the tagger information are delayed and recorded by a 50 MHz, 16 bit sampling ADC (SIS 3320), the "OR" of this 15 channels is delayed and used for the coincidence with the shashlyk modules. If a coincidence between one of the 15 tagger channels and one of the 16 shashlyk cells takes places, a Flip-Flop is set in the I/O logic board and a trigger signal is created. This signal is split into three output branches. While the first two are used for the triggering of the two sampling ADCs for the shashlyk cells and the tagger channels, the third signal is used to submit the event information to the VME bus via the I/O logic board. This step is necessary because the readout is blocked until the acquisition of the event is finished. After the readout is ready again, the I/O logic board gets this information from the VME bus and resets the Flip-Flop, which enables the recoding of the next event. The signal of the plastic paddle is automatically recorded by the sampling ADC of the tagger channels for each event.

For the version A prototype a similar readout with the same sampling ADC has been used. A detailed description can be found in [SD12].

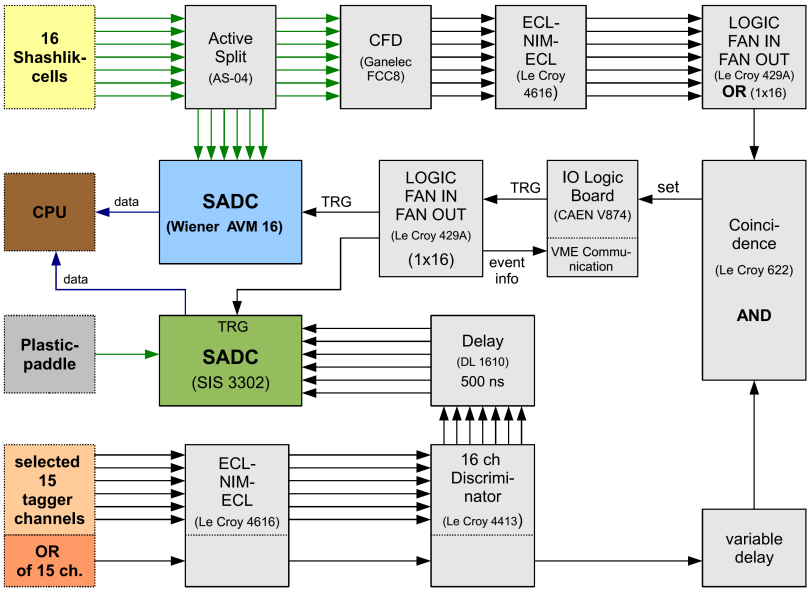

Figure 2.15: Data acquisition scheme for the last shashlyk EMC prototype beam-time. The green arrows show the connection of the raw signals between the detector modules and the sampling ADCs and CFD modules, while the blue arrow shows the internal data submission form the SADCs to the CPU via the VME bus. The black arrows show connections with standard logic ECL or NIM signals.

2.5 Overview over the beam-times

For the tests of the prototypes several beam-times have been used, which are listed in table 2.2. During the beam-times in 2011 and 2012 only the version A prototype of the shashlyk modules was tested. In the 2014 beam-time the first version of PROTO120 as well as the version B prototype of the shashlyk modules have been tested. During the last two beam-times in 2015 only the second and third iteration of PROTO120 has been tested.

beam-time	beam energy (e^-)	radiator	collimator	E_{photon}
07.12. - 09.12.2011	855.0 MeV	5 μm Ni	1.0 mm	102.2 MeV - 769.0 MeV
04.04. - 06.04.2012	855.0 MeV	5 μm Ni	1.0 mm	58.5 MeV - 769.2 MeV
17.07. - 21.07.2014	855.0 MeV	10 μm Cu	1.5 mm	54.7 MeV - 652.7 MeV
30.01. - 02.02.2015	855.0 MeV	10 μm Cu	1.5 mm	49.8 MeV - 743.3 MeV
10.04. - 13.04.2015	883.2 MeV	10 μm Cu	1.5 mm	56.4 MeV - 766.8 MeV

Table 2.2: Overview over the beam-times used for tests of the shashlyk EMC and PROTO120.

Chapter 3

Influence of the feature extraction, calibration and detector inhomogeneities on the performance of the forward shashlyk EMC

The forward shashlyk calorimeter of the PANDA detector has been constructed to detect electromagnetic probes in an energy range from 10 MeV up to 15 GeV. To reach the physics goals of PANDA, a sufficient energy resolution has to be provided for the complete energy range and for all interaction positions on the calorimeter wall. At large energies above 1 GeV electromagnetic showers induced by the incoming electromagnetic probes spread over a large part of an individual detector cell in longitudinal direction and over several cells in lateral direction. In contrast to this, for small energies ($\ll$ 1 GeV) the spread of the shower is limited in longitudinal and lateral directions, which makes the detector more sensitive to local inhomogeneities of the energy response in single detector cells. To test the performance and the homogeneity of the energy response for different interaction points in lateral direction at low photon energies, a first prototype (version A) has been tested with tagged photons below 1 GeV at MAMI in 2011/2012. Since a strong position dependent energy response and a large variation in the longitudinal uniformity of the modules were observed, a second improved prototype (version B), has been tested at MAMI in 2014 (for details of the prototypes see section 2.4).

The results of the version A prototype have already been presented in detail in the master-thesis of the author "Response of a Shashlyk Calorimeter to High Energetic Photons in the Energy Range from 100 MeV up to 770 MeV" [SD12] and will be shortly reviewed as a basis for a comparison. The main part of this chapter will show the performance of the improved version B prototype and the influence of the improvements on the energy resolution and the homogeneity of the energy response. A comparison of the two prototypes, pointing out the improvements which have been achieved can be found in the discussion (sec. 5.1).

3.1 Review: Performance of the version A prototype

The response to high energetic photons of the version A prototype has been tested in the energy range from 100 MeV up to 770 MeV [SD12]. To investigate the position dependence of the energy response, different interaction points have been scanned with the photon beam. Figure 3.1 shows the interaction positions of the tagged photon beam on the front face of a module in the center of the prototype, consisting of 3 × 3 modules with in total 6 × 6 individual cells. Details on the data acquisition, the feature extraction and the calibration can be found in [SD12].

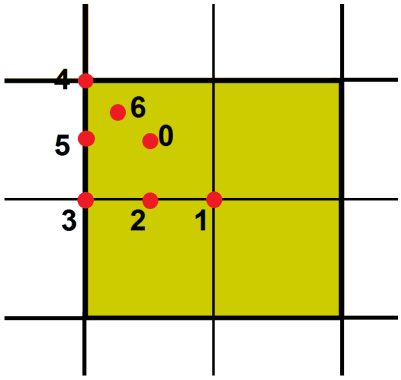

Figure 3.1: Interaction positions of the photon beam within a module of the version A prototype during the beam-time in 2012 [SD12]. The shown module is positioned in the center of the 6×6 matrix.

3.1.1 Linearity and homogeneity of the energy response

For the energy reconstruction, the complete 6 × 6 matrix has been considered with a reconstruction threshold of the individual cells of approximately 3 MeV, which was determined by the noise-level of the individual channel. Figure 3.2 (left) shows the reconstructed energy as a function of the incident photon energy for the positions marked in figure 3.1, while the right part of figure 3.2 shows the reconstructed energy, absolutely calibrated for position 0 for a fixed energy of 103 MeV, as a function of the interaction position. The figures illustrate that the reconstructed energy strongly depends on the interaction position over the entire energy range with an absolute variation of up to 25 % [SD12]. A comparison of the positions shows that the deduced energy is reduced for the inner positions of the cell and increased for the positions at the outer border and the outer corner. This behavior can be related to having only one fixation pin per cell and a different reflector concept for the inner and outer edges of the scintillator tiles. For more details see section 2.4 and [SD12].

3.1.2 Position dependence of the energy resolution

The energy resolution was also extracted from the complete 6 × 6 matrix with a threshold of the individual cells of approximately 3 MeV. Figure 3.3 shows the relative energy resolution as a function of the incident photon energy for the different interaction positions. Even the relative energy resolution shows a large variation. In accordance to the reconstructed

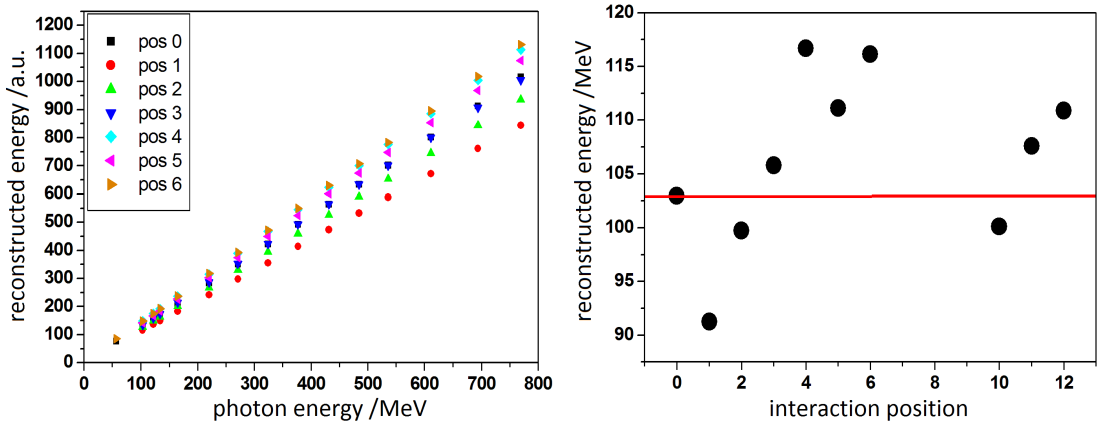

Figure 3.2: Linearity of the energy response of the complete 6 × 6 matrix of shashlyk cells for different interaction positions within one of the central cells (left) [SD12] and reconstructed energy as a function of the interaction position for an incident photon energy of 103 MeV, with an absolute calibration for position 0 (right) [SD12]. Position 10, 11 and 12 are measured for an interaction of the photon beam in a different cell and correspond to position 0, 5 and 4 in the original cell, respectively. The bold line in the right figure show the reconstructed energy in the center of the primary target cell.

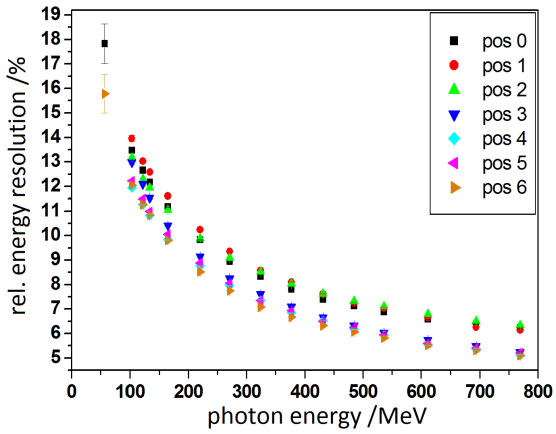

Figure 3.3: Dependence of the relative energy resolution on the interaction position within one module for different incident photon energies [SD12]. For the reconstruction, the complete 6 × 6 array of the version A prototype has been used.

energy in figure 3.2 and the directly correlated light yield, a better energy resolution can be achieved for interaction positions in between two modules or in the corner of the module, while the positions inside the module show a significantly worse energy resolution [SD12]. For an interaction in the center of the cell (pos 0), the relative energy resolution can be described by [SD12]:

$$\frac{\sigma}{E} = \frac{4.22\ \%}{\sqrt{E/GeV}} \oplus 3.82\% \tag{3.1}$$

Smearing the incoming photons over the entire front face would further degrade the resolution due to the lateral non-uniformity of up to ± 12.5 %. For more details on the energy resolution see [SD12].

3.1.3 Longitudinal homogeneity

Another critical issue which was found for the version A modules is a strong module dependent variation of the longitudinal homogeneity of the energy response from around 5 % up to more than 30 %, depending on the individual cell [SD12]. Figure 3.4 shows this variation in the longitudinal response for different cells, which has been measured by a coincidence of cosmic muons between two thin plastic scintillator bars above the module and the module itself. More details on the measurement technique can be found in section 3.5.1.

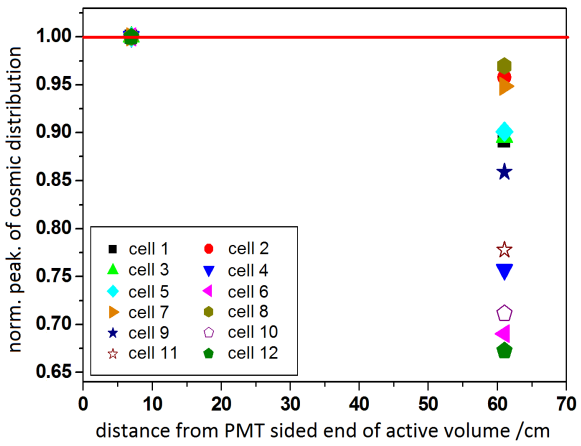

Figure 3.4: Position of the cosmic muon peak for a transverse interaction of the muons close to the PMT sided end of the active volume and close to the front side of the cells, normalized to the point close to the PMT [SD12].

The strong variation between the cells can be explained by different intensities of cracks in the bending region of the WLS fibers at the front end of the modules, which were caused by a not optimized bending procedure [SD12]. In addition, a possible damage of the fibers inside the modules by the scintillator tiles, which were not stabilized enough by a single fixation pin, is possible.

3.2 Energy response of the version B prototype

The version B prototype described in section 2.4.2 has been tested as a 4×4 array of cells (2×2 modules) with a tagged photon beam in the energy range from 55 MeV up to 650 MeV at the MAMI accelerator complex in Mainz in July 2014. To scan different interaction positions of the photon beam, it has been placed on a remote controlled xy-table and adjusted to the beam center with a laser system. Figure 3.5 shows the arrangement of the modules during the beam-time and the interaction positions of the tagged photon beam within the prototype. Since the photon beam has to pass several meters of air before it hits the prototype, a plastic scintillator paddle has been placed in front of the prototype to reject electrons and positrons created by conversion of photons in air or by an interaction with other materials in the photon beam. This paddle is only responding if a charged particle is passing it, or if a photon undergoes a conversion within the paddle, which happens with a probability of less than 1 %.

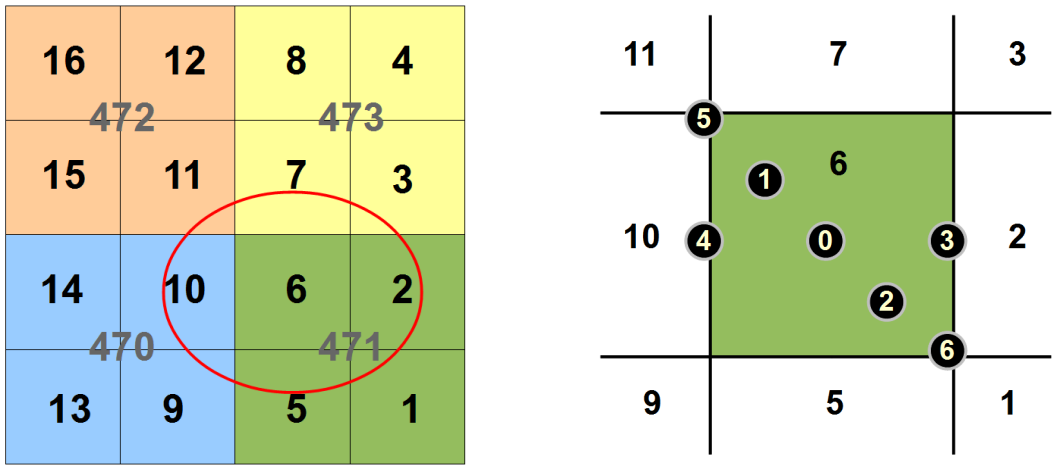

Figure 3.5: Arrangement of the modules of the version B prototype (left) and interaction positions of the photon beam within cell number 6 (right).

To ensure the exclusive detection of photons an anti-coincidence between the detector and the paddle is required.

3.2.1 Feature extraction methods

The signals created by the PMT readout are recorded with a 160 MHz, 12 bit sampling ADC (WIENER AVM 16). Depending on the shaping of the signals by the connection cables, the typical rise time is in the order of 1.4 - 3.0 ns, while the decay time is in the order of 10 - 15 ns [SD12]. Figure 3.6 shows typical traces for different incident photon energies recorded with the sampling ADC. The undershoot after the main signal becomes dominant for high energies and is caused by a not proper impedance of the sampling ADC entrance. Since this effect is nearly proportional to the energy, it has no effect on the results, even if it is included in the integration region. To avoid pile up events, a low electron beam current of $\sim$ 15 nA was used to produce the tagged photon beam. The total rate of the fifteen, selected tagger channels was at a level of 15 kHz. Considering the total tagger rate of $\sim$ 390 kHz the pile-up probability is negligible.

For the feature extraction of the energy information several methods have been performed and compared. For all methods the pedestal has been deduced by averaging over the first 50 channels of the sampling ADC trace, which corresponds to a time interval of 312.5 ns. Based on this value for the pedestal there are several methods to extract the energy information.

Peak sensing feature extraction

The first and easiest method for the extraction of the energy information is the peak sensing feature extraction. Since the leading edge trigger of the sampling ADC places the leading edge of the signal trace at approximately the same position in each event, only a relatively sharp window has to be considered for the position of the maximum of the trace. Therefore, the maximal SADC value of the trace is searched in a region of 18 ADC channels (112.5 ns) around the expected position. The energy information is then extracted by subtracting the

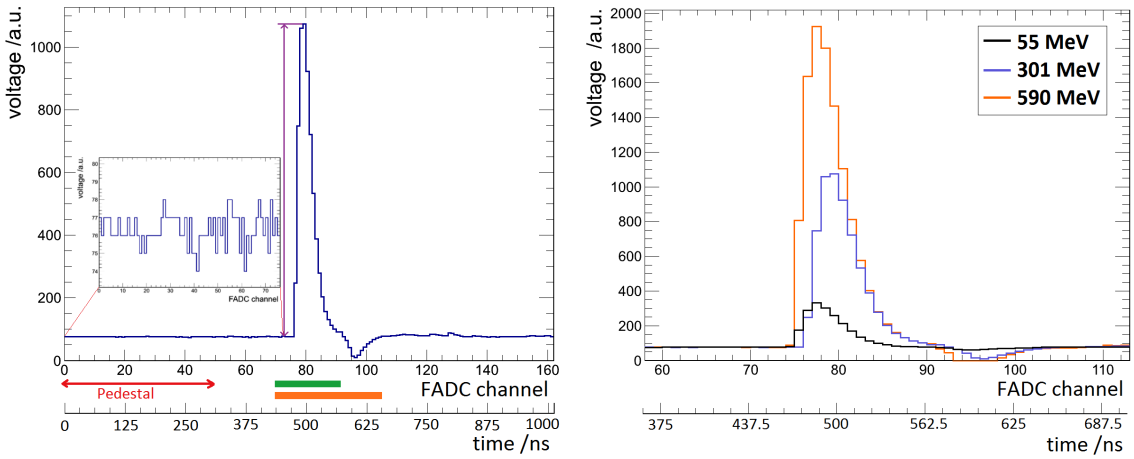

Figure 3.6: Signal-trace, recorded by the sampling ADC for an energy of around 300 MeV over a time range of 1 μs (left). The time region for the pedestal extraction is shown in red and the different integration regions in green (method 2) and orange (method 3). The peak sensing feature extraction (method 1) is illustrated by the purple arrow. The right figure shows a detailed view on traces corresponding to different incident photon energies. One SADC channel is corresponding to 6.25 ns.

pedestal from the maximal value in this region. This method will further on be referred to as "AMP" feature extraction.

The main advantages of this method are given by its stability and by the low computing effort which is needed for this feature extraction. A disadvantage can be seen in the high sensitivity to electronic noise overlapping the signal trace since only one bin is considered for the energy extraction. The electronic noise influences on the one hand the resolution which can be extracted from the signal and on the other hand also the threshold level which has to be set to calculate the energy sum of a cluster. Another disadvantage are sampling variations of the signal height introduced by the ADC due to the short signal length. The signals in figure 3.6 show that the height of the bins next to the maximal bin is significantly reduced. Therefore, small variations in the leading edge timing of the sampling ADC can cause a variation of the height of the central bin, if the signal is shifted by a few nanoseconds on the time axis. For a pure peak sensing feature extraction only a faster sampling rate of the ADC or a larger signal width can reduce the impact of this effect. However, there are methods to correct these effects based on the recorded data, considering the height of the neighboring bins [MK14]. Nevertheless, since these effects are in the order of less than ± 0.6 % [MK14] they have no significant impact on the energy resolution of the shashlyk EMC and can be neglected in the feature extraction.

Fit of the signal trace

The problem of the sampling variations introduced by the limited sampling frequency of the ADC can be solved by considering not only the highest bin, but also the neighboring bins. In the most accurate case this would lead to a fit of the complete signal trace with a theoretical function. The advantage of this method is the very accurate determination of the signal height for well developed signal traces. At low energy depositions with signals close to the noise level

a fit of the signal trace can be used to average the noise contribution, which might result in an improvement of the energy resolution compared to a peak sensing feature extraction. On the other hand, a fit of the signal trace in each event consumes a lot of computing power and can therefore only be considered for a second level or off-line analysis of the data. A more detailed discussion of the fit procedure and an application of the method can be found in the analysis of PROTO 120 in chapter 4.

Integration of the signal trace

The integration of the signal trace uses the fact that for a PMT the area of the pulse is proportional to the total charge collected by the PMT. The integration can be performed by summing the height of the single bins in relation to the pedestal:

$$E = \sum_{\mathrm{i}\,=\,\mathrm{bin}_{min}}^{\mathrm{bin}_{max}} (\mathrm{height[i]} - \mathrm{pedestal}) \tag{3.2}$$

In a first version of this method the undershoot of the signal trace behind the main signal (see fig. 3.6) has been ignored and the integration starting in front of the signal has been performed for only 23 SADC channels, corresponding to approximately 144 ns, stopping just before the start of the undershoot. In a second case the undershoot has been included in the integral with a total integration window of 36 SADC channels, corresponding to 225 ns. The integration regions are shown in figure 3.6 (left). Since this integration emulates the working principle of a charge integrating ADC (QDC) with a given integration gate, these methods are further on referred to as QDC-short and QDC.

The integration of the signal shape has several advantages. On the one hand the sampling fluctuations caused by the ADC are canceled out by summing all bins of the pulse. On the other hand this summation also averages out a part of the electronic noise and therefore improves the energy resolution and reduces the single cell threshold. Another advantage of this method is the reduced sensitivity to saturation effects of the PMT or the ADC, since more bins than the maximal bin which is most affected by these effects are taken into account. A disadvantage is given by the sensitivity of this method to pile-up effects at high interaction rates. Therefore, a pile-up identification and rejection or recovery has to be implemented in these cases.

Since all presented feature extraction methods for the tested prototype provide only small differences in the results, the pictures in the following subsections will be only shown for the case of the integration with a gate of 144 ns (QDC-short), which finally provides slightly better results in terms of energy resolution.

3.2.2 Response of a single cell

The smallest unit of the shashlyk calorimeter is a single cell, read out by one PMT. To characterize the response of each cell and to perform the relative calibration of the cells, the response of each cell with the photon beam hitting exactly in the center of the cell was recorded. In this configuration one expects a similar behavior for each cell, only differing by the different gains of the PMTs, which were adjusted only approximately by a pre-calibration with cosmic muons (see section 3.2.4) before the beam-time.

Line-shape of the energy distribution: Figure 3.7 (left) shows the line-shapes of the energy distribution for a single cell with a photon beam of 1.7 cm in diameter, interacting in the center of the cell for different incident photon energies between 55 MeV and 590 MeV.

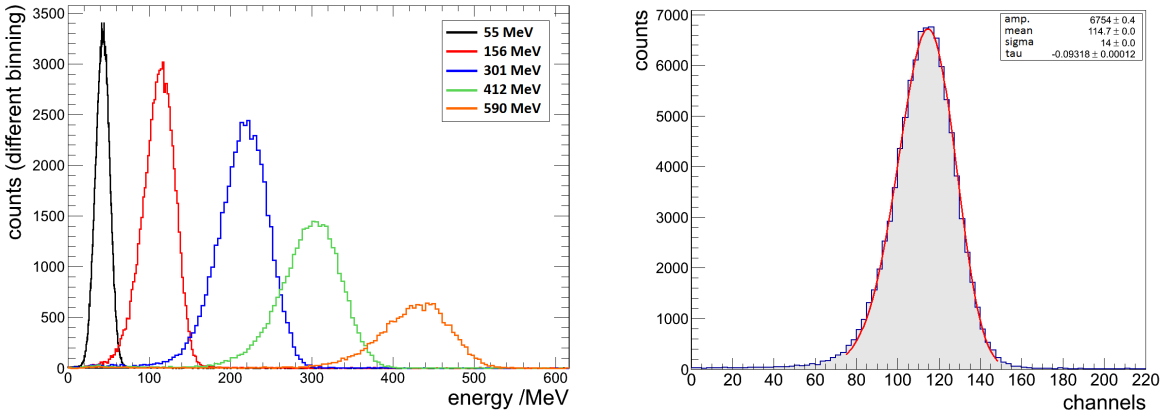

Figure 3.7: Line-shapes of a single cell with the photon beam interacting in the center of the cell for different photon energies (left) and fit of the line-shape recorded for 156 MeV photons by a Novosibirsk function (right).

Since the dimension of a single cell corresponds to around one Molière-Radius, on average only 74 % of the incident photon energy for E $\gg$ 100 MeV and up to 82 % for 50 MeV are deposited in the central cell based on simulations (see section 3.6.3). However, the exact fraction of the energy deposition underlies strong fluctuations from event to event. Therefore, the energy distributions in figure 3.7 are asymmetric with a tail to lower energies. Due to the higher energy deposition fraction in the central cell for $E < 100\ MeV$, these distributions look much more symmetric than the ones for higher energies. To determine the position of the maximum (E_0) and the standard deviation (σ) of such asymmetric distributions, a Novosibirsk function [BW10] has to be used, which is given by

$$f(E) = A \cdot e^{-\frac{ln[1-\Lambda\cdot\tau\cdot(E-E_0)]^2}{2\cdot\tau^2}+\tau^2} \qquad \text{with} \qquad \Lambda = \frac{sinh(\tau\cdot ln(4))}{\sigma\cdot\tau\cdot\sqrt{ln(4)}} \tag{3.3}$$

with the amplitude A and the parameter τ, which parametrizes the low energetic tail of the function. The right part of figure 3.7 shows a typical energy distribution for 156 MeV photons reproduced with a Novosibirsk function.

Linearity of the energy response: For the reconstruction of electromagnetic probes, a linear behavior of the energy response is an important feature. Simulations show (see section 3.6.3) that also the energy deposited in a single cell follows a nearly linear behavior in the energy region above 100 MeV. Figure 3.8 (left) shows the mean of the energy distribution in a single cell as a function of the incident photon energy for the 16 cells of the prototype, before a relative calibration. The figure shows that at least in the energy range below 400 MeV a linear behavior can be observed for all cells. In a more detailed inspection only the two points below 100 MeV show a slightly increased energy like expected from simulations. In the energy range above 400 MeV an increase of the amplitude compared to the linear fit of the points in the region below 400 MeV can be observed which is in contradiction to the behavior

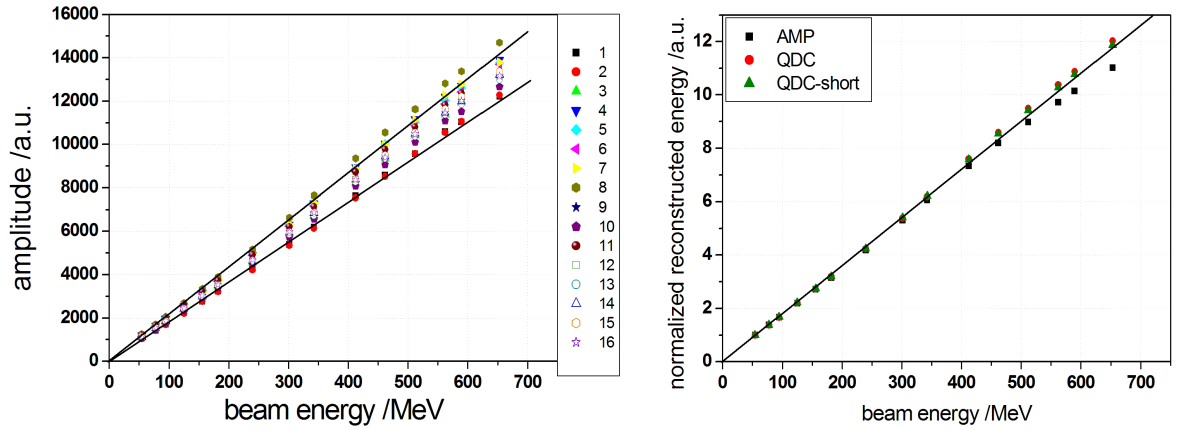

Figure 3.8: Reconstructed energy of a single shashlyk EMC cell for all 16 cells extracted with the QDC-short feature extraction (left) and comparison of the typical behavior of the reconstructed energy with the peak sensing feature extraction (AMP) and the two variants of the integrating feature extraction (QDC and QDC-short) for a selected cell (right). The black line in the right figure indicates the expected linear response.

expected from the simulations. This increase occurs for all cells but is more pronounced if the individual channel has a higher PMT gain. To study the influence of the feature extraction on this effect, figure 3.8 (right) shows the reconstructed energy for the central cell, normalized to the first point as a function of the beam energy for the peak sensing feature extraction (AMP) and the integrating feature extraction with two different gate lengths (QDC and QDC-short). The comparison illustrates that a deviation from the linearity in the region above 400 MeV occurs for all feature extraction methods. While both integrating feature extractions show a slight positive deviation of the reconstructed energy, the peak sensing feature extraction proposes a saturation of the amplitude at high energies. Section 3.2.3 will address these effects to imperfections of the ADC.

Standard deviation of the energy distribution: To check if the standard deviation of the energy distribution is also affected, it has been plotted as a function of the beam energy in figure 3.9. The left part of the figure shows the standard deviation as a function of the beam energy for the 16 cells, while the right part presents the normalized standard deviation for a selected cells as a function of the beam energy for the three different feature extractions. From the parametrization of the energy resolution a behavior like

$$\sigma = a \cdot \sqrt{E} \oplus b \cdot E \tag{3.4}$$

with constants a and b should be expected. However, the figures confirm for all analysis methods a significant deviation from the expectation at higher energies.

Energy resolution of a single cell: The relative energy resolution can be directly deduced from the ratio of the standard deviation and the reconstructed energy. It is shown in the left part of figure 3.10 as a function of the beam energy for the 16 cells and in the right part for different feature extractions applied to a typical cell. As expected, an unphysical behavior is

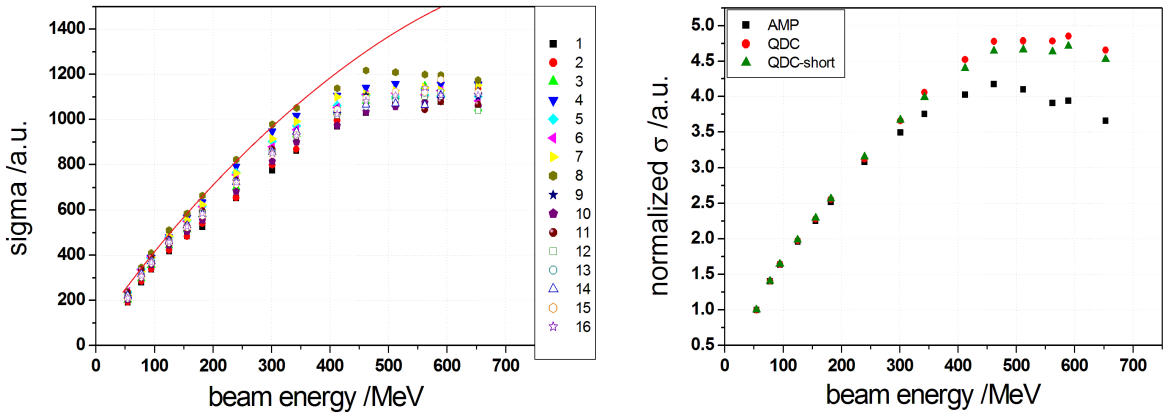

Figure 3.9: Standard deviation of the energy response of a single shashlyk EMC cell for all 16 cells extracted with the QDC-short feature extraction (left) and standard deviation for a selected cell with a typical behavior for the peak sensing feature extraction (AMP) and the two variants of the integrating feature extraction (QDC and QDC-short) (right). The red line in the left picture indicates the expected behavior for cell number 2.

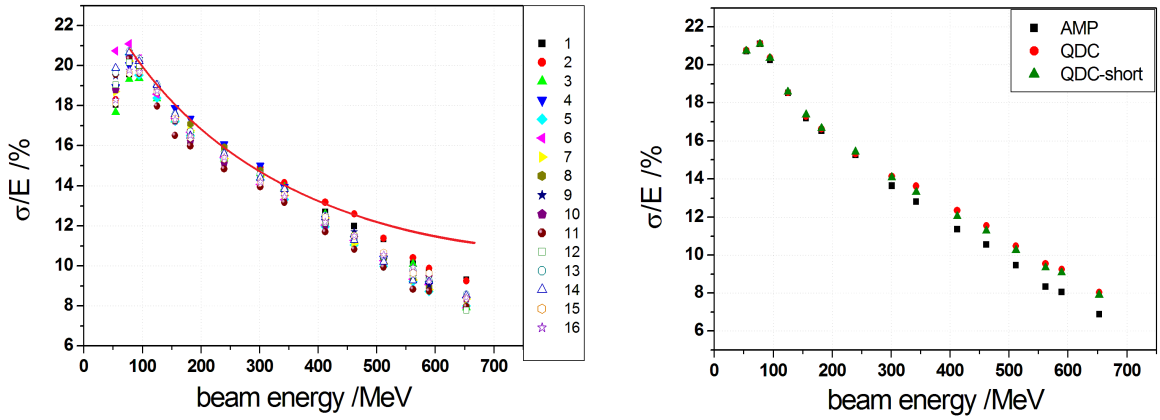

Figure 3.10: Energy resolution of a single shashlyk EMC cell for all 16 cells extracted with the QDC-short feature extraction (left) and energy resolution for a selected cell with a typical behavior for the peak sensing feature extraction (AMP) and the two variants of the integrating feature extraction (QDC and QDC-short) (right). The red line in the left picture indicates the expected behavior of the relative energy resolution of cell number 2.

observed above 400 MeV in all cases. Therefore, values extracted above 400 MeV have to be excluded in the present analysis.

3.2.3 Test of the ADC linearity

Since the effects observed for the response of a single cell for energies higher than 400 MeV can neither be explained by the response of the detector cell nor by its readout, it can only be introduced by the ADC. Therefore, an optical pulse generator, which is shown schematically in figure 3.11, has been used to control the ADC. The pulse generator consists of a pulsed LED and a PMT. Removable gray-filters allow to vary the light intensity. The trigger pulse

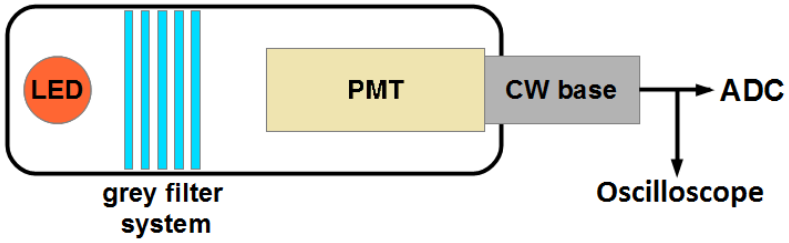

Figure 3.11: Setup of the pulsed LED system for the ADC response tests. The intensity of the light can be controlled by several removable gray-filters in the system. The voltage supply of the PMT is provided by a Cockcroft-Walton (CW) cascade generator like in the experiment.

of the LED has been adapted to create a typical shashlyk pulse. The signal amplitude has been measured simultaneously with an oscilloscope and with the sampling ADC. For the extraction of the signals a peak sensing feature extraction was used. Figure 3.12 shows the reconstructed amplitude and the standard deviation as a function of the amplitude, measured with the oscilloscope.

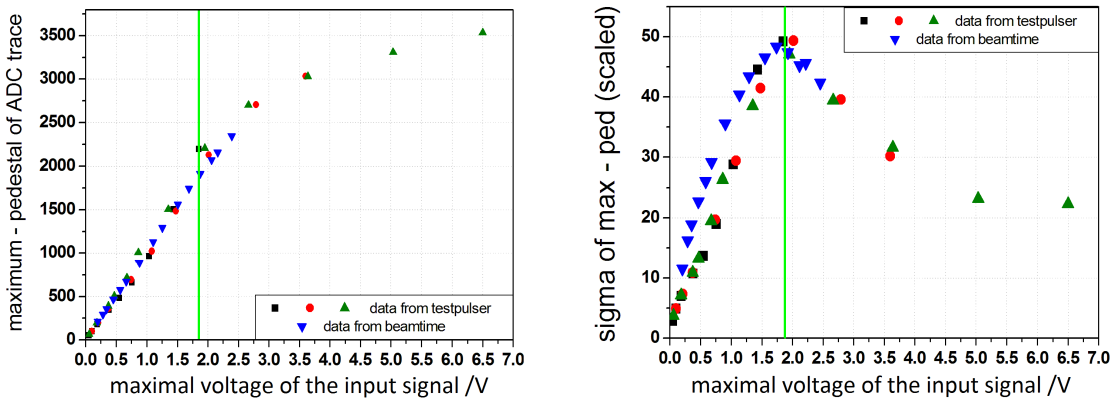

Figure 3.12: Correlation between the reconstructed amplitude and its standard deviation and the voltage amplitude of the input signal.

The similarity of the results illustrates the malfunctioning of the ADC. As stated by the developer of the ADC, the problem is caused by an amplifier, implemented in modules of the first series, which is not linear over the complete dynamic range [PM14]. Therefore, the range of 4096 channels (12 bit) does not correspond to the maximal input voltage of 2.0 V, as it was expected for the settings of the dynamic range during the beam-time. Due to this non-linearity of the amplifier, signals with an amplitude of more than 1.8 V, corresponding to an energy deposition of more than 400 MeV in a single module are strongly influenced by the ADC and have to be excluded in the present analysis.

3.2.4 Calibration methods

The relative calibration of the modules is an important factor for the lateral uniformity of the energy response and therefore also for the achievable energy resolution. Before the beam-time

all modules have been pre-calibrated with cosmic muons, by adjusting the voltage applied to the PMT in a way that all cosmic muon peaks appear at approximately the same ADC value. From the test of the version A prototype it was known that the peak of the energy deposition distribution of a cosmic muon interacting vertically with a horizontally positioned cell can be expected at approximately 23 MeV [SD12]. Based on this experience the ADC range has been set to 1 GeV, which is well suited for photon energies up to 650 MeV. For the final offline calibration different methods have been applied and compared. These methods are in general based on two basic concepts. The first concept follows a relative calibration of all cells to the central cell (cell 6). It can be realized in two ways:

1. By a relative calibration based on photon beam data with energies up to 400 MeV
2. By a relative calibration based on cosmic muons

The second concept is based on an individual calibration of each module and can also be realized on two different ways:

1. By assigning the beam energy to the energy deposited in the cell for a central interaction with beam energies up to 400 MeV[1].
2. By assigning the energy deposition of the photon beam in a single cell simulated in GEANT4 to the experimentally determined amplitude of a single cell for different beam energies below 400 MeV.

In the following part the different calibrations will be explained in more detail.

a) Relative calibration based on beam data

For the relative calibration based on beam data, the photon beam was directed in the center of each cell. For each cell the energy distributions of the 15 tagger channels are fitted with a Novosibirsk function. Afterwards a calibration factor relative to the cell, which is later on used as the central cell (cell 6) is calculated for each tagger energy by

$$c_i(E_{tag}) = \frac{mean_6(E_{tag})}{mean_i(E_{tag})} \tag{3.5}$$

Figure 3.13 shows the calculated calibration factors as a function of the incident photon energy for the 16 cells with the peak sensing and the integrating feature extraction.

The comparison of the two figures shows that up to a small variation of less than 2-3%, caused by fitting uncertainties, both feature extraction methods provide similar results. In the ideal case, the calibration factor should be constant over the complete energy range. Nevertheless, figure 3.13 shows that especially at low and high energies a reduction of the relative calibration factor of up to 5% can be observed. The variations at high energies can be explained by the effects introduced by the ADC which are depending on the gain of the individual cell. In addition, the relatively poor statistics from the short calibration runs introduces an error for

[1]For this method it has to be considered that it is not an absolute calibration, since the assigned energy is approximately 30 % too high.

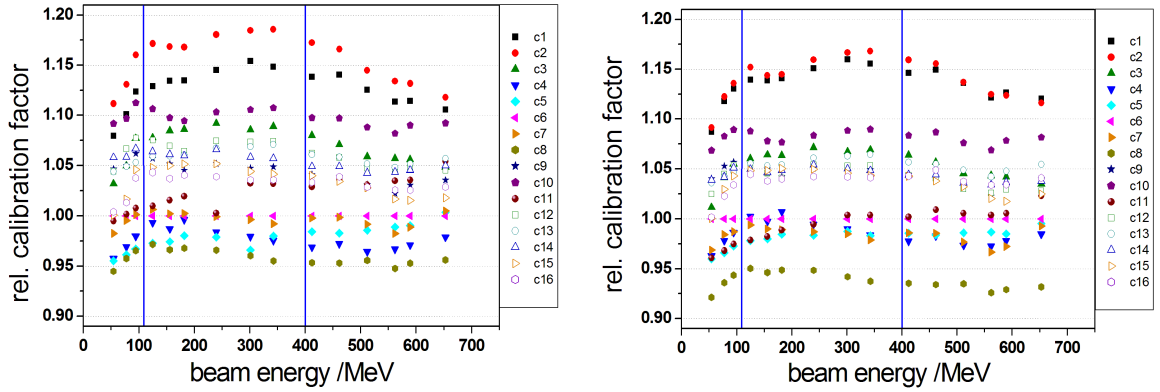

Figure 3.13: Energy dependence of the relative calibration factor for the AMP feature extraction (left) and the QDC-short feature extraction (right) for all 16 cells.

the highest energies. Due to these effects, the values above 400 MeV have to be ignored for the calibration. At energies below 100 MeV local inhomogeneities of the single cells and the exact position of the beam become more important. Therefore, the small drop of the relative calibrations coefficient in this region can be explained by small variations of this parameters.

Since the calibration coefficients of all cells show a nearly constant behavior in the region between 100 MeV and 400 MeV the average of the six points in this region

$$c_{avg}(i) = \frac{1}{6} \cdot \sum_{E_{tag}=100\ MeV}^{400\ MeV} c_i(E_{tag}) \tag{3.6}$$

has been taken as a relative calibration coefficient for each module.

On the other hand, at low energies there is less energy leakage out of the module, which may have a positive impact on the calibration. Therefore, in a second calibration only the relative calibration coefficient for a tagger energy of 78 MeV is used.

b) Relative calibration based on cosmic muons

Another possibility for a relative calibration is the use of the energy deposition spectra of cosmic muons which cross the cells in transverse direction. Cosmic muons are produced during the interaction of cosmic radiation with the atmosphere of the earth. If a high energetic proton from the cosmic radiation hits an oxygen or a nitrogen atom of the atmosphere, pions are produced within the hadronic shower, which finally decay into muons.

$$\pi^+ \rightarrow \mu^+ + \nu_\mu \tag{3.7}$$

$$\pi^- \rightarrow \mu^- + \overline{\nu}_\mu \tag{3.8}$$

The energy distribution of the muons, which reach the surface of the earth shows a mean value at approximately 4 GeV [PDG14] and drops by several orders of magnitude in the sub GeV region. While muons with high energies (E $\gg$ 1 GeV) are able to introduce a hadronic shower in the shashlyk modules, most of the cosmic muons can be assigned to the class of

minimal ionizing particles (MIP) (see section 1.3.1), which deposit a constant fraction of their energy per path length in the shashlyk cells. Since this fraction is small compared to their total energy, a typical Landau-distribution of the deposited energy (see eqn. 1.9) can be expected. However, in reality the observed distribution is smeared by the energy resolution of the detector and therefore a bit wider than expected. In addition, the shashlyk modules are hit by the cosmic muons from all directions and therefore also all possible path lengths of muons in the shashlyk module are possible. This effect causes a strong smearing of the expected Landau-distribution, since the mean deposited energy is directly proportional to the path length of the muons in the plastic scintillator tiles. To reduce this smearing, the shashlyk cells are positioned as a 4×4 array and a plastic scintillator paddle is placed above the front part of the modules which also acts as an external trigger (see figure 3.14). With this configuration it is possible to increase the probability that the cosmic muons are passing the shashlyk modules in vertical direction by requiring a coincidence between the 4 cells of one column and the plastic paddle in the offline data analysis. The condition limits the maximal interaction angle of the muons to around 14° in transverse direction and at least for the two inner rows it is guaranteed that the cosmic muon passes the cell across the complete diameter. In addition, this coincidence is used to reject electronic noise and dark counts of the PMTs. Figure 3.14 (left) shows the possible paths of the cosmic muons.

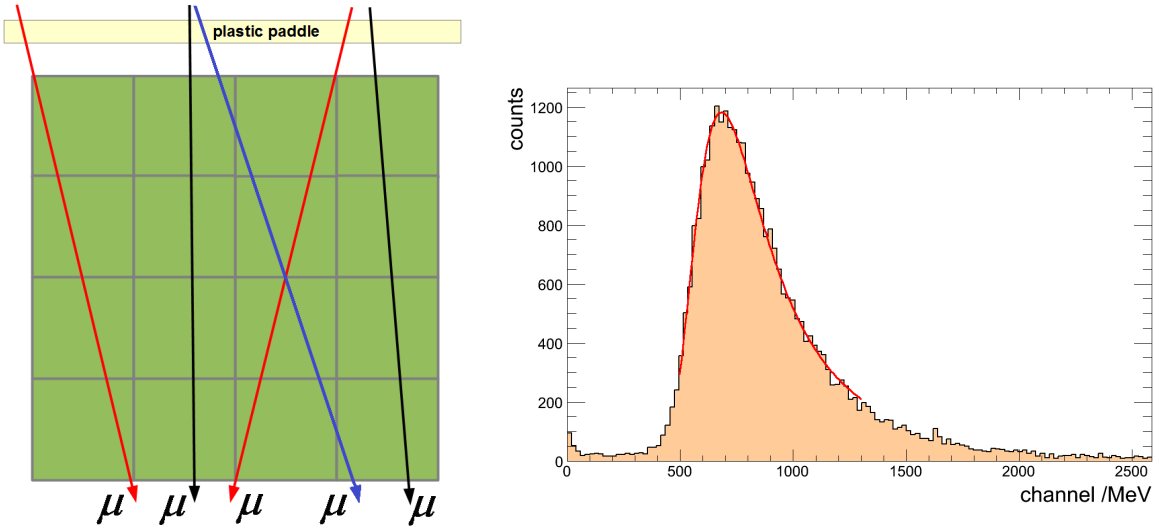

Figure 3.14: Left: Possible paths of cosmic muons through the shashlyk cell in transverse direction, if a coincidence of one column is required. The red arrows show the paths with the maximal angle, which fulfills the coincidence condition if a high threshold ($\sim$ 20 MeV) is required for the coincidence of the cells. If the coincidence threshold is lowered down to around 10 MeV also paths like the blue one become possible and deteriorate the response of the modules in the first and last row. Right: Energy deposition spectrum of cosmic muons in a typical shashlyk cell, fitted with an overlap of a Landau- and a Gaussian- distribution.

However, a perfect Landau-distribution can not be measured with this setup, since the interaction angle of the cosmic muons is only limited in two dimensions, while in longitudinal direction all interaction angles are still possible. Since a non vertical interaction in this direction will deposit more energy in the scintillator tiles than a perfectly vertical interaction, due to the longer total muon path over several scintillator tiles of the shashlyk structure,

this effect will only cause a smearing at higher energies. Concerning the quality of the relative calibration, this smearing will show no effect, since the smearing is the same for all cells. Figure 3.14 (right) shows the energy deposition spectrum of the cosmic muons after the application of the described conditions for a typical cell. All energy deposition spectra are fitted with an overlap of a Landau- and a Gaussian- distribution to take the smearing of the energy deposition by the intrinsic energy resolution of the shashlyk cells into account. The relative calibration coefficient is calculated from the obtained position of the maximum of the distribution with respect to the central cell by:

$$c_{rel}[i] = \frac{\text{maximum of cosmic distribution [6]}}{\text{maximum of cosmic distribution [i]}} \tag{3.9}$$

Earlier measurements with the shashlyk cells showed that the mean amount of scintillation light created by a vertically interacting cosmic muon is equal to the mean energy deposition of a 23 ± 2 MeV photon which interacts with the cell from the front side [SD12]. Based on this empirical value which is also confirmed by simulations, the peak position of a cosmic muon can also be used for a first iteration of an absolute calibration.

All in all, the cosmic muon calibration is a very simple way to gain a calibration without using beam data. However, it provides only a single calibration point at low energies and therefore introduces a large uncertainty, especially at higher energies. Nevertheless, it is important to study this calibration method, since it is an easy way to pre-calibrate and to test the modules.

c) Individual calibration based on the photon beam energy

As a different approach for the calibration, the known energy of the photon beam can be used. The easiest way to perform a calibration with this method is to assign the energy of the photon beam to the energy deposited in the cell in which the photon beam is interacting centrally during the calibration run.

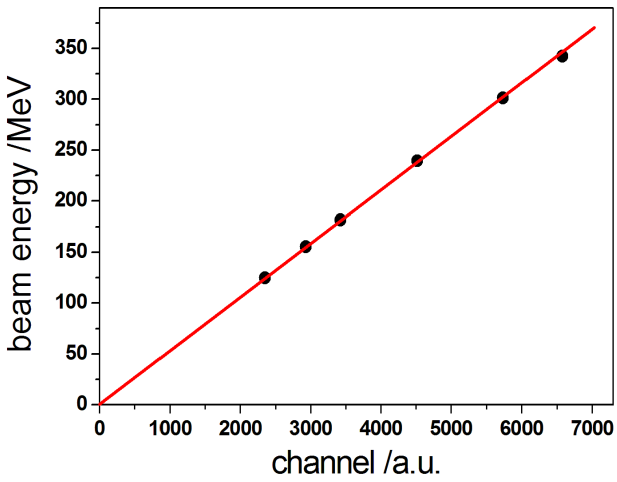

Figure 3.15: Linear calibration fit through the data points of a typical shashlyk cell for energies between 100 MeV and 400 MeV.

However, since one cell has a lateral size of only approximately one Molière-Radius, this method will provide absolute energy values which are between 24 % and 27 % too high (see

section 3.6.3). In addition, the fraction of the energy which is deposited in a single cell is energy dependent. Starting at very low energies, where nearly 100 % of the photon energy are deposited in the central cell, it decreases down to approximately 76 % at 100 MeV and 73 % at 500 MeV (see section 3.6.2). Due to this variation, the method can only be used with a sufficiently small error for energies larger than 100 MeV at which a proper shower development can be assumed. In addition, the energies above 400 MeV have to be ignored due to the ADC effects described in section 3.2.3. Figure 3.15 shows a linear fit through the data points of a typical cell for energies between 100 MeV and 400 MeV, which were used for this calibration. Like expected from the simulation, the data points between 100 MeV and 400 MeV provide a nearly linear behavior. The slope of this linear fit is finally used as the calibration parameter for each cell. The advantage of this calibration is given by the fact that no reference cell is needed, since the energy values of the photon beam are taken as a reference.

d) Individual calibration based on GEANT4 simulations

Like already described for method c), the energy deposited in a single cell is not constant over the complete energy range and shows strong variations especially below 100 MeV. To take this variations into account and to use also the data points below 100 MeV for the calibration, GEANT4 simulations have been performed for the type B modules to determine the energy which is deposited in a single cell for the different energies of the tagged photon beam. By assigning these energies to the peak position of the deposited energy distribution, a linear behavior can be obtained for all energies. Only the data points for energies above 400 MeV have been ignored due to the ADC effects described in section 3.2.3. In addition, this method directly provides a quite good absolute calibration for all cells. Figure 3.16 shows the linear fit through the correlation between the experimental and the simulated data points.

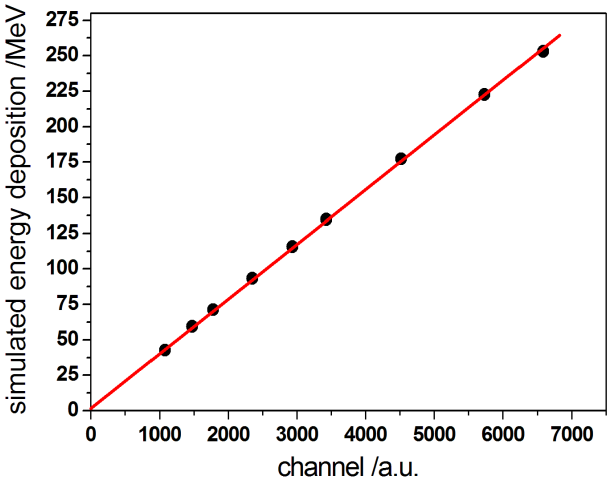

Figure 3.16: Linear calibration fit for a shashlyk cell based on the energy deposition simulated with GEANT4.

The figure shows that the simulated energy values provide a good linear correlation. The slope of this correlation directly provides a combination of the relative and absolute calibration parameter of each cell.

Concepts for the absolute calibration

All presented calibration methods except method d) provide only a relative calibration of the single cells and no explicit value for the deposited energy. For method c) an absolute calibration is easily possible, since the real energy deposited in the central cell can be expressed as a fraction of (74.5 ± 1.5)% of the beam energy, leading directly to an absolute calibration coefficient of $c_{abs} = 0.745$. In contrast to this, method a) and b) provide only a calibration relative to the central cell. Therefore, an absolute calibration is needed for this cell. For method a) this can be realized by comparing the deposited energy with the energy simulated in GEANT4, while for method b) the mean value of the cosmic muon distribution can be assigned to the experimentally determined value from earlier beam tests or to the energy deposition of cosmic muons simulated in GEANT4.

3.2.5 Noise level and threshold

To avoid the inclusion of electronic noise in the energy sum and to define a reconstruction cluster in the final detector setup, a threshold is needed for the single cells. This threshold is directly correlated with the electronic noise level and the feature extraction noise level (also referred to as "noise" or "signal noise"), which has to be determined for each feature extraction method separately. This can be done by looking at the baseline in front of the signal, which represents the behavior of the baseline if no signal is present. Due to the low beam current an additional event in this region is very unlikely. For the peak sensing feature extraction, the signal noise can be determined by searching for the maximum of the baseline in an interval which has the same length like the region from which the main signal is extracted. After subtracting the average value of the baseline, which is also subtracted from a real signal, this method provides a Gaussian distribution around a positive mean value, shown in figure 3.17 (left). For the integrating feature extractions an integration of the baseline in the same time interval like for the signal extraction has to be performed. This method will provide a Gaussian-distribution around a mean value of zero, which provides a cross check for the baseline determined initially. The distribution of the integral values shown in figure 3.17 (right) has nearly the same shape for the QDC and the QDC-short feature extraction.

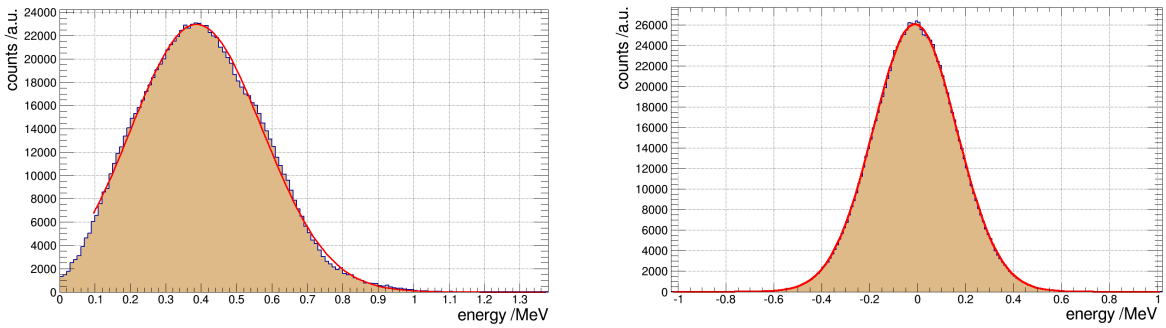

Figure 3.17: Signal noise distribution for a typical shashlyk cell for the peak sensing (left) and the integrating (right) feature extraction.

In both cases, the distribution shows the signal noise, which has been extracted from the electronic noise by the feature extraction method and which will be misidentified as a real

signal, if no energy is deposited in the corresponding cell or if the signal introduced by the deposited energy is below the electronic noise level of the SADC trace. For the peak sensing feature extraction, like in a peak sensing ADC, a signal noise distribution around a positive mean value can be observed, since the maximum of the signal noise over several SADC bins has a positive expectation value $mean_{p-noise}$ with an event-wise standard deviation $\sigma_{p-noise}$. To exclude the complete signal noise from the energy sum, the threshold can be approximated to:

$$E_{p-thr.} = mean_{p-noise} + 3 \cdot \sigma_{p-noise} = 0.39\ MeV + 3 \cdot (0.19 \pm 0.03\ MeV) \approx 1.0\ MeV \quad (3.10)$$

For the integrating feature extractions, the signal noise is distributed around zero. Therefore, the threshold in this case is given by:

$$E_{i-thr.} = 3 \cdot \sigma_{i-noise} = 3 \cdot (0.18 \pm 0.03)\ MeV = (0.54 \pm 0.09)\ MeV \quad (3.11)$$

The comparison of the two methods shows that the integrating feature extraction provides a significantly lower threshold than the peak sensing feature extraction, since the electronic noise is averaged over several bins.

Another method to determine the optimal threshold is to perform a threshold scan. For this purpose the data of a run with the photon beam interacting in the center of one of the inner cells is used and the energy sum of the calibrated 4 × 4 array is calculated for different thresholds. Since the electronic noise level and the threshold have the largest impact at the lowest beam energies, the threshold scan has been performed for the lowest beam energy of 55 MeV. The obtained relative energy resolution of the 4 × 4 energy sum with the QDC-short feature extraction is plotted in figure 3.18 as a function of the software threshold.

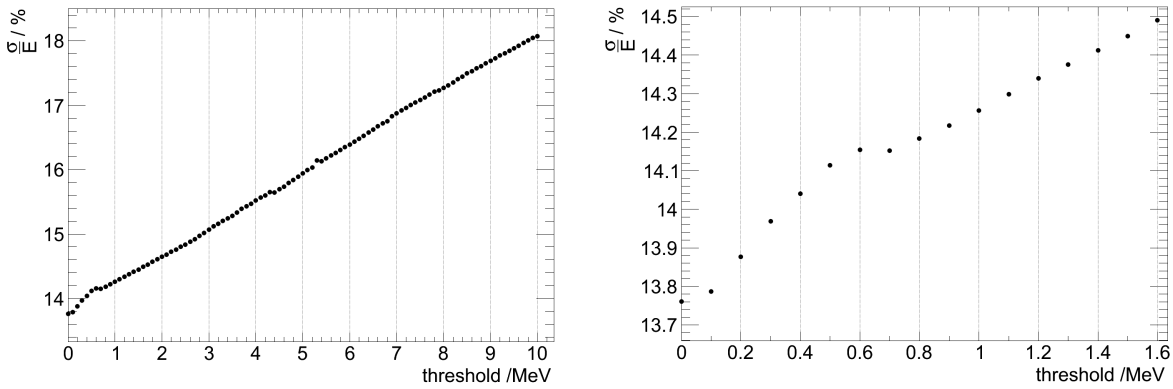

Figure 3.18: Threshold scan for a photon beam energy of 55 MeV with the QDC-short feature extraction. The relative energy resolution has been calculated for the complete 4 × 4 array with the photon beam interacting in the center of one of the central cells. The left picture shows the behavior of the energy resolution over a threshold range from 0 to 10 MeV, while the right figure shows a detailed view of the lowest thresholds.

The threshold scan shows that the relative energy resolution is deteriorated for an increase of the threshold over the complete range. However, after a strong increase of the relative energy resolution for low thresholds, a step and a change of the slope can be observed for a threshold of approximately 0.6 MeV. Since this value fits to the threshold obtained from the

signal noise distribution in figure 3.17, this step can be interpreted as the point after which a higher threshold cuts off mostly energy information in the outer cells of the cluster. For larger clusters one would expect that adding signal noise to the energy sum deteriorates the energy resolution, since it broadens the energy distribution. Due to this effect, the resolution should be worse if no threshold is applied and should improve with higher thresholds, until the complete signal noise distribution is cut off and a further cutting of the energy information deteriorates the energy resolution again. For the shown resolution scan, the relative energy resolution does not show such a minimum. This can be explained by the fact that only a very small cluster of 4×4 cells is used and in addition a very low single cell noise level of only $\sigma_{noise} \approx$ (0.2-0.3) MeV has been achieved. As a combination of this two conditions one can assume that the detected deposited energy, even in the outer cells of the 4×4 array, exceeds the noise level in most of the cases or creates at least a comparable signal height. Only for the lowest incident photon energies a slight impact of the noise can be observed, since due to shower fluctuations not all neighboring cells show a response above the noise level.

For the final shashlyk calorimeter wall in the forward spectrometer of the PANDA detector a threshold is needed for the cluster formation. Therefore, the threshold of 0.6 MeV for the integrating feature extractions and 1.0 MeV for the peak sensing feature extraction, have been fixed for the following analysis.

3.2.6 Line-shape of the reconstructed energy

Figure 3.19 shows selected energy distributions for the energy sum of the complete 4×4 array for the threshold settings discussed in the previous section.

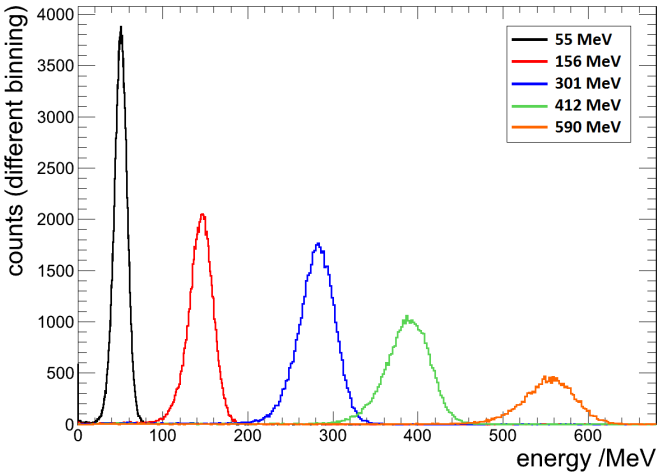

Figure 3.19: Energy distributions of the reconstructed energy sum of the complete 4×4 array with the photon beam interacting in the center of cell 6 for different photon energies extracted with the QDC-short feature extraction.

Compared to the energy deposition distribution of the central module, which is shown in figure 3.7, a significant reduction of the low energetic tail of the distributions can be observed, since more than 95 % of the total deposited energy are now included in the energy sum. Nevertheless, a small low energetic tail is still observable due to the incomplete shower absorption in the 4×4 array, especially at high energies.

3.2.7 Linearity and homogeneity of the cluster energy response

The energy information of the calorimeter has been reconstructed by summing the energy response of all cells within a 3 × 3 or 4 × 4 array. A linear response of the reconstructed energy is a key requirement, which is confirmed in figure 3.20 for a 3 × 3 array of shashlyk cells.

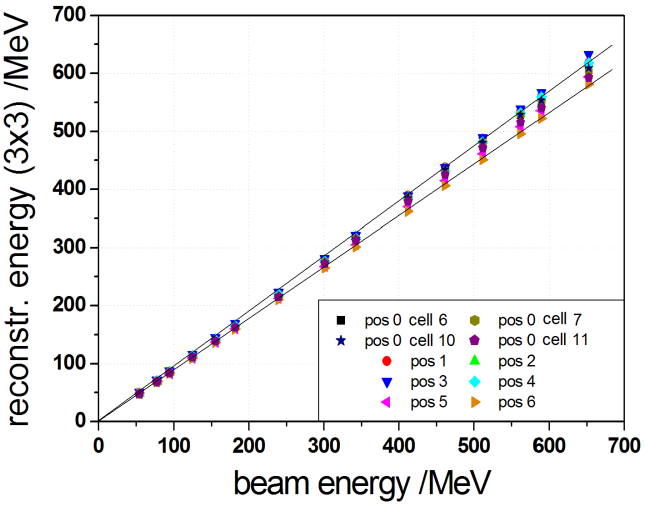

Figure 3.20: Linearity of the cluster energy response for different interaction positions. The positions 1 to 6 are indicated in figure 3.5. For these six positions the energy sum is calculated for a 3 × 3 array around cell 6. Position 0 ("pos 0") indicates a central interaction of the photon beam in a cell. For this case an interaction in cells 6, 7, 10 and 11 was chosen with the corresponding 3 × 3 arrays around these cells. The energy information has been extracted with the QDC-short feature extraction.

The figure shows that the response is nicely linear for the beam positions 1 to 6. Only if the photon beam is interacting in the center of a module and a relatively large signal is produced in a single cell, as in the case of position 0 in the four different cells, a small increase of the reconstructed energy at high photon beam energies can be observed due to the non-linearity of the ADC response in this region. The relatively strong variation of the amplitude in particular at high energies can be addressed to different amounts of energy leakage for the different interaction positions within the 3 × 3 array. The non-linearity of the ADC contributes in addition. To exclude these effects, only energies below 400 MeV will be used to determine the homogeneity of the energy response. Since the homogeneity of the energy response does not depend on the feature extraction, only the QDC-short feature extraction is used. To avoid an influence of the limited lateral size of the prototype only points with the same expected leakage will be compared. Therefore, the interaction points are grouped according to their distance to the center of the 3 × 3 array. Figure 3.21 shows the deviation of the different positions at different energies below 400 MeV from the mean value. A maximum variation of approximately ± 4% is observed including all interaction positions. For comparable points with the same distance to the center the variation decreases to less than ± 2%.

To study the influence of the calibration method on the homogeneity of the energy response the maximal and the average variation for different cases have been calculated in the energy range below 400 MeV. In the first case only the interaction in the center of the 3 × 3 ar-

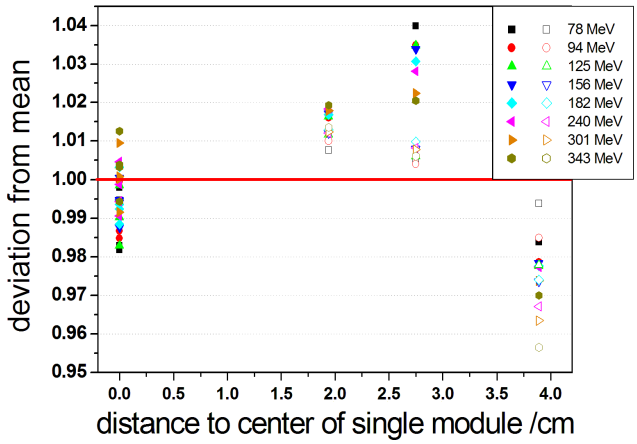

Figure 3.21: Variation of the reconstructed energy from its overall average for different interaction positions and different photon beam energies, determined with a relative calibration of the cells based on beam data. The full and the open points represent two different interaction points with the same distance to the center of the cell.

rays around the 4 central cells of the prototype are compared. In the second case the total variation for all classes of comparable points is considered, while in the third case the overall variation of all measured points is compared. Since the interaction points in the corner of the central cell are expected to show the largest energy leakage, a fourth case compares the overall variation without these points. Figure 3.22 shows the variation from the mean deposited energy, averaged over the different relevant positions and all energies below 400 MeV for the different cases and for the different calibration methods described in section 3.2.4. The behavior for the different cases is nearly the same for all compared calibrations. While

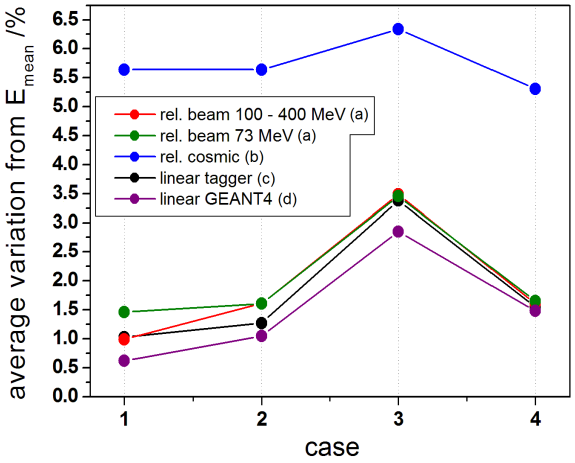

Figure 3.22: Average variation of the reconstructed energy value from the mean value for different cases and different calibrations (case 1: Interactions in the center of the four possible 3 × 3 arrays, case 2: Variation within comparable points in a 3 × 3 array [same distance to the center], case 3: Combination of all measured interaction points within a 3 × 3 array, case 4: Same as case 3, but without the points in the corner of the central cell). The used calibration methods, labeled with (a) to (d), are explained in section 3.2.4.

the comparison of the central interactions shows the lowest variation, the variation increases slightly if all comparable points are taken into account. Like expected, a comparison of all points deteriorates the homogeneity due to energy leakage of the outer points. If these outer points are ignored, the homogeneity becomes significantly better again and reaches nearly the level of case 2. A comparison of the different calibrations shows that all calibrations which are based on the calibration run show a comparable homogeneity of the energy response. Only the cosmic calibration causes a significantly worse homogeneity with variations of more than ± 5 %, which can be explained by the not ignorable calibration error, which is introduced by this method, based on a fit of a single energy spectrum with a relatively wide energy distribution. However, the accuracy of this calibration method is already sufficient to serve as a pre-calibration for the detector setup and can be further improved by requiring a coincidence between more cells in the final detector wall and by a coincidence detector positioned below and above the shashlyk wall to select cosmic muons with a smaller path variation. A comparison of the other calibrations shows that the relative calibration averaged over several energies between 100 MeV and 400 MeV shows a slightly better performance for a central interaction (case 1) than the relative calibration only based on the energy point at 73 MeV. For all other cases the homogeneity is comparable for both methods. The linear calibration based on the tagger energy information shows a comparable or in some cases slightly better homogeneity than the relative calibration method. This can be explained by the use of a fixed reference, which causes that only the error of the calibrated cell is included in the calibration, while a calibration relative to another cell includes the fit error of both cells. The best results concerning the homogeneity can be achieved by using the energy deposition information simulated with GEANT4 for the calibration, since in this case a real linear correlation between the deposited and the simulated data can be expected and therefore a much better linear fit can be applied for all energies in the selected range. Table 3.1 summarizes the achieved maximal and average variation for the calibration based on GEANT4 in the different cases.

case	average variation	maximal variation
1	± 0.7 %	± 1.0 %
2	± 1.1 %	± 1.7 %
3	± 2.9 %	± 3.6 %
4	± 1.5 %	± 1.7 %

Table 3.1: Maximal and average variation of the reconstructed energy for different cases (case 1: Interactions in the center of the 4 possible 3 × 3 arrays, case 2: Variation within comparable points in a 3 × 3 array [same distance to the center], case 3: Combination of all measured interaction points within a 3 × 3 array, case 4: Same as case 3, but without the points in the corner of the central cell).

A comparison of the different cases shows that the homogeneity corrected for the energy leakage is well below ± 2 % for the type B modules. The average variation of points with the same distance to the center stays even in the order of ± 1 %.

3.2.8 Energy resolution

Besides the homogeneity of the energy response, the energy resolution is one of the most important characteristics of an electromagnetic calorimeter. The energy resolution on the one hand strongly depends on the calorimeter type and design as well as on the readout. On

the other hand also the feature extraction method and the calibration of the cells influence the energy resolution. To estimate how the relative energy resolution of a 3×3 and 4×4 array is influenced by the ADC effects observed for a single module (see section 3.2.3), the standard deviation (σ) of the energy sum for a 3×3 array is plotted in figure 3.23 as a function of the beam energy.

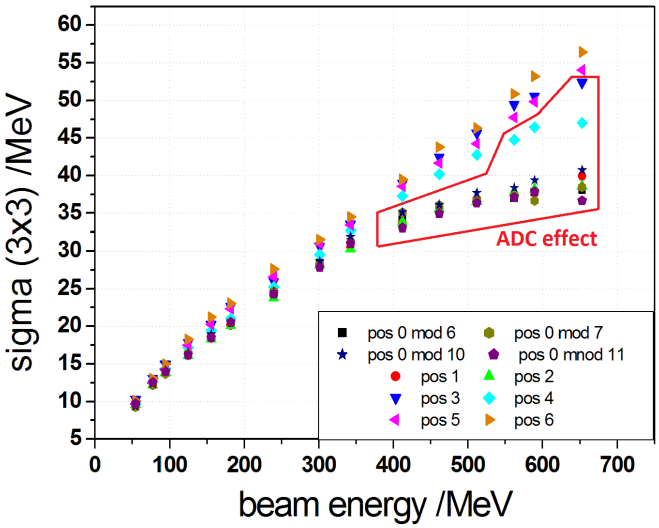

Figure 3.23: Standard deviation of the energy sum of a 3×3 array as a function of the beam energy for different interaction positions (see figure 3.5), extracted with the QDC-short feature extraction and relatively calibrated based on beam data.

As expected from the behavior of a single cell, the values for energies above 400 MeV have to be ignored for an interaction of the photon beam in the center of a cell (pos 0) due to the non-linearities of the ADC (see section 3.2.3). For the other positions a significantly lower impact of the ADC non-linearity can be observed. For positions in between two cells only the highest energies are affected, while for an interaction in the corner of a cell almost no deterioration can be observed.

To find the optimal feature extraction and calibration method, the relative energy resolution (σ/E) has been determined for a peak sensing (AMP) and an integrating (QDC-short) feature extraction and for different calibration methods. The comparison of the different cases of the feature extractions in figure 3.24 shows that concerning the energy resolution there is no significant difference between a peak sensing and an integrating feature extraction. Also the difference in the threshold of 0.4 MeV of both methods has no observable impact. Since the integrating feature extraction showed a slightly better performance concerning the linearity and also enables a lower threshold, all the following plots are based on the QDC-short feature extraction. For a central interaction of the photon beam (pos 0) most of the calibration methods show approximately the same performance. Only the calibration based on GEANT4 simulations shows slightly better results in the relevant energy range below 400 MeV. For an interaction in between two cells (pos 3) nearly the same behavior can be observed. Again the calibration based on GEANT4 simulations provides the best results. In addition, the linear calibration based on beam data shows slightly better results than the relative calibrations. For the interaction of the photon beam in the corner of the cell (pos 5) the picture is more

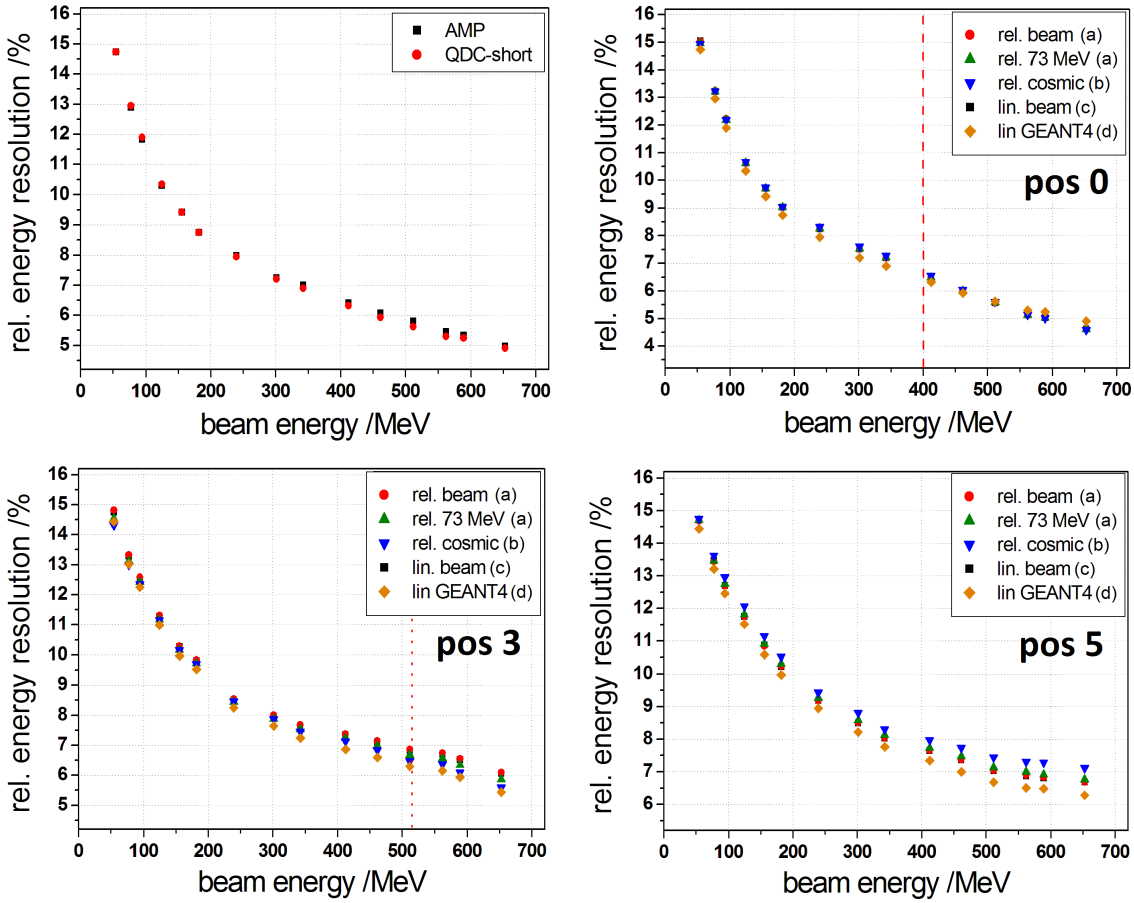

Figure 3.24: Influence of the feature extraction and the calibration method on the relative energy resolution of a 3×3 array. **Upper row left:** Energy resolution for a peak sensing (AMP) and an integrating (QDC-short) feature extraction at pos0 calibrated with the relative calibration based on beam data. **Upper row right and lower row:** Energy resolution for different calibration methods at the position 0, 3 and 5. For the comparison of the calibrations the QDC-short feature extraction has been used. The values behind the dashed red lines have to be ignored due to the described non-linear ADC response for high signals. The calibration methods labeled with (a) to (d) are described in section 3.2.4.

diverse. It is clearly visible that the best results can be obtained with the calibration based on GEANT4 simulations. In addition, it can be observed that the calibration based on cosmic muons provides significantly worse results compared to all other calibrations. This can be explained by the fact that the energy for position 5 is nearly equally split between four cells and therefore the calibration errors of all cells contribute. Based on this comparison and on the results for the homogeneity of the energy response, the calibration with GEANT4 simulations will be used further on.

The final result for the energy resolution obtained for a 3×3 and a 4×4 array with this calibration and the QDC-short feature extraction are shown in figure 3.25. Excluding the data points which are effected by the ADC, both sub-figures show that the interaction points in the center of the cell (pos0, cell7, cell10, cell11) or close to the center (pos1, pos2) show comparable relative energy resolution values. Only the points in between two cells (pos3,

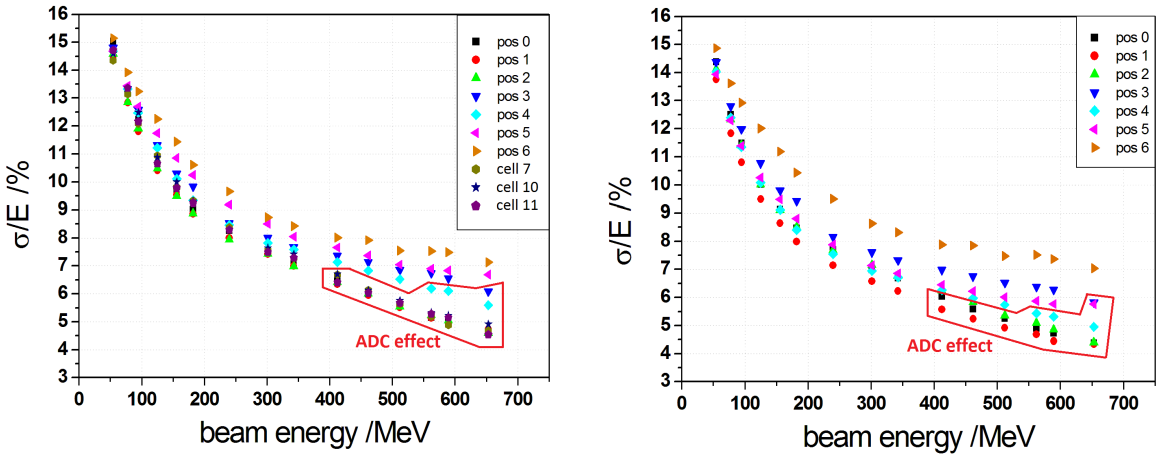

Figure 3.25: Relative energy resolution for a 3×3 (left) and a 4×4 (right) array of shashlyk cells as a function of the photon beam energy for different interaction positions. The interaction positions 0 - 6 are indicated in figure 3.5. Cell 7, 10 and 11 represent the central cells of the different 3×3 arrays. The data points in the red frame have to be ignored due to the ADC effects.

pos4) and in the corner of the cell (pos5, pos6) show slightly worse resolutions due to the increased energy leakage out of the 3×3 array for these positions. This effect is especially visible for pos6 and the use of a 4×4 array, since for this position in both directions only a distance of one module remains to the edge of the array on one side, while the other opposite corner of the cell (pos5) is in this configuration in the center of the array. The same consideration can also explain the difference between position 3 and 4 for the case of a 4×4 array.

As it has been discussed in section 1.3.2, the relative energy resolution can be described by

$$\frac{\sigma}{E} = \frac{a}{\sqrt{E}} \oplus b = \sqrt{\frac{a^2}{E} + b^2} \tag{3.12}$$

with the fit parameters a and b, representing the stochastic and the constant term of the energy resolution. Due to the readout with a PMT any contributions of electronic noise can be neglected. Figure 3.26 shows a fits of the energy resolution for an interaction of the photon beam in the center of a 3×3 array and in the center of the complete 4×4 array of shashlyk cells.

Table 3.2 summarizes the fit parameters obtained for the different cluster sizes and interaction positions. The table shows that the obtained fit parameters are similar for most of the interaction positions. Only interaction positions closer to the sides of the prototype show slightly increased values due to the increase of the shower leakage for these positions like it has already been observed in figure 3.25.

For a central interaction in a 3×3 array the average parametrization is given by:

$$\frac{\sigma}{E} = \frac{3.52\%}{\sqrt{E/GeV}} \oplus 4.09\% \tag{3.13}$$

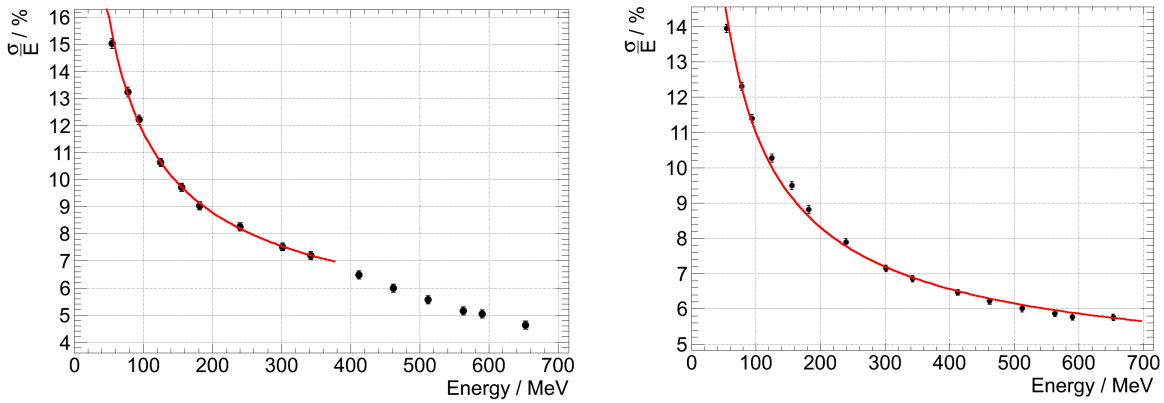

Figure 3.26: Fit of the relative energy resolution of a 3×3 array (left) and a 4×4 array of shashlyk cells with the photon beam interacting in the center of each array. Due to ADC effects, the fit range for the left figure is limited to the range between 50 MeV and 400 MeV.

array size	position	range in MeV	**a** in $(\% \cdot \sqrt{GeV})$	**b** in %
3×3	pos 0 (6)	50 - 400	3.49	4.02
3×3	pos 0 (7)	50 - 400	3.55	4.00
3×3	pos 0 (10)	50 - 400	3.52	4.27
3×3	pos 0 (11)	50 - 400	3.51	4.08
3×3	pos 1	50 - 400	3.41	3.93
3×3	pos 2	50 - 400	3.43	3.87
3×3	pos 3	50 - 580	3.55	4.78
3×3	pos 4	50 - 500	3.57	4.42
3×3	pos 5	50 - 700	3.91	4.55
3×3	pos 6	50 - 700	3.78	5.55
4×4	pos 0	50 - 400	3.31	3.57
4×4	pos 1	50 - 400	3.16	3.11
4×4	pos 2	50 - 400	3.89	3.26
4×4	pos 3	50 - 600	3.44	4.22
4×4	pos 4	50 - 550	3.35	3.39
4×4	pos 5	50 - 700	3.35	3.79
4×4	pos 6	50 - 700	3.69	5.55

Table 3.2: Energy resolution fit parameters for the different interaction positions and array sizes. The range gives the region of the fit and therefore also the region in which the energy resolution can be described with this parametrization. The number in brackets gives the central cell of the 3×3 array. If nothing is stated, cell 6 is the central cell. The interaction positions 0 - 6 are indicated in figure 3.5.

For a 4×4 array two cases can be considered for a comparison. On the one side the interaction in the center of the array and on the other side the interaction in the center of one of the central modules. Equations 3.14 and 3.15 show the corresponding parametrizations:

$$\frac{\sigma}{E} = \frac{3.35\%}{\sqrt{E/GeV}} \oplus 3.79\% \tag{3.14}$$

$$\frac{\sigma}{E} = \frac{3.31\%}{\sqrt{E/GeV}} \oplus 3.57\% \tag{3.15}$$

The parametrization shows that a 4 × 4 array provides significantly better values for the energy resolution than a 3 × 3 array due to the larger containment of the electromagnetic shower.

3.3 Position resolution of the version B prototype

Besides the energy resolution, the position resolution is a very important requirement for an electromagnetic calorimeter as well. While the traces of charged particles, including electrons, can be exactly reconstructed by the inner tracking detectors, the emission angle of photons can only be reconstructed from the position information of the electromagnetic calorimeter. Therefore, the position resolution is a key feature for the reconstruction of the invariant mass of neutral mesons, for example.

3.3.1 The center of gravity algorithm and its limitations

To achieve a reliable position reconstruction, the incident photon energy has to be well above the critical energy E_C to guarantee a proper shower development across several cells. With this limitation reliable results can only by achieved for the shashlyk cells, if the incident photon energy is above 100 MeV. For electromagnetic probes with significantly lower energies, especially for those which interact close to the center of a cell, the position resolution is limited to half of the module size, since the energy deposited in the neighboring cells is below the threshold and therefore no center of gravity can be calculated. As described in section 1.3.2, the resolution of the position reconstruction for probes with sufficient energy is mainly determined by the size of a single cell, which has to be not significantly larger than one Molière-Radius. Since this is fulfilled for the shashlyk modules, a center of gravity algorithm with logarithmic weighting can be applied to reconstruct the position information (see section 1.3.2). This algorithm is given by [TCA92]

$$x_{ln} = \frac{\sum_i \omega_i \cdot x_i}{\sum_i \omega_i} \quad \text{with} \quad \omega_i = \left\{ \begin{array}{ll} 0 & \text{if} \quad W_0 + ln\left(\frac{E_i}{E_{sum}}\right) \leq 0 \\ W_0 + ln\left(\frac{E_i}{E_{sum}}\right) & \text{else} \end{array} \right\} \tag{3.16}$$

with the cluster energy

$$E_{sum} = \sum_i E_i \qquad \text{for} \quad E_i \geq E_{thr} \tag{3.17}$$

and the threshold parameter for the position reconstruction W_0. The event-wise position reconstruction is done for the x- and y- direction separately. The threshold parameter W_0 represents the logarithm of the fraction of the single crystal threshold E_{thr} of the energy sum of the cluster E_{sum}. It can be expressed as

$$W_0 = -ln(E_{thr}/E_{sum}) \tag{3.18}$$

Figure 3.27 shows this correlation between W_0 and the single cell threshold for different photon energies. The figure illustrates the strong energy dependence of W_0 for a fixed single

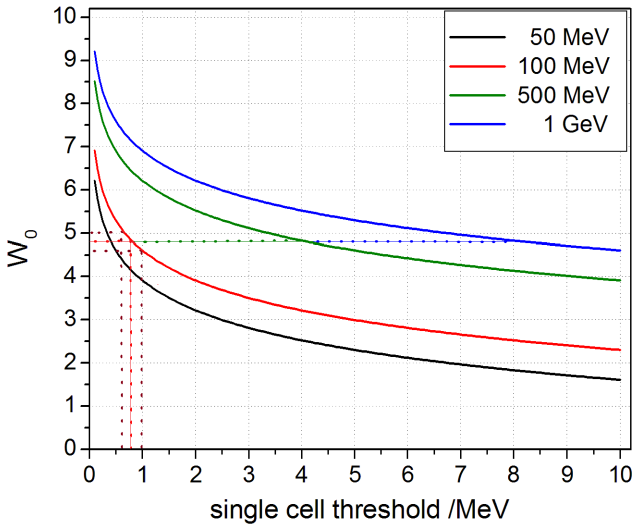

Figure 3.27: Correlation between W_0 and the single cell threshold for different cluster energies. The orange, red and magenta dashed lines indicate the W_0 value corresponding to a single cell threshold of 0.8 ± 0.2 MeV for the lowest reasonable photon energy of 100 MeV. The green and blue dashed lines approximate the corresponding threshold for higher cluster energies.

cell threshold. Considering the experimentally determined energy threshold of around 0.6 - 1.0 MeV, the figure shows that a W_0 value between 4.6 and 5.0 has to be used. For higher photon energies this value corresponds to significantly higher single cell thresholds of up to 8 MeV for an incident photon energy of 1 GeV. This section will discuss the optimal W_0 value based on a scan of the reconstructed position and of the position resolution and present the energy dependence of the obtained position resolution of the version B shashlyk prototype.

3.3.2 Obtained position resolution

The center of gravity algorithm can only deliver reliable results, if a symmetric cluster around the interaction point is used for the position reconstruction. Since the version B prototype has only a limited size of 4×4 cells, an asymmetric cluster would be reconstructed for most of the interaction points, especially at high energies. Therefore, the size of the reconstruction region has been limited to a 3×3 array around the cell on which the photon beam is interacting. Nevertheless, also with this configuration asymmetries of the non-central interaction points have to be taken into account. Figure 3.28 shows the two-dimensional distribution of the reconstructed positions for a photon beam interacting in the center of a module with an energy of 177 MeV and 436 MeV, respectively. The center of the distribution reproduces the expected position of the photon beam, indicated by the black circle, quite well for both energies.

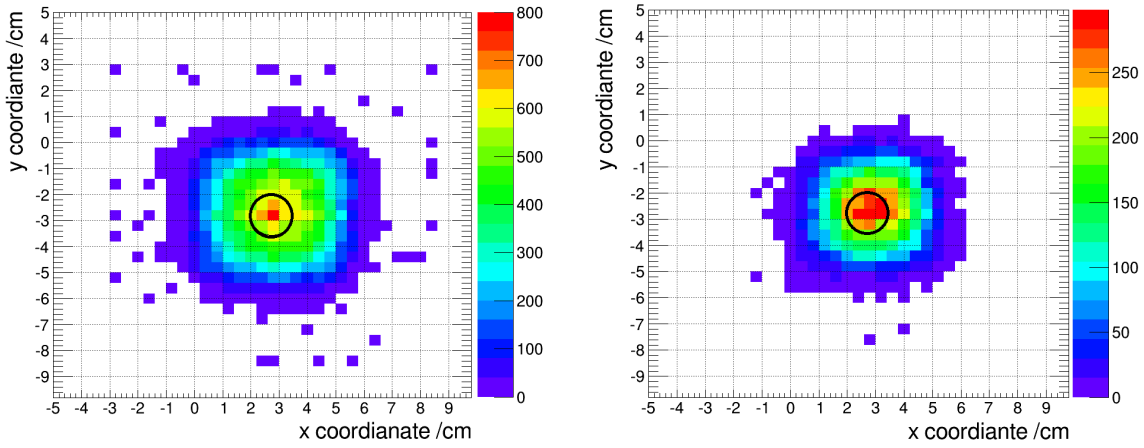

Figure 3.28: Reconstructed position information of the shashlyk prototype in two dimensions for a photon beam interacting in the center of a shashlyk cell at (2.75 cm | -2.75 cm) for a beam energy of 177 MeV (left) and 436 MeV (right) and a W_0 value of 4.8. The black circle indicates the expected position of the photon beam spot.

To determine the position resolution, projections of the distributions shown in figure 3.28 on the x- and the y-axis have been performed. The projection on the x-axis is shown in figure 3.29.

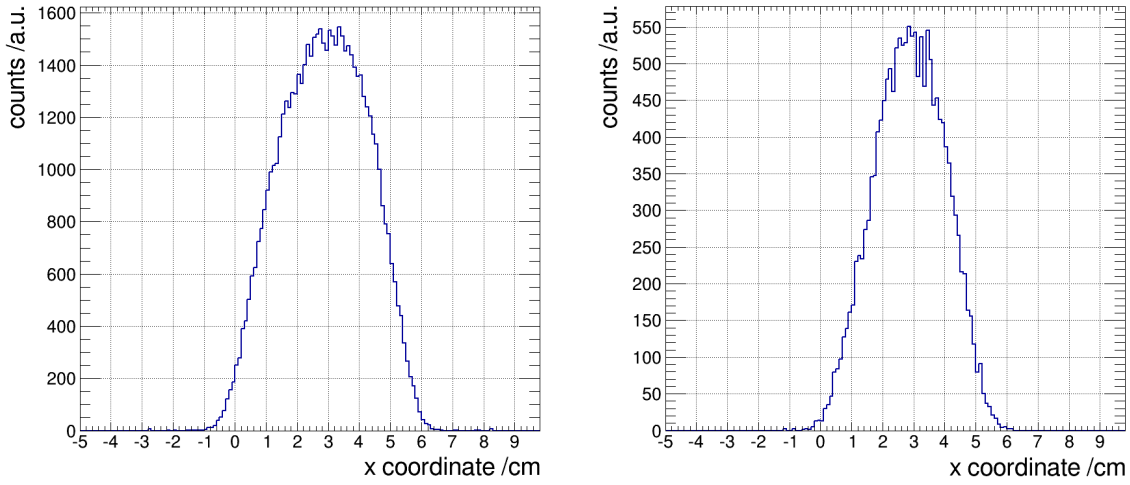

Figure 3.29: Projection of the reconstructed position of the shashlyk prototype in x- direction for a photon beam interacting in the center of a shashlyk cell (x = 2.75 cm) with a beam energy of 177 MeV (left) and 436 MeV (right) and a W_0 value of 4.8.

Since the obtained distributions are not perfectly Gaussian for the lowest energies, the root-mean-square (RMS) value calculated from the distribution has been taken as the position resolution, while the calculated mean value of the distribution is taken as the reconstructed position. Due to the limited shower development, the center of gravity algorithm is not applicable for low photon beam energies. The reason is illustrated in figure 3.30 (left) for a photon beam energy of 43 MeV. In this case, photons interacting close to the center of the cell deposit most of their energy in the central cell, while the energy deposited in the neighbors

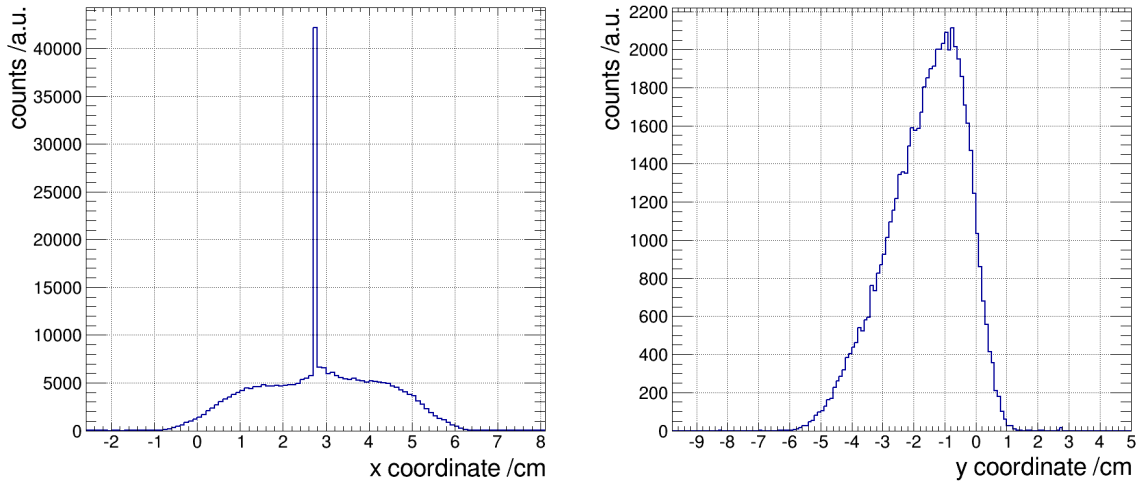

Figure 3.30: Projection of the reconstructed position ($W_0 = 4.8$) of the shashlyk prototype in x-direction for a central interaction of the lowest photon energy of 43 MeV (left) and for the interaction of a 177 MeV photon beam in the upper quarter of the central cell (pos. 1). The events contained in the spike of the distribution in the left figure are generated, if only the central cell detects an energy above the threshold.

is below the single cell threshold. As a result, no center of gravity can be calculated for these events and the algorithm delivers the center of the cell as the reconstructed position, leading to a spike in the center of the position distribution. To minimize such events, only photons with an energy above 100 MeV are considered for the position reconstruction. Another effect which has been observed is the asymmetry of the position distribution due to the limited cluster size which is illustrated in figure 3.30 (right) for interaction position 1 in the upper quarter of the central cell. In this case, the mean and RMS values are calculated with the standard procedure, taking into account that the asymmetry introduces a small error.

As a first step, the optimal W_0 value has to be determined. For this purpose a scan of the threshold parameter W_0 has been performed for the reconstructed position and the position resolution at the non-central interaction position 1 in the upper quarter of the central cell. Figure 3.31 shows the obtained results for the x- and y-direction. The left part of the figure shows that the reconstructed position for both directions shows the smallest deviation from the expected position if a value of W_0 between 4.4 and 4.8 is chosen. Since a value of 4.8 nicely fits to the single crystal threshold at the lowest considered energies (see fig. 3.27), this value was selected for the position reconstruction threshold W_0. The right part of figure 3.31 shows that the selected value is located in the region of the maximum of the scan for the position resolution. This can be explained by the fact that lower W_0 values introduce a higher single cell threshold, resulting in a dominance of the central cell which causes a better RMS value of the position distribution by introducing a spike at the position of the central cell. Like already discussed, this can be seen as a systematic error and the calculated RMS value cannot be taken as a real position resolution. In the other direction, higher W_0 values introduce a lower reconstruction threshold, resulting in a larger influence of the noise from the surrounding cells and therefore also in a systematic shift of the reconstructed position. With a W_0 value of 4.8 the energy dependent position resolutions shown in figure 3.32 have been obtained for the different interaction positions of the photon beam in the shashlyk cell (see fig. 3.5).

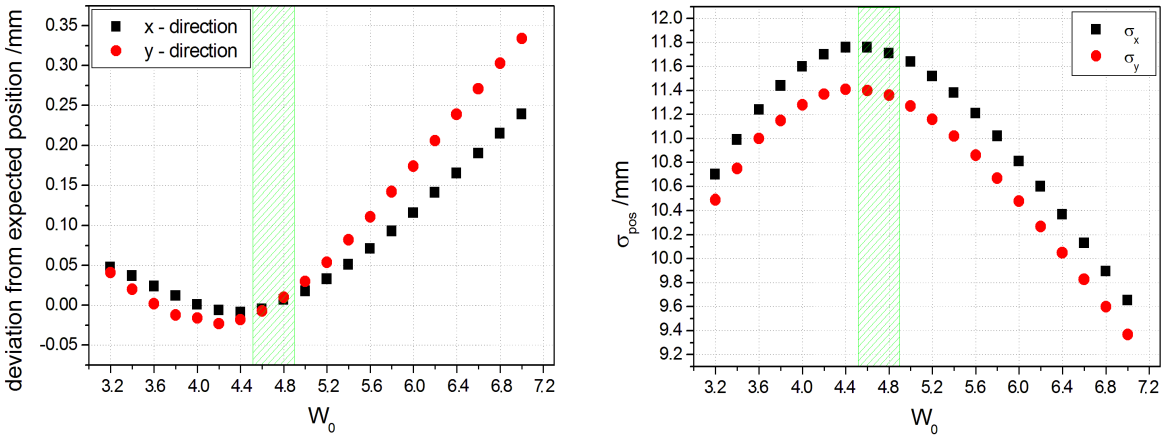

Figure 3.31: Scan of the threshold parameter W_0 for position 1 (see figure 3.5) of the shashlyk prototype at an energy of 343 MeV. Left: Deviation of the reconstructed position from the expected position as a function of W_0. Right: Dependence of the position resolution from the threshold parameter W_0.

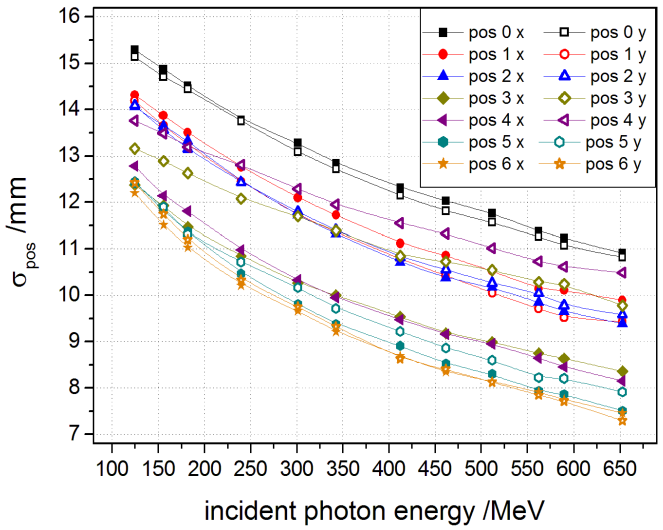

Figure 3.32: Energy dependence of the position resolution of the version B shashlyk prototype for different interaction positions (see fig. 3.5) in x- and y-direction. Due to the large beam spot in the experiment, all values are folded with the beam radius and therefore only represent an upper limit of the position resolution.

Figure 3.32 shows that the position resolution strongly depends on the interaction position of the photons. The best position resolution can be achieved if the photon beam is interacting in the corner between four cells (position 5 and 6), since the deposited energy is spread equally between the four cells and all four neighboring cells detect an energy deposition which is significantly above the threshold. A similar situation exists for the x-direction, if the photon beam is interacting in between two cells (position 3 and 4). In contrast to this, the worst position resolution is obtained for an interaction of the photon beam in the center of a shashlyk cell (position 0), since in this case most of the energy is deposited in the central cell, while all neighboring cells detect only relatively small energy fractions with large fluctuations,

deteriorating the position resolution. For the y-direction of position 3 and 4 a similar situation like for position 0 can be observed. Compared to position 0, there are only more neighbors above and below the interaction point, which slightly improve the position resolution. For the positions not exactly in the center of the cell (position 1 and 2) an average position resolution can be observed for both directions, in accordance to the considerations made for the other points.

3.3.3 Influence of the beam diameter on the position resolution

According to section 2.1.2 a collimator positioned at the end of the tagger with a diameter of 1.5 mm has been used for the beam tests of the version B shashlyk prototype. At the position of the prototype 14.5 m away from the collimator the spread of the photon beam passing the collimator leads to a beam spot with a maximal radius of 8.7 mm (for details see section 2.1.2). For the investigation of the effect of this widened photon beam on the position resolution, a Gaussian beam-spot with a standard deviation σ_{beam} is assumed. Based on the approach that the radius corresponds to $(2.5 \pm 0.5) \cdot \sigma_{beam}$, the standard deviation is determined to

$$\sigma_{beam} = (3.6 \pm 0.7)\ mm \tag{3.19}$$

The values obtained for the position resolution in the last section (σ_{mes}) are an overlap of the beam profile (σ_{beam}) and the intrinsic position resolution of the detector (σ_{pos}).

$$\sigma_{mes} = \sigma_{beam} \oplus \sigma_{pos} \tag{3.20}$$

Due to this overlap, they can only be considered as an upper limit of the position resolution. To obtain more realistic values for the position resolution, the obtained values have to be corrected by the standard deviation of the Gaussian beam profile according to:

$$\sigma_{pos} = \sqrt{\sigma_{mes}^2 - \sigma_{beam}^2} \tag{3.21}$$

Figure 3.33 shows a comparison of the position resolution for four typical cases of the interaction position before and after the correction. The size of the beam spot shows the strongest influence on the measured position resolution, if the resolution is comparable to the standard deviation of the beam spot. Since the position resolution of the shashlyk EMC is significantly larger than the beam spot, the correction causes only a small shift of the measured values. However, since the correction has a larger influence on better resolutions it is more important for higher incident photon energies.

According to section 1.3.2 the energy dependence of the position resolution can be described by

$$\sigma_{pos} = \frac{a}{\sqrt{E/GeV}} \oplus b = \sqrt{\frac{a^2}{E/GeV} + b^2} \tag{3.22}$$

Due to the incomplete shower development for energies below 300 MeV, a fit of the complete resolution curves shown in figure 3.33 is not applicable. Therefore, the fit has been limited to the region above 300 MeV. Table 3.3 shows the fit parameters of the position resolution before and after the beam profile correction.

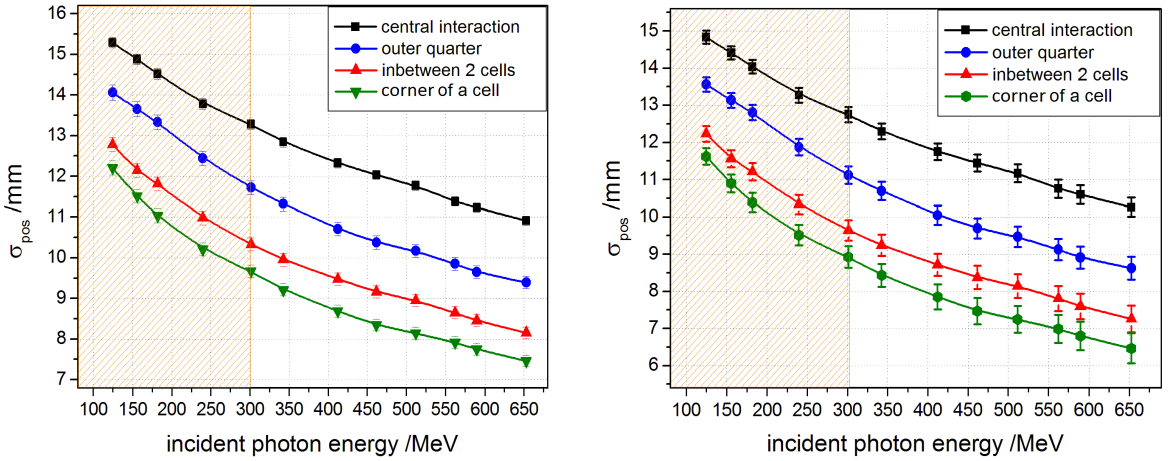

Figure 3.33: Positions resolution for typical interaction positions before (left) and after (right) the beam profile correction according to equation 3.21. The large error bars for the corrected values have been introduced by the uncertainty of the standard deviation of the photon beam. The area below 300 MeV is shaded, since the center of gravity algorithm can only be applied conditionally in this region, since a proper shower development can not be guaranteed in the shashlyk EMC for such low energies.

interaction position	**a** in mm	**b** in mm	$\mathbf{a}_{corr}$ in mm	$\mathbf{b}_{corr}$ in mm
central (i.e. pos 0_x)	5.6 ± 0.2	8.5 ± 0.2	5.7 ± 0.4	7.6 ± 0.6
outer quarter (i.e. pos 1_x)	5.3 ± 0.1	6.9 ± 0.2	5.3 ± 0.4	5.7 ± 0.7
in between two cells (i.e. pos 4_x)	4.7 ± 0.1	5.9 ± 0.3	4.8 ± 0.3	4.4 ± 0.8
corner of a cell (i.e. pos 6_x)	4.5 ± 0.1	5.0 ± 0.3	4.5 ± 0.2	3.4 ± 0.7

Table 3.3: Position resolution fit parameters according to equation 3.22 at different typical interaction positions for an incident photon energy between 300 MeV and 700 MeV. The subscript x after the position indicates the x-direction.

The comparison of the corrected and uncorrected values indicates that the stochastic term of the fit is nearly independent of the correction, while the constant term can be significantly reduced by the beam profile correction. The large errors of the fit parameters for the corrected values are introduced by the estimated error of the standard deviation of the beam profile.

3.4 Time resolution of the version B prototype

The time resolution is an important requirement for the event building algorithms which assign the detected signals to the primary event. Especially at high event rates, an exact separation of events is only possible if the detector provides a sufficient time resolution. In addition, a precise reconstruction of the detection time is important for time of flight measurements of charged particles. The extraction of the time information from a calorimeter signal can be done by two methods. The first method is given by a leading edge timing, determining the time stamp of the signal at the point at which the rising part of the signal exceeds a certain threshold. A problem of this method is the dependance of the result on the signal amplitude. Alternatively, a constant fraction timing (CFD) is used to gain an amplitude independent time information.

In the final detector setup the forward shashlyk calorimeter and also the target electromagnetic calorimeter of PANDA will have no separated timing branch in the readout. Therefore, only the signal traces recorded with the sampling ADC can be used to extract the time information. For this purpose a CFD timing trace (CFD(n)) is calculated bin wise from the pedestal (PED) corrected sampling ADC trace (SADC(n)) by equation 3.23:

$$CFD[n] = (SADC[n - D] - PED) - R \cdot (SADC[n] - PED) \tag{3.23}$$

The constants D and R have been optimized to D = 4 corresponding to a delay of 25 ns of the first branch, and R = 0.5 attenuating the second branch by a factor two. Figure 3.34 (left) shows typical CFD traces obtained by this method for selected energies.

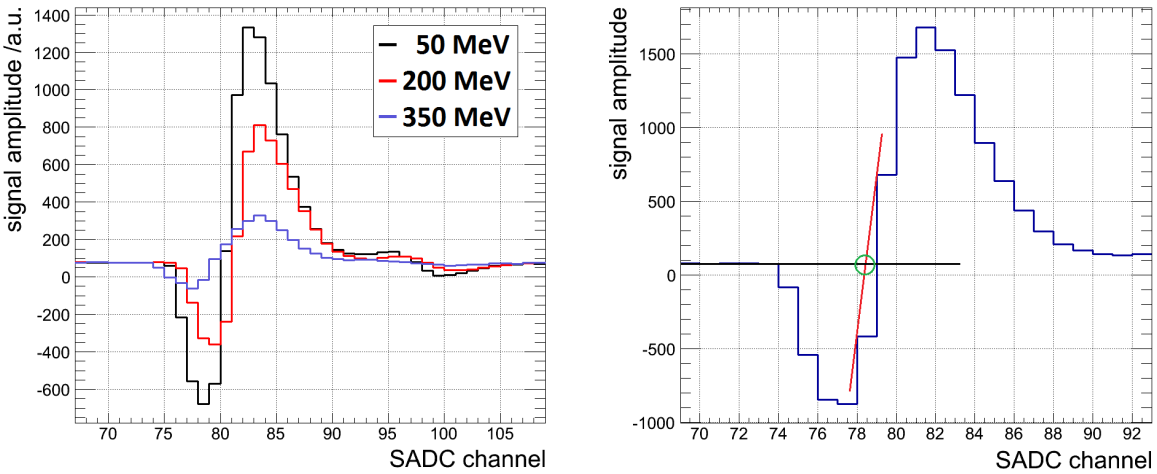

Figure 3.34: Left: Calculated CFD trace for the response of a shashlyk cell to different photon energies. Right: Extraction of the time information by a linear extrapolation of the first bin below and above the baseline. The green circle indicates the point from which the time information is extracted.

For the extraction of the time information a linear extrapolation between the first point of the central rising edge below the baseline and the first point above the baseline is performed. Based on this correlation, the time information can be extracted as the zero crossing point of the obtained linear function. The green circle in figure 3.34 (right) shows this point for a selected CFD trace. The main limiting factor of this method compared to analogue electronics is given by the sampling rate of the SADC.

To extract a time resolution from the timing of a single detector cell, a time reference is needed. For the prototype the time difference between two neighboring cells is used. If both cells detect comparable energy information, both channels should show the same time resolution σ_t. In this case the standard deviation of the time difference $\sigma(\Delta t)$ can be expressed as

$$\sigma(\Delta t) = \sqrt{\sigma_t^2 + \sigma_t^2} = \sqrt{2} \cdot \sigma_t \tag{3.24}$$

Which leads to a description of the time resolution by

$$\sigma_t = \frac{\sigma(\Delta t)}{\sqrt{2}} \tag{3.25}$$

To guarantee a similar energy deposition, only the two runs with the photon beam interacting in the center between two cells (run 3 and 4) were used for the extraction of the time information. In addition, it is required that the energy deposited in both neighboring cells has a difference of less than 10 %. Figure 3.35 shows the obtained time difference spectra for an energy deposition of 30 MeV and 150 MeV in a single shashlyk cell.

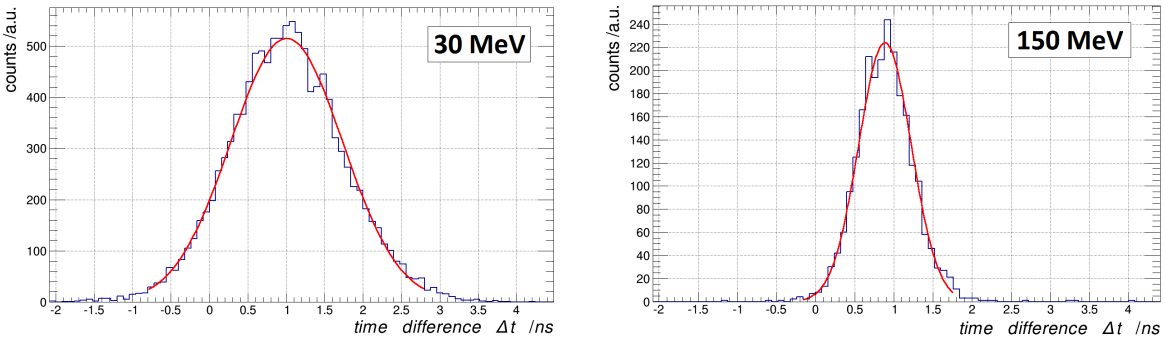

Figure 3.35: Time difference distribution for two neighboring shashlyk cells with a photon beam interacting in the center between the two cells. In each cell an energy of 30 MeV (left) and 150 MeV (right) is deposited.

The comparison of the two figures nicely illustrates the improvement of the time resolution for increasing energies. The standard deviation has been determined by fitting a Gaussian distribution to the time difference spectra and the time resolution can be finally calculated according to equation 3.25. The obtained time resolutions for the two interaction positions (pos 3 and 4) in between two modules are shown in figure 3.36. For comparison, the TDR requirement of 100 $ps/\sqrt{E/GeV}$ is shown as a solid line.

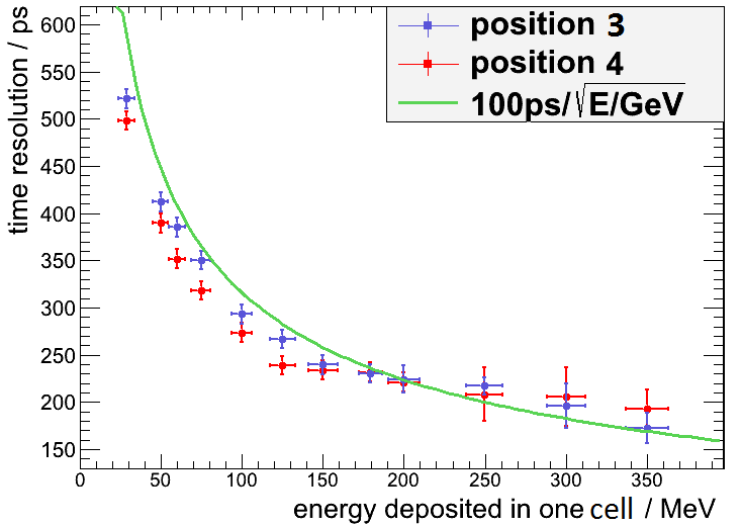

Figure 3.36: Time resolution of the type B shashlyk prototype for two different interaction positions in between two cells (position 3 and 4). The errors of the energy deposition indicate the intervals which have been set for the energy deposited in one cell. For comparison the TDR requirement of 100 ps/$\sqrt{E/GeV}$ [TDf15] is shown as a solid line.

The figure shows that the TDR requirement can be achieved with the version B shashlyk modules. Especially at very low energies the time resolution is even better than the required value. For the highest energies, a relatively large uncertainty is introduced by the poor statistics.

3.5 Additional performance aspects

After the performance of the prototype in terms of energy, position, and time reconstruction has been presented in the last sections, this section will present a detailed investigation of different aspects which can influence the performance of the calorimeter.

3.5.1 Longitudinal uniformity of the energy response

Since incoming high energetic electrons and photons create an electromagnetic shower inside the shashlyk cells, the energy deposition is spread over a large part of the cell. The center of gravity of the energy deposition moves deeper into the module for an increase of the energy. Therefore, the amount of scintillation light detected by the PMT at the rear side of the module per deposited energy unit should be the same for all longitudinal positions to achieve a proper energy reconstruction and to avoid a non-linear energy response. In reality this goal is limited by the longitudinal non-uniformity of the cells. In case of the shashlyk cells this longitudinal non-uniformity is mainly introduced by the light attenuation in the WLS fibers, since light produced in the front part of the cell undergoes a higher attenuation than light produced in the rear part of the cell, due to the longer path in the fibers. Considering the double sided readout of the fibers, the amount of photons coupled into the fiber at a certain position is split and the photons propagate in both directions, indicated as the paths x_1 and x_2 in figure 3.37.

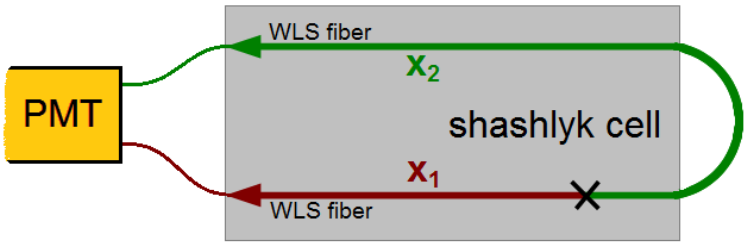

Figure 3.37: Schematic diagram of the light attenuation. The light produced in the cell at the position of the cross is coupled into the WLS fiber and propagates in both directions along the paths x_1 and x_2.

With the attenuation length λ of the WLS fibers, the total light yield detected by the PMT from both ends of the fiber can be described as:

$$LY_{PMT} = \frac{LY_{fib}}{2} \cdot e^{-\frac{x_1}{\lambda}} + c \cdot \frac{LY_{fib}}{2} \cdot e^{-\frac{x_2}{\lambda}} \tag{3.26}$$

with the total light coupled into the fiber LY_{fib} and an empirical reduction factor $0 \leq c \leq 1$

describing additional light losses in the bending region on the path x_2. The value of this factor strongly depends on the bending radius of the fibers and on the fiber treatment.

Since the light propagation lengths x_1 and x_2 are connected by the total fiber length via $L = x_1 + x_2 \approx 190\ cm$, formula 3.26 can be expressed as

$$LY_{PMT} = \frac{LY_{fib}}{2} \cdot \left(e^{-\frac{x_1}{\lambda}} + c \cdot e^{-\frac{L}{\lambda}} \cdot e^{\frac{x_1}{\lambda}} \right) = A \cdot e^{-\frac{x}{\lambda}} + B \cdot e^{\frac{x}{\lambda}} \tag{3.27}$$

with constants A and B and the distance x between the PMT sided end of the active volume and the region of the shower deposition. The total light yield detected by the PMT is the sum over all 36 fibers. With an attenuation length λ of 3.5 m [KUR15] and if a light loss in the bending region of 30 % is assumed, a light reduction in the front part of the module compared to the rear part of 8% has to be expected.

To study this effect experimentally, the energy deposition of cosmic muons at fixed positions of horizontally aligned cells has been investigated. For the selection of cosmic muons with a well defined interaction position, two 4 cm wide and 1 cm thick plastic scintillator paddles have been positioned at a distance of 10 cm directly above the shashlyk module. The schematic setup is shown in figure 3.38.

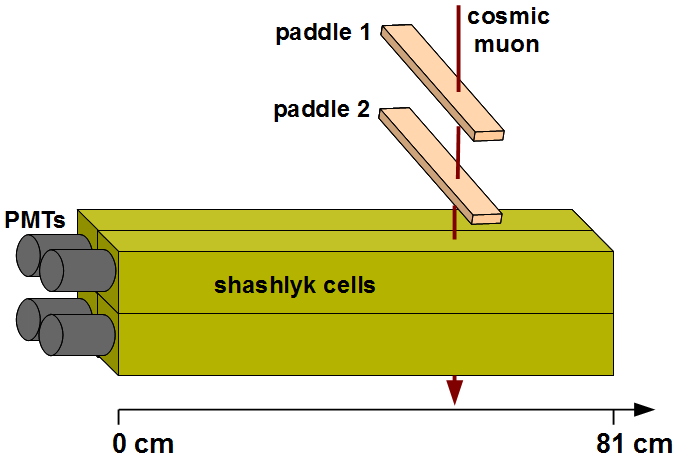

Figure 3.38: Setup for the measurement of the longitudinal homogeneity of the energy response with cosmic muons. To determine the interaction position of the cosmic muons, two plastic scintillator paddles (paddle 1 and 2) are used as coincidence detectors.

By requiring a coincidence between these two paddles and one of the shashlyk cells, the interaction position in longitudinal direction can be limited to approximately four centimeters. With this setup the light yield of all 16 shashlyk modules has been measured close to the PMT sided end of the active volume and close to the front end of the shashlyk cells. Figure 3.39 shows a picture of the energy deposition spectra of cosmic muons for both interaction positions in a typical cell.

The obtained light yield, normalized to the interaction position close to the PMT, and the change of the light yield for all 16 modules is shown in figure 3.40. The average light yield reduction for an energy deposition in the front part of the cell compared to the rear part is in the region of 12 %. For most of the cells it varies between 8 % and 16 % with only a few

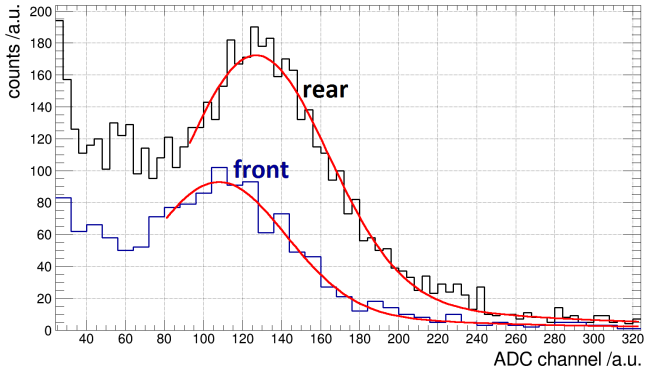

Figure 3.39: Energy deposition spectra of cosmic muons interacting in the front and in the rear part of a typical shashlyk cell.

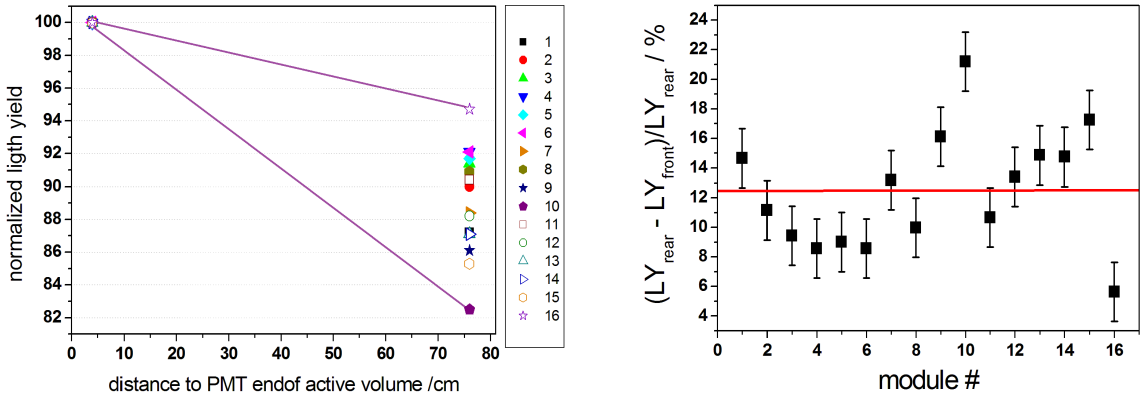

Figure 3.40: Longitudinal non-uniformity of the version B shashlyk cells. Left: Normalized light yield for all 16 cells, measured at the front and rear side of the cells. The solid purple lines indicate the maximal variation of the points. Right: Relative variation of the mean light yield of cosmic muons between the front and the rear side of the cells.

exceptions. The lowest values are therefore consistent with the prediction of 8%, calculated from the attenuation length of the WLS fibers. The higher values of the other fibers can be explained by additional light losses in the bending region of the fibers and by light which is scattered out of the fibers by other defects.

3.5.2 Cross-talk between single cells

For a reliable relative calibration of the single cells and also for an exact position reconstruction it is important that there is no optical cross-talk between the single cells of the shashlyk calorimeter. The modules consisting of four cells are wrapped with black paper on the outer surface and therefore expected to be nearly light tight. In contrast to this, the inner edges of the scintillator tiles of the single cells are only painted with white color and the bent front parts of the WLS fibers of all four cells are in a common volume under the front cover of the module, which may cause optical cross-talk. To check if optical cross-talk occurs between the single cells and to quantify the strength of the cross-talk, a test measurement has been performed. For this purpose one module has been made completely light tight and one cell

of the module has been equipped with a PMT. Figure 3.41 shows the arrangement of the module with the PMT equipped to cell number 2.

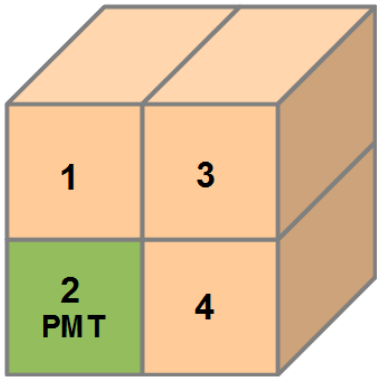

Figure 3.41: Setup for cross-talk measurements in a shashlyk module. The PMT is equipped to cell number 2.

As a first configuration the fiber bundles in the rear part of all cells, expect the one coupled to the PMT were covered with a PVC cap and black tape to make them light tight. If the outer wrapping of the module is light tight, no ambient light should be detected by the PMT in this configuration. To check if this is the case, the dark count spectrum of the PMT coupled to cell 2 has been recorded without any additional coverage of the module and in a second configuration with a cover of three layers of black towel around the module. The results, shown in figure 3.42 (left), demonstrate that the dark counts are only slightly reduced by an additional covering of the module. Therefore, it can be assumed that the outer cover of the modules is nearly light tight. The observed dark count spectrum under the absence of ambient light can be explained on the one hand by the dark counts of the PMT and on the other hand by the intrinsic activity of the lead plates in the shashlyk cell.

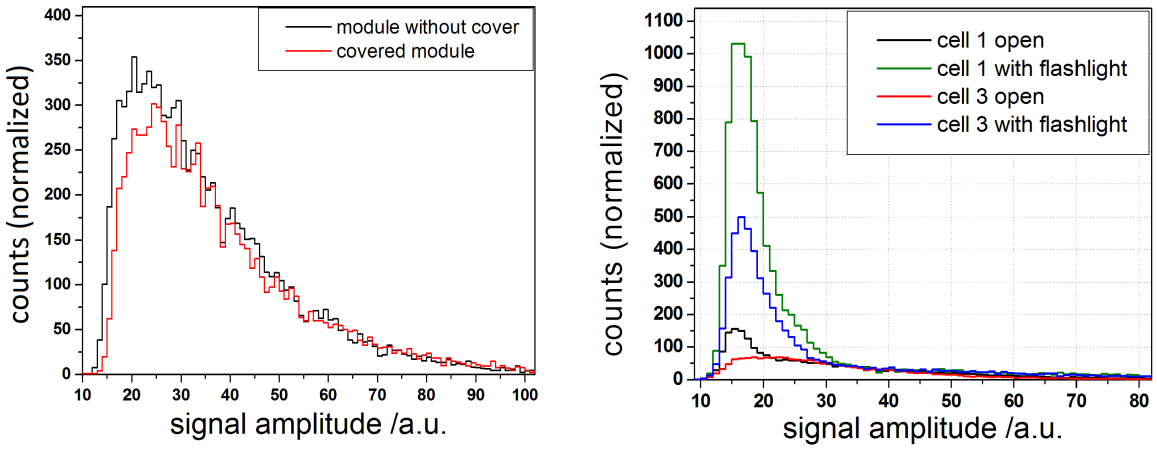

Figure 3.42: Dark counts of a shashlyk module with and without a cover of black towel (left) and cross-talk between the cells of a shashlyk module (right). All spectra are normalized relative to each other at an amplitude of 35, where the intrinsic dark counts of the PMT dominate the response in all cases.

As a second step, the WLS fiber bundle of one of the closed cells has been opened to let ambient light enter this cell. In this configuration the dark count spectrum of the PMT coupled to cell 2 has been recorded. To enhance the amount of light in the open cell, a pulsed flashlight has been used to inject additional light inside the cell. The spectra recorded with the PMT are shown in figure 3.42 (right) for cell 1, directly above the cell with the PMT and for cell 3 in the opposite corner of the module. The spectra show that if cell 1 is open, already without a flashlight, additional noise is detected by the PMT on cell 2 in the amplitude region below 20 channels. The noise level can be additionally increased if external light is coupled into the cell by a flashlight. For cell 3 no significant effect can be observed if the end of the cell is open but after injecting light by a flashlight also for this configuration a significant increase of the counts detected by the PMT coupled to cell 2 can be observed in the region below 30 channels. To quantify the increase of the noise level for the different cases, the ratio of the counts between channel 20 and 40 and channel 20 and 60 has been calculated. Figure 3.43 shows this ratio for the different cases.

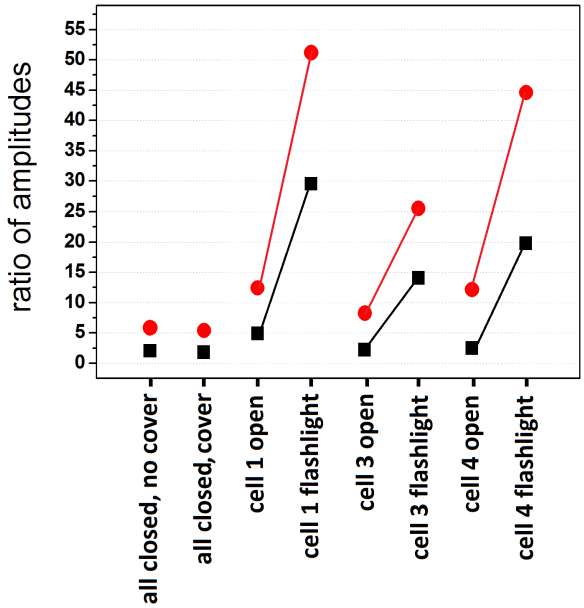

Figure 3.43: Quantization of the cross-talk for different configurations. The black points represent the ratio of the counts at channel 20 and 40, while the red points show the count ratio between channel 20 and 60.

The figure illustrates that cells 1 and 4 with a common side face to cell 2 show a similar behavior with a significant increase of the amplitude ratio after the injection of light into the cells. In contrast to this, the increase is significantly lower for cell 3 which is positioned in the opposite corner of the module. This behavior confirms crosstalk, introduced by a mixing of light from the different cells in the bent front region of the fibers and since a coverage of the side faces of the scintillator tiles with white paint does not make them completely light tight. While the cross-talk of cell 3 is mainly caused by the first effect, the cross talk from cells 1 and 4 is caused by both effects and therefore higher than for the other cell. However, the absolute amount of light transferred to the neighboring cells is not known, since the light coupled into the cells is not pulsed and therefore mainly contributes to the recorded noise distribution.

From the observed spectra, it can only be estimated that the impact of the cross-talk is quite low, since the amount of photons from the external light, even without a flashlight, is many orders of magnitude larger than the typical photon yield of the scintillator. Based on these observations, it can be expected that the crosstalk is negligible, but for a final clarification a test with a calibrated light pulser has to be performed.

3.6 GEANT4 simulations of the version B prototype

To develop a model which reproduces the experimentally achieved energy resolution of the shashlyk prototype and to study the distribution of the energy deposition and the effect of the module length on the energy resolution, the version B prototype has been implemented in GEANT4 (v. 4.9.4) [AAA03, AAA06]. This section will present the simulation setup as well as the results.

3.6.1 Simulation setup

Like the real version B prototype, the simulated one consists of a 4×4 array of $5.5 \times 5.5\ cm^2$ large cells grouped in four modules with 2×2 cells each. Each cell is implemented as a series of 380 layers consisting of a 175 μm thick TYVEK sheet, followed by a 1.5 mm thick scintillator tile, another 175 μm thick TYVEK sheet and the 275 μm thick lead plate. The air gap between the scintillator tiles and the neighboring TYVEK sheets is set to a thickness of only 1 μm, since the layers were closely spaced in the real modules. Figure 3.44 shows the setup for one of the 380 layers of one cell.

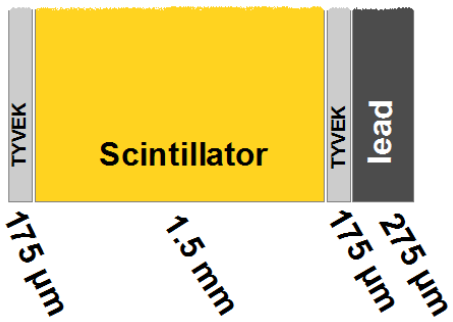

Figure 3.44: Schematic view on the dimensions of one layer of the version B shashlyk cells.

According to the given dimensions, the total thickness of one layer sums up to 2.125 mm, which results in a total module length of 80.75 cm. Table 3.4 lists the properties of the single implemented materials, which are important for the interaction cross-sections used by GEANT4.

With the implemented model it is only envisaged to study the energy deposition and not the light propagation and collection in the modules, since such simulations would require a detailed knowledge of the optical properties of all relevant components and would cause an enormous computing effort. Therefore, the WLS fibers and the support structures of the modules are not implemented in the model, since they show only a minor influence on the

material	chem. formula	density	Z_{eff}
scintillator (polystyrene)	$(C_8H_8)_n$ (+ dopands)	1.04 g/cm^3	3.5
lead	Pb	11.342 g/cm^3	82
TYVEK [DP08]	$C_{12}H_{20}O_{10}$	0.304 g/cm^3	4.1

Table 3.4: Properties of the materials of the shashlyk modules. For composite materials only the chemical formula of the main component is given. In the case of the scintillator material the chemical composition of the dopands can be ignored, since their concentration is less than 1.5 % and they are also organic materials with similar density and similar effective nuclear charge.

overall energy deposition in the module and can be neglected in these simulations. To simulate the influence of the longitudinal non-uniformity, the position dependence of the light yield is parametrized and implemented in a model which calculates the light output based on the energy deposition and its longitudinal position in the module.

The implemented single cell is duplicated 16 times and positioned with a gap of 0.5 mm in between the cells as a 4×4 array, shown in figure 3.45. The TYVEK layer in between the four modules has been neglected, since it has no significant effect on the energy deposition.

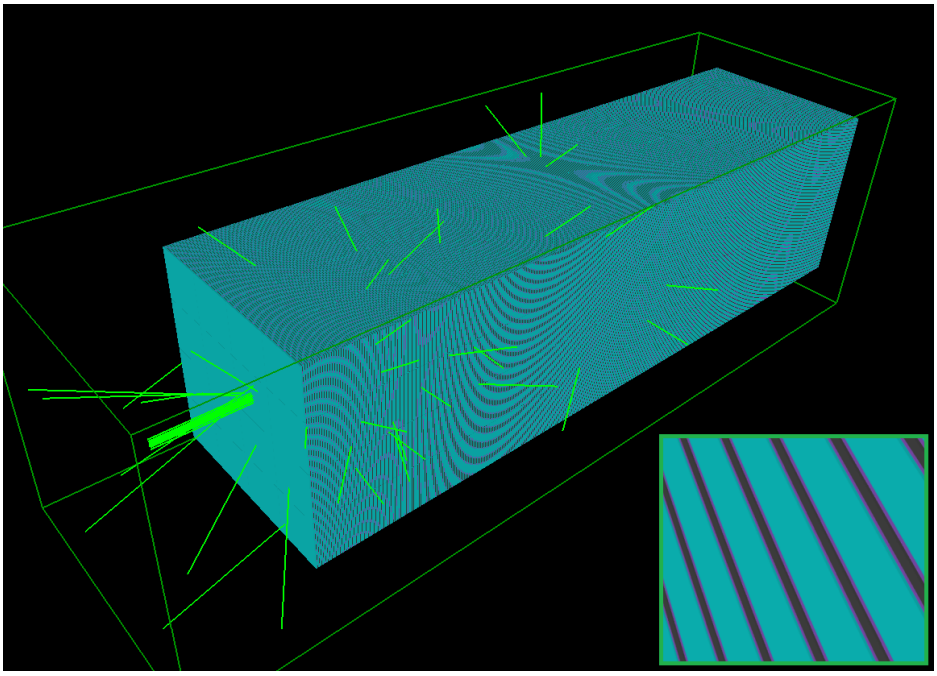

Figure 3.45: Three-dimensional model of the simulation setup of the version B shashlyk EMC prototype. The insert in the right lower corner shows a detailed view on the implemented layer structure of the cells.

For the simulations a photon beam with a Gaussian beam profile and a standard deviation of 3.6 mm is used, which approximately reproduces the photon beam provided by the tagger of the A2 hall in Mainz after a distance of 12-15 m between tagger and detector (see section 2.1.2). In the standard configuration the beam is interacting in the center of the right lower central cell (number 6 in figure 3.5), which was also the central cell in the test experiment.

3.6.2 Lateral and longitudinal energy deposition distribution

The longitudinal energy deposition profile in the modules is a very important property to make a decision about the optimal module length, to approximate the influence of longitudinal non-uniformity based on the implemented light yield model and to approximate the leakage to the rear side of the module for higher energies. In contrast to this, the lateral energy deposition profile can be used to study the influence of lateral inhomogeneities like variations between single cells or within a cell and calibration errors. As another application, it can be used to approximate the lateral leakage out of the relatively small prototype. This leakage is especially important if only small (i.e. 3×3) clusters are considered for the energy reconstruction. In addition, the energy deposition distribution in lateral directions is the basis for all position reconstruction algorithms. Figure 3.46 shows a GEANT4 simulation of the two-dimensional shower profile within the shashlyk prototype for a relatively low photon energy of 100 MeV and for the highest design energy of 15 GeV.

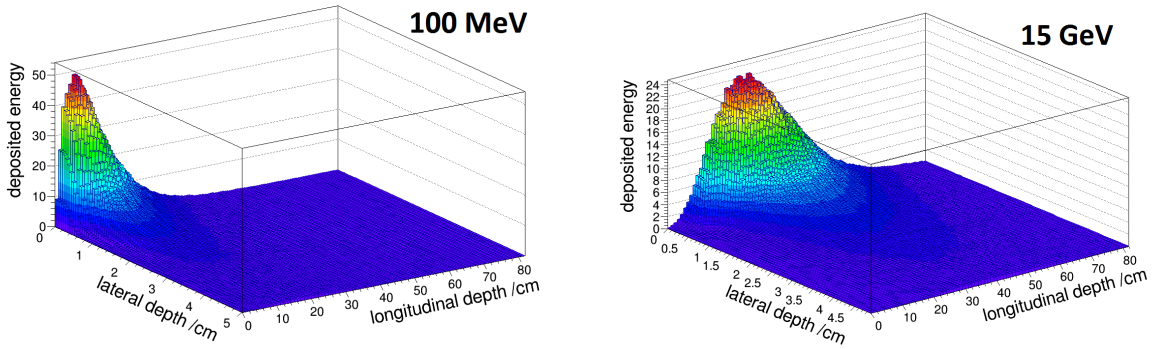

Figure 3.46: GEANT4 simulation of the two-dimensional shower profile within the shashlyk prototype for an incident photon energy of 100 MeV (left) and 15 GeV (right).

As expected, the figure shows that for low energies around 100 MeV the main part of the shower is concentrated in the first third of the cell in longitudinal direction. Also in lateral direction a limited expansion can be observed. However, even for such low energies a significant part of the shower energy is deposited in the neighboring cells starting at a lateral depth of 2.25 cm. For the highest design energy of 15 GeV a significantly larger spread of the shower in both directions can be observed. Especially the maximum of the shower moves deeper into the module and the shower is distributed over the complete cell in longitudinal direction.

Longitudinal energy deposition distribution

For a comparison of the shower distribution in longitudinal direction for different energies a projection of the shower profile on the longitudinal axis has been applied. Figure 3.47 (left) shows the obtained shower profiles for selected incident photon energies between 50 MeV and 15 GeV. The figure illustrates the variation of the position of the shower maximum within the cell and the overall shower depth. For energies $\gg 1$ GeV the distribution shows that a significant part of the shower energy leaks out of the cell in longitudinal direction resulting in a negative influence on the achievable energy resolution at high energies.

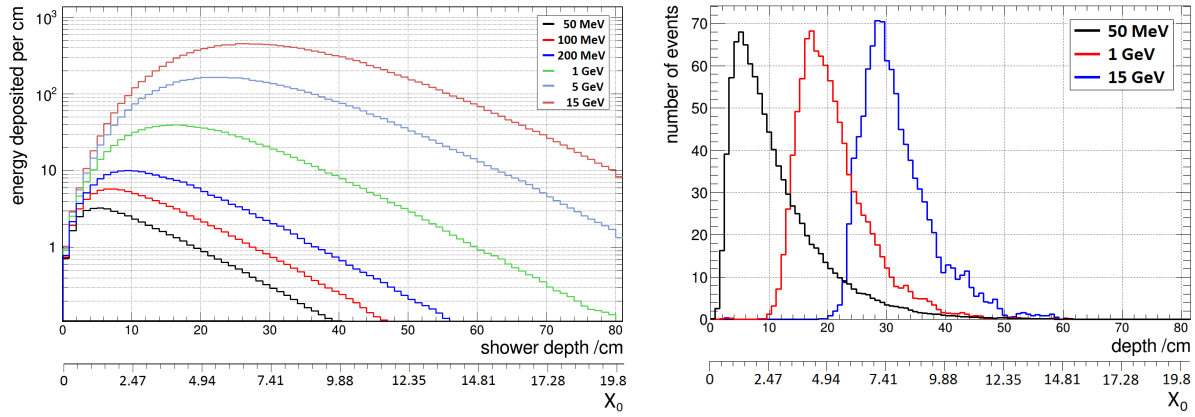

Figure 3.47: Electromagnetic shower profiles of the total deposited energy in a shashlyk cell for selected incident photon energies between 50 MeV and 15 GeV (left) and event-wise variation of the mean energy deposition position on the longitudinal axis of a shashlyk cell for different energies (right).

In addition to these energy deposition distributions, especially for the approximation of the influence of longitudinal non-uniformity effects, it is important to know how the mean value of the energy deposition position x_{mean} is varying from event to event. Therefore, this value has been calculated event-wise from the energy ΔE deposited at position x by formula 3.28.

$$x_{mean} = \frac{\sum(\Delta E \cdot x)}{\sum \Delta E} \tag{3.28}$$

The resulting distribution is shown in figure 3.47 (right) for selected energies. The distributions show that, like expected, also the mean value of the energy deposition is moving deeper into the cell with increasing energy. At the same time, the variation of the mean energy deposition position becomes slightly smaller with increasing energy. Especially for low energies, where no real shower development can be expected, a large spread of the mean energy deposition position can be observed. For a more qualitative discussion the shower maxima as well as the position of the mean energy deposition and its standard deviation have been plotted as a function of the incident photon energy in figure 3.48.

As expected from formula 1.36 and 1.37, the position of the shower maximum as well as the position of the mean energy deposition show a logarithmic dependence on the incident photon energy. In the range above 100 MeV this dependence can be described by:

$$\begin{aligned} x_{max} &= -(11.7 \pm 0.2)\ cm + (4.0 \pm 0.1)\ cm \cdot ln(E/MeV) \\ &= -(2.89 \pm 0.05)\ X_0 + (0.99 \pm 0.02)\ X_0 \cdot ln(E/MeV) \end{aligned} \tag{3.29}$$

$$\begin{aligned} x_{mean} &= -(4.6 \pm 0.2)\ cm + (3.9 \pm 0.1)\ cm \cdot ln(E/MeV) \\ &= -(1.14 \pm 0.05)\ X_0 + (0.96 \pm 0.02)\ X_0 \cdot ln(E/MeV) \end{aligned} \tag{3.30}$$

The comparison of the two parametrizations shows that, like expected, the maximum and the mean value scale with the same factor. The two values are only shifted by around 1.75 X_0 relative to each other. Below 100 MeV the condition $E \gg E_C$ is no longer fulfilled. Therefore,

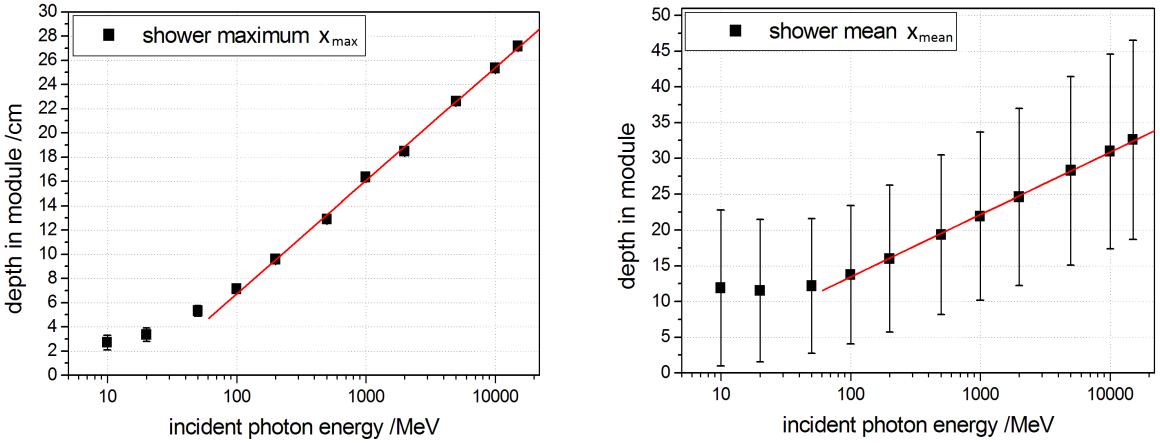

Figure 3.48: Energy dependence of the longitudinal position of the shower maximum (left) and energy dependence of the point of the mean energy deposition within a shashlyk module (right). The error bars in the right figure illustrate the standard deviation of the mean energy deposition distribution for different events.

a proper electromagnetic shower development is not possible any more and other interaction effects have to be considered. As a result the parametrizations are not applicable any more. In addition, GEANT4 is not completely optimized for calorimeter physics in this energy region, which makes the values below 100 MeV only conditionally trustworthy.

Lateral energy deposition distribution

To compare the lateral energy deposition profiles for different energies, a projection of the shower profile on the lateral coordinate has been performed, shown in figure 3.49.

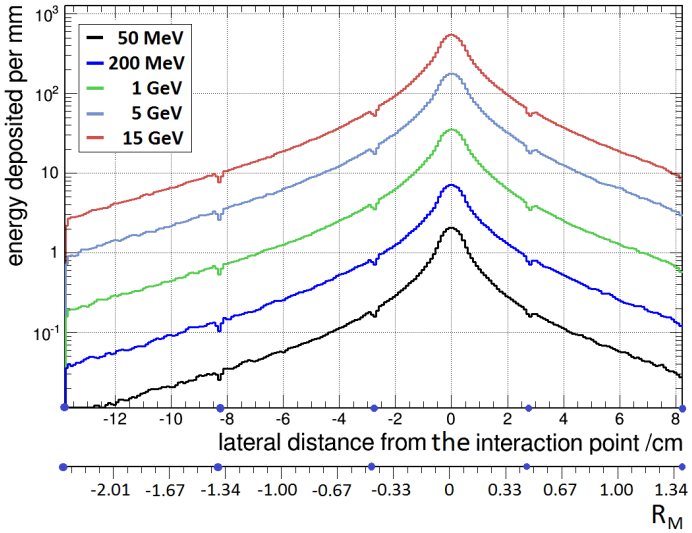

Figure 3.49: Lateral energy deposition profile within the version B prototype for selected incident photon energies. The blue points on the first axis show the borders of the single cells.

The distributions show the two components of the lateral shower expansion with the core component within $\pm$ 0.3 X_0 and the outer tales. The lateral shower expansion is mainly dominated by multiple scattering of the electrons and positrons in the shower. The dips in the distributions indicate the gaps between the modules which are marked with blue points on the x-axis. The figure also shows that for small energies $\ll$ 1 GeV most of the deposited energy, which exceeds the threshold, is contained within a 3 $\times$ 3 array of cells (1.3 R_M). In contrast to this, for the highest energies at least a 5 $\times$ 5 (2.2 R_M) or even a larger array of cells is needed to cover the complete shower with all cells in which the energy deposition exceeds the single cell threshold.

For a quantitative description of the shower containment the fraction of the energy contained in a single cell and in a 3 $\times$ 3 array of cells has been calculated and plotted in figure 3.50.

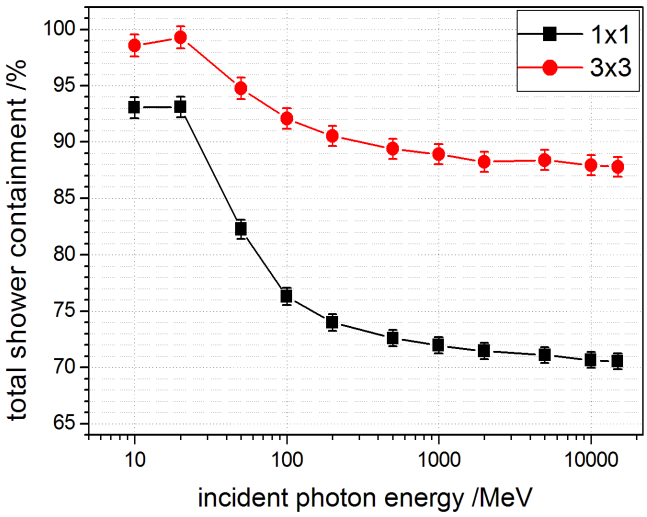

Figure 3.50: Energy deposition fraction in a single shashlyk cell (1 $\times$ 1) and in a 3 $\times$ 3 array of cells. A threshold of 0.9 MeV has been applied for the energy sum of the 3 $\times$ 3 array.

The figure shows that for energies $<$ 100 MeV the fraction of the contained energy strongly varies with the incident photon energy. While for energies below 25 MeV more than 93 % of the energy is deposited in the central cell and almost the complete energy is contained in a 3 $\times$ 3 array, this fraction decreases for an increase of the energy until it reaches a value of around 76 % for the central cell and 92 % for a 3 $\times$ 3 array at an energy of 100 MeV. This behavior at low energies can be explained by a very limited shower development in this energy region and for a 3 $\times$ 3 array also the influence of the threshold plays an important role. For energies $\ll$ 50 MeV there is even a high possibility that no electromagnetic shower is introduced by the interacting electromagnetic probes at all. For energies above 100 MeV the fraction only shows a relatively slight decrease down to 71 % for a single cell and 88 % for a 3 $\times$ 3 array at 15 GeV. This variation of the energy containment is a direct result of the implemented cluster threshold in case of a 3 $\times$ 3 array and of the intrinsic low energetic detection threshold of the simulation for a single cell.

While the longitudinal shower profile is not accessible in the experiment due to a common readout of all scintillator tiles via the WLS fibers, the lateral energy deposition distribution can be at least partly compared with the experiment due to the lateral segmentation of the

calorimeter in single cells. For this purpose the average number of cells in a 3 × 3 array which give a signal above the threshold of 1 MeV have been calculated. This quantity which is also referred to as multiplicity of the cells is plotted in figure 3.51 as a function of the incident photon energy.

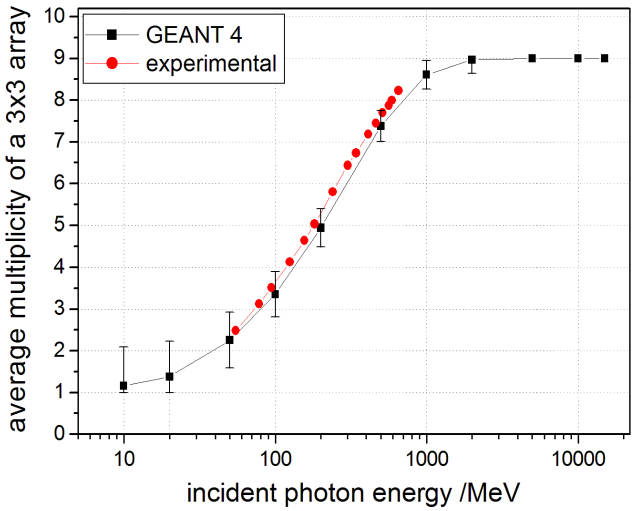

Figure 3.51: Energy dependence of the cell multiplicity in a 3 × 3 array of shashlyk cells for a threshold of 1 MeV. The red points show the multiplicity values which have been obtained with the type B prototype for the same single cell threshold.

The figure shows that for the lowest energies only a few cells are responding, while the cell multiplicity rises rapidly in the range between 100 MeV and 1 GeV. For energies $\gg$ 1 GeV in most of the cases the energy deposited in all cells of the 3 × 3 array is above the threshold of 1 MeV. For the measured energy range between 50 MeV and 700 MeV the obtained values from the type B prototype show a good agreement with the simulated ones.

3.6.3 Energy deposition in the active and passive volumes

For the energy resolution only the energy deposited in the scintillator tiles plays a role, since only this part of the energy produces scintillation light, which is collected by the WLS fibers and finally detected by the PMTs. However, the fraction of the energy deposited in the scintillator tiles and lead/TYVEK sheets is not constant, it varies from event to event. These variations are also known as “sampling fluctuations”. The strength of these sampling fluctuations is one of the main factors which limit the energy resolution of a sampling calorimeter compared to a homogenous calorimeter. The smaller the fraction of the energy deposited in the scintillator tiles is, the higher sampling fluctuations can be expected. Therefore, thick scintillator tiles and only relatively thin lead plates have been chosen for the shashlyk calorimeter of the PANDA detector to achieve the required energy resolution in the complete energy range. Figure 3.52 shows the fraction of the energy deposited in the active and passive volumes of a single version B cell as a function of the incident photon energy. For the experimentally studied energy range from 50 MeV up to 700 MeV a nearly constant fraction of 33 % to 35 % of the energy is deposited in the scintillator tiles, while the remaining energy is lost in the lead

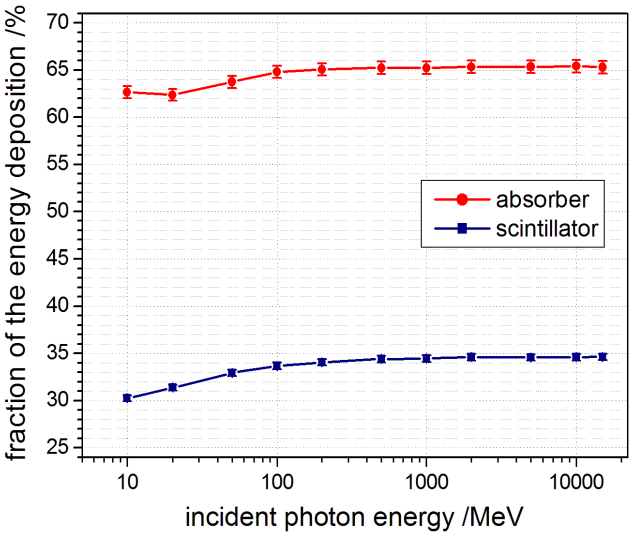

Figure 3.52: Energy fraction deposited in the active and passive parts of a single shashlyk cell, relative to the total energy deposition in a single cell. The values have been extracted from the maxima of the distributions.

and TYVEK sheets. For energies above 1 GeV the two fractions stabilize at 35 % and 65 % for the active and passive materials. In contrast to this, the energy fractions, corresponding to the maxima of the deposited energy distributions become slightly lower for the active and passive parts at energies below 50 MeV.

3.6.4 Influence of the module length on the energy resolution

Due to the additional TYVEK sheets in between the scintillator tiles and the lead plates, the version B shashlyk modules show a total length of the active detector part of approximately 81 cm, which is around 13 cm longer than the 68 cm long version A modules. Since the design of the forward spectrometer of PANDA is already fixed based on the version A module length, such a significant increase of the length is not feasible any more. One of the possible solutions for this problem would be a reduction of the active module length by removing a certain amount of layers. To get a feeling how such a reduction of the active module length would influence the achievable energy resolution of the version B modules, the response has been simulated for different module lengths. To gain a model independent result, only the resolution of the pure energy deposition in the scintillator tiles is considered for this study.

Starting with the original length of the version B modules of 80.75 cm ($\sim 20\ X_0$) several layers have been removed to reduce the module length to 78 cm ($\sim 19.3\ X_0$), 75 cm ($\sim 18.6\ X_0$), 72 cm ($\sim 17.8\ X_0$) and finally 68 cm ($\sim 16.8\ X_0$). In each case the energy dependent relative energy resolution of the energy deposited in all scintillator tiles of a 3×3 array of cells has been determined. Figure 3.53 shows the results for the different module lengths. The figure illustrates that a reduction of the module length shows nearly no impact on the energy resolution for energies below 1 GeV since most of the incoming energy is deposited before a length of 68 cm in this low energy region. For energies larger than 1 GeV an increasing impact of the module length on the energy resolution can be observed with an increase of the

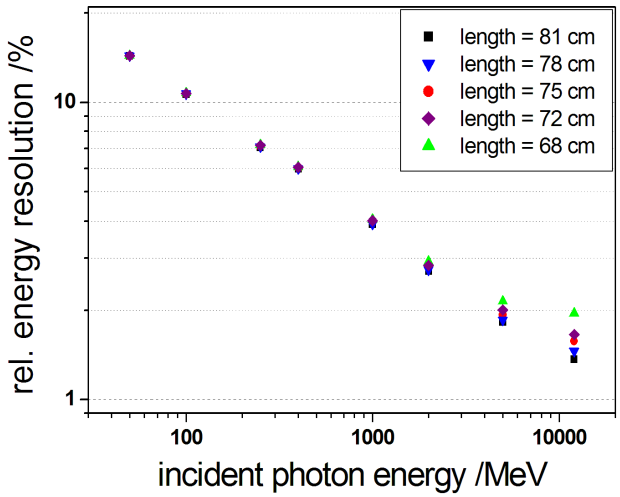

Figure 3.53: Simulated relative energy resolution of a 3 × 3 array of shashlyk cells for different module lengths between 82 cm (∼ 20 X_0) and 68 cm (∼ 16.8 X_0).

incoming photon energy. A reduction to 68 cm would introduce a significant increase of the constant term of the energy resolution. For a more quantitative view, figure 3.54 shows the dependence of the relative energy resolution on the module length for a photon beam energy of 1 GeV, 5 GeV and 12 GeV.

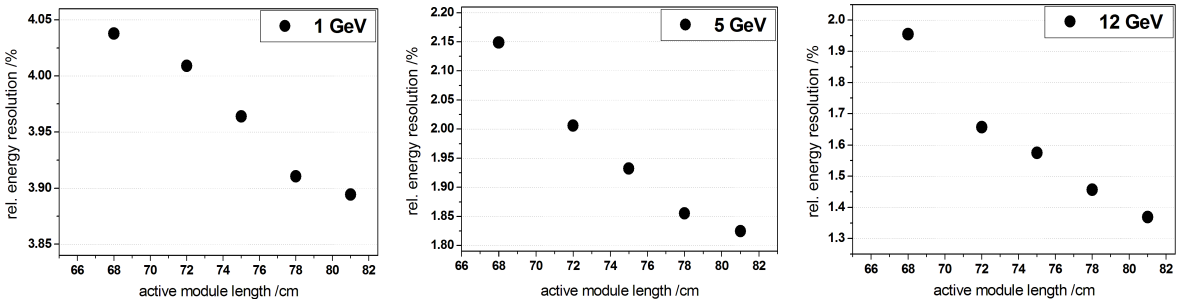

Figure 3.54: Dependence of the relative energy resolution of the deposited energy in a 3 × 3 array of shashlyk cells on the module length for an energy of 1 GeV (left), 5 GeV (middle) and 12 GeV (right).

While the increase of the relative energy resolution between 80.75 cm and 68 cm at 1 GeV is only in the order of 0.15 percent points, it becomes significantly larger for 5 GeV and 12 GeV. At 12 GeV it increases from less than 1.4 % up to nearly 2.0 %. Especially below 72 cm (∼ 17.8 X_0) a strong increase can be observed at energies > 1 GeV. On the other side a reduction of the length to 78 cm (∼ 19.3 X_0) is still acceptable for energies up to 5 GeV, while it already causes a significant increase of the energy resolution at 12 GeV.

The study shows that a moderate reduction of the active module length (< 3 cm ≈ 1 X_0) would be acceptable for most of the energy range but also such a moderate reduction would cause a realizable increase of the energy resolution at the highest energies. A reduction of the module length down to 68 cm would lead to unacceptable results for the energy resolution at energies in the GeV region and should therefore be avoided. However, a reduction of the module length can also be achieved by thinner TYVEK sheets and a shortening of the

Cockcroft-Walton high voltage supply without a reduction of the active module length in terms of radiation lengths, which is the preferable solution.

3.6.5 Influence of the longitudinal non-uniformity on the energy resolution

The measurements of the longitudinal homogeneity of the light yield in section 3.5.1 show that the scintillation light produced in the front part of the version B modules is on average reduced by 12.4 % compared to the light produced close to the PMT sided end of the active volume. This effect can be explained by the absorption and scattering of the scintillation light in the WLS fibers and has a similar effect on the energy response like the absorption of light in a scintillation crystal. The slope of the attenuation curve can in first order be approximated by an exponential function based on the measured values (see section 3.5.1).

$$LY(z) = LY_0 \cdot e^{-0.00178\frac{1}{cm}\cdot z} \tag{3.31}$$

with the light yield per energy unit LY_0 for a position close to the PMT sided end of the active volume an the distance z between the PMT sided end of the active volume and the position of the energy deposition.

To simulate the influence of this non-uniformity (NUF) in light collection on the energy resolution two variants of the light yield (LY_{cell} and $LY_{cell-nuf}$) have been calculated by GEANT4. For the first variant, the energy deposited in each of the 380 scintillator tiles (E_{tile}) is summed up without any weighting and multiplied by the light yield per energy unit (LY_0).

$$LY_{cell} = LY_0 \cdot \sum \cdot E_{tile} \tag{3.32}$$

For the second variant, the energy deposited in each scintillator tile is weighted with the corresponding position dependent factor of the light yield per energy unit $LY(z)$ from equation 3.31, including the non-uniformity, before the values are summed up.

$$LY_{cell-nuf} = \sum LY(z) \cdot E_{tile} \tag{3.33}$$

For a comparison of the two calculations no light yield statistics will be considered and LY_0 will be set to 1.0. With this condition, the results correspond to the resolution of the pure energy deposition. Figure 3.55 shows a comparison of the simulated energy resolution with and without the implementation of the non-uniformity for a single cell and for a 3 × 3 and a 4 × 4 array of shashlyk cells for an energy range from 50 MeV up to 400 MeV. For a single cell nearly no effect of the non-uniformity in light collection on the relative energy resolution can be observed since the shower fluctuations provide the dominant contribution. Even for a 3 × 3 and a 4 × 4 array of cells only a small increase of the resolution is observable if the non-uniformity in light collection is included. This behavior can be explained by the relatively worse intrinsic energy resolution of the shashlyk modules in relation to the strength of the smearing of the energy response by the non-uniformity in light collection. The total non-uniformity is in the order of 12.4 % over a length of around 81 cm, leading to an average change of the light yield of only 0.61 %/X_0. According to section 3.6.2 the longitudinal position of the mean energy deposition within the shashlyk module has a typical standard deviation of approximately 12 cm (∼3 X_0), resulting in a smearing of the energy response

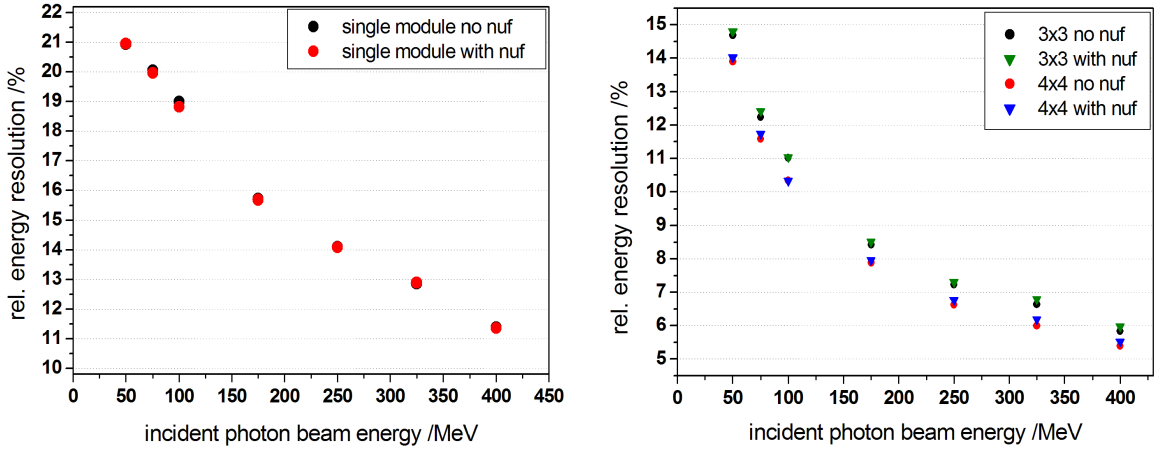

Figure 3.55: Influence of the light collection non-uniformity (nuf) on the energy resolution of the shashlyk calorimeter for a single cell (left) and for a 3 × 3 and a 4 × 4 array of cells (right).

by approximately 1.8 %. Since this smearing is significantly smaller than the relative energy resolution of the shashlyk modules in the region below 400 MeV, no significant influence can be observed. Nevertheless, in the energy region above 1 GeV the relative energy resolution reaches a comparable level, resulting in a significantly stronger impact of the non-uniformity.

3.6.6 Reproduction of the experimental energy resolution

For a detailed understanding of the behavior of the shashlyk modules and for an implementation of the shashlyk calorimeter in physics simulations with the complete PANDA detector it is important to develop a model which reproduces the experimental data. For this purpose two methods are feasible, the implementation of a light collection simulation of the complete module with all optical properties of the different materials, or the development of a model, based on empirical properties, which enables the calculation of the effects and statistics of the light collection and detection based on the pure energy deposition distribution provided by GEANT4.

For practical purposes a complete light collection simulation based on ray tracing in the optical components is quite complex, since a lot of optical and surface properties of the different materials have to be measured and implemented. In addition, a simulation of the light production and propagation in all 380 scintillator tiles of a module and the transportation of this light in the 18 WLS fibers of the module consumes a huge amount of computing power and is therefore very time consuming. Based on this disadvantages it is only feasible to use such simulations for the basic understanding and optimization of the light collection and propagation in a module. For the implementation in physics simulations a much more simple model is needed which provides a fast simulation of the energy response and resolution. This section will present such a model for the energy range between 50 MeV and 400 MeV based on two different approaches. For both approaches the energy deposition including the non-uniformity in light collection described in section 3.6.5 will be used as a basis for the calculations. In both cases the experimentally determined noise level of $\sigma_{noise} \sim 0.3$ MeV is considered by adding a Gaussian noise distribution with a mean value of 0 and a standard

deviation of 0.3 MeV. In addition, also the experimentally determined single cell threshold of 1 MeV has been used for the reconstruction of the simulated energy

1. Gaussian smearing of the energy resolution

A first approach for the reproduction of the experimental energy resolution is a simple Gaussian smearing of the simulated energy deposition by a certain fraction of the simulated value. The calculation of the smeared energy including the Gaussian noise distribution can be described by

$$E_{smeared} = Gaus(E_{\text{scint}}\ ,\ c \cdot E_{\text{scint}}\ )\ +\ Gaus(0\ ,\ 0.3\ \text{MeV}) \tag{3.34}$$

with a constant value c as a free parameter. A comparison between the simulated and the experimental values shows that $c = 0.036$ corresponding to a smearing by 3.6 % of the energy value, provides the best results. Figure 3.56 shows the experimental energy resolution as well as the simulated energy resolution for the pure energy deposition including the non-uniformity in light collection and the resolution of the smeared energy.

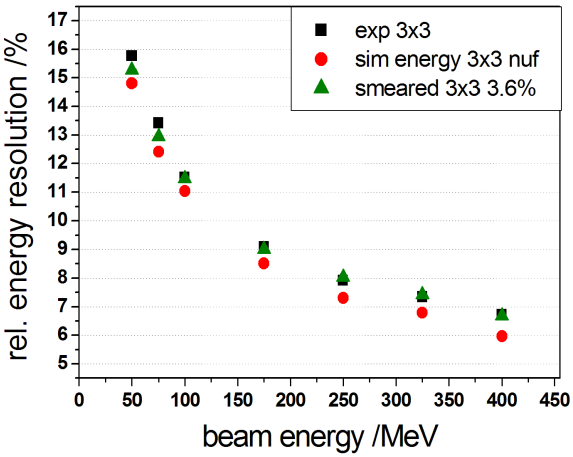

Figure 3.56: Comparison of the experimental energy resolution of a 3 × 3 array of cells (black points) with the simulated resolution of the pure energy deposition including the longitudinal non-uniformity (red points) and the resolution values obtained by a Gaussian smearing of the energy information by 3.6 % of the detected energy (green points).

The figure shows a good agreement of the simulated values with the experimental results for energies between 100 MeV and 400 MeV. Only for the lowest energies between 50 MeV and 100 MeV the simulated energy resolution is slightly too low.

2. Light yield calculation based on empirical values

The second approach uses the light yield detected by the PMT per deposited energy unit to calculate the total light yield smeared by its statistical distribution. The number of photo electrons produced in the photocathode of the PMT per MeV of deposited energy in the shashlyk cell can be easily measured by recording the single photo electron distribution in the dark-count spectrum of the PMT at the same voltage and temperature like during the beam

measurement and comparing the channels between two photo electrons with the number of channels of the peak introduced by a fixed beam energy. With this method a value of (2.8±0.3) photo electrons per MeV has been determined with a Philips XP 1911 PMT for the version B cells. Since this PMT is a few years old and was already in use for other experiments, it shows a reduced quantum efficiency of only $\sim$ 11 % at 530 nm. During the beam-time new Hamamatsu R7899 PMTs with a quantum efficiency of $\sim$ 14 % at 530 nm [Ham00] have been used. Therefore, the number of photo electrons (PE) has to be corrected to consider the higher quantum efficiency (QE) of the new PMTs:

$$PE_{corr} = PE \cdot \frac{QE_{\text{Philips}}}{QE_{\text{Hamamatsu}}} = PE \cdot \frac{14\ \%}{11\ \%} = (3.6 \pm 0.4)\frac{1}{\text{MeV}} \tag{3.35}$$

In addition, it has to be considered that GEANT4 provides the energy deposited in the scintillator tiles, while the measured number of photo-electrons has been calculated for the energy deposited in the complete cell. According to section 3.6.3 only 34 % of the energy deposited in a cell are deposited in the scintillator tiles. Considering this fraction, a transformation of the measured photo electrons can be performed:

$$PE_{scint} = \frac{PE_{corr}}{0.34} \approx 10.5\frac{1}{\text{MeV}} \tag{3.36}$$

Based on this value the light yield in photo electrons for a given energy E_{scint}, deposited in the scintillator tiles of the cell can be calculated by

$$LY_{PE} = E_{scint} \cdot PE_{scint} \approx E_{scint} \cdot 10.5\frac{1}{\text{MeV}} \tag{3.37}$$

Since the light yield is a statistical property, it follows a Gaussian distribution with a standard deviation corresponding to the square-root of the light yield. Applying this distribution and adding the noise distribution transformed in photo electrons, the statistically distributed light yield detected by the PMT can be calculated by

$$\begin{aligned} LY &= Gaus\left(E_{scint} \cdot PE_{scint}\ ,\ \sqrt{E_{scint} \cdot PE_{scint}}\ \right) \\ &\quad + Gaus(0\ ,\ 0.3\ MeV \cdot PE_{scint}\ ) \\ &= Gaus\left(E_{scint} \cdot 10.5\tfrac{1}{MeV}\ ,\ \sqrt{E_{scint} \cdot 10.5\tfrac{1}{MeV}}\ \right) \ +\ Gaus(0\ ,\ 3.15) \end{aligned} \tag{3.38}$$

The application of this calculation to the energy deposited in the scintillator tiles in each event provides the measured light yield distribution, which can be fitted by a Novosibirsk function to determine the energy resolution. Figure 3.57 shows that the energy resolution of a single shashlyk cell can be completely reproduced with this method in the energy range from 50 MeV up to 400 MeV. In contrast to this, the energy resolution of a 3 × 3 and a 4 × 4 array is only exactly reproduced for energies above 200 MeV while the simulated values below 200 MeV are a bit to high, but still within the error bars calculated from the uncertainties of the simulation and calculation procedure.

The main reason for this difference between the simulated and the experimental energy resolutions at low energies may be the uncertainty in the number of photo electrons which has been used for the calculation. In addition, the implemented characteristics of the electronic noise strongly influence the relative energy resolution for low energies.

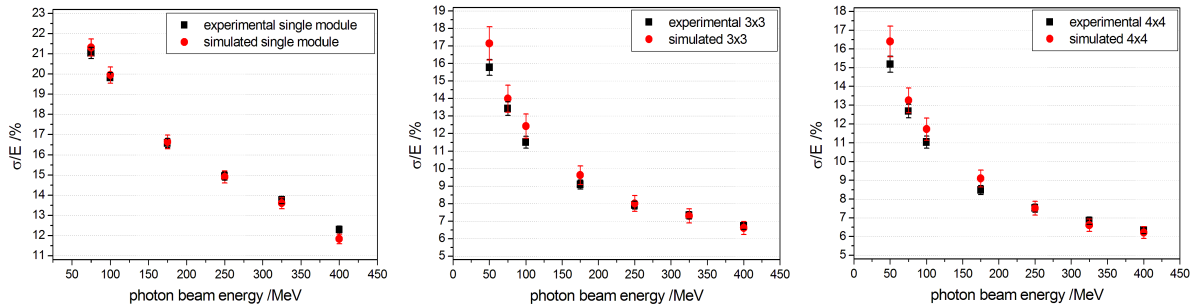

Figure 3.57: Comparison of the experimental energy resolution with the simulated values based on the measured light yield for a central interaction in one module (left), for a 3×3 array (middle) and for a 4×4 array (right).

Conclusion

Both methods for the reproduction of the experimental energy resolution show a good agreement with the experimental values in the energy range above 200 MeV. Only for lower energies a complete reproduction is not possible. In this energy region special correction terms have to be applied to fit to the experimental values. However, for an implementation in physics simulations, the Gaussian smearing of the energy resolution provides the easiest and fastest method for a reliable calculation of the energy under consideration of the experimental resolution.

Chapter 4

Influence of the feature extraction, calibration and light collection non-uniformity on the energy resolution of the barrel EMC

Inhomogeneities of the energy response are a critical issue for all types of calorimeters. In the last chapter it has been presented how the lateral and longitudinal inhomogeneity influences the response of a shashlyk calorimeter and how several optimization of the shashlyk cells resulted in a significant improvement of the homogeneity and the energy resolution. Besides sampling calorimeters, a non-uniform energy response is also an issue for homogeneous crystal calorimeters. In lateral directions the inhomogeneity of a crystal calorimeter is mainly introduced by a variation of the crystal quality and by the segmentation of the calorimeter and the resulting dead material and gaps in between the crystals. In case of the PANDA barrel EMC the crystals will be wrapped with a 63.5 μm thick mirror reflective VM2000 foil and placed in a carbon fiber alveole, acting as a mechanical support structure. The overall distance between two crystals introduced by the 400 μm thick carbon layer, the two VM2000 foils and small air gaps will be in the order of 680 μm [TDe09]. To avoid an interaction of particles or photons directly in these gaps, the interaction point of the anti-protons with the target is shifted relative to the center of the barrel. Nevertheless, even an interaction of electromagnetic probes close to the edge of a crystal causes an energy leakage of the electromagnetic shower due to this gap and the included dead material. Therefore, the detected energy in this region is slightly reduced compared to a central interaction and the energy resolution is deteriorated. Detailed investigation of the influence of this effect on the energy resolution of the PANDA barrel EMC and methods for the correction of the energy loss can be found in [DAB13] and [TE13].

In longitudinal direction a non-uniformity is naturally introduced by the absorption of the scintillation light in the crystal, causing a reduction of the light produced in the front part of the crystal compared to light generated in the rear part. To realize an uniform energy response and to achieve a high light output, scintillation crystals are optimized for a low intrinsic absorption of the scintillation light. In case of the PANDA barrel EMC, the geometrical realization of the barrel requires the application of tapered crystals. Due to the tapering,

scintillation light produced in the front part of the crystal is enhanced when focused to the LAAPDs glued to the rear side of the crystal [ACL02]. As a combination of this focusing effect and the intrinsic absorption of the light in the crystal, a non-uniformity curve with an increase of the light yield from the front part of the crystal of up to 50% for the most tapered PANDA crystals can be observed [DAB13]. Since the electromagnetic shower, especially at high energies, spreads over a large part of the crystal and also varies from event to event, this non-uniformity causes a smearing of the energy response of the crystal and therefore a deterioration of the resolution.

This section will demonstrate the influence of the light collection non-uniformity in tapered PWO crystals on the energy resolution of the PANDA barrel EMC at energies below 1 GeV and present the effect of a reduction of the non-uniformity by de-polishing of one lateral side face of the crystals on the energy resolution. For a test experiment with high energetic photons, performed in the A2 hall of the MAMI accelerator in Mainz, the section with type 2 crystals of the current close to final barrel EMC prototype "PROTO 120" has been used. Based on the data recorded with a 3×3 sub-array with de-polished crystals, the influence of different feature extractions and calibration methods on the energy resolution will be compared and optimized. The results will be compared to a 3×3 sub-array with polished crystals, analyzed in an identical manner. For a more detailed understanding of the results, GEANT4 simulations of single PWO crystals and of PROTO 120 have been performed and a special model has been developed to reproduce the experimental energy resolution.

4.1 The light collection non-uniformity in tapered PANDA PWO crystals

Like introduced in section 1.3.4, the barrel part of the PANDA target EMC will consist of 11 different crystal geometries[1] with a different degree of tapering. The most tapered crystals (type 1) will be placed in the center of the barrel, while the degree of tapering decreases for crystals positioned further away from the center (type 2 - 11) [TDe09]. As a result of the tapering of the crystals side face, scintillation light generated in the front part of the crystal is focused to the LAAPDs glued to the crystals rear side. The focusing effect decreases the incident angle of photons relative to the crystals rear side, on their way to the LAAPDs, resulting in a shortening of the photon paths, a reduction of the number of reflections and an increase of the optical aperture. In combination, this effects increase the probability that photons generated in the front part of the crystal are detected by the LAAPDs, compared to photons generated closer to the rear face of the crystal [BRQ05, DAB13]. The decrease of the incident photon angle on the way to the LAAPDs and therefore also the strength of the focusing effect are directly proportional to the degree of tapering of the crystals side face [DAB13, BRQ05], which makes the effect most dominant for the most tapered crystals (type 1). In addition to the focusing of the light, there is also the intrinsic absorption of the scintillation light in the crystal, which depends on the path length of the photons and therefore introduces the strongest reduction to scintillation photons produced in the front part of the crystal. The combination of these two effects results in a non-uniformity curve for the light detected by the photo sensor, depending on the position were it is generated [BRQ05].

[1] Each geometry will be produced in a mirror symmetric left and right version.

Figure 4.1 illustrates the contributing effects and the resulting non-uniformity curve. The green line within the crystal illustrates the influence of the focusing effect on a typical photon path.

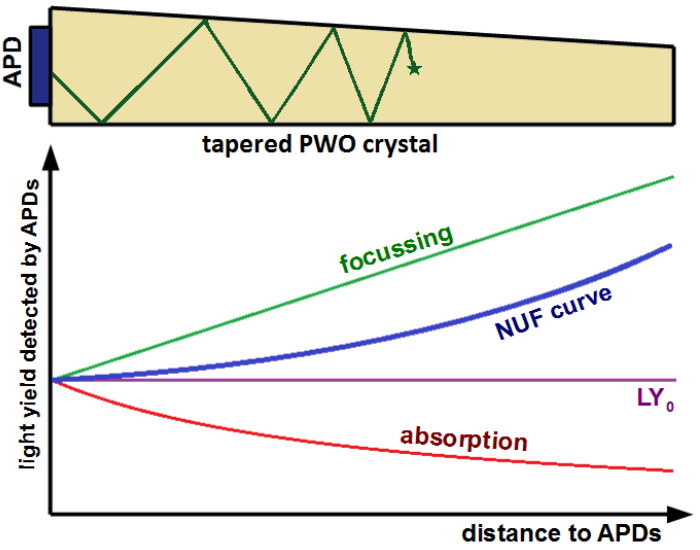

Figure 4.1: Effects contributing to the light collection non-uniformity in tapered PWO crystals. The combination of the focusing effect (green) and the absorption (red) leads to the non-uniformity curve in light collection (blue). The purple curve shows the light yield (LY_0) which would be measured under the absence of all influencing effects. General concept taken from [BRQ05]. The green line in the crystal illustrates the decrease of the incident photon angle relative to the rear face of the crystal due to the focusing effect of the tapered side face.

Since the absorption of the scintillation light is comparable for all crystal types, the slope of the non-uniformity curve mainly depends on the focusing effect. Due to this dependence, also the non-uniformity curve varies with the crystal type and shows the highest slope for the most tapered type 1 crystals, while it decreases gradually for less tapered crystals (type 2 - 11). For the only very slightly tapered crystals of the forward end-cap, a nearly flat non-uniformity curve is observed [DAB13]. The existence of the non-uniformity in light collection has already been observed by the CMS-ECAL collaboration at LHC [BRQ05], which is also using an electromagnetic calorimeter barrel made of tapered PWO crystals [CMS97]. A more detailed discussion and a mathematical model of the focusing effect and the non-uniformity of the crystals in general can be found in [DAB13] and [BRQ05].

For the crystals of the PANDA barrel EMC, several setups have been tested to measure the non-uniformity [DAB13], [MMa09]. In a first setup a coincidence of cosmic muons, passing a horizontally positioned crystal and two small plastic scintillators positioned above and below the side face of the crystal, has been applied to realize well defined interaction positions of the cosmic muons along the longitudinal crystal axis [DAB13]. To realize a fast non-uniformity measurement, another setup using low energetic gamma sources interacting on the side face of the crystals has been constructed. In case of a ^{22}Na gamma-source, also a coincidence of the two 511 keV gamma rays with a series of small BGO detectors has been tested to perform a simultaneous measurements of several well defined interaction positions [DAB13]. All these measurements showed comparable results for the non-uniformity of a

certain crystal type [DAB13]. A first experiment with an APD based readout of the crystals and a 80 MeV proton beam, interacting on the side face of the crystal, performed at the Accelerator Groningen-Orsay (AGOR) facility at Kernfysisch Versneller Institut Groningen (KVI) Groningen [DAB13], enabled a measurement of the non-uniformity curve of type 1 and type 6 crystals with much higher accuracy. Figure 4.2 compares the non-uniformity curves for type 1 crystals measured with 80 MeV protons interacting on the side face of a crystal with a readout via two $7 \times 14\ mm^2$ large APDs in the final arrangement and the non-uniformity curve measured with 511 keV gamma rays from a ^{22}Na source.

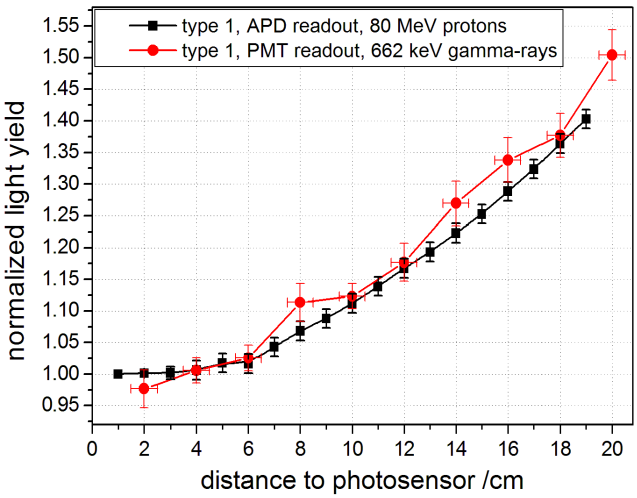

Figure 4.2: Non-uniformity curve of a type 1 crystal with an APD based readout, measured with a 80 MeV proton beam interacting on the side face of the crystal (black points) in comparison to the non-uniformity curve of a type 1 crystal with a PMT based readout, measured with a ^{22}Na gamma source placed in a position defining coincidence setup on the side of the crystal (red points). The curves are normalized relative to each other at a position 4 cm away from the photo-sensor to provide an optimal overlap of the curves within the error bars. Data taken from [DAB13].

The comparison of the two curves shows that the error with low energetic gamma rays is significantly larger than for the measurement with 80 MeV protons. However, if the curves are normalized to each other at a distance to the photo-senor of 4 cm, a good agreement of the average slope can be observed within the error bars (see also [DAB13]).

For the experimental test of the influence of the non-uniformity in light collection on the energy resolution, the section of PROTO 120 with type 2 crystals is used. Since the non-uniformity of these crystals has not been characterized experimentally so far, it has been measured for several samples with a ^{137}Cs source positioned on the side face of the crystals with PMT readout. Figure 4.3 shows the obtained non-uniformity curves for four typical samples. After the normalization, all curves show approximately the same behavior within the error bars. Figure 4.4 compares the resulting average non-uniformity curve of a type 2 crystal to the curves for a type 1 and a type 6 crystal measured with 80 MeV protons in [DAB13]. Since the curves for type 1 and type 6 crystals show comparable values for a distance of less than 5 cm to the photo-sensor, the curve for type 2 crystals is normalized to the other curves in this region and the value at a distance of 1 cm is assumed as the reference point.

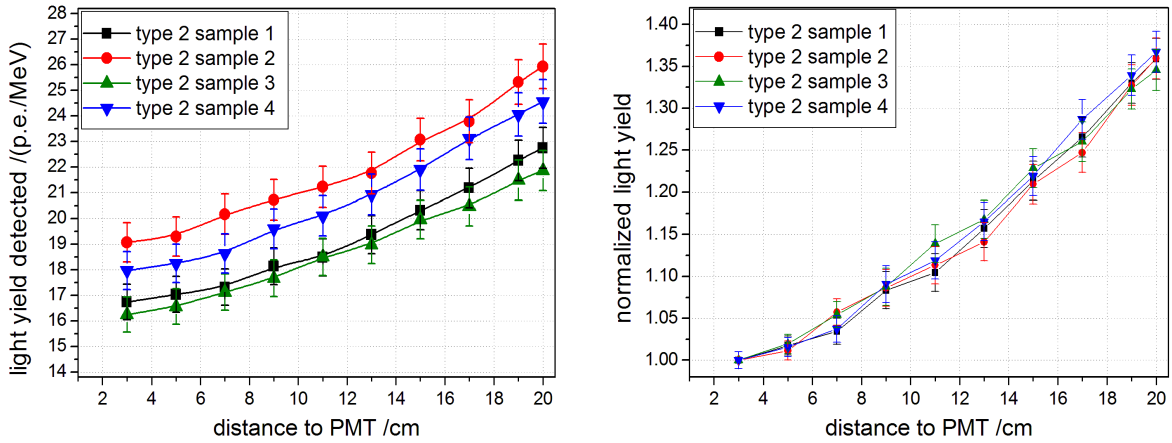

Figure 4.3: Left: Light yield non-uniformity curve of type 2 crystals, measured with a photomultiplier tube with bi-alkali photo-cathode at +18°C. The crystals were wrapped with mirror reflective VM2000 foil. Right: Non-uniformity curves normalized at a distance of 3 cm to the photo-sensor.

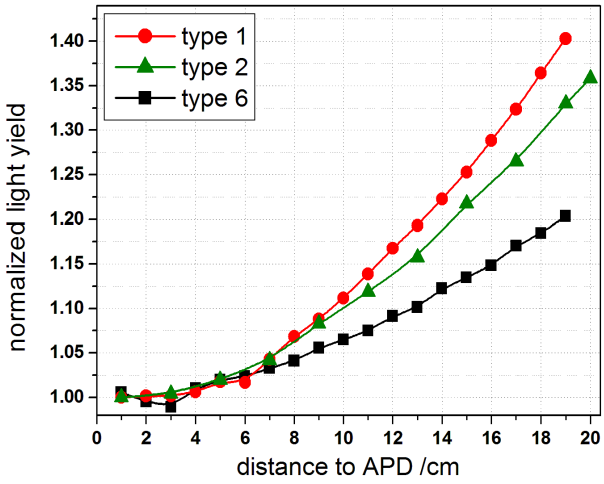

Figure 4.4: Non-uniformity curves, measured for a type 1, type 2 and type 6 crystal. The curves of type 1 and type 6 were measured with an APD based readout and a 80 MeV photon beam interacting on the side face of the crystal. The curve for type 2 represents the average of figure 4.3. It is normalized to the other two curves at a distance of 4 cm to the photo-sensor. The data for type 1 and type 6 has been taken from [DAB13].

The non-uniformity curves shown in figure 4.4 can be parametrized with a second order polynomial function. The results of the fit are given in the following equations for a type 1, type 2 and type 6 crystal, respectively.

$$NUF_{\text{type 1}}(z) = 1.0 - 9.72 \cdot 10^{-4} \cdot z + 1.19 \cdot 10^{-3} \cdot z^2 \tag{4.1}$$

$$NUF_{\text{type 2}}(z) = 1.0 + 1.08 \cdot 10^{-3} \cdot z + 8.58 \cdot 10^{-4} \cdot z^2 \tag{4.2}$$

$$NUF_{\text{type 6}}(z) = 1.0 + 1.29 \cdot 10^{-3} \cdot z + 5.10 \cdot 10^{-4} \cdot z^2 \tag{4.3}$$

The average slope of the non-uniformity has been calculated by:

$$\Delta NUF(x) = \frac{2 \cdot (NUF(x + (X_0/2)) - NUF(x - (X_0/2))}{NUF(x + (X_0/2) + NUF(x - (X_0/2)} \tag{4.4}$$

The position dependence of the calculated values for the different crystal types in the region more than 6 cm away from the photo-sensor can be approximated by the following linear functions:

$$\Delta NUF_{\text{type 1}} = 1.57 \ \frac{\%}{X_0} + 0.05 \ \frac{\%}{X_0 \cdot cm} \ \cdot \ x \tag{4.5}$$

$$\Delta NUF_{\text{type 2}} = 1.04 \ \frac{\%}{X_0} + 0.057 \ \frac{\%}{X_0 \cdot cm} \ \cdot \ x \tag{4.6}$$

$$\Delta NUF_{\text{type 6}} = 0.31 \ \frac{\%}{X_0} + 0.06 \ \frac{\%}{X_0 \cdot cm} \ \cdot \ x \tag{4.7}$$

For a type 2 crystal, this parametrization leads to a slope of 2.2 $\%/X_0$ in the front part and to an average slope in the front half of the crystal of 1.9 $\%/X_0$.

4.1.1 Reduction of the non-uniformity in light collection

The non-uniformity in light collection introduces in principle two effects. On the one hand the light yield from the front part of the crystal is increased by up to 45 % for the most tapered PANDA EMC crystals, which is of great advantage for the photon statistics at low energies. On the other hand, the non-uniformity causes a smearing of the energy response due to the spread of the electromagnetic shower and its fluctuations within the crystal, resulting in a significant deterioration of the constant term of the parametrization of the energy resolution. This effect is especially dominant for higher energies above a few hundred MeV due to the increasing shower dimensions in this energy region and due to the reduced impact of light yield statistics and electronic noise on the energy resolution at higher energies.

This deterioration of the energy resolution by the non-uniformity of the energy response and methods for the reduction of the non-uniformity have already been studied by the CMS-ECAL collaboration [ACL02, ABB98, PA07]. For the CMS ECAL which primarily detects high energetic electromagnetic probes, a reduction of the non-uniformity was an essential task to achieve the resolution requirements of the barrel EMC, since the constant term dominates the energy resolution in the important energy range above several GeV [ABB98]. On the other hand, due to the low energetic threshold of more than 200 MeV [FT14] used for the CMS-ECAL, photon statistics plays only a role for the lowest energies and can be nearly completely neglected at several tens of GeV and for even higher energies. Due to this considerations, the CMS-ECAL collaboration decided to equalize the light yield detected by the APD by a de-polishing of the most tapered side face of the crystals, which provided excellent results for the constant term of the energy resolution [ABB98, PA07].

The PANDA barrel EMC has to detect electromagnetic probes in a much lower energy range, starting at 10 MeV up to only a few hundred MeV or a few GeV, depending on the position of the crystals within the barrel. In this energy range, the photon statistics plays an essential role, especially for energies below 100 MeV. Therefore, a de-polishing of a crystal side face like for the CMS crystals has not been considered initially, due to the expected overall reduction

of the light yield. However, compared to CMS crystals, PANDA crystals show a higher degree of tapering and have a slightly shorter length, leading to a steeper non-uniformity curve with a slope in the front part of the crystals of typically 2.2 $\%/X_0$ for type 2 crystals and up to 2.6 $\%/X_0$ for the most tapered crystals (type 1). For comparison, CMS crystals show a typical slope of 1.5 $\%/X_0$ in the front part [ACL02]. Since this high slope of the non-uniformity curve also introduces strong smearing effects at lower energies down to the threshold, an investigation has been started to study experimentally the effect of a reduced non-uniformity on the energy resolution.

For PANDA crystals already in [DAB13], [OLu11] and [SGr08] several methods have been investigated to reduce the non-uniformity. However, the de-polishing of the crystals applied by the CMS-ECAL collaboration [ACL02] showed the most promising results, since it reduces the non-uniformity in the front part of the crystal, but keeps the light yield from the rear part at a comparable level [ACL02]. To determine the optimal roughness of the de-polished side face, the correlation between the average roughness R_a of the de-polished side face and the slope of the non-uniformity curve of CMS crystals, which is shown in figure 4.5, has been used.

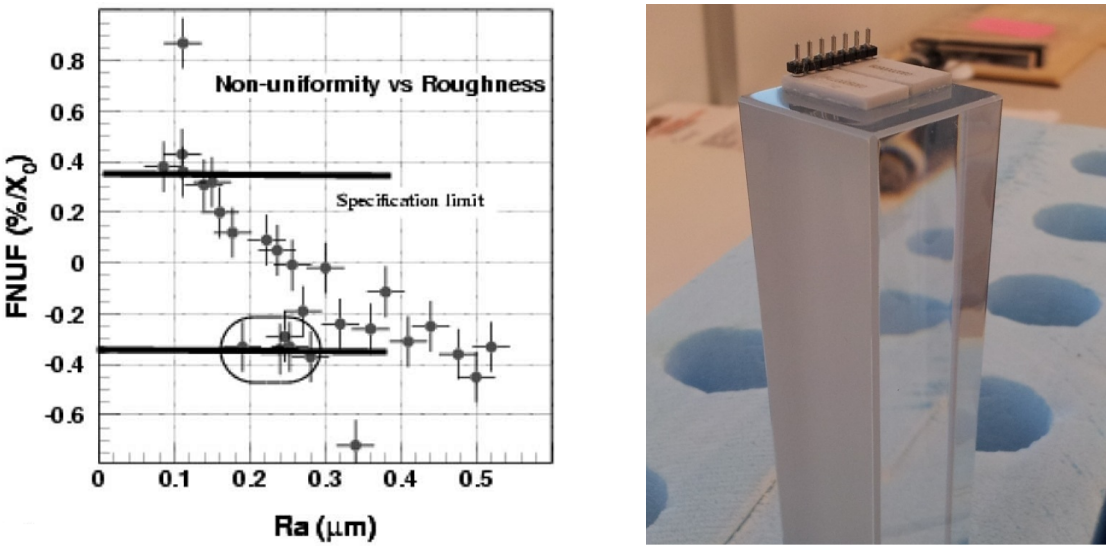

Figure 4.5: Left: Correlation between the slope of the non-uniformity curve (FNUF) and the roughness of the de-polished side face (R_a) of CMS crystals. Figure taken from [ACL02]. Right: Picture of the rear part of a crystal with a de-polished side face with the LAAPDs glued to the end face of the crystal.

Taking the higher slope of the non-uniformity in light-collection of type 2 PANDA crystals compared to a typical CMS crystal into account, an average surface roughness R_a of 0.3 μm has been selected for a de-polishing test. For a first test experiment with a 3 $\times$ 3 array of crystals implemented in PROTO 120, the most tapered side face of nine type 2 crystals has been de-polished in a similar manner like the CMS crystals. For the de-polishing the crystal is first leaped on a resin wheel with 15 μm diamond grain. After this it is polished on a hard fabric wheel with the same diamond grain for 10-20 min [ACL02]. In this process, the average roughness is directly proportional to the polishing time [ACL02]. A complete description of the procedure has been published by Auffray et. al in [ACL02]. Figure 4.5 (right) shows a

picture of the rear part of such a de-polished crystal. After the successful test of this first array, a second set of twelve type 2 and six type 3 crystals has been de-polished to implement a 5 × 5 array of de-polished crystals within PROTO 120.

To investigate the change of the light yield after the de-polishing procedure, the position dependent light yield of six type 2 and six type 3 crystals has been measured with a 662 keV ^{137}Cs source positioned at different interaction points on the side face of the crystal before and after the de-polishing. To avoid systematic errors, exactly the same setup with the same PMT has been used for the measurement. All measurements have been performed in a temperature stabilized environment at +18°C with an integration windows of the charge to digital converter of 100 ns. The crystals were wrapped with eight layers of reflective white teflon (PTFE) tape and an outer layer of aluminum foil. For the coupling of the crystals rear face to the PMT, optical grease is used. Figure 4.6 shows the obtained position dependent light yield, as well as the normalized light yield, relative to the first point and the change of the light yield for the different samples of type 2 and type 3 crystals before and after the de-polishing procedure.

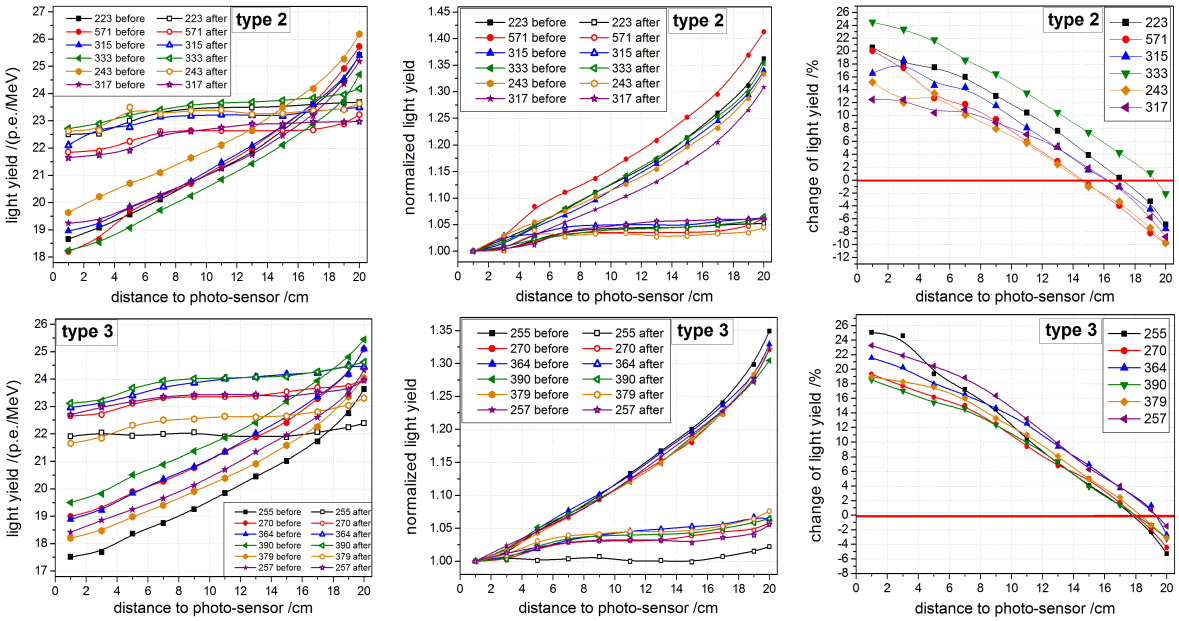

Figure 4.6: Left: Position dependent light yield before and after the de-polishing procedure. Middle: Normalized light yield before and after the de-polishing procedure. Right: Position dependent change of the light yield. The upper row shows the results for six samples of type 2 crystals, while the lower row presents the results for type 3 crystals. The error of the light yield measurements is typically in the order of ± 0.5 photo-electrons.

The measured light yield shows that the de-polishing of one lateral side face of the crystals to $R_a = 0.3$ μm increases the light yield in the rear part of the crystals, close to the photo-sensor, by approximately 20 % while a slight decrease of the light yield of typically 2 % to 10 % can be observed in the front part of the crystals for both types. Since the measurements have been performed with the same setup under controlled conditions and since the typical measurement error of the light yield measurement is in the order of ± 0.5 photo-electrons, this changes are significant and cannot be related to an uncertainty of the measurement method.

A more detailed explanation of the observed effects based on GEANT4 simulations can be found in section 4.3.4.

The normalized light yield shows a ratio between the front and the rear part of the crystals of typically 1.35 for polished type 2 crystals and 1.32 for polished type 3 samples. After the de-polishing procedure this non-uniformity is significantly reduced to values of less than 5 % for all samples of both investigated crystal types. Especially the nearly uniform repose for distances to the photo-sensor between 7 cm and 20 cm has to be noted. Since in the envisaged energy regime of the PANDA barrel EMC, the main part of the energy deposition within the electromagnetic shower will take place in this region, the de-polishing proves a nearly ideal result.

4.2 Energy resolution of a 3 × 3 sub-array of PROTO120 with de-polished crystals

To investigate the influence of the reduced non-uniformity of the de-polished crystals on the energy resolution, a 3 × 3 array of these crystals has been implemented in a corner of the type 2 section of PROTO120. Unfortunately one crystal was damaged during the preparation process. Therefore, one corner of the array contains a normal polished crystal. For comparison another 3 × 3 array with polished crystals directly below the other one has been used. Figure 4.7 shows the arrangement of the de-polished crystals and the position of the two arrays within the type 2 section of PROTO 120. During the beam test the upper 4 × 3 array, which contains the de-polished crystals and the lower 4 × 4 array containing the polished crystals were read out separately due to a limited number of available ADC channels. The numbers in brackets indicate the numbers of the readout channels. Like described in section 2.3 each crystal is equipped with two APDs with independent sub channels in the ASIC and an independent high voltage supply. The ASIC finally provides two output channels for each APD with a low gain and a high gain branch. The high gain was set to an amplification of 16 relative to the low gain. In each event, the complete traces of all four branches have been recorded for all crystals of the array. Sub-branches of single crystals which were out of function during the beam-time due to defect cables or problems with the ASIC programming are also noted in figure 4.7. The described setup has been tested during the beam-time from 10.04.2015 to 13.04.2015 at the A2 hall of the MAMI accelerator in Mainz. An energy marked photon beam with 16 equally distributed energies between 56.4 MeV and 766.8 MeV has been provided by the Glasgow-Mainz Bremsstrahlungs-Tagger.

The following section will show the optimization of the energy resolution of the 3 × 3 array of de-polished crystals by an optimization of the feature extraction, the calibration and the noise suppression. Based on this optimization, the energy sum of the 3 × 3 array will be determined and compared to a 3 × 3 array of polished crystals, analyzed in the same optimized manner.

4.2.1 Tagger-, veto- and trigger- conditions

A scheme and a detailed description of the readout electronics which have been used for the PROTO 120 beam-test can be found in section 2.3.2. During the measurements with the photon beam, a coincidence between a logic OR of the 16 selected tagger channels and the

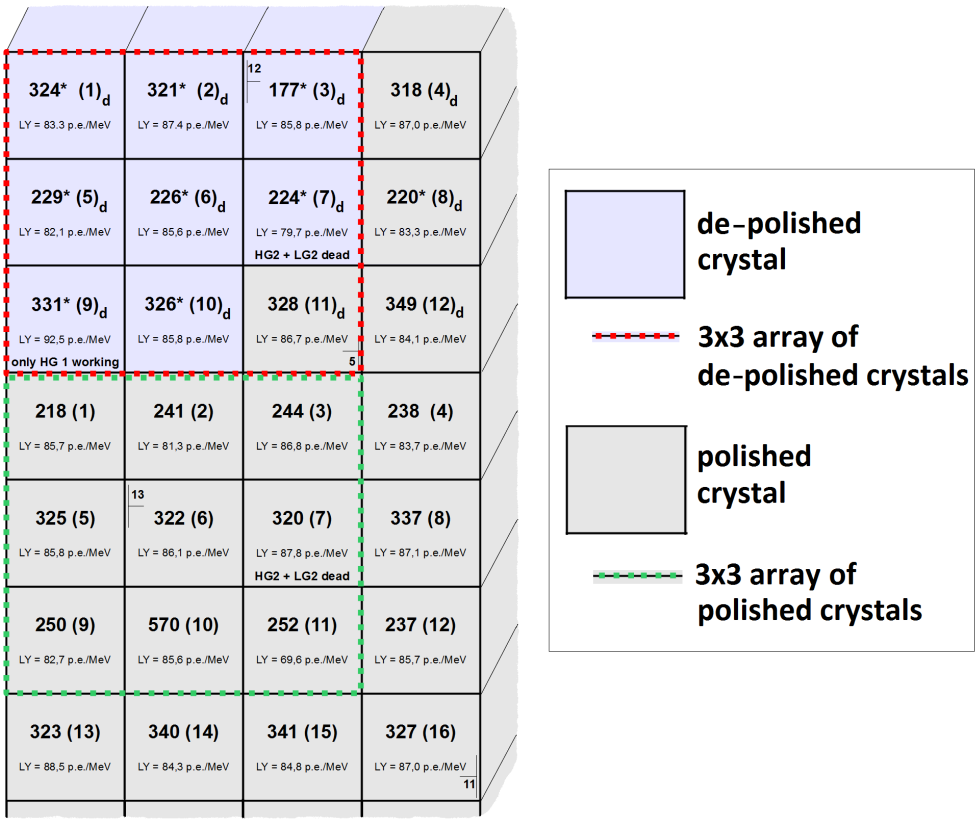

Figure 4.7: Arrangement of the two arrays with polished and de-polished crystals within the type two section of PROTO 120. The 3 × 3 arrays of de-polished and polished crystals are marked with a red and a green dotted line, respectively. The array of de-polished crystals contains one polished sample in the lower corner. For each crystal the crystal ID is shown. The numbers in brackets indicate the number of the readout channel. Since two different readout sections were used, the numbers of the first section are market with a "d" for de-polished in the subscript. The rectangles in some crystals show the position and the number of the temperature sensors.

crystal which was hit by the beam was adjusted and used as a trigger. Since the lowest selected photon beam energy is 56 MeV, the trigger threshold could be set to approximately 10 - 15 MeV, which is well above the electronic noise level. All other channels are read out in a common mode. To identify random coincidences, the time spectra of the 16 tagger channels have been recorded with a TDC to reduce random events offline. In addition, the multiplicity of the 16 selected tagger channels is calculated in the analysis software to identify and to reject events in which two tagger channels are responding at the same time. Figure 4.8 (left) shows the distribution of the amount of channels within the selected 16 which are responding at the same time. The distribution of the tagger multiplicity shows that in most of the events only one tagger channel is responding, while the response of two tagger channels at the same time is suppressed by three orders of magnitude. For the offline data analysis only events were exactly one tagger channel responds will be accepted. Nevertheless, the possibility that two photons hit the detector at the same time still exists, since the photon beam which interacts with the prototype contains all possible photon energies and the rejection criterion can only be set for the selected sixteen channels.

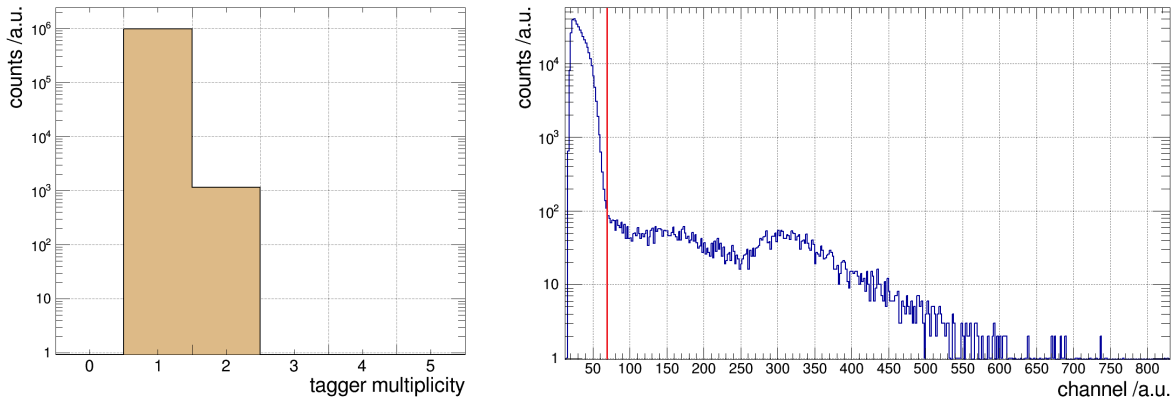

Figure 4.8: Multiplicity distribution of the 16 selected tagger channels after the rejection of random coincidences by a time cut (left) and response of the plastic scintillator paddle, which was placed in front of the prototype as a VETO detector (right). The red line marks the cut between the electronic noise and the events in which the paddle has responded.

To reject charged particles created by photon conversions in air due to the long distance between tagger and prototype, a plastic scintillator paddle has been mounted in front of the prototype. Figure 4.8 (right) shows the response of this paddle, which has been read out in each event. The paddle only responds, if it is crossed by a charged particle or if a photon is converted inside the paddle. Therefore, such events can be rejected by requiring that the response of the paddle is within the electronic noise level, which can be observed in the first 70 channels of figure 4.8 (right). For the analysis only events with a response of the paddle below the red line have been accepted, leading to a rejection rate of less than 1 %.

For the measurement of cosmic muons the plastic paddle has been placed on top of the prototype and used as trigger for the readout. In this case it is required that the paddle shows a response above the electronic noise level, introduced by a passing cosmic muon.

4.2.2 Feature extraction

During the beam-time, the complete traces of all signals have been recorded. Therefore, the method for the extraction of the energy information can be optimized offline based on this data. Selected traces for different photon beam energies between 56 MeV and 743 MeV recorded in the central PWO crystal can be found in figure 4.9. The readout is set to create negative pulses. A closer look on this traces shows that the length of the signal is increasing for an increase of the incident photon energy since the falling tail of small signals disappears within the electronic noise much earlier. In addition, the leading edge trigger implemented in the sampling ADCs causes a walk of the position of the maximum of the pulse. Figure 4.10 illustrates the energy/amplitude dependence of this two effects. The left part of the figure shows the length of the pulse, starting at the point where the baseline is exceeded by the pulse and ending at the point, where the baseline is reached again. Due to the threshold, introduced by the electronic noise which exceeds the signal at some point of the falling tail, the signal length is significantly reduced for low energies. For the highest energy depositions, the signal length stays nearly constant at a level of $\sim$ 154 channels, since the impact of noise is significantly lower.

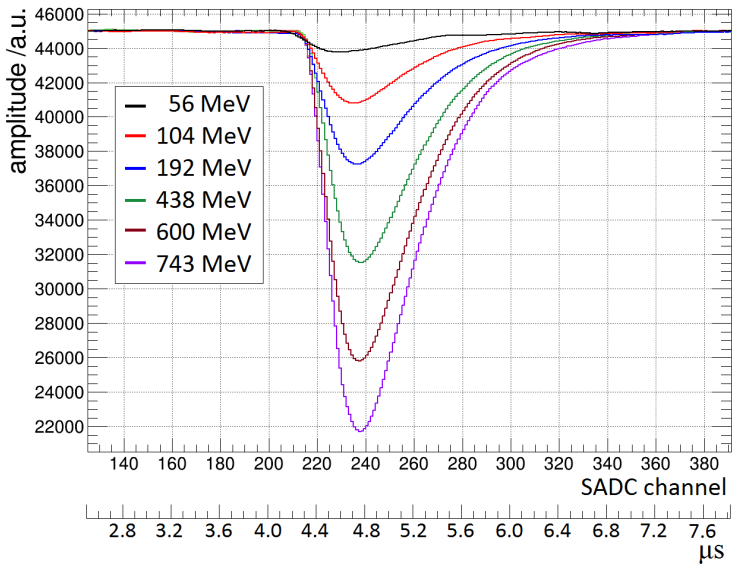

Figure 4.9: Signal traces from a single high gain ASIC channel recorded with a 50 MHz sampling ADC for selected photon energies between 56 MeV and 743 MeV.

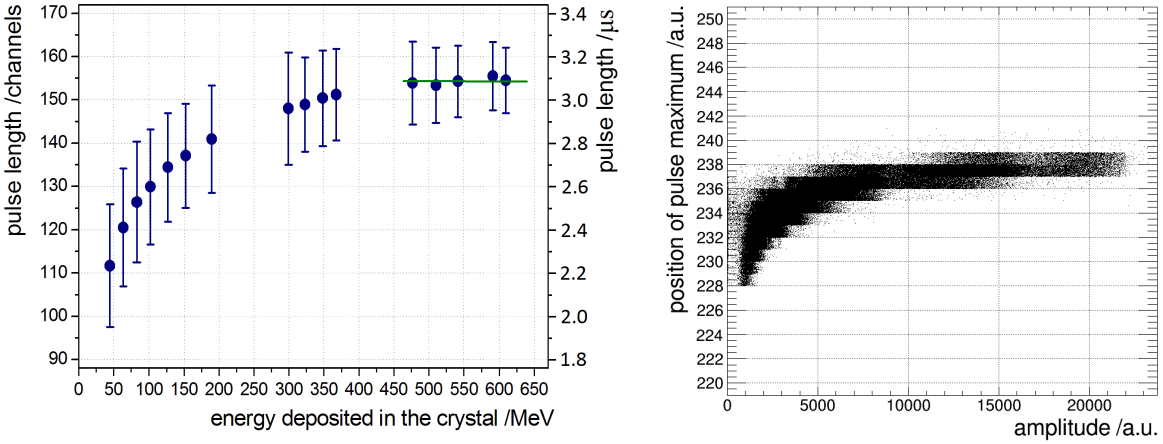

Figure 4.10: Energy dependence of the average pulse length (left) and dependence of the position of the pulse maximum in the triggering detector from the amplitude (right).

The right part of figure 4.10 shows that the absolute position of the pulse maximum varies by around 10 channels (200 ns), depending on the signal amplitudes in the central crystal, since the trigger is set on the leading edge which causes a walk of the signal position. However, for the test experiment the trigger was created commonly by the central crystal. Due to this common readout, the signals of all channels generated by the same event appear at the same position.

Based on this basic observations different feature extraction methods like a peak sensing extraction, an integration of the pulse or a fit of the pulse shape can be applied and will be compared in this section.

Peak sensing feature extraction

The fastest feature extraction method is given by a peak sensing extraction, which works in principle like a peak sensing ADC. In a first step, the pedestal, describing the level of the baseline without any signal, is calculated by averaging the first 130 channels (2.6 μs) of the trace before the signal. To guarantee that no other signals are appearing in this range, the same procedure is repeated for the 100 channels (2.0 μs) following the signal and the obtained values are compared. Figure 4.11 (left) shows a typical signal trace with the two pedestal regions marked in red and purple, respectively. The right part of figure 4.11 shows a detailed view on a typical baseline before the signal, with the averaging range marked in red.

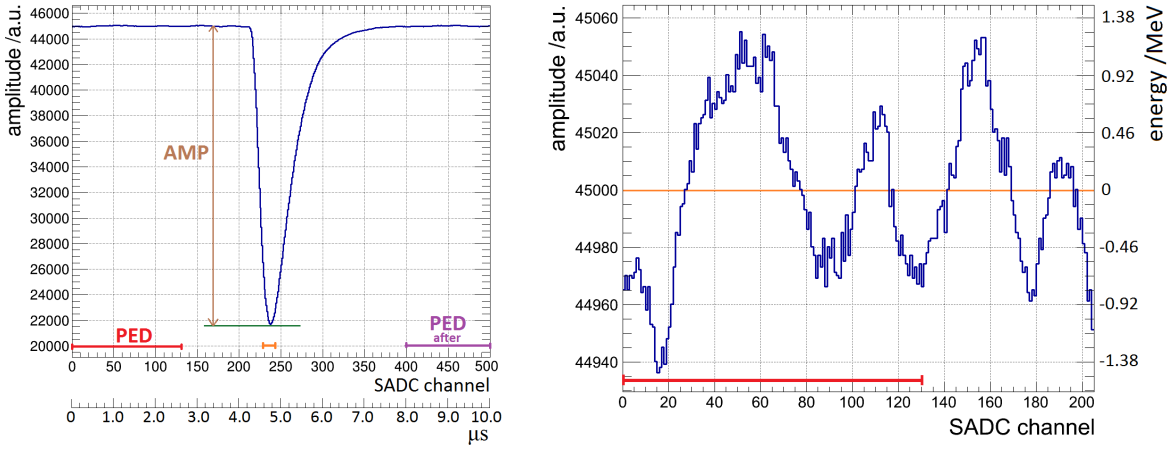

Figure 4.11: Intervals for the signal and pedestal extraction (left) and picture of a typical baseline before the signal (right). The red and the purple line illustrate the region, in which the pedestal is extracted before and after the signal. The signal is searched in the region marked by the orange line.

After the extraction of the pedestal, the minimum of the trace is searched within a window of (120 - 200) ns, depending on the photon energy. In addition, the outer crystals have to fulfill a time-correlation cut, which will be discussed in section 4.2.6. The energy information is extracted for each channel as the difference between the pedestal and the minimum of the trace:

$$\mathrm{E} = \mathrm{pedestal} \; - \; \mathrm{minimum} \tag{4.8}$$

Integral of the signal trace

Another method for the extraction of the energy information is the integration of the signal trace, exploiting the fact that the area of the shaped signal still scales with the deposited energy corresponding to the decay time of the scintillator. Also for this method, the pedestal is calculated in a first step. Based on this value, the difference between the pedestal and the bin value is summed up for a given range of SADC trace bins according to equation 4.9.

$$E = \sum_{\mathrm{i}=\mathrm{bin}_{min}}^{\mathrm{bin}_{max}} (\mathrm{pedestal} - \mathrm{bin\_value[i]}) \tag{4.9}$$

For the considered range of the integral different methods have been compared to optimize the energy resolution and the applicable threshold.

As a first step, a fixed range of 300 SADC channels (6.0 μs), starting before the signal and covering the complete signal range (channel 150 - 450 (see figure 4.11)) has been used. The range is chosen significantly longer than the signal length, since it is assumed that the cancellation of the noise fluctuations below and above the baseline improves for a longer range. However, due to the characteristics of the noise fluctuations from the ASIC which can be observed in the right part of figure 4.11 a significantly longer integration range may be necessary to fulfill this assumption. Therefore, also an integration of the complete recorded range of 500 SADC channels has been investigated.

As a second method, a combination of the peak sensing feature extraction and the integration is used. In that case the minimum of the trace is searched with the method described for the peak sensing feature extraction. Based on this minimum, the integral is calculated for an increasing region of bins ($\pm$ 1, $\pm$ 2, ... , $\pm$ 20) around the minimum to find the optimal integration range.

As a third method, an integration of the complete signal is implemented. For this purpose, the length of the signal has been determined by starting at the minimum of the trace and searching the points at which the baseline minus a fixed threshold is reached for the first time in both directions. Since the minimum of the trace has been determined by the peak sensing feature extraction, a threshold less or equal the value applied for this method has to be used. The two determined points can then be used as the start and end point of the integration. The aim of this approach is, to integrate only the signal itself and no surrounding noise. Nevertheless, electronic noise fluctuations will influence the integration length, especially for a threshold below the noise level.

Fit of the recorded signal shape

As a third method, a theoretical function can be fitted to the recorded signal trace. According to [IVV04] and [MK15] the shaped APD signal can be described mathematically by

$$A(t) = A \cdot e^{-N \cdot \frac{(t-t_0)}{\tau}} \cdot \left(\frac{t-t_0}{\tau}\right)^N \tag{4.10}$$

with the starting point of the rising signal edge t_0, the time constant τ and the parameter N, which describes the behavior of the rising signal edge. Due to the normalization of the pulse-shape, the amplitude A_0 is given by

$$A = A_0 \cdot e^N \tag{4.11}$$

Figure 4.12 shows several examples for a fit of this function to the signal trace for the high and low gain output and different signal heights. To reduce the influence of the electronic noise, a fit range similar to [IVV04], which covers only approximately the upper half of the signal has been selected. The fitted trace in figure 4.12 illustrates that the signal shape can be completely described by the theoretical function in the selected range. Especially for small signals, the fit nicely averages the statistics of the signal bins around the maximum. However, for even lower signals close to the threshold the low frequent oscillation which can

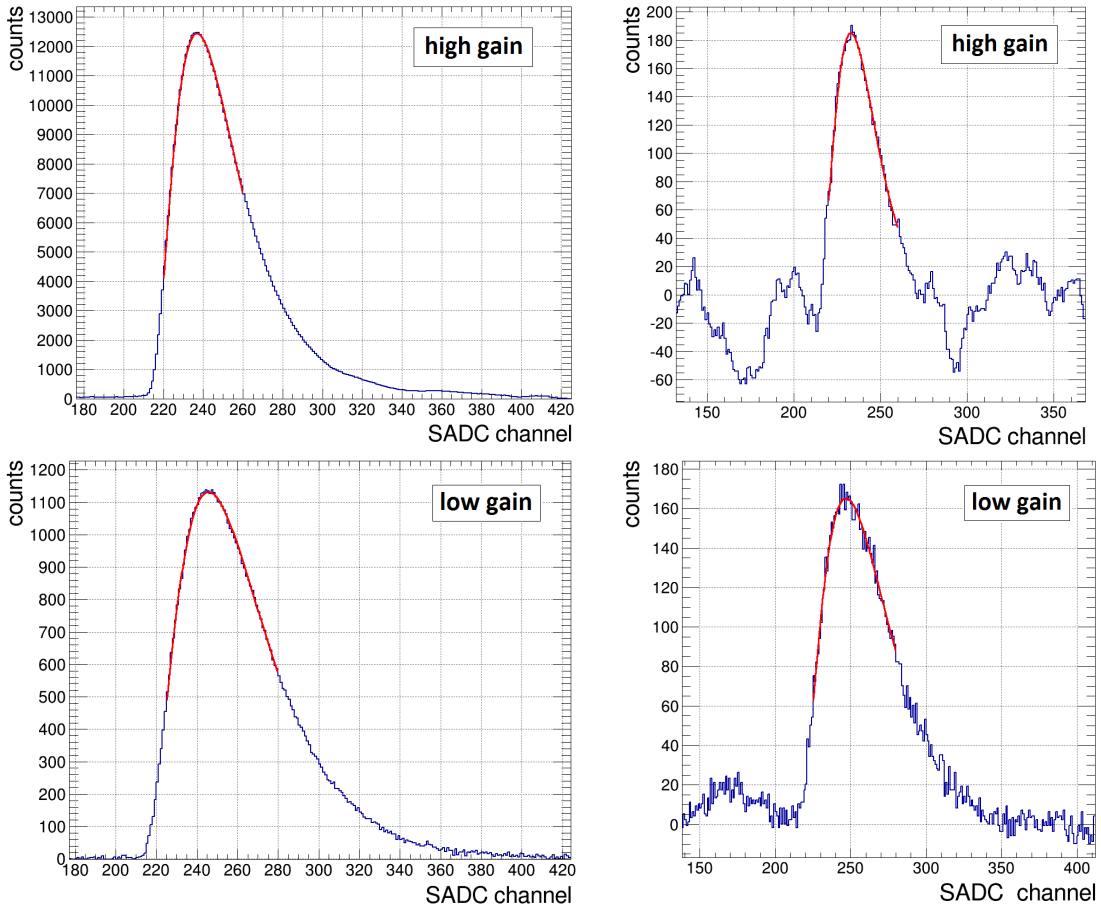

Figure 4.12: Fit of the recorded signal trace for the high (upper row) and low (lower row) gain output of the ASIC. In both cases a fit for a high signal (left) an a relatively small signal (right) are shown. Before the fit procedure, all traces are inverted and the baseline is shifted to zero.

be especially seen in the upper right signal of figure 4.12 can have a dominant influence on the fit quality. To reduce this influence for low signals, the fact can be used that N and τ are defined by the signal shaping and show approximately the same value for all crystals. They only differ between the high- and low- gain branch due to the different amplification and shaping. Therefore, they have been filled in a histogram for signals significantly larger than the noise level. Based on this results, the parameter range has been set to the most probable value of the relative narrow distributions. To compensate binning effects of the recorded signal trace and differences of the electronics, a small variation of the values has been allowed.

The obtained parameter values, which have been used for the fit are:

$$\tau_{HG} = (22.3 \pm 0.1)\ ch = (446 \pm 2)\ ns\ , \qquad N_{HG} = 1.79 \pm 0.01 \tag{4.12}$$

$$\tau_{LG} = (30.3 \pm 0.1)\ ch = (606 \pm 2)\ ns\ , \qquad N_{LG} = 1.83 \pm 0.01 \tag{4.13}$$

The start position of the pulse shape, described by the parameter t_0 has been limited to a range between channel 200 and 240 to take the variation of the pulse position for low amplitudes,

shown in figure 4.10 into account. For the amplitude parameter A_0 only a positive value is required, since the traces which have been prepared for the fit are inverted compared to the original traces.

4.2.3 Response of a single crystal and performance of the ASIC

As a basis for the calculation of the energy sum of larger crystal arrays, the response of a single crystal with a photon beam interacting in the center of the front face of the crystal will be treated. For this purpose a calibration run has been performed with the photon beam interacting in the center of the front face of all crystals within the de-polished array. Based on the data of this run a relative calibration of the two APD and ASIC channels of each crystal and a characterization of the ASIC amplification will be performed.

Relative calibration of the two APDs

Based on a study of the optimal gain of a PANDA LAAPD in [MM13], it has been decided to use a gain of 150 for all APDs of the prototype. Relying on the data from the screening of the APD characteristics [AW14], the two APDs of each crystal have been matched in a way that the bias voltage for a gain of 150 does not differ by more than 0.5 V, corresponding to a gain variation of less than ± 3.5 % if the same average voltage is applied for both APDs.

Due to this gain variation, due to differences in the quality of the gluing of the APDs and due to the statistical variation of the ASIC amplification, the output signals of the two APDs are not identical. Therefore, a relative calibration has to be performed. For this purpose the correlation between the high gain (HG) output of APD 1 and APD 2, overlapped for all tagger channels is used. By applying a slice fit to this correlation shown in figure 4.13 (upper row, left) and finally a linear fit to the results from the slice fit (upper row, right), a correlation coefficient c_{APD} can be obtained, which is used as the relative calibration coefficient of the two APDs.

$$HG_2 = c_{APD} \cdot HG_1 \tag{4.14}$$

Based on this coefficient the mean value of the two APDs is calculated for each crystal:

$$HG_{sum-avg} = (HG_2 + c_{APD} \cdot HG_1)/2 \tag{4.15}$$

The same procedure is repeated for the low gain (LG) output of the APD (figure 4.13, lower row). The correlation for the high gain shows that the response is completely linear up to approximately 24000 ADC channels, which corresponds to an energy of approximately 550 MeV. After this value the high gain output of the ASIC starts to show saturation effects. Due to this saturation, the low gain output, which shows a completely linear response over the entire energy range, has to be used for signals with an amplitude higher than 24000 channels.

The obtained calibration coefficients for both gains are compared in figure 4.14. The figure shows, as expected that most of the coefficients are close to one. Only in two cases, a deviation of more than 30 % can be observed (green circles). For crystal 11 this deviation can be explained by a saturation of the high gain output for energies above 70 MeV due to a programming problem with the ASIC. Since this crystal is in the outer ring of the

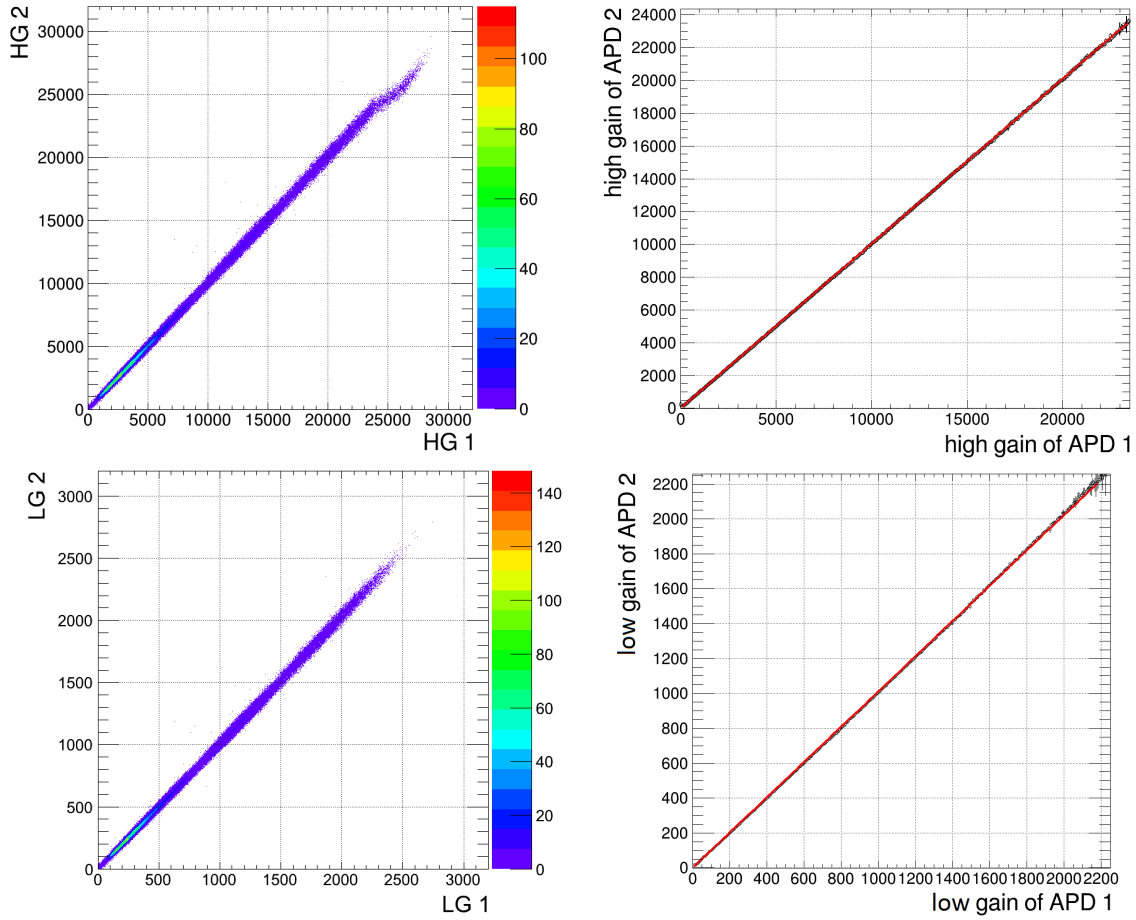

Figure 4.13: Correlation between the output of the two APDs of one crystal for the high gain (upper row) and the low gain (lower row). The right pictures show a linear fit trough the mean values of the slice fit applied to the correlations shown in the left pictures.

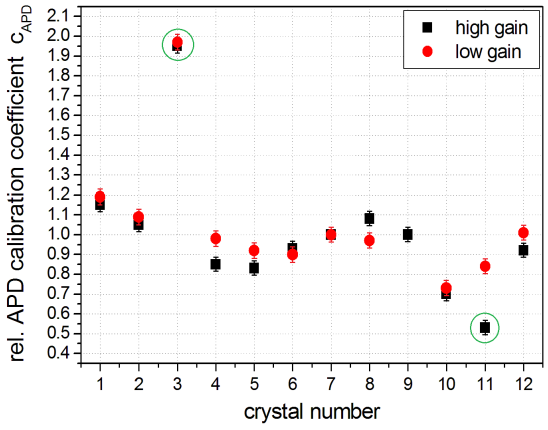

Figure 4.14: Distribution of the relative APD calibration coefficients for the high and low gain output of the de-polished crystal array. Crystals which show an irregular behavior are marked with a green circle. The error range is represented by the size of the dots.

3 × 3 array, it will never detect energies above this value if the photon beam interacts in the center of the 3 × 3 array. For crystal 3 one APD showed only half of the signal amplitude compared to the other APD, which can be caused by a defect of the ASIC or by an imperfect optical coupling of the APD. Nevertheless, the obtained signals from this crystal show no abnormalities. Excluding these channels, the calibration coefficients show a mean value of 0.95 ± 0.05 for the high gain and 0.98 ±0.04 for the low gain branch, which are both close to the expectation value of 1.0 for a statistical distribution of the coefficients. The standard deviation around the mean value is approximately 13-14 % for both branches. Since the high and the low gain output are quite good correlated for most of the channels, an effect of the ASIC is unlikely and it has to be assumed that this variation is due to the uncertainty of the voltages used for the APD matching to preset an identical gain.

Pile-up identification

Despite the low rates used for the beam-test, there is a certain probability for pile-up events. To quantify the fraction of such events and to reject them, a pile-up identification and rejection according to [GT13] has been implemented into the analysis. For the identification of pile-up events, the integral over amplitude ratio is plotted as a function of the amplitude. Since the pulses of the high and low gain output have different characteristics it is done separately for the two branches. The result is shown in figure 4.15.

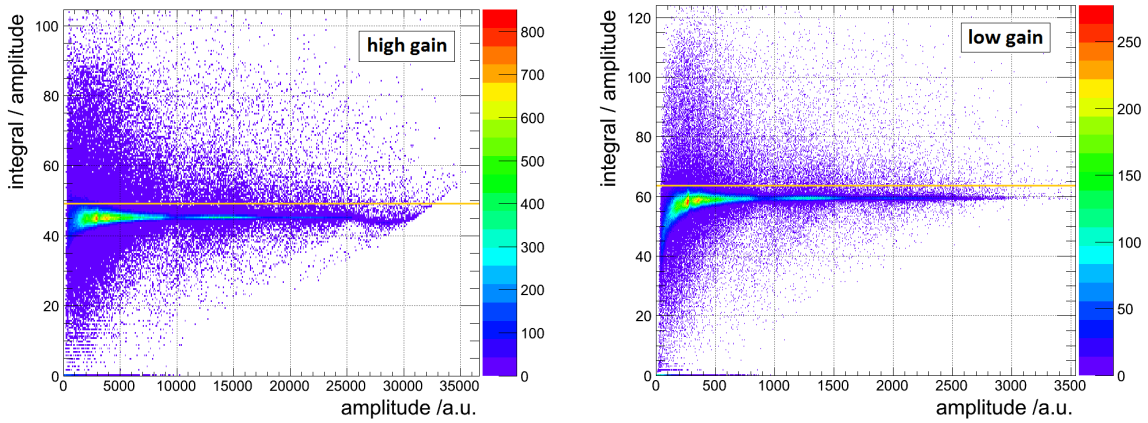

Figure 4.15: Integral over amplitude ratio as a function of the amplitude for the high gain (left) and low gain (right) output of the ASIC. Pile-up events can be expected for a ratio of I/A > 49 for the high gain and I/A > 63 for the low gain branch (indicated by the orange line in the pictures).

For regular pulses, this ratio should stay at the same level for all amplitudes [GT13]. However, for very low amplitudes, the influence of the electronic noise causes a drop and smearing of the ratio, which is especially visible for the low gain in figure 4.15. If a second pulse overlaps the first pulse, the amplitude stays at the same level, but the integral becomes larger. Therefore, the integral over amplitude ratio is higher than expected for pile-up events [GT13]. The plots in figure 4.15 show that the integral over amplitude ratio for regular pulses is somewhere around 45 for the high gain and around 59 for the low gain output. Taking the statistical variation of this value into account, pile-up can be expected for a ratio of I/A > 49 for the high gain and I/A > 63 for the low gain output. Therefore, in the analysis all events with

a ratio of the central crystal higher than this values have been rejected. However, the plots show that like expected for the low photon rates, this events represent only a quite small fraction ($\ll 2\%$) of the total events, resulting in a non-significant influence on the energy resolution. Like the correlation of the high gain branch of the two APDs in figure 4.13, also the drop of the integral over amplitude ratio for high gain amplitudes above 25000 channels in figure 4.15 (left) shows that the high gain branch of the ASIC starts to saturate for the highest energies.

Line-shapes for a single crystal

Based on the considerations of the last subsections, the energy distributions of the sum of both APDs have been plotted in figure 4.16 for the high gain output of a single crystal with the Gaussian shaped photon beam ($\sigma = 3.6$ mm) interacting in the center of the crystal.

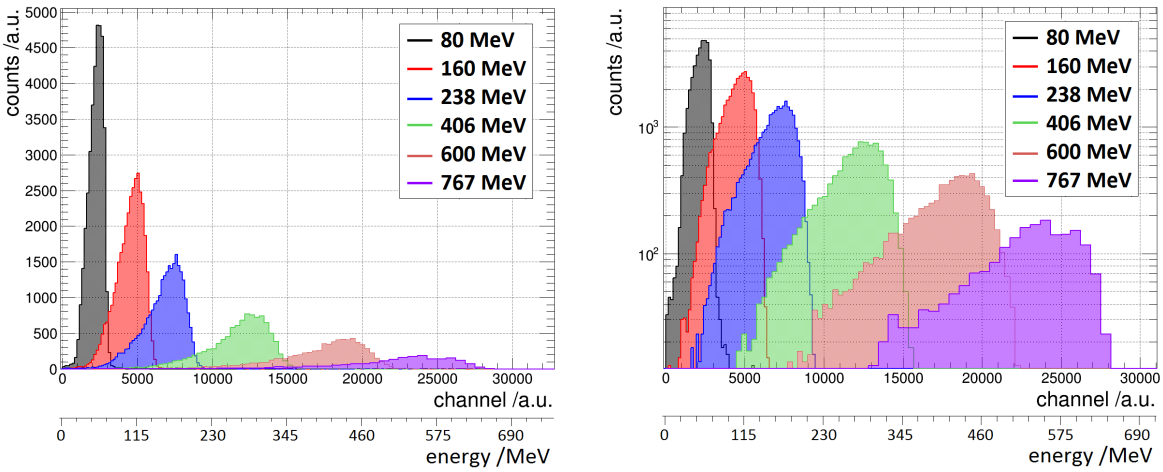

Figure 4.16: Response of a single PWO crystal for a photon beam interacting in the center of the crystal for selected photon energies between 80 MeV and 767 MeV shown on a linear scale (left) and a logarithmic scale (right).

The figure illustrates that due to the small lateral dimension of a single crystal, a lot of energy is lost by the leakage of the electromagnetic shower to the crystals side faces, resulting in dominant tails of the energy distribution towards lower energies. The influence of this effect is even more amplified by the large photon beam spot which covers more than half of the crystal front face and causes a strong variation of the energy leakage due to variations of the non-central interaction positions. To take this tails, which are especially visible in the logarithmic plot of the energy distribution, into account, the distributions have been fitted with a Novosibirsk-function (see equation 3.3) to determine the peak position and the energy resolution.

Comparison of the high- and low- gain branch of the ASIC

To realize the required energy resolution for low energies and a coverage of the complete dynamic range at the same time, the APFEL ASIC provides a high gain and a low gain branch

for each APD channel. For the recent beam-test, the high gain branch has been programmed to an amplification of 16 relative to the low gain branch. Due to this amplification, a better signal to noise ratio, resulting in a better energy resolution, can be expected for low energies.

Since the high gain branch of the central crystal starts to saturate for energies above a certain level of approximately 500-600 MeV, the low gain information has to be used for amplitudes exceeding this level. For this purpose, the relative amplification of the high gain relative to the low gain output has been characterized. This parameter can also be used as a good indication for the variation of the ASICS relative to each other. To determine the amplification, the ratio between the high- and low- gain branch is calculated in each event and filled in a histogram in figure 4.17 (left).

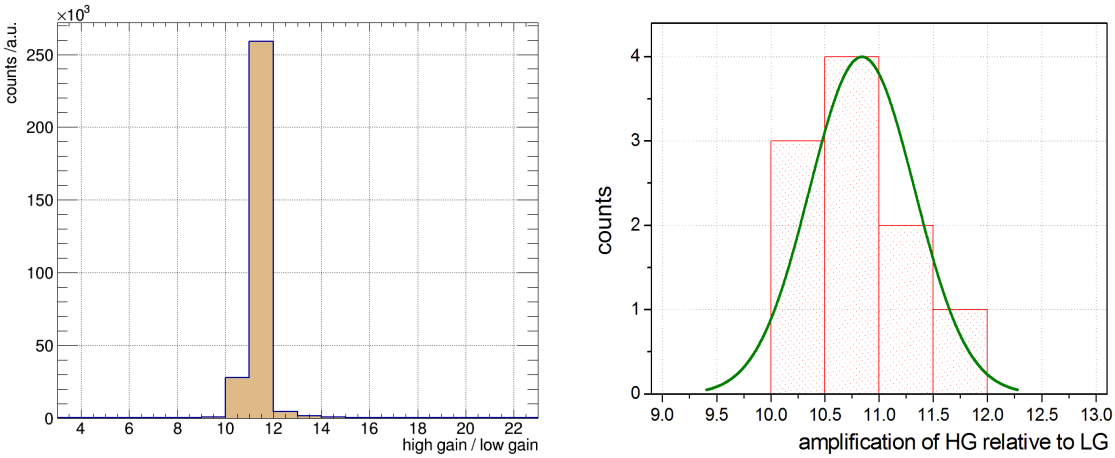

Figure 4.17: Left: Amplification of the high gain output relative to the low gain output for a single ASIC. Right: Histogram of the amplification of all ASICS used for the readout of the de-polished crystal array.

The mean value of the obtained distribution is taken as the amplification of the ASIC. The distribution of these amplifications for all ASICS of the array with de-polished crystals is shown in figure 4.17 (right). It indicates that the used ASICs have an average amplification of 10.8 with a standard deviation of 0.8. Based on this relative calibration values for the two branches, the energy extracted from the low gain branch is scaled up to the level of the high gain branch and used instead of this one, if the energy of a channels exceeds a level of 500 MeV. With the application of this method a linear response over the complete dynamic range can be guaranteed.

Linearity and energy resolution for different feature extractions

As a next step, the linearity and the energy resolution of the central crystal, obtained for the different feature extractions, introduced in section 4.2.2, will be compared. Figure 4.18 shows the obtained normalized amplitudes (left) and the relative energy resolution as a function of the incident photon energy (right) for the different feature extractions. With the combination of the high- and low- gain data all feature extractions provide a good linearity over the complete energy range. The relative energy resolution obtained with the different feature extractions is shown just for completion. Since the central crystal ever detects an energy

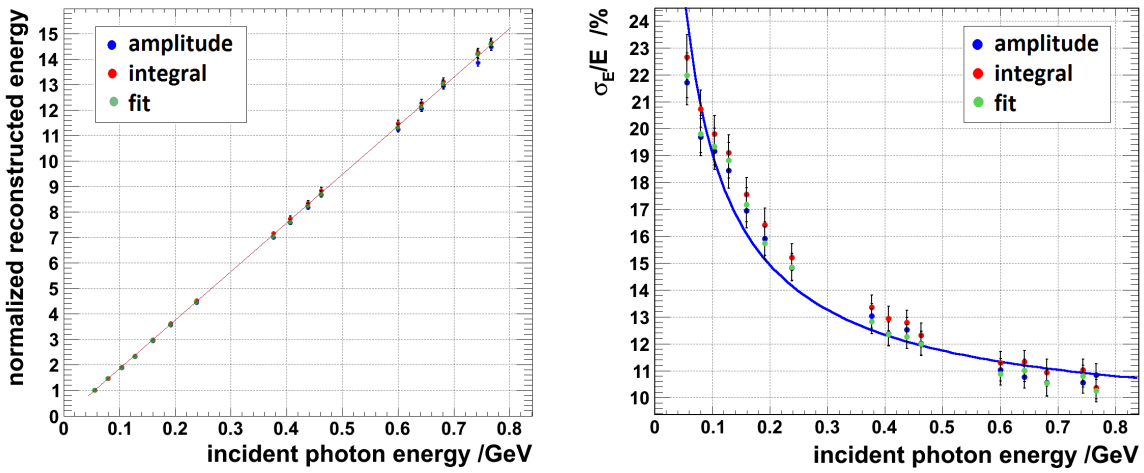

Figure 4.18: Linearity of the energy response (left) and relative energy resolution (right) of a single crystal with the photon beam interacting in the center of the crystal. The different colored points represent the peak-sensing (blue), the integral (red) and the fit (green) feature extraction. The blue line shows a fit of the points obtained with the peak-sensing feature extraction.

significantly above the background for the investigated range of photon energies and since the energy resolution of a single crystal is dominated by the energy leakage, no significant difference can be observed for the relative energy resolution obtained from the different feature extractions and therefore, no judgment of the performance of the different feature extraction is possible based on this data. A detailed comparison and discussion of the performance of the different feature extractions will be given in section 4.2.6 based on the energy resolution obtained for the complete 3 × 3 array. Since the linearity of the reconstructed energy is comparable for all feature extractions and due to the results presented in section 4.2.6, the peak sensing feature extraction will be applied for the calibration of the cells and the other studies, if nothing else is stated. The blue line in figure 4.18 (right) shows a fit of the relative energy resolution obtained with this method for a single crystal. The parametrization of the fit is given by:

$$\frac{\sigma}{E} = \frac{0.27\%}{E/GeV} \oplus \frac{5.25\%}{\sqrt{E/GeV}} \oplus 9.08\% \tag{4.16}$$

The high constant and statistic term can be explained by the lateral energy leakage out of the single crystal and its fluctuations, like already discussed in the explanation of the energy distributions.

4.2.4 Relative and absolute energy calibration

The most critical parameter for the calculation of the energy sum of a crystal array is the relative calibration of the single detector cells. This section will present and compare different approaches for a relative and an absolute calibration of the array with de-polished crystals within PROTO 120. For this purpose the data obtained from a calibration run with the photon beam during the experiment and the data from the interaction of cosmic muons, recorded after the experiment will be used.

Calibration based on beam data

To gain information about the response of all crystals in the 4 × 3 array containing the de-polished sub-array and especially about their readout, a calibration run has been performed at the beginning of the beam-time. During this run, the photon beam was aligned to the longitudinal axis of the central crystal of the de-polished array and the prototype was moved with the x-y-table in several steps, focusing the photon-beam on the center of each crystal of the array for approximately 20 minutes. Due to the low statistics for the highest photon energies in this short measurement period, only the first 13 of the selected tagger channels have been used for the calibration. To characterize the response of each crystal, a fit of the energy distribution for each tagger channel has been performed with a Novosibirsk-function. Based on this data, the relative calibration constant for each outer crystal has been extracted from a linear fit to the correlation between the obtained peak positions of the central crystal and the peak positions of the outer crystals, shown in figure 4.19 (left).

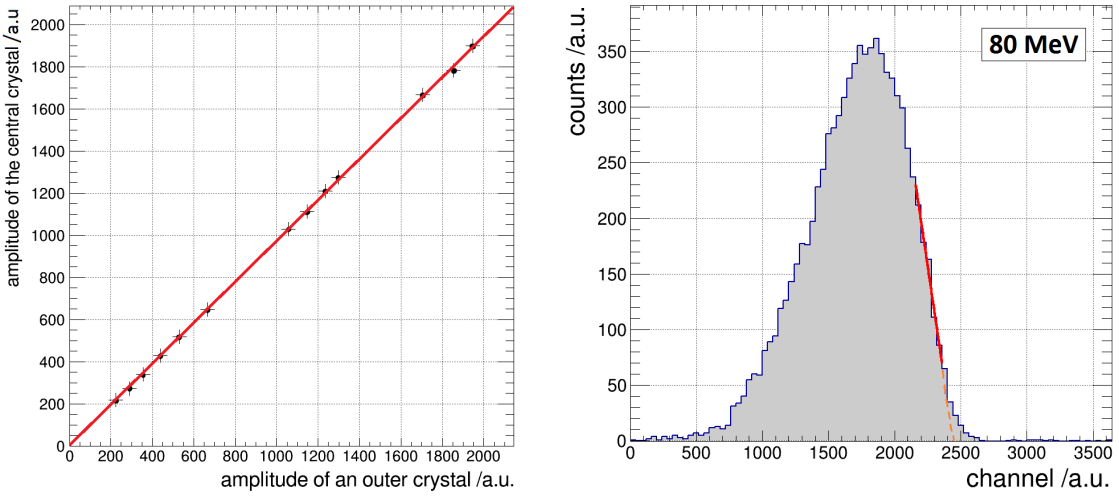

Figure 4.19: Linear fit to determine the relative calibration constant between a selected outer crystal and the central crystal for a typical low gain output (left) and linear fit to the falling tail of the energy distribution (right).

This method provides a linear correlation for all crystals, with a slope corresponding to the relative calibration coefficient. To apply these values extracted from the calibration run for a relative calibration, one has to assume that the same amount of energy is deposited in each crystal. This would be true for a perfect alignment of the beam position and the beam angle to each crystal axis. In reality, during the calibration run for the outer crystals, the alignment of the angle was fixed to the initial setting for the central crystal, since a manual adjustment for each crystal would be very time consuming. Therefore, it has to be considered that this misalignment of the interaction angle of approximately 2.2° and an additional uncertainty of the interaction position of the beam center of approximately ± 2 mm for the outer crystals introduces a variation of the average energy deposition in the different crystals, causing an error of the relative calibration based on this values.

A method to reduce these variations is given by a relative calibration based on the maximal energy deposition in the crystals. Since the maximal energy is most probably deposited by

photons interacting close to the center, the variation due to the misalignment of the interaction angle is significantly reduced, especially for the lowest incident photon energies. To obtain a reproducible value for the maximal energy deposition, a linear fit has been applied to the falling tail of the energy distributions for the lowest photon energies of 56 MeV, 80 MeV and 104 MeV between a height of approximately 1/3 and 2/3 of the maximal amplitude. A typical example for such a fit is shown in figure 4.19 (right). Since the real point of the maximal energy deposition can only be determined with a large error, the zero crossing point of this fit is taken as the energy deposition value for the single detectors. Based on these values the relative calibration coefficients have been calculated for the three photon energies and averaged. Figure 4.20 compares the obtained average calibration coefficients with the coefficients extracted from the peak positions of the energy distributions.

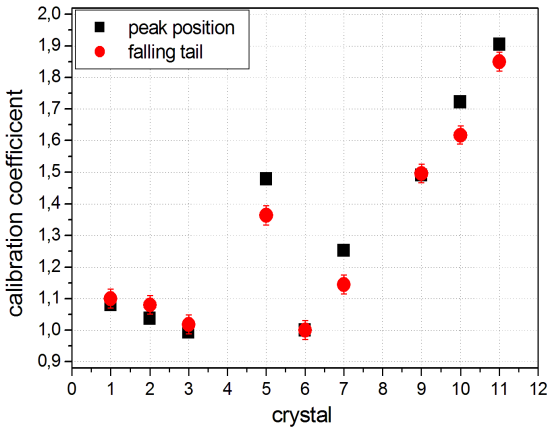

Figure 4.20: Comparison of the relative calibration coefficients obtained from the peak position of the energy distributions (black points) and from the falling tail of the energy distribution (red points).

A systematic shift of the two sets of coefficients can be observed. The coefficients of the first row (crystal 1-3) are slightly increased, while most of the coefficients of the last row (crystal 9-11) and the neighboring crystals of the central row (crystal 5 and 7) are decreased. This effect clearly shows that the detectors showing a decrease for the new calibration suffer from an energy leakage due to the misalignment of the beam angle, which reduces the most probable energy deposition. Considering this observation, it can be expected to obtain a better calibration from the second method.

Calibration based on cosmic muons

Another method for a relative calibration is given by the energy deposition of cosmic muons. Cosmic muons are minimal ionizing particles produced during the interaction of cosmic radiation in the atmosphere of the earth (for more details see also section 3.2.4). In lead tungstate, cosmic muons which can be observed from all atmospheric directions with a varying intensity, deposit approximately 10.2 MeV/cm [PDG14].

To gain two calibration points at different energies, PROTO 120 has been oriented in horizontal and vertical direction in two different runs and the energy deposition spectra of cosmic muons, interacting with the prototype, have been recorded for both orientations. As a trigger

for the readout, a plastic scintillator paddle which covers the complete array has been placed on top of the prototype. To reduce the background events, introduced by a non-correlated triggering of the paddle, and to limit the interaction angle of the cosmic muons, additional coincidences between the crystals of the array have been required in the analysis. For the horizontal orientation of the prototype, all three crystals of one column (see figure 4.21) have to show a response above a threshold of 15 MeV, if the event is accepted for the crystals in this column (*column cut*). With this condition it can be assured that the muon passes at least

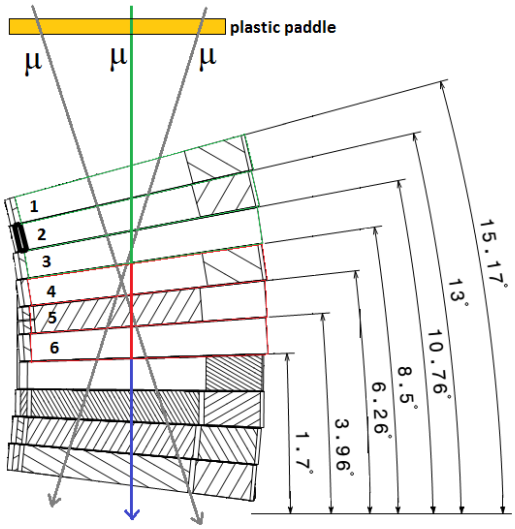

Figure 4.21: Schematic drawing of the orientation of PROTO 120 in horizontal direction during the measurement of cosmic muons. The green crystals represent the de-polished array, while the polished crystal array is marked in red. A plastic scintillator paddle was placed on top of the prototype to act as a trigger. The arrows show a selection of possible paths of cosmic muons.

the central crystals over the full width, while events in which only a corner of the crystal is passed are rejected. Nevertheless, a variation of the interaction angle along the longitudinal crystal axis is still possible, causing a smearing of the energy deposition distribution. For a vertical orientation of the prototype those cosmic muons should be selected, which deposit there energy along the complete longitudinal axis of a crystal. In this case, all neighboring crystals should detect no significant energy deposition. To realize this condition, it has been required that an event is only accepted for a crystal, if all neighbors detect an energy of less than 10 MeV, which corresponds to a path length of less than 1 cm (*exclusion cut*).

Figure 4.22 shows typical examples of the distributions which have been generated in the central crystal under the conditions for a horizontal and vertical orientation of the prototype. However, in vertical direction no neighbors exist in some directions for non central crystals, causing a higher amount of background events and a stronger smearing of the energy deposition distribution. To determine the channel of the most probable energy deposition, the distributions have been fitted with an overlap of a Landau-distribution, describing the energy deposition of the minimal ionizing particles and a Gaussian-distribution, which describes the intrinsic energy resolution of the detector and the smearing from the different path lengths for different interaction angles. However, since the distributions are quite broad and show

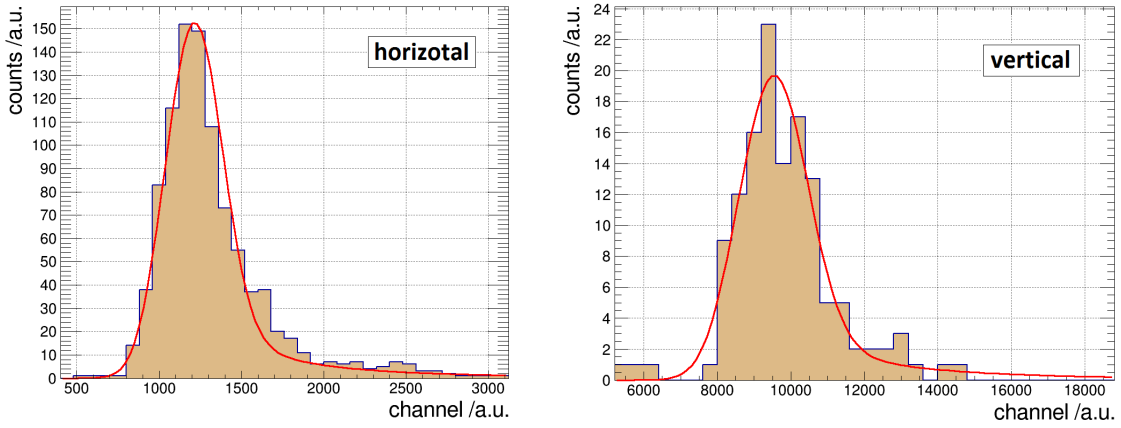

Figure 4.22: Spectra of the energy deposition distribution of cosmic muons, interacting with a crystal aligned in horizontal (left figure) and vertical (right figure) direction. In both cases the distribution is fitted with an overlap of a Landau- and a Gaussian- distribution.

poor statistics, an error of a few percent can be expected for the determination of the most probable energy deposition by the fit.

In addition, due to the different orientation of the three crystal rows of the array (see figure 4.21), a correction based on the path length variation of the muons has to be applied to the obtained peak positions of the upper and lower row for a horizontal orientation and to the outer crystals for a vertical orientation, if they are used for a relative calibration. The relative path length for a horizontal orientation is calculated based on the average angle α of the crystal by

$$\frac{l_{outer}}{l_{central}} = \frac{cos(\alpha_{central})}{cos(\alpha_{outer})} \tag{4.17}$$

Table 4.1 shows the obtained path length variation and the resulting correction coefficients $f_{cor.}$, representing the inverse of the relative path length, for a horizontal orientation of the prototype. The coefficients show that the introduced correction is in the region of less than

row	avg. crystal angle α	path length rel. to central row	$f_{cor.}$
1	14.09°	100.9 %	0.99
2	11.88°	100.0 %	1.00
3	9.63°	99.3 %	1.01

Table 4.1: Correction coefficients for the relative calibration of the array with de-polished crystals oriented in horizontal direction.

one percent and therefore below the estimated fitting error of the energy distributions. Also for a vertical orientation of the prototype, the calculated correction coefficients are on a comparable level and have no significant impact on the result.

Based on the corrected peak positions obtained from the fit of the energy deposition distributions, the relative calibration coefficients can be calculated by

$$c_{rel}[i] = \frac{f_{cor.} \cdot \text{maximum of cosmic distribution [central]}}{\text{maximum of cosmic distribution [i]}} \tag{4.18}$$

Comparison of the calibrations

Figure 4.23 compares the relative calibration coefficients extracted from the in-beam calibration run and from the energy deposition of cosmic muons. The figure shows that the cosmic

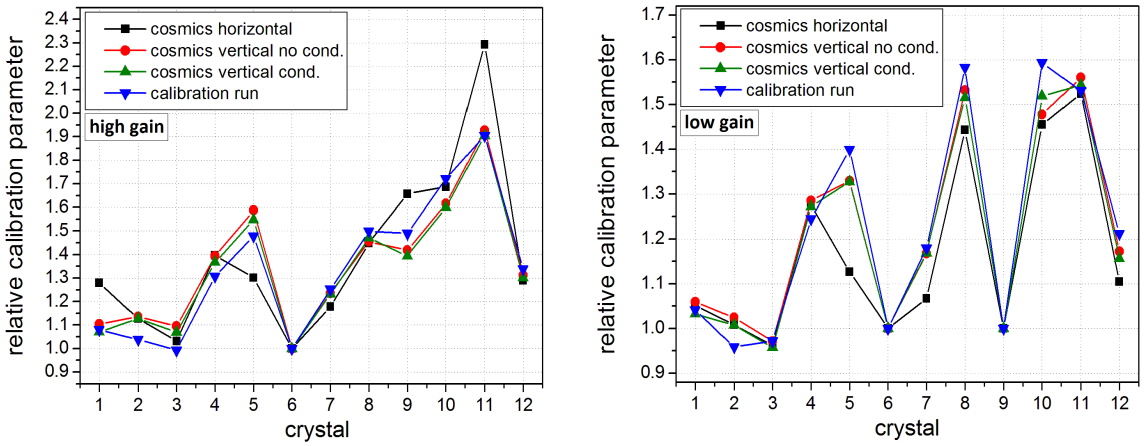

Figure 4.23: Comparison of the relative calibration coefficients obtained from the in beam calibration run and from the energy distribution of cosmic muons interacting with the horizontally and vertically oriented crystals. For the vertical orientation, the obtained coefficients are shown with and without the described condition for the neighboring crystals. The left picture shows the values for the high gain, while the low gain values are compared in the right picture. The error range, which is not shown in the pictures for clarity reasons, can be approximated to ± 0.04 for the cosmic calibrations. For the calibration based on the in-beam calibration run, a fit error of less than ± 0.02 can be obtained. However, an additional systematic error of up to 10 % has to be considered for these points due to the different amount of energy leakage initiated by the variation of the beam alignment (see figure 4.20).

muon calibration for a vertically aligned prototype provides approximately the same values with and without the condition that the neighboring crystals have to detect an energy below 10 MeV. A comparison of the cosmic muon calibration for a vertical and a horizontal orientation shows that most of the crystals provide comparable values for both methods. Only a few samples show a significant variation. The strong variation of the high gain of crystal 11 can be explained by the different energy deposition in horizontal and vertical direction of approximately 26.5 MeV and 220 MeV, respectively. While the response of the detector is still linear for the lower energy, it already shows a slight saturation for the higher energy, causing a different calibration coefficient. This effect is especially dominant for the high gain of crystal 11, since for this sample, the ASIC starts saturating after approximately 60 MeV due to a programming problem of the baseline. However, this saturation is no problem for the energy sum, since the crystal is in the outer ring and does not detect energies above 60 MeV for a central interaction of the investigated photon energies. For the low gain, the coefficients of the different calibration approaches are much more comparable, since the saturation of the AISC response does not occur in this amplitude region. The calibration with beam data shows a similar behavior like the cosmic calibration with a vertically oriented prototype, with small variations for some crystals, initiated by the systematic uncertainties of the calibration run.

The influence of the different calibrations on the relative resolution of the energy sum will be compared in section 4.2.6.

Absolute energy calibration

After the relative calibration of the crystals, an absolute calibration has to be performed to assign an energy to the reconstructed values. For this purpose different methods can be applied, which will be described and compared in the following section. Since all outer crystals are calibrated relative to the central crystal, an absolute calibration is only needed for the central one.

i) Absolute calibration based on GEANT4: The first method compares the energy deposited in the central crystal and in the 3 × 3 array with the energy deposition expected from GEANT4 simulations. The simulated energy fractions f_E for both cases can be found in figure 4.61 of the simulation section. Based on the expected energy deposition, calculated for the peak positions of the central crystal and the energy sum of the 3 × 3 array with this fractions, the absolute calibration coefficients shown in figure 4.24 have been extracted from the reconstructed peak positions of the experimental energy distributions by.

$$c_{abs} = \frac{\text{reconstructed amplitude}}{f_E \cdot E_{beam}} \tag{4.19}$$

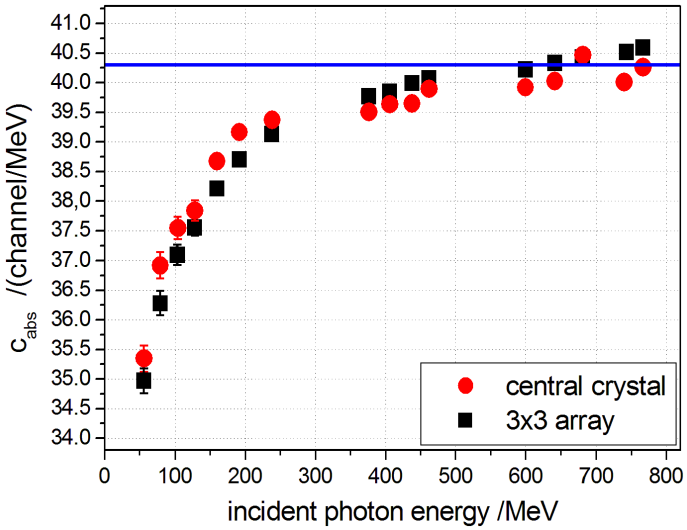

Figure 4.24: Energy dependence of the absolute energy calibration coefficient calculated based on the energy deposition of the photon beam in comparison with GEANT4 simulations.

A comparison of the calibration coefficients obtained from the central crystal and from the 3 × 3 array shows that both methods provide approximately the same values. In both cases, the coefficients increase for increasing energies. Only for energies above approximately 600 MeV they reach a nearly constant level of **(40.3 ± 0.8) ch/MeV**. For low energies a strong decrease of the calibration coefficient of up to 13 % can be observed. Since this effect also occurs for the central crystal, it can not be introduced by the experimental threshold but may be an effect of the shower simulation in GEANT4.

ii) Absolute calibration based on the maximal energy deposition: As another possibility to perform an absolute energy calibration based on beam data but without using GEANT4, it can be assumed that there is a certain probability that the complete energy is deposited in the 3 × 3 array. In the energy distribution, this case corresponds to the end of the high energetic tail of the distribution. The amplitude of this position can be determined directly from the distribution or it can be approximated as the peak position plus three times the standard deviation. Figure 4.25 (left) shows the relevant point, marked as a red bar in the energy distribution. The obtained absolute calibration coefficients

$$c_{abs-max} = \frac{\text{maximal reconstructed energy}}{E_{beam}} \tag{4.20}$$

for both methods can be found in figure 4.25 (right).

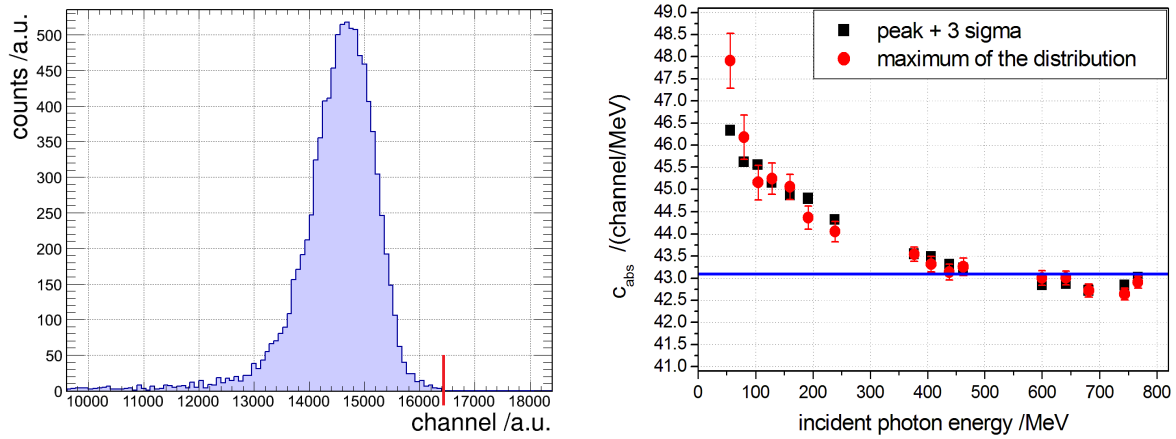

Figure 4.25: Left: Energy distribution for an incident photon energy of 377 MeV. The point of the highest reconstructed energy is marked as a red bar. Right: Absolute calibration coefficients determined from the highest points of the reconstructed energy distributions. The red points are extracted from the position determined from the energy spectrum by eye and the black points are calculated from the position obtained from the fit parameters of the peak position and the standard deviation of the energy distribution. The blue line indicates the average value for incident photon energies higher than 300 MeV.

The figure shows that both methods provide approximately the same coefficients. For low incident photon energies the coefficient slightly increases, while it stays nearly constant above 300 MeV. This increase for low energies of less than 8 % can be explained by the smearing of the distribution introduced by the electronic noise, which has less impact for higher energies. To exclude this effect, the absolute calibration coefficient has been determined as the average of the plateau, starting at approximately 300 MeV to a value of **(43.1 ± 0.4) ch/MeV**.

iii) Absolute calibration based on cosmic muons: For the absolute calibration, also the energy deposition of cosmic muons can be used. Based on the constant energy deposition of 10.2 MeV per centimeter [PDG14], the mean energy deposition for the different orientations can be calculated.

For the horizontal positioning of the crystals, the average thickness of the tapered type 2 crystals depends on the longitudinal position (x) and can be described by

$$d(x) = 2.128\ cm + 0.0379 \cdot x \tag{4.21}$$

The central crystal of the de-polished crystal array is oriented under an angle of 11.88° to the horizontal axis, which leads to an effective thickness for vertically crossing cosmic muons of

$$d_{eff}(x) = 2.175\ cm + 0.0387 \cdot x \tag{4.22}$$

Due to the position dependence of the thickness, also the deposited energy shows a position dependence, which can be described by

$$E_{dep}(x) = 10.2\ MeV/cm \cdot d_{eff}(x) = 22.19\ MeV + 0.395\ MeV/cm \cdot x \tag{4.23}$$

This parametrization leads to an average energy deposition of the cosmic muons of 26.14 MeV. Including the average non-uniformity of the de-polished crystals of 1.023 ±0.008, this results in a photon equivalent energy deposition of (26.7 ± 0.2) MeV. With this energy, the peak position of the cosmic muons in the central crystal of 1165 ± 15 channels, directly provides the calibration coefficient of **(43.6 ± 0.6) ch/MeV**.

For the vertical orientation of the crystals, the cosmic muons deposit energy along the complete crystal length of 20 cm. Including the angle of the central crystal relative to the vertical axis of 10.34°, this leads to an average length of 20.33 cm. Along this path length, cosmic muons deposit a mean energy of 207.4 MeV. Under consideration of the average non-uniformity of the de-polished crystals of 1.023 this results in an energy deposition, equivalent to the energy reconstructed for high energetic photons of (212.1 ± 1.7) MeV. With the peak position of the cosmic muons of 9228 ± 100 channels, a calibration coefficient of **(43.5 ± 0.5) ch/MeV** can be obtained.

As another method, the two calibration points obtained from horizontally and vertically interacting cosmic muons can also be combined to reduce the individual error range and to achieve a calibration which is also reliable for higher energies above a few hundred MeV incident photon energy. For this purpose the fact can be exploited that both data points have to fit to a linear function starting at zero. The slope of this fit, shown in the left part of figure 4.26 for the central crystal, directly provides the inverse of the absolute calibration coefficient for the considered detector. If the same procedure is repeated for all detectors of the array, a relative calibration is directly included in the obtained values. The resulting absolute calibration coefficients, defined as the inverse of the slope of the linear fit function are shown for all crystals in figure 4.26 (right). For most of the detectors a quite good linearity could be observed. Only for a few samples, which also showed deviations for the two data points of the relative calibration coefficients in figure 4.23 due to saturation effects, a discrepancy from the linear fit occurred for the data point at 212 MeV. In this cases the fit is primarily determined by the first data point at 26 MeV. For the central crystal, the linear fit provides an absolute energy calibration coefficient of **(43.7 ± 0.5) ch/MeV** for the high gain and **(3.9 ± 0.1) ch/MeV** for the low gain. The average calibration coefficient for all detectors, which can be used to approximate the dynamic range has been determined to (33.3 ± 6.5) ch/MeV for the high gain and (3.3 ± 0.6) ch/MeV for the low gain.

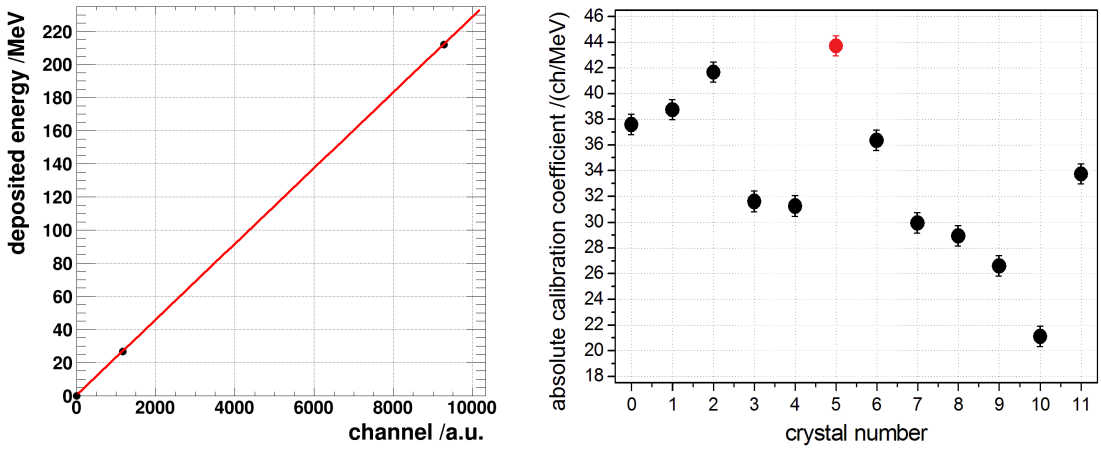

Figure 4.26: Linear fit of the two calibration points obtained with cosmic muons for the central crystal (left) and resulting absolute calibration coefficients for all crystals (right). The calibration coefficient of the central crystal is marked in red.

Comparison: The comparison of the different absolute calibration approaches shows that all absolute calibration coefficients are in good agreement within the error limit, except the one obtained by a comparison of the reconstructed energy with GEANT4 simulations of the prototype. The value obtained from the simulations provides an approximately 7.4 % lower calibration coefficient than the average of all other approaches and also shows a relative strong energy dependence especially for the lowest energies. An application of the calibration obtained by the simulations to the energy distributions also leads to significantly too high reconstructed energies. Therefore, it has to be assumed that GEANT4 simulates a slightly too small shower expansion, leading to an increased energy fraction contained in the central crystal and in the 3 × 3 array. Due to this behavior, this calibration approach will not be considered. The average of the other methods leads to a calibration coefficient of

$$c_{abs} = (43.5 \pm 0.4)\ \frac{ch}{MeV} \tag{4.24}$$

which will be taken for the further analysis. The correctness of this coefficient is confirmed by the good agreement with the coefficient obtained for the reproduction of the maximal energy deposition point of the 3 × 3 array. However, due to the non-uniformity in light collection a dependence of the absolute calibration coefficient on the incident photon energy and on the shower profile has to be expected. In the final calorimeter setup this energy dependence has to be compensated by the application of correction functions adjusted to the non-uniformity of the individual crystal types. For the de-polished crystals implemented in the 3 × 3 array of the present analysis, only a quite small energy dependence and therefore also a small error of the absolute calibration is expected from the missing correction, due to the nearly uniform response of the crystals.

4.2.5 Noise level and threshold

For the calculation of the energy sum of a crystal array, the electronic noise level and the threshold of a single channel have to be determined. The electronic noise can be defined as

the standard deviation of the recorded trace under the absence of any signal. To guarantee this condition, the baseline in front of the signal is used to calculate the standard deviation for each event. The obtained distributions are shown in figure 4.27. The left sub-figure compares the values for a single trace of the high gain branch (HG) and for the direct sum of the high gain raw traces of the two APDs of one crystal (add-HG), while the right figure compares the standard deviations of a single trace of the high gain (HG) and the low gain (LG) branch.

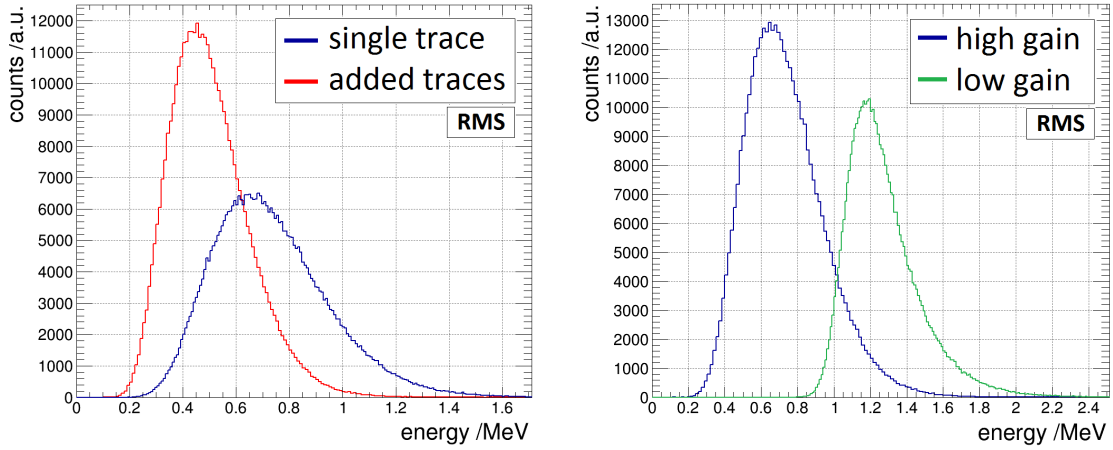

Figure 4.27: Distribution of the standard deviation of the electronic noise in units of the incident photon energy, exploiting the absolute calibration from section 4.2.4. The left picture shows a comparison between a single trace of the high gain branch (blue) and the direct sum of the two APDs of the high gain branch of one crystal (red). The right pictures illustrates the difference of the electronic noise between the high gain (blue) and the low gain (green) output.

All distributions show a slight asymmetry to higher energies, which indicates that different noise components are contributing. The obtained maxima and standard deviations[2] of the high energetic tail of the distributions are

$$\begin{aligned} \sigma_{HG} &= (0.67 \ \pm \ 0.28) \ MeV, \\ \sigma_{LG} &= (1.22 \ \pm \ 0.38) \ MeV, \\ \sigma_{add-HG} &= (0.46 \ \pm \ 0.21) \ MeV \end{aligned} \tag{4.25}$$

The comparison of the values shows that the electronic noise of the low gain branch is approximately 1.8 times higher than for the high gain branch. However, since the low gain branch is only used for energies above a few hundred MeV, this increase plays only a minor role. The ratio between the standard deviation of a single trace and the sum of the two high gain traces of one crystal is given by

$$\frac{\sigma_{HG}}{\sigma_{add-HG}} \approx 1.46. \tag{4.26}$$

As expected from statistical considerations, the noise level in units of the incident photon energy improves by approximately a factor $\sqrt{2}$ if two uncorrelated noise distributions are added.

[2]Stated as the error range of the maxima

In case of the peak-sensing feature extraction, the maximum of the trace is searched in a given time interval. Therefore, under the absence of additional cuts and conditions, also for a trace without a signal, the maximal bin will be miss-identified as a signal. To get a feeling for the distribution of the height of the maximal bin of the traces, the maximum of the baseline has been searched in a time-interval with the same length like for a real signal. The obtained distributions are shown in figure 4.28. Like for the standard deviation, the left sub-figure compares the values for a single trace of the high gain branch (HG) and for the direct sum of the high gain raw traces of the two APDs of one crystal (add-HG), while the right figure compares the standard deviations of a single trace of the high gain (HG) and the low gain (LG) branch.

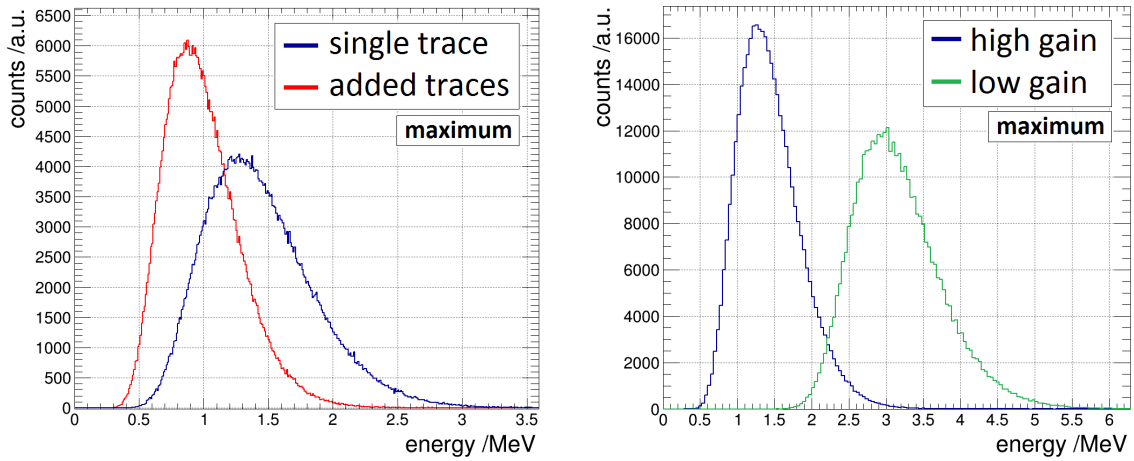

Figure 4.28: Distribution of the maximum of the electronic noise, searched in a time interval of the baseline with the same length like for a real signal. The left picture shows a comparison between a single trace (blue) and the direct sum of the two APDs of one crystal (red). The right pictures illustrates the difference between the high gain (blue) and the low gain (green) output.

The maxima and standard deviations[3] of the high energetic tails of this distributions are

$$\begin{aligned} \max_{HG} &= (1.29 \ \pm \ 0.54) \ MeV, \\ \max_{LG} &= (2.97 \ \pm \ 0.73) \ MeV, \\ \max_{add-HG} &= (0.88 \ \pm \ 0.42) \ MeV \end{aligned} \tag{4.27}$$

In this case the difference between the high and the low gain branch is a factor of 2.3. The ratio between the most probable maximal value of a single trace and the sum of the two high gain traces of one crystal stays with a value of

$$\frac{\sigma_{HG}}{\sigma_{add-HG}} \approx 1.47 \tag{4.28}$$

approximately at the same level, close to $\sqrt{2}$, like for the standard deviation of the values.

Based on the obtained maximal values of the traces and their standard deviations in 4.27, the single crystal threshold can be calculated. To reject the complete electronic noise, three

[3]Stated as the error range of the maxima

times the standard deviation of the high energetic tail is added to the most probable maximal values of the traces.

$$\text{thr} = \max + 3 \cdot \sigma_{max} \tag{4.29}$$

For the different branches and for the direct sum of the high gain traces, the following thresholds can be obtained with this method:

$$\begin{aligned} \text{thr}_{HG} &\approx 2.9\ MeV, \\ \text{thr}_{LG} &\approx 5.2\ MeV, \\ \text{thr}_{add-HG} &\approx 2.1\ MeV \end{aligned} \tag{4.30}$$

Similar values can be calculated, if the standard deviations of the baselines from equation 4.25 are used. To exclude 99.7 % of the noise, a threshold corresponding to three times the standard deviation σ has to be taken. Since the standard deviation shows a distribution around the most probable value, at least a single error range $\Delta(\sigma)$ has to be added to the standard deviation, leading to the equation:

$$\text{thr} = 3 \cdot (\sigma + \Delta(\sigma)) \tag{4.31}$$

Using this definition, approximately the same values like in 4.30 can be obtained for the threshold. Only for the low gain, the relatively large high energetic tail increases the threshold based on the maximal value a little bit.

Integral feature extraction

The electronic noise level determined in the last paragraph is focused on a peak-sensing feature extraction. For an integrating feature extraction, a summation of several bins of the trace is performed. Since the baseline represents the average value of the trace, an integral with the baseline set to zero should reproduce a value of zero, if no signal appears on the trace. In reality, the baseline is calculated over a limited sample of the trace of only 130 ADC channels and the signal is integrated over another limited sample of 300 bins. Due to this limited range, both values will show variations from event to event, resulting in a distribution of the integral value around zero, with a standard deviation strongly influenced by the characteristics of the electronic noise. To estimate the strength of these variations, the integral has been determined for traces without a signal over a fixed range of 300 channels, differing from the range in which the baseline is extracted. Figure 4.29 shows the resulting distributions for the high gain and the low gain branch. The distributions show a standard deviation of 1.8 MeV for the high gain and 2.5 MeV for the low gain branch, respectively. These values are significantly higher than for the peak sensing feature extraction, which can be explained by components of the electronic noise with a length comparable to small signals (see figure 4.11), causing a strong variation of the integral value extracted from a limited range of bins. Due to the high noise level, thresholds of 5.4 MeV and 7.5 MeV are expected for an integral feature extraction of the high and low gain branch, respectively.

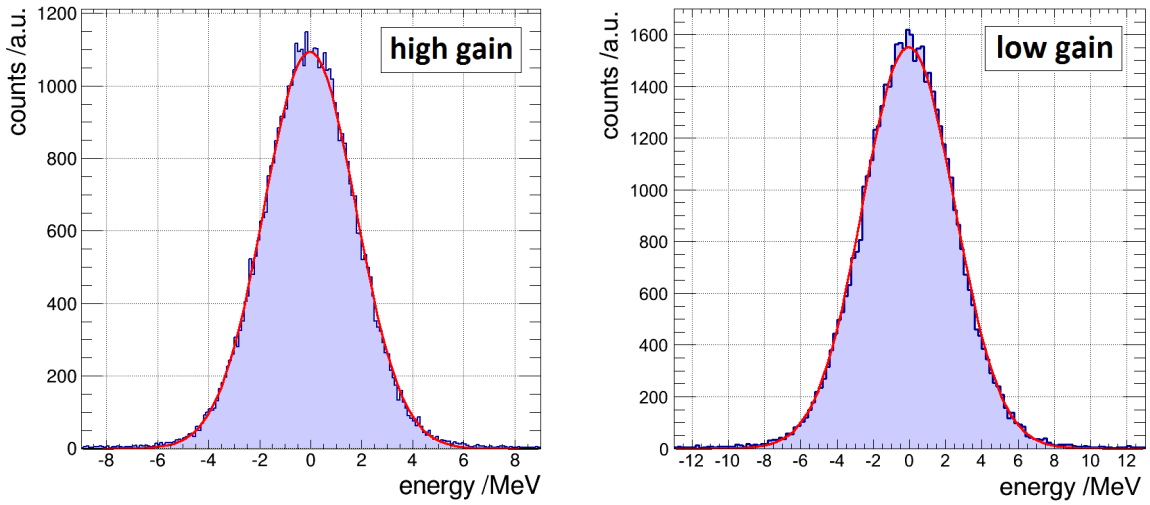

Figure 4.29: Electronic noise distribution of the high gain (left) and the low gain (right) branch for an integrating feature extraction over a fixed range of 300 bins.

In contrast to this, the second method for an integral feature extraction presented in section 4.2.2, which integrates only a limited range of bins around the minimum of the trace, enables the combination of the threshold of an peak sensing feature extraction and the advantages of an integral feature extraction. For an individually triggered readout of each detector, the same threshold like for the peak-sensing feature extraction has to be applied with this method, independent from the integration range. However, if a common readout of all detectors within the cluster is performed, this threshold can be further reduced by adjusting the reconstruction threshold to the signal noise determined from the application of the method to a trace without any signal. To determine the optimal integration length, a scan of the threshold which is required to reject noise misidentified as a signal has been performed as a function of the integration range, which is positioned symmetrically around the minimum. The result is shown in figure 4.30. The figure shows that an integration of the neighboring bins around the minimum of the trace can reduce the reconstruction threshold from originally 2.8 MeV down to less than 2.6 MeV for an integration region of approximately 400 ns, since up to this point the signal to noise ratio is improved by the integration. For a larger integration region the increase of the integral is lower than the increase of the fluctuations of the integral for traces without any signal. Therefore, the reconstruction threshold increases again. An improvement of the threshold by the integration is only possible for integration regions of less than 0.9 μs, since after this point even the threshold of the peak sensing feature extraction is exceeded and the threshold of the peak sensing algorithm has to be used to obtain optimal results. This is especially the case, if the complete signal is integrated. However, the observed threshold behavior strongly depends on the characteristics of the electronic noise and has to be optimized for each setup. The minimum of the threshold for a certain integration range is caused by the irregular oscillations of the trace which can be observed in the right part of figure 4.11. This oscillations are introduced by the amplification and shaping process within the ASIC and show a behavior similar to small signals, making a smoothing of the trace by filter algorithms hardly possible without deteriorating real signals. If the electronic noise only consisted of single bin fluctuations, an increase of the integration range would cause a reduction of the threshold.

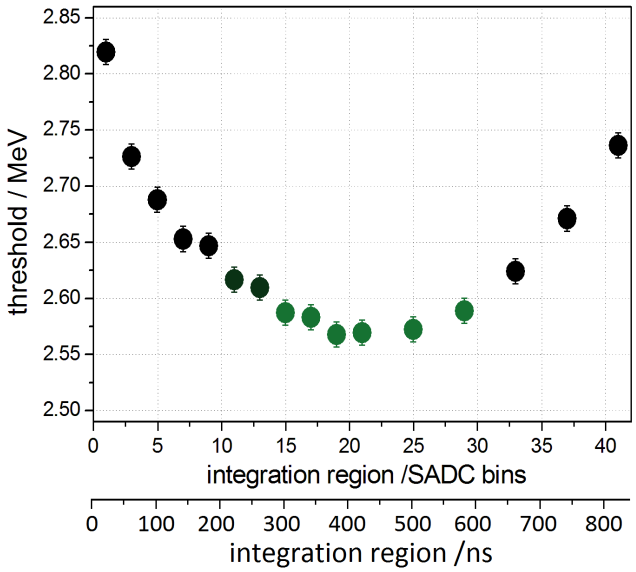

Figure 4.30: Software threshold of the cluster reconstruction versus integration range. The integral is positioned symmetrically around the minimum of the trace. An integration region of 1 SADC bin (20ns) represents the peak sensing feature extraction. The green points mark the integration region, which provides an optimal reconstruction threshold.

4.2.6 Response of a 3 × 3 array

After the performance of a single crystal and the electronic noise have been characterized and several methods for a relative and an absolute calibrations have been presented in the last sections, this section will present the energy resolution of a 3 × 3 array of crystals with a de-polished side face, obtained with the different feature extraction and calibration methods. Finally, the optimized results will be compared to another array with polished crystals to estimate the influence of the non-uniformity in light collection on the energy resolution.

Time correlation cut

To optimize the noise rejection for the calculation of the energy sum, a time correlation cut has been applied. In addition to the time gate for the feature extraction of the central crystal, which has already been limited to (120 - 160) ns, depending on the incident photon energy, the signals of the outer crystals of the 3 × 3 array have to be in coincidence with the signal of the central crystal to be accepted for the energy sum. Figure 4.31 shows the distribution of the time difference between the signals in an outer crystals and in the central crystal for the lowest and the highest incident photon energy. Both distributions show a clear peak around zero which contains the correlated events. For energies above a few hundred MeV, most of the outer crystals of the 3 × 3 array detect a signal above the electronic noise level. Therefore, at 743 MeV nearly no non-correlated signals can be observed. In contrast to this, for 56 MeV the signal in some of the outer crystals is below the electronic noise level and noise is miss-identified as a signal if no threshold is applied. To reject such miss-identified signals, a sharp window has been set to the time difference. The width of the window has been optimized for each tagger energy to gain an optimal energy resolution. For the two examples

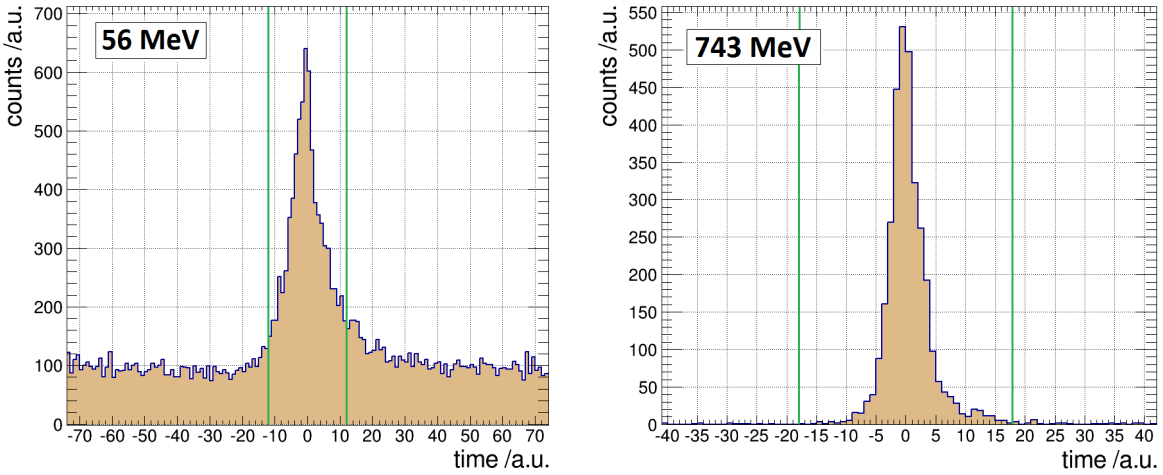

Figure 4.31: Time difference distributions between the central and an outer crystals for an incident photon energy of 56 MeV (left) and 743 MeV (right). The time cuts, which have been individually optimized for each energy are shown as a green line in both figures.

in figure 4.31, the cuts are shown as green lines. Especially at low energies, this method can provide a significant improvement of the energy resolution and due to the common readout of all channels also a reduction of the effective offline threshold.

Threshold scan

The thresholds of all channels of the 3 × 3 array show only small deviations, except two outer channels which show low frequent (≈ 100 kHz) periodic oscillations. Since this effect deteriorates the energy resolution, a correction has been applied. For this purpose a sinus-function has been fitted to the oscillating baseline before and after the main signal to correct the complete trace. For one of the detectors it was possible to remove the oscillation completely, but for the other one, only a reduction to a certain level was possible. The remaining oscillations mainly deteriorate the energy resolution at low energies. Therefore, the threshold of the affected crystal in the upper left corner of the array had to be increased to 6 MeV to exclude an influence at least at low energies.

To verify the threshold calculated for the other crystals on the basis of the electronic noise distribution in section 4.2.5 and to check, if the time correlation cut described in the last paragraph reduces the optimal setting, a threshold scan has been performed for the relative energy resolution of the 3 × 3 array. Figure 4.32 shows the obtained results for the response of the high gain sum of both APDs of each crystal for an incident photon energy of 80 MeV and 462 MeV, respectively. For both incident photon energies, a similar behavior can be observed. For very low thresholds, up to a value of approximately 2 MeV the relative energy resolution stays constant or slightly increases. Between 2.3 MeV and 3 MeV a slight drop appears, before a steep increase of the relative energy resolution sets in. This behavior can be explained by a comparison with the electronic noise distributions from section 4.2.5. For thresholds below 2.3 MeV noise is added for most of the outer crystals. This uncorrelated noise causes a shift of the amplitude and an increase of the standard deviation by approximately the same factor. As a result, the resolution, representing the ratio of this two properties, stays at the same level

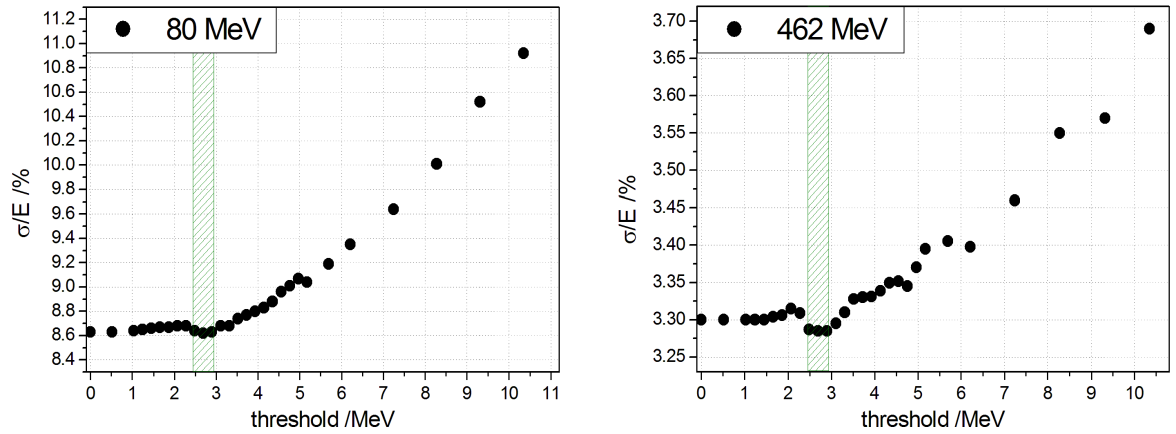

Figure 4.32: Threshold scan of the relative energy resolution for an incident photon energy of 80 MeV (left) and 462 MeV (right).

or becomes even slightly better at low thresholds. Between 2.4 MeV and 2.9 MeV, marked by the green shaded area in figure 4.2.5, less noise is added and a balance between the added noise and real signals sets in. For a threshold above 2.9 MeV the complete noise is suppressed and more and more true energy information is rejected, resulting in a deterioration of the relative energy resolution.

Based on the minimum of the threshold scan, the **optimal threshold** can be set to **2.7 MeV**. A comparison to the 2.9 MeV determined from the noise distribution without any cut (see equation 4.30) shows that the applied time-correlation cut helps to reduce the offline threshold.

Energy distribution within the array

Based on the time-correlation cut and the optimal threshold of 2.7 MeV, the energy sum of the 3 × 3 array has been calculated. Figure 4.33 shows the obtained energy distributions for the 3 × 3 array in comparison to a single crystal for selected photon energies between 56 MeV and 743 MeV.

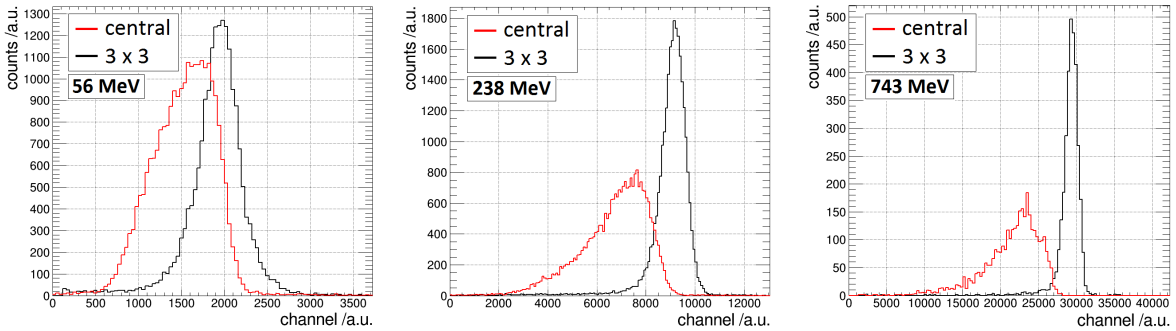

Figure 4.33: Energy distribution of the 3 × 3 energy sum in comparison to the energy distribution of a single crystal for an energy of 56 MeV (left), 238 MeV (middle) and 743 MeV (right). A threshold of 2.7 MeV has been applied for the reconstruction of the energy sum.

The comparison of the figures shows that for low energies, due to the applied threshold, only a quite small difference of the maxima of the energy distribution between the central crystal and the 3 × 3 array can be observed, while the difference is much more pronounced for higher energies. In all cases it is clearly visible that the energy distribution for the 3 × 3 array is much narrower and the low energetic tail, introduced by the energy leakage, is significantly reduced due to the larger energy fraction, which is contained in the 3 × 3 array. The relatively wide energy distributions for the central crystal, especially at low energies, are also a result of the energy deposition variation, introduced by the large area covered by the photon beam. This effect is nearly completely compensated for the 3 × 3 energy sum.

The experimentally determined **energy fraction** contained in the central crystal of the 3 × 3 array in relation to the energy deposited in the complete array is shown in figure 4.34.

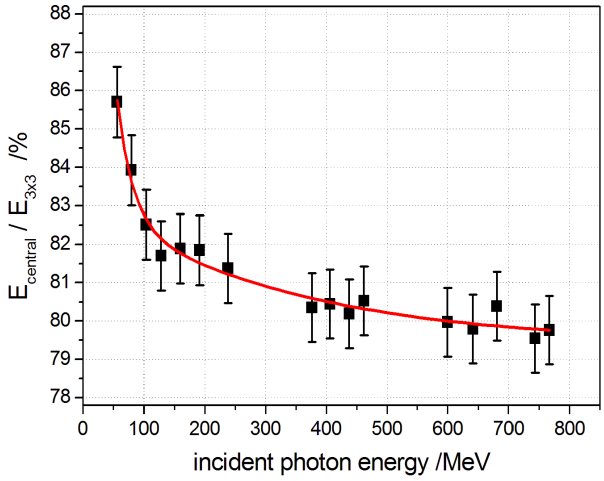

Figure 4.34: Energy fraction, deposited in the central crystal of a 3 × 3 array as a function of the incident photon energy.

As expected from figure 4.33 the ratio increases for low energies and stays nearly constant for higher energies. The steep increase at low energies is partly a physical effect but for the shown data also strongly amplified by the threshold, which has been applied to the energy sum of the 3 × 3 array.

Another sensitive value to estimate the shower expansion is given by the **multiplicity** of the responding crystals. To determine the multiplicity, the number of crystals which are added to the energy sum have been counted in each event. Like for the energy sum, also for the multiplicity the noise rejection by the time-correlation cut between the central and the outer-crystals is applied. Figure 4.35 shows the distributions of the crystal multiplicity for all events at energies between 56 MeV and 767 MeV with a threshold of 2.7 MeV. The shift of the multiplicity distribution illustrates the increasing lateral shower expansion for increasing incident photon energies. For the highest incident photon energy of 767 MeV on average almost 90 % of the crystals within the 3 × 3 array provide a response above the threshold. To obtain a more quantitative picture of the multiplicity, the energy dependence of the mean value of the crystal multiplicity is plotted in figure 4.36 for different thresholds between 0 MeV and 2.8 MeV. For all thresholds, the typical increase of the multiplicity with increasing incident photon energies can be observed. As expected, a decrease of the

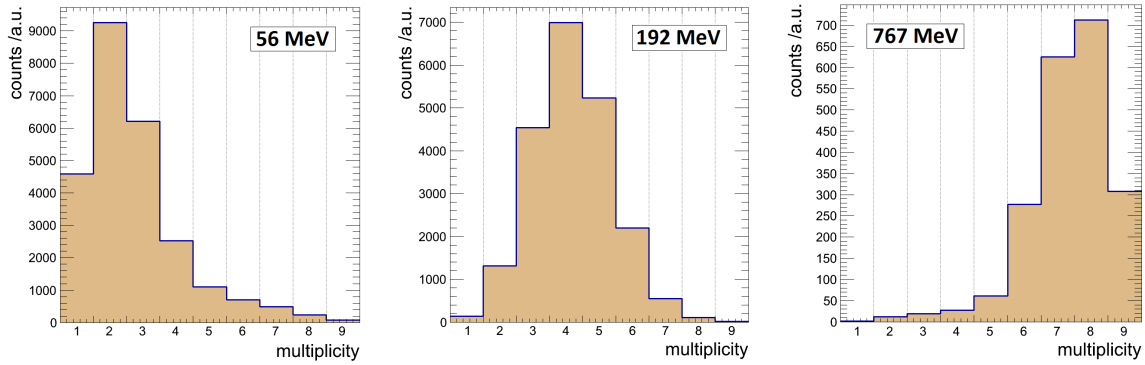

Figure 4.35: Distribution of the multiplicity of the responding crystals above a threshold of 2.7 MeV for an energy of 56 MeV (left), 192 MeV (middle) and 767 MeV (right).

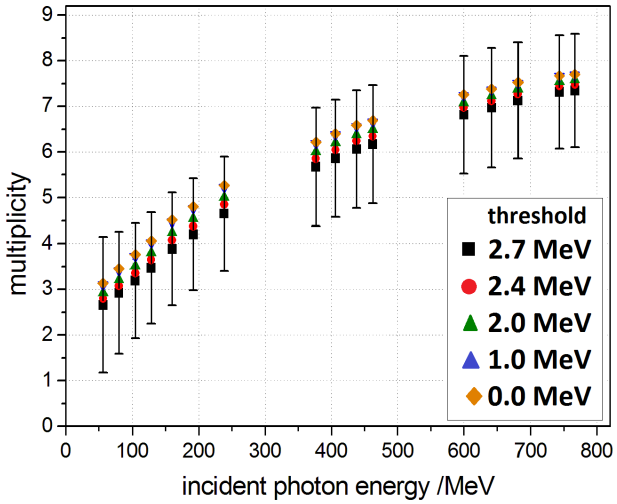

Figure 4.36: Energy dependence of the mean multiplicity of the crystals with a response above the threshold, for thresholds between 0 MeV (orange points) and 2.7 MeV (black points). The time-correlation cut of the energy sum is also applied for the calculation of the multiplicity. The error bars, only shown for a threshold of 2.7 MeV, represent the standard deviation of the multiplicity distribution.

threshold leads to an increase of the multiplicity due to noise contributions. Nevertheless, the unexpected small increase for a reduction of the threshold, especially at low energies shows that most of the noise is rejected from the energy sum by the time-correlation cut. Without this cut a significant increase for thresholds below 2 MeV, especially for the lowest incident photon energies was observed.

Line-shape of the energy sum

Figure 4.37 shows selected energy distributions for the energy sum of the 3 × 3 array of de-polished type 2 crystals operated at -25°C for energies between 80 MeV and 767 MeV. For all energies only quite small low energetic tails can be observed, since more than 94 % of the incident photon energy are deposited within the 3 × 3 array. Like for the central crystal, also these distributions are fitted with a Novosibirsk-function to determine the energy resolution.

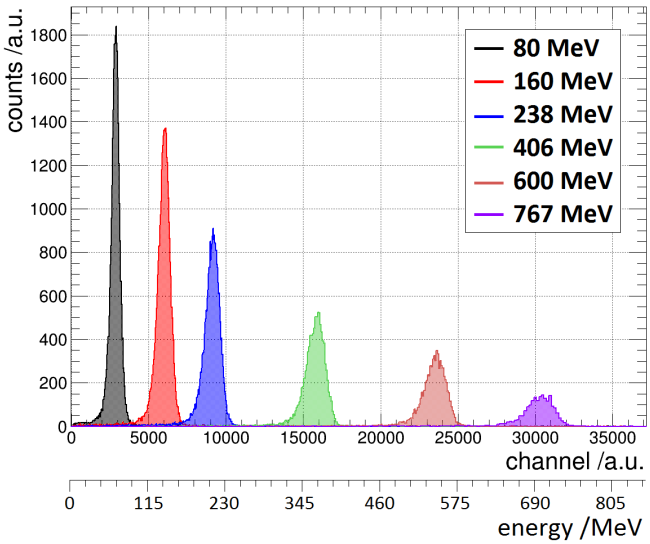

Figure 4.37: Line-shape of the energy sum of a 3 × 3 array of de-polished type 2 crystals operated at -25°C for selected incident photon energies between 80 MeV and 767 MeV.

Influence of the calibration and the feature extraction on the energy resolution

Uncertainties of the relative energy calibration can have a significant influence on the energy resolution. To compare the different calibration methods described in section 4.2.4, the relative energy resolution of the 3 × 3 array has been determined for all methods and compared in figure 4.38.

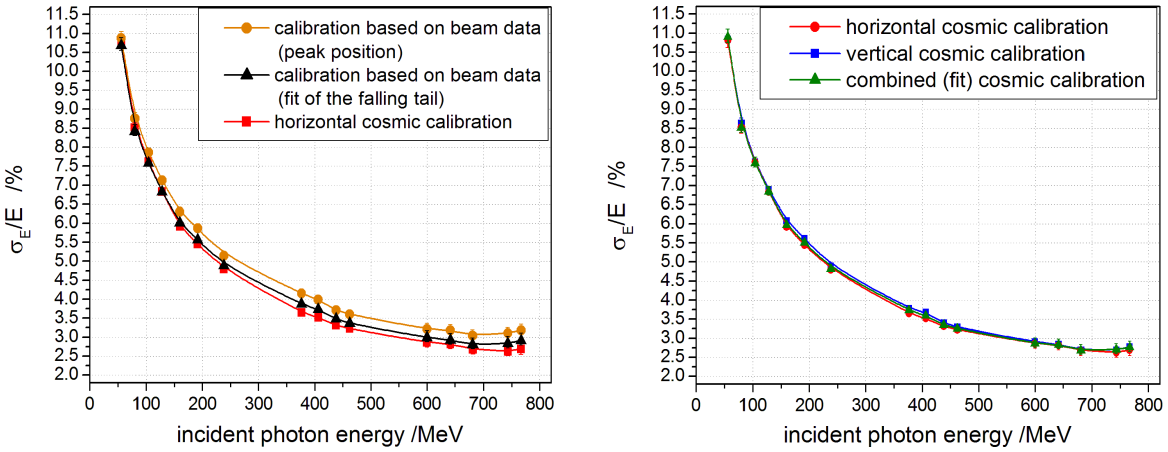

Figure 4.38: Left: Comparison of the energy resolution of the 3 × 3 array, achieved with the two variants of the calibration based on beam data from the calibration run (orange and black points) with the result of the calibration using cosmic muons interacting on an horizontally oriented prototype (red points). Right: Comparison of the different calibration variants based on cosmic muons interacting with and horizontally (red points) and vertically (blue points) oriented prototype and for a combination of both calibration points with a linear fit (green points). For more details on the calibrations see section 4.2.4. In all cases the peak sensing feature extraction and a threshold of 2.7 MeV have been applied.

The comparison of the energy resolution curves for the two options of the relative calibration based on beam data in figure 4.38 (left) shows that the calibration using the maximal energy deposition in the crystals, determined with a linear fit to the falling tail of the energy distributions, provides significantly better results than the calibration based on the peak positions of the energy distributions of the single crystals. This difference shows that a misalignment of the photon beam can not be neglected for the outer crystals, since it influences the most probable value of the energy deposition in a single crystal due to a variation of the shower leakage. The deteriorating effect of the misalignment of the photon beam on the energy resolution can only be compensated if the maximal energy deposition is used for the calibration, since it is less sensitive to the interaction angle. However, compared to a calibration based on cosmic muons interacting on a horizontally oriented prototype, the energy resolution obtained with the calibration based on the maximal energy deposition is still slightly worse, especially at higher energies. This difference can be explained by the uncertainty of the determination of the position of the maximal energy deposition by a fit of the falling tail of the energy distributions and by a more homogeneous response of the cosmic muons, which interact along the complete crystal.

A comparison of the results for the different concepts of the calibration based on cosmic muons in figure 4.38 (right) shows that all methods provide comparable results. A closer look on the results for the calibration with a horizontally and a vertically oriented prototype shows that the interaction on a horizontally oriented prototype provides slightly better results for the relative energy resolution, since the deposited energy of 26.1 MeV is closer to the energy deposited in the outer crystals of the array. The calibration based on a linear fit of the two data points obtained from the peak positions of the cosmic muons, presented in section 4.2.4, provides energy resolution values in between the results obtained for the other two calibrations. Nevertheless, a slight improvement can be expected for this calibration at higher energies, due to the lower error of the calibration coefficients. As a conclusion of the comparison, the calibration based on cosmic muons interacting on a horizontally aligned prototype will be used for the further analysis.

Based on the optimized calibration, the relative energy resolution curves obtained for the 3 × 3 array with the peak sensing feature extraction and the **fit of the pulse shape** are compared in figure 4.39. For energies above 130 MeV, the fit of the pulse-shape and the peak-sensing feature extraction provide approximately the same results within the error bars. Only for energies below 130 MeV a small improvement can be achieved by a fit of the pulse-shape. This improvement increases for decreasing energies and reaches a significant value of 0.6 percent points for the lowest energy of 56 MeV. A threshold scan for the energy resolution, obtained from the pulse-fit, showed that the optimal threshold decreases from 2.7 MeV to 2.3-2.4 MeV introducing an additional improvement of the energy resolution for the lowest energy in the order of 0.1 percent point. The improvement of the relative energy resolution by the pulse-fit at low energies can be explained by an averaging of noise contributions and statistical fluctuations of single sampling ADC bins, deteriorating the energy resolution at low amplitudes. In addition, the pulse-fit can recover pulses close to the threshold or even slightly below the original threshold, which were misidentified as noise by the peak-sensing feature extraction and can now be added to the energy sum. For energies well above 100 MeV, the announced effects play only a minor role, even in the outer crystals of the 3 × 3 array. Therefore, no significant difference between the peak-sensing feature extraction and the fit can be observed in this energy region.

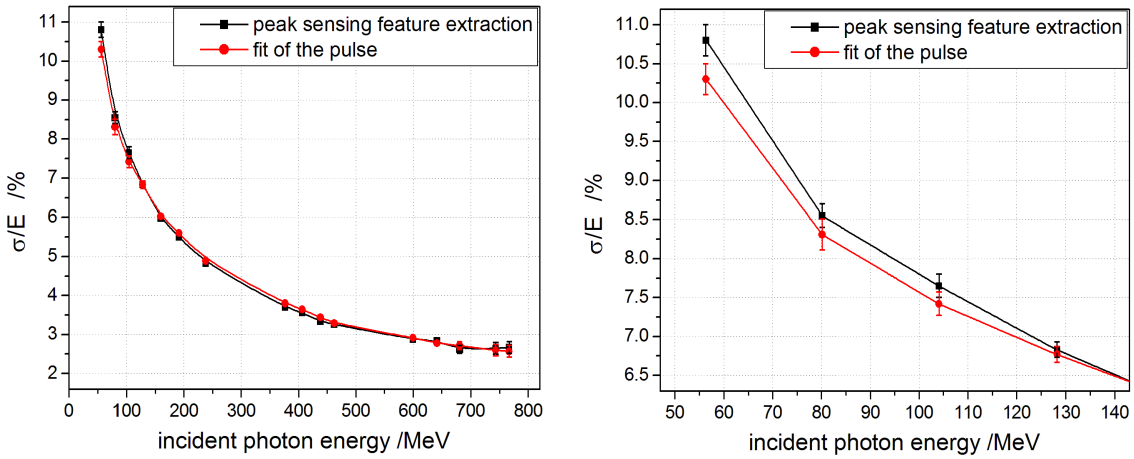

Figure 4.39: Comparison of the energy resolution obtained for a 3 × 3 array with the peak sensing feature extraction (black points) and the fit of the pulse shape (red points). The left figure shows the complete energy range, while the right figure presents the energy range below 150 MeV in which a fit of the pulse shape improves the energy resolution. In both cases the cosmic calibration for a horizontally aligned prototype and a threshold of 2.7 MeV are used.

Besides the fit of the pulse-shape, also the **integral feature extraction** can be used to average over noise fluctuations and to include more signal information into the extracted energy values. Since an integration of the signal needs much less computing effort, it can be easily implemented in an online feature extraction algorithm. Therefore, different integration methods have been compared to study the improvement of the relative energy resolution with this method in comparison to the other feature extraction procedures. The most simple integration method is the integration of a fixed region of 300 SADC bins, including the expected range of the pulse. However, for this method it has been already shown in section 4.2.5 that the characteristics of the electronic noise introduced by the ASIC lead to a significant increase of the reconstruction threshold from 2.7 MeV for the peak sensing feature extraction to 5.4 MeV for the high gain branch of the integral feature extraction. The obtained relative energy resolution under consideration of the different threshold is shown in figure 4.40 in comparison to the values obtained with the peak sensing feature extraction. As expected from the increased threshold, significantly worse energy resolution values have been obtained compared to the peak sensing feature extractions, especially at low energies. This increase of the energy resolution for the integral feature extraction can be explained by the structure of the electronic noise, containing low frequent oscillations with a width comparable to the width of small pulses (see figure 4.11). In addition to the increased effective threshold of the integral feature extraction, the electronic noise from the ASIC also causes a smearing of the integral at low amplitudes which additionally deteriorates the energy sum for a cluster. This effect is much more critical for the integral than for the amplitude or the fit value, since the integration of the bins multiplies the influence of such noise components at low signal amplitudes. Figure 4.41 illustrates this smearing of the integral value with the correlation of the extracted integral and amplitude values. If only high energies are deposited in the crystal, like for the center of the 3 × 3 array (left plot), a quite good correlation can be observed. In this case only a slight deterioration of the energy resolution for the integral feature extraction, compared to the peak sensing feature extraction has been observed in section 4.2.3 for the

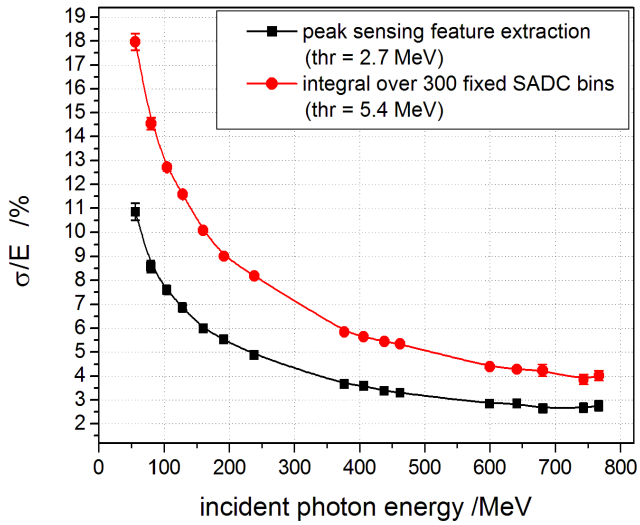

Figure 4.40: Comparison of the relative energy resolution for an integration over 300 bins (red points) and for a peak sensing feature extraction (black points). According to 4.2.6 and 4.2.5 a threshold of 5.4 MeV is used for the integrating feature extraction.

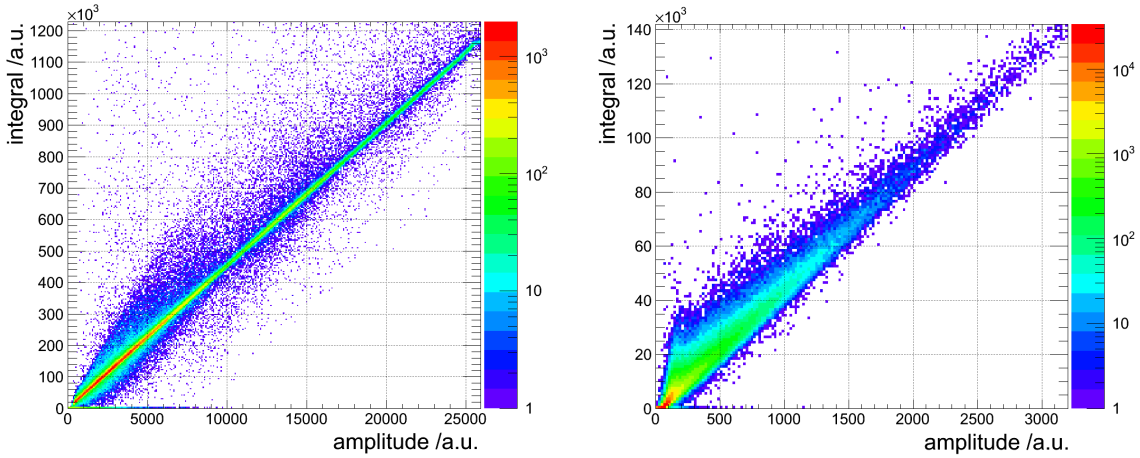

Figure 4.41: Correlation between the integral over 300 SADC bins and the amplitude of a signal pulse for the central crystal (left) and an outer crystal (right).

response of the central crystal. In contrast to this, in the outer crystals (right plot), where only a small part of the energy is deposited, a quite large smearing of the correlation can be observed. This smearing directly leads to a deterioration of the cluster energy resolution over the complete investigated energy range.

To reduce the influence of the electronic noise, a combination of the peak sensing and the integrating feature extraction has been introduced in section 4.2.2. For this method primarily the threshold of the peak sensing feature extraction can be used. Nevertheless, in section 4.2.5 it has been shown that a reduction of the effective cluster threshold is possible with an optimized integration range for a common readout of the cluster. To investigate the influence of the integration region around the minimum of the trace on the relative energy resolution, a

scan of the relative energy resolution as a function of the integration range has been performed for selected incident photon energies between 56 MeV and 681 MeV in figure 4.42.

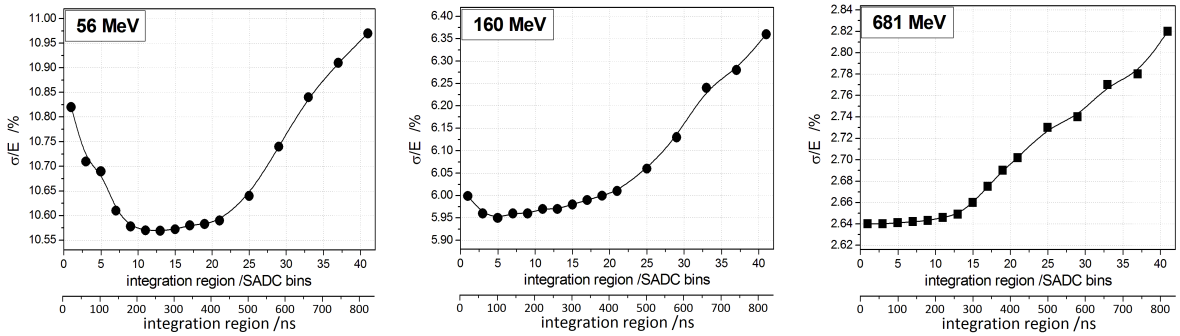

Figure 4.42: Dependence of the relative energy resolution of a 3 × 3 array on the integration length for selected incident photon energies of 56 MeV (left), 160 MeV (center) and 681 MeV (right).

The resolution scan shows that for an energy of 56 MeV a slight improvement of the energy resolution can be achieved for an increasing integration region. However, after a minimum is reached between 180 ns and 420 ns a deterioration of the relative energy resolution sets in. This behavior is consistent with the scan of the threshold as a function of the integration region in figure 4.30 which also showed a minimum in this region and an increase of the threshold for larger integrals. This minimum can be explained by an optimum of the signal to noise ratio for this integration region around the minimum. After this minimum, due to the signal shape the increase of the integral value becomes smaller and smaller for larger integration regions, while the signal noise does not show this behavior, causing a deterioration of the signal to noise ratio. Nevertheless, the observed behavior is a direct result of the noise characteristics observed for the ASIC signals and has to be adjusted to the individual noise of each setup. For the highest investigated energy of 681 MeV no minimum can be observed since most of the signal amplitudes in the outer crystals of the 3 × 3 array are significantly higher than the noise level, but also here a deterioration of the resolution takes place for integration regions larger than 220 ns. To obtain an optimal energy resolution an integration region of 220 ns is selected. The corresponding relative energy resolution curve in comparison to the results of the peak sensing feature extraction is shown in figure 4.43 The left part of the figure shows that the energy resolution is identical over most of the energy region. The slight improvement at the highest energies is caused by the compensation of the saturation of the amplitude for the highest energies by the integration. For energies below 130 MeV an increasing improvement of the relative energy resolution can be observed, which is shown in an amplified view in the right part of the figure. For 56 MeV an improvement of approximately 0.3 percent points can be observed which is approximately half of the improvement which has been achieved for this photon energy by the fit of the pulse shape.

An extreme case of the combination of the peak sensing and the integrating feature extraction is the integration of the complete pulse around the minimum. For this method, the pulse is integrated to both directions until the absolute value of the amplitude is lower than a certain threshold. Figure 4.44 sows the relative energy resolution obtained for a threshold of $3{\cdot}\sigma_{\mathrm{noise}}$ = 2.7 MeV and $1{\cdot}\sigma_{\mathrm{noise}}$ = 0.9 MeV in comparison to the results of the peak sensing feature extraction.

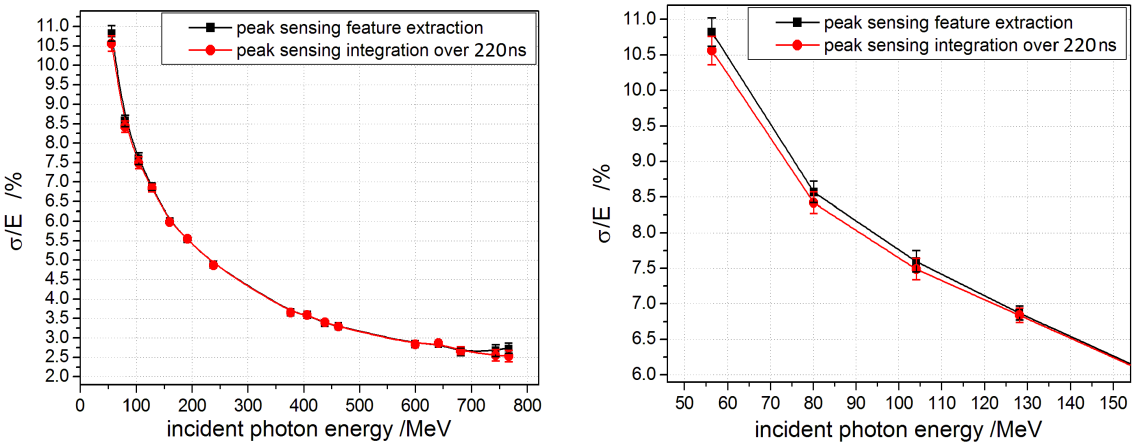

Figure 4.43: Comparison of the energy resolution obtained for a 3 × 3 array with the peak sensing feature extraction (black points) and the integration of the pulse shape in a region of 220 ns around the minimum of the negative pulse. The left figure shows the complete energy range, while the right figure presents the energy range below 150 MeV in which an integration of the pulse shape improves the energy resolution. In both cases the cosmic calibration for a horizontally aligned prototype and a threshold of 2.7 MeV are used.

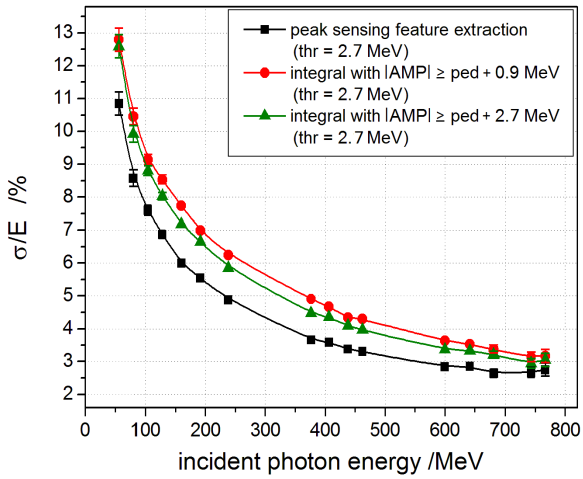

Figure 4.44: Energy resolution obtained from the integration of the complete pulse. The pulse is accepted for the energy sum if the amplitude of the pulse exceeds a threshold of 2.7 MeV. The pulse is integrated to both directions until the absolute value of the amplitude is lower than $3{\cdot}\sigma_{\text{noise}} = 2.7$ MeV (green points) or $1{\cdot}\sigma_{\text{noise}} = 0.9$ MeV (red points). For comparison the energy resolution obtained with the peak sensing feature extraction with a threshold of 2.7 MeV is shown (black points).

As expected from the resolution scan in figure 4.42 the electronic noise within the relatively large integration region deteriorates the relative energy resolution. The impact of the electronic noise is especially obvious if the two curves with different integration thresholds are compared, showing an improved resolution for a threshold corresponding to $3{\cdot}\sigma_{\text{noise}}$ compared to a threshold of $1{\cdot}\sigma_{\text{noise}}$.

The comparison of the different methods of the integrating feature extraction shows that for the noise characteristics provided by the ASIC implemented in the present prototype, only an

integration over a limited range around the extremum of the trace provides an improvement of the relative energy resolution compared to the peak sensing feature extraction.

Another possible approach to extract the energy information of a 3 × 3 array is the **direct sum of the recorded sampling ADC traces** of all crystals included in the array. Since a common readout with a trigger on only one APD of the central crystal has been applied during the experiment, all traces appear at the same time and can be added bin wise in each event. In a first step, the baseline is determined and the signals of the single channels are inverted and shifted to zero to generate a common baseline for all traces. For the relative calibration of the two APDs, the factors obtained in section 4.2.3 and for the relative calibration of the crystals, the horizontal cosmic calibration from section 4.2.4 has been applied. No threshold has been applied to the trace sum, since in an ideal case the positive and negative components of the symmetric electronic noise distribution around the baseline should cancel themselves out in the energy sum. Figure 4.45 (left) shows a typical sample of the sum of the calibrated traces of the high gain output.

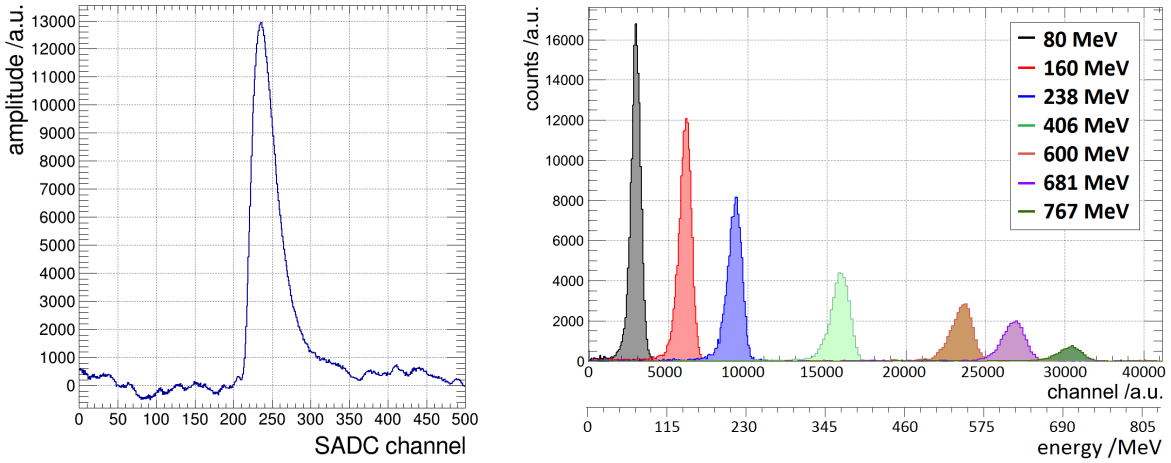

Figure 4.45: Added trace for all detectors of the 3 × 3 array (left) and resulting energy distributions for selected energies between 80 MeV and 767 MeV (right).

The fluctuations of the baseline already indicate that the noise is even increased in some regions and not reduced as it can be expected for an ideal statistical averaging. This effect can be explained by the irregular behavior of some traces, especially from detectors 1 and 4 which show a correlated oscillation of the trace which could not be completely corrected. On the other hand, a nicely smooth signal pulse has been obtained. The energy distributions, obtained from this pulses with the peak sensing feature extraction are shown in the right part of figure 4.45. No significant difference to the energy distributions obtained with the peak sensing feature extraction in figure 4.37 can be observed by eye. Also for these distributions, the peak positions and the relative energy resolution have been extracted by a fit with a Novosibirsk-function. The results for the linearity of the energy response and the relative energy resolution in comparison to the classical method are shown in figure 4.46. The amplitudes show a quite good linearity. Only for the lowest energies, a slight deviation with a trend to lower values can be observed. For the relative energy resolution, comparable or even slightly better values can be obtained for energies above 150 MeV, compared to the classical peak-sensing feature extraction of the individual detectors. Only for energies below 150 MeV,

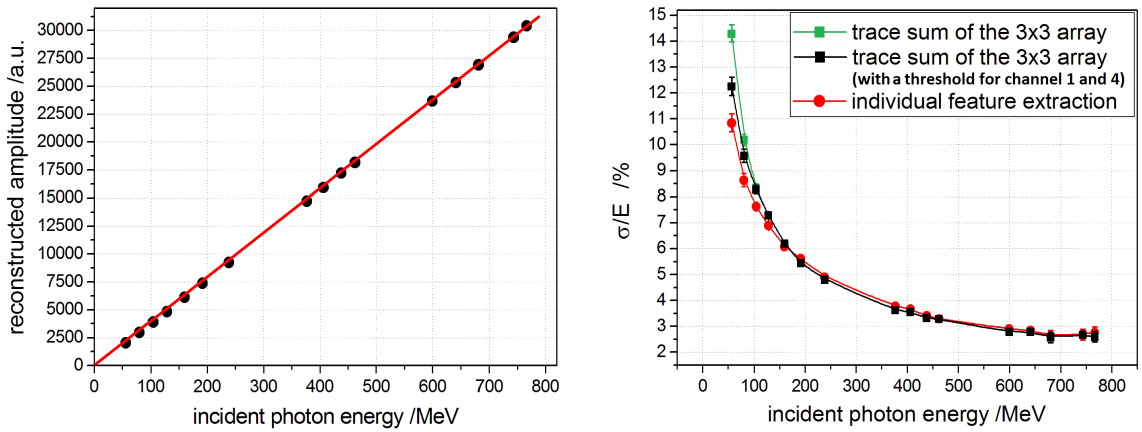

Figure 4.46: Linearity (left) and relative energy resolution (right) for the direct sum of all traces of the 3 × 3 array without any threshold (green points) and with a threshold of 6 MeV for channel 1 and 4 (black points). For comparison the energy resolution for an individual feature extraction of all detectors is shown.

the relative energy resolution is significantly deteriorated. This increase of the energy resolution at low energies in combination with the increased fluctuations of the baseline in figure 4.45 (left) shows that the electronic noise is not canceled out completely in the energy sum. This can be explained on the one hand by the low frequency oscillations, observed in the traces of channel 1 and 4 and on the other hand by partly correlated noise contributions in some channels which have a significant influence on the trace sum at low energies due to the missing threshold. To investigate the impact of correlated noise, a second trace sum has been calculated, in which the traces of channel 1 and 4 are only added if they exceed a threshold of 6 MeV, which is above the level of the correlated noise. Figure 4.46 (right) shows that this method improves the energy resolution at low energies compared to the complete trace sum, which directly proofs that the deterioration is caused by correlated noise. Under the absence of correlated noise the same or even a slightly better energy resolution than for an individual feature extraction can be expected, also for low energies. The same behavior of the energy resolution at low energies can be observed, if no threshold is applied and negative values are allowed in the peak sensing feature extraction of the individual detectors. This proofs that all peaks appear at the same position due to the common readout. Therefore, a deterioration of the energy resolution at low energies due to a shift of the recorded pulse can be excluded.

For the following analysis, the peak-sensing feature extraction has been used, since it requires the lowest computing effort and provides one of the best results over the complete energy range.

Comparison of the low- and high- gain branch

As a next step, the relative energy resolution obtained for the 3 × 3 array with the information extracted from the low- and high- gain branch of the ASIC will be compared. Figure 4.47 shows the obtained energy resolutions for the two branches and for the combination of the two branches, using the low gain data for energies in a single channel above approximately 400 MeV. For the high gain and the combination of the two branches, a threshold of 2.7 MeV

has been used, while for the low gain a threshold of 5.2 MeV has been applied due to the increased signal to noise ratio. For crystal 9 which has no low gain output, the scaled high gain information was used to substitute it.

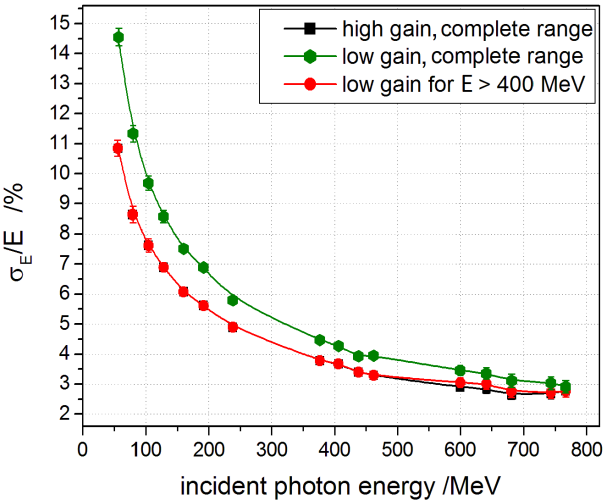

Figure 4.47: Comparison of the energy resolution of the high gain (black) and the low gain (green) branch. Like determined earlier, a threshold of 2.7 MeV for the high gain and 5.2 MeV for the low gain has been applied. The red curve represents a mixture of both branches, for which the low gain information is used for a channel, if the detected energy in this channel exceeds 400 MeV. For most of the points, the red curve overlaps the black one, since the values are identical.

As expected, due to the worse signal to noise ratio and the resulting high single crystal threshold, the resolution of the 3 × 3 energy sum, extracted from the low-gain branch for all crystals of the array, is significantly worse than for the high-gain branch, especially at low energies. However, if the two branches are combined and the low gain branch is only used for a single channel if its amplitude exceeds a level of 400 MeV, approximately the same energy resolution like for the high-gain branch can be achieved for the complete energy range.

Linearity and resolution of the energy response

If the combination of the high- and low- gain branch is used, a completely linear response, shown in figure 4.48 (left), can be achieved for the energy sum of the 3 × 3 array. Also the standard deviation of the energy distribution, shown in figure 4.48 (right), shows the expected $\sqrt{E}$ dependence.

Based on the discussed optimizations, the final energy resolution is shown in figure 4.49 for the sum of both APDs of each crystal (blue points) and for a readout of only one APD per crystal (red points). For crystal seven and nine only one APD is available in both cases. The comparison of the two cases shows that especially at high energies no significant difference can be observed. Only for the lowest energies, a slightly better resolution can be achieved with both APDs. The average improvement factor between the resolution for one APD and for two APDs is in the order of 0.96 and improves for the lowest energies down to 0.94. For the interpretation of this results, it has to be considered that the resolution with both APDs can still be influenced by the two channels with one missing APD. Nevertheless, the use of

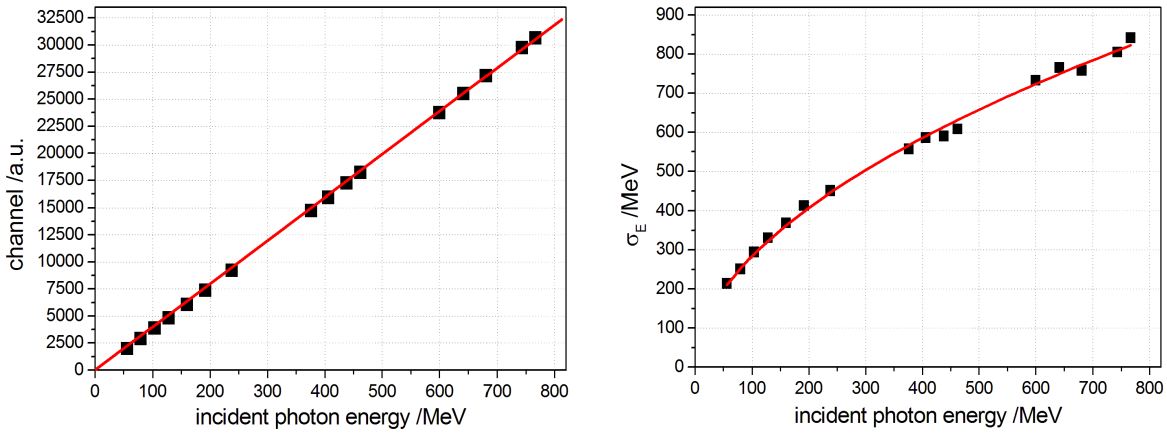

Figure 4.48: Linearity of the reconstructed amplitude (left) and behavior of the standard deviation (right) for the energy sum of a 3 × 3 array of de-polished type 2 crystals within PROTO 120 at a temperature of -25°C.

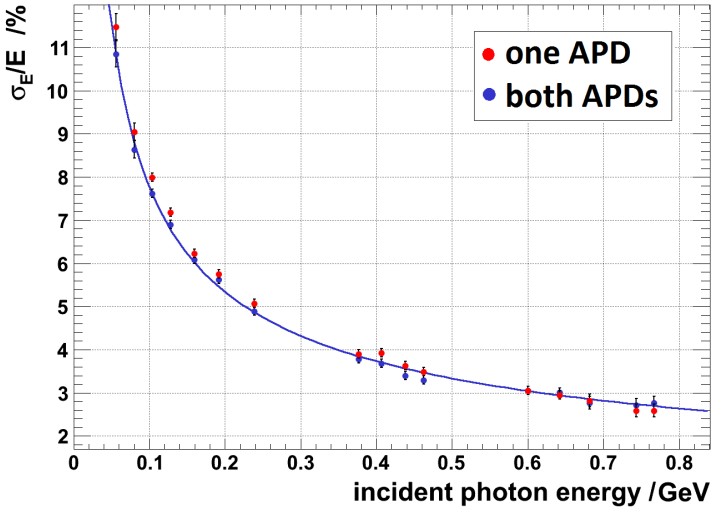

Figure 4.49: Relative energy resolution for a 3 × 3 array of de-polished type 2 crystals within PROTO 120 at a temperature of -25°C for a readout of only one (red points) and for the sum of both (blue points) APDs per crystal. A threshold of 2.7 MeV has been applied. The blue line represents a fit of the points obtained for a readout with both APDs.

two APDs per crystal helps to reduce the single crystal threshold, which has been shown in section 4.2.5. A more detailed discussion on the improvement by two APDs compared to a single APD and a comparison to simulated values will be given in section 4.3.5. The energy resolution obtained with both APDs has been fitted with the blue curve and can be described by the following parametrization:

$$\frac{\sigma_E}{E} = \frac{0.27\%}{E/GeV} \oplus \frac{2.30\%}{\sqrt{E/GeV}} \oplus 0.5\% \tag{4.32}$$

4.2.7 Comparison of the energy resolution of a 3 × 3 array with de-polished and a 3 × 3 array with polished crystals

For comparison with the de-polished crystals, another 3 × 3 array with polished type 2 crystals has been tested within PROTO 120. The performance of polished crystals will be discussed in detail in [CR16]. The array with polished crystals has been analyzed with the same optimizations and time cuts like the array with de-polished crystals, presented in this work. Also for the array with polished crystals a relative calibration with cosmic muons, interacting on a horizontally oriented prototype showed the best results and the peak-sensing feature extraction has been applied. The optimal threshold for the array with polished crystals has been determined to (2.7-2.8) MeV, like for the array with de-polished crystals. To provide identical conditions, also for the array with polished crystals, the threshold of the crystal in the upper left corner has been set to 6 MeV. The fact that the threshold stays at approximately the same level for both arrays, directly reflects the results from the measurement of the position dependent light yield in section 4.1.1 which showed for polished and de-polished type 2 crystals on average a comparable light yield for a distance to the photo-sensor between 14 cm and 18 cm. Since this region contains the center of gravity of the electromagnetic shower in the investigated energy range, a comparable signal to noise ratio can be expected for polished and de-polished crystals.

A comparison of the energy distributions obtained with a 3 × 3 array of polished and a 3 × 3 array of de-polished crystals for incident photon energies of 160 MeV and 681 MeV is shown in figure 4.50.

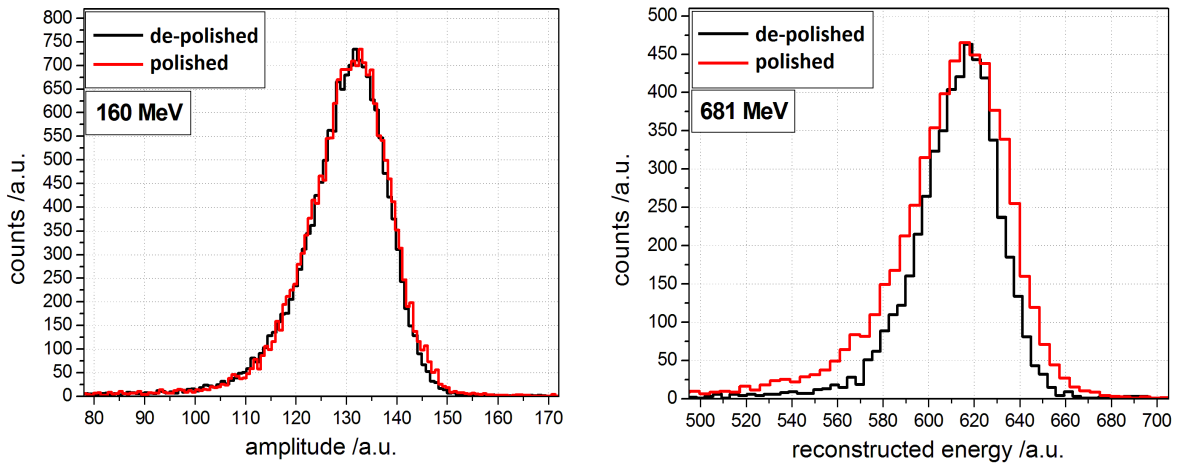

Figure 4.50: Comparison of the energy distributions obtained with a 3 × 3 array of polished and a 3 × 3 array of de-polished crystals for incident photon energies of 160 MeV (left) and 681 MeV (right). The reconstructed energy is scaled to the position of the distributions maximum.

While the distributions obtained from both arrays show a comparable shape at 160 MeV, a significant reduction of the width can be observed for the array with de-polished crystals at 681 MeV. This behavior is also reflected by the relative energy resolution curves, which are compared for the two 3 × 3 arrays with polished and de-polished crystals, analyzed under identical conditions, in figure 4.51.

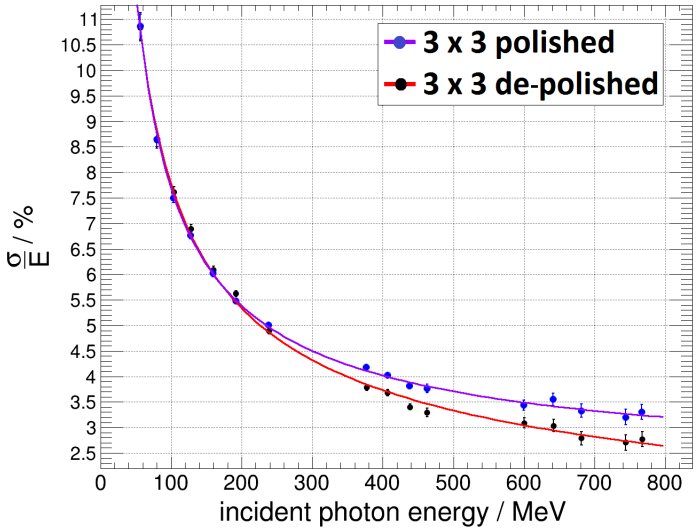

Figure 4.51: Relative energy resolution for a 3 × 3 array of polished and a 3 × 3 array of de-polished type 2 crystals within PROTO 120 at a temperature of -25°C with a single crystal threshold of 2.8 MeV for both cases.

The two resolution curves show that a significant improvement of the relative energy resolution can be achieved with de-polished type 2 crystals in the energy range above 200 MeV. In the energy range from 200 MeV down to 50 MeV approximately the same energy resolution values have been obtained. Especially, no significant deterioration of the energy resolution can be observed for de-polished crystals down to an incident photon energy of 50 MeV. The purple and red lines in figure 4.51 show a fit of the two energy resolution curves. The parametrization for the 3 × 3 array of polished crystals is given in equation 4.33. As a direct comparison equation 4.34 provides the parametrization of the de-polished array, which was already obtained in section 4.2.6.

$$\frac{\sigma_E}{E} = \frac{(0.34 \pm 0.05)\%}{E/GeV} \oplus \frac{(2.07 \pm 0.09)\%}{\sqrt{E/GeV}} \oplus (2.18 \pm 0.20)\% \tag{4.33}$$

$$\frac{\sigma_E}{E} = \frac{(0.27 \pm 0.03)\%}{E/GeV} \oplus \frac{(2.30 \pm 0.04)\%}{\sqrt{E/GeV}} \oplus (0.50 \pm 0.20)\% \tag{4.34}$$

The main effect of the reduced non-uniformity can be seen in a significant reduction of the constant term of the energy resolution parametrization from above 2 % down to 0.5 %. This reduction of the constant term shows that the uniformity of the light yield has the strongest impact at high energies. Also the reduction of the light yield in the front part of the crystal has a direct effect on the parametrization. It causes a slight increase of the stochastic term from 2.07 % to 2.3 %. Only the electronic noise term, introduced by the APD readout stays at the same level, since comparable APDs and the same readout electronics have been used for both arrays. A more detailed discussion and a comparison to simulations can be found in section 4.3.5.

4.3 GEANT4 simulations of PROTO 120

To obtain a better understanding of the energy deposition distribution within the lead tungstate crystal array and to study the influence of the light collection non-uniformity on the energy resolution, a model of PROTO 120, including the scintillation and surface properties of the materials has been implemented in GEANT4 (v. 4.9.4) [AAA03, AAA06]. Since a reproduction of the experimental non-uniformity of the crystals with the ray-tracing model provided by GEANT4 is only possible under certain assumptions, and since a simulation of the complete light collection, especially for high energetic probes, requires a significant amount of computing power, a special model will be presented which enables the calculation of the detector response based on the energy deposition distribution provided by GEANT4, combined with the measured non-uniformity curve and other empirical properties of the crystals, the APDs and the readout.

4.3.1 Implementation of a single PANDA PWO crystal and PROTO 120

As a first step, single PANDA lead tungstate crystals with the different geometries of the barrel have been implemented. Finally the overall geometry of PROTO 120 has been reproduced.

Implementation of a single crystal: Each crystal is realized as an independent detector cell. For this purpose the crystal volume has been implemented with the dimensions given in table 1.5 for the different geometries. In a second step, the scintillation and optical properties have been assigned to the material. The wavelength dependent refraction index and absorption length of PWO are shown in figure 4.52.

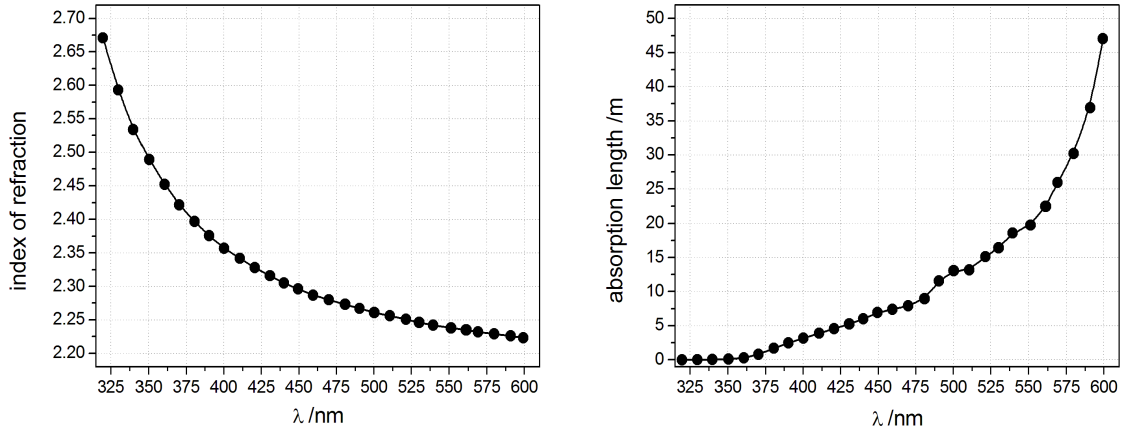

Figure 4.52: Average index of refraction [BBB97] (left) and absorption length [TDe09] (right) of PWO.

Lead tungstate is a double refractive material, showing two slightly different indices of refraction, depending on the crystal orientation [BBB97]. Since presently no model for a double refractive material is available in GEANT4, the average of the two indices is used. The implemented luminescence spectrum of PWO can be found in figure 1.30. For the light yield, a value of 2.5 % of NaI(Tl) has been determined for PWO-II at -25°C in [TDe09], which

corresponds to 950 photons/MeV. The crystal is surrounded by an air volume with identical geometry, of 0.1 mm thickness. The air volume is covered by a 0.6 mm thick polymeric ($C_{14}O_4H_{10}$) VM2000 foil with a density of 1.36 g/cm^3, acting as a mirror reflective layer (reflectivity $\sim$ 0.94 [JM08]) for the scintillation photons. For the implementation in PROTO 120, a carbon fiber alveole with a density of 1.8 g/cm^3 is added as an outer cover. To achieve the total alveole thickness of 0.3 mm between two neighboring crystals in the prototype, the cover thickness of a single crystal is set to half of this value. For the front side of the crystal, the same structure is used since the concept of the front stoppers is not finalized yet. On the rear side, the active areas of the two APDs are placed at the correct positions with a thin layer of silicon based glue (n=1.413 at 420 nm) between the APDs and the crystal. The other parts of the crystals rear face are covered by an air layer and a VM2000 layer like the side faces of the crystal. Behind the APDs is the plastic capsule added. Figure 4.53 (left) shows a three-dimensional model of a type 1 crystal positioned in a rectangular box, visualizing the tapering of the side faces.

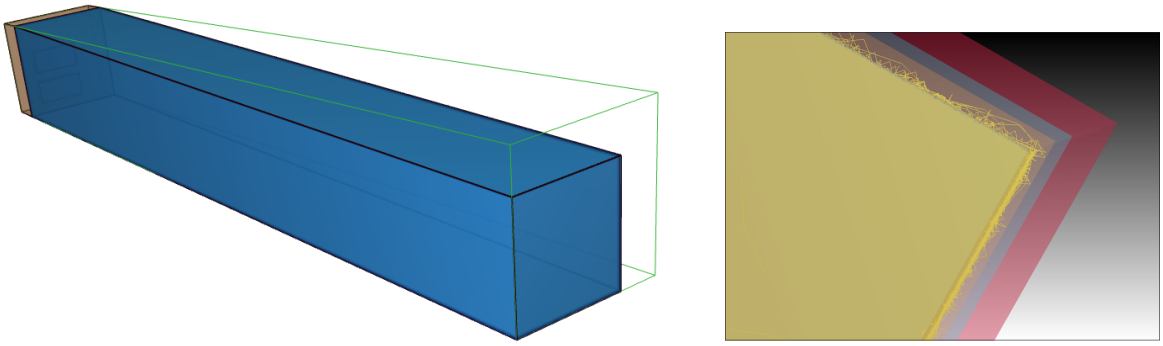

Figure 4.53: Left: Model of a type 1 PANDA PWO crystal with the APDs glued to the end face of the crystal. The tapering of the crystal is visualized by the rectangular box shown in green. Right: Detailed structure of the crystal wrapping, with the air-gap (brown), the VM2000 reflector foil (gray) and the carbon fiber alveole (red). The yellow lines represent single photon tracks. If a photon leaves the crystal volume, it is reflected by the VM2000 layer.

The right part of figure 4.53 illustrates the layer structure of the materials surrounding the crystal. The yellow lines illustrate the tracks of optical photons within the crystal and in the air-gap between crystal and reflector.

Implementation of PROTO 120: For the realization of the complete prototype with 120 crystals, a sample of each of the first three crystal types of the PANDA geometry is implemented in a mirror symmetric left and a right configuration. Each of the 2 $\times$ 3 different crystal samples is then duplicated twenty times and arranged on the basis of the dimensions and angles obtained from CAD drawings of PROTO 120. Figure 4.54 shows a three-dimensional drawing of the implemented prototype in a front view (top) and from both sides (bottom). The different colored arrays represent the 4 $\times$ 10 arrays with the different crystal geometries. The small rectangles, visible on the rear side of some crystals, represent the APDs.

The 3 $\times$ 3 array with de-polished crystals is positioned in the lower left edge of the type 2 section (red). Compared to the experimental setup, the prototype is rotated by 180°.

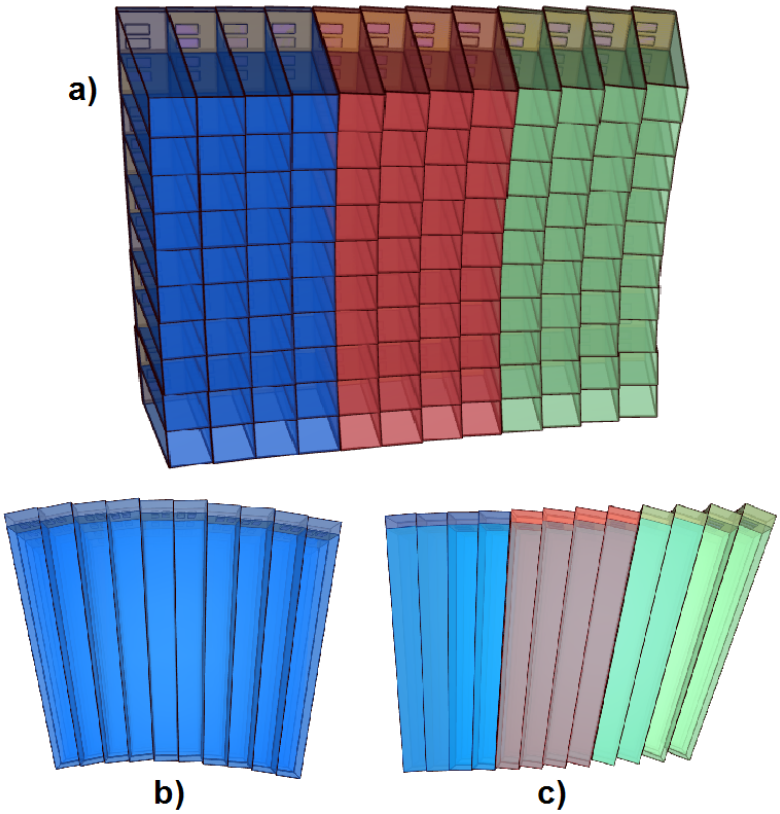

Figure 4.54: Three dimensional model of PROTO 120 implemented in GEANT4. a) Front view of the complete prototype. The different crystal geometries are marked in blue (type 1), red (type 2) and green (type 3). b) Side view of the type 1 section. c) Top view of the different crystal geometries.

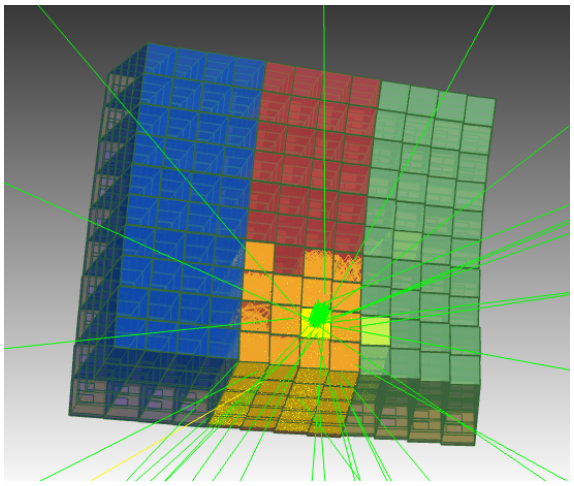

Figure 4.55: Integral picture of 50 events of a 25 MeV photon beam interacting in the center of the array with de-polished crystals. The direction of the incident high energetic photons is aligned to the axis of the target crystal. The incident photons as well as the scattered photons are shown in green, while scintillation photons propagating within the crystal are shown as yellow lines.

To simulate the experimental results, the photon beam is aligned to the central crystal of the 3 × 3 array. For the photon beam a Gaussian beam profile with a standard deviation of 3.6 mm is implemented. Figure 4.55 shows an integral picture of the interaction of 50 events of a 25 MeV photon beam. The responding crystals are highlighted by the yellow color introduced by the traces of the scintillation photons, generated in this crystals. Due to the low energy, several back scattered photons can be observed.

4.3.2 Longitudinal and lateral shower distributions

The influence of the non-uniformity in light collection on the energy resolution is mainly determined by the distribution of the energy deposition within the crystal. To get a feeling for this distribution and especially for its variation from event to event and its energy dependence, the electromagnetic shower has been simulated in GEANT4. In each step of the simulation, the deposited energy and the three-dimensional coordinate of the energy deposition have been recorded. Figure 4.56 shows the obtained two-dimensional shower profiles for an incident photon energy of 50 MeV and 10 GeV within PROTO 120 averaged over 10000 events. The photons are impinging from the right hand side.

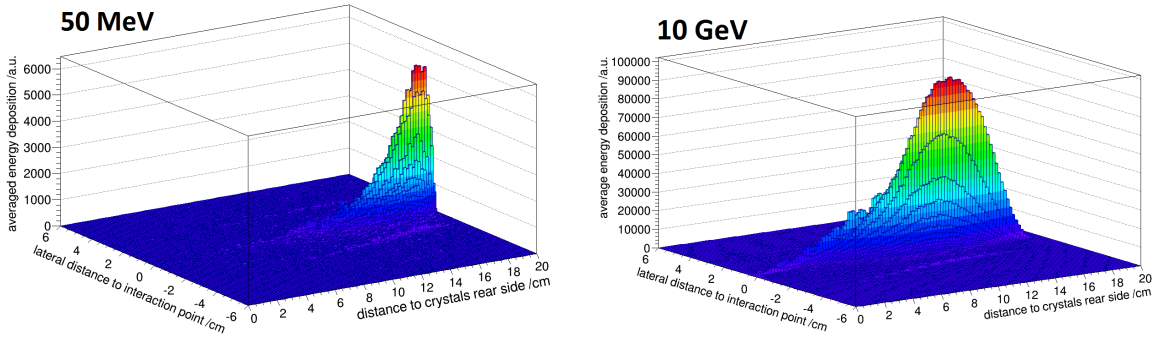

Figure 4.56: Three dimensional shower profile of 50 MeV (left) and 10 GeV (right) photons interacting with PROTO 120, averaged over up to 10000 events. The photons are impinging from the right hand side on the front face of the crystal.

The shower profiles show that for a photon energy of 50 MeV the maximal energy deposition occurs within the first two centimeters of the crystal and most of the energy is deposited in the first half of the crystal. For an incident photon energy of 10 GeV the shower shows a significantly larger spread in longitudinal and lateral direction and also the position of the maximal energy deposition moves significantly deeper into the crystal.

Longitudinal shower distribution

To obtain a more qualitative picture of the shower profile, a projection of the energy deposition has been performed on the longitudinal axis. Figure 4.57 (left) shows this projection for selected photon energies between 50 MeV and 10 GeV. The comparison of the shower profiles illustrates the increasing width of the shower for higher energies, which is also documented by the increase of the shower spread, defined as the standard deviation of the energy deposition position within the crystal, for an increasing incident photon energy in figure 4.57 (right).

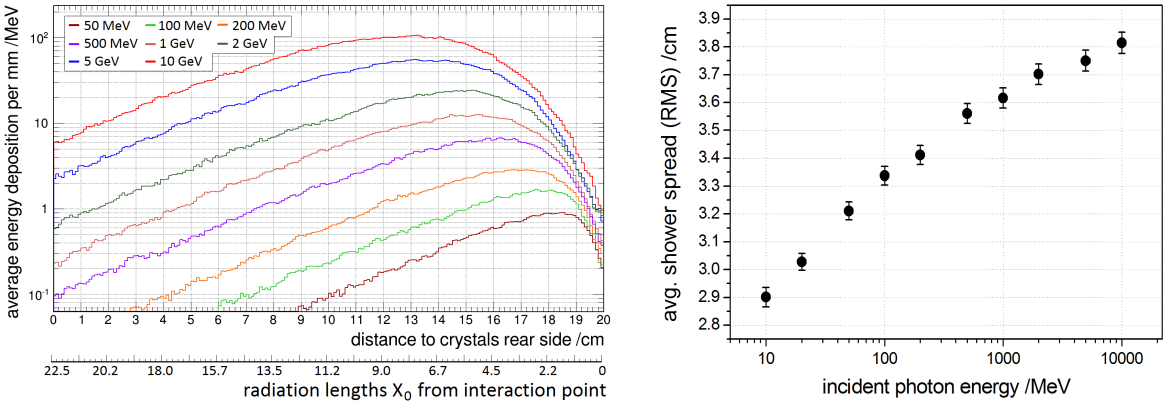

Figure 4.57: Left: Shower profile of the pure energy deposition for selected incident photon energies between 50 MeV and 10 GeV in longitudinal direction. Each distribution is averaged over up to 2000 events. The photon beam interacts from the right hand side at a distance to the crystals rear face of 20 cm. Right: Energy dependence of the average shower spread, defined as the standard deviation of the energy deposition position within the crystal.

The slight saturation of the increase of the shower spread at high energies can be explained by the shower leakage to the rear side of the crystal for the highest energies, which is clearly observable in figure 4.57 (left). In addition to this larger spread of the shower, also the point of the maximal energy deposition and the center of gravity of the shower move deeper into the crystal if the incident photon energy increases. Figure 4.58 shows the energy dependence of this two quantities.

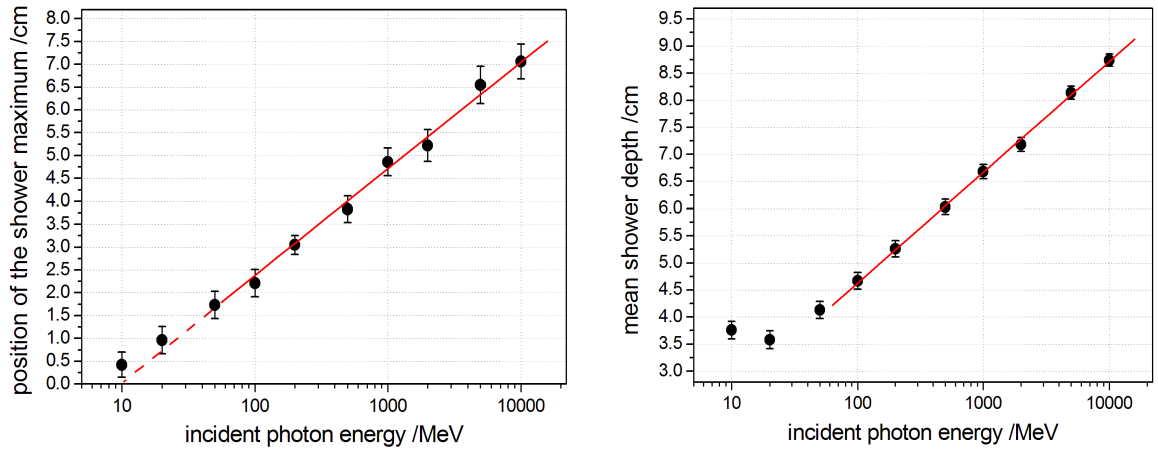

Figure 4.58: Energy dependence of the shower-maximum (left) and the showers center of gravity (right) for a photon beam interacting with PROTO 120.

As expected from the theoretical model in equations 1.36 and 1.37, the point of the maximal energy deposition as well as the center of gravity of the shower follow a logarithmic energy dependence if the incident photon energy is significantly larger than the critical energy E_C. For lead tungstate ($E_C = 9.6$ MeV), this condition is fulfilled for energies above approximately 100 MeV. The obtained parametrization of the energy dependence of the shower maximum x_{max} and the center of gravity of the shower x_{mean} in the applicable energy range above

100 MeV are given by the following expressions:

$$\begin{aligned} x_{max}(E) &= (-1.68 \pm 0.16)\ cm + (0.92 \pm 0.03)\ cm \cdot ln(E/MeV) \\ &= (-1.89 \pm 0.18)\ X_0 + (1.03 \pm 0.03)\ X_0 \cdot ln(E/MeV) \end{aligned} \tag{4.35}$$

$$\begin{aligned} x_{mean}(E) &= (0.47 \pm 0.14)\ cm + (0.896 \pm 0.018)\ cm \cdot ln(E/MeV) \\ &= (0.53 \pm 0.16)\ X_0 + (1.01 \pm 0.02)\ X_0 \cdot ln(E/MeV) \end{aligned} \tag{4.36}$$

with the radiation length X_0 of lead tungstate. Both parametrization show approximately the same slope, but an absolute shift of 2.4 X_0 relative to each other. Compared to theory (see eqn. 1.36 and 1.37), the slope parameter completely agrees with the expectation of 1.01 X_0. Only the relative shift of the two curves is a bit larger than the theoretically expected 1.7 X_0, which can be explained by the longitudinal and lateral energy leakage out of the prototype, especially at high energies in contrast to an infinitely large single crystal assumed in theory. In addition, the offset parameter strongly depends on the fit and on the error range of the determined positions of the shower maximum.

For the smearing of the detector response by the light collection non-uniformity also the variation of the shower from event to event plays an important role. For a more detailed investigation of this variation, the distribution of the center of gravity of the electromagnetic shower

$$z_{cg} = \frac{\sum_i E_i \cdot z_i}{\sum_i E_i} \tag{4.37}$$

with the energy deposition E_i at the longitudinal position z_i of the crystal, is plotted in figure 4.59 (left) for several events at incident photon energies of 56 MeV, 437 MeV and 5 GeV.

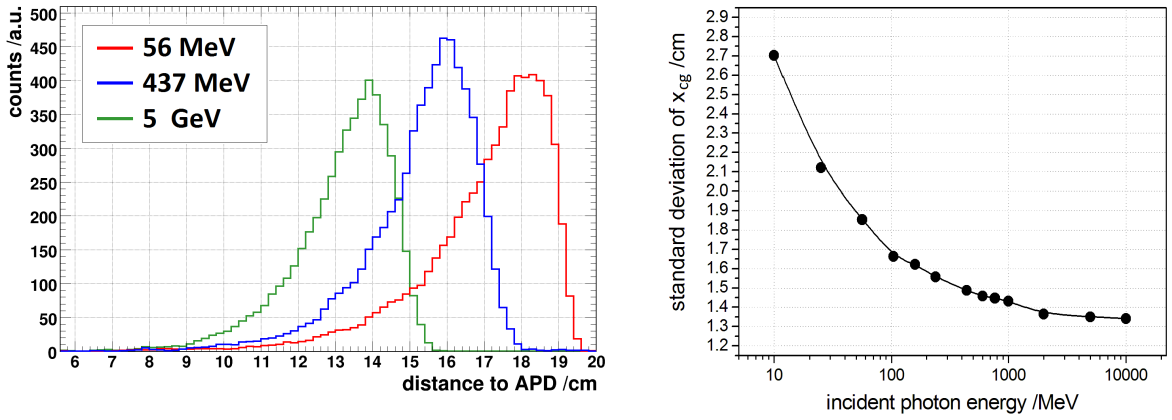

Figure 4.59: Left: Distribution of the center of gravity of the energy deposition for several events at selected incident photon energies between 56 MeV and 5 GeV. The photon beam interacts from the right hand side at a distance to the APDs of 20 cm. Right: Energy dependence of the standard deviation of the center of gravity of the energy deposition within the crystals.

The energy dependence of the standard deviation of the distributions, shown in figure 4.59 (right) demonstrates that the variation of the center of gravity becomes smaller for higher energies. This is in contrast to the spread of the average shower itself (see figure 4.57), which

increases for higher energies, and can be explained by a stronger impact of shower fluctuation at low energies.

In summary, the shower profiles and the distributions of the center of gravity of the shower indicate that the energy deposition is spread over the complete crystal at high energies and still over a significant part of the crystal at low energies. In addition, a significant variation of the center of gravity of the shower from event to event can be observed for all energies. The combination of this longitudinal spread of the shower with a longitudinal non-uniformity in light collection causes a smearing of the energy response, resulting in a deterioration of the energy resolution. Additionally a non-linearity of the energy response is introduced by the energy dependence of the average shower profile in combination with the non-uniform light collection. Therefore, an unification of the light collection can help to improve these properties.

Lateral shower distribution

To estimate the lateral energy leakage caused by a limited cluster size and to determine the fraction of the energy deposited in a single crystal and in clusters of different sizes, also the lateral energy distribution of the electromagnetic shower is an important characteristic for a calorimeter. Figure 4.60 shows a projection of the shower in lateral direction for selected incident photon energies between 50 MeV and 2 GeV.

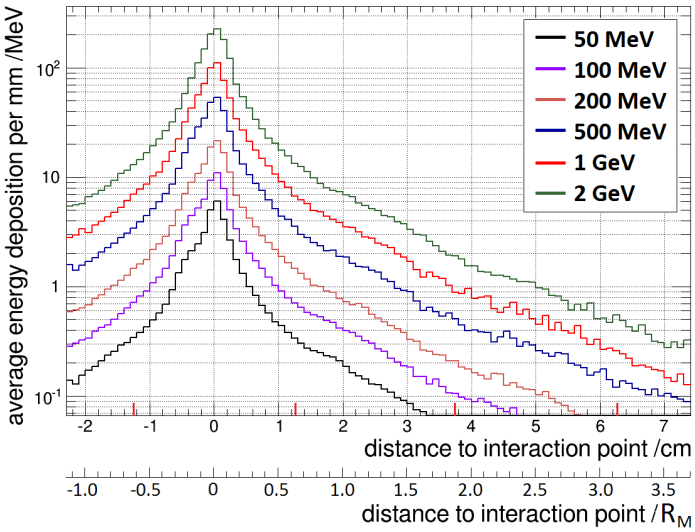

Figure 4.60: Energy deposition profile of the electromagnetic shower in lateral direction for selected energies between 50 MeV and 2 GeV. The photon beam with a Gaussian profile ($\sigma = 3.6$ mm) interacts in the center of a crystal. The red bars on the first axis indicate the average positions of the crystal edges.

The figure illustrates that also in lateral directions a larger spread of the shower can be expected for an increase of the incident photon energy. The red bars on the first axis show the average dimension of one crystal. The bar at 3.75 cm, marking the edge of the 3×3 array, illustrates the increasing amount of the lateral shower leakage out of the 3×3 array for increasing energies. The energy dependence of the energy fraction deposited in a single

crystal and in a 3 × 3 array of crystals is shown in figure 4.61 for the peak position and the mean value of the energy distribution of the contained energy.

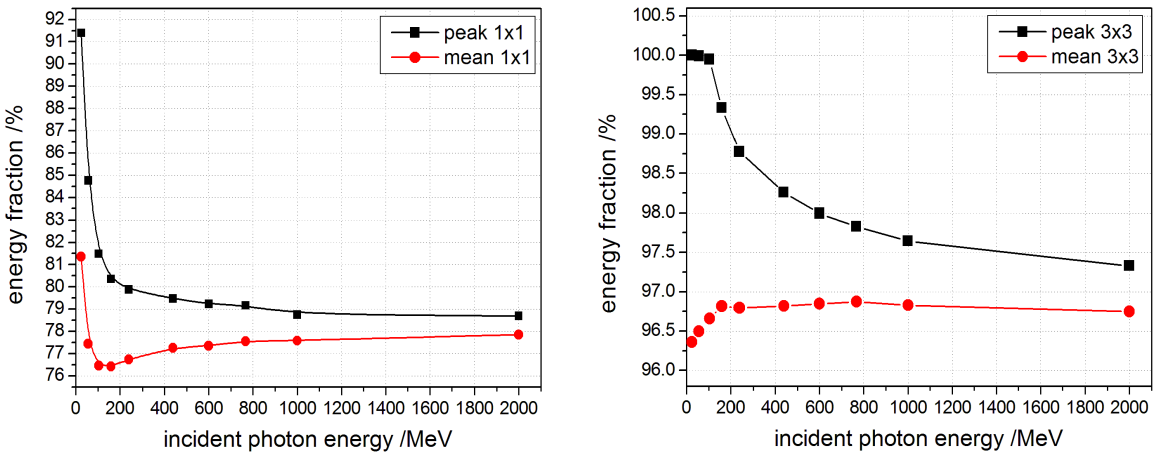

Figure 4.61: Simulated energy dependence of the energy fraction deposited in a single crystal (left) and in a 3 × 3 array of crystals (right) for a Gaussian beam profile with a standard deviation of 3.6 mm interacting in the center of the crystal.

The average lateral thickness of a type 2 crystal in its center is approximately 2.5 cm and its diagonal has a length of approximately 3.5 cm. This leads to an inner radius of a 3 × 3 array of approximately 3.75 cm (1.86 R_M) and to an outer radius in the order of 5.3 cm (2.65 R_M). According to this values, an energy containment between 94 % and 98 % can be theoretically expected for the 3 × 3 array in the energy region around 1 GeV. The simulated values nicely fit in this expectation range.

As a comparison with the experimental values, also the fraction of the energy deposited in the central crystal relative to the energy contained in a 3 × 3 array has been calculated. The obtained values in comparison to the experimental values from figure 4.34 are shown in figure 4.62. A good agreement between the experimental and simulated values can be observed within the experimental error bars. Nevertheless, the simulation provides at low energies a slightly lower and at high energies a slightly higher fraction, compared to the general trend of the experimental values. This deviations may be introduced by a slight misalignment of the interaction angle in the experiment, resulting in a different behavior of the energy leakage. Otherwise, they can also be caused by a not completely realistic shower simulation of GEANT4, especially at low energies.

Another value which characterizes the shower distribution in lateral directions and which can be compared to the experiment is the multiplicity of the responding crystals above the threshold. Figure 4.63 shows a comparison of the experimental and simulated values for a threshold of 2.7 MeV. Also for the multiplicity, a good agreement between simulation and experiment can be observed. As expected due to the larger shower spread, the multiplicity increases with increasing incident photon energies. The variation of the multiplicity for different events displayed by the error bars of the simulated multiplicity in figure 4.63 is a direct indication for the strength of the shower fluctuations in lateral direction.

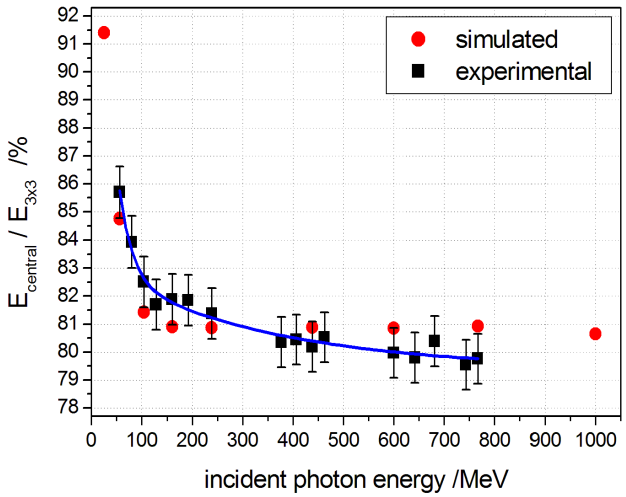

Figure 4.62: Simulated fraction of the energy deposited in the central cell of a 3 × 3 array (red points) in comparison to the experimental values from figure 4.34 (black points). The blue curve shows a fit of the experimental values.

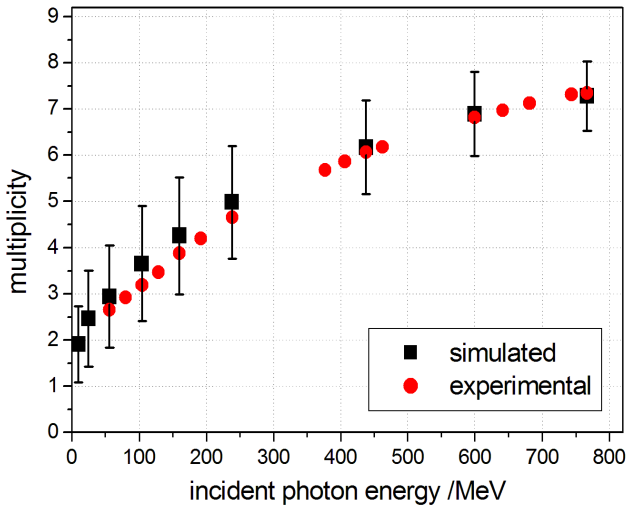

Figure 4.63: Comparison of the energy dependence of the simulated and the experimental crystal multiplicity for a 3 × 3 array. The error bars of the simulated values show the standard deviation of the value for different events. In the experiment a comparable standard deviation has been achieved, which is not shown in the figure due to clarity reasons.

4.3.3 Non-uniformity simulation based on ray tracing of optical photons

To investigate the influence of different optical properties on the non-uniformity in light collection in a tapered PWO crystal, the response of a single crystal has been simulated, using the ray tracing model for optical photons included in GEANT4. For this purpose a 80 MeV proton beam with a diameter of 2 mm has been shot at different positions on the side face of a single crystal. The advantage of low energetic protons is the localized energy deposition in the center of the crystal at a well defined longitudinal position. Figure 4.64

(left) shows the obtained non-uniformity curves for different transmissions of the crystal at 420 nm in comparison to the experimental curve measured with a 80 MeV proton beam at the AGOR facility at KVI Groningen [DAB13].

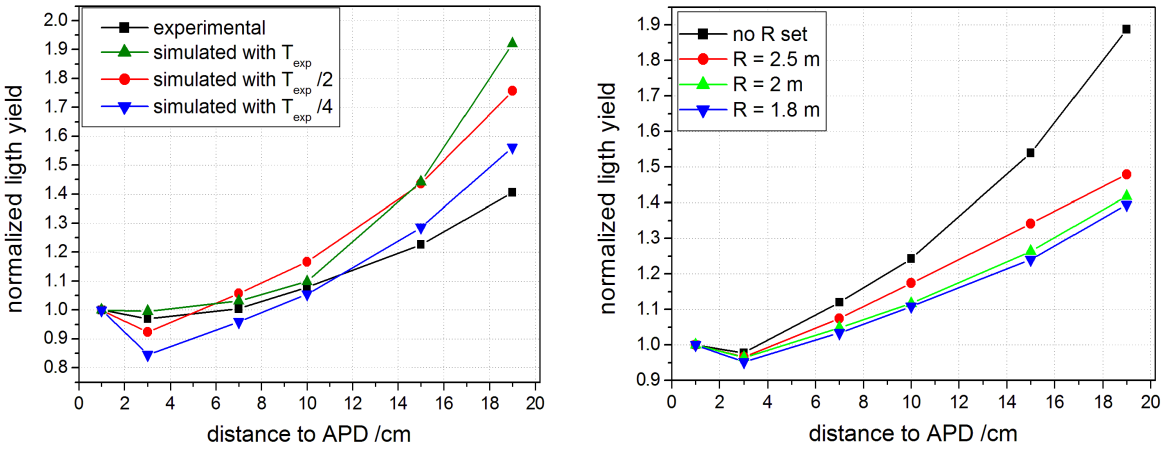

Figure 4.64: Simulated dependence of the non-uniformity in light collection on the transmission and the Rayleigh scattering in a type 1 PANDA crystal.

The figure shows that the simulated non-uniformity curve with the measured wavelength dependent transmission value T_{exp}, measured for a completely annealed crystal, provides a significantly too high non-uniformity factor in the front part of the crystal compared to the experimental values. Especially due to aging effects of the crystal introduced by radiation damage, the transmission of a crystal can be reduced over the time. To study the effect of such a reduction on the non-uniformity, the simulation has been repeated with half and a quarter of the measured transmission. With such a significantly reduced transmission, the non-uniformity in the front part of the crystal is strongly reduced, but at the same time the reduced transmission introduces a dip to the non-uniformity curve on the APD sided half of the crystal.

Another effect which can be introduced to the crystal by radiation damage, especially by hadrons is an increase of the amount of Rayleigh scattering in the crystal [HLL05]. This diffuse scattering of the photons by small defect centers in the crystal has been implemented with its typical λ^{-4} dependence, normalized to the mean free path lengths R of the scattering process at 420 nm. The effect of the different strengths of the Rayleigh scattering is shown in figure 4.64 (right). A comparison of the different curves shows that the implementation of the Rayleigh scattering reduces the non-uniformity in the front part of the crystal significantly to a level comparable to the experimentally measured curve without a strong increase of the dip which has been observed for a reduced transmission.

The observed behavior shows that the discrepancy between the experimental and and the simulated values is introduced by a diffuse scattering of the light in the real crystal. However, for a completely annealed crystal no significant impact of Rayleigh scattering is reported in literature [HLL05]. Therefore, the observed difference can not be described by the implementation of Rayleigh scattering. The diffuse scattering of the light, which reduces the non-uniformity of a real crystal compared to the simulation has to be introduced by the depolished chamfers of the crystal, covering all crystal edges and by macroscopic defects of the

crystal structure. While macroscopic defects can not be implemented into GEANT4, the implementation of the chamfers has been performed for the side faces, but only a slight decrease of the non-uniformity could be observed. At the same time, the complex geometry caused a significant increase of the computing effort. Also a simulation with SLITRANI [FXG02] in [DAB13] under consideration of more details, like the two refraction indices, provided higher values for the non-uniformity in light collection than the experiment.

4.3.4 Influence of a de-polished side face on the light collection

The comparison of the experimental position dependent light yield before and after the de-polishing procedure in section 4.1.1 showed a significant increase of the light yield in the rear part of the crystal and only a relatively small decrease of the light yield in the front part, compared to a perfectly polished crystal. To understand these effects, a simulation based on the ray-tracing model of GEANT4 has been performed. To reproduce the experimental conditions for the measurement of the position dependent light yield, the two LAAPDs in the setup of an individual crystal described in section 4.3.1 have been replaced by a PMT, covering the complete rear face of the crystal. In addition, a separate air layer has been placed on the most tapered side face of the crystal, enabling an individual definition of the surface properties of this side face. Within the UNIFIED model [LM96] GEANT4 provides basically two surface types, a perfectly polished surface and a rough surface. If a "polished" surface is selected, a perfectly flat surface with a normal vector orthogonal to the surface in all cases is simulated [LM96]. In contrast to this, a "ground" surface contains micro-facets with an angle α between the micro facets and the mean surface [LM96]. As an extension of this model a Gaussian smearing of the micro facet angle α by an user defined standard deviation σ_α can be implemented to define different degrees of roughness [LM96]. For the simulation three different configurations will be compared:

1. A perfectly polished crystal with all side faces defined as "polished".
2. A crystal with one of the tapered lateral side faces de-polished ("ground") and all other side faces "polished".
3. A crystal with all lateral side faces and the front face de-polished ("ground").

In addition, the simulation has been performed with and without the implementation of Rayleigh scattering, since section 4.3.3 showed that only the implementation of a diffuse scattering within the crystal can reproduce the experimentally measured non-uniformity of a tapered crystal. Therefore, it can be assumed that also for a de-polished crystal more realistic results can be obtained if Rayleigh scattering is implemented. For the mean free path of the Rayleigh scattering, section 4.3.3 showed that a value of 2.0 m at 420 nm provides the best agreement with the experimental results. The implemented Rayleigh scattering can be partly seen as a kind of substitution for irregularities of the crystal structure or surface quality, but also for other effects which cause a diffuse scattering during the light collection but cannot be implemented in the simulation model directly.

In a first step, the position dependent light yield of a type 2 crystal is simulated with the different configurations. The results are shown in figure 4.65 (left). The simulated position dependent light yield shows that the implementation of Rayleigh scattering only shows an

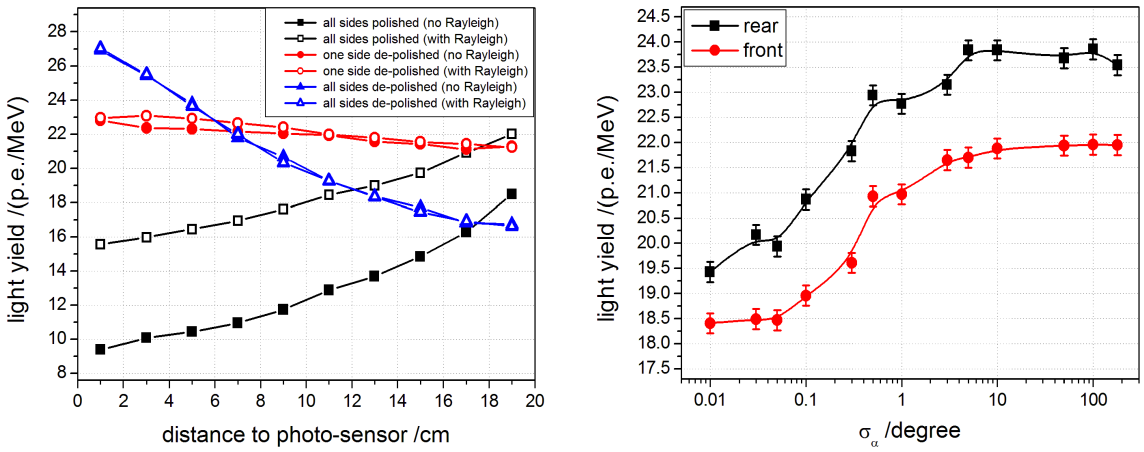

Figure 4.65: Left: Simulated position dependent light yield of a type 2 crystal with all side faces polished (black), with one de-polished lateral side face (red) and with all side faces de-polished (blue). The full points are simulated without the implementation of Rayleigh scattering an the open points with Rayleigh scattering. The readout is performed with a PMT covering the complete rear face of the crystal. Right: Light yield from the front and the rear part of a crystal with one de-polished side face for different degrees of smearing of the micro facet angle of the de-polished surface.

effect in a completely polished crystal. In this case the diffuse scattering interrupts the de-focusing of light propagating to the front face of the crystal and therefore increases the light yield. If one or more side-faces are de-polished, this de-focusing is already suppressed by the scattering of the light on the de-polished side face(s) and therefore no significant change can be observed. If the curves simulated with the implementation of Rayleigh scattering for a polished crystal and a crystal with one de-polished side face are compared, a good agreement with the experimental trend (see section 4.1.1) can be observed. Nevertheless, in contrast to the experimental results, the simulation shows a slightly negative slope of the position dependent light yield for a crystal with one de-polished side face. For CMS crystals it has been shown with the program LITRANI [FXG02] in [CG02] that this slope strongly depends on the implemented characteristics of the de-polished side face. To improve the reproduction of the experimental data by the simulation, different smearing parameters σ_α have been scanned for the de-polished side face. The results, shown in figure 4.65 (right), indicate that the absolute light yield can be influenced by this parameter, but no significant change of the slope can be observed. Therefore, the UNIFIED model of GEANT4 can be only used to proof the general trend and no exact light changes can be predicted. Since a de-polishing of a single side face shows an improvement of the light yield, also a de-polishing of all side faced has been simulated. Figure 4.65 shows that a further improvement of the light yield is possible for light produced close to the PMT, but at the same time a strong non-uniformity with a negative slope and a significant decrease of the light yield in the front part of the crystal are introduced, making a de-polishing of all side faces unattractive for an optimization of the crystals uniformity.

To investigate why a crystal with a de-polished side face provides nearly optimal results for the light yield and uniformity, another simulation has been performed without any reflective wrapping around the crystal. The position dependent light yield is shown in figure 4.66. Without a reflective wrapping around the crystal, the light can reach the PMT either directly

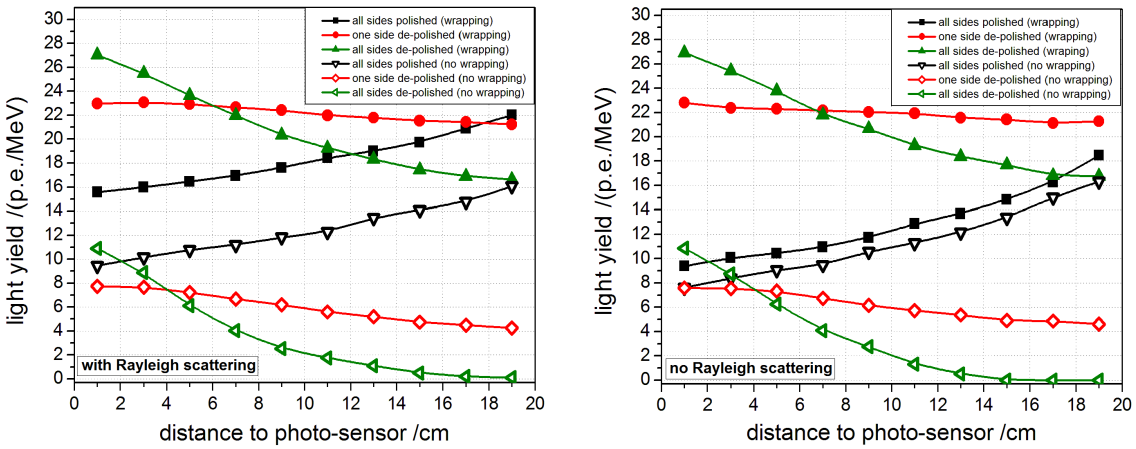

Figure 4.66: Simulated position dependent light yield of a completely polished type 2 crystal (red), a type 2 crystal with one de-polished lateral side face (black) and a type 2 crystal with all side faces de-polished (green). The open points show the results for a crystal placed in an air environment without any wrapping, while the solid points show the results with a reflective wrapping around the crystal. The left figure is simulated with Rayleigh scattering and the right figure without the implementation of Rayleigh scattering.

or totally reflected. Therefore, the light yield is significantly reduced, especially if the total reflection is interrupted by one or more de-polished side faces. However, the direct comparison shows that if a reflective wrapping is added around the crystal, most of the light which escapes the crystal trough the de-polished side faces can be recovered since it is reflected back into the crystal. In contrast to a wrapped crystal, Rayleigh scattering shows only a small impact on the light yield of a completely polished crystal, since the part of the light which is scattered out of the crystal is lost and cannot contribute to the increase of the light yield. The comparison between a crystal with and without a reflective wrapping also shows that the slope of the position dependent light yield is comparable in both cases. Only for the configurations with one or more de-polished side faces, the slope becomes a bit steeper due to an increased light loss probability for light which is generated in the front part of the crystal and has to travel a longer distance to the PMT. Nevertheless, the comparison shows that the slope of the position dependent light yield is mainly determined by the totally reflected light, while a reflective wrapping just causes a nearly position independent increase of the light yield. Without any reflective wrapping the light yield of a crystal with one de-polished side face is even lower than the light yield of a polished crystals. The observed amplification effect in the rear part of the crystal becomes only possible by an interplay between the scattering and refraction of the light on the micro-facets of the de-polished side face and the reflection of the transmitted light on the highly reflective wrapping, which strongly contributes to the observed result.

As a second step, the path length of the scintillation photons from their emission until they reach the PMT has been recorded for the different configurations of the surfaces. The results for a type 2 crystal with reflective wrapping are filled in a histogram in figure 4.67. For comparison the results with and without the implementation of Rayleigh scattering are shown. To describe the light propagation, the isotropically emitted scintillation light has to be divided into two fractions. The first group of the light is emitted in the direction of the photo-sensor, while the second group is emitted towards the front face of the crystal. If the light is

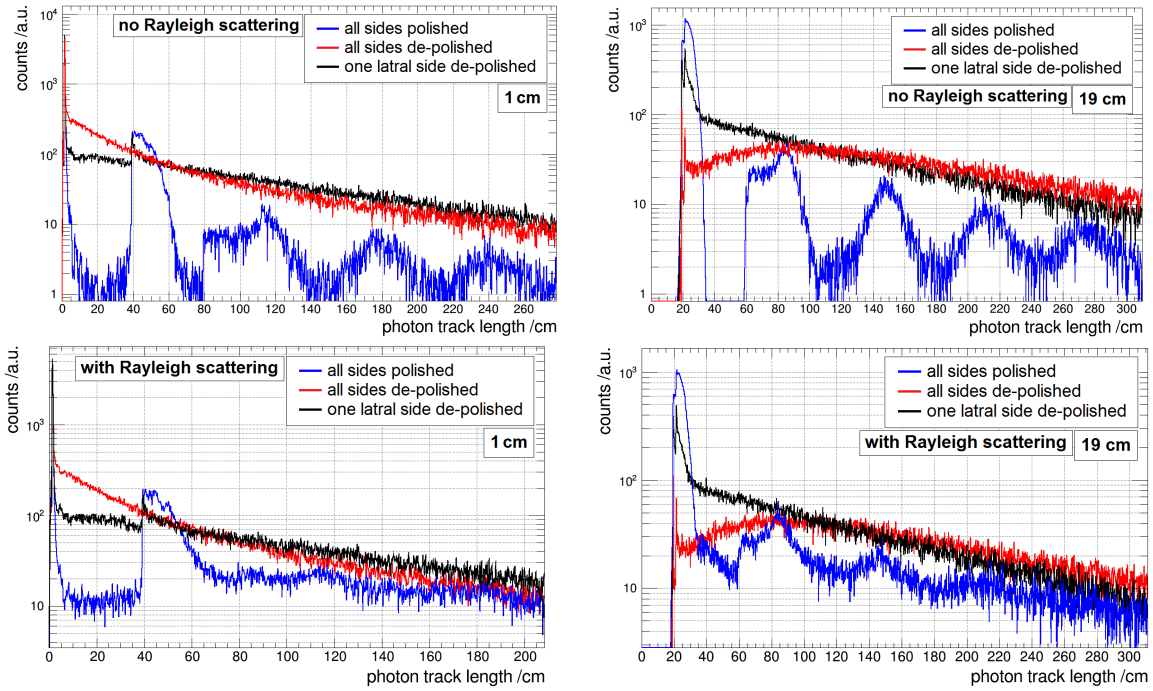

Figure 4.67: Track length of photons which reach the photo-sensor in a crystal with reflective wrapping for photons generated 1 cm (left) and 19 cm (right) away from the photo-sensor. The upper row shows the result without the implementation of Rayleigh scattering and the lower row with Rayleigh scattering. For all configurations the same number of photons has been generated.

generated directly in front of the PMT a strong peak of photons reaching the PMT without any reflection can be observed. This peak shows approximately the same intensity for all surface configurations. However, the behavior of the light which is emitted towards the front face of the crystal is quite different for the three surface configurations. In a completely polished crystal most of the light will travel the complete path to the front face of the crystal and back before it reaches the PMT again. These photons are represented by the peak starting at a path length of approximately 40 cm in the blue distribution of figure 4.67 (left). Due to the de-focusing of the light on the path to the front face of the crystal, a significant amount of light is lost. In a perfect crystal without the implementation of Rayleigh scattering also multiple forward and backward reflections can be observed in form of the following peaks. If diffuse scattering is implemented on the one side a small part of the light changes its direction on the first way to the front face and on the other side the light which undergoes multiple reflections is smeared out and increased, since the focusing effect and also the de-focusing in the other direction are partly disturbed. In contrast to this, a de-polished side face provides a certain probability, that photons which are emitted towards the front face in a special cone change their direction and are reflected back to the PMT. Therefore, they have a shorter path and a lower probability to be absorbed, which finally increases the light yield. Due to the tapered side face the probability and the size of the emission cone for a direction change of the photons is significantly larger in forward direction than on the way back to the PMT, causing an increase of the light yield even for photons emitted further away from the PMT. Photons which have changed their direction due to the de-polished side face can be clearly identified by the significant increase of the photon intensity between 5 cm and 40 cm in

the black distribution in figure 4.67 (left). Also for multiple reflections, this increase can be observed. If all side faces are de-polished, this effect is even more increased for scintillation light emitted close to the PMT, since the amount of photons which change their direction on their first path towards the crystals front face is even larger (red distribution in figure 4.67 (left)). Like already observed in figure 4.65 no significant impact of Rayleigh scattering can be observed for crystals with one or more de-polished side faces. If the light is emitted in the front part of the crystal (figure 4.67 (right)), the picture changes a bit. Now the number of photons which reach the PMT after the first passage of the crystal is significantly increased for a polished crystal due to the focusing effect of the tapered side face (blue distribution). If Rayleigh scattering is implemented, a comparable effect like for the first position can be observed. For a crystal with one de-polished side face the focusing effect still contributes, but is significantly reduced. On the other hand the intensity of photons reaching the PMT after a distance of 35 cm to 80 cm is still higher than for a polished crystal due to the change of direction of the reflected photons on their way back to the front face (black distribution). Due to this effect and due to the still partly existing focusing effect only a slight reduction of the overall light yield in the front part of the crystal can be observed for a crystal with one de-polished side face compared to a perfectly polished crystal. For a crystal with all side faces de-polished, the light which reaches the PMT after the first passage of the crystal and therefore also the overall light yield are significantly reduced due to the light loss on the rough surfaces, which suppress regular reflections (red distribution). For comparison, the same histograms like in figure 4.67 have been created for a crystal without any wrapping. The results with and without the implementation of Rayleigh scattering are shown in figure 4.68.

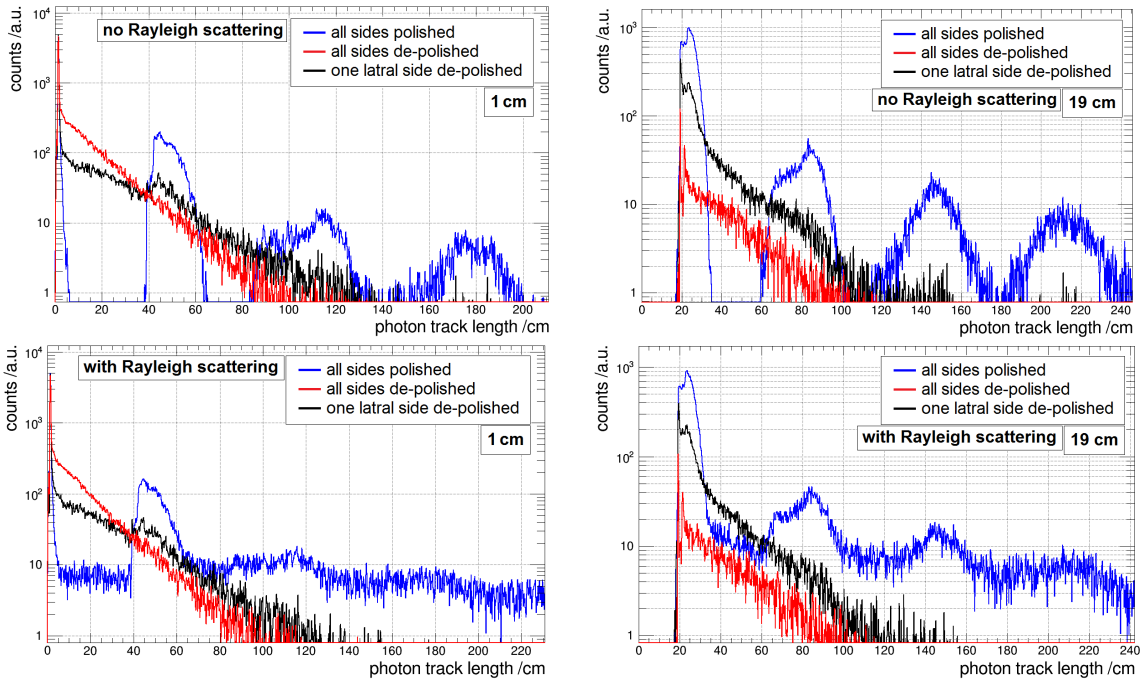

Figure 4.68: Track length of photons which reach the photo-sensor in a crystal without reflective wrapping for photons generated 1 cm (left) and 19 cm (right) away from the photo-sensor. The upper row shows the result without the implementation of Rayleigh scattering and the lower row with Rayleigh scattering. For all configurations the same number of photons has been generated.

For a completely polished crystal a comparable behavior like for a crystal with reflective wrapping can be observed. The peaks are only a bit more narrow and the overall light yield is reduced, since only totally reflected light is detected. If one or more side faces are de-polished, the overall light yield is significantly reduced. Also the amount of photons which undergo a direction change due to the micro facets of the de-polished side face(s) is reduced but still causes an observable increase of the number of detected photons with path length between 5 m and 40 cm if the light is generated directly in front of the PMT. For light which is generated in the front part of the crystal this effect can be still observed on the first reflection back to the front face but due to the low number of remaining photons the impact is significantly reduced. Due to the interruption of the total reflection by the de-polished surface(s) most of the photons have left the crystal after one or two reflections between the end faces if the crystal is not covered by a reflective wrapping.

For a better visualization of the effects which contribute to an increase of the light yield in the rear part of the crystal if one lateral side face is de-polished, a simple two dimensional simulation of the photon path with a not to scale crystal and a highly amplified surface roughness has been performed. Figure 4.69 shows two examples of effects which cause an increase of the light yield.

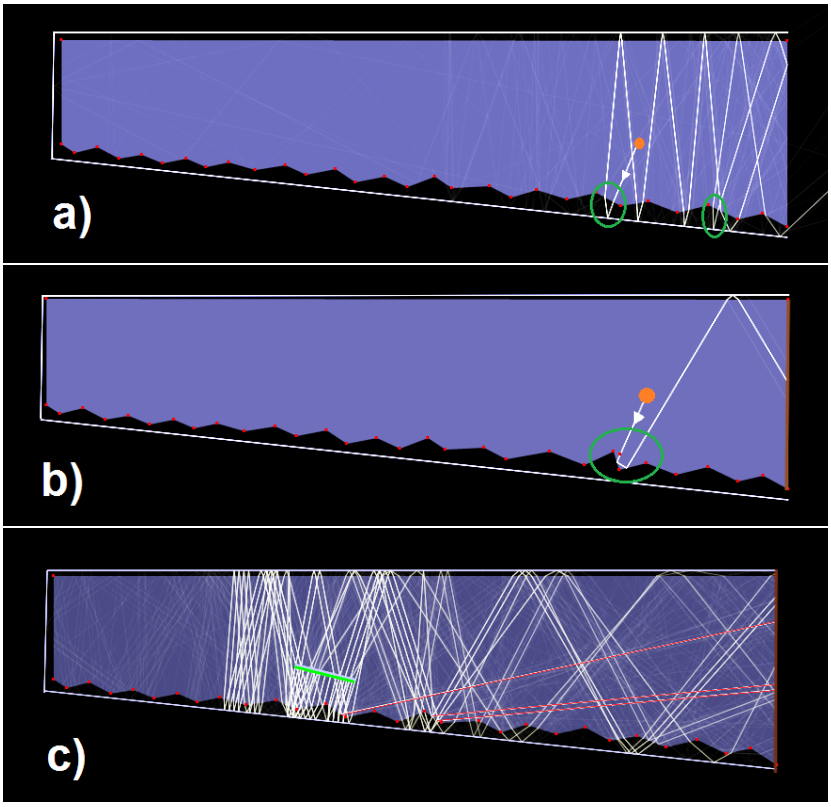

Figure 4.69: Propagation of light in a not to scale tapered crystal with one de-polished side face and a highly amplified surface roughness. Figure a) and b) show the path of a single ray changing its direction by a combination of the refraction on a micro facet and the reflection on the wrapping (case a) and by the total reflection on two micro facets (case b). Figure c) illustrates several parallel rays hitting the surface at different positions.

In part (a) possible photon paths causing a direction change in a wrapped crystal can be observed within the green circles. The figure illustrates that the change of direction is caused by a combination of the refraction on the micro facet and the reflection on the reflective wrapping which surrounds the crystal. If the facets and the incident rays are properly oriented, such a direction change is also possible without a reflective wrapping (figure 4.69 b), but due to the limited range of possible incident angles and facet orientations, the probability is significantly reduced. An additional effect which is contributing to the amplification of the light by the de-polished surface can be observed in case of the red light tracks in figure 4.69 c, showing a strong focusing of the light if the micro-facet is properly oriented. Figure 4.69 c also illustrates the direction change of a complete bundle of rays. In addition to these effects also the de-focusing which can be observed for light traveling to the front face in a completely polished crystal is interrupted by the de-polished side face, which results in a shorter length of the photon path and therefore reduces the absorption probability.

Up to now all simulations and experimental tests for the de-polishing of a crystal side face have been performed with type 2 and type 3 crystals. To investigate the influence of the degree of tapering on the results, additional simulations have been done with type 6 crystals (average degree of tapering) and with the least tapered type 11 crystals. The results are shown in figure 4.70.

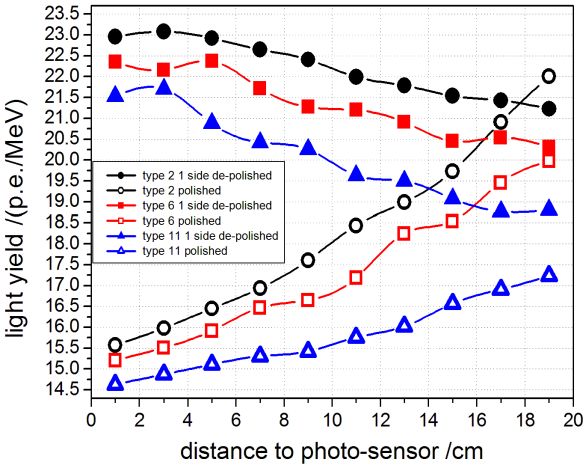

Figure 4.70: Influence of a de-polished lateral side face on the position dependent light yield for different degrees of tapering. The open symbols represent crystals with one de-polished side face, while the full symbols have been simulated with completely polished crystals. In all cases Rayleigh scattering is implemented.

The simulated position dependence of the light yield shows that the relative change of the light yield in the rear part of the crystals is comparable for all crystal types. In contrast to this, the light yield in the front part of the crystal shows a stronger decrease for completely polished crystals than for crystals with one de-polished lateral side face, if the degree of tapering is reduced. This behavior shows that the impact of the focusing effect is significantly reduced if one side face is de-polished and also light generated in the front part of the crystal is partly enhanced by the de-polished side face. Nevertheless, also the negative slope of the position dependent light yield becomes larger for less tapered crystals, which shows that a reduced roughness of the de-polished surface is needed to homogenize the response of less tapered

crystals. Altogether, the observable trend for less tapered crystals is quite promising, but still has to be verified experimentally.

As a last point, the simulations of a type 2 crystal with the different surface configurations have been repeated with the final readout concept for the PANDA barrel EMC consisting of two rectangular LAAPDs like it is described in section 4.3.1. Figure 4.71 shows the obtained results.

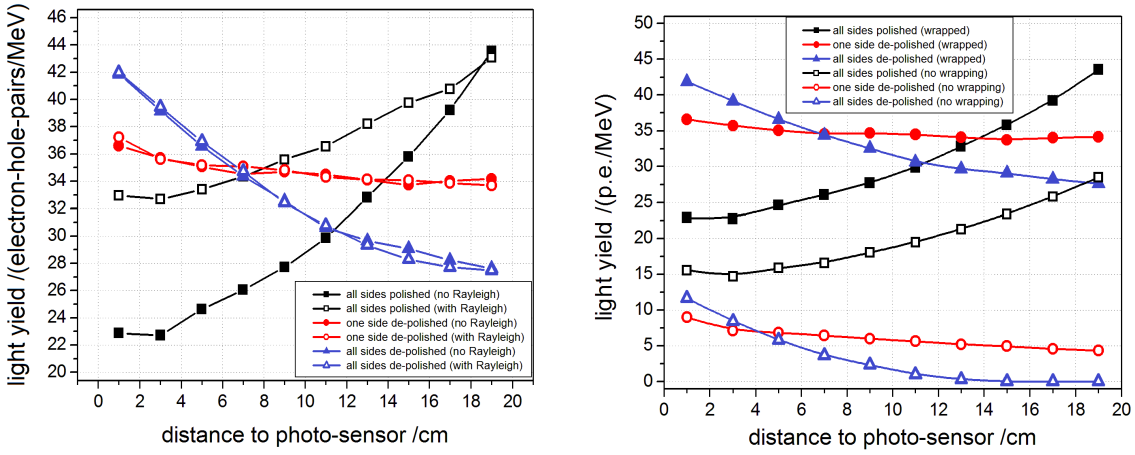

Figure 4.71: Simulated position dependent light yield of a type 2 crystal with all side faces polished (black), with one de-polished side face (red) and with all side faces de-polished (blue). In the left figure, the full points are simulated without the implementation of Rayleigh scattering an the open points with Rayleigh scattering. In both cases the crystal is covered by a reflective wrapping. The readout is performed with two 1 cm^2 LAAPDs and the plotted light yield represents the sum of the electron hole pairs generated in both LAAPDs. The right figure compares the results without the implementation of Rayleigh scattering for a crystal with (solid points) and without (open points) reflective wrapping.

The comparison of the left figure with the results of a PMT based readout in figure 4.65 shows in principle the same trend, but with a change of the relative light yield between the different surface configurations. Especially the light loss in the front part of a crystal with one de-polished side face compared to a completely polished crystal is increased up to 20 % and also the relative gain of the light yield in the rear part is reduced. This change of the light yield for the different surface configurations relative to each other is caused by the relative small area of the rear face covered by the LAAPDs. In contrast to the PMT, the two LAAPDs are covering only approximately 25 % of the crystals rear face, while the other parts are covered with reflective VM2000 foil which reflects the photons back into the crystal. Since the detection efficiency of this reflected photons is different for the individual surface configurations, a different relation of the light yield occurs for the different cases. The difference of the collection efficiency can be also observed in the right part of figure 4.71, which compares the position depended light yield with and without a reflective wrapping. Here an over-proportional increase of the light yield in the front part of the crystal can be observed compared to the rear part for a completely polished crystal, while the slope for a crystal with one de-polished side face is much more comparable with and without a reflective wrapping. Since for a PMT based readout more or less a parallel shift of the curves has been observed, this difference in the collection efficiency of the light which is not directly detected by the photo-sensor can explain the different relation of the light yield for the two readout

concepts. However, due to the uncertainties of the simulation model, the simulated light loss in the front part of the crystal of 20 % can only be seen as a trend and has to be verified in future experimental tests with an APD based readout.

4.3.5 Calculation of the energy response based on the energy deposition distribution

Since the ray-tracing implemented in GEANT4 generates a too high non-uniformity of the light collection if realistic values for the transmission and the mean free path of the Rayleigh scattering are implemented, also the simulated energy resolution based on ray-tracing would be significantly worse than expected, especially for high energies. This discrepancy can only be avoided, if the effects which contribute to the light collection and cannot be implemented directly into GEANT4 are compensated by an optimization of the mean free path of the Rayleigh scattering. In addition, the experimental results for the position dependent light yield for a crystal with one de-polished side face can not be reproduced completely in the ray tracing model. To avoid these problems and uncertainties and to obtain a more reliable and especially a faster simulation of the energy resolution, a model has been implemented which enables the calculation of the energy response based on the distribution of the deposited energy simulated by GEANT4 and empirical values for the position dependent light yield, the excess-noise factor of the LAAPDs and the electronic noise level. A similar model has also been applied for the simulation of PROTO 60 in [MM13].

A model to calculate the detected signal and its fluctuations

Without the occurrence of a non-uniformity in light collection, the total light yield of a crystal shows a linear relation to the deposited energy. In this case, the energy deposited along the shower paths can be summed up and the total energy deposition can be multiplied by the light yield per energy unit to obtain the average light yield generated by the incoming electromagnetic probe. If the light collection shows a position dependent non-uniformity, this concept cannot be applied any more, since the amount of light detected by the photo-sensor depends on the position where the energy is deposited. To take this effect into account, the position of the energy deposition along the longitudinal crystal axis, provided by GEANT4 is used to determine the position dependent amplification factor of the detected light based on the experimental non-uniformity curve $NUF(z)$. This factor, which is displayed in figure 4.4 and parametrized for the investigated crystal geometries in equations 4.1 - 4.3 as a function of the longitudinal crystal axis z is multiplied with the light yield close to the rear side of the crystal LY_0 and with the deposited energy $E_{dep}(z)$ to calculate the light yield detected by the photo-sensor from each energy deposition point within the crystal.

$$LY(z) = E_{dep}(z) \cdot LY_0 \cdot NUF(z) \tag{4.38}$$

The light yield of the crystals has been measured for the implemented samples of the type 2 section with a ^{137}Cs source placed on top of the crystal and a photo-tube with standard bi-alkali photo-cathode. The obtained distribution for the light yield created in the front part of each crystal at -25°C is shown in figure 4.72 (left). Based on the average light yield of the implemented type 2 crystals of mean$\pm\sigma$ = 84.5 $\pm$ 3.8 photo-electrons per MeV and under

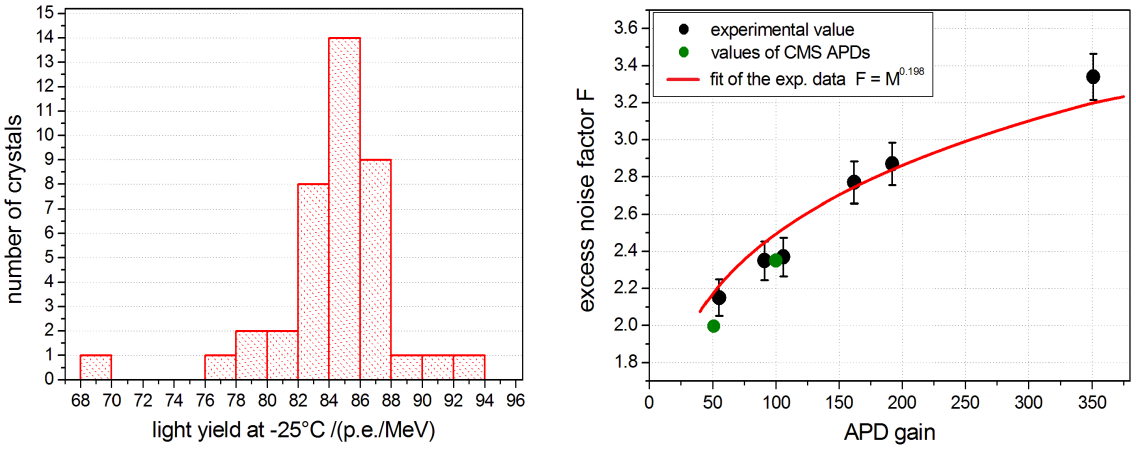

Figure 4.72: Light yield distribution of the type 2 crystals implemented in PROTO 120 (left) and gain dependence of the excess noise factor of the PANDA APDs (right).

consideration of the different active area and quantum efficiency of an APD and a PMT, the detected light of a single 1 cm^2 APD at a temperature of -25°C has been determined to mean$\pm\sigma$ = 31.2 $\pm$ 1.8 electron-hole pairs per MeV. To obtain the value of the detected light yield for an interaction close to the APD, this value has to be corrected by the amplification factor of 1.35, introduced by the non-uniformity. Considering this correction, a value of LY_0 = 23.1 electron-hole pairs per MeV has been implemented.

To obtain the total detected light yield LY_{det}, the light portions detected from all segments $LY_i(z)$ are summed up:

$$LY_{det} = \sum_i LY_i(z) \tag{4.39}$$

Up to now, this value only includes the statistical shower fluctuations of the energy deposition and the smearing of the energy due to the light collection non-uniformity. Figure 4.73 illustrates how this smearing of the pure energy response with different degrees of non-uniformity affects the relative energy resolution of a 3 $\times$ 3 array within the prototype. For type 1, type 2 and type 6 the non-uniformity parametrizations from equations 4.1 - 4.3 have been used. For the de-polished crystals, the non-uniformity curves from figure 4.6, which have been individually measured for the crystals of the implemented 3 $\times$ 3 array have been applied. The simulation has been performed under the conditions of the experimental test, with a Gaussian beam profile with a standard deviation of σ = 3.6 mm. The comparison of the curves for different strengths of the non-uniformity shows that the slope of the non-uniformity has a major impact on the achievable energy resolution. Compared to the de-polished array, the resolution of the pure energy deposition, without light collection statistics, of a 3 $\times$ 3 array with type 1 crystals is increased by more than a factor 2 over the complete energy range below 1 GeV.

In reality, also the statistics of the light collection, the excess-noise factor of the APDs and the electronic noise level play an important role for the energy resolution, especially at low energies. Since the light collection and the noise of the APDs are statistical processes, their influence can be implemented by a Gaussian smearing of the response. While the detected light yield LY_{det} is set as the mean value, the standard deviation is determined as the square-

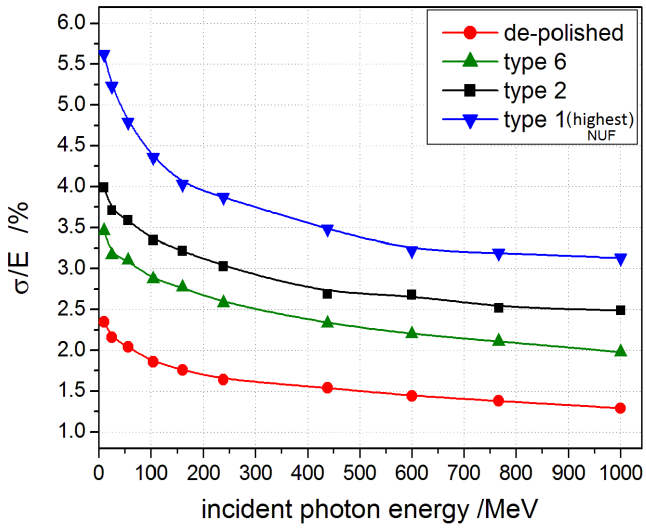

Figure 4.73: Influence of smearing of the pure energy response with the non-uniformity curve of the light collection on the energy resolution. The implemented non-uniformity curves can be found in figure 4.4 and 4.6.

root of the excess-noise factor of the APDs F times the detected light yield. The electronic noise, which is also a statistical quantity is considered by adding a Gaussian distribution around zero, with the experimentally determined standard deviation of the electronic noise $\sigma_{\text{Noise}} = 0.9$ MeV. The resulting equation for the detected signal including all statistics is given by:

$$LY_{final} = Gauss\left(LY_{det},\ \underbrace{\sqrt{F \cdot LY_{det}}}_{\sigma}\right) + Gauss\,(0,\ \sigma_{Noise}) \tag{4.40}$$

The gain dependence of the excess-noise factor of the APDs, which is shown in figure 4.72 (right) has been determined experimentally with a calibrated light-pulser. The obtained values are comparable to the values measured for CMS APDs [DIM00]. The dependence on the gain M can be described with the theoretical potential behavior [HP15] by:

$$F(M) = M^{0.2} \tag{4.41}$$

For a gain of 150, used for PROTO120 during the beam-test, a value of F $\approx$ 2.70 can be calculated.

The described method can be used to calculate the response of a single APD. To calculate the response of two APDs per crystal, the statistical smearing of the light yield in equation 4.40 has to be performed two times with the same detected light yield LY_{det}. A summation of the obtained values with uncorrelated noise statistics leads to the response of both APDs. The same method has been used for the analysis of the experimental data.

Comparison of the simulated and the experimental energy resolution

The simulation has been performed under the same conditions for the setup like the experiment. The photon beam with a Gaussian beam profile ($\sigma = 3.6$ mm) interacts in the center of

the polished and de-polished 3 × 3 arrays under the same angle, parallel to the central crystal axis, like in the experiment. For the analysis only the 3 × 3 array has been considered and the experimental threshold of 2.7 MeV has been applied. Like in the experiment, the noise of one crystal in a corner of the array has been doubled and its threshold was set to 6 MeV. For the de-polished crystals, the measured non-uniformity curves from figure 4.6 have been implemented. For the array with polished crystals and for the polished crystal in one corner of the array with de-polished crystals, the non-uniformity parametrization for type 2 crystals from equation 4.2 has been applied. Figure 4.74 (left) shows the simulated relative energy resolution for the 3 × 3 array with polished and the one with de-polished type 2 crystals in comparison to the experimental results from section 4.2.7.

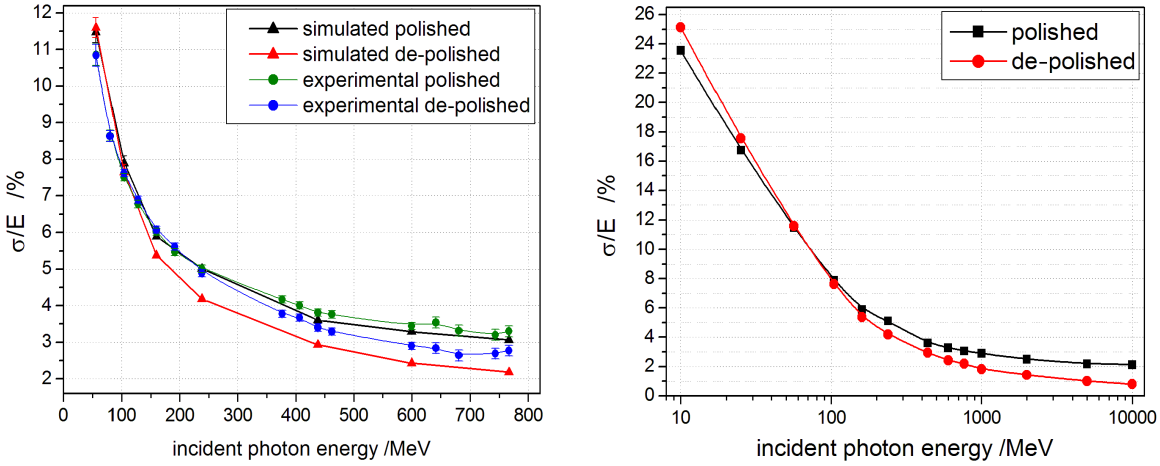

Figure 4.74: Comparison of the simulated and experimental values of the relative energy resolution for a 3 × 3 array of polished and de-polished type 2 crystals in the experimental energy range (left) and simulated energy resolution for a 3 × 3 array of polished and de-polished crystals over the complete energy range from 10 MeV up to 10 GeV (right). Both APDs of each crystal have been used for the simulation.

The comparison of the simulation and the experimental values shows that the energy resolution of the array with polished crystals is in good agreement with the experiment. The small variation at high energies is strongly influenced by the implemented non-uniformity curve. Since an average curve is implemented for the type 2 crystals, the difference between experiment and simulation can be explained by a slight variation of the non-uniformity of the individual crystals. For the lowest energies, the results are strongly influenced by the implemented noise distribution. The difference therefore shows that a simple uncorrelated Gaussian-noise distribution implemented in the simulation can not completely describe the experimental noise. In addition the reduction of the noise by the experimental requirement of a time correlation between the central crystal and the outer detectors of the 3 × 3 array can not be considered in the simulation. In contrast to the array with polished crystals, the simulation of the array with de-polished crystals shows a significantly better energy resolution at energies above 100 MeV, than the one obtained in the experiment. This observation can lead to two conclusions. On the one hand it has to be considered that the simulation is not completely correct in this case. On the other hand different effects occurred to the array with de-polished crystals during the experiment, which may result in a deterioration of the

experimental energy resolution. Especially the low frequent oscillation of the traces of two detectors, which has been corrected as good as possible, and the failure of the readout of one APD of two crystals may cause a deterioration of the energy resolution. Therefore, it can be assumed that a further improvement of the experimental results of the array with de-polished crystals can be achieved under the absence of the mentioned effects.

The right part of figure 4.74 extends the simulation to lower and higher energies. It shows that the improvement of the energy resolution by the de-polishing has a significantly stronger impact in the sub-GeV range due to the reduced impact of the statistical term and the dominance of the constant term of the energy resolution parametrization in this region. Like the experiment, also the simulation shows an increase of the constant term from 0.4-0.5 % for the de-polished crystals to nearly 2 % for polished type 2 crystals. In contrast to this, at energies below 50 MeV statistical effects dominate. For these energies, the light loss from the front part of the crystal, introduced by the de-polishing of the crystals side face, leads to a deterioration of the energy resolution. However, this deterioration stays in an acceptable range below one percent point down to 25 MeV.

Comparison of a readout with one and two APDs

Each crystal of the barrel EMC will be read out with two APDs. To compare the energy resolution with one and two APDs, a simulation has been performed for both cases. The results for the 3 × 3 array with polished and de-polished type 2 crystals with the experimental noise level of 0.9 MeV and a threshold of 2.7 MeV are shown in figure 4.75 (left).

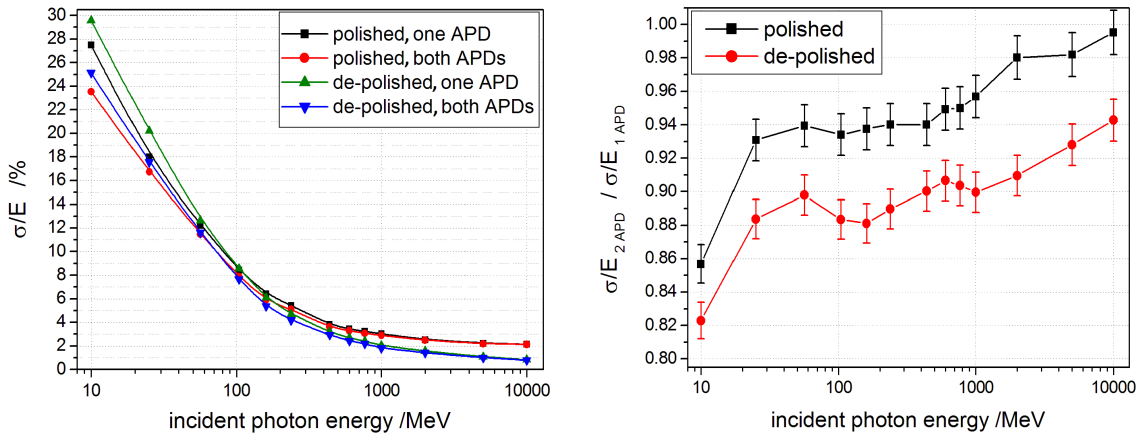

Figure 4.75: Comparison of the simulated energy resolution for a readout with one and two APDs for a 3 × 3 array of polished and a 3 × 3 array of de-polished type 2 crystals (left) and resulting energy dependence of the improvement factor of the energy resolution for a readout with two APDs compared to one APD for a 3 × 3 array of polished and a 3 × 3 array of de-polished type 2 crystals (right).

Especially in the energy region below 50 MeV, a significant improvement can be observed due to the improved light collection statistics for two APDs. For the lowest energy of the experimental data range of 56 MeV, the effect is already reduced down to approximately one percent point in the simulation with a decreasing trend for an increase of the photon energy.

At energies above 1 GeV, light yield statistics and therefore also the improvement by a second APD play only a minor role.

Figure 4.75 (right) shows the improvement factor of the relative energy resolution between one and two APDs obtained from the simulations for the polished and the de-polished crystal array. For a pure statistical contribution one would expect an improvement factor of $1/\sqrt{2} = 0.71$. In the experiment, also the electronic noise and the smearing of the energy by the non-uniformity and other factors, resulting in a constant term of the parametrization of the energy resolution, contribute to the measured energy resolution and reduce the impact of the light yield statistics. The deterioration of the improvement factor for increasing energies also indicates that as expected, the influence of the statistical contribution is more and more reduced at higher energies. The comparison of the factors for polished and de-polished crystals shows that a reduction of the energy smearing by a reduced non-uniformity of de-polished crystals leads to a stronger impact of the light collection statistics due to the reduced constant term and therefore to better improvement factors for the readout of de-polished crystals with two APDs.

For the experimental values (see figure 4.49) the improvement of a readout with two APDs is even smaller than the expectations from the simulation, but also in the experiment a stronger improvement can be observed for the lowest energies. The reduced improvement between one and two APDs in the experiment is expected to be introduced by the non-functional second APD of two crystals and by correlated noise components introduced by some ASICs.

Influence of the strength of the non-uniformity on the energy resolution

To compare the impact of the non-uniformity of the different crystal geometries within the barrel EMC on the energy resolution, a simulation under the same conditions like in section 4.3.5, but with different non-uniformity curves has been performed. For the crystal types 1, 2 and 6 and for the de-polished crystals, the experimentally measured non-uniformity curves from section 4.1 and 4.1.1 have been implemented. The resulting energy resolution is shown in figure 4.76 (left). The figure shows that nearly no difference of the relative energy resolution can be observed between the de-polished crystals and crystals with a completely uniform light yield. This behavior indicates that a de-polishing of the most tapered side face of the type 2 crystals to an average roughness R_a of 0.3 μm provides an optimal result. All non-uniformity curves lead to approximately the same energy resolution for energies between 50 MeV and 100 MeV. Only the most tapered type 1 crystals show a slight deterioration of the energy resolution by the non-uniformity even at this low energies. For all other crystal types, a balance between the deteriorating influence of the non-uniformity and the improved light yield statistics due to the non-uniformity can be observed in this region. For energies above 100 MeV, a deterioration of the energy resolution can be observed for the tapered crystal geometries. The strength of this deterioration is directly correlated with the degree of tapering and the non-uniformity, like the correlations in figure 4.77 illustrate for the relative energy resolution at an incident photon energy of 1 GeV.

The strength of the non-uniformity in light collection also directly influences the constant term of the parametrization of the relative energy resolution which has been determined form a fit of the simulated energy resolution curves in figure 4.76 for the different crystal types. The obtained correlation between the constant term of the energy resolution of a 3 $\times$ 3 array

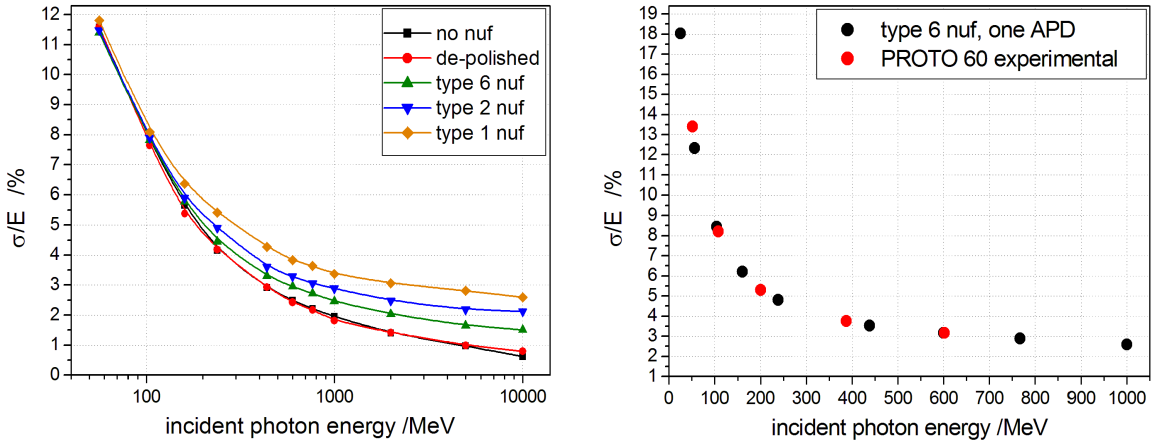

Figure 4.76: Left: Influence of the strength of the non-uniformity in light collection on the relative energy resolution of a 3 × 3 array. For type 1, type 2 and type 6 the non-uniformity curves shown in figure 4.4 have been used. For the de-polished crystals, the non-uniformity curves from figure 4.6, which have been individually measured for the crystals of the implemented 3 × 3 array have been applied. For the case without non-uniformity, the light yield close to the rear side of the crystal has been used for all positions. Right: Comparison of the results simulated for a 3 × 3 array of type 6 crystals with a readout of only one APD to the results obtained during the experiments with PROTO 60. In both cases a threshold of 2.7 MeV has been applied.

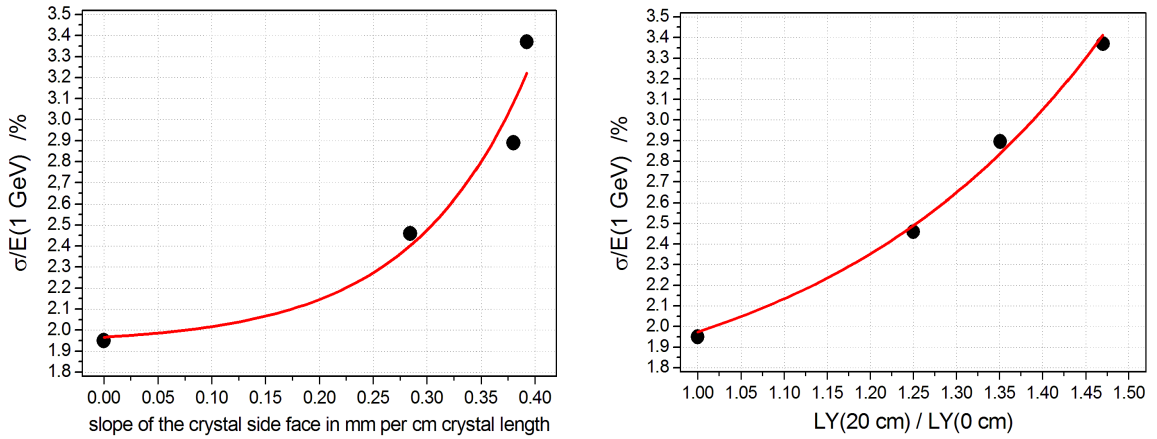

Figure 4.77: Correlation between the simulated relative energy resolution of a 3 × 3 array at 1 GeV and the slope [(d(20 cm)-d(0 cm))/20 cm] of the most tapered crystal side face (left) and correlation between the simulated relative energy resolution of a 3 × 3 array at 1 GeV and the factor of the increase in light yield in the front part compared to the rear part of a crystal [LY(20 m)/LY(0 cm)], introduced by the non-uniformity of the light collection.

and the ratio of the light yield in the front and rear part of the crystals is shown in figure 4.78. The experimental values for de-polished and polished type 2 crystals, taken from the parametrizations of the relative energy resolution in equation 4.33 and 4.34, show a good agreement with the simulated correlation.

As another proof for the correctness of the simulation model, a simulation with the non-uniformity curve of type 6 crystals and a readout of only one APD per crystal has been

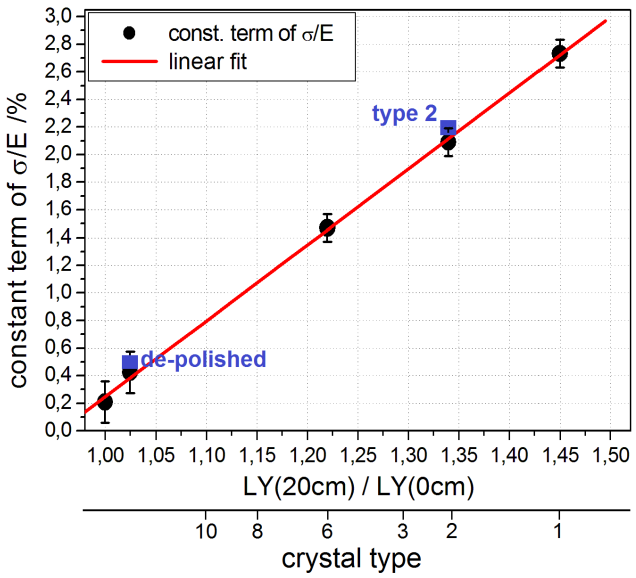

Figure 4.78: Correlation between the constant term of the relative energy resolution of a 3 × 3 array and the ratio of the light yield in the front and rear part of the crystals. For comparison the corresponding crystal type of the PANDA geometry is given. The experimental values determined for de-polished and polished type 2 crystals in this work are shown as blue points.

performed and compared to the results obtained with PROTO 60, representing exactly these conditions. The comparison of the simulated and experimental data points in figure 4.76 (right), both obtained with the same noise level and a threshold of 2.7 MeV, shows a quite good agreement over the complete energy range, which is a good proof of the applicability of the simulation model.

Chapter 5

Discussion and Outlook

The performance of the most recent prototypes of the forward shashlyk EMC and the barrel EMC of the PANDA detector has been presented in the last two chapters. For both prototypes, an optimization of the feature extraction method and the relative calibration has been performed. In addition, a special focus has been set to the investigation and the improvement of detector inhomogeneities in longitudinal and lateral direction. The investigations showed that a lateral or longitudinal non-uniformity of the detector response can cause a significant deterioration of the energy resolution. To solve this issue, concepts which reduce the non-uniformity and improve the energy resolution have been presented and verified for both calorimeter types. This section will discuss the impact of the different investigated aspects on the calorimeter performance and estimate the impact of additional parameters on the results. In addition, a comparison to earlier measurements and already existing detector setups with a comparable design will be given.

5.1 Forward shashlyk calorimeter

The response of a prototype of the forward shashlyk calorimeter of PANDA to tagged photons in the energy range below 1 GeV has been tested for the first time in the A2 hall of the MAMI accelerator in Mainz in 2012. The characterization of this so called "version A" prototype showed a strong variation of the reconstructed energy, depending on the interaction position of the photon beam. In addition a significant variation of the longitudinal non-uniformity has been observed for the single cells. Based on the obtained results it was figured out that the observed lateral variations of the energy response were an effect of a misalignment of the scintillator tiles and a different treatment of the side faces of this tiles, while the variation of the longitudinal homogeneity was caused by cracks in the bending region of the WLS fibers and a possible damage of the fibers due to the misaligned scintillator tiles. To remove these inhomogeneities, a second "version B" prototype with significant improvements of the longitudinal and lateral homogeneity has been constructed at IHEP Protvino and tested at the MAMI accelerator in 2014. The focus of the first part of this work was the characterization of the response of this prototype. The following section will compare the obtained results to the first prototype and to other comparable shashlyk calorimeters. In addition, the impact of different aspects influencing the homogeneity of the energy response and playing a critical role for the general detector performance will be discussed.

5.1.1 Performance of the current prototype in comparison to the version A prototype

With the current prototype, a significant improvement of the performance at low energies could be achieved. The main problems which were figured out for the version A prototype during the beam-test in 2012, were the missing alignment of the scintillator tiles, fixed by only one pin-hole per tile, the different treatment of the outer side faces of these tiles and the occurrence of cracks in the bending region of the WLS fibers. All theses points could be successfully solved for the version B modules, constructed at IHEP Protvnio. The scintillator tiles are produced now separately for each cell with two fixation pins per tile and a coverage of all outer side faces with white paint to guarantee a homogenous light collection [TDf15]. To improve the longitudinal homogeneity, the WLS fibers from BICRON (BCF-91A) have been replaced by new ones from KURARAY (Y-11(200)) with a better light attenuation behavior. To reduce the light loss in the bending region, a special crack-free bending procedure has been developed [TDf15]. In addition to the light collection improvements by the new WLS fibers, an additional improvement of the light yield could be achieved by the insertion of reflective TYVEK paper sheets in-between the scintillator tiles and the lead plates. With these improvements, especially the homogeneity of the energy response, the energy resolution, but also the position resolution could be significantly improved.

Energy response

A main problem of the version A prototype was the high position dependence of the reconstructed energy of up to ± 10-17 % of the mean energy [SD12]. With the version B prototype, this variation could be significantly reduced down to less than ± 2 % for points with the same energy leakage. Due to the new fibers with a higher attenuation length and less cracks in the bending region, also the longitudinal non-uniformity, introducing a light yield reduction in the front part of the cell of up to 33 % compared to the rear part, with strong variations from cell to cell for the version A modules [SD12] could be reduced to an average value of 12 % with a good homogeneity for most of the cells for the version B modules. As a direct result of this improved light collection in combination with the reflective TYVEK paper between scintillator tiles and lead plates, the light yield measured with a PMT with bi-alkali photo-cathode could be increased by nearly 90 % to (2.8 ± 0.3) p.e./MeV, which is comparable to other shashlyk calorimeter (KOPIO: 3.2 p.e./MeV (24 e.h. pairs with an APD) [ADI04], LHCb: 3 p.e./MeV [ABB08] CMS: 2.46 p.e./MeV [LD94]). However, with special green sensitive PMTs the detected light yield could be improved even more. With the new modules a threshold of 0.6 - 1.0 MeV, depending on the feature extraction method could be achieved, which is significantly below the requirement of the TDR [TDf15] of 3 MeV.

As a result of the improved homogeneity and the increased light yield, also the energy resolution of the version B modules could be significantly improved. For incident photon energies of 100 MeV and 300 MeV typical improvements from 13.4 % to 12.2 % for the first energy and 8.5 % to 7.2 % for 300 MeV can be observed. Table 5.1 compares the parametrization of the relative energy resolution of the two prototypes for different cluster sizes. The comparison indicates a significant improvement of the stochastic term of the parametrization due to the increase of the light yield. The effect of the reduced lateral and longitudinal non-uniformity of the cells is contained in a reduced constant term, at least for a 4 × 4 array. In case of

clsuter size	**version A** [SD12]	**version B**
3×3	$\frac{(4.0-4.4)\ \%}{\sqrt{E/GeV}} \oplus (3.1-4.5)\ \%$	$\frac{(3.4-3.9)\ \%}{\sqrt{E/GeV}} \oplus (3.1-4.8)\ \%$
4×4	$\frac{(4.49 \pm 0.03)\ \%}{\sqrt{E/GeV}} \oplus (4.34 \pm 0.05)\ \%$	$\frac{(3.35 \pm 0.04)\ \%}{\sqrt{E/GeV}} \oplus (3.79 \pm 0.09)\ \%$

Table 5.1: Comparison of the parametrization of the relative energy resolution of the version A and B shashlyk prototypes for an interaction of the photon beam in the center of a 3×3 and a 4×4 array of cells. The data for the version A prototype is taken from [SD12]. The range of the values given for the 3×3 arrays shows the variation between the different investigated arrays within the prototype.

a 3×3 array no significant improvement can be observed, since the constant term of the energy resolution is mainly limited by the lateral energy leakage due to the too small cluster size.

For a comparison of the two prototypes, it has to be considered that the parametrization of the resolution has been determined for a fixed interaction position of the beam spot, which is significantly smaller than the size of the cell. If the photon beam would illuminate the complete cell, also the variation of the reconstructed energy would contribute to the energy resolution. For the version B modules this inhomogeneity has only a minor impact, since the variation of less than $\pm$ 2 % is significantly smaller than the constant term of the energy resolution. In contrast to this a variation of $\pm$ 10-17 % for the version A modules causes a significant smearing of the overall energy resolution. This effect is illustrated in figure 5.1 for an overlap of Gaussian distributions with the same standard deviation but a variation of the mean value of up to 15 %.

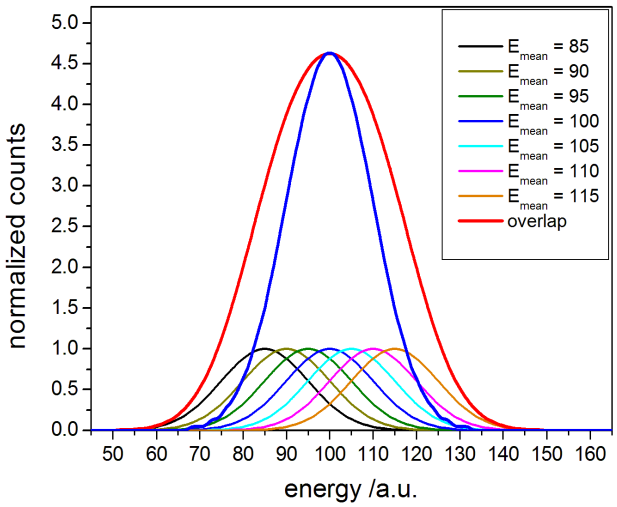

Figure 5.1: Smearing of the overall energy resolution by a position dependence of the reconstructed energy. The blue curve shows the energy resolution for a fixed mean value of the reconstructed energy, while the red curve shows the overlap of different single energy distributions with the same width like the blue one but with a variation of the mean energy of $\pm$ 15 % (small distributions).

The difference between the red and the blue distribution indicates the significant increase of the standard deviation if the mean value shows a position dependent variation. Due to this effect, the improvement in energy resolution for the version B modules is even larger than the difference of the parametrization for fixed interaction position in table 5.1.

Position and time resolution

Also the position resolution of the version B prototype has been improved by the increased light yield and especially by the improved lateral homogeneity. For an interaction of a 400 MeV photon beam in the center of a cell, a reduction of the position resolution from 16 mm down to 12.3 mm has been achieved and for an interaction of the same photon beam in the corner of a cell, the position resolution has been improved from 10.2 mm down to 9.6 mm. All given resolution values are folded with the beam profile, which was comparable for both test-experiments. Table 5.2 compares the parametrization of the two extreme cases for an interaction of the photon beam in the center of a cell and in the corner between 4 cells.

position	**version A** [SD12]	**version B**
center	$\frac{(8.9 \pm 0.9)\ mm}{\sqrt{E/GeV}} \oplus (7.7 \pm 0.6)\ mm$	$\frac{(5.6 \pm 0.2)\ mm}{\sqrt{E/GeV}} \oplus (8.5 \pm 0.2)\ mm$
corner	$\frac{(5.5 \pm 0.6)\ mm}{\sqrt{E/GeV}} \oplus (5.8 \pm 1.3)\ mm$	$\frac{(4.5 \pm 0.1)\ mm}{\sqrt{E/GeV}} \oplus (5.0 \pm 0.3)\ mm$

Table 5.2: Comparison of the parametrization of the position resolution of the version A and B shashlyk prototype for an interaction of the photon beam in the center of a cell and in the corner between four cells. The data for the version A prototype is taken from [SD12].

The comparison of the parametrizations of the two prototype versions shows an improvement of the stochastic term for both interaction positions, which can be explained by the improved light output. In contrast to this, the constant term, which is mainly influenced by the beam profile stays at approximately the same level within the error bars. By a correction of the position resolution with the estimated beam profile, a significant reduction of the constant term of the parametrization for the version B prototype down to (7.6 ± 0.6) mm for a central interaction and (3.4 ± 0.7) mm for an interaction in the corner of a cell is possible.

For the time resolution, a value comparable to the version A prototype was obtained. For low energies the results are even better than the TDR requirement of 100 ps/$\sqrt{E/GeV}$.

5.1.2 Comparison of the results to the performance at higher energies and to the KOPIO prototypes

Since the version B prototype has never been tested at energies above 1 GeV, it will be compared to the results of the version A prototype in this energy range. The test of this prototype with energies above 1 GeV was performed at IHEP Protvino and the results are presented in [TDf15]. Due to the improvements of the version B prototype even better results than the values obtained with the version A prototype can be expected also in the energy range

above 1 GeV. On the other side, the reduced influence of light collection statistics on the energy resolution at high energies will limit the improvement. Nevertheless, the resolution values of the version A prototype can be taken as an upper limit for the expected performance of the version B prototype. Also in the energy range below 1 GeV, the resolution values obtained with the version B prototype are only an upper limit for the expected performance due to the limited cluster size. The relative energy resolution obtained for the version A prototype at high energies [TDf15] in comparison to the results at energies below 1 GeV presented in this work is shown in figure 5.2.

Figure 5.2: Energy resolution of the shashlyk calorimeter over the entire energy range. The green points have been taken from [TDf15]. The error bars of the blue points represent the variation for different interaction positions.

The red line, representing a global fit of the data points indicates a quite good agreement of the energy resolution at low and high energies. The increase of the relative energy resolution for the highest energies in the range below 1 GeV can be explained by the lateral energy leakage due to the limited size of the prototype. The complete resolution curve, can be described by the following parametrization:

$$\frac{\sigma}{E} = \frac{3.54\ \%}{\sqrt{E/GeV}} \oplus 1.34\ \% \tag{5.1}$$

A comparison to the requirements stated in the TDR shows that the envisaged values of (2-3) % for the stochastic term and 1 % for the constant term can not be achieved with this upper limit. However, the resolution values at low energies, obtained from a 3×3 array, can be further improved with a larger cluster size, which will directly result in a reduction of the stochastic term. In addition, a PMT with a green enhanced photo-cathode which is better optimized for the emission region of the WLS fibers can increase the detected light yield and additionally improve the stochastic term. Considering these improvements, a value close to the required 3 % should be possible. The constant term is mainly influenced by the data points at high energies. Since these values have been measured with the version A prototype, an improvement can be expected for the version B modules due to the significantly improved longitudinal and lateral uniformity.

For an incident photon energy of 19 GeV, a position resolution of 1.5 mm was reported with the version A prototype in the corner between four cells [TDf15]. Due to the overlap with the beam profile, the values for the position resolution of both energy ranges can not be directly compared. To enable a comparison, a correction of the influence of the beam profile has been performed. After this correction a constant term of the parametrization of the position resolution of (3.4 ± 0.7) mm has been obtained for the energy range below 1 GeV. The difference to the value at 19 GeV, representing mainly the contribution of the constant term, can be explained by the limitation of the position reconstruction due to the limited size of the version B prototype.

Most of the shashlyk calorimeters which have been in operation in high energy physics experiments like at LHCb [ABB08], CMS [LD94] or COMPASS [CKO14] were designed for the detection of electromagnetic or hadronic probes in an energy range above a few hundred MeV. To achieve a high stopping power with a short module length, they are designed with a low sampling fraction, leading to large sampling fluctuations and a worse energy resolution at low energies. The COMPASS modules for example show a stochastic term of the energy resolution in the order of 4.8 $\%/\sqrt{E}$ [VP06], which is far away from the requirements of PANDA. The only design of a shashlyk calorimeter for an energy range comparable to PANDA has been investigated for the KOPIO experiment [ADI04], [GSA08], which was planed for the AGS facility of the Brookhaven National Laboratory but was never built due to funding issues. However, the design of the PANDA modules is based on these developments. Besides geometrical changes, the main difference of these modules was an APD based readout, providing a significantly higher quantum efficiency. With the latest version of these modules an energy resolution of

$$\frac{\sigma}{E} = \frac{2.74\ \%}{\sqrt{E/GeV}} \oplus 1.96\ \% \tag{5.2}$$

could be achieved in test-beam experiments [GSA08]. The smaller stochastic term compared to the PANDA modules is a direct result of the higher quantum efficiency provided by the APDs, while the relatively high constant term can be probably explained by the short length of these modules of only 15.9 X_0 [GSA08].

Due to a significantly larger lateral cell size the position resolution of the KOPIO modules is not directly comparable with the PANDA modules. For the time resolution a value of (90 ± 10) $\mathrm{ps}/\sqrt{E/GeV}$ was achieved with the KOPIO modules [GSA08]. Considering the higher amount of detected light by the APDs, this value is consistent with the results obtained with the current PANDA prototype.

5.1.3 Influence of different factors on the detector response

The comparison of the performance of the version A and version B prototype has shown that detector inhomogeneities can have a significant impact on the energy response and can deteriorate the energy resolution over the complete energy range.

Influence of the module design

The main source of detector inhomogeneities in lateral direction in the case of sampling calorimeters is besides the transition area between the modules also the design of the modules

itself. In case of the version A shashlyk modules, a misalignment of the scintillator tiles by a missing second fixation pin on each tile, resulting in a partial contact to the lead plates and a possible damage or a reduced coupling to the WLS fibers and also a different surface quality and treatment of the side faces of the scintillator tiles caused a strong lateral inhomogeneity of the energy response due to a varying collection efficiency for scintillation light produced in different regions of the cell. This inhomogeneity, which also varied from cell to cell caused a direct deterioration of the energy resolution but also introduced an additional error to the relative and absolute calibration of the cells. Since an uncertainty of the relative calibration can introduce additional inhomogeneities in lateral direction, it can also deteriorate the energy resolution.

In addition to the lateral inhomogeneity also a longitudinal inhomogeneity with strong variations from cell to cell has been observed for the version A prototype. As a reason for this inhomogeneity, the WLS fibers have been identified. They may have been damaged by the misaligned scintillator tiles and also showed cracks in the bending region at the front side of the modules due to a non-optimized bending procedure. As it has been shown with respect to the barrel EMC, such a longitudinal inhomogeneity can also deteriorate the energy resolution and becomes dominant for high energies due to an increased constant term of the resolution.

For the version B modules all these inhomogeneity issues have been resolved by a new design of the scintillator tiles with two fixation pins and a homogeneous coverage of all side faces with white paint. In addition new fibers and an improved bending procedure have been applied. However, to increase the light yield and to improve the lateral homogeneity, diffuse reflective TYVEK paper sheets have been inserted between the scintillator tiles and the lead plates, resulting in an increase of the module length from approximately 68 cm to 81 cm. Due to the fixed dimensions of the forward spectrometer, these enlarged modules will not fit in the foreseen gap. A GEANT4 simulation, investigating the influence of a shorter active module part showed that a reduction of the active length can not be performed without a deterioration of the energy resolution at high energies due to the increased longitudinal shower leakage. Therefore, the module has to be shortened by the application of thinner TYVEK sheets and by a redesign of the Cockcroft-Walton high voltage generator boards, which are positioned directly behind the PMTs.

Since several aspects have been changed in parallel, the impact of the individual improvements on the energy resolution and the homogeneity can not be clearly addressed. Altogether, it has been shown that a homogenous module design is the key requirement for an optimum energy response.

Influence of long term effects

For the optimization of the detector response, also long-term effects have to be considered, since an operation of PANDA is planed for at least 10 years. Due to the high radiation background in the forward spectrometer, radiation damage will be the main reason for a change of the detector performance with time, but also normal aging effects of the components have to be considered.

The most critical components for radiation damage are the scintillator tiles and the WLS fibers. For the WLS fibers from KURARAY [Y11(200)], radiation hardness tests have been performed in [DGM96], showing a reduction of the light output after an irradiation with a

dose of 1.3-1.4 kGy of 11 % for a fiber length of 180 cm [DGM96]. For modules close to the beam-pipe, this dose corresponds to approximately one and a half year of operation of PANDA and for the outer modules it represents an even longer time-scale. Due to the spread of the dose over such a long time, also spontaneous recovery of the radiation damage takes place, which may probably reduce the effective light loss to less than 10 %. A more critical issue for the light loss can be the radiation damage of the scintillator tiles. The chosen scintillator material shows a radiation stability up to a dose level of 1.2 kGy and a recovery time of approximately 80 days [GSA08], [BVL01]. In the shashlyk modules close to the beam line, a dose rate of 0.25 Gy/h can be expected [TDf15], resulting in a dose of 480 Gy for a permanent operation of 80 days. Since this dose is significantly below 1.2 kGy and an additional recovery is possible during breaks of the operation, it can be expected that the light loss stays at an controllable level, at least for the non-central detectors of the shashlyk wall. Nevertheless, since the radiation damage is stronger in the front part of the modules than in the rear part, it will also increase the longitudinal non-uniformity of the cells in addition to the deterioration of the light collection statistics.

Another source for long term changes of the performance is the natural aging of the components. Especially the surfaces of the lead plates will be covered by a layer of lead-oxide, changing their optical properties, if they are exposed to air. If no TYVEK sheets are interlard, this may influence the light output of the scintillator tiles. Finally, also the reduction of the quantum efficiency of the PMTs over time, caused by the aging of the photo-cathodes, can have a significant impact on the detected light yield. To control the influence of the light loss on the relative calibration, a light monitoring system will be implemented in the modules.

Additional critical long term effect can be introduced by the activation of the lead plates. Lead in its natural composition consists of four isotopes: 52.4 % ^{208}Pb, 24.1 % ^{206}Pb, 22.1 % ^{207}Pb and 1.4 % ^{204}Pb [SRA09]. All these isotopes can be activated with neutrons, with cross-sections ranging from a few milli-barn up to a few barn, strongly depending on the isotope and the neutron energy [SRA09]. In the decay, following the activation with half-lifes ranging from a few seconds to a few weeks, gamma quanta or alpha particles with energies from a few hundred keV up to nearly 1 MeV are emitted [SRA09]. To improve their rigidity, the lead plates used for the shashlyk calorimeter are doped with 3 % of antimony [TDf15] which additionally provides a cross section for the capture of thermal neutrons of 4.9 barns [VFS92]. Since the radiation background hitting the forward spectrometer of PANDA contains in addition to electromagnetic interacting particles also hadrons and especially neutrons, the activation of the lead plates will introduce a radioactive background in the shashlyk modules. A result of such a radioactive background can be a significant increase of the low energetic threshold of the calorimeter. Thus, a more detailed experimental investigation of the activation of the modules by neutrons and the effects of such an activation on the radiation background and the energy threshold has to be performed.

5.1.4 Dynamic range, energy threshold and readout electronics

Another open topic for the design of the shashlyk calorimeter is the coverage of the complete dynamic range by the sampling ADC. A single cell of the shashlyk calorimeter has to cover an energy range from the threshold of approximately 3 MeV up to a maximal energy of 12 GeV [TDf15]. For the test of the prototypes with photon energies below 1 GeV, a 12 bit sampling ADC (WIENER AVM 16) was used. The gain of the PMTs has been adjusted in a way that

a maximal energy of 1 GeV covers the complete dynamic range of 4096 channels. With this setting a noise level of 0.6-1.0 MeV has been achieved. If the same sampling ADC would be used for the final readout, the gain of the PMT would have to be reduced by a factor 12, since with the applied configuration only 8.3 % of the total dynamic range are covered. This reduction would reduce the signal to noise ratio and increase the threshold to a value of more than 7.2 MeV, which is significantly above the TDR [TDf15] limit of 3.0 MeV. To stay within the TDR limits for the threshold, the dynamic range has to be increased at least by a factor 7.2 MeV/3.0 MeV $\approx$ 2.5, which can only be realized by a 14 bit ADC. With this configuration a threshold of approximately 2 MeV can be expected. Compared to the threshold of 0.6 MeV applied for the prototype, this increase of the threshold would cause a deterioration of the energy resolution for 55 MeV photons by 0.5 percent points, which is still in an acceptable range for the forward region.

As an alternative, also a concept similar to the readout of the barrel of the target spectrometer with 2 ADCs, covering a low and a high gain branch would be possible. In this case two 12 bit ADCs could be used and a threshold of 1 MeV could be realized for the high gain branch, covering the lowest energies.

5.2 Barrel electromagnetic calorimeter

Up to now, two large scale prototypes have been constructed and tested for the PANDA barrel EMC. The first large scale prototype "PROTO 60" was mainly designed to test the performance of the improved PWO crystals with an APD based readout at a temperature of -25°C. It consists of 60 type 6 crystals with an average degree of tapering, read out with a single quadratic 1 cm^2 APD. With this prototype, the complete energy range from 50 MeV up to 15 GeV has been tested in several experiments at MAMI in Mainz, at the Elektronen-Stretcher-Anlage (ELSA) in Bonn and at the Super Proton Synchrotron (SPS) of CERN. The current large scale prototype "PROTO 120" was designed with the aim to realize a close to final design of the PANDA barrel EMC with all mechanical and cooling components. It consists of 120 crystals of the three most tapered crystal geometries, read out with two rectangular 1 cm^2 APDs and the current version of the APFEL ASIC chip-set version 1.5. In addition to the test of the performance with the final APDs and ASICS, also the influence of the non-uniformity in light collection of the strongly tapered crystals on the energy resolution has been tested with this prototype. The following section will discuss the different parameters contributing to the performance of this prototype and compare the results to PROTO 60 and to the electromagnetic calorimeter of CMS, which also consists of PWO crystals in a similar geometry.

5.2.1 Achieved energy resolution and influence of the non-uniformity in light collection

The focus of this work is the investigation of the influence on the energy resolution of a reduced non-uniformity in light collection achieved by a de-polishing of one lateral crystal side face. For this purpose two 3 $\times$ 3 arrays, one with de-polished and the other one with polished crystals have been tested within PROTO 120. The achieved energy resolutions show

a clear difference which can be nicely visualized with the parametrization functions shown in equations 5.3 and 5.4.

$$\left(\frac{\sigma_E}{E}\right)_{pol} = \frac{0.34\%}{E/GeV} \oplus \frac{2.07\%}{\sqrt{E/GeV}} \oplus 2.18\% \tag{5.3}$$

$$\left(\frac{\sigma_E}{E}\right)_{depol} = \frac{0.27\%}{E/GeV} \oplus \frac{2.30\%}{\sqrt{E/GeV}} \oplus 0.5\% \tag{5.4}$$

Due to the reduced non-uniformity, a significant reduction of the constant term, initiated by a more homogenous energy response could be achieved. At the same time, the reduced light yield from the front part of the crystal, which is mainly critical for low energies causes a slight increase of the stochastic term. As a result, an improvement of the relative energy resolution has been achieved for energies above 200 MeV, while the energy resolution stays nearly at the same level within the error bars for the energy range between 50 MeV and 200 MeV. An approximation of the experimental data to lower energies based on the parametrization shows that for an energy of 20 MeV only a very slight deterioration of 1.4 percent points, from 21.1 % to 22.5 % has to be expected. To obtain a deeper understanding of the processes, GEANT 4 simulations have been performed, applying a specially developed model to reproduce the energy response. With these simulations, a reproduction of the experimental energy resolution of the polished 3 × 3 array is possible within the error bars. For the de-polished 3 × 3 array, compared to the experimental results an even better energy resolution and therefore a higher improvement factor between the two arrays has been simulated. In contrast to the experiment, the improvement by de-polishing of the crystals in the simulation already takes place for energies above approximately 75 MeV. This discrepancy between the experiment and the simulations shows that an additional improvement of the energy resolution for the de-polished crystals may be possible independent of contributions from electronic noise.

The simulations of the energy distribution of the electromagnetic shower within the prototype also showed that the effect of the non-uniformity on the energy resolution is even higher for low energies than for higher energies. The reason for this behavior can be seen in the event-wise variation of the position of the showers center of gravity, which is mainly responsible for the deterioration of the energy resolution by the non-uniformity in light collection. While the spread of the average shower profile becomes larger for increasing energies, the event-wise variation of its center of gravity has its largest value for the lowest energies, since low energetic showers are subject to the strongest fluctuations. In addition to this increased variation of the center of gravity, also the non-uniformity curve of the light collection shows its highest slope in the front part of the crystal, which additionally increases the impact of the non-uniformity on the energy resolution at low energies. In the experiment this cannot be directly observed, since also the $1/E$-dependent electronic noise and the $1/\sqrt{E}$-dependent photon statistics of the collected light influence the energy resolution. For low energies, these contributions can be significantly higher than the contribution of the non-uniformity. For increasing energies their impact becomes smaller and smaller, and the influence of the non-uniformity in light collection becomes dominant. The difference of the polished- and de-polished crystal array clearly confirms these effects. While the deterioration of the light collection statistics is dominant at energies below 50 MeV, providing slightly worse results for the de-polished array, a trade off between the deteriorated light collection statistics and the improved uniformity can be observed between 50 MeV and 200 MeV, resulting in comparable

results for both arrays. For higher energies, the dominance of the decreased constant term due the improved homogeneity of the energy response becomes clearly visible.

The simulation for different crystal geometries showed that a de-polishing makes even sense for less tapered crystals. For such crystals the de-polishing on the one hand causes a smaller improvement, but on the other hand also a smaller light loss is introduced to the front part of the crystals. Altogether comparable results should be observable with de-polished crystals of all types.

To make a decision for which crystals within the barrel a de-polishing provides an improvement, the energy distribution at different scattering angles has to be considered. The left part of figure 5.3 shows the differential single crystal rate spectrum of the energy for different angles of 25°, representing the most forward region of the barrel equipped with type 11 crystals, 90° in the center of the barrel and 135° in the backward region of the barrel.

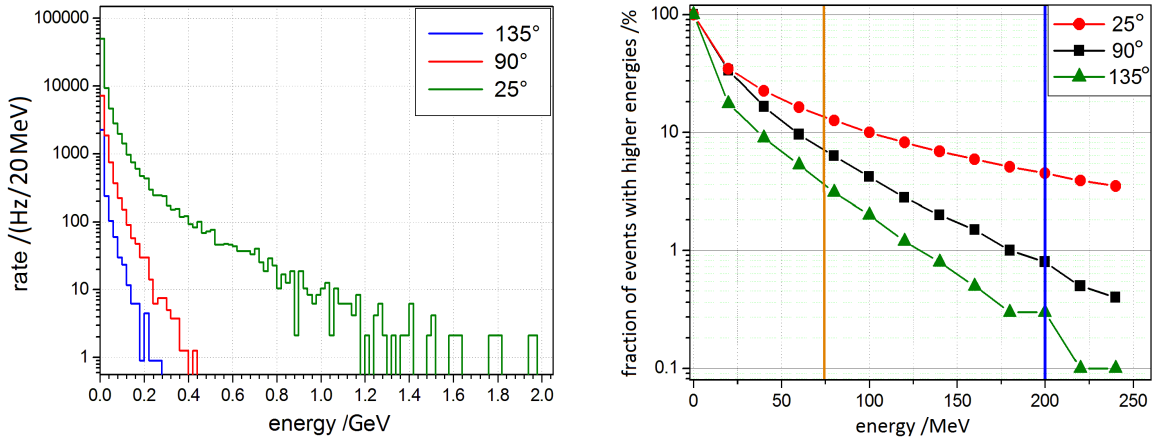

Figure 5.3: Left: Differential rate spectrum of the energy for a single crystal positioned under a polar angle of 25° (green), 90° (red) and 135° (blue). The data is taken from [TDe09]. The simulation is performed with the Dual-Parton-Model (DPM) event generator for an incident anti-proton beam momentum of 15 GeV/c [TDe09]. Right: Fraction of events with an energy above the given energy for different polar angles. The energy above which an improvement of the energy resolution by a de-polishing of the crystals has been observed is marked as a blue line for the experiment and as an orange line for the simulation.

The figure shows the strong impact of the polar angle on the energy distribution. For all distributions a strong increase of the intensity can be observed for energies below 100 MeV. To quantify this distributions, the fraction of events with an energy above a certain energy limit is plotted in figure 5.3 (right) for different polar angles. For comparison, the energy limits above which an improvement of the energy resolution can be observed according to the experimental results and the simulations are marked as a blue and an orange line. The rate distribution for a polar angle of 135° shows that a de-polishing of the crystals in backward direction will provide an improvement for only a very small fraction of events. In contrast, in the most forward region of the barrel at least 4.5 %, according to the experimental results, and up to 13 % of the photons, according to the simulations, can gain in energy resolution by de-polishing one lateral side face of the crystals. In the center of the barrel the number of events which gain in resolution is reduced to 0.8 % according to the experiment and approximately 7 % according to the simulations. On the other hand, the energy distributions for all polar angles

show a significantly larger fraction of photons with energies below approximately 40 MeV, which will be effected by a slight deterioration of the energy resolution. In addition to this loss in resolution, also a slight increase of the low energetic threshold can be expected for de-polished crystals due to the reduced light yield from the front part of the crystal, resulting in a reduction of the detection efficiency (for a more detailed discussion see section 5.2.6).

In addition to the fraction of events which gain from an improved light collection uniformity, also the absolute gain in resolution for the different crystal types is an important argument pro or contra a de-polishing. Figure 4.77 shows that the gain in resolution is directly correlated with the strength of the non-uniformity of a polished crystal, which is shown in figure 5.4 (left) for the different crystal types of the barrel.

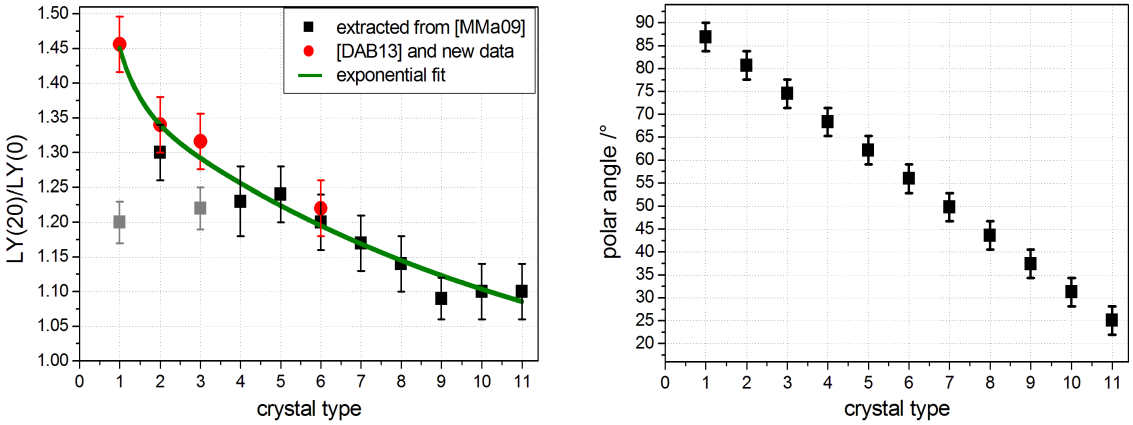

Figure 5.4: Left: Ratio of the light yield extrapolated to the front and rear side of a crystal for the different crystal types of the barrel EMC. The degree of tapering decreases gradually with increasing type number. The black points are extracted from the non-uniformity curves presented in [MMa09], while the red points are based on [DAB13] and the measurements presented in this work. The gray points are excluded from the fit, since they are obviously influenced by a systematic error. Right: Average polar angle of the different crystal types in the forward part of the barrel.

For the least tapered crystals (type 10 - 11) an enhancement of the light created in the front part of the crystal compared to the rear part of only ∼10 % has been measured. According to the simulations in figure 4.77 a de-polishing of these crystals leads to an improvement of only ∼0.2 percent points at 1 GeV. On the other hand improvements of up to 1.4 percent points at 1 GeV and still 1.2 percent points at 240 MeV have been simulated for the most tapered type 1 crystals. To connect these values with the rate distributions in figure 5.3, the average polar angle under which the different crystal types are positioned in the forward region of the barrel is shown in figure 5.4 (right). Since the most tapered crystals with the strongest non-uniformity are positioned in the center of the barrel, only relatively few events can gain from the improvements. On the other side the increased number of events with an improved resolution due to the de-polishing in the forward region will gain only a relatively low absolute improvement. Considering these opposing trends, crystals with an average degree of tapering which are positioned in the middle of the forward region of the barrel at around 55° may gain the largest overall benefit from de-polishing.

Based on the presented studies a decision for or against a de-polishing of certain crystal types in the forward direction of the barrel has to be made under consideration of the importance of

the different energy ranges and the impact on the detection efficiency for the physics program of PANDA.

5.2.2 Comparison of the energy resolution with PROTO 60 and the CMS ECAL

The energy response of the first large scale prototype of the PANDA barrel EMC, PROTO 60, has been analyzed and described in detail in the PhD thesis of Markus Moritz, "Measurements and improvements of the response of the PANDA-EMC prototype PROTO60 to high energetic particles and photons in accelerator experiments" [MM13]. According to this work, the parametrized energy resolution of all 60 crystals over the complete energy range from 50 MeV up to 15 GeV can be described by [MM13]:

$$\frac{\sigma}{E} = \frac{0.25\ \%}{E/GeV} \oplus \frac{1.86\ \%}{\sqrt{E/GeV}} \oplus 1.46\ \% \tag{5.5}$$

Since for PROTO 120 only 3 × 3 arrays have been tested so far, the results are not directly comparable. The only parametrization for a 3 × 3 array and different thresholds given in [MM13] are obtained from an earlier experiment with photon energies above 200 MeV and non optimal conditions. Therefore, the data obtained with PROTO 60 during the beam-time at MAMI in 2011 has been re-analyzed under the same conditions like PROTO 120, considering only a 3 × 3 array of crystals and applying thresholds of 2.8 MeV and for comparison also 1.0 MeV. The other details of the analysis are identical to [MM13] and can be found in this work. However, in contrast to PROTO 120 the data obtained with PROTO 60 in 2011 has been recorded with peak-sensing ADCs. To obtain a better comparability, also the results obtained with a sampling ADC readout of PROTO 60, presented in [KBD11] will be considered for a comparison. For this readout method a minimal threshold of 2 MeV has been determined for PROTO 60 [KBD11]. Figure 5.5 shows the obtained energy resolution curves for 3 × 3 arrays of PROTO 60 with the different data acquisition methods and thresholds in comparison to the curves obtained for the polished and de-polished crystal arrays of PROTO 120.

If for the signals of PROTO 60, which are recorded with a peak-sensing ADC, a threshold of 2.8 MeV is applied, approximately the same energy resolution like for the two arrays within PROTO 120 can be achieved in the energy range from 50 MeV to 200 MeV. However, if the lower experimental noise level in the case of PROTO 60 is considered and a threshold of only 1 MeV is applied, a significantly better energy resolution can be achieved with PROTO 60 for this energy range. An even more significant improvement of the resolution is possible, if the data acquisition of PROTO 60 is performed with a sampling ADC. For the highest investigated energies above 500 MeV the energy resolution of PROTO 60, obtained with a peak-sensing ADC, shows values in-between the resolution of the polished type 2 crystals and the resolution of the de-polished crystal array. Also in this energy range the resolution of PROTO 60 extracted from sampling ADC data is still slightly better than the values from the peak-sensing ADC readout. Compared to the de-polished crystal array of PROTO 120 also the sampling ADC readout provides an inferior resolution. Besides the different electronic noise level, this behavior at high energies can be explained by the influence of the non-uniformity in light collection, which shows a slope of type 6 crystals in-between the slope

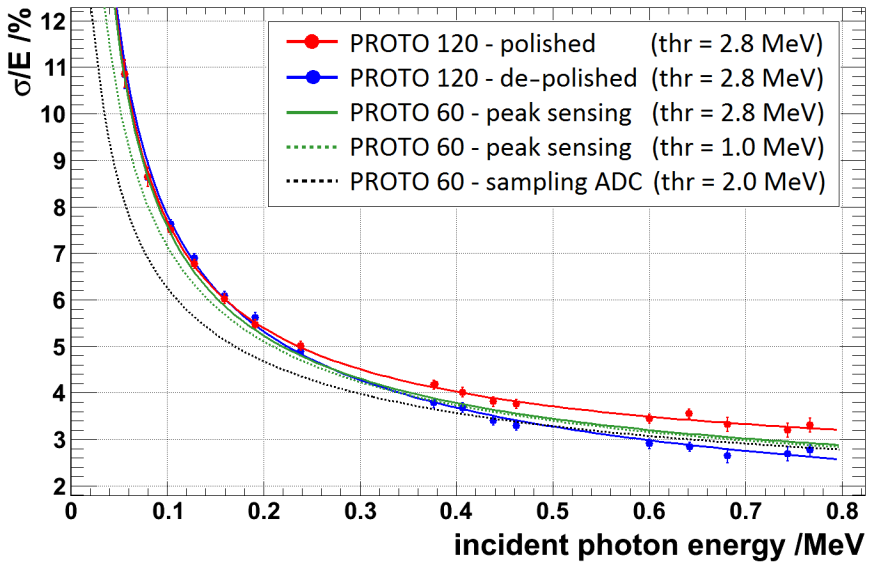

Figure 5.5: Comparison of the energy resolution of a 3 × 3 array of de-polished and polished type 2 crystals within PROTO 120 with the energy resolution obtained with different data acquisitions and thresholds for a 3 × 3 array of polished type 6 crystals within PROTO 60. Both prototype have been operated at -25°C. The data for a sampling ADC readout of PROTO 60 is taken from [KBD11].

of type 2 crystals and the slope of de-polished crystals. In summary, the comparison of the energy resolution of PROTO 120 and PROTO 60 shows that a significant improvement is possible for energies below 500 MeV if the noise level and the threshold are further reduced. In the current configuration the intrinsic noise level of the ASIC clearly provides a limitation of the achievable energy resolution at low energies compared to the discrete pre-amplifiers applied in PROTO 60.

A fit of the parametrization

$$\frac{\sigma}{E} = \frac{a}{E/GeV} \oplus \frac{b}{\sqrt{E/GeV}} \oplus c \tag{5.6}$$

with the electronic noise term a, the stochastic term b and the constant term c provides the parameters given in table 5.3 for the different cases. For comparison, the energy resolution parameters obtained for a 3 × 3 array of straight 20 × 20 × 200 mm^3 crystals with a single APD readout, measured at a temperature of 0°C [NDD08] are given. If the same threshold of 2.8 MeV is applied, a comparable electronic noise term can be obtained for PROTO 60 and PROTO 120. However, a reduction of the threshold of PROTO 60 to 1 MeV, leads to a significantly better electronic noise term, while the electronic noise term nearly disappears for a sampling ADC readout of PROTO 60. For the stochastic term only a non-significant improvement can be observed between the polished crystals of PROTO 60 and the polished array within PROTO 120, although PROTO 120 is equipped with two APDs instead of one in the case of PROTO 60. This is consistent with the observed small improvement factor between a readout with one and two APDs for PROTO 120. The improvement of the stochastic term for a sampling ADC readout of PROTO 60 compared to the readout with a peak sensing ADC can be explained by a different fit of the energy resolution with nearly no

case	ADC	thresh. /MeV	**a** in %	**b** in %	**c** in %
PROTO 60 (type 6)	peak sensing	1.0	0.15	2.16	1.47
PROTO 60 (type 6)	peak sensing	2.8	0.32	2.11	1.6
PROTO 60 (type 6) [KBD11]	sampling	2.0	$< 10^{-4}$	2.01	1.66
PROTO 120 polished	sampling	2.8	0.34	2.07	2.18
PROTO 120 de-polished	sampling	2.8	0.27	2.30	0.5
straight crystals [NDD08]	peak sensing	1.0	$< 10^{-4}$	2.10	1.1

Table 5.3: Comparison of the fit parameters of the energy resolution curves of a 3 × 3 array with de-polished and another one with polished crystals within PROTO 120 with a 3 × 3 array within PROTO 60 and a 3 × 3 array of straight 20 × 20 × 200 mm^3 crystals [NDD08]. The parameters for PROTO 60 with a sampling ADC readout and the parameters for the array with straight crystals have been obtained from a fit of the data points presented in [KBD11] and [NDD08] with the parametrization in equation 5.6. PROTO 60 and PROTO 120 have been operated at -25°C. The array of straight crystals has been operated at a temperature of 0°C.

contribution from the electronic noise term. Within the error range of the data points it is possible to obtain a value for the stochastic term, which is comparable to the value obtained for the readout with a peak sensing ADC. The constant term of the energy resolution directly reflects the slope of the non-uniformity in light collection. Only for de-polished crystals it is possible to fulfill the TDR requirement of a value less than 1 % [TDe09] for this term. On the other hand the array with polished type 2 crystals shows the highest value for the constant term. For the array with completely straight crystals an improvement of the constant term compared to PROTO 60 but a higher constant term compared to the de-polished crystals within PROTO 120 has been obtained. However, a direct comparison is not possible due to the different electronic noise level and the approximately 40 % smaller volume of this array in lateral direction. Nevertheless, even under this conditions the constant term is close to 1 % and thereby significantly lower than for the tapered crystals.

A similar electromagnetic calorimeter like for PANDA is implemented in the Compact Muon Solenoid (CMS) spectrometer at CERNs LHC. The crystals also consist of lead tungstate, but in an earlier, less optimized version with a significantly lower light yield. Also the operation at room temperature causes an additional reduction of the light yield compared to the operation at -25°C in the PANDA experiment. The design of the CMS barrel EMC uses a similar but significantly less tapered crystal geometry like PANDA. To provide enough stopping power for the detection of high energetic electromagnetic probes produced in proton-proton collision with several TeV center of mass energy, the crystals are 3.3 X_0 longer than the PANDA crystals [FC11]. Since CMS is mainly focused on the detection of energies in the region from several GeV up to the TeV region, the constant term plays the most important role for the energy resolution. To minimize this term, all crystals were de-polished on one side surface to a slope of the light collection non-uniformity in the center of the crystal below 0.35 %/X_0 [ACL02]. In test-beam studies the following parametrization of the relative energy resolution could be obtained for the CMS ECAL [FC11]:

$$\frac{\sigma}{E} = \frac{12\ \%}{E/GeV} \oplus \frac{2.8\ \%}{\sqrt{E/GeV}} \oplus 0.3\ \% \tag{5.7}$$

Due to the de-polishing of the crystals, a constant term of only 0.3 %, comparable to the result for the de-polished PANDA crystals, could be achieved. Due to the lower light yield, the

stochastic term is significantly higher. Since CMS is focused on high energies, the electronic noise term has no relevance and is therefore not optimized by a special low noise pre-amplifier, like in the case of PANDA.

5.2.3 Influence of the feature extraction and the calibration on the energy resolution

The feature extraction can have a significant impact on the influence of the electronic noise on the energy resolution and the single crystal threshold and is therefore especially important for low energies with a reduced signal to noise ratio. Especially for higher energies, also the relative calibration of the crystals has a significant influence on the achievable energy resolution, since an uncertainty of the relative calibration can introduce lateral inhomogeneities to the calorimeter. Due to their possible impact on the energy resolution, a strong focus has been set on the optimization of these parameters.

Influence of the feature extraction

In section 4.2.6 different feature extraction methods have been compared to optimize the energy resolution. The comparison of the methods shows that a simple peak sensing feature extraction and a fit of the pulse shape, as well as the integration of the pulse over a limited region around the extremum provide approximately the same energy resolution for a 3×3 array at energies above 100 MeV. Only for incident photon energies below 100 MeV an improvement can be observed if the amplitude is extracted by a fit of the pulse-shape or by an integration of a limited region of the signal. For an energy of 55 MeV the improvement by a fit of the pulse compared to a peak sensing feature extraction is in the order of 0.6 percent points, with an increasing trend for lower energies. This improvement, which is introduced by the averaging of trace fluctuations and noise contributions for low signals in the outer detectors of the array is expect to be even more significant for larger cluster sizes due to the higher contributions of small energy depositions in the outer crystals. For larger clusters also an improvement up to even higher energies is expected. Based on these observations, a fit of the pulse shapes at low energies can be recommended. On the other hand a fit like it has been applied for the prototype causes a significant computing effort which may only be possible in an online feature extraction as a modified version with an optimized fitting routine and a reduced set of data-points. In contrast to this, it is much simpler to implement the integration of a fixed region of the pulse around the extremum in the online feature extraction. However, the integration provides a significantly lower improvement of the relative energy resolution of only 0.2 percent points at 55 MeV and shows a higher sensitivity to the noise characteristics of the ASIC.

Independent of the difference in energy resolution at low energies it can be assumed that the fit of the pulse and the integration of a limited signal region provide a more reliable absolute value of the energy information, since a larger fraction of the signal is included in the feature extraction and a reduced influence of electronic noise can be expected. Like for the relative energy resolution this is especially important for larger clusters, since the small signal amplitudes in the outer detectors can be significantly better reconstructed with these feature extraction methods, compare to a simple search of the extremum.

Influence of the relative calibration

The relative calibration of the prototype has been performed with different approaches based on the data from an in-beam calibration run and from the interaction of cosmic muons. The comparison of the methods indicated that the calibration with cosmic muons provides the most promising results for the energy reconstruction. The worse results for the calibration based on the data from the in-beam calibration run can be explained by the strong dependence of the response of a single crystal on the alignment of the photon beam, which was not adjusted for the outer detectors during the calibration run.

In the final calorimeter barrel, the crystals will be oriented in all azimuthal and polar angles, making a calibration with cosmic muons more complicated. One possibility to use cosmic muons at least for the pre-calibration of the detectors is a comparison of the energy deposition distribution of each crystal to simulations (see also the following subsection). However, since this simulations have to include the correct non-uniformity in light collection for each crystal, a certain error will be introduced to the obtained calibration coefficients. Another possibility for a more accurate calibration with cosmic muons is a coincidence of the crystals from the upper half of the barrel with their counterparts from the lower half of the barrel, oriented in the same direction. This method exploits the fact that the angular distribution of cosmic muons covers the complete upper half square of the horizon. However, the coincidence rate will be significantly reduced for crystals with an orientation close to the horizon and will also not work for the most forward crystals, having no counterpart in backward direction. Altogether, a combination of both approaches has to be used for the pre-calibration. A final relative calibration can be performed for example by using the reconstruction of the invariant mass of photon pairs from neutral pions and eta mesons, from the decays

$$\pi^0 \to \gamma\gamma \qquad \text{and} \qquad \eta \to \gamma\gamma. \tag{5.8}$$

The CMS collaboration was able to obtain an uncertainty of the relative calibration with this method significantly below 1 % [CMS13].

An optimized cosmic muon calibration of PROTO 120 based on a GEANT4 simulation with the cosmic-ray shower library

For the relative calibration of crystals with a different non-uniformity in light collection and a different orientation relative to the horizontal or vertical axis, a varying effective signal height has to be expected from the energy deposition of cosmic muons. In addition, conditions like the column cut for the horizontal orientation or the exclusion cut for the vertical orientation of the prototype (see section 3.2.4) also influence the effective value of the most probable energy deposition. To estimate the impact of this effects on the present analysis and to provide a calibration model for future prototype tests, including also larger clusters with a significant difference of the crystal orientation as well as a mixture of different crystal types, a GEANT4 simulation of the interaction of cosmic muons has been executed. For this purpose the particles of the cosmic shower, including muons, and their distributions have been generated with the cosmic-ray shower library (CRY) [HLV12]. The CRY library uses data tables to generate cosmic ray shower particles for primary energies ranging from 1 GeV to 100 TeV and secondary particle energies between 1 MeV and 100 TeV [HLV12]. For the

simulations an altitude of 0 m, corresponding to the see level as best approximation for the real altitude and an latitude of 50° for Mainz, Germany are set. In addition, the date has been set to April 2015 to adjust the cosmic-ray distributions to the eleven year cycle of the sunspots. A detailed description of the physics used to generate the data tables of the CRY library can be found in [HLW12]. The particles are emitted from an area corresponding to the plastic scintillator paddle, which was positioned on top of the detector and used as a trigger for the readout during the measurement. For the prototype the model presented in section 4.3 with the same crystal orientation like in the experiment is used. Figure 5.6 shows the interaction of several events from the cosmic shower with a horizontally and a vertically oriented prototype.

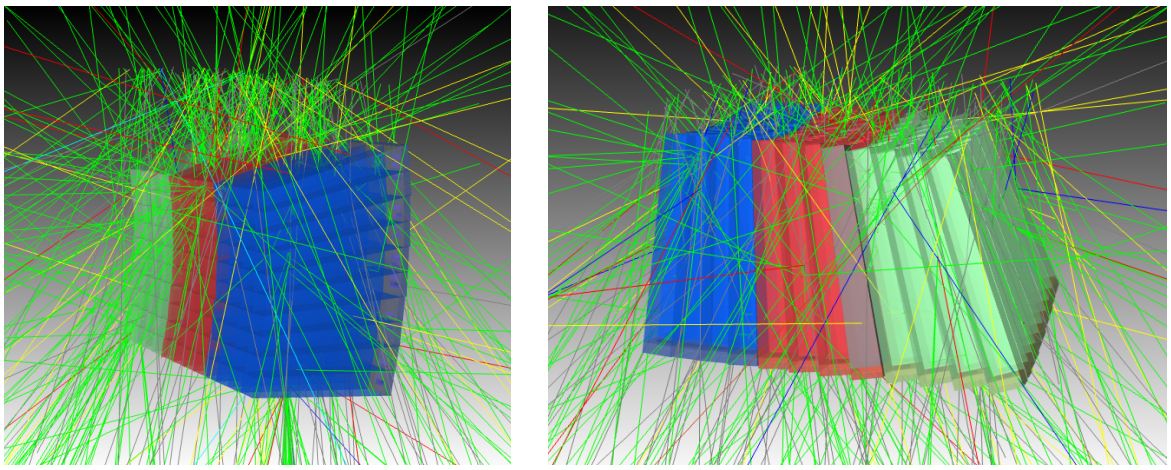

Figure 5.6: Interaction of 200 events from a cosmic-ray shower with a horizontally (left) and a vertically (right) oriented prototype. The cosmic shower particles are emitted from an area on top of the detector, corresponding to the plastic scintillator paddle used as a trigger of the readout in the experiment.

To obtain sufficient statistics, for a horizontal orientation of the prototype six million events and for a vertical orientation twenty million events have been simulated. For the deposited energy, the column cut for a horizontally oriented prototype and the exclusion cut for a vertically oriented prototype have been applied with the same thresholds like for the experimental data (see section 3.2.4). Figure 5.7 shows the simulated energy distributions under the announced conditions. The figures show that like for the experimental data the applied cuts provide the best results for the central detectors, since only here a neighbor, on which the condition can be applied, exists in all directions. In contrast to this for the outer crystals still shorter muon paths with a smaller energy deposition are possible.

The most probable values of the deposited energy detected in the single crystals for a horizontal orientation of the prototype are given in the left part of figure 5.8. The pure deposited energy in the single crystals shows that the column cut increases the most probable detected energy in the central row, since it rejects all events in which not the complete width of the crystal is passed by the cosmic muons. Due to the non-uniformity in light collection the effectively detected signal amplitude is strongly influenced by the non-uniformity curves of the individual crystals. To consider this effect for a relative calibration, the non-uniformity weighting model presented in section 4.3 has been applied to the deposited energy during the

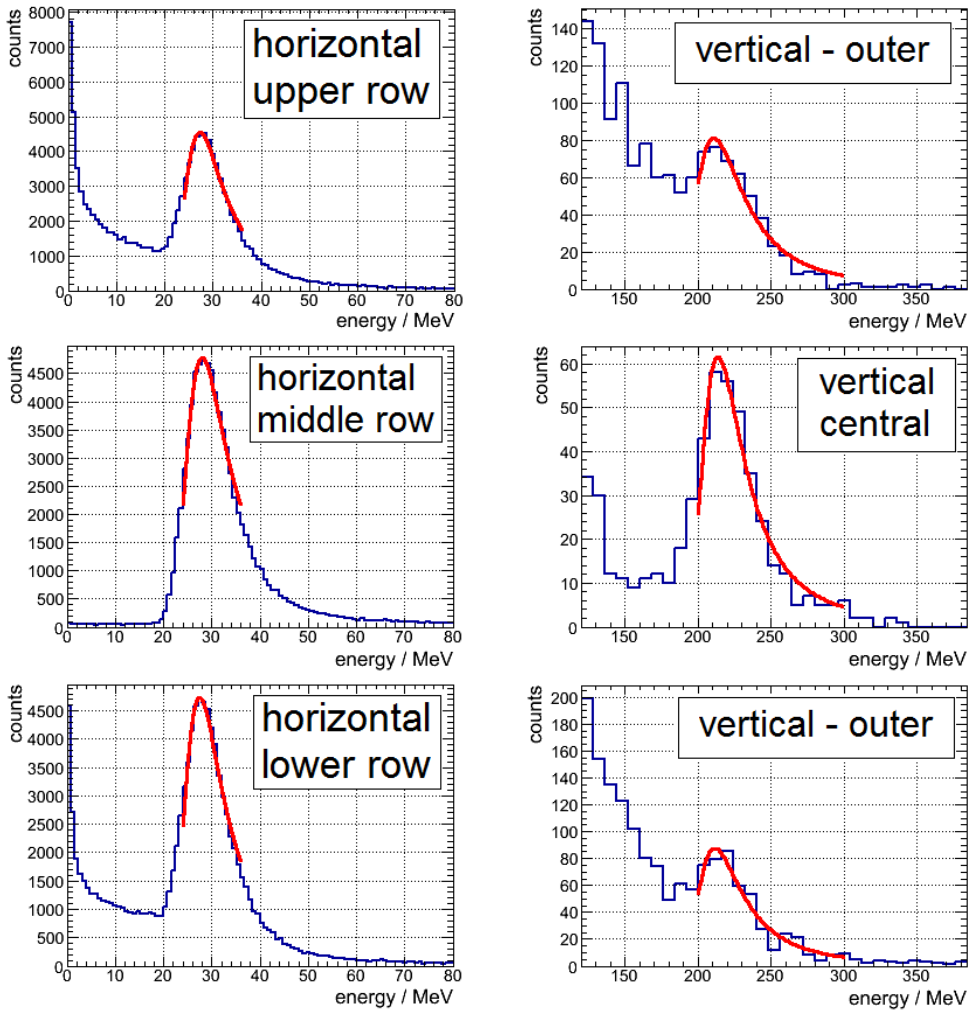

Figure 5.7: Simulated energy distributions of cosmic muons for a horizontally (left column) and a vertically (right column) oriented prototype. For the horizontal orientation a column cut and for the vertical orientation an exclusion cut (see section 3.2.4) has been applied. For both orientations the energy distributions for a crystal positioned in the center of the array and for two crystals positioned in the outer ring of the array are shown. The distributions are fitted with an overlap of a Gaussian- and a Landau- distribution (red line).

simulation. The obtained results are shown in the left part of figure 5.8. For this points a clear difference between de-polished crystals (red points) and polished crystals (orange points) can be observed. Like expected, due to the non-uniformity in light collection the polished crystals detect significantly higher signal amplitudes than the de-polished crystals. To visualize the difference between a relative calibration based on the simulated signal amplitudes under consideration of the non-uniformity and a relative calibration relying on the assumption of an nearly identical energy deposition in all crystals, the deviation of the most probable deposited energy in the individual crystals relative to the energy deposition in the central crystal is shown in the right part of figure 5.8. The de-polished crystals show a typical difference below 3 % compared to the central crystal. Only for the polished crystals, like expected a

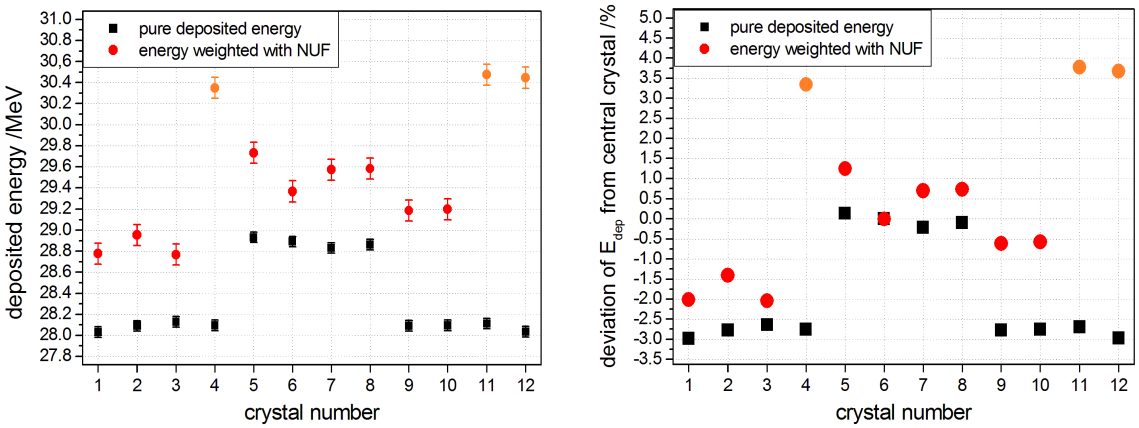

Figure 5.8: Left: Simulated values of the pure energy deposition of cosmic muons and of the non-uniformity weighted response after the application of a column cut for a horizontal orientation of the prototype. The red point represent de-polished crystals and the orange points indicate polished samples. Right: Deviation of the simulated response of the single crystals from the response of the central crystal.

significantly higher difference can be observed compared to the de-polished samples. This observation shows that an exact simulation of the response is especially important, if samples from different types or polished and de-polished crystals are included in the same cluster. However, in the final calorimeter barrel the individual non-uniformity curves of the single crystals will not be available. Nevertheless, the average non-uniformity curve of each crystal type should provide results with an acceptable error of the simulation.

A comparable conclusion can be drawn for the vertical orientation of the prototype. The values obtained in this case for the deposited energy and the non-uniformity weighted response under the application of the exclusion cut are shown in figure 5.9.

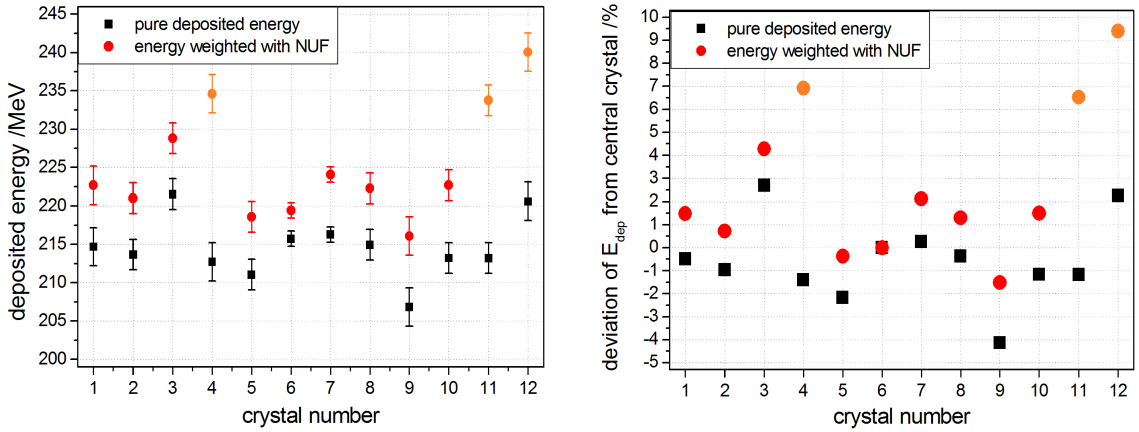

Figure 5.9: Left: Simulated values of the pure energy deposition of cosmic muons and of the non-uniformity weighted response after the application of an exclusion cut for a vertical orientation of the prototype. The red points represent de-polished crystals and the orange points indicate polished samples. Right: Deviation of the simulated response of the single crystals from the response of the central crystal.

Also for this orientation of the prototype the simulated values show a typical deviation below 3-4 % for the de-polished crystals. Only the polished crystals show a significantly higher deviation of up to 10 %.

Since only one of the three polished crystals is included in the analyzed 3 × 3 array it can be assumed that the variation of the relative calibration parameters under consideration of the simulation results is within the error bars of the fit of the experimental energy deposition distribution of the cosmic muons for most of the crystals in the present analysis. The left part of figure 5.10 shows that a calibration of the 3 × 3 array with de-polished crystals based on the simulated amplitudes of the cosmic muon interaction, including the non-uniformity in light collection, obtained from a horizontally and a vertically oriented prototype and also for a calibration based on a linear fit of both simulated data points causes a difference of the reconstructed signal amplitude of the 3 × 3 array of less than half a percent compared to a calibration based on the assumption of a nearly identical energy deposition of cosmic muons in all crystals. Nevertheless, a slight variation of the linearity of the energy response at low incident photon energies can be observed if the simulated non-uniformity weighted response is used for the relative calibration.

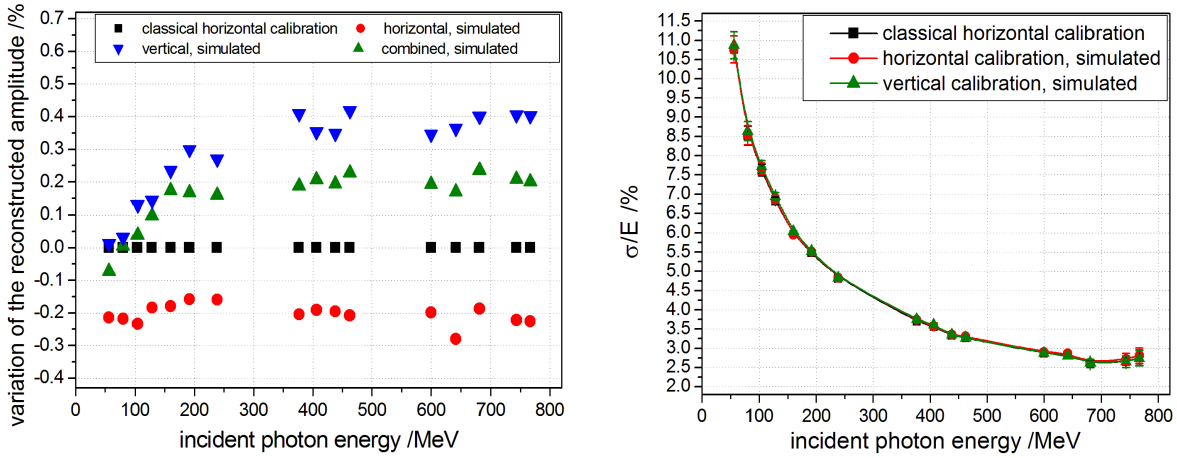

Figure 5.10: Left: Variation of the reconstructed energy response of a 3 × 3 array obtained with the calibrations based on the simulated values relative to the energy reconstructed with a calibration, assuming an approximately identical energy deposition in each crystals (classical case). Right: Relative energy resolution for the different calibration approaches with and without the consideration of the simulated response.

Also for the relative energy resolution obtained with the different calibration approaches, shown in the right part of figure 5.10, no significant difference can be observed. This can be explained by the small change of the calibration parameters and since the relative energy resolution at energies significantly below 1 GeV is dominated by the light collection statistics and the electronic noise at very low energies. However, especially for higher energies an exact calibration is a key requirement for an accurate reconstruction of the energy and for an optimal energy resolution. Therefore, a more significant impact of the improved calibration is expected in the energy region of several GeV and above.

5.2.4 Accuracy of the absolute energy calibration

The absolute energy calibration coefficient has been determined with different methods. Especially the calibrations based on the energy deposition of cosmic muons in a horizontally and vertically oriented prototype and the calibration based on the maximal energy deposition in the 3 × 3 array show a good agreement, if the calculated value for the most probable energy deposition of cosmic muons is used. Nevertheless, the simulation of the interaction of cosmic muons with the prototype, based on the CRY library provides slightly higher energy values than the ones which have been obtained by a simple calculation of the most probable path length. Table 5.4 compares the absolute calibration coefficients obtained for the different cases.

case	E_{dep} /MeV	amplitude ch 6	abs calib. coefficient
horizontal - calculated	26.7 ± 0.2	1165 ± 15	(43.6 ± 0.6) ch/MeV
horizontal - simulated - pure energy	28.9 ± 0.05	1165 ± 15	(40.3 ± 0.5) ch/MeV
horizontal - simulated - with NUF	29.4 ± 0.1	1165 ± 15	(39.6 ± 0.5) ch/MeV
vertical - calculated	212.1 ± 1.7	9230 ± 100	(43.5 ± 0.6) ch/MeV
vertical - simulated - pure energy	215.7 ± 2.0	9230 ± 100	(42.8 ± 0.6) ch/MeV
vertical - simulated - with NUF	219.4 ± 2.5	9230 ± 100	(42.1 ± 0.7) ch/MeV

Table 5.4: Absolute calibration coefficients based on the energy deposition of cosmic muons. The calculated values have been derived in section 3.2.4, while the simulated values are based on the cosmic muon simulation with the CRY library in section 5.2.3. All values are given for the central detector (channel 6).

The table shows that for a horizontal orientation of the prototype a difference of the absolute calibration coefficient of up to 9 % can be observed between the simulated and the calculated energy deposition. In contrast to this, the values obtained for a vertical orientation of the prototype are much more comparable with the calculated value and show only a reduction of the absolute calibration coefficient of approximately 3 %, with all single values contained in the error range of the mean value. This difference shows, that an error of a few percent has to be assumed for an absolute calibration of the prototype based on cosmic muons. Besides this error, also the influence of the non-uniformity has to be considered for an absolute calibration, since the mean energy deposition position of the electromagnetic shower generated by high energetic probes interacting in the front of the crystal, shows a dependence on the incident photon energy. Due to the non-uniform light collection, this energy dependence directly results in an energy dependence of the detected signal amplitude per deposited energy, causing a non-linear energy response. Taking the logarithmic dependence of the shower depth on the incident energy and the high slope of the non-uniformity curve of the light yield in the front part of the crystal into account, this effect will be especially dominant at low energies close to the threshold, while the prototype test showed that for energies above 50 MeV no significant deviation from the linearity of the reconstructed energy can be observed for the investigated 3 × 3 arrays with polished and de-polished crystal. As another effect of the non-uniform light collection, also the relation between the signal generated by cosmic muons and the signal generated by an electromagnetic shower show a dependence on the non-uniformity curve. Only for an uniform light collection the signal amplitude per deposited energy unit would be identical. Therefore, this effect should introduce only a small error to the absolute calibration

of the de-polished crystals analyzed in this work, since their response is nearly uniform. On the other side, for polished crystals with a high non-uniformity a correction has to be applied for this effect, since the signal generated by the uniformly distributed energy deposition of cosmic muons per deposited energy unit is not identical to the signal generated per deposited energy unit by high energetic gammas which deposit the main part of their energy in the first half or even in the first third of the crystal, resulting in a stronger amplification of the signal by the focusing effect.

5.2.5 Coverage of the dynamic range with the low- and high- gain branch

A single crystals of the barrel part of the PANDA electromagnetic calorimeter has to cover an energy range from the single crystal threshold of 3 MeV up to a few hundred MeV or even a few GeV, depending on the polar angle of its position. The coverage of this dynamic range with sufficient accuracy for the lowest energies, would require a quite high maximal output voltage of the preamplifier and a sampling ADC with a high dynamic input range. To avoid the technical limitations and high costs of this solution, two branches with different amplifications have been implemented in the ASIC chip-set. The high gain branch with a programmable amplification of 16 or 32 can be used to cover the lowest amplitudes, while the low gain branch is used for higher amplitudes.

The analysis of the test experiment showed that an amplification programmed to 16 provides an effective amplification of the high gain relative to the low gain branch of 10.8 $\pm$ 0.8 for the current ASIC version 1.5. The reason for this deviation from the programmed value is not finally understood. With this amplification the high gain branch starts to saturate at approximately 24.000 sampling ADC channels. According to the absolute calibration for the single detectors in figure 4.26, this corresponds to an energy deposition of approximately (720 $\pm$ 170) MeV in a single crystal. Considering the average amplification between the low and high gain branch of 10.8, the low gain branch should be able to cover a dynamic range up to (7.8 $\pm$ 1.8) GeV of energy deposition in a single detector, which is sufficient for the maximal expected photon energy of 7.3 GeV for the most forward region of the barrel.

The decision for an amplification of the high gain branch of 16 or 32 has to be made based on the polar angle of the individual detector units and the expected corresponding energy distributions. To reduce the impact of a possible variation between neighboring energies reconstructed from different branches, it should be set in a way that the transition point between the high and low gain branch appears at an energy where only a low fraction of events is expected. On the other hand the amplification should be set as high as possible to improve the signal to noise ratio. According to the experimental data, a real amplification of 16 would set the transition point to (486 $\pm$ 115) MeV, while an amplification of 32 leads to a transition pint at (243 $\pm$ 57) MeV energy deposition in a single crystal. A comparison with the differential rate spectrum in figure 5.3 shows that an amplification of 32 is suitable for the backward directions and the center of the barrel, while in forward directions an amplification of 16 better fits to the energy spectrum. Even at a polar angel of 25° only less than 2 % of the events will exceed the range of the high gain with this setting. Under this consideration an amplification of 10.8 like it has been observed for the latest ASIC version 1.5 is too low for an application in the barrel.

In general, the combination of the two branches makes it possible to apply the good signal to noise ratio and the low threshold of the high gain branch at low energies and the high dynamic range of the low gain branch for the highest energies. In addition the use of two standard sampling ADCs per channel is more cost efficient than the application of a single high dynamic range sampling ADC. According to figure 4.47 the combination of the two branches causes only a very small deterioration of the relative energy resolution in the transition region but no overall deterioration at high energies.

5.2.6 Influence of threshold and noise level on the detector performance

The electronic noise, recorded by the sampling ADC is determined by different factors. On the one hand the APD introduces a gain dependent dark current to the signal. On the other hand also the ASIC introduces a certain noise level due to the switching of digital transitions in the CMOS circuits. Especially digital rise and fall transitions which take place during the switching of gates under clock control, like it is common in integrated circuits, can cause a high bandwidth of noise [JT00]. The applied APFEL ASIC chip-set is designed to provide a noise level as low as possible. For the ASIC version 1.4 a noise of 0.74 fC for a maximal input charge of 8 pC could be achieved [PW12]. Considering the energy at which the saturation in an average detector starts for the high gain branch during the last prototype test of (720 ± 170) MeV, this leads to a photon equivalent noise level of

$$\sigma_{noise} = \frac{(720 \pm 170)\ MeV \cdot 0.74\ fC \cdot 10.8}{8\ pC} = (0.72 \pm 0.17)\ MeV \tag{5.9}$$

for an amplification of the high gain of 10.8 relative to the low gain. In addition to this intrinsic noise contributions of the electronic components, also a pick-up of noise from surrounding electronic components by the APD, the ASIC and the wiring is possible. While the intrinsic noise of the components can not be influenced, the pick-up noise can be reduced by a proper shielding and grounding concept. After an application of such a concept for the recent beam test with a common star like grounding of all components and a shielding of all electronic components with copper foil, it was possible to reduce the noise level of the high gain branch down to (0.67 ± 0.28) MeV, which is comparable to the intrinsic noise of the ASIC. This shows that it was possible to reduce the influence of pick-up noise by the applied shielding and grounding concept to a level significantly below the intrinsic noise of the ASIC, which now acts as the limiting factor of the noise level.

The single crystal threshold is directly correlated with the electronic noise level. It has to be set to a level at which most of the noise contribution is rejected. For a Gaussian distribution of the electronic noise, more than 99.7 % of the events are included in a range covering three times the standard deviation (sigma) of the distribution. Knowing this statistical condition, the threshold is normally set to a three sigma level. Including the variation of the standard deviation, this leads to a value of 2.85 MeV, which can be seen as a maximal threshold to reject the complete noise in the current setup. This value is already below the single crystal threshold of 3.0 MeV required by the TDR [TDe09] for a cluster reconstruction threshold of 10 MeV. However, exploiting the common readout of all detectors applied during the test beam experiment with the prototype, an even lower threshold can be achieved for the calculation of the cluster energy by a rejection of noise with a time-difference condition between the central

and the outer crystals of the cluster. For the tested 3 × 3 array a threshold scan indicated that a value of 2.7 MeV provides the optimal results for a peak-sensing feature extraction after the implementation of a time-difference condition. If the feature extraction is done by an integration of a fixed 220 ns wide region of the pulse around the extremum, a further reduction of the threshold to 2.5-2.6 MeV is possible. Applying a fit of the pulse shape with fixed parameters for the feature extraction can reduce the optimal threshold even down to 2.4 MeV for the 3 × 3 array, since pulses slightly below the original threshold level can be partly recovered by the fit, which is especially important for low incident photon energies.

For the barrel part of the final calorimeter, up to now a trigger less readout of all channels which exceed the implemented threshold is foreseen. With this method a threshold above the noise distribution like the given maximal threshold of 2.85 MeV has to be set for each channel to avoid a permanent triggering of single channels due to the detection of electronic noise misidentified as a signal. Since this concept rejects all signals below the threshold, a recovery of small pulses for example by a fit of the pulse shape is not possible in later analysis stages. An alternative to the foreseen independent triggering of all channels would be a cluster trigger readout, initiating the readout of a pre-defined cluster of crystals with an energy dependent size, if one crystal exceeds a certain threshold. With this readout scheme, also channels with a response slightly below the threshold could be recovered and added in the energy sum. Like figure 4.39 proofs for the feature extraction based on a fit of the pulse-shape, a clear improvement of the energy resolution at incident photon energies below 100 MeV can be achieved with this method in addition to the reduction of the reconstruction threshold. However, since a cluster readout requires a more complex data processing, another alternative, enabling a recovery of small pulses, would be a slight reduction of the trigger threshold, resulting in a triggering on a certain amount of noise events. Since this method would cause an increase of the count rate of the detector, a careful investigation of the rate capability of the data processing electronics is necessary to determine the possible reduction capability. To estimate the possible increase of the count rate by a reduced threshold, the noise rejection rate is plotted as a function of the threshold, based on the noise distribution of the present PROTO 120 run, in figure 5.11.

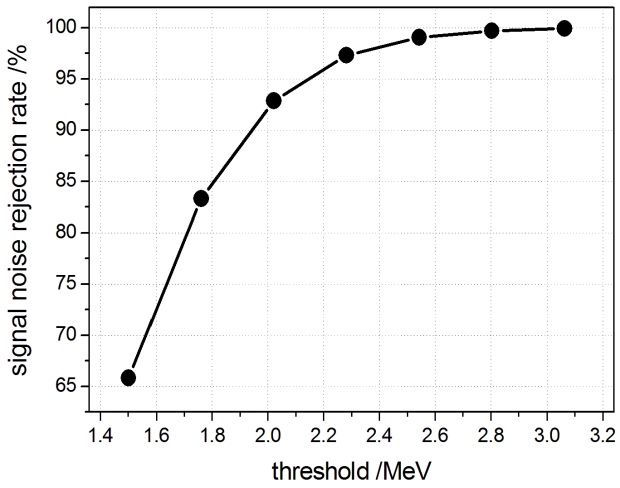

Figure 5.11: Rejection rate of the signal noise as a function of the trigger threshold.

The figure shows that with a trigger threshold of 2.4 MeV still approximately 98 % of the electronic noise, misidentified as a signal, are rejected. A further reduction of the threshold is not recommendable due to the steep decrease of the rejection rate for lower thresholds.

Influence of the threshold on the reconstruction efficiency

Since the threshold level directly influences the detection efficiency of the calorimeter, a low threshold will also improve this property. Figure 5.12 shows how the photon energy threshold effects the reconstruction loss of π^0 mesons for different momenta of the meson [TDe09].

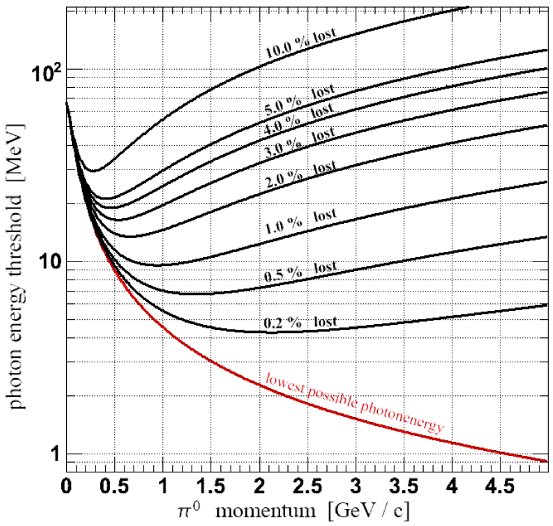

Figure 5.12: Dependence of the π^0 reconstruction loss on the energy threshold and the particle momentum. The picture has been taken from [TDe09]

A fixed single crystal threshold of 2.85 MeV would lead to a photon reconstruction threshold of approximately 9.5 MeV, while a single crystal threshold reduction to 2.4 MeV would also reduce the reconstruction threshold to 8.0 MeV. According to figure 5.12 this improvement would result in a reduction of the π^0 reconstruction loss from less than 1 % down to less than 0.7 %.

Influence of the de-polishing on the light yield and the threshold

The measurements of the position dependent light yield before and after the de-polishing of one lateral side face of type 2 and type 3 crystals in section 4.1.1 showed that the reduction of the non-uniformity in light collection does not cause a significant decrease of the light yield in the crystals. Only in the front part of the crystals a slight reduction of the light yield of less than 10 % can be observed, while the light yield in the rear part of the crystal increases by approximately 20 %. However, GEANT4 simulations show that for an APD based readout the light loss in the front part may increase up to 20 % while the light gain in the rear part decreases compared to the values measured with a PMT. This difference can be explained by a different collection efficiency of the scintillation light which is reflected back from the parts of the rear face which are not covered by the two APDs. Figure 5.13 shows the

average light yield of six selected type 2 PANDA crystals before and after the de-polishing procedure, measured with a PMT. For comparison the light yield of a CMS crystal before the de-polishing procedure and after the de-polishing of one lateral side face to different average roughness values is shown.

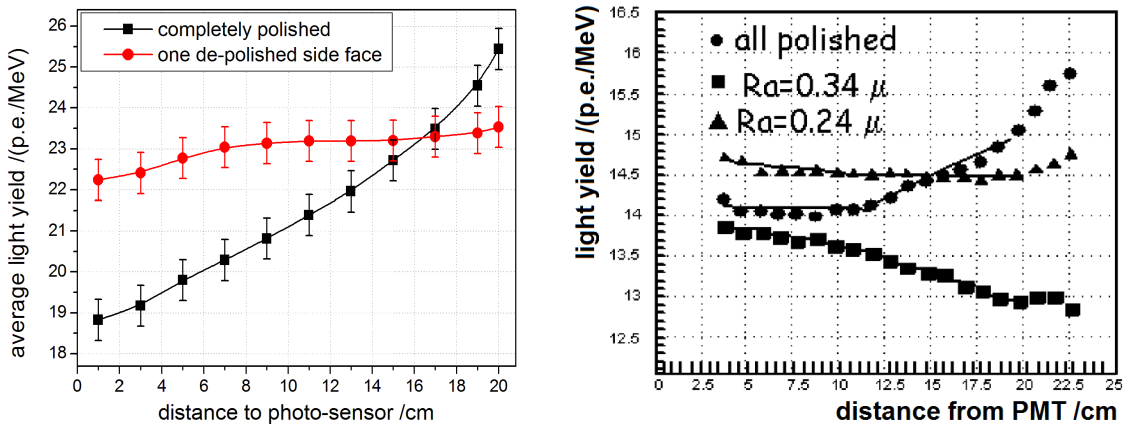

Figure 5.13: Left: Position dependent light yield of type 2 PANDA crystals before and after the de-polishing of one lateral side face to $R_a = 0.3$ μm. The crystals are wrapped with eight layers of white teflon (PTFE) tape and the values are averaged over 6 samples. Right: Position dependent light yield of a CMS barrel crystal before the de-polishing procedure and after the de-polishing of one lateral side face to $R_a = 0.34$ μm and $R_a = 0.24$ μm. The crystal is covered by a carbon fiber alveole with reflective coating. The right picture is taken from [DG10].

The position dependent light yield of the CMS crystal indicates a strong dependence of the light yield and its uniformity on the average roughness of the de-polished side face. For an average roughness of 0.34 μm an overall reduction of the light yield and a negative slope of the position dependent response can be observed. In contrast to this, an average roughness of 0.24 μm causes an increase of the light yield in the rear part of the crystal and a nearly uniform response. This behavior is comparable to the results for the PANDA crystals with one lateral side face de-polished to an average roughness of 0.30 μm. However, for the PANDA crystals the absolute increase of the light yield in the rear part of the crystals is much more pronounced due to the significantly higher non-uniformity in light collection and due to the higher overall light yield. In addition the adjustment of the average roughness to the strength of the non-uniformity of the crystals plays an important role to achieve optimal results for the uniformity and the light collection efficiency.

The GEANT4 simulations of the influence of the de-polished side face on the light collection in section 4.3.4 showed that the increase of the light yield in the rear part of the crystal due to the de-polished side face is caused by an improvement of the light collection efficiency in this region. This improvement can be explained on the one side by the reduction of the de-focusing of photons emitted in the direction of the front face of the crystal and since photons emitted in the direction of the front face have a certain probability to change their direction when they hit an appropriately oriented facet of the de-polished side face. Only in the most forward region the focusing of the light by a perfectly polished side face provides an advantage for the light collection efficiency compared to a de-polished side face with an optimized roughness and therefore a higher light yield.

Since the signal to noise ratio is directly proportional to the light yield per energy unit, the single crystal threshold strongly depends on the light yield, too. In the experiment, a comparable electronic noise level has been determined and therefore also a comparable threshold of 2.7-2.8 MeV has been set for the two 3 × 3 arrays with polished and de-polished crystals. Considering that both arrays were placed in the same prototype and that the same readout has been used, this observation is a direct indication for a similar light yield of polished and de-polished crystals in the investigated energy range. From the simulations of the longitudinal shower profile in section 4.3.2 it is known that the center of gravity of the electromagnetic shower in the investigated energy range below 1 GeV is positioned in the first third of the crystal. According to figure 5.13 an average light yield difference of less than 10 % can be expected for this region with a PMT based readout and also for an APD based readout the simulated average light loss of a crystal with one de-polished side face, compared to a completely polished crystal is expected to stay below 15 % in this region. Considering an error of the energy value of the optimal threshold of a few percent due to uncertainties of the absolute calibration and intrinsic variations of the noise level of the different ASICs, this is in good agreement with the observed similar threshold for both arrays. However, in the worst case an increase of the threshold of up to 15 %, which corresponds to 0.4 MeV, has to be expected for de-polished type 2 crystals. To obtain a more reliable comparison of the threshold, a 5 × 5 array of de-polished crystals will be tested in future test experiments.

Influence of the threshold on the energy resolution for different cluster sizes

Since the limited lateral dimension of the characterized 3 × 3 array limits the energy resolution due to lateral shower leakage, a study of the effect of the cluster size on the energy resolution has been performed based on data taken with PROTO 60 at the MAMI facility in 2011. The detailed analysis of the data from this beam-time is shown in [MM13]. The left part of figure 5.14 shows a threshold scan for the lowest incident photon energy of 52 MeV for different array sizes of 9, 25 and 60 crystals. The noise level for this experiment was in the order of 0.25 MeV, leading to an applied threshold of 0.75 MeV [MM13].

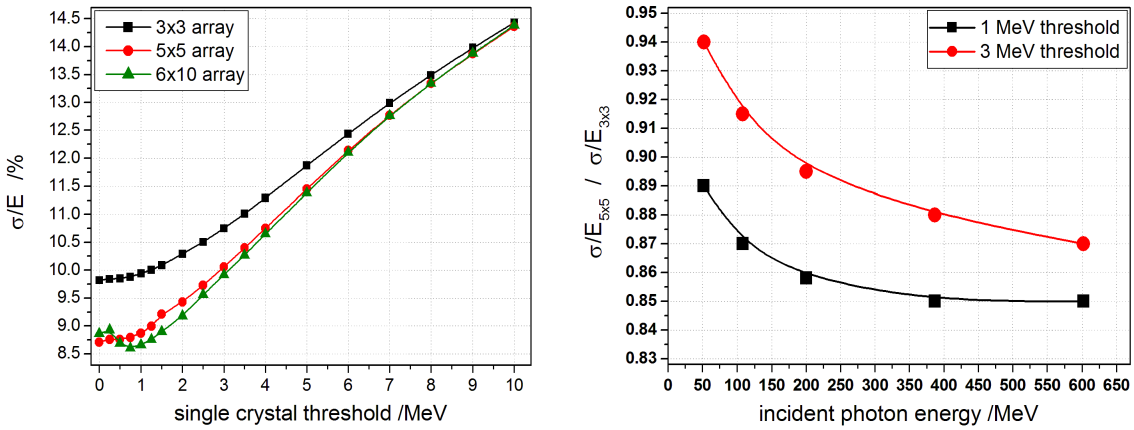

Figure 5.14: Left: Threshold scan of the relative energy resolution for different array sizes for an incident photon energy of 52 MeV. Right: Improvement factor of the energy resolution between a 5 × 5 and a 3 × 3 array for a threshold of 1 MeV and 3 MeV. The plots have been prepared with data obtained with PROTO 60 in 2011 (for details see also [MM13]).

The threshold scan shows that the deterioration of the energy resolution by an increasing threshold is much more significant for larger clusters. For an increase of the threshold from 0.75 MeV to 2.8 MeV, the relative energy resolution of a 3 × 3 array for a photon energy of 52 MeV is deteriorated by 0.9 percent points and in a 5 × 5 array even by 1.2 percent points. This effect can be explained by the deposition of lower energies in the outer detectors of a 5 × 5 array compared to a 3 × 3 array, which are rejected by lower thresholds than energies contained in the 3 × 3 array. To illustrate the energy and threshold dependence of the improvement of the energy resolution between a 3 × 3 and a 5 × 5 array, the improvement factor of the energy resolution is shown in the right part of figure 5.14 for a threshold of 1 MeV and 3 MeV. Due to the larger spread of the electromagnetic shower at high energies, both curves show a significant improvement for an increase of the energy. A comparison between the two thresholds illustrates that a higher threshold deteriorates the improvement between a 3 × 3 and a 5 × 5 array. According to this observation, due to the higher threshold, a smaller improvement of the energy resolution can be expected for PROTO 120 compared to PROTO 60, if a larger array is read out. The investigation of the threshold dependence of the energy resolution shows that a low threshold will be a great benefit for the energy resolution, especially if larger clusters are considered.

5.2.7 Influence of radiation damage on the non-uniformity

In section 4.1.1 it has been shown that a de-polishing of one lateral side face of the crystals can uniform the light collection in tapered PWO crystals for the price of a reduced light yield from the front part of the crystals. However, all non-uniformity measurements up to now have been performed with completely annealed crystals. Since radiation damage reduces the transmission of the crystals, it is still an open question, how it influences the non-uniformity in light collection of polished and especially de-polished crystals. To obtain a first indication for the expectable influence, the non-uniformity curves of several polished and de-polished crystals have been measured before and after an homogeneous irradiation with a dose of 30 Gy gamma radiation from a ^{60}Co-source. Since the crystals had to be transported from the irradiation facility to the laboratory and since the crystals were kept at room temperature during the non-uniformity measurement, spontaneous recovery of the radiation damage may influence the result and introduce systematic errors. Under these considerations, the non-uniformity curves shown in figure 5.15 (upper row) have been obtained before and after the irradiation. After the irradiation with a dose of 30 Gy, the light yield of polished and de-polished crystals is significantly reduced. For both crystal types an average light yield reduction between 36 % and 56 %, depending on the radiation hardness of the crystal, takes place. According to [DKK14], this light loss can increase to more than 65 % for crystals close to the rejection limit of the radiation induced absorption coefficient (see equation 5.10) of 1.1 m^{-1}. To compare the slope of the non-uniformity before and after the irradiation, the measured position dependent light yield has been normalized at a position in the center of the crystal in figure 5.15 (lower row). The comparison of the curves shows that the irradiation has only a minor impact on the non-uniformity. While the non-uniformity of de-polished samples stays nearly constant within the error bars, a trend towards a slight increase of the non-uniformity after the irradiation can be observed for the polished samples. Since the observed variation is still within the error bars and since a systematic effect due to the spontaneous recovery can not be excluded, a more detailed investigation, including a measurement of the

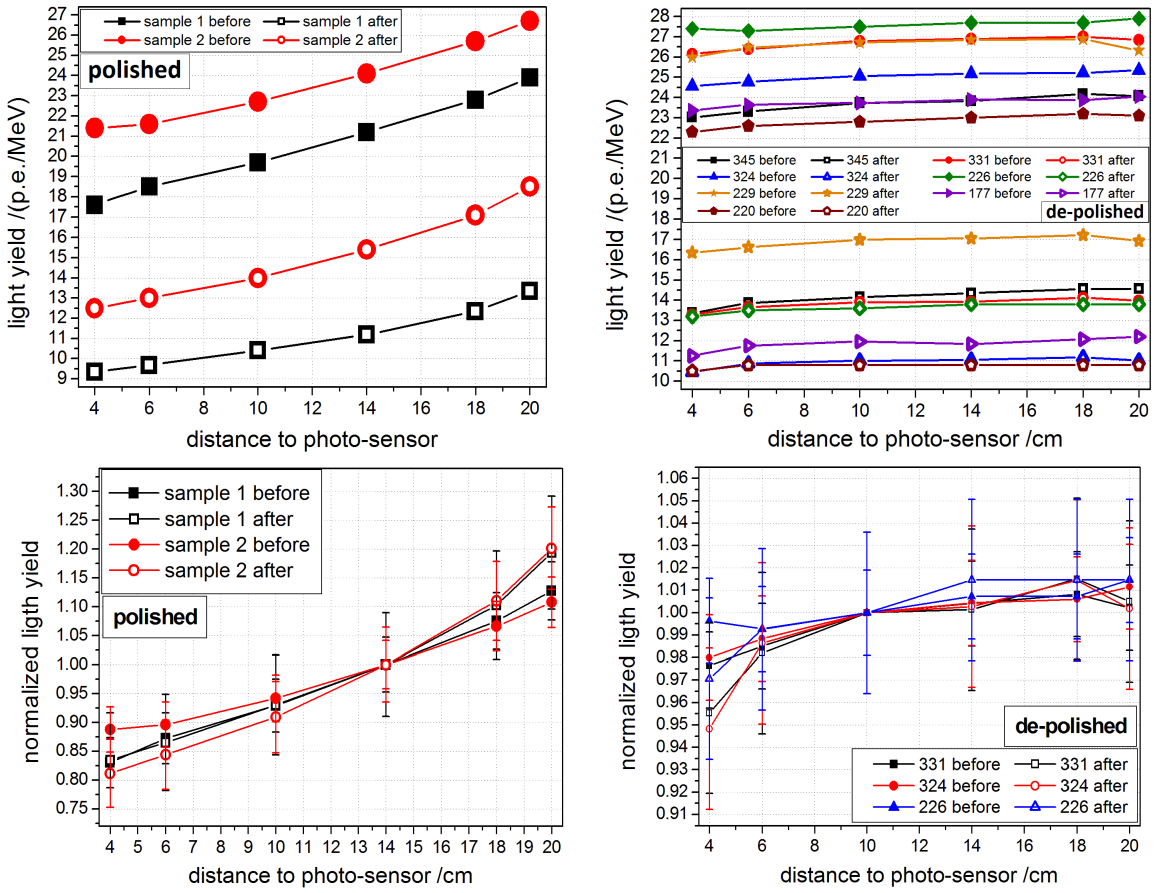

Figure 5.15: Position dependent light yield of polished (left) and de-polished (right) crystal before and after an irradiation with 30 Gy gamma radiation from an ^{60}Co source. In both cases, the data points before the irradiation are plotted as solid points and the data points after the irradiation as open points. The upper row shows the light yield measured with a PMT with bi-alkali photo-cathode at +18°C and the lower row the normalized light yield of typical samples. To provide a better comparison of the slope of the non-uniformity curve before and after the irradiation, the normalization has been performed at a central position of 14 cm for the polished samples and 10 cm for the de-polished samples. The assumed measurement error of half a photo electron, which is not shown in the upper row due to a better clarity of the figures is used to calculate the error bars of the normalized curves in the lower row.

non-uniformity curve of cooled crystals directly after the irradiation has to be performed to study this effect.

The presented measurements show that for a homogenous irradiation, at least for the de-polished crystals no significant change of the slope of the non-uniformity can be expected. Nevertheless, in reality the front part of the crystal will suffer from a higher radiation damage than the rear part, since a huge amount of low-energetic photons will deposit there energy mainly in the front region. To estimate the influence of this effect on the non-uniformity in light collection, the position dependence of the radiation induced absorption coefficient dk has been calculated for the center and the most forward region of the barrel. As a basis for this calculation, the normalized dose distribution within the crystal, simulated with a dual

patron model based event generator in [TDe09] and the dose dependence of the radiation induced absorption coefficient (dk) [VD15], shown in figure 5.16 are applied.

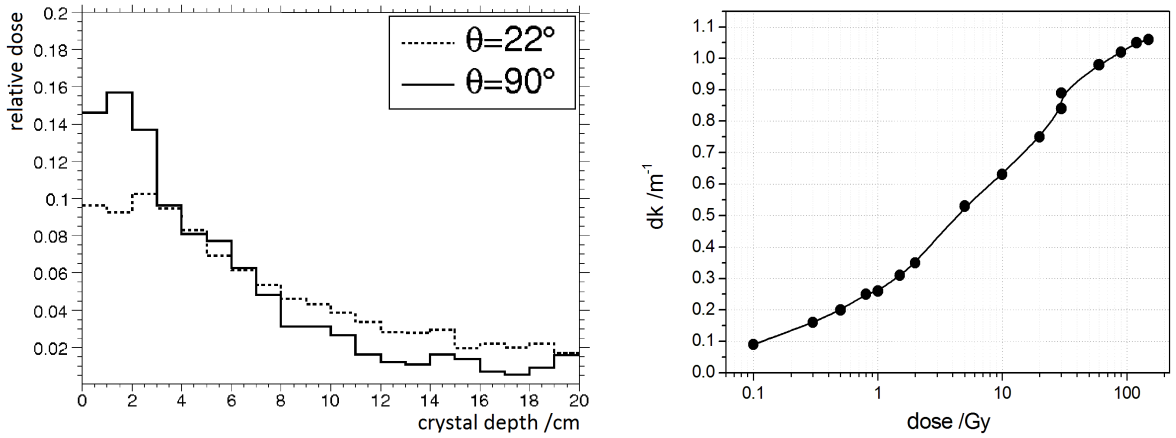

Figure 5.16: Left: Normalized dose distribution within the crystal for a polar angle of 22° and 90°. Picture modified from [TDe09]. Right: Dose dependence of the absorption coefficient introduced by radiation damage [VD15] for a crystal with an average radiation hardness of dk = 0.85 m^{-1} at 30 Gy.

The radiation induced absorption coefficient is defined with the crystal thickens d, the transmission of the crystal before the irradiation T_b and the transmission after the irradiation T_a as

$$dk = \frac{1}{d} \cdot ln\left(\frac{T_a}{T_b}\right) \tag{5.10}$$

According to [TDe09] a radiation dose-rate of 0.16 mGy/h for a polar angle of 90°, representing the center of the barrel and a dose-rate of 1.83 Gy/h for the most forward region of the barrel at a polar angle of 22° can be expected. For operation times between 14 days and 1 year, these dose-rates lead to the total doses given in table 5.5. A permanent operation without recovery is assumed. However, for longer time frames a duty-cycle of 50 % is realistic, doubling the time intervals which are needed to collect the given doses.

angle	14 days	1 month	2 month	6 month	1 year
90° (type 1)	0.05 Gy	0.11 Gy	0.22 Gy	0.65 Gy	1.29 Gy
22° (type 11)	0.61 Gy	1.23 Gy	2.46 Gy	7.38 Gy	14.76 Gy

Table 5.5: Radiation dose deposited under a polar angle of 90° and 22° for different time frames. A permanent operation is assumed.

Together with the data from figure 5.16, these doses can be used to calculate the position dependence of the radiation induced absorption coefficient dk. The results for a polar angle of 90° and 22° are shown in figure 5.17. The figure shows that the absorption of scintillation light induced by radiation damage is concentrated in the front part of the crystal, if the crystal is positioned in the center of the barrel, while it is distributed more homogeneously over the crystal in the most forward region of the barrel. Due to this dependence of the induced absorption coefficient on the longitudinal position within the crystal, a stronger reduction of light produced in the front part of the crystal, compared to the rear part is expected,

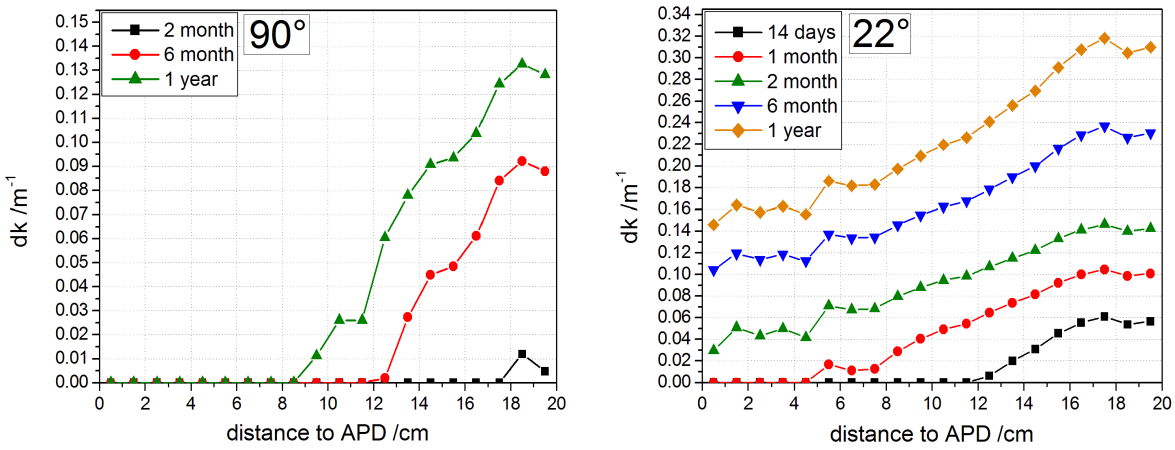

Figure 5.17: Calculated position dependence of the absorption coefficient introduced by radiation damage for polar angles of 90° (left) and 22° (right).

leading to a slightly reduced slope of the non-uniformity curve. Due to the dependence of the induced absorption profile on the polar angle, also for the influence of the radiation damage on the non-uniformity a strong position dependence can be expected within the barrel. In addition, the quality control of the crystals [TE13] showed a distribution of the radiation induced absorption coefficient from 0.2 m^{-1} up to 1.4 m^{-1} which causes a different light loss for the single crystals [DKK14], but also a strong variation of the impact of radiation damage on the non-uniformity curve from crystal to crystal. Due to these variations and since approximately 70 % of the scintillation photons are scattered within the crystal one or more times before they reach the APDs, reliable estimations of the strength of the influence of a position dependent radiation damage on the non-uniformity are not easily possible. However, the calculated doses show that the radiation damage accumulated within 2 weeks or even within a month will only show a considerable impact in the most forward region of the barrel. If a stimulated recovery of the radiation damage with LED light [VD11] is performed at least one time per month, the impact of radiation damage on the non-uniformity can be more less ignored for most of the crystals within the barrel.

5.3 Conclusion and Outlook

The performance tests of the prototypes of the forward shashlyk calorimeter and the barrel electromagnetic calorimeter for energies below 1 GeV showed that the current version of both prototypes fulfill the requirements for the PANDA detector. The new, improved design of the shashlyk modules provides a good lateral homogeneity and a small variation of the light attenuation in the modules. With this improvements of the detector homogeneity, a comparable energy response and resolution can be achieved for all interaction positions, which is the basis for a reliable calorimeter. To optimize the energy resolution, different feature extraction methods have been compared and an integral of the recorded PMT pulses was identified as the optimal solution. Also the position- and time- resolution show the expected values in the investigated energy range. Altogether it has been proven that the shashlyk calorimeter can be used for the detection of low energetic photons at least down to 50 MeV with an acceptable energy resolution.

For the barrel EMC different feature extraction and calibration concepts have been compared. It has been shown that an integration of a limited signal region and a fit of the pulse-shape can improve the energy resolution and reduce the optimal threshold, if a common readout of a pre-defined array of crystals is applied. Due to this observations a modification of the trigger-less readout concept from an individual trigger of all channels above a threshold to a readout of a pre-defined cluster, if a single channel exceeds a certain threshold, would reduce the effective cluster threshold and improve the energy resolution at low energies. For the current version 1.5 of the APFEL ASIC it has been experimentally proven that a noise level of less than 1 MeV, resulting in a single crystal threshold of less than 3 MeV, can be achieved under real conditions. With an identical threshold and a limitation to a 3×3 array an energy resolution comparable to the first large scale barrel prototype PROTO 60 has been obtained, if the data acquisition of PROTO 60 is performed with a peak-sensing ADC. However, the energy resolution obtained with the optimal threshold of 0.75 MeV achieved with a pre-amplifier with discrete components implemented in PROTO 60 and especially the resolution obtained with a sampling ADC readout of the prototype at energies below 500 MeV can not be reproduced with PROTO 120. In addition, the threshold of approximately 3 MeV enables only a very small improvement of the energy resolution at low energies, if larger clusters are considered. Therefore, the relatively high threshold of PROTO 120, mainly caused by the intrinsic noise contribution of the ASIC, is a limitation not only for the detection efficiency but also for the energy resolution of the calorimeter. The difference to former prototypes in terms of the constant term of the parametrization of the energy resolution could be identified to be a result of the non-uniformity in light collection. Concerning this longitudinal uniformity of the crystals it has been shown that a de-polishing of the most tapered lateral side face of the crystals to an average roughness of $R_a = 0.3$ μm reduces the non-uniformity in light collection of type 2 crystals down to a level of less than 5 % with a nearly homogenous response in the front part of the crystals. The comparison of the light yield of polished and de-polished crystals showed that the de-polished surface causes only a relatively small decrease of the light yield in the front part of the crystals, while the light yield in the rear part of the crystals is even significantly improved. Based on the de-polished crystals, implemented in the current barrel EMC prototype, the influence of the light collection uniformity on the energy resolution for energies below 1 GeV has been investigated for the first time. It has been proven experimentally that a reduction of the non-uniformity by the de-polishing procedure improves the relative energy resolution for energies above 200 MeV, while the energy resolution between 50 MeV and 200 MeV stays approximately at the same level and only a slight deterioration is expected for energies below 50 MeV. Simulations even predict an improvement of the relative energy resolution under more ideal experimental conditions, starting at 75 MeV. The experiment especially showed a similar threshold for polished and de-polished crystals, which is in good agreement with the expected only slightly different light yield of the crystals for both surface configurations in the investigated energy range. A comparison to the photon energy distributions in the barrel showed that a de-polishing of the crystals can make sense in the forward region of the barrel even for the energy regime expected for the PANDA barrel EMC. Altogether it has been shown that the close to final design of the prototype in combination with the new APFEL ASIC fulfills the requirements of the Technical Design Report. Besides the application for PANDA, the investigation of the influence of an homogenized light collection on the energy resolution at energies significantly below 1 GeV can be also applied for other future calorimeter projects using a barrel design with tapered crystals.

Currently different new concepts for shashlyk calorimeters and also other calorimeters based on lead tungstate crystals are under investigation or already planed for new detector projects. To gain a more compact design of the modules and a better radiation hardness, the use of small slices of inorganic scintillation crystals like the radiation hard LYSO:Ce as active component of a shashlyk calorimeter is currently under investigation [RYZ12]. Also the use of inorganic fibers or small crystal rods, intersected in a heavy absorber made for example of tungsten is under investigation [LMP13]. In the field of homogeneous calorimeters there is still a huge interest in lead tungstate as a compact and fast scintillation crystal for future high energy physics experiments. Especially for the neutral particle spectrometer at Jefferson National Laboratory (USA) the use of a wall of lead tungstate crystals is currently in the R&D phase [TH15].

Appendix

Crystal and APD configuration of the complete PROTO 120

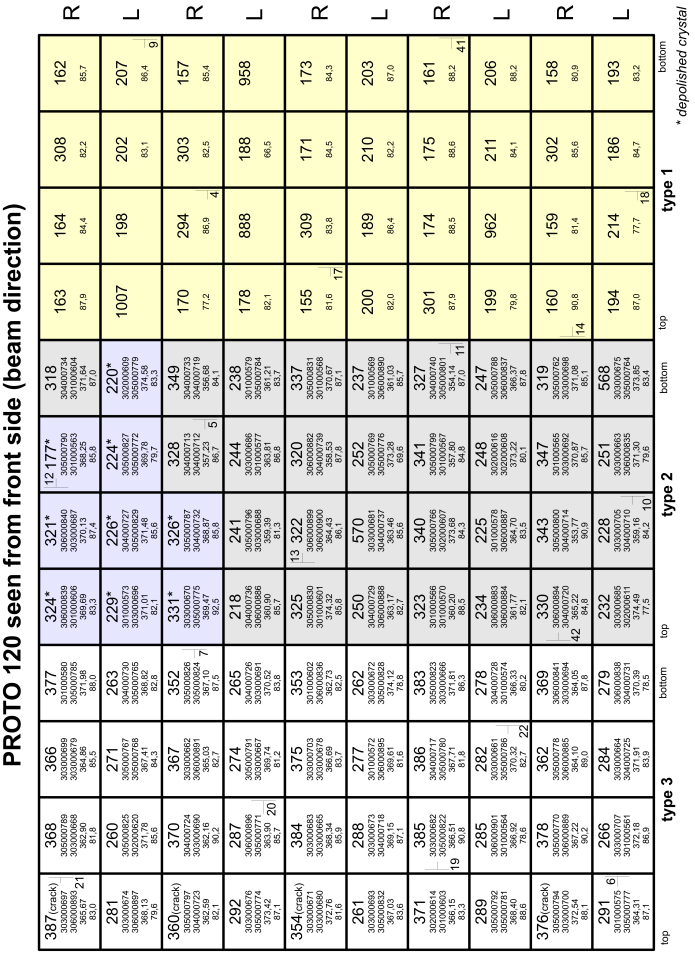

Crystal and APD configuration of the complete PROTO 120. The first number indicates the crystal number, while the second and third number show the APD IDs. The fourth number represents the average APD voltage for a gain of 150 at -25°C. The fifth number indicates the light yield of the crystal at -25°C in photo electrons measured with a bi-alkali photo-cathode during the quality control. The rectangles with numbers show the ID and the position of the temperature sensors.

List of Acronyms

ADC	Analogue to Digital Converter
AGOR	Accelerator Groningen-Orsay
APD	Avalanche Photo Diode
APFEL	ASIC for PANDA Front End Electronics
CERN	European Center for Nuclear and Particle Research
CFD	Constant Fraction Discriminator
CMS	Compact Muon Solenoid
DAQ	Data Aquisition
DIRC	Detection of Internally Reflected Cherenkov Light
EMC	Electromagnetic Calorimeter
FAIR	Facility for Antiproton and Ion Research
FPGA	Field Programmable Gate Array
GPDs	Generalized Parton Distributions
GSI	GSI, Helmholtzzentrum für Schwerionenforschung Darmstadt
HESR	High Energy Storage Ring
KVI	Kernfysisch Versneller Institut Groningen
LAAPD	Large Area Avalanche Photo Diode
MAMI	Mainzer Mikrotron
MVD	Micro Vertex Detector
NIM	Nuclear Instrumentation Module
PANDA	Antiproton Annihilation at Darmstadt
PID	Particle Identification
PMT	Photomultiplier Tube
PWO	lead tungstate ($PbWO_4$)
PWO-II	lead tungstate (second generation)
QCD	Quantum Chromodynamics
QDC	Charge to Digital Converter
RICH	Ring Imaging Cherenkov Counter
SADC	Sampling Analogue to Digital Converter
SiPM	Silicon Photomultiplier
SIS100	Schwerionensynchrotron 100
SIS18	Schwerionensynchrotron 18
TDC	Time to Digital Converter
TOF	Time Of Flight
VPT	Vacuum Photo Triode
VPTT	Vacuum Photo Tetrode

List of Figures

List of Tables

Bibliography

[AAA98] A. Abele et al., *Exotic η π State in antiproton-deuterium Annihilation at Rest into $\pi^-\pi^0\eta$ $p_{spectator}$*, Phys. Lett. B 423, pp. 175 (1998).

[AAA03] S. Agostinelli et al., *Geant4 - a simulation toolkit*, Nucl. Instr. and Meth. in Phys. Res. A 506, pp. 250-303 (2003).

[AAA06] J. Allison et al., *Geant4 developments and applications*, IEEE Transactions on Nuclear Science 53 No. 1, pp. 270-278 (2006).

[AB14] G. D. Alexeev, Maria Pia Bussa, official PANDA homepage, *www-panda.gsi.de/framework /det_iframe.php?section=Forward*

[ABB98] E. Auffray, P. Baillon, D. Barney et al., *Beam tests of lead tungstate crystal matrices and a silicon strip preshower detector for the CMS electromagnetic calorimeter*, Nuclear Instruments and Methods in Physics Research A, vol, 412, iss. 2-3, pp. 223-237, (1998), doi: 10.1016/S0168-9002(98)00464-1

[ABB08] A. V. Arefev, I. M. Belyaev, B. M. Bobchenko et al., *A Study of Light Collection in "Shashlik" Calorimeters*, Instruments and Experimental Techniques, vol. 51 (2008).

[ABP12] P. Achenbach, S. Bleser, J. Pochodzalla, A. Sanchez Lorente, M. Steinen, *Hyper nuclear Physics at PANDA*, Hyperfine Interactions 209, pp. 99-104 (2012), doi: 10.1007/s10751-012-0571-1

[ACH05] N. Akchurin, K. Carrell, J. Hauptman, H. Kim, A. Penzo, R. Thomas, R. Wigmans, *Comparison of high-energy electromagnetic shower profiles measured with scintillation and Cherenkov light*, Nuclear Instruments and Methods in Physics Research A 548, pp. 336-354 (2005).

[ACL02] E. Auffray, F. Cavallari, M. Lebeau, P. Lecoq, M. Schneegans, P. Sempere-Roldan, *Crystal conditioning for high-energy physics detectors*, Nuclear Instruments and Methods in Physics Research A, vol. 486, pp. 22-43, (2002), doi: 10.1016/S0168-9002(02)00670-8.

[ADI04] G. Atoian, S. Dhawan, V. Issakov, A. Poblaguev, M. Zeller, G.I. Britvich, S. Chernichenko, I. Shein, A. Soldatov, O. Karavichev, T. Karavicheva, V. Marin, *Test Beam Study of the KOPIO Shashlyk Calorimeter*, talk at CALOR 2004, Perugia, Italy, *http://hallaweb.jlab.org/12GeV/SoLID/download/ec/Shashlyk/perugia_ap.pdf*

[ADe12] Achim Dening, Institut für Kernphysik, JGU Mainz, *The Mainz Microtron MAMI - Ein einzigartiger Teilchenbeschleuniger an der JGU Mainz*, talk at Rotary Club Mainz (2012), *http://slideplayer.de/slide/891539/* (accessed Nov. 2015).

[AG94] A. Golutvin et al., *HERA-B Tech. Note 94-073* (1994).

[AGG92] G.S. Atoyan, V.A. Gladyshev, S.N. Gninenko et al., *Lead-scintillator electromagnetic calorimeter with wavelength shifting fiber readout*, Nucl. Instrum. and Meth. A 320:1-2, pp. 144 (1992).

[AIK04] G. S. Atoian, V. V. Isakov, O. V. Karavichev, T. L. Karavicheva, A. A. Poblaguev and M.E. Zeller, *Development of Shashlyk calorimeter for KOPIO*, Nucl. Instr. and Meth. in Phys. Res., A 531 (2004).

[AK14] Andreas Künsken, on behalf of the CMS Collaboration, *MPPC Photon Sensor Operational Experience in CMS*, talk at CALOR 2014, Journal of Physics: Conference Series 587, 012022 (2015).

[AKL02] A. A. Annenkov, M. V. Korzhik, and P. Lecoq, *Lead tungstate scintillation material*, Nucl. Instrum. and Meth. A 490, pp. 30 (2002).

[AN13] A2 collaboration (Andreas Neiser), *A2 ugcal Tagger calibration*, fortran program, *https://github.com/A2-Collaboration/ugcal* (published 2013, accessed Nov. 2015).

[ANA97] K. Aulenbacher, Ch. Nachtigall, H. G. Andresen et al., *The MAMI source of polarized electrons*, Nucl. Instr. and Meth. in Phys. Res. A 391, pp. 498 (1997).

[AP10] A. J. R. Puckett et al., *Recoil Polarization Measurements of the Proton Electromagnetic Form Factor Ratio to Q^2=8.5 GeV^2*, Phys. Rev. Lett. 104, 242301 (2010).

[ASL13] A. Sanchez Lorente on behalf of the PANDA collaboration, *High precision γ spectroscopy of $\Lambda\Lambda$-Hypernuclei at the PANDA experiment*, Journal of Physics: Conference Series 426, 012030 (2013).

[ASL14] Alicia Sanchez Lorente on behalf of the PANDA collaboration, *Hypernuclear physics studies of the PANDA experiment at FAIR*, Hyperfine Interactions 229, 1-3, pp. 45-51 (2014).

[AW14] Andrea Wilms, GSI Darmstadt, *private communication* (2014).

[B115] B1 collaboration, *Parameter table*, *http://portal.kph.uni-mainz.de/B1/params.php* (web page - Nov. 2015).

[BBB97] S. Baccaro, L. M. Barone, B. Borgia et al., *Ordinary and extraordinary complex refractive index of the lead tungstate ($PbWO_4$) crystal*, Nucl. Instr. and Meth. A 385, pp. 209-214 (1997).

[BDG14] R. Becker, G. Dissertori, A. Gendotti et al., *Proof-of-principle of a new geometry for sampling calorimetry using inorganic scintillator plates*, Proceedings of CALOR 2014, Giessen (Germany), Journal of Physics: Conference Series 587, 012039 (2015), doi: 10.1088/1742-6596/587/1/012039

[BGM14] S. E. Brunner et al., *Time resolution below 100 ps for the SciTil detector of PANDA employing SiPM*, Journal of Instr. 9, C03010 (2014), doi: 10.1088/1748-0221/9/03/C03010

[BGS05] T. Barnes, S. Godfrey, E. S. Swanson, *Higher Charmonia*, Phys. Rev. D72, 054026 (2005), arXiv:hep-ph/0505002

[BHS14] M. J. Berger, J. H. Hubbell, S. M. Seltzer et al., *XCOM: Photon Cross Sections Database*, NIST Standard Reference Database 8 (XGAM), *http://www.nist.gov/pml/data/xcom/index.cfm* (accessed Nov. 2015).

[BKM05] N. Brambilla, M. Krämer, R. Mussa, A. Vairo et. al, *Heavy Quarkonium Physics*, CERN Yellow Report, CERN-2005-005, Geneva: CERN (2005), arXiv:hep-ph/0412158

[BKS05] R. Bär, U. Krause, V. Schaa, P. Schütt, *The new FAIR accelerator complex at GSI: Project, Controls, Challenges and First Steps*, Proceedings of ICALEPCS07, Knoxville, Tennesse (2007), *https://accelconf.web.cern.ch/accelconf/ica07/PAPERS/TOAB01.PDF* (accessed Nov. 2015).

[BRQ05] D. Britton, M. Ryan, X. Qu, *Light collection uniformity of lead tungstate crystals for the CMS electromagnetic calorimeter*, Nuclear Instruments and Methods in Physics Research Section A: Accelerators, Spectrometers, Detectors and Associated Equipment, vol. 540, iss. 2-3, pp. 273-284 (2005), doi: 10.1016/j.nima.2004.11.038

[BVL01] G. I. Britvich, V. G. Vasil'chenko, V. A. Lishin, V. A. Polyakov, A. S. Solov'ev, *New Scintillation Materials for Particle Detectors*, Instr. Exp. Tech. 44, pp. 472 (2001).

[BW10] Adrian Bevan, Fergus Wilson, *A Fit User Guide*, *http://pprc.qmul.ac.uk/∼bevan/afit/afit.pdf* (published 2010, accessed Nov. 2015).

[CAD05] Y. Chen et al, *Glueball Spectrum and Matrix Elements on Anisotropic Lattices*, Phys. Rev. D 73, 014516 (2006).

[CFP07] C. F. Perdrisat, V. Punjabi and M. Vanderhaeghen, *Nucleon electromagnetic form factors*, Prog. Nucl. Part. Phys. 59, pp. 694 (2007).

[CG93] Claus Grupen, *Teilchendetektoren*, BI Wissenschaftsverlag, Manheim, Leipzig, Wien, Zürich (1993), ISBN-13: 978-3411165711

[CG02] R. Chipaux, F.-X. Gentit, *Simulation of light collection in the CMS lead tungstate crystals with the program Litrani: coating and surface effects*, Nuclear Instruments and Methods in Physics Research A 486, 48-54 (2002).

[CKO14] I. Chirikov-Zorin, Z. Krumshtein, A. Olchevski, V. Utkin, P. Zhmurin, *The design of a module of a new electromagnetic calorimeter for COMPASS II*, Physics of Particles and Nuclei Letters, vol. 11, iss. 3, pp. 252-258, (2014).

[CMS97] CMS collaboration, *The Electromagnetic Calorimeter - Technical Design Report*, Technical report CERN-LHCC-97-33 (1997).

[CMS13] CMS collaboration, *Energy calibration and resolution of the CMS electromagnetic calorimeter in pp collisions at* $\sqrt{s}$ *= 7 TeV*, Journal of Instrumentation 8 (2013), P09009, arXiv:1306.2016 [hep-ex]

[CR16] Christoph Rosenbaum, *PhD thesis*, Justus Liebig University Giessen (to be submitted, 2016).

[CRN14] C. R. Nave, *Hyper Physics*, *http://hyperphysics.phy-astr.gsu.edu/hbase/forces /funfor.html*, Geogia State University (accessed Nov. 2015).

[CS14] Carsten Schwarz, *The PANDA Detector - Particle ID*, official PANDA homepage, *https://panda.gsi.de/oldwww/framework/det_iframe.php?section=Particle%20ID* (accessed Nov. 2015).

[DAB13] Daniel Andreas Bremer, *Measurements and Simulations on Position Dependencies in the Response of Single PWO crystals and a Prototype of the PANDA EMC*, PhD thesis, University Giessen (2013), *http://geb.uni-giessen.de/geb/volltexte/2014/10582/pdf/BremerDaniel_2014_01_09.pdf*

[DB05] Diego Bettoni, *Physics with the PANDA detector at GSI*, Journal of Physics: Conference Series 9, pp. 309-314 (2005) doi: 10.1088/1742-6596/9/1/059

[DBP10] Govindhan Dhanaraj, Kullaiah Byrappa, Vishwanath Prasad, Michael Dudley, *Springer Handbook of Crystal Growth* (2010) ISBN: 978-3-540-74182-4

[DCZ07] D. C. Zhou (for the ALICE Collaboration), *PHOS, the ALICE-PHOton Spectrometer*, J. Phys. G: Nucl. Part. Phys. 34, pp. 719 (2007) doi: 10.1088/0954-3899/34/8/S81

[DG10] Dan Green (editor), *At the Leading Edge: The ATLAS and CMS LHC Experiments*, World Science Publishing Co. Pte. Ltd. (2010), ISBN: 978-9814277617

[DGM96] M. David, A. Gomes, A. Maio, *Dose rate effects in WLS fibers*, ATLAS internal note (1996) *http://citeseerx.ist.psu.edu/viewdoc/download?doi=10.1.1.29.6858&rep=rep1 &type=pdf*

[DIM00] K. Deiters, Q. Ingram, Y. Musienko, S. Nicol, P. Patel, D. Renker, S. Reucroft, R. Rusack, T. Sakhelashvili, J. Swain, P. Vikas, *Properties of the avalanche photodiodes for the CMS electromagnetic calorimeter*, Nucl. Instr. and Meth. A, vol 453, pp. 223-226 (2000).

[DKK14] Valera Dormenev, Mikhail Korjik, Till Kuske, Vitaly Mechinski, Rainer W. Novotny, *Comparison of Radiation Damage Effects in PWO Crystals Under 150 MeV and 24 GeV High Fluence Proton Irradiation*, IEEE transactions on nuclear science, vol. 61, no. 1 (2014).

[DP08] DuPont de Nemours (Luxembourg) S.à r.l., *DuPont^{TM} Tyvek^{C} Graphics - Typical Properties of Tyvek^{C} style 10*, data sheet (2008).

[EP14] E. Prencipe, *Status and Perspectives for PANDA @ FAIR*, talk at ICHEP 2014, Valencia (Spain), *www – panda.gsi.de/db/talksDBr/EP*19 – 140701_*Prencipe_ICHEP*2014.*pdf*

[ER11] E. Rutherford, *The scattering of alpha and beta particles by matter and the structure of the atom*, Philosophical Magazine, volume 21, 669-688 (1911).

[FAIRexp] Facility for Antiproton and Ion Research in Europe, *http://www.fair-center.de/de/oeffentlichkeit/experimenteprogramm.html* (accessed Nov. 2015).

[FC11] Francesca Cavallari, *Performance of calorimeters at the LHC*, Journal of Physics: Conference Series 293, pp. 012001 (2011) doi: 10.1088/1742-6596/293/1/012001

[FKM96] A. Fyodorov, M. Korzhik, O. Missevitch et al., *Progress in $PbWO_4$ Scintillating Crystal*, Radiation Measurements 26-1, pp. 107-115 (1996) doi: 10.1016/1350-4487(95)00283-9

[FRS03] A. Freund, A. V. Radyushkin, A. Schäfer, and C. Weiss, *Exclusive annihilation $p\bar{p} \to \gamma\gamma$ in a generalized parton picture*, Physical Review Letters 90(9):092001 (2003), doi: 10.1103/PhysRevLett.90.092001 .

[FT14] Federica Tarsitano, *Study of the Noise and Thresholds in CMS ECAL*, CMS DPG ECAL Meeting 17.072014, CERN, *http://www.researchgate.net/publication/269105856_Study_of_the_Noise_and_Thresholds_in_CMS_ECAL* (2014).

[FXG02] François-Xavier Gentit, *Litrani: a general purpose Monte-Carlo program simulating light propagation in isotropic or anisotropic media*, Nucl. Instr. and Meth. A, vol. 486, iss. 1-2, pp. 35-39 (2002).

[GAA77] G.A. Akopdjanov et al., *Determination of photon coordinates in a hodoscope cherenkov spectrometer*, Nuclear Instruments and Methods, 140(3) (1977).

[GB12] C. Grupen, I. Buvat (eds.), *Handbook of Particle Detectors and Imaging*, Springer Verlag (2012), ISBN-13: 978-3642132704

[GD96] G. David et al., *Performance of the PHENIX EM calorimeter*, Technical report, PHENIX Tech. Note 236 (1996).

[GGK07] Y. Gilitsky, A. Golutvin, A. Konoplyannikov, J. Lefrancois, P. Perret, A. Schopper, M. Soldatov, V. Yakimchuk, *LHCb calorimeter high voltage system*, Nuclear Instruments and Methods in Physics Research A 571, pp. 294 (2007).

[GL94] M. A. Green, S. J. St. Lorant, *Estimating the Cost of Large Superconducting Thin Solenoid Magnets*, Advances in Cryogenic Engineering Vol. 39, pp. 271-276 (1994).

[GL02] Gan Liping, *Development of a high precision hybrid electromagnetic calorimeter at Jlab*, American Physical Society, April Meeting, New Mexico (2002) (Bibliographic Code: 2002APS..APRE13003G)

[GM64] M. Gell-Mann, *A Schematic Model of Baryons and Mesons*, Physics Letters, vol. 8.3, pp. 214-215 (1964).

[GOS11] K. Goetzen et al., *Proposal for a Scintillator Tile Hodoscope for PANDA*, Darmstadt (2011) *https://panda-wiki.gsi.de/pub/Tof/SciTil/scitil.pdf* (accessed Nov. 2015).

[GSA08] G.S. Atoian et al., *An improved Shashlyk calorimeter*, Nuclear Instruments and Methods in Physics Research A 584 (2008).

[GSI14] Helmholtzzentrum für Schwerionenforschung GmbH Darmstadt, *www.gsi.de /start/fair/aufbau_der_fair_beschleunigeranlage.htm* (2014).

[GT13] G. Tambave, *Electromagnetic Calorimeter Studies for Charmonium Physics*, PhD thesis, Rijksuniversiteit Groningen (2013), *https://panda.gsi.de/oldwww /db/thesesDB/GT14-130510_ganesh_thesis_5-April_2013.pdf*

[H197] H1 SpaCal Group, *The H1 Lead/Scintillating-Fibre Calorimeter*, DESY Red Report 96-171, published in Nucl. Instr. and Meth. A 386, pp. 397-408 (1997).

[HDG14] M. Hoek, R. Dzhygadlo, A. Gerhardt et al., *The PANDA Barrel DIRC detector*, Nuclear Instruments and Methods in Physics Research Section A 766, pp. 9-13 (2014) ISSN 0168-9002, http://dx.doi.org/10.1016/j.nima.2014.04.006

[HHG06] H. H. Gutbrod (Edt.), *FAIR Baseline Technical Report*, Facility for Antiproton and Ion Research, ISBN: 3-9811298-0-6 (2006).

[HK85] H. Koch et al., *Proposal: meson spectroscopy at LEAR with a 4 π neutral and charged detector*, Technical Report CERN-PSCC-85-56. PSCC-P-90, Geneva (1985).

[HLL05] M. Huhtinen, P. Lecompte, D. Luckey, F. Nessi-Tedaldi, F. Pauss, *High-energy proton induced damage in Lead Tungstate calorimeter crystals*, Nucl. Instr. and Meth. A 545, 63-87 (2005).

[HLV12] Chris Hagmann, David Lange, Jerome Verbeke, Doug Wright, *Cosmic-ray Shower Library (CRY)*, Lawrence Livermore National Laboratory, UCRL-TM-229453, *http://nuclear.llnl.gov/simulation/* (2012).

[HLW12] Chris Hagmann, David Lange, Doug Wright, *Monte Carlo Simulation of Proton-induced Cosmic-ray Cascades in the Atmosphere*, Lawrence Livermore National Laboratory, UCRL-TM-229452, *http://nuclear.llnl.gov/simulation/* (2012).

[HP15] Hamamatsu Photonics, *Handbook on Si APD and MPPC*, chapter 3, p. 5, *https://www.hamamatsu.com/resources/pdf/ssd/e03_handbook_si_apd_mppc.pdf* (Nov. 2015).

[Ham00] Hamamatsu, *Tentative Data, Photomultiplier Tube R7899/ R7899-01* (2000).

[Ham15] Hamamatsu, *Data sheets of the delivered Hamamatsu R2059 and R329-EGP PMTs* (2015).

[IKP15] Institut für Kernphysik Mainz, *Mainzer Mikrotron-Bildergalerie http://www.kph.uni-mainz.de/Bildergalerie/mami_06.jpg* (accessed Nov. 2015).

[IM09] Irina Machikhiliyan for the LHCb calorimeter group, *The LHCb electromagnetic calorimeter*, Journal of Physics: Conference Series 160, 012047 (2009) doi: 10.1088/1742-6596/160/1/012047

[IVV04] Ivo van Vulpen, *Pulse (Energy) and Position Reconstruction in the CMS ECAL*, talk at CALOR 2004, Perugia (Italy), *http://www.nikhef.nl/∼ivov/Talks/Calor2004.pdf* (2004).

[JA08] J. R. M. Annand (editor), *The Glasgow/Mainz Bremsstrahlung Tagger Operations Manual*, University of Glasgow (2008) *http://wwwa2.kph.uni-mainz.de/images/internal/detectors%20and%20setup/Tagger/TaggerManual.10.08_opt.pdf*

[JC32] J. Chadwick, *Possible Existence of a Neutron*, Nature 192, pp. 312 (1932).

[JKA13] J. K. Ahn et al. (E373 (KEK-PS) collaboration), *Double-hypernuclei observed in a hybrid emulsion experiment*, Phys. Rev. C 88, 014003 (2013).

[JM08] Martik Janecek, Wiliam M. Moses, *Optical Reflectance Measurements for Commonly Used Reflectors*, IEEE Transactions on Nuclear Science, vol. 54, iss. 4, pp. 2432-2437, doi: 10.1109/TNS.2008.2001408 (2008).

[JR01] J. Reinnarth, *Evidence for an exotic partial wave in $\pi\eta$'*, Nucl. Phys. A 692, p. 268c (2001).

[JS09] Jan Schulze, *Prototypenentwicklung für das elektromagnetische Kalorimeter des PANDA-Experimentes*, diploma thesis, Ruhr-University Bochum (2009).

[JS14] Jerzy Smyrski, official PANDA homepage, *https://panda.gsi.de/oldwww/framework/det_iframe.php?section=Forward* (accessed Nov. 2015).

[JT00] Jerry Twomey, *Noise Reduction Is Crucial To Mixed-Signal ASIC Design Success*, *http://electronicdesign.com/analog/noise-reduction-crucial-mixed-signal-asic-design-success* (published Oct. 2000, accessed Nov. 2015).

[JVJ55] J. V. Jelle, *Cerenkov Radiation and Its Applications*, British Journal of Applied Physics 6, pp. 277 (1955).

[KBD11] M. Kavatsyuk, D. Bremer, V. Dormenev, P. Drexler, T. Eissner, W. Erni, E. Guliyev, T. Hennino, B. Krusche, B. Lewandowski, H. Löhner, M. Moritz, R. W. Novotny, K. Peters, J. Pouthas, P. Rosier, M. Steinacher, G. Tambave, A. Wilms, on behalf of the PANDA Collaboration, *Performance of the prototype of the electromagnetic calorimeter for PANDA*, Nucl. Instr. and Meth. in Phys. Res. A 648, pp. 77 (2011).

[KHK11] M. Kavatsyuk, M. Hevinga, I. Konorov, P. J. J. Lemmens, P. Marciniewski, P. Schakel, F. Schreuder, R. Speelman, G. Tambave, T. Johansson, H. Loehner, *Trigger-less readout electronics for the PANDA Electromagnetic Calorimeter*, Proceedings of IEEE Nuclear Science Symposium and Medical Imaging Conference, Valencia 2011, pp. 43-47, doi: 10.1109/NSSMIC.2011.6154360

[KOP15] The KOPIO collaboration at BNL, *http://hep.lancs.ac.uk/ athans/resinterests/KOPIO.html* (accessed Nov. 2015).

[KRS14] M. Kube, M. Rossbach, C. Schmidt, U. Thoma, G. Urff, *Summary of VPTT activities*, talk, EMC Session at Panda Collaboration meeting XLIX (June 2014).

[KSM09] Yu. V. Kharlov, P. A. Semenov, Yu. A. Matulenko et al., *Performance of a fine-sampling electromagnetic calorimeter prototype in the energy range from 1 to 19 GeV*, Nucl. Instrum. and Meth. A 606:3, pp. 432 (2009), arXiv:0809.3671v1 [physics.ins-det]

[KUR15] Kuraray Co., Ltd., Plastic Scintillating Fibers, Plastic imaging fibers, *web page: http://kurarayps f.jp/psf/ws.html* (accessed Nov. 2015).

[LB86] L. M. Brown, *Hideki Yukawa and the meson theory*, Physics Today 1200, p. 55 (1986).

[LD94] L. Dobrzynski, *Shashlik calorimeter Response to high energy electrons*, Nuclear Instruments and Methods in Physics Research A, 344 (1994).

[LGR13] S. Lange, M. Galuska, S. Reiter, E. Prencipe, S. Spataro, *New Studies of XYZ States at PANDA*, proceedings of the 6th International Workshop on Charm Physics (CHARM 2013), arXiv:1311.7597

[LHCb14-1] LHCb collaboration, *Observation of overlapping spin-1 and spin-3* $\bar{D}^0 K^-$ *resonance at mass 2.86* GeV/c^2, Phys. Rev. Lett. 113, 162001 (2014), arXiv:1407.7574

[LHCb14-2] LHCb collaboration, *Dalitz plot analysis of* $B_s^0 \to \bar{D}^0 K^- \pi^+$ *decays*, Phys. Rev. D 90, 072003 (2014), arXiv:1407.7712

[LL85] E. Longo, L. Luminari, *Fast electromagnetic shower simulation*, Nucl. Instr. and Meth. 239, iss. 3, pp. 506-512 (1985).

[LM96] A. Levin, C. Moisan, *A More Physical Approach to Model the Surface Treatment of Scintillation Counters and its Implementation in DETECT*, Conference Record IEEE Nuclear Science Symposium, Anaheim (USA) (1996).

[LMP13] M. Lucchini, T. Medvedeva, K. Pauwels, C. Tully, A. Heering, C. Dujardin, K. Lebbou, P. Lecoq, E. Auffray, *Test beam results with LuAG fibers for next-generation calorimeters*, JINST 8 P10017 (2013), doi: 10.1088/1748-0221/8/10/P10017

[LR09] C. Leroy, P. G. Rancoita, *Principles of radiation interaction in matter and detection*, 2nd edition, World Scientific, Singapore (2009).

[LS75] Egidio Longo, Ignazio Sestili, *Monte Carlo calculation of photon-initiated electromagnetic showers in lead glass*, Nucl. Instr. and Meth. 128, iss. 2, pp. 283-307 (1975).

[MA99] E835 Collaboration (M. Ambrogiani et al.), *Measurements of the magnetic form-factor of the proton in the time like region at large momentum transfer*, Phys. Rev. D 60, 032002 (1999), doi: 10.1103/PhysRevD.60.032002

[MDG14] O. Merle, R. Dzhygadlo, A. Gerhardt et al., *Development of an Endcap DIRC for PANDA*, Nuclear Instruments and Methods in Physics Research Section A: 766, pp. 96-100 (2014), doi: 10.1016/j.nima.2014.04.016

[MK14] M. Kavatsyuk, *Overview of the EMC Readout*, talk at the PANDA EMC - workshop in Rauischholzhausen (Dec. 2014), *https://indico.gsi.de/getFile.py/access?contribId=8&resId=0&materialId=slides &confId=3516* (accessed Nov. 2015).

[MK15] Myroslav Kavatsyuk, KVI Groningen, private communication (2015).

[MKA08] J. C. McGeorge, J. D. Kellie, J. R. M. Annand et al., *Upgrade of the Glasgow photon tagging spectrometer for Mainz MAMI-C*, The European Physical Journal A 37:1, pp. 129-137, arXiv:0711.3443v3 [nucl-ex] (2008).

[MKJ00] M. K. Jones et al., G_{E_p}/G_{M_p} *Ratio by Polarization Transfer in e p* $\rightarrow$ *e p*, Phys. Rev. Lett. 84, 1398 (2000).

[MM13] Markus Moritz, *Measurements and improvements of the response of the PANDA-EMC prototype PROTO60 to high energetic particles and photons in accelerator experiments*, PhD thesis, University Giessen (2013), *http://geb.uni-giessen.de/geb/volltexte/2013/10105/pdf/MoritzMarkus-2013-09-24.pdf*

[MMa09] María Marteinsdóttir, *Light Yield Nonuniformity in PWO Scintillators*, Master thesis, Stockholm University (2009).

[MRR95] G. Musiol, J. Ranft, R. Reif und D. Seliger, *Kern- und Elementarteilchenphysik*, 2. Auflage, Verlag Harri Deutsch, Frankfurt am Main (1995).

[MS05] D. Motta, S. Schönert, *Optical properties of bialkali photocathodes*, Nucl. Instr. and Meth. in Phys. Res. A 539, pp. 217 (2005).

[MU09] Marc Unverzagt, for the Crystal Ball at MAMI Collaboration, *eta and eta-prime Physics at MAMI*, Nucl. Phys. Proc. Suppl. 198, 174 (2010) doi: 10.1016/j.nuclphysbps.2009.12.034

[NDD08] R. W. Novotny, W. Döring, V. Dormenev, P. Drexler, W. Erni, M. Rost, M. Steinacher, M. Thiel, A. Thomas, *Performance of PWO-II Prototype Arrays for the EMC of PANDA*, IEEE Transactions on Nuclear Science 55(3), pp. 1295-1298 (2008).

[OLu11] Olle Lundberg, *Measures to Improve the Light Yield Uniformity of Tapered PWO Crystals*, master thesis, Stockholm University (2011).

[OP47] G. P. S. Occhialini and C. F. Powell, *Nuclear Disintegrations Produced by Slow Charged Particles of Small Mass*, Nature 159, pp. 186-190 (1947).

[PA07] P. Adzic et al., *Energy resolution of the barrel of the CMS Electromagnetic Calorimeter*, Journal of Instrumentation 2, P04004, (2007), doi: 10.1088/1748-0221/2/04/P04004

[PAN14] PANDA collaboration, *https://panda.gsi.de/oldwww/framework/detector.php* (official web page - Nov. 2015).

[PANp14] PANDA collaboration, *https://panda.gsi.de/oldwww/framework/content/physics/phys_nucstruc.php* (official web page - Nov. 2015).

[PB12] P. Bühler on behalf of the PANDA collaboration, *Studying hadrons in matter with PANDA*, EXA 2011 Springer Netherlands, 105-110 (2012) doi: 10.1007/978-94-007-4890-3_17

[PBS11] Josef Pochodzalla, Alexander Botvina, Alicia Sanchez Lorente, *Studies of Hyperons and Antihyperons in Nuclei*, Proceedings of Science XLVIII International Winter Meeting on Nuclear Physics in Memoriam of Ileana Iori (2010), arXiv:1101.3181 and http://pos.sissa.it/archive/conferences/103/033/BORMIO2010_033.pdf

[PDG14] K. A. Olive et al. (Particle Data Group), *Particle Physics Booklet*, Chin. Phys. C 38, 090001 (2014) *http://pdg.lbl.gov*

[PDGbb12] J. Beringer et al., *PDG: chapter 32 - PASSAGE OF PARTICLES THROUGH MATTER*, Physical Review D 86, 010001 (2012) (http://pdg.lbl.gov)

[PDGbb14] K. A. Olive et al., *PDG: chapter 32 - PASSAGE OF PARTICLES THROUGH MATTER*, Chin. Phys. C38, 090001 (2014) (http://pdg.lbl.gov)

[PDGdet14] K. A. Olive et al., Particle Data Group, *Review: PARTICLE DETECTORS AT ACCELERATORS*, Chin. Phys. C38, 090001 (2014) (http://pdg.lbl.gov/2014/reviews/rpp2014-rev-particle-detectors-accel.pdf)

[PM14] Pawel Marciniewaki, Uppsala University, private communication (2014).

[PPR09] PANDA collaboration, *Physics Performance Report for: PANDA*, Darmstadt (2009), arXiv:0903.3905

[PW12] Peter Wieczorek, *Preliminary Results of the APFEL 1.4 Measurements*, talk, PANDA collaboration meeting, Paris (September 2012), *https://indico.gsi.de/getFile.py/access?contribId=4&resId=0&materialId=slides &confId=1871* (accessed Nov. 2015).

[RFR06] L. Rossi, P. Fischer, T. Rohe, N. Wermes, *Pixel Detectors: From Fundamentals to Applications*, Springer Verlag (2006) ISBN: 3-540-28332-3

[RKB98] R. K. Bock, *Energy Resolution in Calorimeters*, CERN web page, *http://rd11.web.cern.ch/RD11/rkb/PH14pp/node63.html* (1998).

[RM11] R. Maier for the HESR Consortium, *The High-Energy Storage Ring (HESR)*, Proceedings of 2011 Particle Accelerator Conference, New York, NY, USA (2011).

[RM12] Ryan Mitchell, *Charmonium Spectroscopy and the Role of BESIII*, MIAMI 2012 conference talk, Fort Lauderdale, Florida (2012), *https://cgc.physics.miami.edu/Miami2012/Mitchell.pdf*

[RYZ12] Ren-Yuan Zhu, *LYSO Crystal Based Shashlik Calorimeter Cell Design*, talk given at CMS forward calorimetry task-force meeting (2012), *http://www.hep.caltech.edu/žhu/talks/ryz_120830_shashlic.pdf* (accessed Nov. 2015).

[RYZ13] Ren-Yuan Zhu, *The Next Generation of Crystal Detectors*, white paper for DOF Snowman study 2013, arXiv:1308.4937 [physics.ins-det] and http://www.slac.stanford.edu/econf/C1307292/docs/submittedArxivFiles/1308.4937.pdf (accessed Nov. 2015).

[SB14] S. Belostotski, Petersburg Nuclear Physics Institute, *Status of ETOF detectors*, talk at the PANDA collaboration meeting (March 2014), *https://indico.gsi.de/getFile.py/access?contribId=28&sessionId=13&resId=0 &materialId=slides&confId=2363* (accessed Nov. 2015).

[SD12] Stefan Diehl, *Response of a Shashlyk Calorimeter to High Energetic Photons in the Energy Range from 100 MeV up to 770 MeV*, Masterthesis, JLU Gießen (2012).

[SGK08] Savely G. Karshenboim, *Precision Physics of Simple Atoms and Molecules*, Springer: Lecture Notes in Physics, vol. 745 (2008).

[SGr08] Sophie Grape, *PWO Crystal Measurements and Simulation Studies of $\bar{\Lambda}$ Hyperon Polarisation for PANDA*, PhD thesis, Uppsala University (2008).

[SMB10] M. Sudol, M. C. Mora Espi, E. Becheva, J. Boucher, T. Hennino, R. Kunne, D. Marchand, S. Ong, B. Ramstein, J. Van de Wiele, T. Zerguerras, F. Maas, B. Kopf, M. Pelizaeus, M. Steinke, J. Zhong, E. Tomasi-Gustafsson, *Feasibility studies of the time-like proton electromagnetic form factor measurements with PANDA at FAIR*, Eur. Phys. J. A44: 373-384 (2010), doi: 10.1140/epja/i2010-10960-8

[SRA09] V. Semkova, P. Reimer, T. Altzitzoglou, A. J. M. Plompen, C. Quétel, S. Sudár, J. Vogl, A. J. Koning, S. M. Qaim, D. L. Smith, *Neutron activation cross sections on lead isotopes*, Physical Review C 80, 024610 (2009).

[ST99] S. Teige, *Corrections to the Radϕ mass scale*, Radiative Phi Decay experiment notes, JLAB, *userweb.jlab.org/∼radphi/notes/1999-1201.ps.gz* (1999).

[STT07] K. Saitoa, K. Tsushimab, A.W. Thomasc, *Nucleon and hadron structure changes in the nuclear medium and the impact on observables*, Prog. Part. Nucl. Phys. 58, 1 (2007).

[TAA93] E760 Collaboration (T.A. Armstrong et al.), *Measurement of the proton electromagnetic form-factors in the timelike region at 8.9 GeV^2 - 13 GeV^2*, Phys. Rev. Lett. 70, 1212-1215 (1993), doi: 10.1103/PhysRevLett.70.1212

[TAS14] Toshi-Aki Shibata, for the HERMES collaboration, *Ring imaging Cherenkov counter of HERMES for pion, kaon, proton and anti-proton identification*, Nuclear Instruments and Methods in Physics Research Section A 766:1, 267-269 (2014).

[TCA92] T. C. Awes et al., *A simple method of shower localization and identication in laterally segmented calorimeters*, Nuclear Instruments and Methods in Physics Research Section A: Accelerators, Spectrometers, Detectors and Associated Equipment, 311 (1992).

[TDe09] PANDA collaboration, *Technical Design Report for: PANDA Electromagnetic Calorimeter (EMC)*, Darmstadt (2009), arXiv:0810.1216 [physics.ins-det]

[TDf15] PANDA collaboration, *Technical Design Report for: Forward Spectrometer Calorimeter (FSC)*, (collaboration internal preliminary version), Darmstadt (2015).

[TDg12] PANDA GEM-TPC collaboration (Editors: B. Ketzer, L. Fabbietti), *Technical Design Study for the PANDA Time Projection Chamber*, Darmstadt (2012), arXiv:1207.0013 [physics.ins-det]

[TDl15] PANDA collaboration, *Technical Design Report for the PANDA Luminosity Detector*, (preliminary version), Darmstadt (2015), *http://www.staff.uni-mainz.de/jasinsk/temp/lmd_tdr.pdf*

[TDm11] PANDA collaboration, *Technical Design Report for the: PANDA Micro Vertex Detector*, Darmstadt (2011), arXiv:1207.6581 [physics.ins-det]

[TDma09] PANDA collaboration, *Technical Design Report for the PANDA Solenoid and Dipole Spectrometer Magnets*, Darmstadt (2009), arXiv:0907.0169 [physics.ins-det]

[TDta12] PANDA collaboration, *Technical Design Report for the PANDA Internal Targets: The Cluster-Jet Target and Developments for the Pellet Target*, Darmstadt (2012).

[TDtr12] PANDA collaboration, *Technical Design Report for the: PANDA Straw Tube Tracker*, Darmstadt (2012), arXiv:1205.5441 [physics.ins-det]

[TE13] Tobias Eissner, *The new PWO Crystal Generation and Concepts for the Performance Optimisation of the PANDA EMC*, PhD thesis, University Giessen (2013), *http://geb.uni-giessen.de/geb/volltexte/2013/10382/pdf/EissnerTobias_2013_11_18.pdf*

[TGP12] O. A. Tarasenco, N. Z. Galunov, V. D. Panikarskaya, E. V. Sanin, V. A. Tarasov, V. L. Volkov, *Luminescence energy yields of organic solid materials excited by photons of light or gamma-radiation*, Functional Materials 19:3, pp. 404 (2012).

[TH15] Tanja Horn, *A $PbWO_4$-based Neutral Particle Spectrometer in Hall C at 12 GeV JLab*, Journal of Physics: Conference Series 587, 012048 (2015), doi: 10.1088/1742-6596/587/1/012048

[TPR05] PANDA collaboration, *Technical Progress Report for: PANDA*, Darmstadt (2005), *https://panda.gsi.de/oldwww/archive/public/panda_tpr.pdf*

[UW11] Ulrich Wiedner, *Future Prospects for Hadron Physics at PANDA*, Prog. Part. Nucl. Phys. 66, pp. 477-518 (2011), arXiv:1104.3961

[VD11] Valera Dormenev, Till Kuske, Rainer W. Novotny, A. Borisevich, A. A. Fedorov, Mikhail Korzhik, Vitaly Mechinsky, O. Missevitch, S. Lugert, *Stimulated recovery of the optical transmission of $PbWO_4$ scintillation crystals for electromagnetic calorimeters after radiation damage*, Nucl. Instr. and Meth. in Phys. Res. A, 623(3), pp. 1082-1085 (2011) doi: 10.1016/j.nima.2010.08.092

[VD15] Valera Dormenev, JLU Giessen, *private communication* (2015).

[VFS92] Varley F. Sears, *Neutron scattering lengths and cross sections*, Neutron News, vol. 3, no. 3 , pp. 29-37 (1992) doi: 10.1080/10448639208218770.

[VM10] V. Metag, *The search for in-medium modifications of mesons-experimental status*, AIP Conf. Proc. 1322, pp. 73 (2010), http://dx.doi.org/10.1063/1.3542034

[VM13] V. Mochalov, on behalf of the $\bar{P}$ANDA collaboration, *Physics with antiprotons at $\bar{P}ANDA$*, Nuclear Physics B Proceedings Supplement 245, pp. 124-131 (2013), ISSN 0920-5632, doi: 10.1016/j.nuclphysbps.2013.10.023

[VP06] V. Polyakov, *Shashlik calorimeter in COMPASS*, talk at the PANDA collaboration meeting (2006), see also V. Polyakov, *Radiation hard Shashlik calorimeter for COMPASS experiment*, 21.10.2010, *http://hallaweb.jlab.org/12GeV/SoLID/download/ec/Shashlyk/shashlik_NA62_2010_mod.ppt* (accessed Nov. 2015).

[VR09] Valery Rodionov, *PANDA Muon System (Range System)*, ITEP (Russia), talk (2009), *http://www.itep.ru/rus/FRRC/present/Rodionov.pdf* (accessed Nov. 2015).

[WRL94] W. R. Leo, *Techniques for Nuclear and Particle Physics Experiments*, Springer-Verlag New York Inc., edition: 2nd Rev (1994), ISBN-13: 978-0387572802

Acknowledgements

First of all I want to thank Prof. Dr. Kai-Thomas Brinkmann and Dr. Rainer Novotny who enabled my work in the PANDA collaboration and who ever supported me during my time at the 2nd physics institute. I especially want to thank them for the possibility to take on responsibility for different projects also beyond the work presented in this thesis. I really enjoyed the nice and efficient working atmosphere in our group. Special thanks also to my present and former colleagues from the EMC group Peter, Valera, Hans, Christoph, Till, Tobias, Daniel, Markus, Svetlana and Benny for the good and harmonic cooperation during the complete time. I also want to thank the colleagues from the MVD and CB-ELSA/TAPS groups, Robert, Andreas, Tommaso, Matrin, Erik, Marianna, Volker and Stefan for the pleasant atmosphere in the complete group and the good cooperation. For the thorough reading of the thesis I especially want to thank Rainer and Stefan. Special thanks also to Anita who ever had the overview over all bureaucracy issues and to Rene, Ulli, Marcel and Thomas for the technical support as well as the people from the machine shop who ever provided mechanical parts of the experimental setups in an excellent quality. I also want to thank Dr. Etiennette Auffray from CERN who enabled the de-polishing of the test crystals. Last but not least I want to thank my family, especially my mother who ever supported me during my time as a student and during my PhD thesis.

Erklärung der Urheberschaft

Ich erkläre: Ich habe die vorgelegte Dissertation selbstständig und ohne unerlaubte fremde Hilfe und nur mit den Hilfen angefrtigt, die ich in der Dissertation angegeben habe.
Alle Textstellen, die wörtlich oder sinngemäß aus veröffentlichen Schriften entnommen sind, und alle Angaben, die auf mündlichen Auskünften beruhen, sind als solche kenntlich gemacht.
Bei den von mir durchgeführten und in der Dissertation erwähnten Untersuchungen habe ich die Grundsätze guter wissenschaftlicher Praxis, wie sie in der "Satzung der Justus-Liebig-Universität Gießen zur Sicherung guter wissenschaftlicher Praxis" niedergelgt sind, eingehalten.

Stefan Diehl

Giessen, im Dezember 2015